IGSHPA

IGSHPA SWEDEN

Research Conference Proceedings

International Ground Source Heat Pump Association
Research Conference
September 18-19, 2018

Editors:
Jeffrey Spitler, José Acuña, Michel Bernier, Zhaohong Fang, Signhild Gehlin, Saqib Javed, Björn Palm, Simon J. Rees

IGSHPA SWEDEN

2018 Research Conference

IGSHPA Research Conference

September 18-19, 2018

KTH Royal Institute of Technology
Stockholm, Sweden

International Scientific Committee:

I.W. Johnston, U. Melbourne, Australia
G.A. Narsilio, U. Melbourne, Australia
L. Helsen, KU Leuven, Belgium
M. Cimmino, Polytechnique Montréal, Canada
P. Eslami-nejad, CANMET Energy, Canada
P. Pasquier, Polytechnique Montréal, Canada
J. Raymond, INRS, Canada
P. Cui, Shandong Jianzhu University, China
G. Zhang, Hunan University, China
M. Philippe, BRGM, France
D. Bauer, German Aerospace Center, Germany
H. Yang, HKPU, Hong Kong
M. Fossa, University of Genoa, Italy
K. Midttømme, CMR, Norway
R. K. Ramstad, NTNU, Norway
J. Corberán, UPV, Spain
C. Montagud, UPV, Spain
J. Claesson, Lund University, Sweden
G. Hellström, NeoEnergy, Sweden
H. Madani, KTH, Sweden
B. Olofsson, KTH, Sweden
H. Witte, GroenHolland, The Netherlands
H.Ö. Paksoy, Cukurova University, Turkey
R. Curtis, GeoScience, UK
C. Underwood, U. Northumbria, UK
R. Beier, Oklahoma State University, USA
A. Chiasson, University of Dayton, USA
X. Liu, Oak Ridge National Laboratory, USA

Executive Scientific Committee:

Jeffrey Spitler, Oklahoma State University, USA - Chair
Michel Bernier, Polytechnique Montréal, Canada
Zhaohong Fang, Shandong Jianzhu University, China
Simon J. Rees, University of Leeds, UK
Björn Palm, Kungliga Tekniska Högskolan, Sweden
José Acuña, Kungliga Teknikska Högskolan, Sweden
Signhild Gehlin, Svenskt Geoenergicentrum AB, Sweden
Saqib Javed, Chalmers Tekniska Högskola, Sweden

Conference Organizing Committee:

Per Lundqvist, Kungliga Tekniska Högskolan, Sweden - Chair
José Acuña, Kungliga Teknikska Högskolan, Sweden
Dominika Rydel, Sveriges Avanti Borrare Förening, Sweden

Proceedings Book Designed by:

Peyton Haley
IGSHPA Publications Intern

DOI : 10.22488/okstate.18.000001

IGSHPA®

International Ground Source Heat Pump Association

1201 S. Innovation Way Drive, Suite 400
Stillwater, OK 74074
405-744-5175 or 800-626-4747
Fax- 405-744-5283

Foreword

José Acuña
KTH Royal Institute of Technology

During the IGSHPA Conference in Denver, I volunteered to host a second research conference in Sweden in order to give continuity to the fantastic idea of IGSHPA Research Conferences. I received support and interest from many researchers, some IGSHPA board members as well as people from the research and international chapters committee. Since then, it has been a long story and an enriching experience to materialize this event. I am happy it became true!

It has been a pleasure to co-organize the event with Energiforsk, Christian Michelsen Research and the Avanti Drillers Association. The IGSHPA Research Conference is organized this year in connection to the Swedish drillers day and the first common workshop between two new research programs: Termiska Energilager and ROCKSTORE, financed by the Swedish Energy Agency and Norway's Research Council, respectively.

KTH and IGSHPA Sweden are honored to host this meeting, an event with a glimpse back in time as well as insights into the future of ground source heat pumps and borehole thermal energy storage. Almost three generations of GSHP researchers and energy industry representatives from all over the world are now meeting here in Sweden, a country where many of the first seeds for ground source heat pump research were planted about four decades ago. We are here, in Stockholm, one of the borehole heat exchanger densest cities in the world.

This event is a fantastic forum to network and discuss research, innovation and the future of our technology. I would like to believe that IGSHPA research conferences are here to stay for many years to come, helping IGSHPA to grow maturely into international levels at the same time as ground source heat pumps get larger market penetration worldwide.

For supporting this initiative, I would like to thank Prof. Björn Palm, Prof. Per Lundqvist, Erin Portman, Roshan Revankar, Dominika Rydel, John Turley, Ed Kirtley, Garen Ewbank, Michael Albertson, Martin Forsén, all researchers and friends of the industry who manifested interest for the event, and Prof. Jeffrey Spitler for leading and coordinating the review process.

I would also like to acknowledge the conference sponsors: SENS, Swedish Avant-Drillers Association, NIBE, MUOVITECH, THERMIA and BENGT DAHLGREN.

Last but not least, a big thank to the big protagonist of this event, all paper authors and conference participants, for contributing to a nice and interesting conference content.

Welcome to KTH, Welcome to Stockholm, Welcome to Sweden!

José Acuña

Preface

Dr. Jeffrey D. Spitler
Oklahoma State University
Executive Scientific Committee Chairman

This conference organized by IGSHPA Sweden follows on the success of the first "research track" at the 30th annual IGSHPA conference held in Denver in March 2017. This was the first IGSHPA meeting in 30 years to have peer-reviewed scientific papers. It was successful enough that IGSHPA Sweden proposed hosting a research conference; this was approved by the IGSHPA Board in June of 2017.

The organization started with formation of an expanded Executive Scientific Committee. (I'm very glad all the original members agreed to serve for another conference!) We were joined this time by three members from the host country: Saqib Javed, José Acuña, and Björn Palm. Together, we adjusted the list of topics in the call for papers to include the following:

- Design of GHEs
- Performance of alternative GHE designs
- Modeling and simulation of GHE
- Validation of GHE and GSHP models
- Thermal response tests measuring ground thermal properties
- Optimal control, operation and fault detection of GSHP systems
- Modeling and simulation of GSHPs and GSHP systems
- Design and performance of GSHPs and GSHP components
- Measured performance of GSHP systems
- New system configurations and supporting models
- Materials and working fluids used in ground heat exchangers
- Borehole and aquifer thermal energy storage
- Open loop GSHP systems, e.g. standing column wells
- Surface water heat exchangers and heat pump systems
- Oft-neglected phenomena (e.g. moisture transport, groundwater flow, freezing/thawing)
- Environmental aspects of GSHP systems
- History of GSHPs and GSHP technology
- Design of ground heat exchangers
- Performance of alternative GHE designs.
- Modeling and simulation of ground heat exchangers
- Validation of GHE and GSHP system models.
- Thermal response tests for measurement of ground thermal properties
- Optimal control and operation of ground heat exchangers and GSHP systems.
- Modeling and simulation of GSHPs and GSHP systems.
- Measured performance of GSHP systems.
- New system configurations and supporting models.
- Oft-neglected phenomena (moisture transport, freezing/thawing, near-surface effects)

A total of 76 abstracts were submitted, leading to 53 papers submitted, which after the review process finally came to 48 papers scheduled to be presented here in Stockholm. The 48 papers come from 13 different countries on four continents. The review process for each paper was managed by one of the Executive Scientific Committee members and each paper was reviewed by at least two peer reviewers drawn from the International Scientific Committee and other experts. Most of the papers went through two rounds of reviews before being accepted. A big thank you goes out to all the authors, committee members and reviewers!

To help insure that the papers remain widely available, they will be available from both the IGSHPA website and SHAREOK, which is the joint institutional repository for the University of Oklahoma Libraries and Oklahoma State University Libraries. All papers have received digital object identifiers (DOI); these appear on each paper and give a persistent and permanent link to the paper.

I wish everyone a fruitful and productive conference!

Dr. Jeffrey D. Spitler

Table of Contents

IGSHPA SWEDEN
2018 Research Conference

IGSHPA SWEDEN
2018 Research Conference

DOI: 10.22488/okstate.18.000018

Thermal Analysis Models of Deep Borehole Heat Exchangers

Liang Fang, Nairen Diao, Zhukun Shao, Ping Cui, Ke Zhu, and Zhaohong Fang

ABSTRACT

With the advantages of much less land demand and higher temperature available, the deep borehole heat exchanger (DBHE) gets down to a depth of 1000-3000 m below the ground surface, and provides a new variance of ground-coupled heat pump systems especially for applications in cold-climate regions. Coaxial tubes, instead of U-tubes, are usually used in DBHEs. Two models are presented for DBHE thermal analysis in this paper. One follows the traditional approach based on analytical solutions and the concept of the effective borehole thermal resistance for the boreholes with coaxial tubes. The other is a numerical simulation scheme based on the FDM which takes the geothermal gradient into account. The latter features much higher efficiency in computation than most commercially-available software toolkits based on FEM. The performance of DBHEs is then assessed with parameter analyses.

INTRODUCTION

The ground-coupled heat pump (GCHP) technologies have great appeal in offering higher levels of efficiency than traditional HVAC technologies. However, penetration of the GCHP technology into the market has been hindered by its limitations such as higher capital cost, requirement of a certain land plot for installation of the ground loop and concerns over the possible heat or cold accumulation in the ground heat exchangers. The vertical Borehole Heat Exchangers (BHEs) are recognized as the most-widely-used ground heat exchanger for the GCHP system (Rees 2016). A typical borehole is normally drilled down to 40-150 m deep; a single or double U-tube is then inserted in the borehole. This traditional configuration is referred to as the shallow boreholes. The concept of Deep Borehole Heat Exchanger (DBHE) has aroused growing interests from both academic and engineering arenas in China recently. The DBHEs are usually drilled down to depths of 1000-3000 m at present. Rather than the single or double U-tube configurations commonly used in shallow GCHPs, coaxial tubes are used for DBHEs out of construction considerations. As heat carrier fluid, water flows either downward through the central pipe and then returns in the annular channel between the pipes, or in an opposite circulating process.

The DBHEs may go down much deeper below the ground surface; and temperatures at the borehole bottom could reach 60-90℃. Therefore, they have benn considered as a desirable alternative to the traditional shallow BHEs in GCHP systems, with advantages of much less land

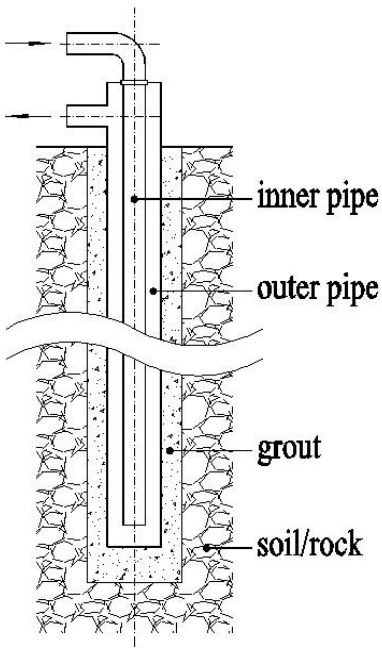

Figure 1 A diagram of a borehole with coaxial tube

Zhaohong Fang and Nairen Diao are professors, Ping Cui and Ke Zhu (zhuke@sdjzu.edu.cn) are associate professors, Liang Fang and Zhukun Shao are graduate students in Shandong Jianzhu University, China.

demand and higher efficiency of the heat pumps. The concept of DBHE has also arisen from the technical sector of the direct use of hydro-geothermal energy. The open hydrothermal system relies heavily on existence of hydrothermal reservoir in specific locations as well as feasibility of recharging the effluent geothermal water back to its original stratum to ensure sustainable exploitation. When no hydrothermal reservoir is found down to a certain depth of strata, or when recharging is not feasible technically or economically, the closed system of DBHE becomes an alternative. The DBHE may also be employed for the purpose of seasonal thermal storage owing to its favorable features of flexibility, higher temperature available and huge storage capacity in limited land plots. A borehole with a coaxial tube is schematically shown in Figure 1.

In spite of its advantages, application of the DBHE in GCHP systems has been out of consideration for its much higher initial drilling cost. However, an abundant surplus deep-drilling capacity in China, which used to serve for oil production, lowers the drilling cost substantially and makes the DBHE application possible. The DBHE is still realatively a new concept, and its technical feasibility and economic competitiveness need to be assessed before its practical applications. It is crucial to develop adequate and convenient means for thermal analysis of the DBHE. An idea is to apply the existing theories and tools of the shallow BHEs to thermal analyses of the DBHE. The two processes of shallow and deep BHEs, however, have a few fundamental distinctions. A uniform initial temperature in the ground is usually assumed in heat transfer models for the shallow boreholes in view of the limited depth of shallow BHEs and limited temperature difference in the longitudinal direction (Lamarche et al. 2010). It seems unreasonable, however, to ignore the geothermal gradient in DBHEs, which constitutes a key factor of their performance. Besides, there are few reports on study of the borehole with the coaxial tubes owing to its rare applications in the shallow BHEs. Beier et al. (2013) has studied the heat transfer in coaxial borehole without intaking into account the geothermal gradient. Numerical models based on FDM with a traditional solution algorithm have been developed by Holmberg et al. (2016) and Dijkshoorn et al. (2013) to study the coaxial BHE. In this study, we explored the DBHE heat transfer with these important features taken into account. An analytical model and a numerical model presented in our recent publications (Fang et al. 2017 and 2018) are compared here, and their respective merits and aplicabilities are disscussed.

THERMAL RESISTANCE OF BOREHOLES WITH COAXIAL TUBES

There have been numerous methods proposed for calculating the effective borehole thermal resistance (Javed and Spitler 2016), most of which deal with the U-tube boreholes. In the traditional approaches of BHE heat transfer analysis the effective borehole thermal resistance can be defined as

$$R_b = \left(T_f - T_b\right)/q_b \tag{1}$$

where T_f is the mean temperature of the fluid, i.e. the average of its inlet and outlet temperatures, and T_b is the borehole wall temperature and q_b the specific heat load. The work presented in this section is to develop an adequate model of heat transfer in coaxial tube boreholes. The traditional approach of BHE analysis on basis of the analytical solutions could be used for the coaxial tube boreholes. The advantages of such an approach are its mature framework and high computational efficiency. Nevertheless, an inherent defect remains that simplifying assumptions are necessary, such as uniform temperature distribution along the borehole wall. The distortion in the temperature responses caused by such a simplification can be assessed by models with higher fidelity such as the numerical model presented in the next section.

It is important to realize that heat transfer inside the borehole is affected by thermal short-circuit, that is, heat transfer between the upward- and downward-flowing fluids of the heat exchanger. Taking thermal short-circuit into account, Hellström (1991) derived relationships between the effective borehole thermal resistance and the local borehole thermal resistance for single U-tube boreholes. Zeng et al. (2003) have developed the methodology and studied effective borehole resistance of double U-tubes in detail. A recent study has been reported by the authors on the effective borehole resistance of coaxial tube boreholes (Fang et al. 2017). An improved version of the study is briefly presented below.

MODEL ASSUMPTIONS

Following analysis will focus on heat transfer inside the borehole with coaxial tubes. To keep the problem

analytically manageable, some simplifications are assumed as in discussions of the U-tube boreholes (Javed et al. 2016). They are as follows.

The heat capacity of the materials inside the borehole is neglected.

The heat conduction in the grout, pipes and fluid along the depth direction is neglected.

The borehole wall temperature, T_b, is uniform along its depth, but may vary with time.

The local thermal resistance between the upward- and downward-flowing fluids and that between fluid in the annular channel and borehole wall can be determined easily on basis of the traditional heat transfer principle, those are

$$\begin{cases} R_1 = \frac{1}{2\pi k_b}\ln\left(\frac{r_b}{r_{1o}}\right) + \frac{1}{2\pi r_{1i}h_1} + \frac{1}{2\pi k_{p1}}\ln\left(\frac{r_{1o}}{r_{1i}}\right) \\ R_2 = \frac{1}{2\pi r_{2i}h_2} + \frac{1}{2\pi k_{p2}}\ln\left(\frac{r_{2o}}{r_{2i}}\right) + \frac{1}{2\pi r_{2o}h_1} \end{cases} \tag{2}$$

where k_b, k_{p1} and k_{p2} are thermal conductivity of the grout and outer and inner pipes; r_b is the radius of the borehole, r_i and r_o are the inner and outer radiuses of the pipe; h_1 and h_2 are the convective heat transfer coefficients of the annular channel and inner tube, respectively. These convective heat transfer coefficients may be counted with correlation formula provided in heat transfer handbooks.

MATHEMATICAL MODEL AND SOLUTION

It is noticed that different flow configurations, i.e. fluid entering the borehole in the annular channel and returning from the inner tube or in a reverse cycle, will lead to different fluid temperature profiles in the tubes. Therefore, both the flow configurations are discussed below. Here the mass flow rate of fluid is denoted in M, and its specific heat in c.

Flow configuration of fluid entering in the annulus and returning from the inner tube. The heat conservation of fluid in the tubes leads to the following equations when the fluid flows downward in the annular channel, and when the z-axis is set downward.

$$0 \le z \le H \quad \begin{cases} -Mc\frac{dT_{f1}(z)}{dz} = \frac{T_{f1}(z)-T_{f2}(z)}{R_2} + \frac{T_{f1}(z)-T_b}{R_1} \\ Mc\frac{dT_{f2}(z)}{dz} = \frac{T_{f2}(z)-T_{f1}(z)}{R_2} \end{cases} \tag{3}$$

The boundary conditions are: $z=0 \quad T_{f1}=T_f'$; $z=H \quad T_{f1}=T_{f2}$. Here T_f' is the inlet temperature of the circulating fluid, H denotes the borehole depth. Equation (3) is a set of ordinary differential equations, and can be solved by Laplace transformation (Diao & Fang 2006). Introduce the dimensionless parameters:$\theta_1 = \left(T_{f1}(z)-T_b\right)/\left(T_f'-T_b\right)$, $\theta_2 = \left(T_{f2}(z)-T_b\right)/\left(T_f'-T_b\right)$, $R_1^* = McR_1/H$, $R_2^* = McR_2/H$, $Z=z/H$, solution of the fluid temperature distributions may be expressed in dimensionless form as

$$\begin{cases} \theta_1(Z) = exp\left(-\frac{Z}{2R_1^*}\right)\left[f_1(Z) + f_2(Z)\frac{2\beta R_1^* ch(\beta)-sh(\beta)}{2\beta R_1^* ch(\beta)+sh(\beta)}\right] \\ \theta_2(Z) = exp\left(-\frac{Z}{2R_1^*}\right)\left[-f_2(Z) + f_3(Z)\frac{2\beta R_1^* ch(\beta)-sh(\beta)}{2\beta R_1^* ch(\beta)+sh(\beta)}\right] \end{cases} \tag{4}$$

where $f_1(Z) = ch(\beta Z) - \frac{1}{\beta}\left(\frac{1}{2R_1^*}+\frac{1}{R_2^*}\right)sh(\beta Z)$, $f_2(Z) = \frac{1}{\beta R_2^*}sh(\beta Z)$, $f_3(Z) = ch(\beta Z) + \frac{1}{2\beta}\left(\frac{1}{R_1^*}+\frac{2}{R_2^*}\right)sh(\beta Z)$ and $\beta = \sqrt{\left(\frac{1}{2R_1^*}\right)^2 + \frac{1}{R_1^*R_2^*}}$. And a simple expression of the outlet temperature of the fluid is obtained as

$$\theta_f'' = \theta_2(0) = \frac{2\beta R_1^* ch(\beta)-sh(\beta)}{2\beta R_1^* ch(\beta)+sh(\beta)} \tag{5}$$

Flow configuration of fluid entering in the inner tube and returning from the annulus. When the fluid flow is arranged in the opposite direction, i.e. downwards in the inner tube, the convective terms in the equations change their signs.

$$0 \le z \le H \quad \begin{cases} Mc\frac{dT_{f1}(z)}{dz} = \frac{T_{f1}(z)-T_{f2}(z)}{R_2} + \frac{T_{f1}(z)-T_b}{R_1} \\ -Mc\frac{dT_{f2}(z)}{dz} = \frac{T_{f2}(z)-T_{f1}(z)}{R_2} \end{cases} \tag{6}$$

Accordingly, the boundary conditions become $z=0 \quad T_{f2}=T_f'$; $z=H \quad T_{f1}=T_{f2}$. With the same dimensionless parameters defined as above, the fluid temperature distributions can be obtained in the dimensionless form as

$$0 \le z \le H \quad \begin{cases} \theta_1(Z) = exp\left(\frac{Z}{2R_1^*}\right)\left[-f_2(Z) + f_3(Z)\frac{2\beta R_1^* ch(\beta) - sh(\beta)}{2\beta R_1^* ch(\beta) + sh(\beta)}\right] \\ \theta_2(Z) = exp\left(\frac{Z}{2R_1^*}\right)\left[f_1(Z) + f_2(Z)\frac{2\beta R_1^* ch(\beta) - sh(\beta)}{2\beta R_1^* ch(\beta) + sh(\beta)}\right] \end{cases} \tag{7}$$

And the outlet temperature of the fluid turns to be identical as in the other configuration, i.e.

$$\theta_f'' = \theta_1(0) = \frac{2\beta R_1^* ch(\beta) - sh(\beta)}{2\beta R_1^* ch(\beta) + sh(\beta)} \tag{8}$$

It can be seen from Equations (4) and (7) that the different flow configurations lead to different temperature profiles in the tubes, but result in the identical outlet temperature of the fluid on the condition of uniform temperature distribution along the borehole wall. This also means that the different flow configurations do not influence on the effective borehole thermal resistance and the BHE performance on the same condition.

Borehole Thermal Resistance. The effective borehole resistance of the coaxial tube boreholes can be determined according to the analytical solutions of fluid temperature profiles (Diao & Fang 2006; Fang et al. 2017), which takes the expression

$$R_b = \frac{H}{2Mc} \cdot \frac{1+\theta_f''}{1-\theta_f''} = \frac{R_1}{2}\beta cth(\beta) \tag{9}$$

NUMERICAL SOLUTION OF DBHE HEAT TRANSFER BASED ON FDM

Modeling Consideration

It is realized that the geothermal gradient in subsurface caused by the geothermal flux plays a key role in DBHE performance, and should not be ignored. This ristricts various approaches of analytical solution; and schemes with numerical solutions have been proved potent for such tasks. Different numerical models on BHE heat transfer have also been presented over the past decades. Recent studies on heat transfer in BHEs make use of commercial software packages more often, such as FLUENT (Congedo et al. 2012), FEFLLOW (Bauer et al. 2010; Welsch et al. 2016) or COMSOL (Zhao et al. 2016) and OpenGeoSys (Kong et al. 2017), which are all based on the Finite Element Method (FEM). However, the heat transfer in BHEs involves diversified spatial and temporal spans. As a result, a few hundred thousand or even millions of nodes (elements) are needed in discretization of the borehole field. The extraordinary slenderness of the DBHE aggravates the dilemma in its discretization. Therefore, innovative models and algorithms have been sought persistently for their practical exploitation for design and optimization of BHEs.

A model has been presented by the authors based on the Finite Difference Method (FDM), which incorporates the coaxial borehole with surrounding soil (Fang et al., 2018). To achieve efficient computation the model takes advantages of the specific features of the problem, these are

The subsurface surrounding the coaxial borehole can be treated as a regular domain in the cylindrical coordinates, and then the FDM can readily be used in discretizing the domain concerned.

It is appropriate and acceptable to treat the flow and convective heat transfer in the long pipes as one-dimensional. As a result, the complex simulation of transient fluid dynamics and convective heat transfer inside the pipes can be greatly simplified.

A coordinate transformation is introduced to realize the variable step sizes in the radial direction.

Large spatial step sizes in the axial direction are possible in FDM scheme owing to the relatively minor temperature gradient in this direction.

An algorithm based on the chasing method is adopted to achieve direct solution of the derived algebraic equation set for the transient two-dimensional heat transfer problem without turning to time-consuming iterations (Jia and Fang 2003).

ASSUMPTIONS AND MATHEMATICAL DESCRIPTION

This study focuses on heat transfer in a single deep borehole with coaxial tubes. Following assumptions are taken in the model.

The soil and rock surrounding the DBHE is regarded as one or a few horizontal layers of homogeneous media.

Groundwater infiltration is neglected, and pure conduction is considered as the only mechanism of heat transfer in the soil/rock.

The temperature fluctuation of the atmosphere and its influence on the top layer of the soil are ignored.

A uniform geothermal heat flux exists throughout the media.

The convective heat transport by circulating water in pipes is the dominant mechanism of heat transfer in the longitudinal direction within the borehole; conduction by grout, pipe wall and water in the borehole is neglected in this direction.

The thermal capacity of the grout, pipe wall and water in pipes is counted in the model, the temperature of grout and pipe wall, however, is assumed to be the same as the water in the same section of the pipe.

According to these assumptions the governing equations of the heat transfer in DBHE may be presented as the follows. For each layer of soil/rock, the radial symmetry is tenable, and the conduction equation takes the form

$$\frac{1}{a}\frac{\partial t}{\partial \tau}=\frac{1}{r}\frac{\partial}{\partial r}\left(r\frac{\partial t}{\partial r}\right)+\frac{\partial^2 t}{\partial z^2} \tag{10}$$

A new coordinate $\sigma = \ln(r/r_b)$ is assigned so as to achieve a variable step size in the radial direction. The conduction equation becomes in the new coordinate system

$$\frac{1}{a}\frac{\partial t}{\partial \tau}=\frac{1}{r^2}\frac{\partial^2 t}{\partial \sigma}+\frac{\partial^2 t}{\partial z^2} \tag{11}$$

A uniform step size in the σ-coordinate, $\Delta\sigma$, corresponds to a geometric progression of step sizes in the r-coordinate. That is $r_{i+1}/r_i = r_1/r_b = \exp(\Delta\sigma) = \mu$.

The governing equations for the circulating water in the outer annulus and the central pipe are expressed respectively as

$$C_1\frac{\partial t_{f1}}{\partial \tau}=\frac{t_{f2}-t_{f1}}{R_2}+\frac{t_b-t_{f1}}{R_1}-Mc_f\frac{\partial t_{f1}}{\partial z} \tag{12}$$

$$C_2\frac{\partial t_{f2}}{\partial \tau}=\frac{t_{f1}-t_{f2}}{R_2}+Mc_f\frac{\partial t_{f2}}{\partial z} \tag{13}$$

Here C_1 and C_2 denote the heat capacity per length of flow channels (J/(m·K)), including water, pipe wall and grout, and can be referred to in reference (Fang et al. 2018). The local thermal resistance between the water in the annular channel and borehole wall, R_1, and that between the two streams of circulating water, R_2, can be determined with Equation (2) as in the discussion of analytical model. It should be noticed that the signs of the convective terms in Equations (12) correspond to the flow configuration of water flowing downwards through the outer annulus and returning in the inner pipe. In the case of reversed circulation the signs in front of the convective term should be changed.

The coupling conditions of the circulating water in the inner pipe and the annulus are also needed, that is

$$t_{f1}=t_{f2},\quad z=H,\tau\geq 0 \tag{14}$$

$$t_{f2}-t_{f1}=Q/Mc_f,\quad z=0,\tau\geq 0 \tag{15}$$

The latter corresponds to the flow configuration of downward-flow in the annulus and returning in the central pipe; and a positive Q means heat extraction from the subsurface. The complete settings of the initial and boundary conditions can be found elsewhere (Fang et al. 2018).

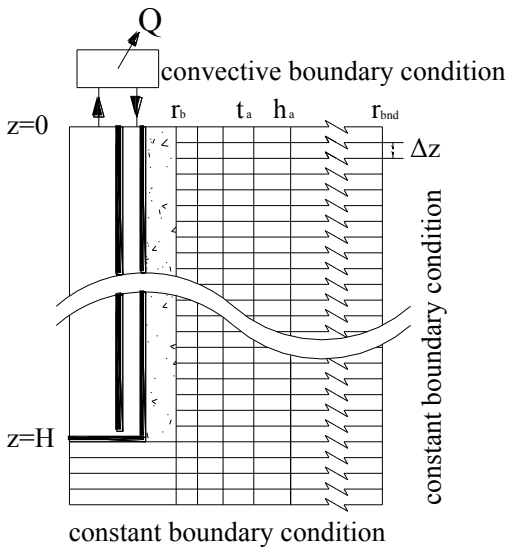

Figure 2 The discretization mesh and boundary conditions of the numerical scheme

FDM ALGORITHM

The thermal analysis of DBHEs mainly deals with a transient two-dimensional heat conduction problem in a regular cylindrical domain, coupled with some specific convective heat transfer on one of the boundaries (borehole wall). The FDM is then chosen to solve the set of governing equations presented above. The considered domain and boundary conditions are depicted in Figure 3 together with the discretization mesh. The radial and axial coordinates are not in proportion in the diagram in consideration of extraordinary slenderness of the interested region.

An alternant time step method is used in establishing the difference equations in order to keep the unknowns in each of the derived difference equations within three. As a consequence, the algebraic equation set obtained can be solved explicitly by the chasing method without turning to time-consuming iterations. Refer to reference (Jia & Fang, 2003) for the algorithm details.computation and simulation

MODEL COMPARISON

In order to compare the numerical scheme presented above with the analytical model, a virtual borehole is set up, served also as a benchmark of the discussion. For this case, the subsurface is assumed as a homogeneous medium; and the circulating fluid is pure water. The geothermal temperature gradient is 0.03℃/m in this scenario. Other involved major parameters include: borehole depth and diameter, H=2000 m, d_b=0.28m; inner and out diameters of the outer steel pipe, d_1=0.188/0.200 m; inner and out diameters of the inner PE pipe, d_2=0.124/0.140 m; thermal conductivity and diffusivity of subsurface, k=2.5 W/(m.K), a=1.2x10^{-6} m^2/s; mass flow rate of water, M=12 kg/s, and average atmosphere temperature, T_a=10℃.

For the analytical model a uniform initial temperature in the subsurface, T_0=40℃, was assumed, equal to the mean temperature throughout the borehole depth. The line source model of transient conduction outside the borehole was employed for determining the borehole wall temperature. Then, the inlet and outlet water temperature were obtained according to the borehole thermal resistance presented above. In the numerical simulation discretization parameters were chosen as Δz=10m, $\Delta\tau$=180s, μ=1.2, and the radial boundary was set at r_{bnd}=68.9m (n=35). A constant heat extraction rate of 200 kW was set to be exerted to the DBHE for 5 months. The temperature responses of the inlet and outlet water were calculated by means of both analytical and numerical schemes, which are plotted in Figure 3.

The temperature responses obtained with the analytical and numerical schemes show similar trend as a whole, but notable quantitative difference remains. The comparison indicates that the geothermal temperature gradient plays an important role in the DBHE performance, and should not be neglected in models describing the heat transfer of the DBHEs. The analytical model with the assumption of a uniform initial temperature, however, can be calculated readily without appealing to computer, may still be useful for rough conceptual estimations.

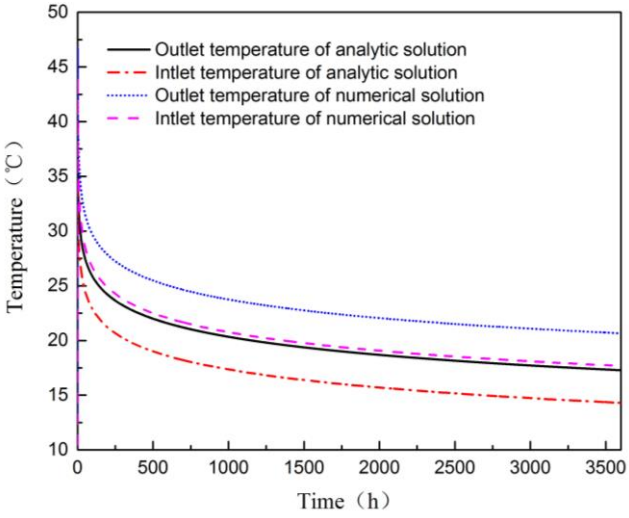

Figure 3 The water temperature responses comparison between the analytical and numerical models

NOMINAL DBHE CAPACITY

The FDM simulation scheme is then used to study performance of DBHEs. The BHEs may be referred to as a thermal-storage-type heat exchanger, and their operating status and performance depend heavily on their working history besides its geometric and physical configurations. Even though it is difficult to precisely quantify the performance or capacity of a certain borehole, a quantitative index is still desirable in parametric analyses of the BHE performance. The concept of "nominal DBHE capacity" has been suggested (Fang et al. 2018), which could be

defined as the maximum continuous heat extraction rate that a deep borehole can undertake on the condition that the inlet temperature of the DBHE should not be less than 5℃ at the end of heat extraction period of 3 months. The DBHE nominal capacity may be determined by means of simulation, but hardly by tests. Iteration in simulation is needed to determine the nominal DBHE capacity. This concept is used in the following discussions.

PARAMETRIC STUDIES

Different from the conclusions drawn by the analytical model where uniform temperature distribution on the borehole wall is predefined, the numerical model indicates that different flow configurations of the circulating water, i.e. flow downward in the annulus or in the central tube, not only make differences in the water temperature profiles in the tubes, but also result in different heat exchanger performance of the coaxial tube boreholes.

Parametric studies may be conducted based on the concept of nominal capacity of DBHEs. As mentioned before, higher thermal resistance of the central pipe wall is desirable to reduce the thermal short-circuit between the upward- and downward-flowing streams. These influences can be quantified by simulation, and the results obtained on the benchmark borehole are plotted in Figure 4. It shows that the thermal resistance of inner pipe affects greatly the DBHE performance. More adequate insulation between the two channels is needed to improve the heat transfer efficiency. Besides, it is clear that the flow configuration of entering in the annulus and returning through the inner pipe when extracting heat from the ground is more efficient than the opposite flow direction. While heat is injected into the ground, simulation shows that an opposite flow is better to enhance the heat transfer. Therefore, in the extraction phase, the cold water should enter the outer annulus to utilize the borehole wall as heat exchanger surface at full length. In heat injection phase, however, the water should reach the bottom of the borehole in the insulated inner pipe before discharging the bulk of its heat into the surrounding subsurface at maximum depth. Thus, seasonally alternating flow directions in the DBHE is beneficial in borehole thermal energy storage systems.

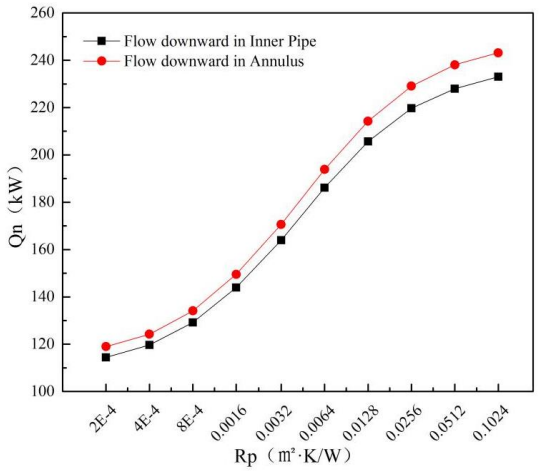

Figure 4 Nominal capacity of DBHE vs. thermal resistance of per length of inner pipe

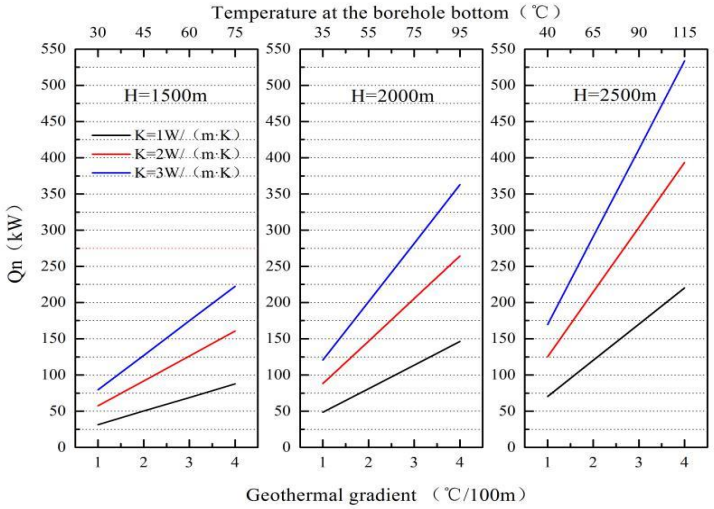

Figure 5 The DBHE nominal capacity diagram

The DBHE capacity is influenced by quite a lot of factors. The undisturbed temperature at the borehole bottom plays an important role in determination of the borehole heat extraction capacity, which depends mainly on the borehole depth, local geothermal heat flux and thermal conductivity of subsurface. The temperature difference across a certain layer of strata is proportional to the geothermal heat flux, but inversely proportional to its conductivity. Lower thermal conductivity of the subsurface will result in a higher temperature at borehole bottom when the geothermal heat flux is fixed. A diagram has been worked out on the assumption of a homogeneous subsurface (Fang et al. 2018). It is convenient for engineers to obtain an estimation of the nominal capacity of a DBHE according to the few key parameters, which is also shown in Figure 5.

PERFORMANCE SIMULATION

The numerical FDM scheme is used to simulate the performance of a GCHP system for 10 years with the benchmark DBHE. The 8000 m² building is located in north-eastern China, and only heating is provided in winter. The annual hourly heating load profile was calculated with a software package DeST developed in China (Yan et al., 2008; Peng et al. 2014). The heat extraction rates were determined then on the assumption of heat pump with a COP of 4.0. The parameters chosen for computation are as follows: μ=1.2 for radial direction discretization, Δz=10m, the time step is 180s. The radial boundary was set at 171.5 m (N=40) away from the borehole center. It took 55 minutes to finish the simulation on a common laptop computer (Intel (R) Core™ i5-2450M CPU @ 2.50GHz，4G memory). Water is arranged to flow downwards in the annular channel and return in the inner tube while extracting heat from the ground. Circulation stops when heating is off. The temperature responses show cyclic fluctuations with rapid drops in the heating seasons and significant recovery in the non-heating periods. It is also noticed that the minimum temperatures, corresponding to the maximum load in winter, become slightly lower in the first 3-5 years, but turn to quite stable in the following years. This feature is understandable because only a single DBHE is involved here. It may be inferred that the annual balance between heat extraction and injection is much less important for DBHEs located far enough from each other.

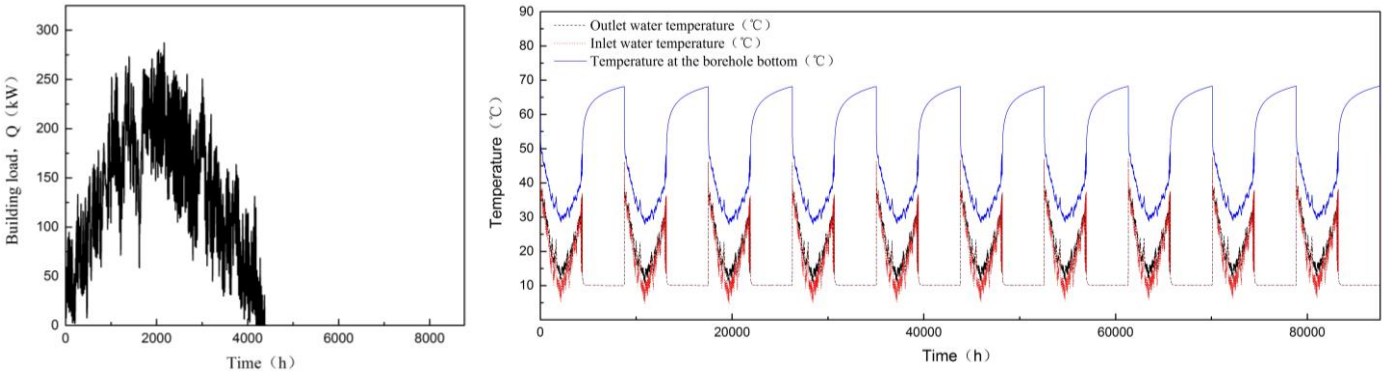

(a) Annual heating load of the building

(b) The temperature responses of the inlet and outlet water as well as that at borehole bottom

Figure 6 Simulation of a DBHE operation for 10 years

CONCLUSIONS

A few conclusions have been drawn from this study.

For BHEs with coaxial tubes, analytical solutions have been derived to calculate temperature profiles in the annulus and inner tube as well as the effective borehole resistance. The solutions indicate that different configurations of the circulation directions result in different fluid temperature profiles in the tubes, but lead to the same fluid outlet temperature and borehole resistance when the temperature distribution on the borehole wall remains uniform.

Numerical simulation seems more appropriate for thermal analysis of DBHE since the geothermal gradient in subsurface could be considered adequately. While a couple of commercial softwares are available to solve complex flow and heat transfer problems, a great amount of elements (nodes) have to be dealt with in problems such as DBHEs, which results in time-consuming computations. Based on the FDM, the numerical scheme developed specifically for coaxial DBHEs in this study is proven to be computationally-efficient, and may provide a useful tool for DBHE design and optimization. Results of the simulation have shown that the configurations of the circulation directions do make difference in the DBHE performance in view of the influence of geothermal gradient. Nominal DBHE capacities are evaluated according to their key parameters such as borehole depth, subsurface conductivity and geothermal heat flux.

More DBHE geometric and physical factors need to be investigated on their impacts on DBHE performances. And economic assessment will also be essential in its feasibility study. A pilot DBHE project is under construction

with technical assistance of this study. Real operation data will be collected to further verify the models.

ACKNOWLEDGMENTS

This work is supported by the National Natural Science Foundation of China (41702325) and Taishan Scholar Project of Shandong Province of China.

REFERENCES

Bauer, D., R. Marx, J. Nußbicker-Lux, F. Ochs, W. Heidemann and H. Müller-Steinhagen. 2010. *German central solar heating plants with seasonal heat storage*. Solar Energy 84(4): 612-623.

Beier, R. A., J. Acuña, P. Mogensen, B. Palm. 2014. *Transient heat transfer in a coaxial borehole heat exchanger*. Geothermics 51: 470–482

Beier, R. A., J. Acuña, P. Mogensen, B. Palm. 2013. *Borehole resistance and vertical temperature profiles in coaxial borehole heat exchangers*. Applied Energy 102: 665–675.

Congedo P.M., G. Colangelo, G. Starace. 2012. *CFD simulations of horizontal ground heat exchangers: A comparison among different configurations*. Applied Thermal Engineering 33-34: 24-32.

Diao, N. and Z. Fang. 2006. *The ground-coupled heat pump technology* (in Chinese), Science Press, Beijing.

Dijkshoorn, L., S. Speer, R. Pechnig. 2013. *Measurements and Design Calculations for a Deep Coaxial Borehole Heat Exchanger in Aachen, Germany*. International Journal of Geophysics: 1–14.

Fang L., Diao N., Shao Z. and Fang Z. 2017. S*tudy on thermal resistance of coaxial tube boreholes in ground-coupled heat pump systems*. Procedia Engineering 205: 3735-3742.

Fang L., N. Diao, Z. Shao, K.Zhu and Z. Fang. 2018. *A computationally efficient numerical model for heat transfer simulation of deep borehole heat exchanger*. Energy & Buildings 167: 79-88.

Hellström, G., *Ground heat storage - Thermal analyses of duct storage systems theory*, Ph.D. thesis. Sweden: University of Lund. 1991.

Holmberg, H., J. Acuña, E. Næss and O. K. Sønju. 2016. *Thermal evaluation of coaxial deep borehole heat exchangers*. Renewable Energy 97: 65–76.

Javed, S., J.D. Spitler. 2016. *Calculation of borehole thermal resistance*. Advances in Ground-Source Heat Pump Systems. Duxford, UK: Woodhead Publishing.

Jia, L. and Z. Fang. 2003. Advanced Heat Transfer (the 2nd Edition). Beijing, China: Higher Education Press.

Kong, Y.L., C.F. Chen, H.B. Shao, Z.H. Pang, L.P. Xiong and J.Y. Wang. *Principle and capacity qualification of deep borehole heat exchangers*. Chinese Journal of Geophysics (in Chinese) 60(12).

Lamarche, L., S. Kajl and B. Beauchamp. 2010. *A review of methods to evaluate borehole thermal resistances in geothermal heat-pump systems*. Geothermics 39 (2): 187-200.

Peng, C., Wang L., Zhang X. 2014. *DeST-based dynamic simulation and energy efficiency retrofitanalysis of commercial buildings in the hot summer/coldwinter zone of China: A case in Nanjing*. Energy & Buildings 78: 123–131.

Rees, S.J. 2016. *An introduction to ground-sourceheat pump technology*, Advances in Ground-Source Heat Pump Systems. Duxford, UK: Woodhead Publishing.

Welsch, B., W. Rühaak, D.O. Schulte, K. Bär and I. Sass. 2016. *Characteristics of medium deep borehole thermal energy storage*. International Journal of Energy Research 40 (13): 1855-1868.

Yan, D., Xia J., Tang Q., Song F., Zhang X., Jiang Y. 2008. *DeST—An Integrated Building Simulation Toolkit Part Ⅰ: Fundamentals*, Build Simul 1: 95–110Zhao, Q., B. Chen and F. Liu. 2016. *Study on the thermal performance of several types of energy pile ground heat exchangers: U-shaped, W-shaped and spiral-shaped*. Energy and Buildings 133: 335–344.

Zeng, H., N. Diao and Z. Fang. 2003. *Heat transfer analysis of boreholes in vertical ground heat exchangers*. International Journal of Heat and Mass Transfer 46 (23): 4467-4481.

[This page has been intentionally left blank]

IGSHPA SWEDEN
2018 Research Conference

DOI: 10.22488/okstate.18.000013

Upgrade of the B2G dynamic geothermal heat exchanger model: optimal location of the ground nodes

Antonio Cazorla-Marín **Carla Montagud** **José M. Corberán**
Francesco Tinti **Sara Focaccia**

ABSTRACT

In order to optimize the design and operation of a ground source heat pump system, the modeling of the Borehole Heat Exchanger (BHE) and its coupling to the heat pump operation becomes crucial. This becomes key for those systems with on/off operation, where it is important to model the short-term response of the BHE accurately. Furthermore, the modeling of the local variation of the ground temperature near the BHE will be highly influenced by ground thermal properties and the operation of the system. In this context, the novel B2G dynamic model was developed and experimentally validated in previous works for a single U BHE and adapted to a novel coaxial spiral configuration. In order to consider the influence of the soil surrounding the BHE, two ground nodes were initially defined and their position (penetration radii) was calculated for a specific type of soil and operating conditions. This paper presents an upgrade of the B2G model, with a descripton of penetration radii calculation. For this purpose, a comparison between the B2G model and the Infinite Cylindrical Source model was carried out to find the penetration radii that reproduce the ground thermal response with a higher accuracy under the corresponding soil thermal properties and operating conditions.

INTRODUCTION

During the last years, the concern about the global warming and the environmental pollution has lead to the research and widespread of renewable energy sources, together with an increase in the efficiency of the energy systems, with the aim of reducing the carbon emissions and reduce the global pollution. In the sector of heating and cooling in buildings, the Ground Source Heat Pump (GSHP) systems represent an efficient alternative to conventional systems (Rees 2016). In these systems, the ground is used in order to provide heat to the system (heat source) or to store the heat injected by the system (heat sink). This heat exchange with the system is performed by the use of a Borehole Heat Exchanger (BHE) field. Inside the BHE, the flowing fluid is heated up or cooled down because of the temperature difference between the surrounding ground and the fluid. In order to assist in the design of the BHEs and the optimal control of GSHP systems, an accurate dynamic model is a helpful tool, being able to reproduce the thermodynamic behavior of the BHE itself and then, couple the BHE model to the rest of the components inside an integrated system model. However, in order to reproduce the BHE behavior accurately, it is important to model not only the long-term response of the BHE and the surrounding ground, but also the short-term. This is especially important in systems with an on/off operation, where the accurate reproduction of the short-term response of the BHE becomes crucial. For this

Antonio Cazorla-Marín (ancamar4@upvnet.upv.es), Carla Montagud and José Miguel Corberán work at I.U.I.I.E. Universitat Politècnica de València, Francesco Tinti and Sara Focaccia work at University of Bologna.

purpose, the temperature variation of the nearer surrounding ground must be well predicted, and it will depend not only on the heat injected or extracted, but also on the ground thermal properties and the operating conditions of the BHE.

In this framework, several BHE models have been developed along the years. Some of them are focused on the prediction of the ground temperature variation under different assumptions, for example, the commonly used analytical models Infinite Line Source (ILS), Infinite Cylindrical Source (ICS) or Finite Line Source (FLS) based on the work carried out by Carslaw and Jaeger (1959). On the other hand, there exist several models with a higher level of detail, able to reproduce also the behavior inside the borehole in terms of water temperature. The analytical models usually include some assumptions and simplifications in order to reduce the computational cost, but also reducing the precision. However, they are easier to couple with other simulation programs (Yang, et al. 2010). Among these models, several of them use a thermal network based on thermal resistances and capacitances in order to model the heat transfer between the borehole and the surrounding ground (Eskilson and Claesson 1988; Yang, et al. 2012; Bauer, et al. 2011; Pasquier and Marcotte 2012; Lamarche, et al. 2010). Furthermore, some short-term analytical solutions have been developed, for example the one developed by Li and Lai (2012). However it can be used in time scales higher than one hour (to several years), not in vey short-term scales (in the range of minutes) in order to reproduce the dynamic behavior of an on/off GSHP. On the other hand, there exist several numerical models (Al-Khoury 2012) with a higher level of flexibility and more accuracy, but also with a higher computational cost, being difficult to couple them with other energy analysis programs. Furthermore, some other computer programs are used in the design and simulation of GSHP systems and the BHE, for example: GLHEPRO, EED, EnergyPlus or TRNSYS (Yang, et al. 2010). Regarding the thermal response of the ground and the amount of soil that is affected by the heat injection during a specific time period, it is usually addressed by adding a number of radial ground nodes and discretizing the soil mass in small radial steps until the far-field radius, where the effect of the heat injection vanishes. This far-field radius calculation has been addressed by several authors, for example, Hart and Couvillion (1986) defined it as $r_\infty = 4\sqrt{\alpha t}$, which depends on the ground thermal diffusivity (α) and the injection period (t). The addition of ground nodes inevitably leads to an increase in the complexity of the model and therefore, an increase in the computational cost. In this context, the novel B2G dynamic model was developed and experimentally validated in previous works for a single U BHE (Ruiz-Calvo, et al. 2015). In order to reduce the computational cost, the simpler 2D thermal network that reproduces the fluid temperature evolution with a high accuracy was used and only the portion of the surrounding ground affected by the heat injection period was considered. This model was adapted to a novel coaxial spiral BHE configuration designed by GEOTHEX® (http://www.geothex.nl/). This BHE has been developed and optimized in the framework of a HORIZON 2020 European Project, GEOTeCH (European Commision 2015). The adaptation to the coaxial spiral BHE was previously presented in the IGSHPA 2017 conference (Cazorla-Marin, et al. 2017a), where a validation of the model with experimental data from a TRT (Witte 2012) was carried out. In order to account for the influence of the thermal properties of the ground and the operating conditions of the system in the soil surrounding the BHE wall, two different penetration diameters were initially defined as an input in the model (now referred as penetration radii). They were determined calculating the distance at which the heat transfer rate in the ground was negligible by using the ICS model for the specific type of soil and different injection times, for example, 15 hours for the second ground node (mid-term) and 3 hours for the first ground node (short-term). The results showed that the B2G approach applied to this configuration produced a model that could accurately predict the behaviour of the BHE, obtaining a Root Mean Square Error (RMSE) of 0.095 K (in the case with no enhanced convective heat transfer). In this work, an upgrade of the B2G model with three ground nodes is presented. The simulation in TRNSYS with the same TRT data produces a RMSE of 0.088 K, lower than the previous work. In order to make the use of the B2G model more general, it should be able to reproduce the effect of any type of soil and system operating conditions. Therefore, their influence in the determination of the corresponding penetration radii needs to be addressed and modelled. This paper presents an upgrade of the B2G model where the determination of the ground nodes location is described. For this purpose, the B2G model was compared to the ICS model, and the penetration radii that minimize the difference between the results of the two models is calculated by using an optimization algorithm implemented in MATLAB®. The future objective of this methodology is to obtain polynomial correllations where the penetration radii could be determined as a function of the soil thermal properties, BHE geometry and operating conditions (heat injection period). These correlations would be further implemented inside the B2G model for its widespread use.

B2G BHE MODEL

U-tube B2G model

The B2G dynamic model was originally developed in order to reproduce the short-term behaviour of a single U-tube BHE in terms of the water temperature evolution throughout the pipe. For this purpose, a thermal network approach is used, together with a vertical discretization of the borehole. In order to reduce the computational cost, a simple 2D thermal network was used and only the portion of the surrounding ground affected by the heat injection/extraction was considered, so that it is possible to reproduce the water temperature evolution with a high accuracy. The thermal network consists of five nodes, connected by six thermal resistances, where each node represents one part of the BHE: downward and upward fluid, two grout sections and the surrounding ground. The thermal properties of the fluid, grout and ground are considered: thermal capacitance (representing the thermal inertia) and conductivity, as well as the BHE geometry. On the other hand, the thermal resistances represent the convective and conductive heat transfer between nodes. Concerning the fluid nodes, the advection is taken into account, but the axial conduction is neglected. The entire model consists of a 5C6R-n model (five thermal capacitances, six thermal resistances and *n* vertical divisions of the BHE), which is a system of ordinary differential equations that is solved by standard numerical procedures. The U-tube B2G model was implemented in TRNSYS and was presented and experimentally validated against different conditions in (Ruiz-Calvo, et al. 2015) and (De Rosa, et al. 2015).

Coaxial B2G model

The single U-tube BHE model was adapted to a standard coaxial configuration as well as to a spiral coaxial configuration. The main difference between them is that, in the spiral coaxial BHE, the fluid flowing through the outer pipe follows a helical path. This is modeled using an equivalent section in the outer pipe, that is, the equivalent hydraulic diameter corresponding to the helical channel is determined in order to calculate the hydraulic and thermodynamic properties. The adaptation of the B2G model to the standard coaxial configuration was previously presented in (Cazorla-Marin, et al. 2017b). On the other hand, the adaptation to the spiral coaxial configuration was presented in (Cazorla-Marin, et al. 2017a), where a more detailed explanation of the model and the calculation of the different parameters can be found, this description is also applicable to the standard coaxial configuration. In order to adapt the B2G model to the coaxial configurations, the thermal network was modified to a simpler linear thermal network with five thermal capacitances and four thermal resistances. Furthermore, the vertical heat conduction between grout and ground nodes is considered by the use of vertical thermal resistances (R_{vb}, R_{vg1} and R_{vg2}). The five thermal capacitances represent the fluid in the inner pipe (T_i), the fluid in the outer pipe (T_o), the grout (T_b), the closer surrounding ground (T_{g1}), which represents the ground affected by a short period of heat injection/extraction and a further ground section (T_{g2}), representing the ground affected by a larger period of heat injection/extraction. The convective and conductive heat transfer between nodes was calculated using radial thermal resistances between nodes (R_{io}, R_{ob}, R_{bg1} and R_{g1g2}). As it can be observed, in the coaxial model, two ground nodes are used instead of only one. In this way, it is possible to obtain a better prediction of the ground temperature evolution during all the heat injection/extraction period, therefore, a better accuracy in the prediction of the fluid temperature. In the last version of the coaxial model, another ground node has been added, representing the undisturbed ground (T_{ug}), where the temperature is constant. Therefore, it is possible to take into account the heat transfer between the second ground node and the undisturbed ground, represented by a thermal resistance (R_{g2ug}), as it is presented in (Cazorla-Marin, et al. 2018). Figure 1 a) shows the linear thermal network for the spiral coaxial model, while the vertical discretization of the borehole is shown in Figure 1 b).

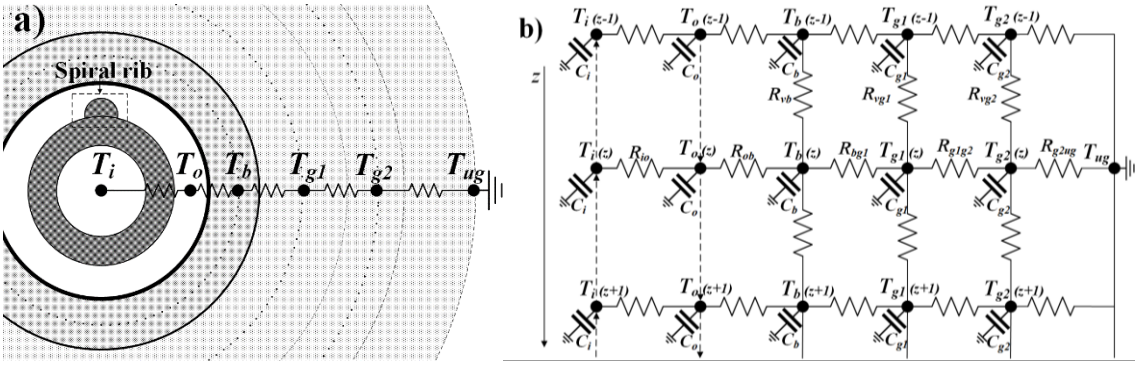

Figure 1 Thermal network of the coaxial configuration model: a) borehole layout (spiral coaxial); b) vertical discretization.

OPTIMAL LOCATION OF THE GROUND NODES

The position of the ground nodes is defined by three penetration radii. The calculation of these penetration radii is not straitghforward, as it will influence in the calculation of the ground temperature and thus, in the water temperature calculation. For example, for the first ground node, the higher the value of the penetration radius, the bigger the amount of ground that the model will consider, therefore, the bigger the heat capacity of this ground section. If the heat capacity is bigger, the temperature of this node will vary slowlier, and it will influence in the short-term evolution of the water temperature. Analogously, the same will occur with the second ground node. However, the position of the undisturbed ground node will only have an influence in the heat transfer between the second ground node and the undisturbed ground node (increasing or decreasing the thermal resitance), as it only represents a temperature boundary, with no temperature variation. In previous works, in order to calculate the radius of the undisturbed ground node (R_{ugp}), the heat flux in the ground was calculated for the whole heat injection period in the radial direction, and the distance where the heat flux was negligible for this period was used to set the undisturbed ground node distance. For this purpose, the equation of the Infinite Cylindrical Source (ICS) (Carslaw and Jaeger 1959) model was used. Regarding the other ground nodes, their position was calculated for a shorter period of heat injection (for example, 1 hour for the first ground node and 5 hours for the second ground node). In this work, a new methodology is proposed, in which a comparison between the B2G model and the ICS model is carried out in order to calculate the penetration radii that reproduce with the highest accuracy the temperature variation of the ground nodes and the heat transfer along the ground. In this comparison, a constant heat flux on the borehole wall during all the heat injection period is assumed, and the ground temperature variation is calculated for the ground nodes position and the heat transfer rate between them, for each time step. The ground nodes position (penetration radii R_{gp1}, R_{gp2} and R_{ug}; corresponding to the ground nodes T_{g1}, T_{g2} and T_{ug}, respectively) will be optimized, so the difference between the results calculated by the two models is minimum. For this purpose, the B2G thermal network has been adapted in order to consider a constant heat flux on the borehole wall instead of the fluid through the BHE tubes. Therefore, a node on this surface is considered (T_b), and a constant heat flux (q_0) is imposed. Figure 2 shows the thermal network corresponding to this problem. The ground nodes T_{g1} and T_{g2} are located, each one, at the average distance between the two concentric circumferences that form each annulus region. These positions are defined by the radii r_{g1} and r_{g2}, respectively.

$$r_{g1} = \frac{R_{gp1} + r_b}{2} \quad ; \quad r_{g2} = \frac{R_{gp2} + R_{gp1}}{2} \tag{1}$$

Where r_b represents the borehole wall radius. On the other hand, q_1 represents the heat transfer between the ground nodes T_{g1} and T_{g2}, while q_2 represents the heat transfer between T_{g2} and T_{ug}.

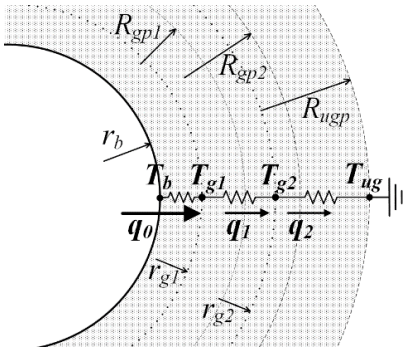

Figure 2 Thermal network used for the calculation of the penetration radii

The main parameters used in the models are the borehole radius (r_b), the ground thermal conductivity (λ), the ground volumetric heat capacity (c_v) and the heat flux (q_0). The main inputs are the three penetration radii (R_{gp1}, R_{gp2} and R_{ug}). The initial ground temperature is assumed to be zero, as only the temperature variation is calculated.

B2G model

In the B2G model, the temperature of the ground nodes T_{g1} and T_{g2} is calculated using the main BHE parameters and penetration radii. First, the thermal capacitances (C) of the two ground nodes are calculated (eq. 2), together with the UA values, which represent the thermal resistance between ground nodes (eq. 3).

$$C_{g1} = \pi \left(R_{gp1}^2 - r_b^2\right) c_v \quad ; \quad C_{g2} = \pi \left(R_{gp2}^2 - R_{gp1}^2\right) c_v \tag{2}$$

$$UA_{bg1} = \frac{2\,\pi\,\lambda}{\ln\left(r_{g1}/r_b\right)} \quad ; \quad UA_{g1g2} = \frac{2\,\pi\,\lambda}{\ln\left(r_{g2}/r_{g1}\right)} \quad ; \quad UA_{g2ug} = \frac{2\,\pi\,\lambda}{\ln\left(R_{ug}/r_{g2}\right)} \tag{3}$$

Second, the ground nodes temperatures (T_{g1} and T_{g2}) are calculated using the energy balance equations. The undisturbed ground temperature is defined as zero ($T_{ug} = 0$).

$$C_{g1}\frac{\partial T_{g1}(t)}{\partial t} = q_0 + UA_{g1g2}\left(T_{g2}(t) - T_{g1}(t)\right) \tag{4}$$

$$C_{g2}\frac{\partial T_{g2}(t)}{\partial t} = UA_{g1g2}\left(T_{g1}(t) - T_{g2}(t)\right) + UA_{g2ug}\left(T_{ug}(t) - T_{g2}(t)\right) \tag{5}$$

Finally, the heat transfer rate between ground nodes is calculated (q_1 and q_2) using the equations 6 and 7.

$$q_1^{B2G}(t) = UA_{g1g2}\left((T_{g1}^{B2G}(t) - T_{g2}^{B2G}(t)\right) \tag{6}$$

$$q_2^{B2G}(t) = UA_{g2ug}\left((T_{g2}^{B2G}(t) - T_{ug}^{B2G}(t)\right) \tag{7}$$

Infinite Cylindrical Source model

The Infinite Cylindrical Source (ICS) model calculates the heat transfer in the region bounded internally by a

circular cylinder and constant heat flux in its surface. In this case, the internal circular cylinder would correspond to the borehole wall, with radius r_b, and the constant heat flux through its surface would be q_0. The solution for the calculation of the ground temperature along the radial distance was provided by Carslaw and Jaeger (Carslaw and Jaeger 1959). This solution is presented in equation (8), where the initial ground temperature is zero, and α represents the thermal diffusivity of the ground ($\alpha = \lambda/c_v$).

$$T^{ICS}(r,t) = -\frac{2q_0}{\pi^2 r_b \lambda}\int_0^{\infty}\left(1-e^{-\alpha u^2 t}\right)\frac{J_0(ur)\,Y_1(ur_b)-Y_0(ur)\,J_1(ur_b)}{u^2[J_1^2(ur_b)+Y_1^2(ur_b)]}du \tag{8}$$

Therefore, the temperature in the ground nodes will be calculated by the equation (9).

$$T_{g1}^{ICS}(t) = T^{ICS}(r_{g1},t) \quad ; \quad T_{g2}^{ICS}(t) = T^{ICS}(r_{g2},t) \tag{9}$$

Regarding the heat transfer between nodes, it is calculated using the Fourier's law applied in the frontier between the ground nodes (R_{gp1} and R_{gp2}), using the equations (10-11), where Δr represents a very small radial distance.

$$q_1^{ICS}(t) = -2\,\pi\,R_{gp1}\,\lambda\frac{T_{R_{gp1}}^{ICS}(t)-T_{R_{gp1}+\Delta r}^{ICS}(t)}{\Delta r} \tag{10}$$

$$q_2^{ICS}(t) = -2\,\pi\,R_{gp2}\,\lambda\frac{T_{R_{gp2}}^{ICS}(t)-T_{R_{gp2}+\Delta r}^{ICS}(t)}{\Delta r} \tag{11}$$

Calculation and validation of penetration radii

Both the B2G model and ICS were implemented in MATLAB and the Root Mean Square Error (RMSE) between the B2G results and the ICS is calculated for a set of penetration radii (R_{gp1}, R_{gp2} and R_{ug}). Therefore, it is possible to find the penetration radii that minimize the RMSE between the two models by using an optimization algorithm. In this case, a pattern search optimization methodology was used by using the solver *patternsearch*, already implemented in the Global Optimization Toolbox in MATLAB (MathWorks 2017). For the calculation, two approaches were used:

a) Ground nodes temperatures optimization. The ground nodes temperatures T_{g1} and T_{g2} are the variables calculated by each model. Therefore, the optimization solver calculates the set of radii that minimizes the RMSE between these temperatures calculated by the B2G and the ICS models.
b) Heat transfer rates optimization. The heat transfer rates q_1 and q_2 are the variables to calculate. Therefore, the optimization solver finds the penetration radii that minimize the RMSE between the heat transfer rates calculated by each model.

Once the penetration radii are calculated, they are used as inputs in the B2G model implemented in TRNSYS. Thus, it can be checked if this set of penetration radii are suitable to reproduce the behavior of the BHE accurately. For this purpose, it is employed the same methodology followed in (Cazorla-Marin, et al. 2017a), using the experimental data from a Thermal Response Test (TRT). So the inlet mass flow rate and fluid temperature are introduced as inputs in the B2G model and the outlet fluid temperature is calculated, together with the total heat transferred to the ground. Then, the calculated results are compared to the experimental ones by calculating the RMSE of the outlet fluid temperature and the percentage difference of the heat transferred to the ground.

Case study parameters

In this study, the spiral coaxial BHE developed by GEOTHEX® was used. The main parameters are calculated

from a TRT carried out in Houten, The Netherlands (Witte 2012). The main parameters used in the calculation of the penetration radii in MATLAB are shown in Table 1. Regarding the main parameters used for the TRT simulation in TRNSYS, they are the same as the ones already presented in a previous work (Cazorla-Marin, et al. 2017a).

Table 1. Main parameters for the calculation of the penetration radii

TRT data		Model parameters	
Ground thermal conductivity	2.13 W/m·K	Heat injection period	15 h
Ground volumetric heat capacity	2410 kJ/m³·K	Time step	3 min
Borehole radius (r_b)	0.044 m	Differential radial distance (Δr)	0.001 m
Average heat flux (q_0)	17.7 W/m	Initial point ($R_{gp1}/R_{gp2}/R_{ug}$)	0.1/0.2/0.3

RESULTS

The calculation of the penetration radii was carried out in MATLAB for the two approaches. The results that were obtained are the following:

a) Ground nodes temperature optimization: R_{gp1}=0.163 m, R_{gp2}=0.362 m, R_{ug}=0.593 m.

b) Heat transfer rate optimization: R_{gp1}=0.165 m, R_{gp2}=0.352 m, R_{ug}=0.517 m.

It can be seen that both approaches produce quite similar results for R_{gp1} and R_{gp2}. However, the ground temperatures approach produces a bigger undisturbed ground radius. The results obtained by each model are shown in Figure 3, for each optimization approach.

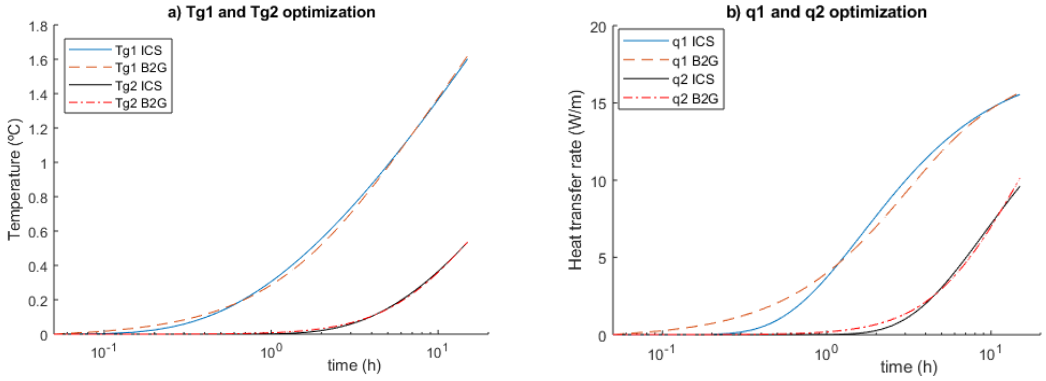

Figure 3 Penetration radii calculation: a) Ground nodes temperature optimization; b) Heat transfer rate optimization.

It can be seen that, for both cases, the results produced by the B2G model are quite similar to the results produced by the ICS model. The accuracy of these results will be validated in the next step, with the simulation of the TRT. Figure 4 shows the comparison between the outlet temperature calculated by the B2G model implemented in TRNSYS and the experimental outlet temperature for the two sets of penetration radii obtained previously.

For both optimization approaches, the calculated outlet temperature is quite similar to the experimental one, with a RMSE of 0.088K in the ground temperatures approach (case a), and 0.087K in the heat transfer rate approach (case b). Regarding the calculated heat transfer to the ground and the deviation with the experimental results, it is summarized in Table 2.

Table 2. Heat transferred to the ground during the TRT

Experimental	B2G model. method a)	Percentage difference	B2G model. Method b)	Percentage difference
43022.6 kJ	41864.5 kJ	-2.69%	41932.2 kJ	-2.53%

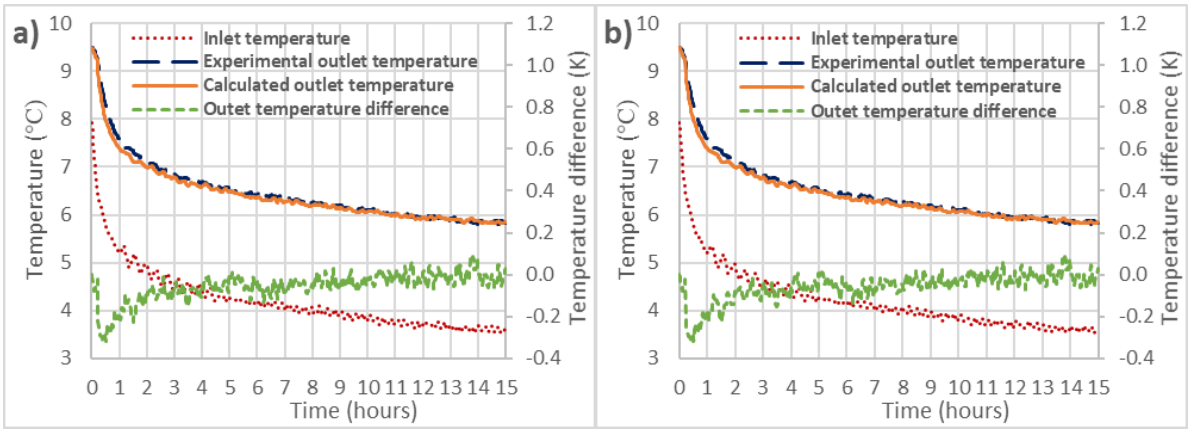

Figure 4 Comparison between the experimental and calculated outlet temperature using the B2G model with the calculated penetration radii. a) Ground nodes temperature optimization; b) Heat transfer rate optimization.

Taking a look at the results, it can be concluded that the 'heat transfer optimization approach' is slightly better.

It should be mentioned that the calculation of the ground nodes position was also carried out with different values of heat injection, producing the same optimal position of the ground nodes. Therefore, it can be concluded that this position is independent of the heat injected and can be applied in the B2G model inside a complete ground source heat pump system model, where the heat load will be variable, also along the borehole depth.

CONCLUSION

The B2G dynamic model was presented previously as an accurate tool to reproduce the short-term behavior of a BHE for different configurations (U-tube, coaxial or spiral coaxial). In this work, a new methodology to calculate the position of the three ground nodes considered in the model is presented. For this purpose, a comparison between the B2G model, adapted to a constant heat flux on the borehole wall surface, and the Infinite Cylindrical Source (ICS) is carried out to find the position of the ground nodes that reproduce with the highest accuracy the ground thermal response. In order to achieve this, two approaches were considered in the calculation of the ground nodes position, depending on the results that are compared between models. In the case a), the values to compare are the ground nodes temperatures; while in the case b), the values to compare are the heat transfer rates between ground nodes. The calculated ground nodes positions (referred as penetration radii) are used in the B2G model implemented in TRNSYS to simulate a thermal response test, reproducing the dynamic thermal response of the BHE with a high accuracy (maximum RMSE of 0.088K and maximum 2.7% deviation in the calculation of the heat exchanged with the BHE). The main objective of this new methodology would be the calculation of several polynomial correlations, which would be implemented in the TRNSYS model, in order to determine the ground nodes positions depending on the ground thermal properties, the borehole geometry and the operating conditions heat injection period).

ACKNOWLEDGMENTS

The present work has been supported by the European Community Horizon 2020 Program for European Research and Technological Development (2014-2020) inside the framework of the project 656889 – GEOTeCH (Geothermal Technology for Economic Cooling and Heating) and by the Generalitat Valenciana inside the program "Ayudas para la contratación de personal investigador en formación de carácter predoctoral (ACIF/2016/131)".

REFERENCES

Al-Khoury, R. 2012. Computational Modeling of Shallow Geothermal Systems. BocaRaton, FL, USA: CRC Press.

Bauer, D., Heidemann, W., Müller-Steinhagen and H., Diersch, H.-J. G. 2011. *Thermal resistance and capacity models for borehole heat exchangers*. Intenational Journal of Energy Research 35(4): 312–320.

Carslaw, H. S. and Jaeger, J. C. 1959. Conduction of heat in solids. New York, NY, USA: Oxford University Press.

Cazorla-Marin, A., Montagud, C., Witte, H., Hylkema, R. and Corberán, J.M. 2017a. *Modelling and Experimental Validation of a Novel Co-axial Spiral Borehole Heat Exchanger*. IGSHPA Technical/Research Conference and Expo 2017. Denver, CO, USA. March 14-16.

Cazorla-Marin, A., Montagud, C., Corberán, J. M. and Acuña, J. 2017b. *Modeling of a coaxial Borehole Heat Exchanger and experimental validation*. 10º Congreso Internacional Ingeniería Termodinámica 10CNIT. Lleida, Spain. June 28-30.

Cazorla-Marin, A., Montagud, C. and Corberán, J. M. 2018. *Adaptation of the B2G dynamic model to new borehole heat exchanger coaxial configurations*. CYTEF 2018 − IX Congreso Ibérico | VII Congreso Iberoamericano de las Ciencias y Técnicas del Frío. *Accepted.*

Eskilson, P. and Claesson, J., 1988. *Simulation model for thermally interacting heat extraction boreholes*. Numerical Heat Transfer 13(2): 149-65.

European Commision. 2015. Geothermal Technology for €conomic Cooling and Heating (H2020-LCE-2014-2, GEOTeCH-656889). Available online at: http://www.geotech-project.eu/.

Hart, D. P. and Couvillion, R. 1986. Earth-Coupled Heat Transfer. Dublin, OH, Ireland: National Water Well Association

Lamarche, L., Kajl, S. and Beauchamp, B. 2010. *A review of methods to evaluate borehole thermal resistances in geothermal heat-pump systems*, Geothermics 39(2): 187-200.

Li, M. and Lai, C.K. 2012. *New temperature response functions (G functions) for pile and borehole ground heat exchangers based on composite-medium line-source theory*. Energy 38: 255-263.

MathWorks. 2017. Global Optimization Toolbox - User's Guide - MATLAB. Available online at: https://es.mathworks.com/help/pdf_doc/gads/gads_tb.pdf.

Pasquier, P. and Marcotte, D. 2012. *Short-term simulation of ground heat exchanger with an improved TRCM*. Renewable Energy 46: 92-99.

Rees, S. J. 2016. Advances in Ground-Source Heat Pump Systems. Duxford, UK: Elsevier / Woodhead Publishing.

De Rosa, M., Ruiz-Calvo, F., Corberán, J.M., Montagud, C. and Tagliafico, L.A. 2015. *A novel TRNSYS type for short-term borehole heat exchanger simulation: B2G model*. Energy Conversion and Management 100: 347–357.

Ruiz-Calvo, F., De Rosa, M., Acuña, J., Corberán, J.M. and Montagud, C. 2015. *Experimental validation of a short-term Borehole-to-Ground (B2G) dynamic model.* Applied Energy 140: 210–223.

Witte, H.J.L. 2012. *The GEOTHEX geothermal heat exchanger, characterisation of a novel high efficiency heat exchanger design*. The 12th International conference on Energy Storage (Innostock 2012). Lleida, Spain. May 16-19.

Yang, H., Cui, P. and Fang, Z. 2010. *Vertical-borehole ground-coupled heat pumps: A review of models and systems*. Applied Energy 87: 16–27.

Yang, W., Shi, M., Liu, G. and Chen, Z. 2012. *A two-region simulation model of vertical U-tube ground heat exchanger and its experimental verification*, Applied Energy 86(10): 2005-2012.

[This page has been intentionally left blank]

IGSHPA SWEDEN
2018 Research Conference

DOI: 10.22488/okstate.18.000043

Extending the Ashrae Tp8 method for vertical borefield design to uniform BHE temperature boundary conditions

Davide Rolando **Marco Fossa** **Antonella Priarone**

ABSTRACT

The Ashrae method is a fast algorithm for calculating the overall length of closed-loop borehole heat exchangers, considering the ground thermal response and the building thermal load profile. The method includes a corrective variable called Temperature Penalty (T_p) to account for the thermal interaction between boreholes. Several authors proposed different approaches for calculating this parameter, but the majority is inaccurate or too complex. Recently, the same Authors suggested a very simple method, called T_{p8}. The coefficients included in the original formula were optimized against g-functions obtained by spatial superposition of a single source always working at the same heat rate. In this paper, the early T_{p8} method is improved by the calculation of new constants based on g-functions calculated for uniform temperature borehole conditions. A large dataset of 300 borefield configurations have been considered for optimization and validation purposes. In this case, all the BHEs are at the same temperature and the overall heat transfer rate of the field is constant in time. Compared with EED software outputs, the results from present T_{p8} method show a good accuracy (within 3% for the overall BHE field length) while maintaining a great simplicity in applying the method at engineering design level.

INTRODUCTION

The sizing process of a Ground Coupled Heat Pump (GCHP) needs the knowledge of the building loads, the heat pump characteristics and the ground thermophysical properties. The element that influences more the profitability of the plant from both the energy efficiency and financial sustainability point of view is the correct design of the boreholes (BHEs) field.

Different methods have been proposed to this aim, including commercial design tools as EED (1994) and GLHEPRO (2000). These softwares are powerful but their algorithms are complex and above all not suitable to be implemented in engineering level calculations (e.g. calculation spreadsheets) or suggested in Standards.

Kavanaugh and Rafferty (1997) proposed a method that later became the Ashrae reference. This method is very simple but contains some critical elements, in particular a correction parameter named temperature penalty T_p. The physical meaning of this parameter is not clearly disclosed in the Ashrae method and the original methodology suggested by Kavanaugh and Rafferty for the T_p calculation appears arguable and inaccurate in the results it is able to provide.

During the years, some critical analyses to the Ashrae method have been carried out, including the ones by Bernier et al. (2008), Fossa (2011) and Capozza et al. (2012).

More recently, Ahmadfard and Bernier (2014, 2018) proposed modifications to the Ashrae method that involve the elimination of the temperature penalty term and the analytical evaluation of the long term ground resistance by the superposition of the finite line source (FLS) solution on borehole segments to obtain the "real" *g*-function for the BHE field at time equal to 10 years.

D. Rolando (davide.rolando@energy.kth.se) is Researcher at KTH Royal Institute of Technology, Sweden
M. Fossa (marco.fossa@unige.it) is Full Professor and A. Priarone (a.priarone@unige.it) is Researcher at DIME, University of Genova, Italy

A different approach has been proposed by Fossa and Rolando (2014, 2015) who kept the temperature penalty parameter and proposed a method based on the original Ashrae implementation. Comparisons with EED software results showed the reliability of the improved T_{p8} method, which maintains with respect to other formulations a great simplicity and the possibility to be implemented in calculation spreadsheets and employed in Standard method (Fossa et al. 2017).

In the present paper, a further improvement to the original version of the method is proposed, with a new set of constants obtained considering as a reference the g-functions calculated for uniform temperature at the BHE wall, hereafter called BC III g-functions (Eskilson 1987, Hellstrom 1989, Cimmino and Bernier 2014, Lamarche 2017).

THEORETICAL BACKGROUND

To size a borehole heat exchangers (BHEs) field, one of the most important elements is the correct modeling of the transient response of the ground to the presence of the heat exchangers. Neglecting the influence of the groundwater, the analysis can be reduced to the resolution of a transient three-dimensional heat conduction problem.

Usually, a single BHE is first considered to obtain a basic solution that can be then superposed in space and time. This basic solution can be achieved analytically or numerically, applying to the BHE suitable boundary conditions and considering the ground domain as one-dimensional (radial direction) or two-dimensional (radial and axial one). In the following, the main models are briefly presented.

The simplest case is the one-dimensional transient response of the ground to an infinite line source (ILS), as discussed by Thomson (Lord Kelvin), (1882, 1911), Carslaw and Jaeger (1947) and Ingersoll et al. (1954). In this case, the applied boundary condition is an imposed constant heat transfer rate for unit length $\dot{Q}'$.

Carslaw and Jaeger (1947) developed a solution for the hallow infinite cylinder and analytically solved the problem for either the constant heat rate or constant temperature boundary condition. Later Ingersoll et al. (1954) provided tabulated values of the related solutions.

To take into account the actual finite length of the BHE, the finite line source (FLS) model has been proposed by Zeng (2002) and then reformulated by Lamarche and Beauchamp (2007). Finally, Claesson and Javed (2011) proposed an analytical solution that is commonly used as basic solution in the space superposition process.

Recently, Priarone and Fossa (2015, 2016) proposed to model the BHE as a finite hallow cylinder (FCS), imposing either constant heat rate or temperature and solving the problem numerically. In particular, the imposed temperature boundary condition provides a non-uniform heat transfer rate along the depth of the BHE.

The transient temperature field in the ground around the BHE, obtained analytically or numerically, can be provided by defining a generic temperature response factor Γ, with reference to the average heat rate per unit length:

$$\Gamma = \frac{2\pi k_{gr}(T - T_{gr,\infty})}{\dot{Q}'_{\text{ave}}} \tag{1}$$

In a similar way, the average temperature at the BHE boundary in a BHEs field can be described by using a family of temperature response factors called *g*-function, first introduced by Eskilson (1987).

The *g*-functions are obtained by superposition of a basic solution and depend on geometrical parameters and operating conditions of the BHEs field:

$$\frac{2\pi k_{gr}\left[T_{\text{ave}}(r_b) - T_{gr,\infty}\right]}{\dot{Q}'_{\text{ave}}} = g\left(\ln(9\text{Fo}_H), r_b / H, B / H, \text{borefield geometry}\right) \tag{2}$$

In the Eskilson original work the superposition was realized numerically to obtain a uniform temperature for all the BHEs and a total heat transfer rate constant in time for the whole borefield. This condition replicates correctly the actual operating condition of the GCHP with BHEs connected in parallel and a nearly constant COP not greatly depending on the temperature of the fluid.

However, usually the building load is variable in time; so, after obtaining the *g*-function for a constant total heat transfer rate of the borefield, the transient ground response to a variable load can be obtained by a superposition in time, according to the method described for example by Yavuzturk and Spitler (1999).

During the years, several efforts have been made in literature to reproduce the Eskilson *g*-functions, according to different approaches, briefly described in the following and sketched in Table 1.

The most common method is to simply superpose in space the FLS solution obtained for a single BHE, keeping uniform heat transfer rate for all the BHE of the field (BC I). Fossa et al. (2009) and Cimmino and Bernier (2013) tried to reproduce the actual behavior of the borefield and calculated the *g*-functions by applying different uniform heat transfer rates to the BHEs according to their position in the field (BC II). Unfortunately, this approach does not yet reproduce the Eskilson *g*-functions.

Thus, Cimmino and Bernier (2014) proposed an improvement to their method. They considered a "segmented" heat transfer rate boundary condition applied to each BHE to obtain a nearly uniform temperature distribution in the whole field again keeping the total heat transfer rate constant in time (BC III.) This method provides results very similar to the Eskilson ones since it applies the original swedish approach. A further improvement to this approach has been proposed by Lamarche (2017) with a piecewise-linear profile applied to each BHE. This method reduces the number of segments and simplifies the matrix inversion process devoted to segment heat transfer rate evaluation.

Table 1. Different approach for the g-functions evaluation

MULTI SOURCE (Γ_{multi})				
Geometry	Boundary Condition	Schematics	Label	Reference
FLS	$\dot{Q}' = \text{const}$	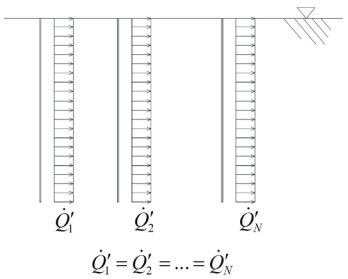	BC I (Cimmino and Bernier 2014)	Cimmino and Bernier (2014)
FLS	$\dot{Q}' = \text{const}$	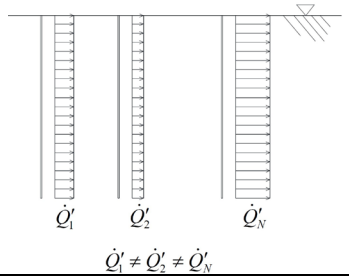	BC II (Cimmino and Bernier 2014)	Fossa et al. (2009), Cimmino and Bernier (2013)
FLS (segmented)	$\dot{Q}' = \dot{Q}'(z)$	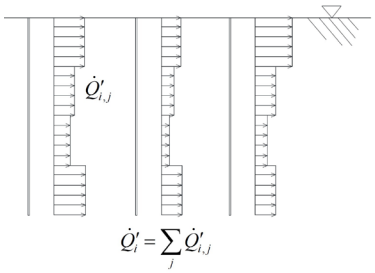	BC III (Cimmino and Bernier 2014)	Eskilson (1987), Hellstrom (1989), Cimmino and Bernier (2014), Lamarche (2017)
FCSTM	$T = \text{const}$	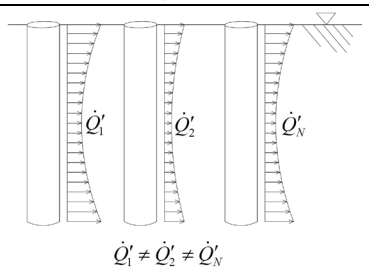	BC IIT	Fossa and Priarone (2018)

A different method is proposed by Fossa and Priarone (Fossa and Priarone 2018) who suggest as basic solution their finite hallow cylinder with imposed temperature boundary condition (FCST). This solution is superposed in space after having iteratively evaluated the heat transfer rate for each BHE of the field to ensure a constant in time global load to the ground (BC IIT).

The peculiarity of the method is that the basic single BHE temperature response factor Γ is provided in tabular form at given radial distances from the source and in a wide range of Fourier numbers, avoiding in such a way the numerical integration of FLS solution.

THE ASHRAE T_{P8} METHOD

The simplest method to size a borefield is the Ashrae method, first proposed by Kavanaugh and Rafferty (1997) and based on the knowledge of the building heat load requirements in time.

Bernier (2006) proposed the following formulation of the Ashrae method:

$$L = \frac{\left\{\dot{Q}_y R_y + \dot{Q}_m R_m + \dot{Q}_h \left(R_h + R_b\right)\right\}}{T_{gr,\infty} - T_{f,ave}(\tau_N) - T_p} \tag{3}$$

where $T_{gr,\infty}$ is the undisturbed ground temperature, $T_{f,ave}$ is the average fluid temperature and R_b is the effective thermal resistance of the borehole.

$\dot{Q}_y$, $\dot{Q}_m$ and $\dot{Q}_h$ are the average heat transfer rates from (or to) the ground in a given period of 10 years, one month and 6 hours, respectively. These basic thermal pulses are assumed suitable to represent the building thermal history. τ_N is the total considered time period (10 years + 1 month + 6 hours).

R_y, R_m, R_h are ground resistances evaluated according to the ICS model at the above time intervals.

Finally, T_p represents the temperature penalty, which accounts for "interference of adjacent borehole" (Ashrae Handbook 2015).

The ICS model (and its well known *G* solution) is suitable to represent the ground thermal response in the short and medium time intervals but not for the long term analysis, i.e. for a time period of 10 years. Thus, evaluating the resistance R_y using the *G* solution provides incorrect results and leads to significant error (up to 100% or more, when the BHE number is large and $\dot{Q}_y$ term is comparable as order of magnitude with $\dot{Q}_m$ and $\dot{Q}_h$) in the calculation of the total borehole length.

Fossa (2011) first pointed out the real meaning of the temperature penalty parameter which represents the needed correction in the long term analysis comparing the *G* solution and the proper *g*-function for the BHE field:

$$T_p(L) = \frac{\dot{Q}_y \left(\frac{g(\tau_N)}{2\pi} - G(\tau_N) \right)}{L k_{gr}} \tag{4}$$

It is interesting to outline that T_p is proportional to the long term heat loads $\dot{Q}_y$ thus, considering a building with balanced heating and cooling request leads to small temperature penalty values.

Therefore, the correct evaluation of the temperature penalty parameter becomes mandatory for the correct sizing of the BHE field, especially for buildings with unbalanced seasonal loads.

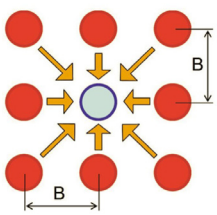

Figure 1. Superposition of thermal effects behind the concept of θ_8 temperature excess.

Fossa and Rolando (2015) and Fossa (2016) proposed a method based on the interaction of each borehole in a field with the eight neighboring ones (for this reason called T_{p8}) according to Figure 1. With respect to the central one, four BHEs are at distance B and four at distance $B\sqrt{2}$.

The excess temperature for the central BHE is calculated by the superposition of the corresponding ILS solution for the other BHEs:

$$\theta_8 = T(r_b) - T_{gr,\infty} = \dot{Q}_y \frac{E_1(\tau_N, B) + E_1(\tau_N, B\sqrt{2})}{\pi k_{gr} L} \tag{5}$$

The T_{p8} formulation is intentionally similar to the Kavanaugh and Rafferty (1997) corresponding one:

$$T_{p8} = \theta_8 \frac{aN_4 + bN_3 + cN_2 + dN_1}{N_{tot}} \tag{6}$$

where N_4, N_3, N_2 and N_1 are the number of boreholes surrounded by only 4 other ones, only 3 other ones, and so on, respectively.

The constant a, b, c, d are evaluated by optimum search by comparison with the "correct" BC III g-functions for a large number of different BHE field configurations, considering a reference BHE depth H_{ref} equal to 100 m. For different BHE depths, Fossa and Rolando (2015) suggest the following correction in the evaluation of the Fourier number to be used in the E_1 calculation (Eq.5):

$$Fo^* = Fo(\tau_N, R) \cdot \left(\frac{H_{ref}}{H} \right) \tag{7}$$

Where R can be either B or $B\sqrt{2}$. Worth noticing, the above correction also works for coping with BHE filed configurations where r_b/H is different from the reference 0.0005 value at which the constants in Eq.(6) have been calculated. A demonstration in this sense is not provided here for the sake of brevity.

BUILDING AND VALIDATING THE NEW TP8 METHOD

A large set of BHE configurations has been considered in order to calculate the 4 constants to be employed in Eq. (6). For each configuration the corresponding BC III g-function has been calculated and adopted as a reference for evaluating the correct value of the T_p according to Eq. (4) and for estimating the uncertainty of the proposed model. Some of these reference g-functions are from Eskilson thesis, some are from EED database, and all of them have been cross checked. As an example in Figure 2a and 2b some reference g-function values are presented together with the original Eskilson profiles for two rectangular configurations and different values of the B/H parameter.

The BHE fields include square and rectangular configurations (up to 10x12 BHEs) and non-rectangular configurations. The non-rectangular configurations include: in-line (up to 16x1), L shaped (up to 10x10L), U shaped (up to 10x10U) and empty rectangles (up to 10x10O).

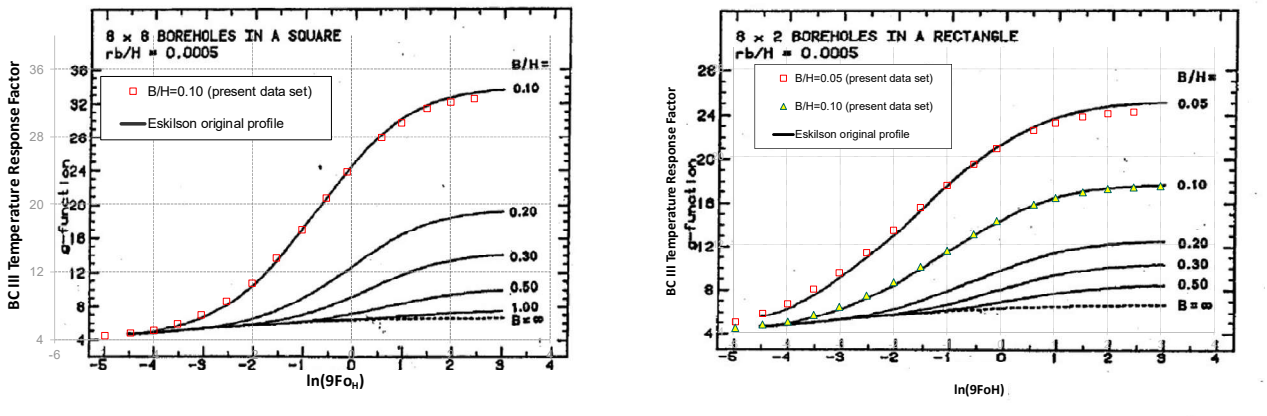

(a) (b)

Figure 2. Comparison between present data set values and original Eskilson g-function profiles for different values of the B/H parameter. (a) 8 x 8 in a square; (b) 8 x 2 in a rectangle.

Similarly, to the work proposed by Fossa and Rolando (2015) slender rectangular configuration with an aspect ratio greater than 3 are accounted as non-rectangular configurations. Compared to the set of configurations employed in Fossa and Rolando (2015) the range considered in this paper is wider and includes slender rectangular shapes with lower dimension greater than 2, such as 10x3 and 12x3.A BHE depth (H) equal to 100 m has been adopted for all the configurations and different BHE spacing (B) has been employed in order to have dimensionless BHE spacings (B/H) of 0.03, 0.05, 0.075, 0.1 and 0.125. As a result, an overall number of 300 BHE fields have been considered, including 150 rectangular configurations and 150 non-rectangular configurations. A dimensionless reference radius $(r_b/H)_{ref}$ has been adopted equal to 0.0005 for all the calculations.

Moreover, for all the calculations a ground thermal conductivity of 2.7 W/(mK) and a ground thermal diffusivity of 1.65E-6 m²/s have been used. A reference unbalanced heat load profile (with no cooling mode) has been adopted to design each of the 300 configurations employing the BC III g-function. Worth noticing, given the implicit nature of Eq. (3), the heat load profile has been scaled for each configuration in order to obtain a design BHE depth of 100m as a result of an iterative calculation. Similarly to Fossa and Rolando (2015), an optimization procedure has been implemented in a proprietary code in order to minimize the objective function F shown in Eq. (8):

$$F(a,b,c,d) = \frac{1}{BHE_k} \sum_{j=1}^{BHE_k} \frac{\left| T_{p,j} - T_{p8,j} \right|}{T_{p,j}} \tag{8}$$

Where k refers either to the 150 rectangular configurations or to the 150 non-rectangular configurations. The 4 constants a, b, c and d that have been iteratively refined in order to minimize the absolute overall percentage error of the T_{p8} with respect to the reference T_p.

RESULTS AND DISCUSSION

The objective function defined in Eq. (8) has been minimized through the refinement of the 4 coefficients a, b, c and d. The optimum search procedure, described in the previous section, has been applied separately to rectangular (R) and non-rectangular (non-R) configurations. The optimization procedure has been performed also considering separately the respective dimensionless BHE spacing, following the same procedure adopted in Fossa and Rolando (2015). Table 2 and Table 3 show the raw value obtained by the performed optimization and no further attempt to level the resulting values has been carried out. The inspection of the constant values, for both R and non-R configurations, reveals the possibility to interpolate the results for any B/H between 0.03 and 0.125.

The whole set of 300 configurations has been used to calculate the overall errors of the proposed new T_{p8} coefficients and to validate the proposed model. Preliminary further comparisons, to be discussed in a future work, confirm the reliability of the present method also outside the perimeter of the reference data set. Figure 3 shows the results of the new T_{p8} model in terms of overall BHE length (Figure 3a) and temperature penalty values (Figure 3b). In particular, Figure 3a shows the very good agreement of the design borehole length evaluated with the T_{p8} model (L_8) compared to the overall length calculated with the reference model based on the BC III g-functions. The overall percentage difference between L and L_8 is only 2.95%. Similarly, Figure 3b shows the same results in terms of temperature penalty values. The comparison shows a good agreement between the T_{p8} and the T_p, especially considering large rectangular configurations. A tendency of exceeding the ±10% agreement can be noticed for rectangular configurations with relatively low values of temperature penalty (i.e. low overall borehole length). The overall percentage difference between the T_{p8} and the T_p values is 9.86%, while the maximum difference is almost 40%, but for only one case among those here considered.

Worth noticing, the results of the overall difference between the proposed method and the reference based on the BC III g-functions are very similar to the results obtained by the parameter estimation analysis carried out by Fossa and Rolando (2015) where the reference models were the BC I and BCII g-functions. In that case, the overall percentage differences between the T_{p8} method and the reference were 2.7% for the overall borehole length and 9.4% for the temperature penalty values.

Figure 4 shows the comparison between the original Kavanaugh and Rafferty method (Ashrae first method) and the reference BC III model in terms of overall BHE length and temperature penalty for all the 300 configurations considered in the present analysis. In terms of design borehole length, the underestimation

tendency and the deviation from the theoretical agreement for medium and large borefield (e.g. L>1000m) is confirmed and shown in Figure 4a. The comparison in terms of temperature penalty shown in Figure 4b confirms also the low agreement between the T_{pA} and the T_p values.

Table 2. Constants to be employed in Eq. (6) for Rectangular (R) configurations

Rectangular configurations					
B/H	**0.03**	**0.05**	**0.075**	**0.1**	**0.125**
a	4.840	3.824	3.194	2.373	2.072
b	0.4132	0.4045	0.4403	0.5069	0.5118
c	0.3041	0.2894	0.2793	0.2618	0.2525
d	0	0	0	0	0

Table 3. Constants to be employed in Eq. (6) for non-R configurations

Non-Rectangular and slender Rectangular configurations (6x2, 7x2, 10x3, 12x3)					
B/H	**0.03**	**0.05**	**0.075**	**0.1**	**0.125**
a	3.173	2.571	2.275	1.752	1.567
b	1.0587	0.9129	0.8241	0.7166	0.6702
c	0.7192	0.6037	0.5140	0.4081	0.3645
d	0.05	0.05	0.05	0.05	0.05

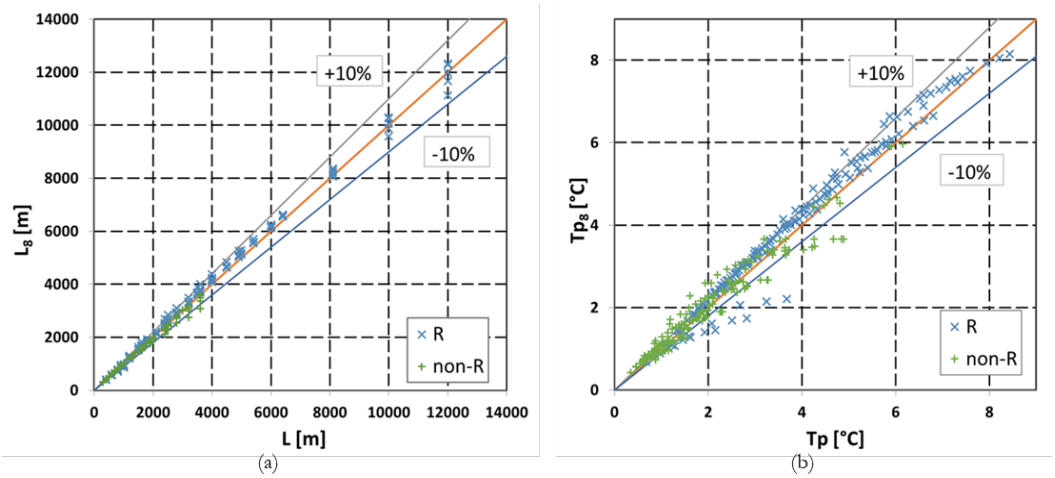

Figure 3. Comparison between calculated overall length L (a) and temperature penalty T_p (b) according to the reference model and the proposed T_{p8} model for 300 BHE configurations.

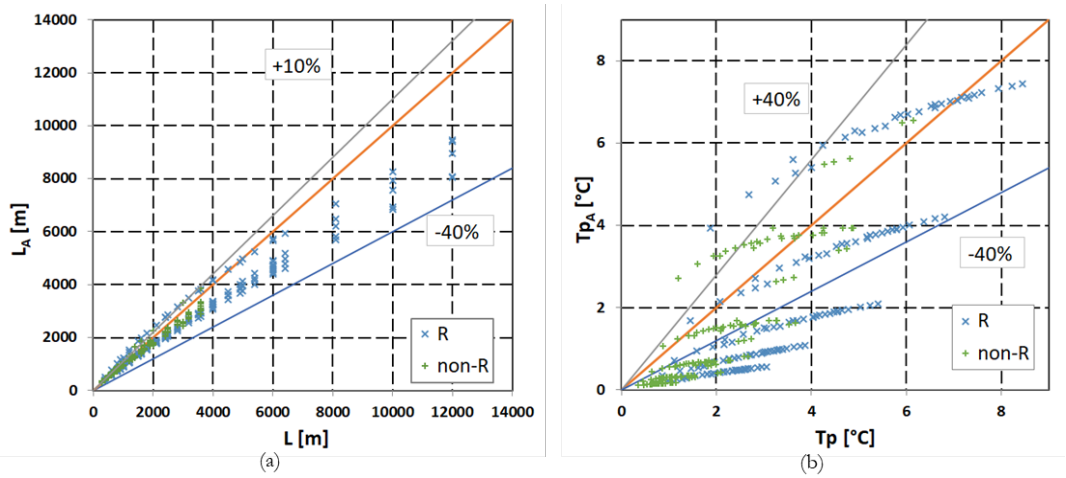

Figure 4. Comparison between calculated overall length L (a) and temperature penalty T_p (b) according to the reference model and the original Kavanaugh and Rafferty model for 300 BHE configurations.

CONCLUSIONS

In this paper a new version of the modified Ashrae method is discussed in order to propose a reliable and simple procedure for the design of BHE fields. The new method is based on the constant refinement procedure already proposed by Fossa and Rolando (2015). In this paper, a new set of constant for the evaluation of the temperature penalty has been obtained through an optimum search procedure based on the BC III *g*-functions and considering 300 BHE configurations. It has been demonstrated that the implemented approach for calculating the new constants used in the evaluation of the temperature penalty values is reliable and consistent.

The average percentage difference of the proposed method is less than 3% compared to the reference one and a very good agreement for a large variety of BHE configurations has been proven. For these reasons, the present method is proposed as a simple and valuable tool for BHE field design.

NOMENCLATURE

B	=	BHE spacing (m)
k	=	Thermal conductivity (W/mK)
Fo	=	Fourier number
H	=	BHE depth (m)
L	=	Overall BHEs length (m)
$\dot{Q}$	=	Heat rate (W)
$\dot{Q}'$	=	Specific heat rate (W/m)
r	=	Radial distance (m)
R	=	Ground resistance (mK/W)
T	=	Temperature (K)

Subscripts

ave	=	average value
b	=	borehole
f	=	fluid
G	=	ICS solution for imposed heat transfer rate boundary condition
gr	=	ground
H	=	based on BHE depth
h	=	referred to 6 hours
m	=	referred to 1 month
y	=	referred to 10 years
ref	=	reference value
∞	=	undisturbed and initial condition

REFERENCES

Ahmadfard, M. and M. Bernier. 2014. *An alternative to ASHRAE's design length equation for sizing borehole heat exchangers*. ASHRAE Annual Conference, Seattle, WA, June 28–July 2, 1–8.

Ahmadfard, M. and M. Bernier. 2018. *Modifications to ASHRAE's sizing method for vertical ground heat exchangers*. Science and Technology for the Built Environment.

ASHRAE. 2015. Chapter 34, Ashrae Handbook-HVAC Applications: Geothermal Energy Atlanta: ASHRAE.

Bernier, M. 2006. *Closed-loop ground-coupled heat pump systems*. ASHRAE Journal 48(9):12–19.

Bernier, M., A. Chahla, and P. Pinel. 2008. *Long-term ground temperature changes in geo-exchange systems*. ASHRAE Transactions 114: 342–350.

Capozza, A., M. De Carli and A. Zarrella. 2012. *Design of borehole heat exchangers for ground-source heat pumps: A literature review, methodology comparison and analysis on the penalty temperature*. Energy and Buildings 55: 369–379.

Carslaw, H.S. and J.C. Jaeger. 1947. Conduction of heat in solids, Claremore Press, Oxford, U.K.

Cimmino, M. and M. Bernier. 2014. *A semi-analytical method to generate g-functions for geothermal bore fields*. J. of Heat and Mass Transfer: 641-650.

Cimmino, M., M. Bernier and F. Adams. 2013. *A contribution towards the determination of g-functions using the finite line source*. Applied Thermal Engineering 51(1-2): 401-412.

Claesson, J. and S. Javed. 2011. *An analytical method to calculate borehole fluid temperatures for time-scales from minutes to decades*, ASHRAE Transactions 117 (2): 279-288.

Eskilson, P. 1987. *Thermal analysis of heat extraction boreholes*. Ph.D. Thesis. Lund University of Technology, Sweden.

Fossa, M. 2016. *Correct design of vertical borehole heat exchanger systems through the improvement of the ASHRAE method*. Science and Technology for the Built Environment. DOI: 10.1080/23744731.2016.1208537.

Fossa, M. and A. Priarone. 2018. *Constant temperature response factors for fast calculation of sparse bhe field G-functions*. Submitted to Renewable Energy. Manuscript number: RENE-D-18-00806

Fossa, M. and D. Rolando. 2014. *Improving the Ashrae method for vertical geothermalborefield design*. 11th International Energy Agency Heat Pump Conference, Montreal, Canada.

Fossa, M. and D. Rolando. 2015. *Improving the Ashrae method for vertical geothermal borefield design*. Energy and Buildings 93: 315–323.

Fossa, M. 2011. *The temperature penalty approach to the design of borehole heat exchangers for heat pump applications*. Energy and Buildings 43:1473-1479.

Fossa, M., D. Rolando, A. Priarone. 2017. *Investigation on the Effects of Different Time Resolutions in the Design and Simulation of Bhe Fields*. In: IGSHPA Conference, Denver (CO).

Fossa, M., O.Cauret and M.Bernier. 2009. *Comparing The Thermal Performance of Ground Heat Exchangers of Various Lengths*. In: Effstock Conference, Stockholm.

Hellström, G. and B. Sanner. 1994. *Earth Energy Designer: Software for Dimensioning of Deep Boreholes for Heat Extraction*, Department of Mathematical Physics, Lund University, Sweden.

Ingersoll L.R., O.J. Zobel and A.C. Ingersoll. 1954. Heat conduction with engineering, geological, and other applications, McGraw-Hill, New York.

Kavanaugh, S.P. and K. Rafferty. 1997. *Ground source heat pumps design of geothermal system for commercial and institutional buildings*. ASHRAE Hanbook, Atlanta, GA.

Lamarche L., and B. Beauchamp. 2007. *A new contribution to the finite line-source model for geothermal boreholes*. Energy and Buildings 39: 188-198.

Lamarche, L. 2017. *g-function generation using a piecewise-linear profile applied to ground heat exchangers*. Int. J. of Heat and Mass Transfer 115(B): 354-360.

Priarone, A. and M. Fossa. 2015. *Modelling the ground volume for numerically generating single borehole heat exchanger response factors according to the cylindrical source approach*. Geothermics 58: 32-38.

Priarone, A. and M. Fossa. 2016. *Temperature response factors at different boundary conditions for modelling the single borehole heat exchanger*. Applied Thermal Engineering 103: 934-944.

Spitler J.D. 2000. *GLHEPRO-a design tool for commercial building ground loop heat exchangers*. in: Proc. of 4th Int. Heat Pumps in Cold Climates Conference, Aylmer, Quebec, 17th–18th August.

Thomson, W. (Lord Kelvin). 1882-1911. Mathematical and Physical Papers. Cambridge University Press, London.

Yavuzturk, C. and J.D. Spitler. 1999. *A short time step response factor model for vertical ground loop heat exchangers*. ASHRAE Transactions 105: 475-485.

Zeng, H., N. Diao and Z. Fang. 2003. *Heat transfer analysis of boreholes in vertical ground heat exchangers*, International Journal of Heat and Mass Transfer 46: 4467–4481.

[This page has been intentionally left blank]

IGSHPA SWEDEN
2018 Research Conference

DOI: 10.22488/okstate.18.000007

On the role of vertical ground heat flux for analytical simulation of borehole heat exchangers

Peter Bayer **Jaime A. Rivera** **Philipp Blum**

ABSTRACT

Analytical modelling techniques are frequently used for prediction of the impacts of borehole heat exchangers (BHEs) on the thermal conditions in the subsurface. They are appealing because they are easy to use, compact and computationally efficient. However, analytical formulations also cut down the complexity of the conditions in the field by limited resolution of variations in space and time, and by often simplified specifications of boundary conditions. In this presentation, we focus on the definition of the land surface boundary condition in line source solutions. As BHEs are thin elongated forms that can be approximated by a linear shape function, main attention is on the radial heat transfer, but less on the axial effects. Given the long operation time, however, the sharp physical boundary at the top may exert a substantial influence on the temperature evolution in the shallow ground and thus influence the performance of the ground source heat pump. We examine different formulations with Dirichlet and Cauchy type boundaries included in the line source equation, with and without horizontal groundwater flow. Both homogeneous as well as inhomogeneous implementations are presented, which offer new flexibilities for simulation of nonuniform land surface impacts such as associated with varying land use types. The presented approach also facilitates to account for the accelerated ground heat flux due to global warming and due to urbanization such as observed in so-called subsurface urban heat islands in many cities.

INTRODUCTION

Shallow geothermal energy use by borehole heat exchangers (BHEs) focus on the heat stored just below the ground surface. Usually, BHEs are drilled to a depth of 80 - 400 m, but for example in Germany, most installations do not reach much deeper than 100 m (Stauffer et al. 2013). Energy balance calculations for such systems show that long term heat extractions source mainly energy stored in the ground (Nouanegue et al. 2009). However, cooling of the ground accelerates heat flux through the ground surface. Considering a full life cycle of a BHE, which covers the period of operation and recovery afterwards, around two thirds of the energy deficit in the ambient ground is filled up by heat transfer from the ground surface (Rivera et al. 2015b). This emphasizes the importance of considering or neglecting heat flux from the ground surface in BHE simulation and design.

The shallow geothermal energy reservoir benefits from global warming. Due to atmospheric temperature increase, ground heat will naturally increase in the future. Beltrami et al. (2002), has estimated that for the last half of the 20th century, the mean continental ground heat flux in the subsurface has been around 39 mW/m². The distribution of the associated ground heat gain is heterogeneous in space and time (Kurylyk et al. 2014; Benz et al.

Peter Bayer (mail@bayerpeter.com) is a professor of geothermics at Ingolstadt University of Applied Sciences, Jaime A Rivera holds a Ph.D. degree in Earth Sciences, and Philipp Blum is a professor of Engineering Geology at the Karlsruhe Institute of Technology (KIT), Germany.

2017). In urban environments, temperatures in shallow ground have been rising even more since industrialization. This is not simply a consequence of urban heat islands in the atmosphere that are thermally coupled with the ground (Kataoka et al. 2009) (Fig. 1a). Recently, attention to the so-called subsurface urban heat islands (Ferguson and Woodbury 2007) has been growing, especially because in cold and moderate climates such as those found in central Europe, large scale thermal anomalies are found beneath cities (Menberg et al. 2013; Benz et al. 2015; Bayer et al. 2016; Mueller et al. 2018). Compared with their counterpart in the atmosphere, much more pronounced permanent thermal anomalies are measured, and thus subsurface urban heat islands have a substantial geothermal potential (Zhu et al. 2010; Radioti et al. 2017; Rivera et al. 2017). As an example, Fig. 1b depicts two typical temperature profiles recorded in BHEs before start of operation, using a wireless temperature logger, in urbanized areas of Switzerland NIMO-T (Rohner et al. 2005). The profiles are site-specific, but all delineate clearly increased temperatures in the uppermost tens of meters. BHE simulation techniques that account for such vertical temperature variations, however, are not common (Bandos et al. 2009).

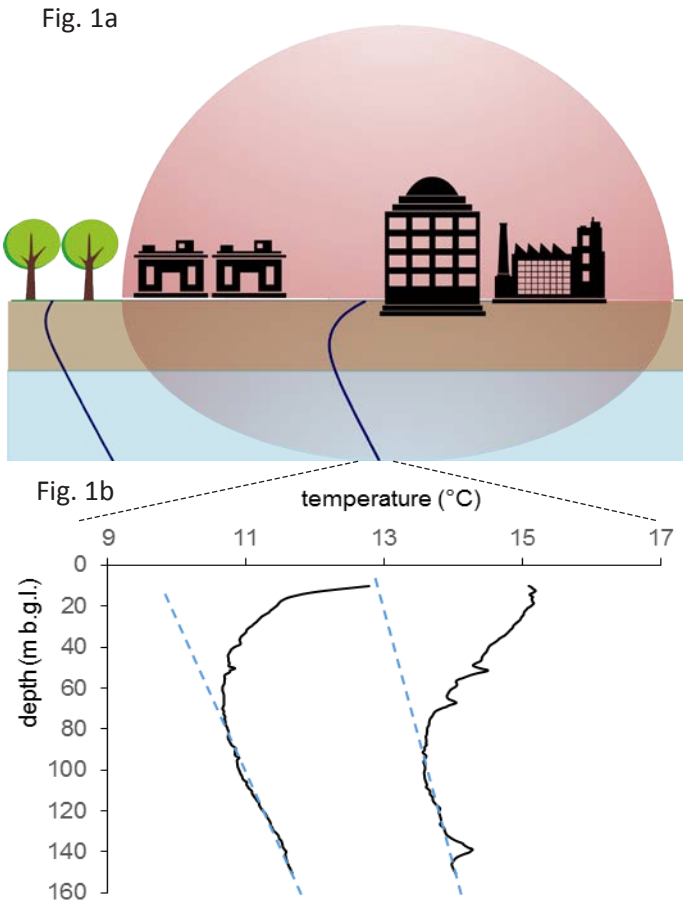

Figure 1 a) Illustration of atmospheric and subsurface urban heat islands with characteristic borehole temperature profiles through the shallow ground and groundwater. The bottom plot (b) depicts two measured profiles in Switzerland (black curves), with comparison of the interpolated temperature trend based on the (expected) ambient geothermal gradient (blue dashed lines).

In a series of recent papers, we presented and applied analytical modelling concepts that account for ambient ground warming in different ways and include ground heat flux processes based on the common line-source equation approach (Rivera et al. 2015a; Bayer et al. 2016; Rivera et al. 2016b, 2016a). We distinguished implementations with fixed temperature and Cauchy (or Robin) type top boundary conditions (BCs) to capture the heat transfer processes at the ground surface. This was complemented by moving line source formulations, including the effect of horizontal groundwater flow. It was revealed that, when taking the city of Zurich as a study case, each degree of ground heating saves 4 m of the borehole to supply a given heat demand. In highly urbanized regions, heat extraction can be increase by 13 % to 40 % depending on BHE layout, depths and physical ground conditions. These values clearly demonstrate the importance of accounting for elevated ground temperatures and heat flux in urban environments for proper BHE planning. In contrast, by ignoring such effects, the renewability of shallow geothermal systems will be undervalued and the performance of BHEs for heat extraction will be underestimated. When the focus is set on cooling by means of BHEs or geothermal wells, however, ambient ground heating in the future represents a clear disadvantage, e.g. (Epting et al. 2013).

In this presentation, we present a line source formulation, which includes a non-homogeneous BC to account for spatially variable heat exchange at the land surface. It is applied to example cases with different heat flux into the subsurface as a consequence of variable land use in the surrounding of a BHE. We inspect the role of different BC formulations on the thermal regime in the ground, including conditions with horizontal groundwater flow. The findings are useful for revealing the consequence of elevated ground heat flux in an urban environment on the long-term performance of BHEs.

METHODOLOGY

The coupled thermal interaction between BHEs and non-uniform transient ground surface effects is accounted for via superpositioning of Green´s functions (Rivera et al. 2016b, 2016a). Considering the model shown in Figure 2 and for the general case where the thermal regimes above and below the ground surface are coupled through Cauchy type BCs, the solution reads:

$$T_C = \omega_C + \beta_C \tag{1}$$

where T_C is temperature at any point in time within the half-space, and ω_C and β_C are respectively solutions of the associated non-homogenous and homogeneous boundary value problems:

$$\beta_C = \beta_{MFLS}(\boldsymbol{x}, \boldsymbol{x}', t) + \Delta\beta_C(\boldsymbol{x}, \boldsymbol{x}', t) \tag{1}$$

$$\beta_{MFLS}(\boldsymbol{x}, \boldsymbol{x}', t) = \frac{q}{8\lambda\pi} exp\left(\frac{x - x'}{2a} v\right) \int_{\frac{r_d^2}{4at}}^{\infty} \frac{1}{\varphi} exp\left[-\varphi - \left(\frac{r_d v}{4a}\right)^2 \frac{1}{\varphi}\right] \left\{2erf\left(\frac{z}{r_d}\sqrt{\varphi}\right) - erf\left(\frac{z - H}{r_d}\sqrt{\varphi}\right) - erf\left(\frac{z + H}{r_d}\sqrt{\varphi}\right)\right\} d\varphi \tag{3}$$

$$\Delta\beta_C(\boldsymbol{x},\boldsymbol{x}',t) = \frac{q}{4\lambda\pi} exp\left(\frac{x-x'}{2a}v\right) \int_{\frac{r_d^2}{4at}}^{\infty} \frac{1}{\varphi} exp\Big(-\varphi - \left(\frac{r_d v}{4a}\right)^2 \frac{1}{\varphi}\Big)\left\{exp\left(hz + \left(\frac{hr_d}{2}\right)^2 \frac{1}{\varphi}\right)\left[erfc\left(\frac{z\sqrt{\varphi}}{r_d} + \frac{hr_d}{2\sqrt{\varphi}}\right) - exp(hH)erfc\left(\frac{z+H}{r_d}\sqrt{\varphi} + \frac{hr_d}{2\sqrt{\varphi}}\right)\right]\right\} d\varphi \quad (4)$$

$$\omega_C(\boldsymbol{x},t) = \frac{Hh}{16} \int_{\frac{H^2}{4at}}^{\infty} T_s\left(t - \frac{H^2}{4a\varphi}\right)\left\{\frac{2}{\sqrt{\pi\varphi^3}} exp\left[-\left(\frac{z}{H}\right)^2 \varphi\right] - \frac{Hh}{\varphi^2} erfc[\sigma(z,\varphi)]\, exp[\rho(z,\varphi)]\right\} \Delta(\boldsymbol{x},\varphi) d\varphi\,, \quad z \neq 0 \quad (2)$$

with:

$$\Delta(\boldsymbol{x},\varphi) = \left[erf\left(\frac{y-y_b}{H}\sqrt{\varphi}\right) - erf\left(\frac{y-y_a}{H}\sqrt{\varphi}\right)\right]\left[erf\left(\frac{x-x_b}{H}\sqrt{\varphi} - \frac{vH}{4a\sqrt{\varphi}}\right) - erf\left(\frac{x-x_a}{H}\sqrt{\varphi} - \frac{vH}{4a\sqrt{\varphi}}\right)\right] \quad (6)$$

$$\sigma(z,\varphi) = \frac{z}{H}\sqrt{\varphi} + \frac{Hh}{2\sqrt{\varphi}} \qquad \rho(z,\varphi) = zh + \frac{(Hh)^2}{4\varphi} \quad (7\ a,b)$$

$$r_d^{\,2} = (x-x')^2 + (y-y')^2 \quad (8)$$

The related solution with prescribed temperature at the ground surface (Dirichlet BCs) can be obtained by considering the coupling coefficient *h* infinite. A more detailed description of this coefficient can be found in Rivera et al. (2016a, 2016b).

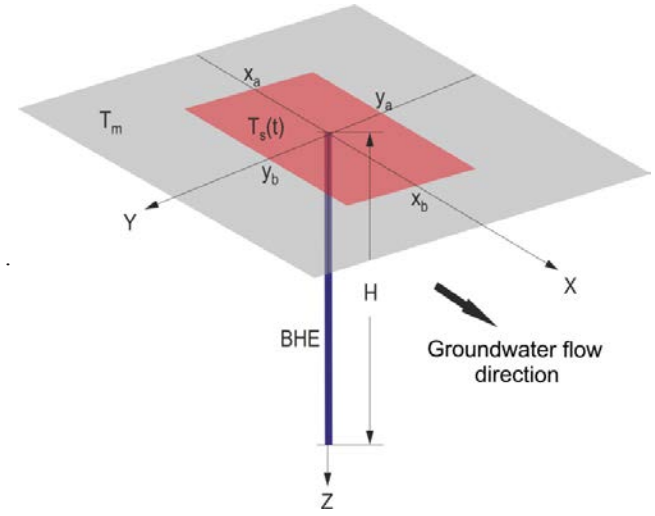

Figure 2 Conceptual model representing spatial variability of above-ground temperatures in urban environments. The red plane within the coordinates $[x_a, x_b]$ and $[y_a, y_b]$ represents a distinctive above-ground temperature, T_s, in comparison to the background conditions, given by the mean reference temperature T_m. BHE denotes the position of the vertical borehole heat exchanger (Rivera et al. 2016b).

MODEL APPLICATION AND RESULTS

By superpositioning the model described in Figure 2, it is possible to estimate transient three-dimensional (3D) temperature fields such as the one illustrated in Figure 3. In this arbitrary scenario, heat is extracted from the ground via a BHE (located at z-arrow), while the basal heat losses from two buildings partially replenish the induced heat deficit. The buildings and the bare soil area are represented as planar sources with periodic above-ground temperatures with mean values of 22 °C and 12 °C respectively. The undisturbed ground temperature is 11°C. Further model parameter settings are oriented at those utilized in (Rivera et al. 2016b). The figure demonstrates a strong influence of permanent local heat sources such as the buildings adjacent to a BHE. It also reveals the resulting non-uniform thermal regime in the ground assuming long term heat extraction by the BHE (30 W/m) and ambient groundwater flow with Darcy flux of 10^{-7} m/s in x-direction.

In the next step, we examine in more detail the role of thermal coupling at the land surface and choose the simple case delineated in Figure 2. The temperature (in dimensionless form) is calculated along the x-axis for different levels of coupling between the thermal fields below and above the ground surface. The coordinates x_a and x_b are also normalized (here x_a = -0.5 and x_b = 0.5) and indicate for instance, the boundaries of a building. Figure 4 describes the coupled thermal effect of a BHE extracting heat and spatially variable ground heat flux on the thermal regime at the ground surface. The BHE is located at x = 0 as it is evident from the induced temperature minimum. The temperature directly above the building slab is 1 (dimensionless). This case is also delineated by the red dashed line corresponding to the solution assuming Dirichlet BCs (T_D). This implies that the ground surface temperature is identical to the temperature directly above it.

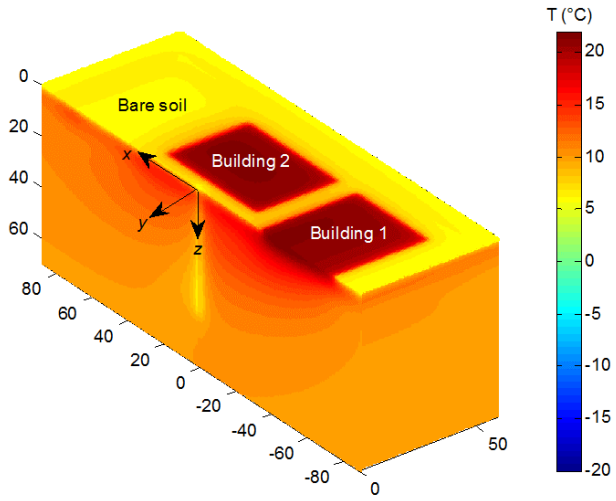

Figure 3 Temperature distribution after 25 years obtained with the analytical model for a synthetic exemplary scenario with two buildings and one BHE. Groundwater flows along the positive *x* direction.

As the level of coupling (represented by the product H·h) decreases, the difference between ground -and above ground surface temperature becomes more evident. This is a crucial point for simulating temperature fields near the ground surface (e.g. during the operation of very shallow geothermal systems) where most commonly prescribed BCs with fixed temperatures are assumed. Such settings have a crucial impact on the computed long term energy balance for geothermal systems since they govern the time-dependent power contribution from the shallow reservoir (Rivera et al. 2015b). The deeper BHEs are installed, the lower is the relative impact of the specification of the top boundary in the model. However, the impact of locally elevated ground heat flux grows with time. Considering BHE life times of decades, so even BHEs operating at a depth of 100 m can be remarkably influenced (Bayer et al. 2016; Rivera et al. 2017).

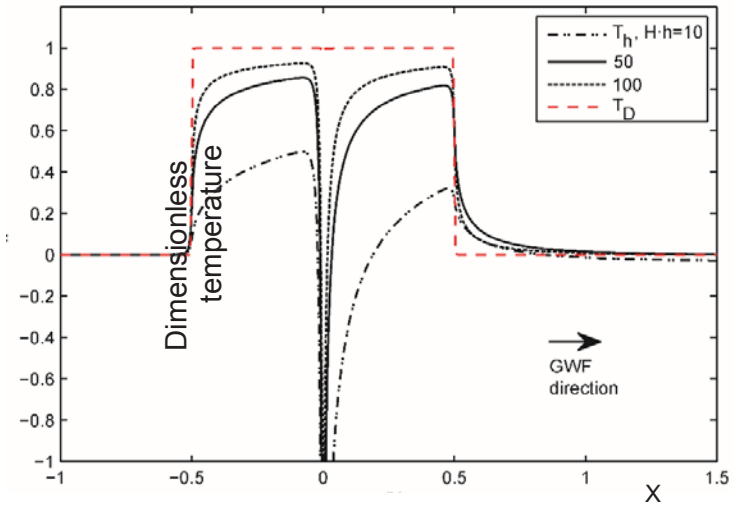

Figure 4 Dimensionless steady state ground surface temperature for the model shown in Figure 2. Dirichlet- (T_D) and Cauchy-type (T_h) BCs are compared changing the product *H·h* via the coupling coefficient *h*..

CONCLUSIONS

The presented discussion of nonuniform, spatially and temporally variable ground heat flux is crucial for facilitating a process-based prediction of the thermal regime evolving during decades of BHE operation. As demonstrated, complex heat transport mechansims at the land surface can be considered in standard line-source formulations by variable formulation of the top boundary condition in a superpositioned BHE model. The presented third type boundary condition (BC) offers more flexibility to the mathematical formulation of heat fluxes at the ground surface. Still, it is clear that any type of BC used in a mathematical model (e.g., the first-, second-, and third-kind BCs) represents a simplified approximation to actual conditions. Therefore, the appropriate choice of BC needs to be decided for each case study individually.

As demonstrated, it is also possible to account for horizontal groundwater flow and advection, as well as multiple BHE fields. The obtained model framework can be used to simulate the transient 3D thermal regime in the ground and, for instance, elaborate in more detail parameter sensitivities. It is suitable for depicting the specific conditions beneath cities, and in particular the role of accelerated heat flux in the ground as observed in urban settlements worldwide. This is important, because in cities with evolving subsurface heat islands the (seasonal) regeneration potential of BHEs is improved. Considering a continuous increase in the density of geothermal installations in cities, proper characterisation of vertical heat flow mechanisms will thus gain interest in the future.

ACKNOWLEDGEMENTS

This work has been supported by the German Research Foundation (project BA2850/3-1).

NOMENCLATURE

a	= thermal diffusivity ($m^2\ s^{-1}$)
b	= coupling coefficient (m^{-1})
H	= borehole length (m)
q	= heat flow rate per unit length ($W\ m^{-1}$)
r_d	= horizontal radial distance from the borehole (m)
t	= time (s)
T	= temperature in the porous medium (°C)
T_m	= reference initial and surrounding temperature (°C)
T_s	= above-ground temperature (°C)
$\boldsymbol{X}$	= coordinates vector where temperature is evaluated (m)
$\boldsymbol{x}'$	= coordinates vector where a heat source is released (m)
x, y, z	= single space coordinates where temperature is evaluated (m)
x_a, x_b, y_a, y_b	= boundary coordinates of the specific land use (m)
x', y', z'	= single space coordinates where heat sources are released (m)

Subscripts

C = referring to Cauchy-type boundary conditions

D = referring to Dirichlet-type boundary conditions

Abbreviations

BC = boundary condition

BHE = borehole heat exchanger

MFLS = moving finite line source

REFERENCES

Bandos, T. V., Á. Montero, E. Fernández, J. L. G. Santander, J. M. Isidro, J. Pérez, P. J. F. de Córdoba and J. F. Urchueguía. 2009. *Finite line-source model for borehole heat exchangers: effect of vertical temperature variations*. Geothermics 38 (2):263-270.

Bayer, P., J. A. Rivera, D. Schweizer, U. Schärli, P. Blum and L. Rybach. 2016. *Extracting past atmospheric warming and urban heating effects from borehole temperature profiles*. Geothermics 64:289-299.

Beltrami, H., J. E. Smerdon, H. N. Pollack and S. Huang. 2002. *Continental heat gain in the global climate system*. Geophysical Research Letters 29 (8):8-1-8-3.

Benz, S. A., P. Bayer and P. Blum. 2017. *Global patterns of shallow groundwater temperatures*. Environmental Research Letters 12 (3):034005.

Benz, S. A., P. Bayer, K. Menberg, S. Jung and P. Blum. 2015. *Spatial resolution of anthropogenic heat fluxes into urban aquifers*. Science of The Total Environment 524:427-439.

Epting, J., F. Händel and P. Huggenberger. 2013. *Thermal management of an unconsolidated shallow urban groundwater body*. Hydrology and earth system sciences 17:1851-1869.

Ferguson, G. and A. D. Woodbury. 2007. *Urban heat island in the subsurface*. Geophysical research letters 34 (23).

Kataoka, K., F. Matsumoto, T. Ichinose and M. Taniguchi. 2009. *Urban warming trends in several large Asian cities over the last 100 years*. Science of the total environment 407 (9):3112-3119.

Kurylyk, B. L., K. T. MacQuarrie and J. M. McKenzie. 2014. *Climate change impacts on groundwater and soil temperatures in cold and temperate regions: Implications, mathematical theory, and emerging simulation tools*. Earth-Science Reviews 138:313-334.

Menberg, K., P. Blum, A. Schaffitel and P. Bayer. 2013. *Long-term evolution of anthropogenic heat fluxes into a subsurface urban heat island*. Environmental science & technology 47 (17):9747-9755.

Mueller, M. H., P. Huggenberger and J. Epting. 2018. *Combining monitoring and modelling tools as a basis for city-scale concepts for a sustainable thermal management of urban groundwater resources*. Science of The Total Environment 627:1121-1136.

Nouanegue, H.-F., A. S. Shirazi and M. Bernier. 2009. *Extracted heat from geothermal boreholes: where does the energy come from*. 4th Canadian Solar Buildings Conference, Toronto, Ontario.227-236.

Radioti, G., K. Sartor, R. Charlier, P. Dewallef and F. Nguyen. 2017. *Effect of undisturbed ground temperature on the design of closed-loop geothermal systems: A case study in a semi-urban environment*. Applied energy 200:89-105.

Rivera, J. A., P. Blum and P. Bayer. 2015a. *Analytical simulation of groundwater flow and land surface effects on thermal plumes of borehole heat exchangers*. Applied Energy 146:421-433.

Rivera, J. A., P. Blum and P. Bayer. 2015b. *Ground energy balance for borehole heat exchangers: vertical fluxes, groundwater and storage*. Renewable Energy 83:1341-1351.

Rivera, J. A., P. Blum and P. Bayer. 2016a. *A finite line source model with Cauchy-type top boundary conditions for simulating near surface effects on borehole heat exchangers*. Energy 98:50-63.

Rivera, J. A., P. Blum and P. Bayer. 2016b. *Influence of spatially variable ground heat flux on closed-loop geothermal systems: Line source model with nonhomogeneous Cauchy-type top boundary conditions*. Applied Energy 180:572-585.

Rivera, J. A., P. Blum and P. Bayer. 2017. *Increased ground temperatures in urban areas: Estimation of the technical geothermal potential*. Renewable energy 103:388-400.

Rohner, E., L. Rybach and U. Schärli. 2005. *A new, small, wireless instrument to determine ground thermal conductivity in-situ for borehole heat exchanger design*. Proceedings World Geothermal Congress.

Stauffer, F., P. Bayer, P. Blum, N. M. Giraldo and W. Kinzelbach. 2013. *Thermal use of shallow groundwater*: CRC Press.

Zhu, K., P. Blum, G. Ferguson, K.-D. Balke and P. Bayer. 2010. *The geothermal potential of urban heat islands*. Environmental Research Letters 5 (4):044002.

IGSHPA SWEDEN
2018 Research Conference

DOI: 10.22488/okstate.18.000011

A hybrid model for generating short-time g-functions

Yves Brussieux **Michel Bernier**

ABSTRACT

A hybrid numerical/analytical approach is proposed to predict short-time g-functions. Transient heat transfer in the borehole is solved numerically while ground heat transfer is evaluated analytically using the infinite cylindrical heat source solution. Grid independence checks indicate that 40 radial nodes and a time step of 3 minutes represent a good compromise between computational time and accuracy. The proposed model is successfully validated against test cases, which include transient heat transfer in a plane wall and experimental data from a sand box.

In the application section of the paper, the classic ASHRAE sizing equation is modified to account for borehole thermal capacity using short-time g-functions. It is shown that the inclusion of borehole thermal capacity has a direct effect on the daily and monthly effective ground thermal resistances which reduces the required borehole length by a few percent. It is concluded that borehole thermal capacity should be included when sizing a bore field.

INTRODUCTION

Heat transfer calculations from vertical ground heat exchangers (VGHE) are typically performed over two distinct regions, within the borehole and in the ground. In the ground, transient heat transfer from the borehole wall to the far-field is evaluated with thermal response factors such as g-functions (Eskilson, 1987). In the borehole, i.e. from the fluid to the borehole wall, calculations are typically performed using a steady-state borehole thermal resistance by neglecting the fluid and grout thermal capacity within the borehole. While the steady-state assumption in the borehole is valid when the borehole operates continuously, it is shown to be inaccurate for rapidly changing borehole inlet conditions (Shirazi and Bernier, 2013) or when sizing a bore field with a short peak pulse (Ahmadfard and Bernier, 2018).

It is possible to extend the traditional (so-called long-term) g-functions to short time-steps to account for borehole thermal capacity. Thus, with this unified g-function curve, heat exchange with the ground can be predicted over time scales ranging from minutes to decades. Examples of such curves are presented in Figure 1 for a 3×2 bore field geometry. This figure is constructed with five long-term g-function curves for five B/H ratios obtained using the techniques described by Cimmino and Bernier (2013, 2014) while the short-term g-function segment is determined with the model proposed in this paper. As mentioned by Yavuzturk and Spitler (1999), much of the original g-functions calculated by Eskilson (1987) did not cover time periods of less than a month. Yavuzturk and Spitler (1999) also mention that Hellström extended the g-functions so that they could be used down to about 100 hours. For a typical borehole, this represents a value of $ln(t/t_s) \approx -8$. For lower values, it is necessary to account for transient effects in the borehole. In this paper, this is accomplished using short-time g-functions.

Yves Brussieux (yves.brussieux@polymtl.ca) is a graduate student and Michel Bernier (michel.bernier@polymtl.ca) is a professor of mechanical engineering at Polytechnique Montréal.

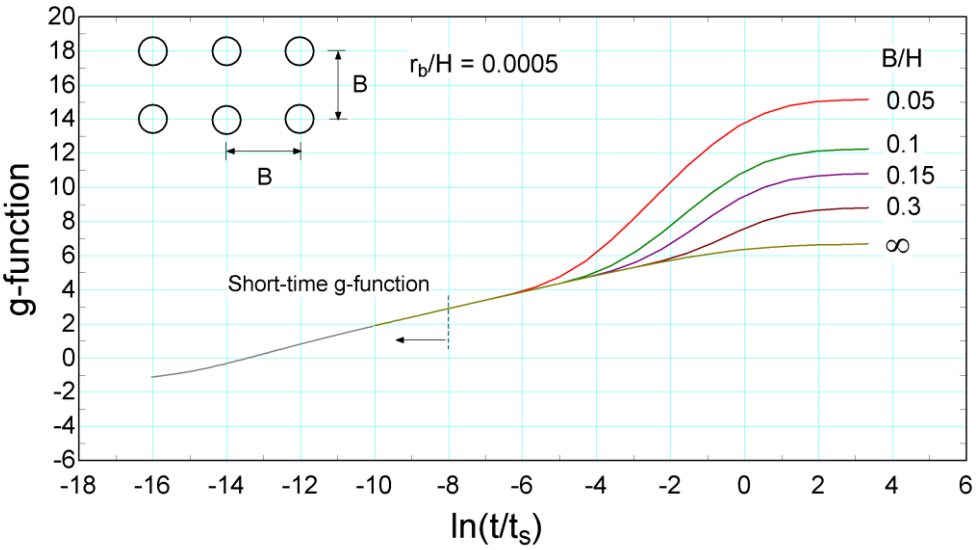

Figure 1 Short and long-term g-functions for a 3 × 2 bore field.

Yavuzturk and Spitler (1999) were the first to extend the concept of g-functions to short time steps taking into account the pipe and grout thermal capacities but neglecting the fluid thermal capacity. Xu and Spitler (2006) extended this work by approximating the U-tube geometry with a series of hollow cylinders representing the fluid, the internal convective resistance, the pipe, the grout and the ground. They have shown that results obtained with this technique compare favorably well with the ones obtained with a two-dimensional model representing the real borehole geometry.

Calculation methods to account for borehole thermal capacity were reviewed by Shirazi and Bernier (2013). Other studies which were not reviewed by these authors will now be briefly discussed.

Javed et al. (2010), Javed and Claesson (2011) and Claesson and Javed (2011) proposed an analytical one-dimensional model to simulate the short and long term thermal response of vertical ground heat exchangers where the U-tube is replaced by a composite cylinder. Borehole heat transfer is solved in the Laplace domain with the use of a circuit of thermal resistances and then inverse transforms are used to revert back to the time domain. Lamarche (2015) used a similar approach and later used his solution (Lamarche, 2016) to study the impact of short time effects on the required length of VGHE. He showed that for a particular case, the required borehole length could be overestimated by about 5% when short-term effects are neglected.

Li and Lai (2013) and Li et al. (2014) proposed a two-dimensional analytical models for U-tube boreholes in which each tube is replaced by an infinite line source. Their results match experimental data with good accuracy for times as short as several minutes. Ma et al. (2015) used a similar composite-medium line source but in three-dimensions to also account for the variation of fluid temperature along the U-tube. However, the fluid thermal capacity is not taken into account in these models. Yang and Li (2014) compared the composite-medium line-source analytical solution of Li and Lai (2013) with a new two-dimensional model using a finite volume approach. This model uses the same assumptions and also considers the influence of the fluid thermal capacity. It is shown that the results are very similar but a better estimation is made with the numerical model for the first few minutes.

Bauer et al. (2011) proposed a three dimensional model based on a thermal resistance and capacity network, however, such a degree of precision imply relatively high computational costs. Rees (2015) presents a two-dimensional model based on the finite volume method to allow for fluctuations of the fluid temperature along the U-tube. Kim et al. (2014) used a hybrid model, numerical inside the borehole and analytical in the ground, to account for borehole thermal capacity. They used an equivalent radius and a state model size reduction technique to limit computation time. Despite these simplifications, they show results quite similar to analytical models. Ruiz-Calvo et al. (2015) proposed a

model called Borehole-to-Ground (B2G) with a thermal network approach to evaluate the internal thermal resistance. This model accounts for grout and fluid thermal capacities and is also combined with long term g-functions (Ruiz-Calvo et al., 2016) to obtain a complete model. Parisch et al. (2015) accounted for the fluid and grout thermal capacities by adding an adiabatic pipe, which accounts for the borehole thermal capacity, upstream of a steady-sate borehole model. Simulations results in TRNSYS performed with this approach show significant improvements.

In the present work, a hybrid approach is proposed to predict short-time g-functions. First, the U-tube geometry is transformed into an equivalent composite cylinder using the approach suggested by Xu and Spitler (2006). Then, heat transfer from the fluid to the borehole wall is evaluated numerically using Patankar's (1980) finite volume approach. Finally, ground heat transfer is evaluated analytically using the infinite cylindrical heat source solution where the heat transfer rate at the borehole wall is obtained from the numerical solution.

After a presentation of the governing equations and the solution methodology, the paper addresses the issue of grid independence and makes recommendations on the number of required nodes and time-step durations to obtain accurate solutions. The approach is then validated against analytical solutions and experimental data. In the application section of the paper, the ASHRAE sizing equation for VGHE is used in conjunction with short-time g-functions to show the impact of borehole thermal capacity on sizing.

PROPOSED MODEL

The following model is based on the equivalent geometry proposed by Xu and Spitler (2006) and illustrated in Figure 2. The two-pipe geometry, with a borehole radius r_b, is converted into a composite cylinder configuration with the same borehole radius. The outer pipe radius of the equivalent geometry, $r_{eq,out,p}$, is set equal to $\sqrt{2}\, r_{out}$. This ensures that the volume occupied by the grout is the same in both the real and equivalent geometry. The inner pipe radius of the equivalent geometry, $r_{eq,in,p}$, is set equal to $r_{eq,out,p}$ minus the pipe thickness Δ ($= r_{out} - r_{in}$). Then a mass-less convection layer with a thickness of $0.25 \times \Delta$ followed by a fully-mixed fluid layer with a thickness of $0.75 \times \Delta$ are used as suggested by Xu and Spitler (2006). An additional radius, r_{far} , is used by Xu and Spitler (2006) to set the far-field radius in the ground for their numerical model. This radius is not required here since ground heat transfer is handled with an analytical solution. An equivalent fluid thermal capacity, $\rho Cp_{eq,f}$, is determined based on the actual fluid thermal capacity, ρCp_f, as follows:

$$\rho Cp_{eq,f} = \frac{2r_{in}^2}{\left(r_{eq,in,c}^2 - r_{eq,f}^2\right)} \rho Cp_f \tag{1}$$

The local fluid is at a temperature equal to the average borehole fluid temperature, T_f, while the undisturbed ground temperature is given by T_g. The steady-state borehole thermal resistance, R_b, is equal for both geometries. It is determined here using the first order multipole method (Hellström, 1991) based on the real geometry. Once the value of R_b is known, each layer are assigned equivalent properties as shown in Table 1.

Governing equations and boundary conditions

One-dimensional transient heat transfer in the composite cylinder, is governed by the following equation:

$$\rho C_p \frac{\partial T}{\partial t} = k \frac{1}{r} \frac{\partial}{\partial r}\left(r \frac{\partial T}{\partial r}\right) \tag{2}$$

where ρ, C_p and k are, respectively, the density, specific heat and thermal conductivity. This equation is subjected to the following initial and boundary conditions:

$$T_{t=0} = T_g \quad ; \quad T_{r=r_b} = T_w(t) \quad ; \quad q_{r=r_{eq,f}} = q_f \tag{3}$$

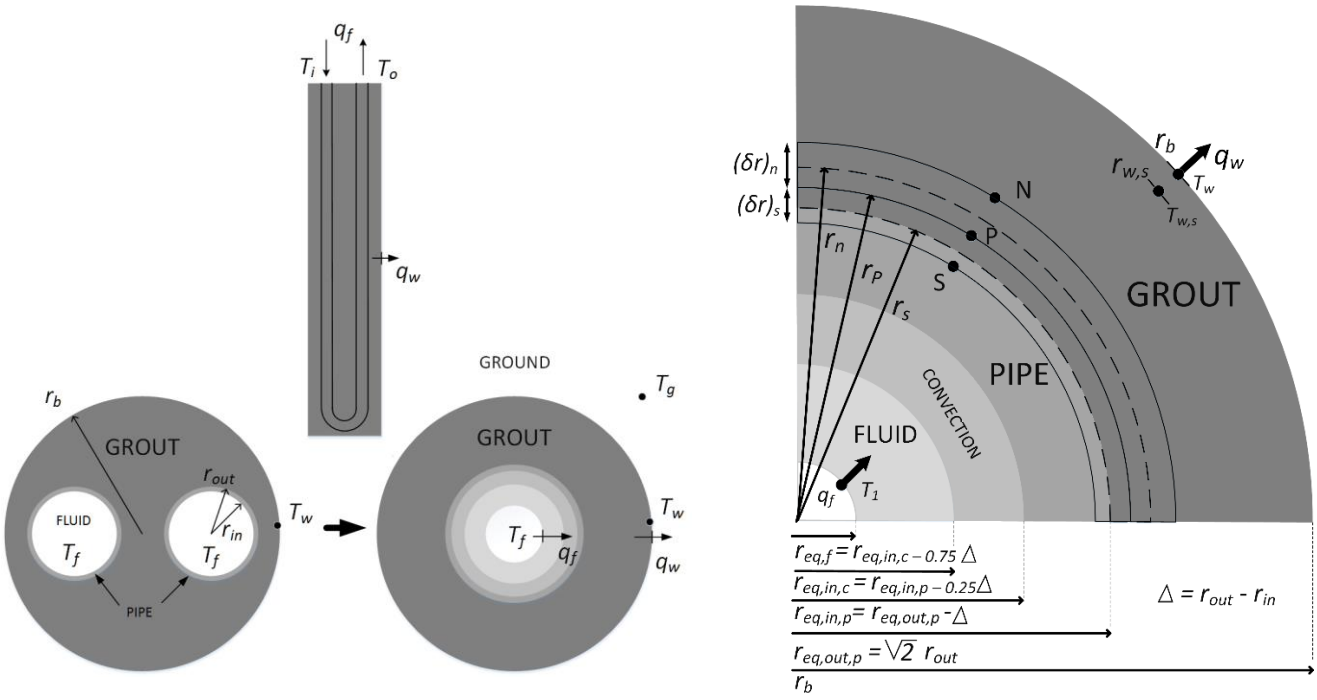

Figure 2 Approximation of the real geometry with an equivalent composite cylinder (left). Dimensions (not to scale) of the various layers and grid layout (right).

Table 1. Equivalent properties for each layer

Layer	Thermal resistance (m-K/W)	Thermal conductivity (W/m-K)	Thermal capacity (ρCp) (kJ/m³-K)
Convection	$R_{eq,c} = \dfrac{1}{2\pi r_{in} h_c n}$	$k_{eq,c} = \dfrac{\ln\left(\frac{r_{eq,out,p}}{r_{eq,in,p}}\right)}{2\pi R_{eq,c}}$	Set artificially to a small value
Grout	$R_{eq,gt+p} = R_b - R_{eq,c}$	$k_{eq,gt} = k_{eq,p} = \dfrac{\ln\left(\frac{r_b}{r_{eq,in,p}}\right)}{2\pi R_{eq,gt+p}}$	Actual thermal capacity
Pipe			Actual thermal capacity
Fluid	negligible	Set artificially to a high value	See equation 1

eq : equivalent geometry; c : convection; gt : grout; p : pipe

Heat transfer in the composite cylinder geometry is solved using the control-volume method of Patankar (1980) with a fully implicit scheme. Using the nomenclature presented in Figure 2, the discretized equation for an internal node *P* is given by:

$$a_P T_P = a_N T_N + a_S T_S + b \tag{4}$$

where,

$$a_N = \frac{k_n}{ln\left(\frac{r_P}{r_{P,n}}\right)}\ ;\ a_S = \frac{k_s}{ln\left(\frac{r_P}{r_{P,s}}\right)} \quad ;\ b = a_P^0 T_P^0 \ ;\ a_P = a_P^0 + a_N + a_S \ ;\ a_P^0 = \frac{\rho Cp}{\Delta t}\frac{(r_n^2 - r_s^2)}{2} \tag{4a}$$

The coefficients a_N and a_S, which are different from the traditional formulation (i.e. $a_i = r_i\, k_i/(\delta r)_i$), are structured so as to account for the logarithmic nature of the temperature profile in a radial configuration. The subscripts "*P,s*" and "*P,n*" refer to the nodes immediately upstream and downstream of node *P*, respectively. The superscript "0" refers to the previous time step and Δt is the time step. Control-volume boundaries are placed at the interface of the different cylinders. The size of the control volumes increases exponentially from the interface to the middle of the layer, then decreases symmetrically until the next interface. Such a configuration prevents inconcistencies due to abrupt temperature changes between two adjacent cylinders with different properties. The boundary condition on the fluid side is entered through the b term for node T_1:

$$b_1 = a_1^0 T_1^0 + r_{eq,f} q_f; \quad \text{where } q_f = r_{eq,f} h_c (T_f - T_1) \tag{4b}$$

where h_c is the internal convection coefficient. Finally, the borehole wall temperature, T_w, is known at each time step and is given by the infinite cylindrical heat source solution (ICS) to ground heat transfer. The infinite cylindrical heat source (ICS) analytical solution requires the heat transfer rate at the borehole wall, q_w. This value is obtained from the numerical solution of borehole heat transfer as follows:

$$q_w = -2\pi k_{eq,gt} \frac{dT}{dr} \approx -2\pi k_{eq,gt} \frac{T_\mathrm{w} - T_\mathrm{w,s}}{ln\left(\frac{r_b}{r_{w,s}}\right)} \tag{5}$$

As shown in Figure 2, the subscript "w,s" refers to the node immediately upstream of the last node. In turn, the value of q_w is used to obtain the borehole wall temperature using temporal superposition as follows:

$$T_w - T_g = \sum_{i=1}^{n_t} (q_{w,i} - q_{w,i-1}) \Gamma(t - t_{i-1}) \tag{6}$$

where n_t is the total number of time steps, $\Gamma = \frac{1}{k_g} G(F_o)$ and $F_o = \frac{\alpha_g t}{r_b^2}$

The value of G is the solution of the ICS. It is given here using the approximation provided by Cooper (1976).

Evaluation of short-time g-functions

The evaluation of short-time g-functions is performed as follows. The real borehole geometry is converted into an equivalent composite cylinder (Figure 2) with corresponding properties for each layer (Table 1). Then, the proposed model is solved with a constant value of q_f which is arbitrarily set at 50 W/m in this study. Values of the mean fluid temperature, T_f, and heat transfer at the borehole wall, q_w are then determined at each time step. The short-time g-functions are calculated here based on the work of Yavuzturk and Spitler (1999):

$$g\left(\frac{t}{t_s}, \frac{r_b}{H}\right) = \frac{2\pi k_g (T_f - R_b q_w - T_g)}{q_w} \tag{7}$$

where t_s is the time scale (= $H^2/9\alpha$)

Grid independence checks

The results of grid independence checks are presented in Figure 3 where short-time g-function values are plotted as a function of $ln(t/t_s)$. The borehole characteristics used for these checks are presented in Table 2. First, the influence of the time step is examined for a fixed number of radial nodes (60). Results for time steps, Δt, of 0.01, 0.05, 0.1, 0.5 and 1 h are reported in Figure 3a. The difference between successive curves diminishes as the Δt is reduced and results for time steps of 0.01 and 0.05 h are very close to each other. A Δt of 0.05 h (3 min.) is a good compromise between computational time and accuracy. It is to be noted that in certain cases it may be required to use a smaller Δt to establish the start of the g-function curve for small values of $ln(t/t_s)$ to capture transient phenomenon occurring over time scales

of seconds. Figure 3b shows the effect of increasing the number of radial nodes from 16 to 60 for a fixed Δt of 0.05 h. The number of nodes is split equally between each of the four cylinders of the equivalent geometry. As shown on Figure 3b, the g-function curve does not change significantly when the number of nodes reaches 40.

Based on this grid independence study, the number of nodes is fixed at 40, i.e.10 nodes per concentric cylinder, and the Δt = 0.05 h.

One final note regarding Figure 3a, concerns the asymptotic value of the g-function for $t = 0^+$, i.e. for $\ln(t/t_s) \rightarrow -\infty$. For the initial conditions ($t = 0$), $q_w = 0$ and $T_f = T_g$ and according to equation 7, $g = -2\pi k_g R_b$. As show in Figure 3a, this is the asymptotic value of short-time g-functions. A few tests were performed with very small time steps (data not shown on Figure 3) and the proposed method does predict the asymptotic value of the short-time g-function when $t = 0^+$.

Table 2. Borehole characteristics used in Figures 1 and 3

Borehole characteristics		Layer properties		
Borehole diameter (mm)	108 (100)	**Layer**	**Volumetric heat capacity (kJ/K-m³)**	**Thermal conductivities (W/m-K)**
Borehole total length (m)	108	*Fluid*	4124	-
U-tube inside diameter (mm)	27.4	*Pipe*	1540	0.45
U-tube outside diameter (mm)	33.4	*Grout*	3900	1.280
Shank spacing (mm)	47.1	*Ground*	2877	2.25

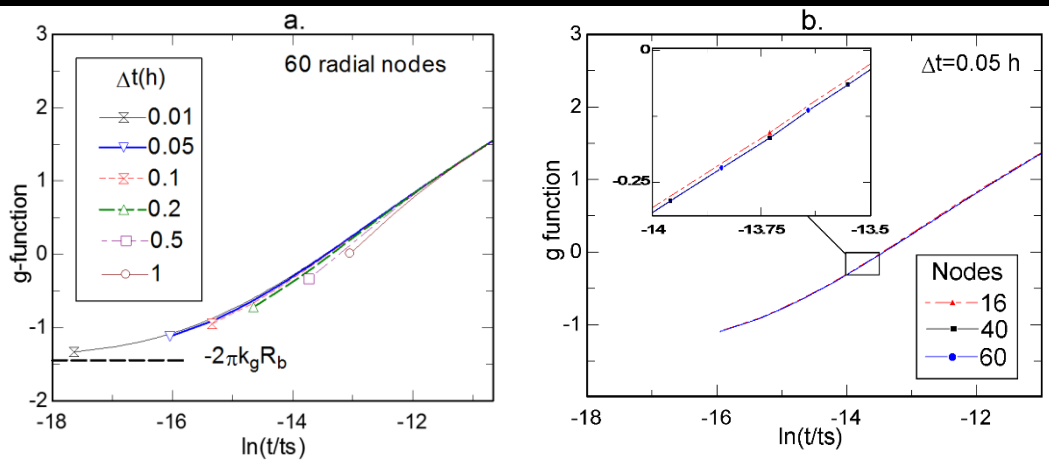

Figure 3 Grid independence checks. a) The number of nodes is fixed at 60 and the time step is varied. b) The time step is fixed at 0.05 h and only number of nodes per layer is varied.

VALIDATION

The proposed model has been validated against several test cases. The first case used test TC3 provided in the building fabric test suite developed by Spitler et al. (2001). This test consists of finding the transient response of a three-layer plane wall. Since the numerical code developed here is for a radial geometry, a large internal radius (1000 m) was used to approximate a plane wall. A fine mesh consisting of 14 nodes per layer and a time-step of 0.02 h were used. The results of this test (not shown here due to a lack of space) indicate that the average relative error on the wall heat flux between the numerical and analytical solution is 0.85%. This comparison indicated that the numerical code was correctly implemented for transient conduction in multi-layer walls.

The experimental data of Beier et al. (2011) is used in the final validation test. The system parameters, geometry and thermal conductivities are taken from Table 1 of Beier et al. (2011). The specific heat capacities for the fluid, pipe, grout and ground are taken as 4.187, 1.77, 3.840, and 3.2 kJ/kg-K, respectively, based on the work of Minaei and Marefat

(2017). The proposed model is used with the experimental values of inlet temperature and flow rate as input. Figure 4 presents the outlet temperature as a function of time predicted by the proposed model and measured by Beier et al. (2011). As shown in the top portion of Figure 4, there is very good agreement between the proposed model and the experiments with maximum and average differences of +0.15 and +0.05 K, respectively.

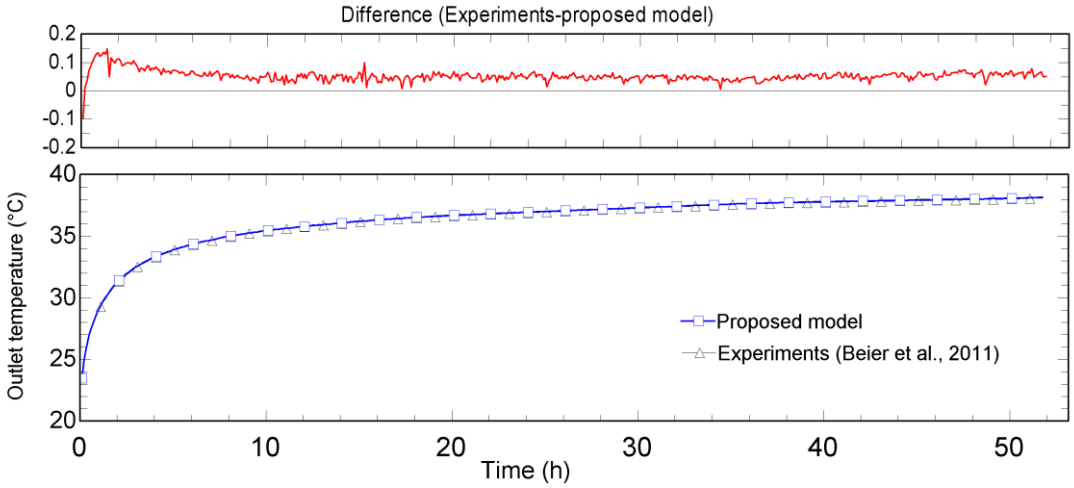

Figure 4 Comparison between the outlet fluid temperature predicted by the proposed model and those measured by Beier et al. (2011).

APPLICATION TO THE ASHRAE SIZING EQUATION

The current ASHRAE sizing equations for vertical boreholes (ASHRAE, 2015) do not account for borehole thermal capacity effects. With short-time g-functions it is possible to account for such effects. When the so-called alternative g-function based design equation (ASHRAE, 2015) is used the required borehole length, L, is given by:

$$L = \frac{q_a R_{ga,g} + q_m R_{gm,g} + q_h R_{gh,g} + q_h R_b}{T_m - T_g} \tag{8}$$

The three ground pulses, q_a, q_m and q_h are applied over time periods which are typically equal to 10 years (t_y), 1 month (t_m), and 1 to 6 hours (t_h), respectively. The corresponding ground thermal resistances, $R_{ga,g}$, $R_{gm,g}$, $R_{gd,g}$ are evaluated as follows (ASHRAE, 2015):

$$R_{ga,g} = \left[g_{(t_f)} - g_{(t_f - t_1)}\right]/2\pi k_g \quad ; \quad R_{gm,g} = \left[g_{(t_f - t_1)} - g_{(t_f - t_2)}\right]/2\pi k_g \quad ; \quad R_{gd,g} = \left[g_{(t_f - t_2)}\right]/2\pi k_g \tag{9}$$

where $t_f = t_y + t_m + t_h$, $t_2 = t_y + t_m$ and $t_1 = t_y$. The subscript "g" denotes that the effective ground thermal resistances are evaluated using g-functions. As noted by Lamarche (2016), short-term g-functions influence the values of $R_{gm,g}$ and $R_{gd,g}$. It is interesting to examine the impact of borehole thermal capacity on the required borehole length for a particular example. In this example, the required length of a single borehole operating in cooling is required for q_a = 0.5 kW, q_m = 3 kW, and q_h=10 kW and t_y = 10 y, t_m =1 month and t_h = 4 hours, and T_m =35 °C and T_g =13 °C. The other borehole characteristics are given in Table 2. The convective heat transfer, h_c, is set at 500 W/m²-K giving a value of R_b = 0.1 m-K/W using the first order multipole method. The corresponding g-function for this geometry is the unified curve for $B/H = \infty$ in Figure 1. Strictly speaking this curve is only applicable for r_b/H=0.0005, thus for a value of H=108 m. Therefore, for different values of the r_b/H ratio, the correction factor suggested by Eskilson is applied. Table 3 presents the required borehole length with and without short-term effects for this case.

Table 3. Short-term effects on borehole length

Parameter	without short-term effects	with short-term effects
Borehole length (m)	109.4	107.3
$R_{ga,g}$ (m-K/W)	0.156	0.155
$R_{gm,g}$ (m-K/W)	0.181	0.187
$R_{gd,g}$ (m-K/W)	0.079	0.072

For this particular example, the design borehole length is slightly oversized (≈ 2%) when short-term effects are not taken into account. Short-term effects decrease the value of $R_{gd,g}$ by about 9 % and increase the value of $R_{gm,g}$ by about 3%. The slight change in the value of $R_{ga,g}$ is not caused directly by borehole thermal capacity but is simply due to the fact that the borehole length varies slightly. The percentage of oversizing is problem dependent and can reach close to 10% (Ahmadfard and Bernier, 2018). It will depend, among other things, on the relative magnitude between q_m and q_h and the duration of the peak pulse.

CONCLUSION

A one-dimensional hybrid model is proposed to generate short-time g-functions for single U-tube boreholes. The two-pipe geometry is first converted into a single equivalent composite cylinder. This cylinder is discretized to numerically solve heat transfer in each layer while ground heat transfer is determined using the infinite cylindrical heat source solution. The influence of the time step and of the number of radial nodes is checked to ensure a good compromise between accuracy and computation time. From this analysis, it appears that 40 nodes and a time step of 3 min is a good compromise between accuracy and computational cost. The numerical part of the model is verified against an analytical solution while the full model is successfully validated against experimental data. Short-time g-functions are generated and used to study the effects of borehole thermal capacity on the required borehole length using the g-function-based ASHRAE sizing equation. It is shown that the inclusion of borehole thermal capacity, using short-time g-functions, reduces the required design borehole length.

NOMENCLATURE

α = thermal diffusivity (m^2/s)
B = borehole spacing (m)
q = heat transfer rate per unit length (W/m)
r = radial distance from the borehole center (m)
T = temperature (°C)
k = thermal conductivity ($W.m^{-1}.K^{-1}$)
a = discretization coefficient ($W.m^{-1}.K^{-1}$)
δr = node spacing (m)
t = time (h or s)
t_s = time scale (day)
H = borehole length (m)
ρ = density ($kg.m^{-3}$)
C_p = specific heat capacity ($J.m^{-3}.K^{-1}$)
R = effective thermal resistance ($m.K.W^{-1}$)
Δ = pipe thickness (m)
b = discretization coefficient

Subscripts

b = borehole
gt = grout
eq = equivalent
c = convection
P = node
f = fluid
w = wall
p = pipe
h = hour
s = southern neighbour
n = northern neighbour
a = year
m = month

REFERENCES

Ahmadfard, M. and M. Bernier. 2018. *Modifications to ASHRAE's sizing method for Vertical Ground Heat Exchangers*. Science and Technology for the Built Environment. In press. 2108.

ASHRAE (2015) Chapter 34 – Geothermal Energy, *ASHRAE Handbook - Applications*, Atlanta, GA: ASHRAE.

Bauer, D., W. Heidemann and H.-J.G. Diersch. 2011. *Transient 3d analysis of borehole heat exchanger modeling*. Geothermics 40: 250-260.

Cimmino, M. and M. Bernier. 2013. *Preprocessor for the generation of g-functions used in the simulation of geothermal systems*. Proceedings of the 13th International IBPSA conference, 25-28 August, Chambery, France, pp.2675-2682.

Cimmino, M. and M. Bernier. 2014. *A semi-analytical method to generate g-functions for geothermal bore fields*. Int. J. Heat Mass Transfer 70(c): 641-650.

Claesson, J. and S. Javed. 2011. *An analytical method to calculate borehole fluid temperatures for time-scales from minutes to decades*. ASHRAE annual conference, paper ML-11-C034.

Cooper, L.Y. 1976. *Heating of a Cylindrical Cavity*. International Journal of Heat and Mass Transfer 19: 575-577.

Eskilson, P. 1987. *Thermal analysis of heat extraction boreholes*. University of Lund, Sweden: Doctoral Thesis.

Javed, S., J. Claesson and P. Fahlén. 2010. *Analytical Modelling of Short-term Response of Ground Heat Exchangers in Ground Source Heat Pump Systems*. 10th REHVA World Congress, Clima 2010, Antalya, Turkey, May 9-12.

Javed, S. and J. Claesson. 2011. *New analytical and numerical solutions for the short-term analysis of vertical ground heat exchangers*. ASHRAE Transaction 117(1): 3-12.

Kim, E.-J., M. Bernier, O. Cauret and J.-J. Roux. 2014. *A hybrid reduced model for borehole heat exchangers over different time-scales and regions*. Energy 77: 318-326.

Lamarche, L. 2015. *Short-time analysis of vertical boreholes, new analytic solutions and choice of equivalent radius*. International Journal of Heat and Mass Transfer 91: 800-807.

Lamarche, L. 2016. *Short-time modelling of geothermal systems*. 29th internation conference on efficiency, cost, optimization, simulation and environmental impact of energy systems, Portoroz, Slovenia, June 19-23, Proceedings.

Li, M. and A. C. Lai. 2013. *Analytical model for short-time responses of ground heat exchangers with U-shaped tubes: Model development and validation*. Applied Energy 104: 510-516.

Li, M., P. Li, V.Chan and A. C. Lai. 2014. *Full-scale temperature response function (G-function) for heat transfer by borehole ground heat exchangers (GHEs) from sub-hour to decades*. Applied Energy 136: 197-205.

Ma, W., M. Li, P. Li and A. C. Lai. 2015. *New quasi-3D model for heat transfer in U-shaped GHEs (ground heat exchangers): Effective overall thermal resistance* Energy 90: 578-587.

Pärisch, P., O. Mercker, P. Oberdorfer, E. Bertram, R. Tepe. and G. Rockendorf. 2015. *Short-term expermients with borehole heat exchangers and model validation in TRNSYS*. Renewable Energy 74: 471-477.

Rees, S. J. 2015. *An extended two-dimensional borehole heat exchanger model for simulation of short and medium timescale thermal response*. Renewable Energy 83: 518-526.

Ruiz-Calvo, F., M. De Rosa, P. Monzo, C. Montagud and J. Corberan. 2016. *Coupling short-term (B2G model) and long-term (g-function) models for ground heat exchanger simulation in TRNSYS. Application in a real installation*. App.Thermal Eng102: 720-732.

Ruiz-Calvo, F., De Rosa, M., Acuña, J., Corberán, J. and C. Montagud. 2015. *Experimental validation of a short-term Borehole-to-Ground (B2G) dynamic model*. Applied Energy 140: 210-223.

Shirazi, A. S. and M. Bernier. 2013. *Thermal capacity effects in borehole ground heat exchangers*. Energy and Buildings 67: 352-364.

Shonder, J.A. and J.V. Beck. 1999. *Determining effective soil formation thermal properties from field data using a parameter estimation technique*. ASHRAE Transactions 105: 458-468.

Spitler, J. D., S.J. Rees and X. Dongyi. 2001. *Development of an analytical verification test suite for whole building energy simulation program - building fabric*. ASHRAE 1052-RP: Final Report.

Spitler, J. D. and X. Xu . 2006. *Modeling of Vertical Ground Loop Heat Exchangers with Variable Convective Resistance and Thermal Mass of the Fluid*. Proceedings of the 10th Int. Conference on Thermal Energy Storage-Ecostock 2006, Pomona, NJ.

Yang, Y. and M. Li. 2014. *Short-time performance of composite-medium line-source model for predicting responses of ground heat exchangers with single U-shaped tube*. International Journal of Thermal Sciences 82: 130-137.

Yavuzturk, C. and J.D. Spitler. 1999. *A short time step response factor model for vertical ground loop heat exchangers*. ASHRAE Transactions. 105(2): 475-485.

Yavuzturk, C. and J.D. Spitler. 2001. *Field validation of a short time step model for vertical ground-loop heat exchangers*. ASHRAE Transactions 107(1):617-625.

[This page has been intentionally left blank]

IGSHPA SWEDEN 2018 Research Conference

DOI: 10.22488/okstate.18.000025

Video inspection of wells in open loop ground source heat pump systems in Norway.

Sondre Gjengedal, Randi K. Ramstad, Bernt Olav Hilmo, Bjørn Frengstad

ABSTRACT

This paper presents results from video inspections of groundwater wells in Melhus and Elverum, in Norway. The method has identified iron hydroxides, bacterial growth and sand production as causes of clogging in different wells. Video inspection has proven itself a reliable, inexpensive and quick method for such investigations. The videos supply documentation for the building owner about the well condition. A video inspection should be incorporated as a standard part of the tender document and an integrated part of the maintenance routine. Finally, open loop GSHP and ATES system wells should be designed and manufactured with integrated video inspection options. This will ease the fault detection process and reduce maintenance costs of the system through the lifetime of the wells.

INTRODUCTION

Ground source heat is a renewable energy source that has a potential for increased use in Norway. Through the ORMEL project, the municipalities of Melhus and Elverum are evaluating their potential for further development, specifically with the open loop ground source heat pump systems (open loop GSHP systems). Melhus has utilized ground water for heating and cooling purposes since 1999, with good results, while Elverum is currently investing in such systems. Aquifer thermal energy storage systems (ATES systems) are vulnerable towards many of the same problems as GSHP systems, but will not be described further in this paper.

The typical open loop GSHP systems in Melhus and Elverum utilize an unconsolidated Quaternary sand and gravel aquifer as a heat source. The production well and injection well connect to the aquifer through customized screens, which withholds the sediments, while groundwater is allowed to flow freely into the wells. A submersible pump in the production well pumps groundwater through a secondary heat exchanger in the building, where a secondary fluid extracts heat. After heat extraction, the groundwater is re-injected to the aquifer in the injection well. Elverum currently has one such open loop GSHP system in operation. Melhus has nine such open loop systems, which utilize groundwater from the same aquifer. Of the nine systems, seven have injection wells, while the remaining two utilize the local drainage system for disposal of the return water.

Unlike domestic water works, there are no requirements regarding water quality in open loop GSHP system in Norway. Specified water quality guidelines do not exist and water quality issues are often disregarded or insufficiently emphasized during the planning and design phase of new projects. Lack of specialist input from a hydrogeologist often leads to insufficient aquifer investigation. The production wells or injection wells are seldom sufficiently tested before or after the construction phase. Insufficient instrumentation and lack of monitoring of the systems during operation also contribute to late discovery of fouling and other water quality issues. All of these factors are likely contributors to increased risks of problems caused by faulty design or inappropriate operational strategies. Similar findings are reported by Bakema (2001) and Banks (2012) who emphasize that most open loop problems are best dealt with through correct system design.

Sondre Gjengedal: Ph.D. at Norwegian University of Science and Technology (sondre.gjengedal@ntnu.no).
Randi Kalskin Ramstad: Associate Professor at Norwegian University of Science and Technology (randi.kalskin.ramstad@ntnu.no).
Bernt Olav Hilmo (Ph.D.): Consultant at Asplan Viak AS (BerntOlav.Hilmo@Asplanviak.no).
Bjørn Frengstad: Professor at Norwegian University of Science and Technology (bjorn.frengstad@ntnu.no).

Since 1999, a wide range of problems has occurred with the systems in Melhus. These problems often involve clogging of the well screens, either the production wells or the injection wells (Riise, 2015). Typically, the injection wells are more prone to clogging than the production wells. All of the seven injection wells in Melhus have had clogging issues. In comparison, clogging have been detected in two out of nine production wells. In Elverum, one planned open loop GSHP system was terminated because three of the four production wells showed severe clogging issues during the pre-investigation phase of the project. The active open loop GSHP system in Elverum has experienced clogging issues in one out of its two production wells. Common for the problems found in Melhus is a lack of monitoring of the wells during normal system operation. Only three of the systems monitor groundwater flow rates and only one system monitor pressure levels in the production well. None of the injection wells is monitored. As a result, the faults are seldom detected before the clogging have had time to develop and have become a sever problem.

Clogging problems can originate from a wide range of sources that yield similar symptoms, such as reduced groundwater flow rates through the system and increased pressure drops in the groundwater flow through the affected components (Bakema, 2001, Banks, 2012, Andersson et al., 1984). It is common to distinguish between mechanical, chemical or microbial causes. Mechanical clogging involves incrustations of sand, silt and other suspended particles, which fill the pore space in the soil and clog system components. Chemical clogging involves precipitation of particles, which in turn incrusts on system components. Microbial clogging, or biofouling, is caused by bacteria, which grow on system components. All of these complications require different cleaning or corrective approaches (Andersson et al., 1984) and there exists a need to distinguish between them. Flow rate and pressure monitoring is not capable of such distinctions. Consequently, such problems often call for investigations by means of water quality analysis or visual inspection of the affected area to identify the problem cause.

EXAMPLES OF SUCCESSFUL VIDEO INSPECTIONS IN MELHUS AND ELVERUM

Video inspection offers a familiar, hands-on, versatile and reliable approach. The method is common in domestic waterworks in Norway, England (Banks, 1992), the Netherlands (van Beek et al., 2017), USA (Jansen and LoCoco, 2007, Gorder, 1963) and most likely other countries. Similar methods are common in other industries such as buildings and constructions, roads and sewage systems where video inspection is a standardized part of any project. Today`s high-resolution color imaging cameras are capable of forward-looking and sideways-looking views with 360 degrees rotation and variable depth of focus. During the inspection, the video is shown in real-time on a monitor with a depth display. Some cameras, like the *Supervision™ SVR 140/SVC100 pan and tilt camera* utilized in this study, are equipped with laser measuring tools, which for example enables measurement of screen slot openings in the well.

In groundwater wells, the usefulness of the method relies on the clarity of the water. Performing a flushing of the well and allowing particles to settle is in some cases recommended before the inspection, especially when inspecting new wells. Figure 1A shows a new well that had been pumped for 14 days and where the pumping ended one week before the video inspection. The 1 mm screen slot openings were measured to confirm that the well was constructed in accordance to the specifications given in the tender document. The lodged sand grains and the clarity of the water indicate that the well was constructed in good agreement with the local soil conditions.

The clarity of the water might be a good indication of a well's current condition and an inspection without pre-flushing might be useful in itself. Figure 1B shows a production well in Elverum where the well screen is clogged by a biofilm of iron bacteria. This particular production well is less than 1 year old and had not yet been connected to the heat pump system. It was not flushed before the inspection. In this case the bacterial growth seems to favor specific parts of the screen and builds on the screen surface in a foam-like structure, effectively clogging some of the openings. These observations might not have been possible if the well was flushed before the inspection. Disinfection with chlorine and cleaning were necessary before the well could be connected to the system.

Precipitated iron and manganese hydroxides is a common problem in Norwegian open loop systems (Riise, 2015). Often these particles accumulate in the injection well, after a journey through the rest of the system. But some examples of hydroxide precipitation is also found in production wells in Melhus. The production well screen in figure 1C is incrusted with precipitated iron hydroxides at the location of the pump inlet. The drawdown in the well was not monitored during operation and the water table was lowered below the suction inlet section of the pump. Mixture of air into the screen area allowed the chemical reaction to occur. Unlike the iron bacteria in figure 1B the precipitated hydroxides seem to evenly cover the screen slots. This well had functioned for 15 years before the problem was discovered and the well had to be abandoned because of faulty design.

The injection well in figure 1D is clogged by fine silt and clay particles. The particles originate from the sedimentary formation around the production well, where they are carried through the production well screen by the flow of water. The particles are unable to infiltrate back through the injection well screen and effectively clog the slots. Before the inspection the well was taken out of service and the suspended particles were allowed to settle. The picture shows some small particles of black manganese hydroxides still settling in the well. The problem was discovered 1.5-2 years after the plant was set in operation. The problem was solved by installing a filter on a part of the pipe section in the machinery room before reinjection of the groundwater back into the aquifer. The filter is regularly cleaned.

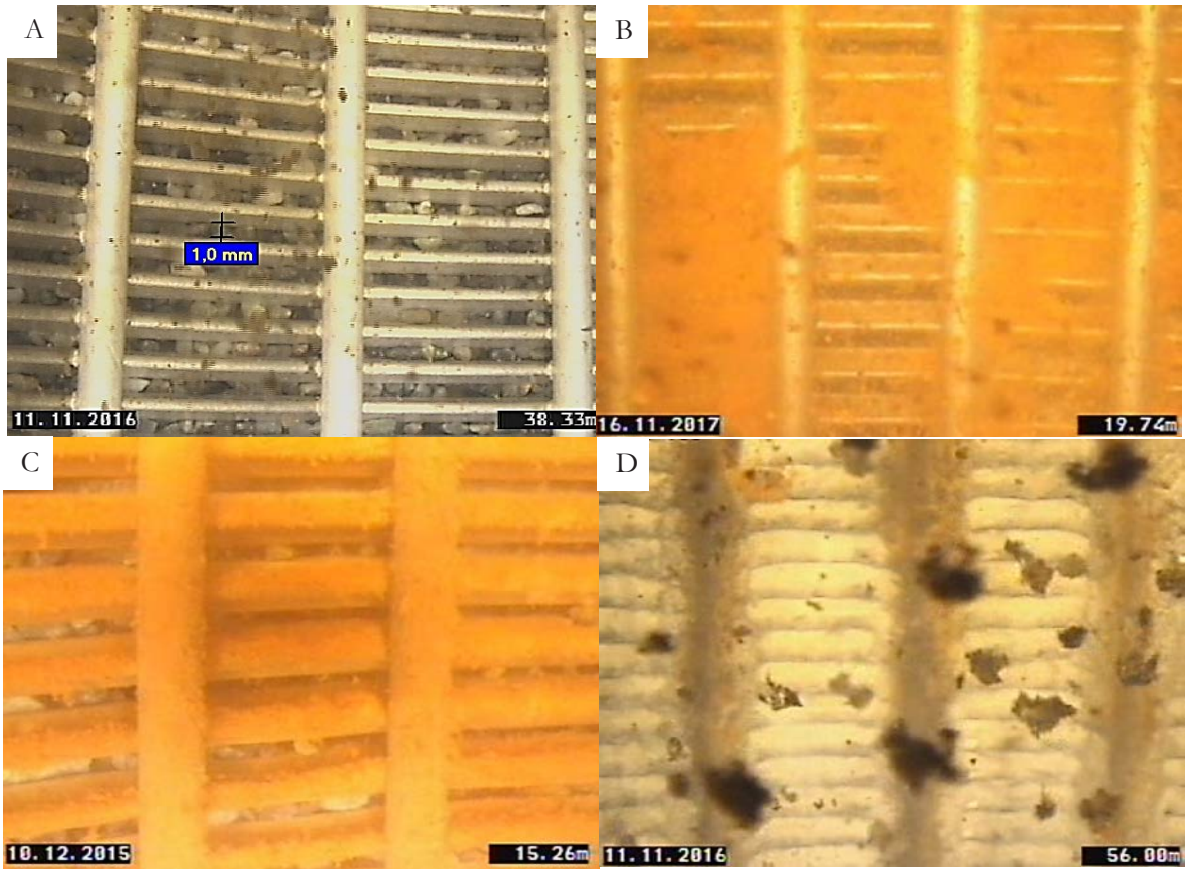

Figure 1 Video inspections of well screens. A: a newly constructed well in Melhus. The 1 mm slots were measured with a built-in laser tool. B: iron bacteria have infected this production well in Elverum. C: precipitated iron hydroxide incrustations on a production well screen in Melhus. D: sand and silt clogging an injection well screen in Melhus. Photos: Gjøvaag AS (part of the ORMEL project).

BENEFITS, COST AND DRAWBACKS

The presented video photos demonstrate the applicability of the method in open loop GSHP system wells. The investigation of newly constructed wells confirms that proper placement of screen, pump and pressure sensors are ensured and that the wells are constructed in agreement with the soil

conditions and the tender documents. The method can identify location and type of debris, scale and biofilm deposits in clogged wells. New vs. old well conditions can be compared and such information supply vital knowledge to the system operator and allow planning of appropriate maintenance and corrective measures. The method has also been applied in real-time to direct rehabilitation operations in the well or to identify sand-production zones in the well while pumping is in progress (Jansen and LoCoco, 2007).

The cost of a video inspection is a function of the actual inspection time and transportation cost to the site. The actual inspection time required for a single well depends mainly on the well depth and clarity of the water. For example, the depth of the wells shown in figure 1A-1D are 40 (A), 22 (B), 24 (C) and 58 (D) meters, respectively. The time needed for the inspections ranged from 15 (A), 15 (B), 23 (C) and 30 (D) minutes, respectively. The total cost of the individual video inspections ranged from 5000-5700 NOK (≈520-590 €) per well. By comparison, similar numbers have been reported by Banks (1992), where an average cost of 2500-6000 NOK (≈260-620 €) was registered in 1991.

A hydrogeologist can interpret the video during the inspection of the well or in the office afterwards. A digital copy of the video can also be sent to an expert (e.g. a microbiologist) for further evaluation.

The main drawbacks of the method involve the cost of preparing the wells for inspection. In Norway, the current open loop GSHP well designs generally follow the more traditional well designs applied for domestic drinking water purposes. Most of these wells are designed around the space required by the submersible pump, with minimum space available for other equipment. The camera utilized in this investigation required 90 mm diameter free space. Normally, the pump or injection pipe have to be dismantled and lifted out of the well for the camera to fit. The heat pump system must shut down during the video inspection, adding additional cost to the investigation.

If the well designs include enough space for a video camera while the pump and pipes are operating, the time needed and the over-all cost of the inspection is greatly reduced. A possible alternative would be to increase the well diameter sufficiently to give space for a camera along the side of the pump or injection pipe. An inspection "hatch" next

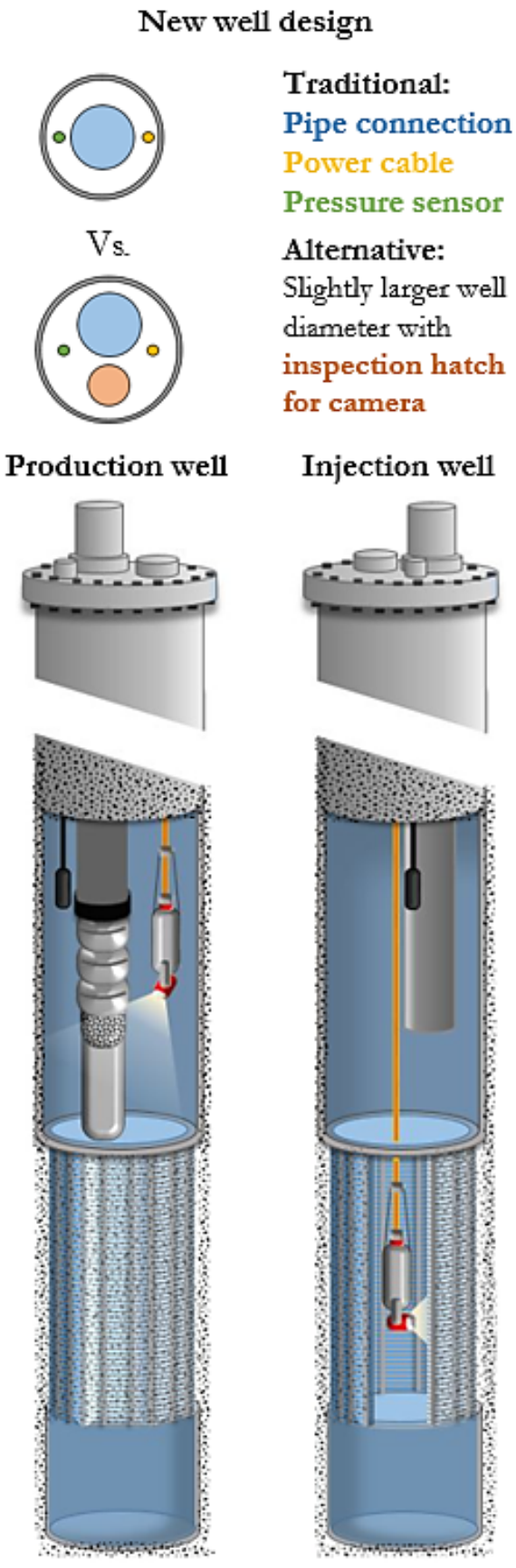

Figure 2 The traditional well design does not have space for a video camera. An alternative design that allows for real-time video inspection can reduce the over-all cost of fault detection.

to the pipe connections is a potential technique. By installing the pump and injection pipe slightly off-center, the additional well diameter needed for the camera might be minimized (figure 2). The video inspection can then be conducted during normal system operations and the actual well behaviors are observed live on the monitor while groundwater flows through the system. The increased installation cost due to a larger well diameter will be more than outweighed by the benefits of regular monitoring of the well conditions during the lifetime of the wells. In addition, a larger screen diameter would in most cases improve the well characteristics.

It might be argued that clogging problems also can be detected by measuring the specific flow or the pumping capacity. Although a reduction of the specific flow is easily understood by a hydrogeologist, a video presentation of the conditions in the well is a much stronger tool when trying to convince the well owner that a costly well rehabilitation is needed. If there is any doubt whether the well is installed according to order, a video inspection of the well can settle the dispute.

A record of routine video inspections from the wells were installed and onwards, will together with data on the performance of the open loop GSHP, be a strong tool for monitoring and documentation of the plant.

CONCLUSION

Video inspection of wells have proven to be a reliable, efficient and relatively low cost method for investigation of production wells and injection wells. A video inspection of the wells should be a standard part of the tender document in new open loop system and an integrated part of the maintenance routines. Open loop GSHP wells should be designed and manufactured with integrated video inspection options. This will ease the fault detection process and reduce maintenance costs of the system through the lifetime of the wells.

ACKNOWLEDGMENTS

The research project *Optimal Utilization of groundwater for heating and cooling in Melhus and Elverum*, the ORMEL project, is a cooperation between the municipalities of Melhus and Elverum, the Norwegian University of Science and Technology, Asplan Viak AS and the Geological Survey of Norway and with funding from the Norwegian Research Council. Erlend Skorstad at Gjøvaag AS performed the video inspection. We would like to thank all the involved institutions and persons for cooperation and financial contributions.

REFERENCES

Journal papers:

Gorder, Z. A. 1963. *Television Inspection of a Gravel Pack Well.* Journal - American Water Works Association*,* 55**,** 31-34.

Van Beek, C., Hubeek, A., De La Loma Gonzalez, B. & Stuyfzand, P. 2017. *Chemical and mechanical clogging of groundwater abstraction wells at well field Heel, the Netherlands.* Hydrogeology Journal*,* 25**,** 67-78.

Book:

Banks, D. 2012. *An introduction to thermogeology : ground source heating and cooling,* Chichester, Wiley-Blackwell.

Book section:

Jansen, J. & LoCoco, J. J. 2007. *Borehole Geophysics.* In: Sterret, R. J. (ed.) *Groundwater and Wells.* 3 ed. New Brighton: JohnsonscreensTM.

State of the art reports:

Andersson, A.-C., Andersson, O. & Gustafson, G. 1984. *Brunnar : undersökning, dimensionering, borrning, drift,* Stockholm.

Bakema, G. 2001. *Well and borehole failures in UTESS*. State of the art 2000. 2 ed. IF Technology bv.

Banks, D. 1992. *Grunnvannsbrønner : kontroll, vedlikehold, rehabilitering,* Trondheim, Norges geologiske undersøkelse.

*Thesi*s:

Riise, M. H. 2015. *Praktisk guide for grunnvarmeanlegg basert på oppumpet grunnvann - Hydrogeologiske forundersøkelser, etablering, drift og oppfølging med utgangspunkt i erfaringer fra etablerte anlegg i Melhus sentrum*. NTNU.

[This page has been intentionally left blank]

IGSHPA SWEDEN 2018 Research Conference

DOI: 10.22488/okstate.18.000009

Hydrogeothermal Characterization and Modelling of a Standing Column Well Experimental Installation

Gabrielle Beaudry **Philippe Pasquier** **Denis Marcotte**

ABSTRACT

Standing column wells (SCW) are efficient ground heat exchangers that offer promising potential for integration in dense urban areas. Recent years have witnessed a growing interest in SCWs, resulting in the development of various simulation models incorporating heat transfer, groundwater flow and geochemical reactions within the well and the surrounding ground. However, these models commonly use a configuration that involves pumping at the bottom of the well and reinjection from its top, which can lead to installation and maintenance difficulties in deep wells. Furthermore, very few SCW models have been validated against reliable field data. This paper presents an original finite element model coupling advection-diffusion of heat and groundwater flow within a top pumped SCW and its surrounding ground as well as the experimental setup used for its validation. Within the scope of this study, experimental data obtained after an extensive field characterization campaign and a thermal response test performed with a large-scale geothermal laboratory were used directly as inputs in the numerical model. Experimental validation shows that without any calibration procedure, the model reproduces the experimental inlet and outlet groundwater temperatures with a mean absolute error of 0.14 °C. It is also shown that the placement of the pump at the top of the well offers a more practical design that has minor impact on the thermal performance of the system.

INTRODUCTION

In Canada, about 17% of secondary energy use and 14% of greenhouse gases emissions are related to space heating and, albeit to a far lesser extent, cooling (NRCan 2018). As they allow for significant energy savings, ground-source heat pump systems offer great potential to alleviate the carbon footprint associated with these activities. Among those systems, standing column wells (SCW) achieve competitive heat exchange rates by recirculating groundwater in a single uncased vertical borehole, thereby minimizing the thermal resistance as well as the size and cost of the system. SCWs performance can be enhanced by discharging or *bleeding* part of the pumped water, an action that promotes groundwater flow and advective heat transfer around the well. This operation has been described as a key feature for maintaining the groundwater temperature within the heat pumps operational range in the peak heating conditions that frequently occur in cold climates (Spitler, *et al.* 2002; Deng, *et al.* 2005; Orio, *et al.* 2005; Nguyen, *et al.* 2015; Pasquier, *et al.* 2016).

Recent years have witnessed a growing interest in SCWs, resulting in the development of various simulation models incorporating heat transfer, groundwater flow (Rees, *et al.* 2004; Deng, *et al.* 2005; Abu-Nada, *et al.* 2008; Croteau 2011; Lee 2011; Ng, *et al.* 2011; Nguyen, *et al.* 2012, 2015) and geochemical reactions (Eppner, *et al.* 2015, 2017a, 2017b) within the SCW and the surrounding ground. However, these models commonly use a configuration that involves pumping at the bottom of the well where higher ground temperatures are found, and recirculation from

Gabrielle Beaudry (gabrielle.beaudry@polymtl.ca) is a Ph.D. candidate at Polytechnique Montréal, Canada.
Philippe Pasquier (philippe.pasquier@polymtl.ca) is professor of geological engineering at Polytechnique Montréal, Canada.
Denis Marcotte (denis.marcotte@polymtl.ca) is professor of geological engineering at Polytechnique Montréal, Canada.

its top. This strategy aims at increasing the heating energy conveyed by the groundwater but can also lead to installation and maintenance difficulties in deep wells (Orio, *et al.* 1999). Furthermore, as some experimental projects involving SCWs exist (Minea 2013; Lee, *et al.* 2016; Chang, *et al.* 2017), only a few authors used long-term field data incorporating bleed for the validation of a predictive simulation model (Deng, *et al.* 2005; Ng, *et al.* 2011). This paper aims to present an original finite element model coupling transient advection-diffusion of heat and groundwater flow within a top pumped SCW and its surrounding ground. The experimental setup and methodology used for its validation, as well as preliminary results, will also be presented.

A STANDING COLUMN WELL EXPERIMENTAL INSTALLATION

As part of an ongoing research program on SCWs in cold climates, a mobile geothermal laboratory (MGL) was assembled in a 12.2 meter marine container located in the city of Varennes at 10 km east of Montreal (Canada) in the spring of 2016. The MGL was designed to mimic the heating and cooling operation of a small commercial building connected to a borehole heat exchanger (closed or open-loop, vertical or horizontal) so as to obtain detailed information about the thermo-hydro-geochemical processes occurring during the operation of open and closed-loop ground heat exchangers. Accordingly, the MGL was equipped with a heating, ventilation and air-conditioning system allowing heat extraction or injection through four 14 kW water-to-air heat pumps connected in a parallel arrangement with a propylene glycol loop. A plate heat exchanger connects the propylene glycol loop to the groundwater loop to prevent fouling in the heat pumps. In addition, the MGL has a 24 kW nominal water heater and a water treatment unit designed to condition groundwater chemistry. A comprehensive control and data acquisition system monitoring the electrical power, flow rate, fluid and air temperatures every minute is also put into place in the MGL.

Next to the MGL, a 300 m deep SCW (Ø165 mm) and a 150 m deep injection well (IW) (Ø165 mm) allowing to return the bleed water to the aquifer were drilled at about 10 m from each other in June 2016. Later in the fall, the wells were equipped with high-density polyethylene pumping and reinjection pipes (SDR 11, Ø50.8 mm) and with distributed fibre optic temperature sensors. The installation delay caused the SCW bottom walls to collapse, resulting in an effective depth of 215 m. For practical and financial considerations, the submersible pump was located near the surface in a pumping chamber (Ø241 mm) at a depth of about 18 m. Figure 1 illustrates the MGL setup.

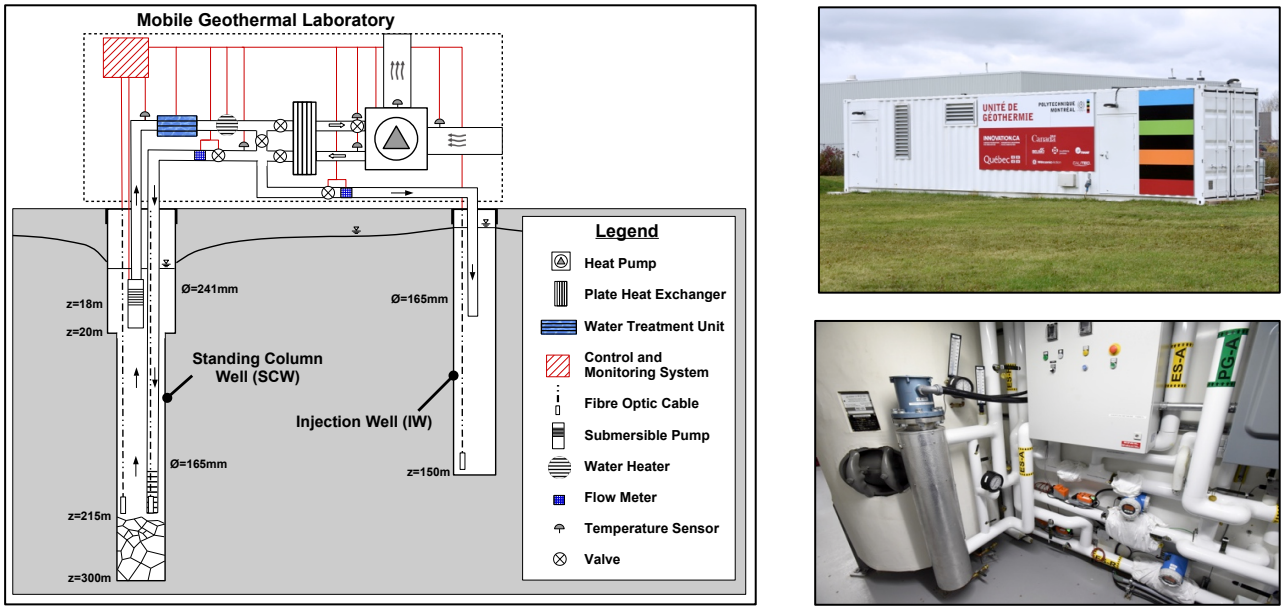

Figure 1 Schematic illustration of the MGL (not to scale) (left), MGL viewed from outside (upper right) and experimental apparatus used for the thermal response test: water heater, flow meters, valves and temperature sensors (lower right).

CHARACTERIZATION OF THE EXPERIMENTAL SITE

A comprehensive characterization of the site was undertaken in 2017 to acquire detailed information about aquifer characteristics. Parameters needed for the development of an accurate numerical model and its validation, namely, the nature, depth and temperature of the bedrock, groundwater static hydraulic head, aquifer specific storage, hydraulic and thermal conductivity, were obtained following the tests listed below.

Geology

A first evaluation of the site hydrogeothermal conditions was made based on local geology. A stratigraphic column was developed following the macroscopic analysis of 54 composite samples coming from drill cuttings, each representing 6.1 m along the SCW. The bedrock was identified at a depth of 3 m and corresponds to a grey fine-grained sedimentary rock intersected locally by beds of siltstone, beige-pink sandstone and beige limestone as well as intermediate to mafic sills and dikes. A gradual transition was observed after a depth of 215 m that leads to a black shaly limestone at a depth of 294 m. Those observations are consistent with regional stratigraphic sequence (Globensky 1987) and correspond, respectively, to the Nicolet Formation and Utica Group of the Ordovician period.

Temperature Profiles

As the local geothermal heat flux and far-field thermal conditions affect groundwater temperatures and thereby SCWs performance, a temperature profile was measured prior to any heating or cooling activity. Temperature sensors with 0.25 °C accuracy and 20 seconds response time were taken down the wells with a thermal stabilization period of 60 seconds between each displacement. Shallow temperatures in the borehole (0-30 m) showed significant variations attributable to seasonal air temperature fluctuations. A geothermal gradient of 2.3°C/100 m associated with the local geothermal heat flux was observed from 60 m depth (8.9°C) down to 215 m (12.4°C).

Hydrogeology

To identify aquifer characteristics and gain better understanding of local groundwater flow, a 6-day pumping test was conducted in October 2017. Groundwater was discharged from the SCW to a nearby storm sewer at a rate of 33 L/min to reflect a typical maximal bleed ratio of 30% (Orio, *et al.* 2005; Pasquier, *et al.* 2016). The water level was located at an initial depth of 2 m and was monitored during the test using pressure sensors with 0.5 cmH_2O accuracy. Upon the test ending, stabilized drawdowns of about 4 m and 2 m were observed, respectively, in the pumping well (SCW) and non-operating IW. These stabilized drawdowns suggest the presence of a recharge boundary nearby that is yet unlocalized. Given the very friable nature of the bedrock along the effective borehole depth, groundwater flow was considered to be taking place in a homogeneous equivalent porous medium. On this basis, hydraulic parameters estimates were obtained from the Cooper and Jacob (1946) solution for confined aquifers after analysis of the drawdowns at the SCW and IW (see Figure 2). Slightly different hydraulic conductivity values resulted from the SCW (5.7e-7 m s^{-1}) and IW (7.8e-7 m s^{-1}), which may reflect heterogeneity of the fractured aquifer. Both values are typical of a moderately permeable sedimentary bedrock (Freeze and Cherry 1979). Specific storage coefficients of 6.4e-4 m^{-1} (SCW) and 7.5e-7 m^{-1} (IW) were obtained. The latter avoids wellbore storage effects and indicates a confined aquifer.

Geothermal

Thermal conductivity of surrounding rocks has been identified as one of the most influential factors affecting SCWs performance alongside borehole length and bleed ratio (Deng, *et al.* 2005). Hence, this parameter was tested under both laboratory and field conditions. Thermal needle probe (TNP) tests were first carried out on the saturated drill cuttings samples in March 2017. The procedure was performed following ASTM D-5334-08 protocol (ASTM 2008) with a Hukseflux™ needle thermal conductivimeter.

A thermal response test (TRT) was also conducted in November 2017 to determine the *in situ* thermal conductivity accounting for conductive as well as advective heat transfer mechanisms. After recirculating groundwater in the SCW for 24 hours to measure initial ground temperature, heat was injected in the borehole for six days using a water heater having a 24 kW nominal capacity, followed by a three-day recovery phase. During the TRT, water was recirculated in the SCW without bleed and flow rate was maintained around 98 L/min. Entering (EWT) and leaving (LWT) groundwater temperatures were monitored at the inlet and outlet of the water heater with temperature sensors having 0.2 °C accuracy. The heating power Q was maintained around 23.4 kW assuming that $Q = \Delta T \dot{V} (\rho C_p)_w$, where ΔT is the difference between the EWT and LWT, $\dot{V}$ is the pumping rate and ρC_p is the water volumetric heat capacity. This value implies a correction that accounts for the heat loss in the horizontal pipes between the well and the MGL.

Both tests were interpreted using Kelvin's infinite line source theory (Mogensen 1983), where the temperature rise only depends on the heating power and thermal conductivity k. This approximation is valid after a short transient period represented by $t \geq 5 r_b{}^2/\alpha$:

$$k_{eq} = \left(\frac{q}{4\pi\Delta T}\right)\ln\left(\frac{t_2}{t_1}\right) \text{ with } k_{eq,hetero} = \prod_{i=1}^{N} k_i^{\phi_i} \text{ and } k_{eq,fractured} = \sum_{i=1}^{N} \phi_i k_i \qquad (1)$$

where $\alpha = k/\rho C_p$ is the thermal diffusivity, r_b is the borehole radius, q is the specific heat load and ΔT is the temperature change between time t_1 and t_2. k_{eq} represents the equivalent thermal conductivity of a composite medium as a function of the volumetric fraction Φ_i and the thermal conductivity k_i of N components. Regarding the TNP tests, the saturated cutting samples were considered a heterogeneous medium composed of rock, 3% of trapped air, and a variable water volumetric fraction estimated after stove-drying the samples. As for the TRT, the *in situ* saturated bedrock was assimilated to a fractured medium with an effective porosity of 2%, which is typical of fine-grained and poorly fissured sedimentary rock (Bear and Cheng 2010).

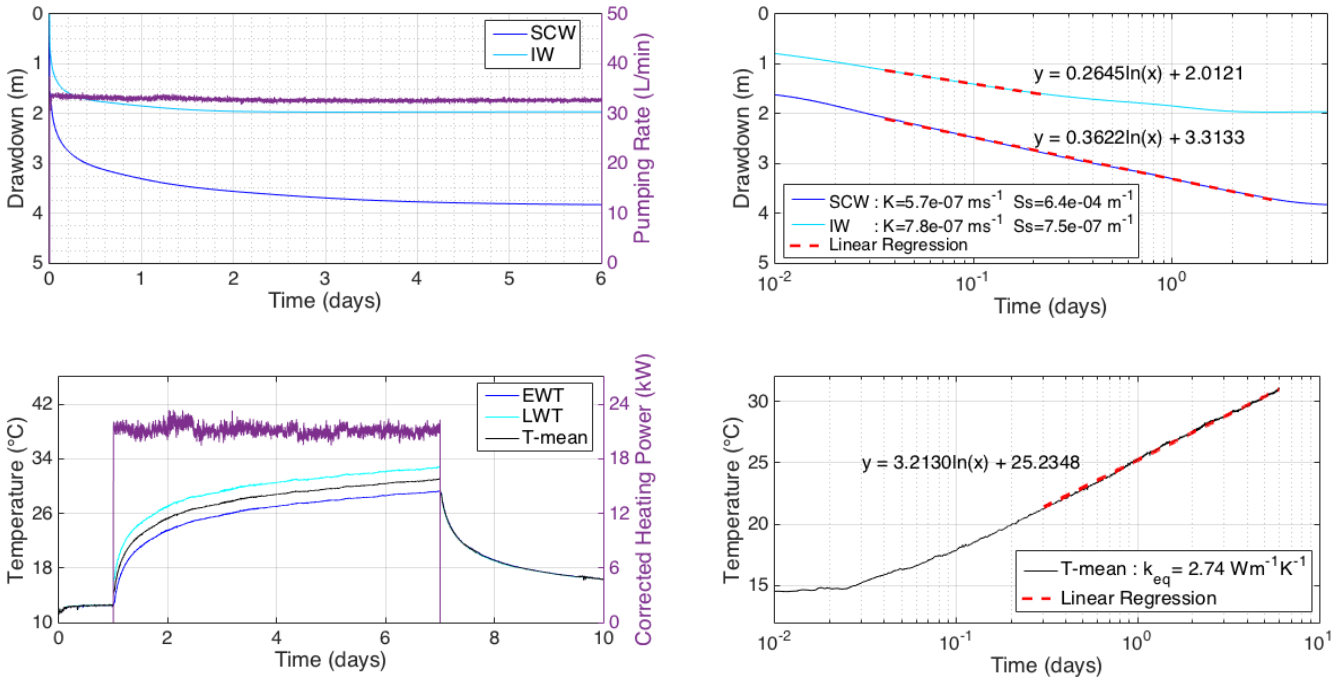

Figure 2 Pumping test data (upper left) and analysis (upper right); Thermal response test data (lower left) and analysis (lower right).

The mean thermal conductivity of the rock fragments was estimated to be 2.49 $Wm^{-1}K^{-1}$ by the TNP tests performed in laboratory. The *in situ* value was rather evaluated at 2.74 $Wm^{-1}K^{-1}$ and 2.78 $Wm^{-1}K^{-1}$, respectively, for the equivalent fractured medium and the rock matrix (see Figure 2). A derivative-based analysis confirmed these values (Pasquier 2018). The difference between the laboratory and *in situ* values is minor and can be attributed to the (1) different borehole length tested by the TNP tests (305 m) and the TRT (215 m), (2) advective heat transfer promoted by the pumping action, (3) scale effects and (4) modified water content of the laboratory samples. Note that no temperature fluctuation was observed in the IW during the test.

NUMERICAL MODELLING STRATEGY

Modelling the complex hydrogeothermal processes occurring in SCWs operation can be achieved by coupling a groundwater flow model and a heat transfer model in the Comsol Multiphysics environment (Nguyen, *et al.* 2012; Eppner, *et al.* 2015, 2017a, 2017b). In the present work, the SCW geometry illustrated in Figure 1 was represented by a simplified 2D axisymmetric configuration in order to minimize computation time. Accordingly, the riser pipe was adapted to a concentric annular space of equivalent cross-sectional area. The model dimensions are listed in Table 2.

Table 2. Geometry of the Numerical Model

Parameter	Aquifer	Upper SCW	Lower SCW	Riser Pipe	Reinjection Pipe
Depth	215 m	20 m	215 m	18 m	215 m
Radius	10 m	121 mm	83 mm	44.58 mm *(outer)*	30.16 mm *(outer)*
Wall thickness	-	-	-	5.82 mm	5.82 mm

The geometrical elements were defined with three distinct materials representing the aquifer, the HDPE pipes and groundwater. The experimental hydraulic and thermal properties provided by the field investigation were directly attributed to the aquifer domain. More specifically, the hydraulic properties derived from the SCW data and the *in situ* thermal conductivity of the rock matrix obtained from the TRT analysis were selected. Typical values for porosity and volumetric heat capacity of most rocks (Banks 2008) were also assigned to the aquifer domain. The pipes and groundwater thermal parameters were obtained respectively from the manufacturer's specifications and the reported standard values at 20°C (see Table 3). The hydraulic paramaters were attributed to represent, respectively, a perfectly impervious solid and a perfectly pervious liquid with very low storage.

Table 3. Hydraulic and Thermal Properties of Model Materials

Parameter	Symbol	Unit	Aquifer	Pipe	Water
Volumetric Heat Capacity	ρC_p	kJ $m^{-3}K^{-1}$	2070	2174	4176
Porosity	n	-	0.02	1e-5	1
Thermal Conductivity	k	W $m^{-1}K^{-1}$	2.78*	0.42	0.59
Hydraulic Conductivity	K	m s^{-1}	5.7e-7*	1e-9	1000
Specific storage	S_s	m^{-1}	6.4e-4*	4e-10	4e-10

*Values provided by the detailed field investigation

Governing Equations

Groundwater motion in the model is assimilated to a saturated flow within an equivalent porous medium. Hence, the governing equations are the continuity equation and Darcy's law as expressed by Equation 2, where ρ is the fluid density, g is the gravitational acceleration, p is the pressure, u is the Darcy velocity, K is the hydraulic conductivity, z is the elevation and S_s is the specific storage :

$$\rho S_s \frac{\partial p}{\partial t} = -\nabla \cdot \left(\rho u\right) \text{ and } u = \frac{-K}{\rho g}\left(\nabla p + \rho g \nabla z\right) \quad (2)$$

Thermal effects in the developed model consider conductive and advective heat transfer mechanisms. The latter accounts for the motion of the water within the well and the surrounding aquifer, and depends on the Darcy velocity computed by Equation 2. The state equation solved for heat transfer is given by Equation 3, where T is the groundwater temperature and k_{eq} and $(\rho C_p)_{eq}$ are respectively the thermal conductivity and volumetric heat capacity of the equivalent porous medium :

$$\left(\rho C_p\right)_{eq}\frac{\partial T}{\partial t}+\left(\rho C_p\right)_w u\cdot\nabla T=\nabla\cdot\left(k_{eq}\nabla T\right) \tag{3}$$

Initial and Boundary Conditions

Boundary conditions used in the model are illustrated in Figure 3. The confined aquifer roof was located 3 m below the surface at the soil-bedrock interface. A constant hydraulic head of 213 m relative to the base of the borehole was set as an initial head for the domain and along the lateral boundary. As the ground below the SCW was not explicitly represented in the model for efficiency purposes, both inflow and outflow boundaries located at the top and the bottom of the well were attributed a normal velocity $v = \dot{V}(1-\beta)/A$ derived from the pumping rate $\dot{V}$, the corresponding cross-sectional area A and a bleed ratio β. The latter was fixed at zero for the riser pipe top boundary.

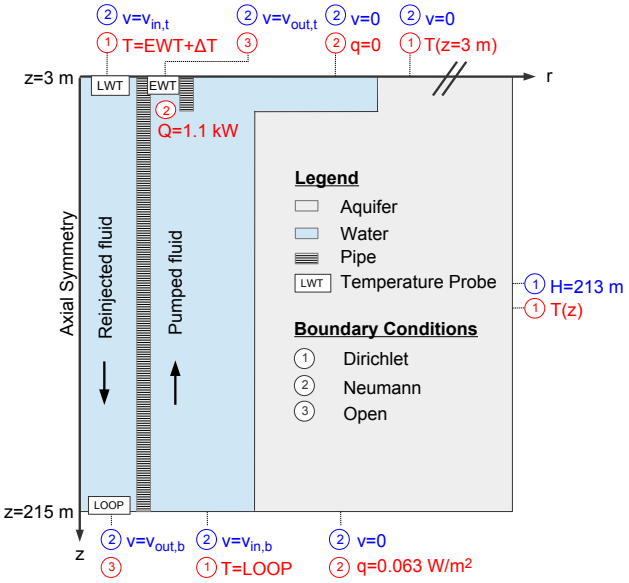

Figure 3 Boundary conditions of the hydraulic (blue) and heat transfer (red) models.

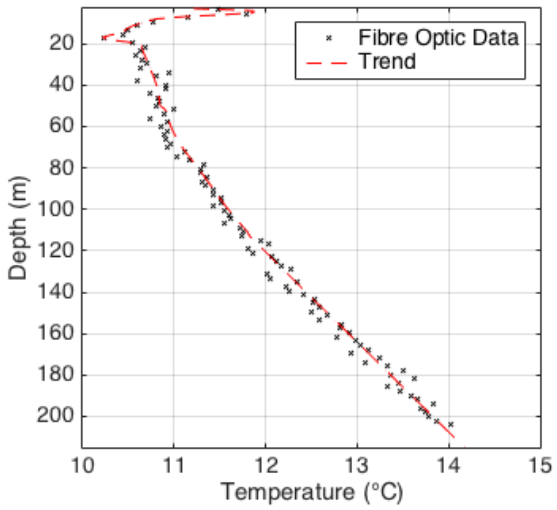

Figure 4 Initial solution and lateral boundary condition T(z) used in the simulation.

As for the thermal conditions, a natural geothermal heat flux (0.063 W m^{-2}) was derived from the equivalent thermal conductivity of the aquifer and the geothermal gradient, and then set as the specific heat load q at the base of the model. The initial solution on the whole simulation domain and temperatures along the outer radial boundary and the aquifer roof were intended to correspond to vertical temperature profiles measured in the SCW (T(z)). The latter, as well as the thermal load Q imposed by the MGL apparatus (the heat pumps or the water heater) can be implemented in the finite element model via interpolation functions. The temperature variation ΔT induced by the thermal load is computed by the model at each time step and considered as the difference between the outlet and intlet fluid temperatures:

$$LWT = EWT + \Delta T \text{ with } \Delta T = \mathcal{Q} \Big/ \left(\dot{V} \left(\rho C_p \right)_w \right) \quad (4)$$

where EWT is integrated along the riser pipe upper boundary. The mean temperature along the well lower outflow boundary is also integrated and then imposed on the adjacent inflow boundary. Ultimately, a heat source equivalent to the power consumption of the submersible pump was set in the annular region at a depth of 18 m.

EXPERIMENTAL VALIDATION OF THE NUMERICAL MODEL

A simple simulation reproducing the previously described TRT was conducted to validate the numerical model. It is important to note that the parameters derived from the field study were directly implemented in the model and that no calibration procedure was performed. The experimental heating loads and pumping rates were also directly implemented at intervals of one minute. A temperature profile measured in the SCW 15 minutes before the test was set as the temperature initial solution on the whole domain and imposed at the lateral boundary and aquifer roof (see Figure 4). This simulation was carried out using a maximum time step of one minute. The difference between the simulated and the experimental temperatures is analyzed and the mean absolute error (MAE) is calculated. Figure 5 shows a very good agreement between experimental and computed groundwater temperatures without any model calibration. The resulting MAE is 0.14 °C.

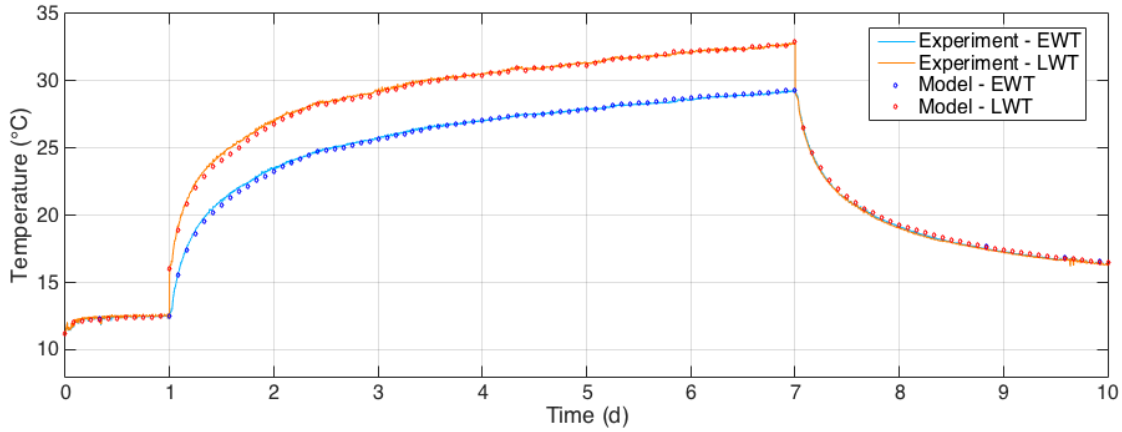

Figure 5 Comparison of EWT and LWT as computed by the numerical model and measured experimental.

FURTHER RESULTS AND DISCUSSION

The modelling strategy described in this work was developed with the intent to reproduce the hydrogeothermal behaviour of an experimental SCW installation. Hence, the real system dimensions and materials were reproduced with minimal simplifications aiming to lighten the computation burden. The ground hydrogeothermal properties obtained from an independent *in situ* investigation of the SCW surroundings were also directly implemented in the model. A simple simulation of the TRT showed that this strategy allows for the computation of groundwater temperatures at the inlet and outlet of the well with a MAE of 0.14 °C, which is smaller than the accuracy of the temperature sensor (0.2 °C).

It was previously mentioned that there is a minor difference between the rock thermal conductivity (2.78 W $m^{-1}K^{-1}$) derived from the *in situ* TRT - which was used for the experimental validation of the model - and the laboratory TNP tests (2.49 W $m^{-1}K^{-1}$). In order to evaluate the impact of this variation on the temperatures computed

by the model, a comparative simulation was carried out using the second value. The resulting inlet and outlet groundwater temperatures were distinctly overestimated and a MAE of 1.04 °C was calculated between the model response and the experimental data. Calibration of the volumetric heat capacity value within a realistic range did not allow a satisfying agreement. These results suggest that a slight variation in ground properties estimates can be a significant source of error and emphasize the advantages conferred by *in situ* tests when evaluating the local values.

In the scope of this study, it was also proposed to evaluate the influence of the pump placement on the performance of the system. A quick modification to the model boundaries allowed for the switch of the pump and reinjection depths, therefore placing the pump inlet at the bottom of the well (215 m) and the reinjection at a depth of 18 m. The TRT simulation was then repeated. Results showed minimal deviation (MAE of 0.12 °C) from the inlet and outlet groundwater temperatures computed by the previous top-pumped simulation presented in Figure 5. These results suggest that installation and maintenance difficulties occasioned by the widespread down-pumped configuration of SCWs (Orio, *et al.* 2005; Pasquier, *et al.* 2016) could be avoided by placing the submersible pump in the annular region at the top of the well since both configurations provide, in the absence of bleed, the same EWT.

CONCLUSION

In this paper, a finite element model coupling transient advection-diffusion of heat and groundwater flow was developed to simulate the behaviour of an experimental SCW connected to a large-scale geothermal laboratory. The thermal conductivity, hydraulic conductivity and specific storage of the aquifer were identified by a comprehensive characterization campaign and were directly integrated in the model. Results of a simple simulation reproducing an *in situ* thermal response test showed that without any calibration procedure, the model reproduces the experimental EWT and LWT with a MAE of 0.14 °C. Further simulations also suggest that the pump inlet depth has little impact on the well heat exchange efficiency in the absence of bleed. Ongoing research activities and incoming experimental data from the MGL operation in the heating and cooling mode should allow further development of the model so as to include the impact of bleed and the potential hydrogeothermal interaction with a nearby injection well.

ACKNOWLEDGMENTS

The authors acknowledge the financial support by Institut de l'Énergie Trottier (IET) and would like to thank Étienne Bélanger and Pierre Beaudry for their technical support.

NOMENCLATURE

α	=	Thermal diffusivity (m^2s^{-1})
β	=	Bleed ratio (-)
$\dot{V}$	=	Flow rate (m^3s^{-1})
ρ	=	Density ($kg\ m^{-3}$)
Φ	=	Volumetric fraction (-)
A	=	Cross-sectional area (m^2)
C_p	=	Specific heat capacity ($J\ kg^{-1}K^{-1}$)
H	=	Hydraulic head (m)
K	=	Hydraulic conductivity ($m\ s^{-1}$)
k	=	Thermal conductivity ($W\ m^{-1}K^{-1}$)
n	=	Porosity (-)
Q	=	Heating power (W)
q	=	Specific heat load ($W\ m^{-1}$)
r_b	=	Borehole radius (m)
S_s	=	Specific storage (m^{-1})
T	=	Temperature (°C)
t	=	Time (s)
u	=	Darcy velocity ($m\ s^{-1}$)
v	=	Normal velocity ($m\ s^{-1}$)
z	=	Depth (m)

Subscripts

b	=	bottom
eq	=	equivalent
t	=	top
w	=	water

REFERENCES

Abu-Nada, E., Akash, B., Al-Hinti, I., Al-Sarkhi, A., Nijmeh, S., Ibrahim, A., & Shishan, A. (2008). Modeling of a geothermal standing column well. *International Journal of Energy Research*, *32*(4), 306–317.

ASTM International. (2008). D5334-08 Standard Test Method for Determination of Thermal Conductivity of Soil and Soft Rock by Thermal Needle Probe Procedure. ASTM International.

Banks, D. (2008). *An introduction to thermogeology: ground source heating and cooling*. Oxford: Blackwell.

Bear, J., & Cheng, A. H. D. (2010). *Modeling groundwater flow and contaminant transport* (Vol. 23). Springer Science & Business Media.

Chang, K. S., Kim, M. J., & Kim, Y. J. (2017). An Experimental Study on the Thermal Performance Evaluation of SCW Ground Heat Exchanger. *International Journal of Air-Conditioning and Refrigeration*, *25*(01), 1750006.

Comsol Multiphysics. (2013). Version 4.4, COMSOL.

Cooper, H. H., & Jacob, C. E. (1946). A generalized graphical method for evaluating formation constants and summarizing well-field history. *Eos, Transactions American Geophysical Union*, *27*(4), 526–534.

Croteau, J. É. (2011). *Évaluation des paramètres influençant les températures d'opération des puits à colonne permanente*. École Polytechnique de Montréal.

Deng, Z., Rees, S. J., & Spitler, J. D. (2005). A model for annual simulation of standing column well ground heat exchangers. *HVAC&R Research*, *11*(4), 637–655.

Eppner, F., Pasquier, P., Baudron, P. (2015). Development of a Thermo-Hydro-Geochemical Model for Low Temperature Geoexchange Applications. In *Comsol Conference, Boston, USA*.

Eppner, F., Pasquier, P., & Baudron, P. (2017). A coupled thermo-hydro-geochemical model for standing column well subject to CO2 degassing and installed in fractured calcareous aquifers. *Geomechanics for Energy and the Environment*.

Eppner, F., Pasquier, P., & Baudron, P. (2017). Investigation of Thermo-hydro-geochemical Processes in a Standing Column Well Intersected by a Fracture. In *Proceedings of the IGSHPA Technical/Research Conference and Expo*.

Freeze, R. A., & Cherry, J. A. (1979). *Groundwater, 604 pp*. Prentice-Hall, Englewood Cliffs, NJ.

Globensky, Y. (1987). Géologie des Basses-Terres du St-Laurent (Geology of the St. Lawrence Lowlands). *Ministry of Energy and Resources, General Direction for Geologic and Mineral Exploration, Québec, Report MM*, 85-02.

Hukseflux Therml Sensors. (n.d.). Multi-purpose Thermal Needle System for Thermal Resistivity/Conductivity Measurment. Hukseflux Thermal Sensors.

Lee, K. S. (2011). Modeling on the performance of standing column wells during continuous operation under regional groundwater flow. *International Journal of Green Energy*, *8*(4), 474–485.

Lee, S., Lee, C., Moon, H., Jeong, J., Lee, Y., Kim, H., Jo, S. (2016). Thermal response performance of the heat exchanger of a standing column well based on the location of the return pipe. *JP Journal of Heat and Mass Transfer*, *13*(4), 559.

Minea, V. (2013). Experimental investigation of the reliability of residential standing column heat pump systems without bleed in cold climates. *Applied Thermal Engineering*, *52*(1), 230–243.

Mogensen, P. (1983). Fluid to duct wall heat transfer in duct system heat storages. *Document-Swedish Council for Building Research*, (16), 652–657.

Natural Resources Canada. (2018). *Energy Use Data Handbook*. Retrieved from :
http://oee.nrcan.gc.ca/corporate/statistics/neud/dpa/showTable.cfm?type=HB&sector=aaa&juris=ca&rn=2&page=0

Ng, B. M., Underwood, C. P., & Walker, S. L. (2011). Standing column wells—Modeling the potential for Applications in Geothermal Heating and Cooling. HVAC&R Research, 17(6), 1089–1100.

Nguyen, A., Pasquier, P., & Marcotte, D. (2012). Multiphysics modelling of standing column well and implementation of heat pumps off-loading sequence. In *Comsol Conference, Boston, USA*.

Nguyen, A., Pasquier, P., & Marcotte, D. (2015). Thermal resistance and capacity model for standing column wells operating under a bleed control. *Renewable Energy*, *76*, 743–756.

Orio, C. D., Chiasson, A., Johnson, C. N., Deng, Z., Rees, S. J., & Spitler, J. D. (2005). A Survey of Standing Column Well Installations in North America. *ASHRAE Transactions*, *111*(2).

Pasquier, P. (2018). Interpretation of the first hours of a thermal response test using the time derivative of the temperature. *Applied Energy*, *213*, 56–75.

Pasquier, P., Nguyen, A., Eppner, F., Marcotte, D., & Baudron, P. (2016). Standing column wells. In *Advances in Ground-Source Heat Pump Systems* (pp. 269–294). Elsevier.

Rees, S. J., Spitler, J., Deng, Z., Orio, C., & Johnson, C. (2004). A study of geothermal heat pump and standing column well performance. *ASHRAE Transactions*, *110*(1), 3–13.

Spitler, J. D., Rees, S. J., Deng, Z., Chiasson, A., Orio, C. D., & Johnson, C. (2002). R&D studies applied to standing column well design. *ASHRAE Research Project*.

[This page has been intentionally left blank]

IGSHPA SWEDEN 2018 Research Conference

DOI: 10.22488/okstate.18.000002

ATES SYSTEM MONITORING PROJECT, FIRST MEASUREMENT AND PERFORMANCE EVALUATION: CASE STUDY IN SWEDEN

MOHAMMAD ABUASBEH **JOSÉ ACUÑA**

ABSTRACT

Performance of Aquifer Thermal Energy Storage (ATES) systems for seasonal thermal storage depends on the temperature of the extracted/injected groundwater, water pumping rates and the hydrogeological conditions of the aquifer. ATES systems are therefore often designed to maintain a temperature difference possible between the warm side and cold side of the aquifer, without risking hydraulic and thermal intrusion between them or thermal leakage to surrounding area, i.e. maximize hydraulic and thermal recovery. Monitoring the operation of pumping and observation wells is crucial for the validation of ATES groundwater models utilized for their design, and measured data provides valuable information for researchers and practitioners working in the field. After months of planning and installation work, selected measurements recorded in an ATES monitoring project in Sweden during the first three seasons of operation are reported in this paper. The ATES system is located in Solna, in Stockholm esker, and it is used to heat and cool two commercial buildings with a total area of around 30,000 m^2. The ATES consists of 3 warm and 2 cold pumping wells that are able to pump up to 50 liters per second.

The monitoring system consists of temperature sensors and flow meters placed at the pumping wells, a distributed temperature-sensing rig employing fiber optic cables as linear sensor and measuring temperature every 0.25 m along the depth of all pumping and several observation wells, yielding temporal and spatial variation data of the temperature in the aquifer. The heat injection and extraction to and from the ground is measured using power meters at the main line connecting the pumping wells to the system. The total heat and cold extracted from the aquifer during the first heating and cooling season is 190MWh and 237MWh, respectively. A total of 143 MWh of heat were extracted during the second heating season. The hydraulic and thermal recovery values of the first year of operation was 1.37 and 0.33, respectively, indicating that more storage volume (50500m^3) was recovered during the cooling season than injected (36900m^3) in the previous heating season. The DTS data showed traces of the thermal front from the warm storage reaching the cold one. Only 33% of the thermal energy was recovered. These losses are likely due to ambient groundwater flow as well as conduction losses at the boundaries of the storage volume. Additionally, the net energy balance over the first year corresponds to 0.12 which indicates a total net heating of the ATES over the first year. It is recommended to increase the storage volume and achieve more hydraulic and thermal balance in the ATES system. This can enhance the thermal recovery and overall performance. Continuous monitoring of the ATES is and will be ongoing for at least 3 more years. The work presented in this paper is an initial evaluation of the system aiming to optimize the ATES performance.

INTRODUCTION

Groundwater stored in glaciofluvial deposits of sand and gravel is a useful source for storing and providing thermal energy to the built environment. The reason is the useful properties of groundwater as heat storage medium with low thermal conductivity and high heat capacity (Lee, 2010, 2013). With increasing pressure on limiting greenhouse gas emissions as Swedish national goals (Regeringskansliet, 2017) and the international climate agreement from Paris 2015 (United Nations, 2015) the interest in renewable energy is growing. Shallow geothermal energy systems such as aquifer thermal energy storage (ATES) systems provides an alternative which usually comprises of a mixture of energy sources such as biofuels, combustible waste but also fossil fuels (Swedish Energy Agency, 2015).

ATES are categorized as open loop systems and normally consists of a cold and a warm well pool. During the summer period, groundwater is extracted from the cold well pool of the aquifer, to cool buildings through a heat exchanger. The heated water is then re-injected and stored into the warm well pool of aquifer. In the winter period, the system is reversed, and stored heat is utilized in the building (often with the help of a heat pump) as cooled

Mohammad Abuasbeh (abuasbeh@kth.se) is a PhD student and José Acuña is a researcher at KTH Royal Institute of Technology, Sweden

groundwater is re-injected. The common range of temperature during operation is between 5° and 20°C (Possemiers, 2014) between winter and summer, respectively.

The main reason for storing energy in groundwater is the favorable properties of thermal capacity and conductivity. Common hard rocks like granite and sandstone have a thermal conductivity of about 2-4 W/(m·K) and a volumetric heat capacity of about 0.5-0.9 (*kWh/m³.K)* (1.8-3.24 M*J/m³.K)* (Svedinger, 1981), respectively, while water has a thermal conductivity of 0.57 (*W/m.K)* and volumetric heat capacity of 1.16 (kWh/m³.K) (4.17 M*J/m³.K)* (Sundberg, J, 1991). This means that water has a larger capacity for storing energy and better properties for storage as less energy will be lost to the surrounding environment through conduction (groundwater movement counter acts the latter). In addition, ATES system allow for larger flowrate and thus higher power production per well in comparison to closed loop systems.

ATES systems are commonly used in combination with a ground source heat pump for achieving what is a sufficient temperature level of space heating. Storage efficiency for an ATES system can be expressed as thermal recovery, defined as the fraction of stored energy that is recovered. To estimate ATES system performance and its impacts on its vicinity, usually groundwater numerical models are developed as well as field measurements for model calibration. Several studies related to ATES have been conducted using numerical and/or monitoring data analysis since the 1980s to evaluate thermal performance of ATES systems, examples of these are (Bakr et al., 2013; Molz et al., 1981; Sauty et al., 1982; W. T. Sommer et al., 2014; Visser et al., 2015). Different values of thermal recovery are reported in the scientific literature, which is natural due to the unique conditions of every aquifer. Field experiments by (Sauty et al., 1982) show recovery values of 18.9 – 68.0%. (Molz et al., 1981) reported 66% and 76%, while values up to 56% and 87% are presented by (Molz et al., 1983) and (Bakr et al., 2013) respectively. (W. Sommer, 2015) reported average thermal recovery values of 82% for cold storage and 68% for hot storage in a monitoring project that was conducted over the period 2005-2012 in the Netherlands. For ATES operating under low temperatures (<25°C) the dominant causes for thermal losses are ambient ground water flow and conduction losses across the boundaries of the storage volume (Bloemendal & Hartog, 2018). With regard to conduction losses from the edges of storage volume, increasing the storage volume enhances the thermal recovery of the system since it is the ratio between the storage volume boundaries area and the storage volume decreases with increasing volume. Additional source of losses can be due to turbulent losses in the well caused by uneven distribution of inflow along the screen section. Therefore, pump placement with respect to the well screen and screen section hydraulic conductivity would improve well efficiency (Houben & Hauschild, 2011).

Measured data in ATES systems is needed to enhance the accuracy of the ATES thermal recovery evaluation, as well as calibrating the thermal properties in the ATES models. Traditionally, temperatures in ATES are measured using one or few local measurement points with respect to the well depth, but there seems to be a growing interest in more refined spatial and long term temporal measured data of ATES systems to better understand the thermal behavior of the systems as well as to calibrate and develop ATES models and design tools. For instance, to take into account the unequal distribution of flowrate along the depth of the well screen due to aquifer heterogeneity as well as to evaluate the proper spacing between wells to avoid thermal break through. In recent years, with the development of distributed temperature sensing (DTS) technology, information about the temperature profiles with depth as well as thermal plume propagation with respect to time became more attainable. An example of monitoring projects that have been conducted using distributed temperature sensing technology (DTS) in ATES system in the Netherlands (W. T. Sommer et al., 2014). Sommer mentioned that no breakthrough was observed in his study but observed preferential flows across the wells screen. Flowrates and well spacing overestimation were used to reduce thermal interference within the ATES. Although this is beneficial for a single ATES system, it would limit the number of other ATES systems to be installed within in the same area. Therefore, the use of DTS technology to monitor ATES system can potentially provide long-term refined spatial and temporal temperature data that can be utilized to improve ATES system design.

This paper presents a full description of an ATES system installation in Stockholm, Sweden as well as few data sets from the first year of ATES operation. The monitoring system consist of groundwater flow meters, water level and temperature sensors. Fiber optical cables and DTS equipment are used to monitor the temperature profile with depth as well as the thermal plume temporal propagation in the aquifer. The system started operating in October 2016 and this data is intended to be used to evaluate the actual ATES performance as well as calibrate and validate a groundwater model that is currently being developed for the site.

DESCRIPTION OF THE ATES INSTALLATION

The study area is located in the northern part of Stockholm, at the north-western side of Lake Brunnsviken, by the E4 highway. The ATES system is positioned on the Stockholm esker in a property that consist of two office buildings with total area of approximately 30,000 m^2, owned by Vasakronan real estate company. The estimated yearly energy consumption are approximately 500 and 600 MWh/year of heating and cooling, respectively. The ATES system is connected to two Carrier heat pumps of 700 and 800 kW cooling capacity. The ATES system has been in operation since autumn 2016 and consists of 4 hot (one of which is not currently used) and 2 cold wells in the north and south of the property respectively. The allowed pumping flowrate for both extraction and injection is up to 50 l/s groundwater.

Hydrogeological Conditions

The main geological feature is the Stockholm esker stretching nearly in the north- northwest direction. The landscape is under the level of the highest marine shoreline giving a more complex soil stratigraphy with deposits of clay but also remains of relic saltwater (Boman & Hanson, 2004). The top of the ridge of the esker has partly been subject to excavation due to a former use as gravel pit. The core of the esker is passing through the southern side of the property. The bedrock is constituted by acidic intrusive rock as well as metamorphic rock of sedimentary origin with varying elevation. Depth from surface to bedrock within the property ranges from 12 to 20 m and aquifer thickness ranges from 8 to 15 m from north to south. It is rather covered by thin layers of soil of foremost clay. The landscape is further characterized by outcrops partly covered with till. The hydraulic conductivity of the esker was estimated from pumping tests to be in the range of 2.5-2.9*10^{-3} m/s. During a pumping test carried out over 35 days with a stable flow of 27 l/s, transmissivity estimates ranges were 4.0-5.8 *10^{-3} m^2/s. Drillings had shown that the main geological material in the esker comprises sand and gravel. However, at the northern part, it was presented that the aquifer have fillings of finer grained material as silt (WSP, 2014). In figure 5, one example of each the cold and the warm side are presented showing the geological stratigraphy, water level and filter section depth of each well. The aquifer is mostly unconfined shallow aquifer with some parts in the north covered with clay. The aquifer showed hydraulic connection with slight delay with the lake Brunnsviken located around 100 m toward the east of the property. The hydraulic gradient vary depending on the water level in Brunnsviken.

Monitoring system

Each well in the ATES system is installed in an underground concrete structure (small room) accessible by a ladder. The concrete structures (rooms) are linked with each other and with the pumps control room by underground pipes. These pipes are used as connection paths for signal and electric cables linking different components installed in the wells with the control room in the building garage. Each well room consists of a pumping and an observation well. Each observation well is equipped with a submerged diver of type STS ATM/N/T DMM029 that measures both the temperature and water level. The diver has a measuring range and accuracy of -25 to 80 ± 1°C and up to 25 ± 0.25% bars. Each pumping well is equipped with a pump of type GRUNDFOS SP 46-4-C for warm wells and GRUNDFOS SP 60-4 for cold wells, as well as a pressure sensor (Siemens QBE2103-P4) and temperature sensor (Siemens QAE2121.010) measuring range and accuracy of up to 4 ± 0.1% bars and -30 to 130 ±0.5°C respectively. The latter sensors are installed on the main pipe just outside the well. All wells on each side (warm and cold) are grouped into one main supply pipe to extend towards the building. The building is equipped with a secondary heat exchanger that separates the ground water loop and the heat pump secondary fluid loop to avoid clogging in the evaporator of the heat pump. Energy meters (Siemens Sitrans F M MAG 5000 & Siemens QAE21) are installed on both sides of the secondary heat exchanger to monitor energy exchange between the ATES and buildings (see Figure 1).

ATES Operation in brief

Heating Mode: The wells are used in injecting or extracting mode depending on the season. During the heating season, water from the warm side of the ATES is extracted and re-injected in the cold side after being cooled

down through heat exchange with the building. Heating is done with the assistance of the heat pumps. If the temperature in the warm wells drop below a pre-defined set point, the heating is supplied through district heating network.

Cooling Mode: Throughout the heating season, cold storage is being accumulated. During the summer, the cycle is reversed and free cooling is utilized. Water from the cold side of the ATES is extracted and re-injected in the warm side after being heated up through heat exchange with the building. If the temperature in the cold wells exceeds a pre-defined set point, the cooling is supplied with the assistance of the heat pumps. During the cooling season, occasional heating loads as well as heat for domestic hot water is provided by district heating network (see figure 1).

Distributed temperature measurements

Two continuous fiber optical cables have been installed in each side of the ATES wells groups. Each cable consists of four fibers two of which are used. Each cable is connected from both sides to the DTS equipment to enable both single and double-ended connection configuration. Along each cable, four sections of the fiber cable are coiled in the beginning, middle and the end of the cable to be used for calibration. The fiber cables are connected to two distributed temperature sensing instruments HALO and SILIXA XT with sampling resolution of 2 and 0.25 m, respectively (see figure 2). The former instrument was used only temporarily while the latter is installed for permanent measurements. Some SILIXA XT data is presented in this paper. Two additional PT100 resistance thermometers with accuracy of ±0.005°C are connected to the DTS and used to provide dynamic measurements of the calibration baths near the DTS. Physical principle used in the DTS equipment is based on the glass fibers sensitivity to temperature change. The DTS equipment sends a laser beam through the fiber and collects the back-scattered signal and translate it into temperature (Suárez et al., 2011). The temperature received from the DTS is averaged over both space and time. The temporal and spatial sampling resolutions of the DTS instrument are set to be 10 minutes and 0.25 m respectively. The DTS has four channels. The first and second channels are connected to the fiber cable installed in cold side. The third and forth channels are connected to the fiber cable installed in warm side (see figure 2). The laser beam is sent from one channel at a time. Therefore, each channel integrates and records the temperatures once every 40 minutes. Since the cable installation was continuous, additional splices along the cable were avoided (except one splice in the beginning of the cable to connect it to the DTS). This significantly avoids the risk of local losses along the fiber cable and make the calibration procedure less complex and temperature measurements more reliable. Channel 1 and 2 (in XT Silixa DTS) are measuring the cold side using the same fiber cable but two different fibers within the cables. The same has been done for channel 3 and 4 (in XT Silixa DTS) on the warm side.

DTS Calibration: the DTS measurement setting used is single ended mode with dynamic calibration using two matching sections in the same bath at the beginning and the end of the fiber cable (Hausner et al., 2011). The DTS equipment is calibrated using equation 1. Where at position z (in m) along the fiber cable length, $P_S(z)$, $P_{aS}(z)$ and $T(z)$ are the signal strength of the Raman-Stokes, Raman-AntiStokes and the temperature at that position, respectively. Additionally, γ (in Kelvin) represents the energy shift between the incident and scattered photon. C is a dimensionless parameter to take into account and calibrate the local losses. These local losses occur in connectors and fiber splices. Δa (in m^{-1}) is the differential attenuation in the fiber along the fiber cable.

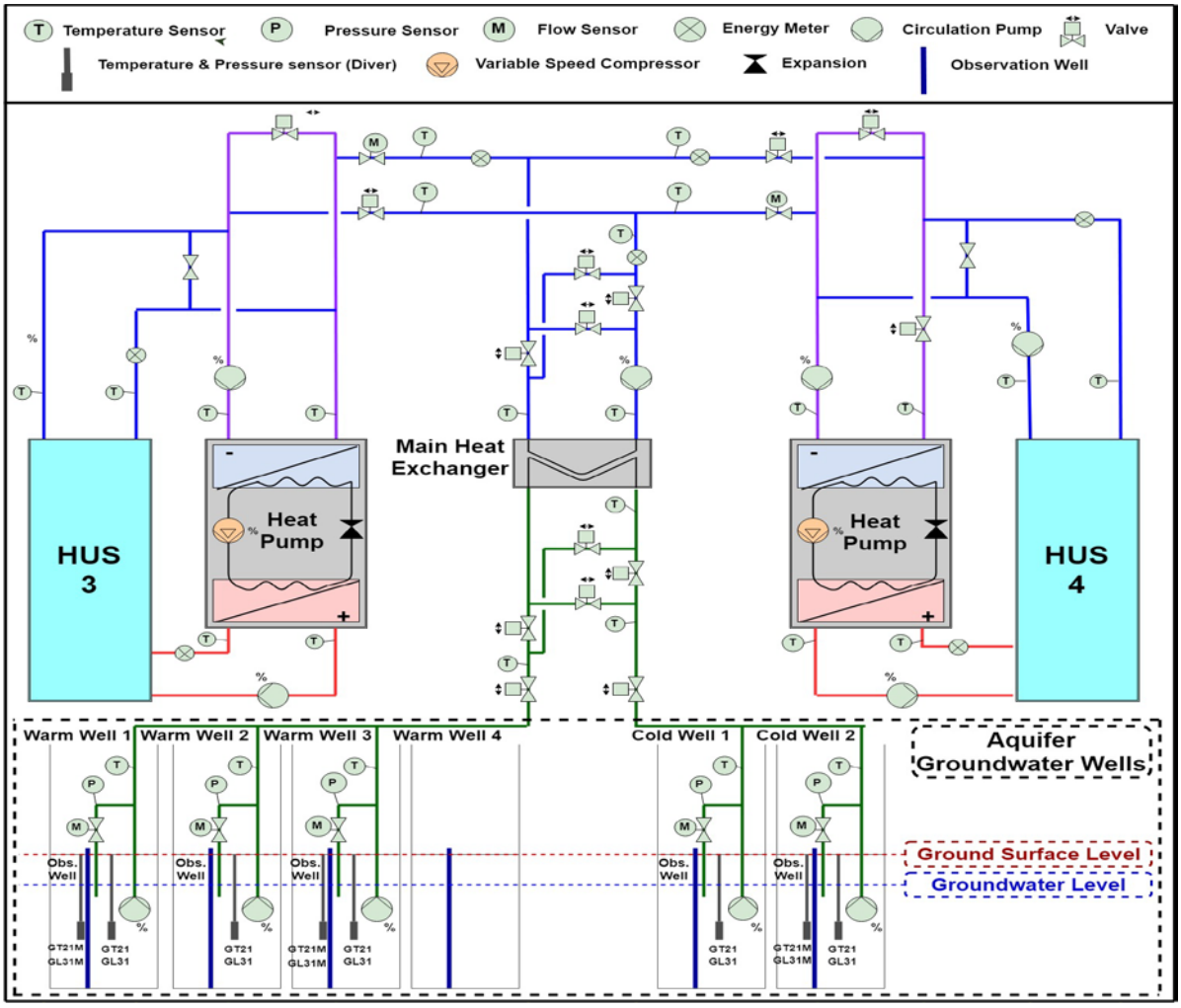

Figure 1 Schematic diagrams that shows the wells in ATES, heat pump and their connection to the building

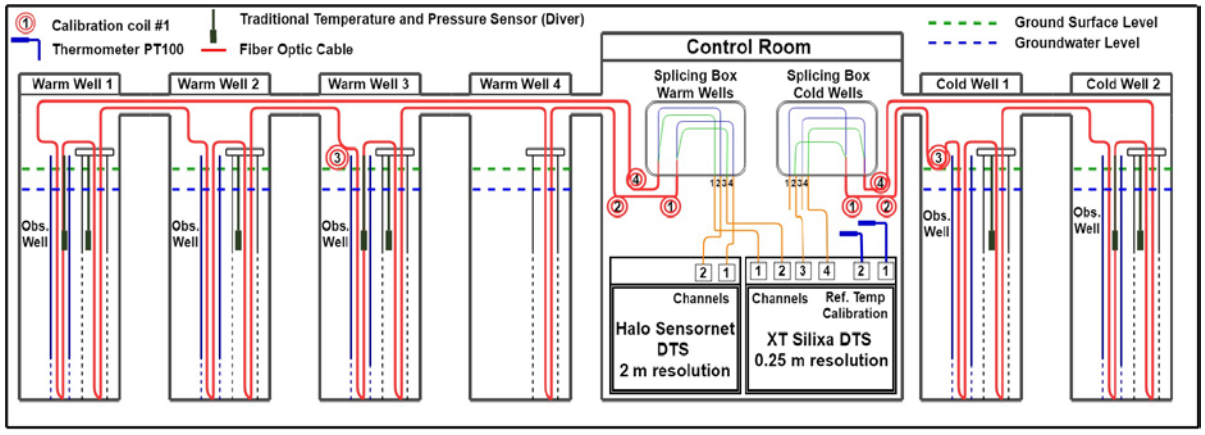

Figure 2 Schematic diagrams that shows the fiber cable installation in warm and cold wells in ATES and channel connections

$$T(z) = \frac{\gamma}{\ln \frac{P_S(z)}{P_{aS}(z)} + C - \Delta\alpha z} \quad (1)$$

The first and fourth calibration coils, for each the warm and cold side, (at the beginning and the end of the cable) are placed in the same calibration bath and used to calibrate $\Delta\alpha$. $C_{internal}$ (loss inside the DTS instrument) is calibrated using the default $\Delta\alpha_{internal}$ given by the instrument as well as the values for γ , $P_S(z)$, $P_{aS}(z)$ and $T(z)$ also given by the instrument for the internal reference section. $C_{internal}$ is then averaged over the internal section. The average value of $C_{internal}$, $\Delta\alpha_{internal}$, γ, and $T(z)$ measured by the thermometer PT100 in the first calibration bath located near the DTS are used to calibrate $C_{external}$. $C_{external}$ accounts for $C_{internal}$, $C_{connector}$ and C_{splice} combined. $C_{connector}$ and C_{splice} refer to the local loss due connecting the fiber cable to the DTS and connecting (splicing) the fibers in the red fiber cable with the fibers in the yellow fiber cable (see figure2). Since the fiber cable is continuous through out the installation, additional splices were avoided and $C_{external}$ is used to calculate the temperature along the rest of the cable. $C_{external}$ is assumed to be constant for each time step. All $\Delta\alpha$, and **C** parameters are calibrated dynamically for each time step. In the other hand, γ and $\Delta\alpha_{interanl}$ is assumed to be constant and default values provided by the manufacture were used. The temperature measurements are validated with the third fiber coil (see figure 2) placed in a validation bath located approximately in the middle of the fiber cable. The calibration and validation process has been conducted over two weeks. The maximum and average deviation achieved between the validation bath temperature and the measured temperature by the DTS are -0.19°C and ± 0.09°C respectively.

FIRST MEASUREMENT

The ATES system has been monitored since March 2016 mainly using water level and temperature sensors and flowmeters. The ATES started operation in the fall of 2016. The fiber optical cables and DTS were installed and started the measurement in the fall of 2017. During the first heating and cooling season October 2016 - September 2017, the total heating and cooling energy consumed from the Aquifer are 189 MWh and 235 MWh respectively. Since the beginning of the second heating season in October 2017 and until March 2018, 147 MWh of total energy was utilized from the ATES the majority of which (143 kWh) for heating.

Power Measurement

Since March 2016, the maximum heating and cooling power used are 469 kW and 610.5 kW respectively. The average groundwater flow utilized throughout the heating and cooling seasons are around 26 m^3/hour and 21 m^3/hour respectively. This accounts for no more than 15% of the allowed pumping flow rate. Figure 3 shows the power (upper side of the figure) and groundwater flow rate (lower side of the figure) during the period October 2017-March 2018. The positive red lines indicate power and flow rate measurements in heating mode while the negative blue ones indicate power and groundwater flow measurement during cooling.

Similarly, figure 4 shows the extraction and injection temperatures for both heating and cooling mode during the period October 2017- March 2018. The red dots indicate extraction and injection temperatures measurement in heating mode while blue dots indicate extraction and injection temperatures measurement in cooling mode. The values presented in figure 3 and figure 4 are measured at the inlet and the outlet of the main heat exchanger (called additional heat exchanger in figure 1) between the ATES the building.

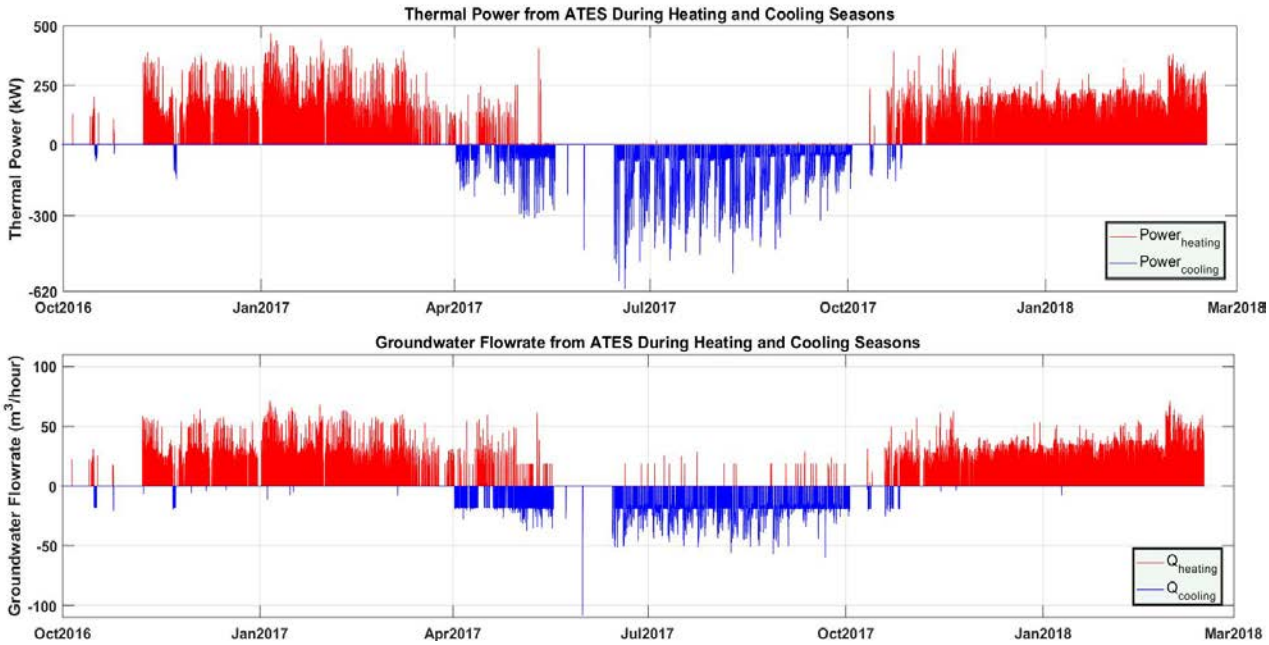

Figure 3 Thermal power and groundwater flowrate for heat and cool for Oct2016-Mar2018

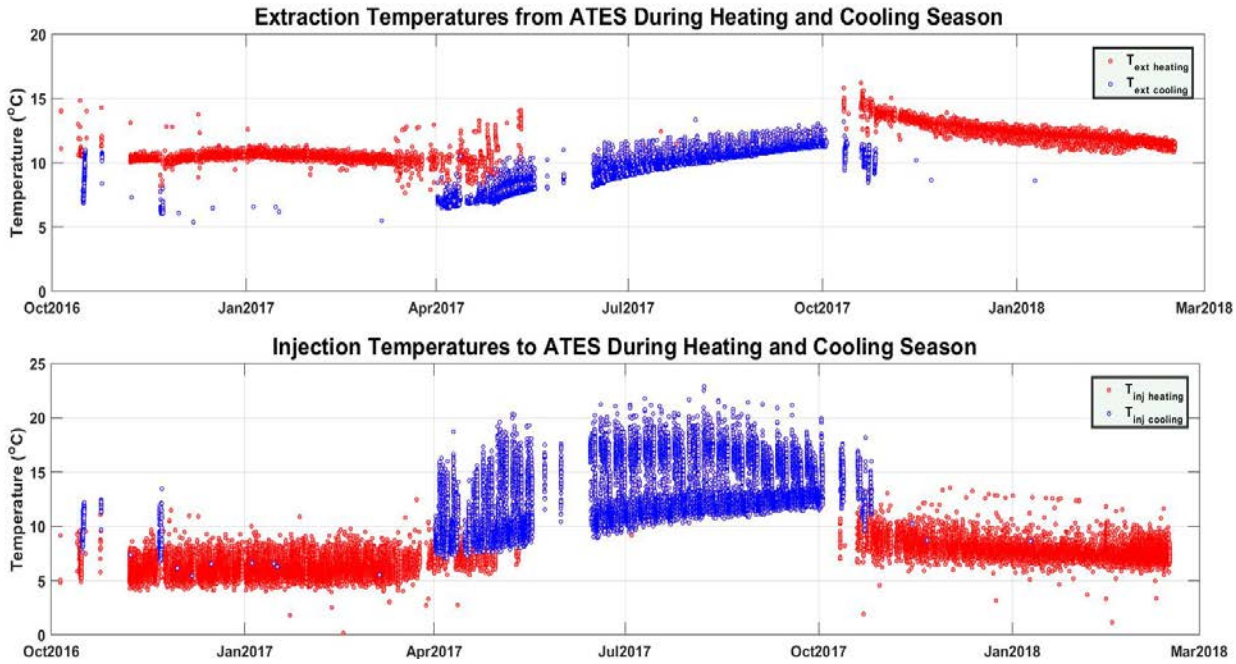

Figure 4 Extraction and injection temperatures for heating and cooling during Oct2016-Mar2018

DTS TEMPERATURE MEASUREMENT

The DTS measurements provided a good insight into the temperature profile with depth as well as the temperature propagation through the ATES. Figure 5 shows the temperature measurements from the fiber cable installed in the observation wells of cold well number two and warm well1 number one as well as the spare pumping

well. The measurements are presented at three different time steps: at the beginning, near the end and during the second heating season of the ATES. Cold well number two and warm well number one are located about 120 m apart at the far end of each side of the ATES. The spare well is located in between them with a distance of approximately 40 m from warm well number one. The negative sign on the y-axis in figure 5 indicate depth below ground surface. The water level in each well is ranging between -2 and -5 m depending on injection or extraction operation. The screen of each well starts at depth -9 m. The well screen depths are 7, 5 and 9 m for the warm, spare and cold wells respectively. Each one of the wells in figure 5 is represented by three lines. The solid, dashed and dotted lines represent measurement dates on 13th Oct 2017, 04th Dec 2017 and 19th Feb 2018 during the beginning, middle and near the end of the heating season. Furthermore, the undisturbed ground temperature profile before ATES started the operation measured on 26th August 2016 is presented in figure 5. The purple solid line shows measured temperature using Oryx DTS (1 m sampling resolution). The blue circles are measurements using divers at several depths within the well filter.

ATES PERFORMANCE EVALUATION

For ATES performance evaluation, energy balance (*EB*), hydraulic recovery (*HR*) and thermal recovery (*TR*) are used as ATES performance indicators.. *EB* is defined as the net energy utilized during heating or cooling divided by the total amount used for one full season of both heating and cooling. *EB* values ranges between -1 and 1. A value of 0 indicates a balanced system over the year. *HR* is defined as the ratio of water volume utilized during one heating or cooling season divided by water volume used in its preceding heating or cooling season during 12 contentious months. *TR* is defined as the ratio between the thermal energy extracted in one heating or cooling season divided by the thermal energy injected to ATES during its preceding heating or cooling season during 12 contentious months. *HR* or *TR* value of 1 indicates the all the water volume or the thermal energy injected in the previous season has been fully extracted (recovered). *TR* and *HR* for the first cooling season are estimated around 0.33 and 1.37 respectively. *EB* of the first full heating and cooling season is 0.12.

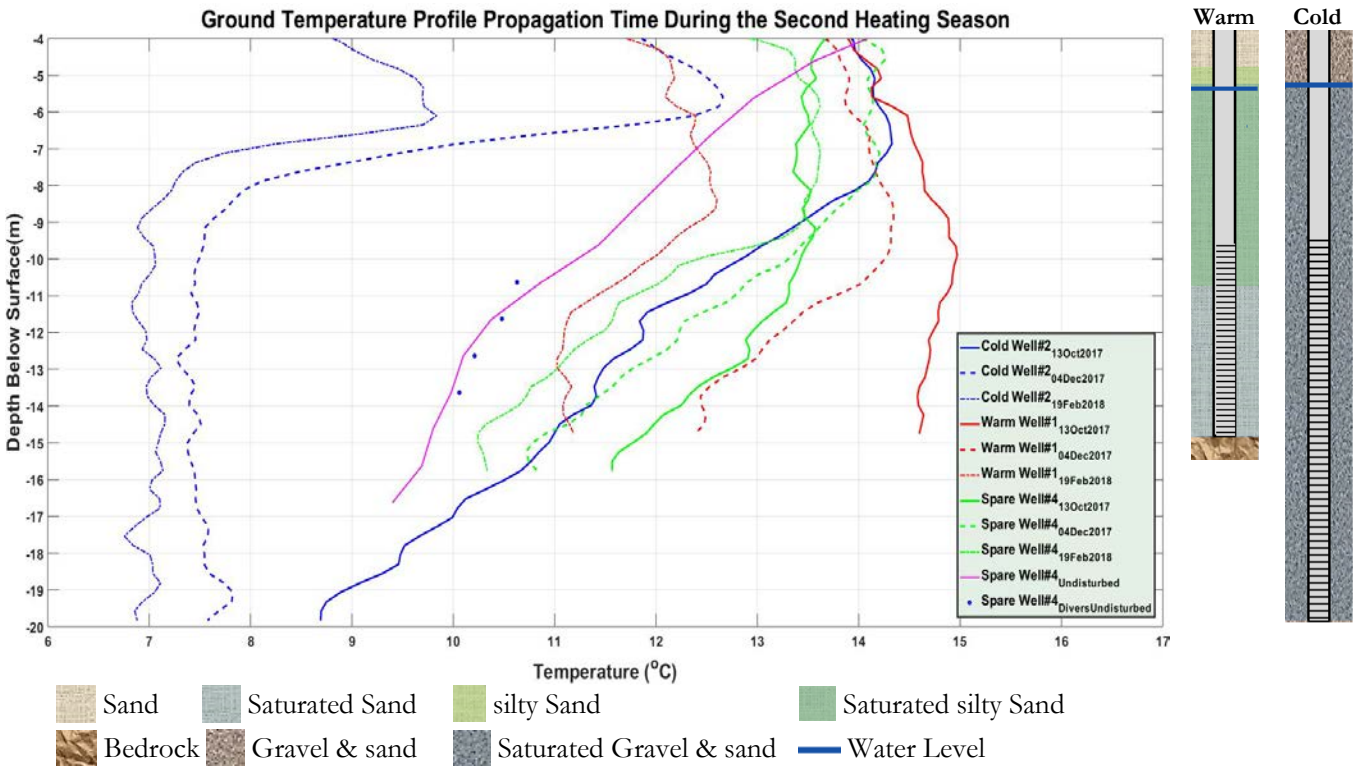

Figure 5 Ground temperatures profile with ATES depth (°C) during the period Oct2017-Feb2018

DISCUSSION AND CONCLUSION

The high hydraulic conductivity and high allowable injection and extraction flowrates, as well as the hydrogeological conditions of a site in Stockholm, Sweden, have been favorable for an ATES system. The real state property is located on top of an Esker formation with a core mostly consisting of gravel and sand. A monitoring set up of the ATES consisting of temperature, pressure and flow meters has been connected to the building control system.

Additionally, for monitoring, a XT Silixa DTS with sampling resolution of 0.25 m and continuous fiber optical cables have been installed in all pumping and some observation wells. DTS is dynamically calibrated using three calibration baths in the beginning and the end of each cable. The DTS temperature measurements are controlled using a bath in the middle of each fiber cable. The maximum and average deviation recorded by the DTS in the temperature measurement when compared to the validation bath are - 0.19°C and ± 0.09°C respectively. These numbers may be improved by mixing the calibration baths temperatures. Proper calibration of the DTS is critical to measure with sufficient accuracy for ATES applications. Therefore, DTS equipment dynamic calibration of signal losses due to length and local effects a recommended.

Traditional local in-well measurement instruments such as divers can be misleading when it comes to temperature. During the cooling season, the building control system is supposed to automatically operate on free cooling mode as long as the temperature in the ATES is low enough. In June 2017, a diver controlling the operation recorded too high temperatures (13°C), and thus the ATES stopped working in free cooling mode. In reality, the temperature in the ATES was suitable (6°C) to operate on free cooling mode as shown by the DTS. The reason behind this was due to diver misplacement since it is located too high in the well and next to the pump.

The highest extraction temperature for the first and second heating season are 14.9°C and 16.3°C and the lowest temperatures are 7.6°C and 10.8°C respectively. The highest and lowest extraction temperature for the first cooling season are 12.1 and 5.4°C, respectively. The average temperature difference between extraction and injection pipe for the first and second heating season are 3.7°C and 3.9°C, respectively, while the average temperature difference for the cooling season is 5°C. Near the end of the cooling season (after mid-August), the extraction temperatures are exceeding average undisturbed temperature (10.7°C) in the aquifer (average temperature along well depth starting at the groundwater water level). This is an indication of thermal break through. The hydraulic recovery value of 1.37 for the first cooling season indicates that more water volume was used during the cooling season than in the first heating season. The storage volume extracted from the warm storage during the first heating season and injected into the cold storage was 36900m^3/year. The storage volume recovered for cooling during the cooling season is 50500m^3/year and thus the imbalanced value of *HR*. This imbalance resulted in water from the warm storage reaching the cold storage (thermal breakthrough). During the summer and before the cooling season ended (mid-August), all the water that was injected in the previous season was recovered and the temperature of the ground return to the undisturbed condition. However, since additional cooling was done until the end of the cooling season (September), the warm water injected in the warm side during the cooling season started to move towards the cold side and eventually reached the cold storage side of the aquifer.

The temperature profile of the cold well in October (end of cooling season) shown in figure 5, shows a sign of thermal break through with temperature values exceeding 13.0°C. It also shows a tilted thermal front with a temperature gradient over the filter depth with 13.3°C at the top and 8.7°C at the bottom. This can likely be due to buoyancy flow caused by the difference in water density between the injected-extracted water and the ambient groundwater density. The shape of the profile is probably also affected by the undisturbed temperature profile. Additionally, pump placement just above the filter section would potentially cause higher inflow rates at the top of the filter than the bottom (Houben & Hauschild, 2011). This could result in a velocity profile along the filter depth having higher velocity at the top of the well screen than the bottom (considering similar sediment, hydraulic conductivity and well screen spacing). Therefore, in addition to aiming for a balance ATES, pump placement optimization can be further investigated. For instance, by lowering the pump at the middle of the filter section, it would potentially result in a more even inflow distribution along the well screen thus reducing the thermal front tilting angle.

Despite the fact that more water volume was recovered in the summer than injected in the preceding winter, the thermal recovery for first cooling season is calculated to be 33% of the total energy injected in the previous heating seasons. When it comes to energy balance over the first heating and cooling season, *EB* value of 0.12 indicates

a net heating of the ATES over the first year. From an individual ATES system stands point, it is beneficial to increase the storage volume. On the other hand, this can also limit the construction of other ATES systems in its vicinity. If such plans are made, careful consideration and coordination with the existing ATES system is necessary. For instance, installing wells with the same type of storage (warm or cold) in the same area. This can enhance the thermal recovery, as the storage volume will increase.

ACKNOWLEDGMENTS

Special thanks to the Swedish Energy Agency and Effsys Expand research program for funding this project. Additionally, our gratitude is extended to our partners for their support to make this work possible: Alverdens, AMF Fastigheter, Asplan Viak, Atlas Copco, AVANTI, Bengt Dahlgren, Cooly AB, Danfoss Heat Pumps, Finspångs Brunnsborrning, HP Borrningar, Geobatteri, Geostrata HB, NGU, NIBE, Nowab, NTNU, Palne Mogensen AB, Stures Brunnsborrningar, SGU, SLU, SWECO, Vasakronan, Värmex, Wilo Sweden AB and WSP.

NOMENCLATURE

P_S = Raman-Stokes (nm)
P_{aS} = Raman-AntiStokes (nm)
T = Temperature (°C)
z = Position along the fiber cable (m)
γ = Energy shift between the incident and scattered photon (K)
$\Delta\alpha$ = Differential attenuation along the fiber cable (m^{-1})
C = Dimensionless parameter for local losses calibration (-)

Subscripts

internal = Internal reference section in the DTS
connector = Connector between DTS and fiber cable
splice = connection (welding) between two fiber cable
external = Refers to the rest of the fiber cable after the splice

REFERENCES

Bakr, M., van Oostrom, N., & Sommer, W. (2013). Efficiency of and interference among multiple Aquifer Thermal Energy Storage systems; A Dutch case study. *Renewable Energy*, *60*(Supplement C), 53–62. https://doi.org/10.1016/j.renene.2013.04.004

Bloemendal, M., & Hartog, N. (2018). Analysis of the impact of storage conditions on the thermal recovery efficiency of low-temperature ATES systems. *Geothermics*, *71*, 306–319. https://doi.org/10.1016/j.geothermics.2017.10.009

Boman, D., & Hanson, G. (2004). *Salt grundvatten i Stockholms läns kust- och skärgårdsområden: metodik för miljöövervakning och undersökningsresultat 2003*. Länsstyrelsen i Stockholms län. Retrieved from http://www.diva-portal.org/smash/record.jsf?pid=diva2:851965

Hausner, M. B., Suárez, F., Glander, K. E., Giesen, N. van de, Selker, J. S., & Tyler, S. W. (2011). Calibrating Single-Ended Fiber-Optic Raman Spectra Distributed Temperature Sensing Data. *Sensors*, *11*(11), 10859–10879. https://doi.org/10.3390/s111110859

Houben, G. J., & Hauschild, S. (2011). Numerical Modeling of the Near-Field Hydraulics of Water Wells. *Ground Water*, *49*(4), 570–575. https://doi.org/10.1111/j.1745-6584.2010.00760.x

Lee, K. S. (2010). A Review on Concepts, Applications, and Models of Aquifer Thermal Energy Storage Systems. *Energies*, *3*(6), 1320–1334. https://doi.org/10.3390/en3061320

Lee, K. S. (2013). Aquifer Thermal Energy Storage. In *Underground Thermal Energy Storage* (pp. 59–93). Springer, London. https://doi.org/10.1007/978-1-4471-4273-7_4

Molz, F. J., Melville, J. G., Parr, A. D., King, D. A., & Hopf, M. T. (1983). Aquifer thermal energy storage : A well doublet experiment at increased temperatures. *Water Resources Research*, *19*(1), 149–160. https://doi.org/10.1029/WR019i001p00149

Molz, F. J., Parr, A. D., & Andersen, P. F. (1981). Thermal energy storage in a confined aquifer: Second cycle. *Water Resources Research*, *17*(3), 641–645. https://doi.org/10.1029/WR017i003p00641

Possemiers, M. (2014). Influence of Aquifer Thermal Energy Storage on groundwater quality: A review illustrated by seven case studies from Belgium. *Journal of Hydrology: Regional Studies*, *2*(Supplement C), 20–34. https://doi.org/10.1016/j.ejrh.2014.08.001

Regeringskansliet, R. och. (2017, April 27). Övergripande mål och svenska mål inom Europa 2020 [Text]. Retrieved October 24, 2017, from http://www.regeringen.se/sverige-i-eu/europa-2020-strategin/overgripande-mal-och-sveriges-nationella-mal/

Sauty, J. P., Gringarten, A. C., Fabris, H., Thiery, D., Menjoz, A., & Landel, P. A. (1982). Sensible energy storage in aquifers: 2. Field experiments and comparison with theoretical results. *Water Resources Research*, *18*(2), 253–265. https://doi.org/10.1029/WR018i002p00253

Sommer, W. (2015). *Modelling and monitoring of Aquifer Thermal Energy Storage: Impacts of heterogeneity, thermal interference and bioremediation.pdf* (PhD thesis). Wageningen University, Wageningen, Netherlands. Retrieved from http://library.wur.nl/WebQuery/wurpubs/fulltext/342495

Sommer, W. T., Doornenbal, P. J., Drijver, B. C., Gaans, P. F. M. van, Leusbrock, I., Grotenhuis, J. T. C., & Rijnaarts, H. H. M. (2014). Thermal performance and heat transport in aquifer thermal energy storage. *Hydrogeology Journal*, *22*(1), 263–279. https://doi.org/10.1007/s10040-013-1066-0

Suárez, F., Aravena, J. E., Hausner, M. B., Childress, A. E., & Tyler, S. W. (2011). Assessment of a vertical high-resolution distributed-temperature-sensing system in a shallow thermohaline environment. *Hydrology and Earth System Sciences; Katlenburg-Lindau*, *15*(3), 1081.

Sundberg, J. (1991). *Termiska egenskaper i jord och berg* (p. 18). Linköping: Swedish geotechnical institute. Retrieved from http://www.swedgeo.se/globalassets/publikationer/info/pdf/sgi-i12.pdf

Svedinger, B. (1981). *Värme i jord, berg och vatten : utvinning och lagring*. Stockholm: Statens råd för byggnadsforskning :

Swdish Energy Agency. (2015). Energy Outlook. Retrieved October 24, 2017, from https://www.energimyndigheten.se/contentassets/50a0c7046ce54aa88e0151796950ba0a/energilaget-2015_webb.pdf

United Nations. (2015). *Paris Agreement*. Retrieved from http://unfccc.int/files/essential_background/convention/application/pdf/english_paris_agreement.pdf

Visser, P. W., Kooi, H., & Stuyfzand, P. J. (2015). The thermal impact of aquifer thermal energy storage (ATES) systems: a case study in the Netherlands, combining monitoring and modeling. *Hydrogeology Journal*, *23*(3), 507–532. https://doi.org/10.1007/s10040-014-1224-z

WSP. (2014). Miljökonsekvensbeskrivning: akvifärlager Rosenborg 3, Solna stad. Ansökan om tillstånd för vattenverksamhet. Retrieved October 24, 2017, from http://hydrologie.org/redbooks/a154/iahs_154_04_0068.pdf

[This page has been intentionally left blank]

IGSHPA SWEDEN 2018 Research Conference

DOI: 10.22488/okstate.18.000046

A Design and Simulation Tool for Ground Source Heat Pump Systems Considering Groundwater Advection

Yutaka SHOJI **Takao KATSURA, PhD** **Takashi HIGASHITANI**

Katsunori NAGANO, PhD **Yoshitaka SAKATA, PhD**

ABSTRACT

Calculation of the underground temperature resulting from heat injection/extraction into/from ground heat exchangers (GHEXs) with hourly variation is one of the most noteworthy challenges to address when simulating and designing a ground source heat pump (GSHP) system. Especially in Japan, considering the groundwater flow is desirable because there is the possibility to reduce the installation cost for GSHP system. In order to overcome this challenge, the authors introduce a method to calculate the underground temperature, by considering heat injection/extraction into/from GHEXs with hourly variation. The method applies the superposition of the Moving Infinite Cylindrical Source (MICS) solution and the Moving Infinite Line Source (MILS) solution to calculate the temperature change due to heat injection/extraction into/from the certain GHEX and other neighboring GHEXs, respectively. In this paper, the outlines of the MICS and the method that calculate the MICS solution were firstly introduced. Next, the calculation method of underground temperature and the simulation model for the GSHP system were explained. Finally, the temperature variations of the heat carrier fluid were calculated by changing the conditions the geological layer and groundwater velocity.

INTRODUCTION

GSHP systems have gained attention in Japan since ground thermal energy was defined as one of the renewable energies in 2009. However, the number of GSHPs installed in Japan is much smaller than the number in other countries such as the USA, China, and Sweden due to the expensive installation cost of GHEXs. In order to reduce the installation cost, considering the groundwater flow in the design process is the one of effective methods. There are several research works related to the effect of ground water flow to the GHEXs (Gehlin and Hellström, 2003), (Diao et.al, 2004), (Molina-Giraldo et.al, 2011). However, the research works related to the simulation tool for the GSHP system considering groundwater flow are hardly observed. The authors developed the simulation tool for the GSHP system considering groundwater flow. In this paper, the outlines of calculation method and example of simulation for the GSHP system are explained.

CALCULATION OF UNDERGROUND TEMPERATURE CONSIDERING SINGLE GEOLOGICAL LAYER WITH GROUNDWATER FLOW

Types of groundwater flow

There are several types of groundwater flow (Gehlin and Hellström, 2003). In Japan, Darcy flow through the porous media is majority and there is quite a lot of case where the the groundwater flow with the Darcy velocity of more than 100 m/year is observed. Therefore, in this paper, the calculation of underground temperature considering groundwater flow of

Yutaka SHOJI (yutaka-soy@eis.hokudai.ac.jp) is a master course student at Graduate School of Engineering, Hokkaido University.

Darcy flow through the porous media is treated.

Calculation of underground temperature considering heat injection into GHEX with constant heat flux and groundwater advection

The groundwater flow is regarded as Darcy flow through the porous media. In this case, an incompressible, constant-property fluid flow passes through a saturated, homogeneous, and infinite porous medium. The incoming free velocity of the fluid u_∞ is parallel to the x axis and the following equation is obtained.

$$u = -k\frac{dh}{dx} \tag{1}$$

On the other hand, the GHEX is regarded as a hollow cylinder in the porous media. In this case, the fluid dynamics is analogous to the one referring to the traditional problem of the two-dimensional, incompressible, irrotational flow past a circular cylinder. The analytical expression of the velocity potential is (Bruce et.al, 2009);

$$\emptyset = u_\infty\{1 + r_{p-out}/(x^2 + y^2)\}x \tag{2}$$

With regard to the heat transfer in the ground surrounding GHEX, we firstly consider a constant heat flux q at the cylinder surface. The energy equation can be formulated according to the local thermal equilibrium, in which both solid and fluid phases have the same local temperature. Under the assumption, the following equations can be obtained.

$$c_s\rho_s\frac{\partial T_s}{\partial t} + c_w\rho_w(\nabla T_s)(\nabla\emptyset) = \nabla(\lambda_s\nabla T_s) \tag{3}$$

And in the case of $r = 0$, this problem becomes the moving infinite line source (MILS). Carslaw and Jeager introduce the analytical solution of this problem (Carslaw and Jaeger, 1959). Diao et.al., apply the MILS to the calculation of underground temperature surrounding the GHEX, which is affected by the groundwater advection (Diao et.al, 2004). The energy equation can be translated as Equation (4).

$$c_s\rho_s\frac{\partial T_s}{\partial t} + c_w\rho_w\left(\frac{\partial T_s}{\partial x}\right)\left(k\frac{\partial h}{\partial x}\right) = \nabla(\lambda_s\nabla T_s) \tag{4}$$

Then, the analytical solution of MILS $\Delta T_{s-MILS}(x, y, t)$ can be expressed by the following equation if the constant heat q is generated at $r = 0$ (Diao et.al, 2004).

$$\Delta T_{s-MILS}(x, y, t) = \frac{q}{4\pi\lambda_s}\int_0^{\frac{4a_s t}{r^2}}\frac{1}{(t-t')}exp\left[-\frac{\{x-U(t-t')\}^2+y^2}{4a_s(t-t')}\right]dt' \tag{5}$$

Here, $U = u_\infty c_w\rho_w/(c_s\rho_s)$.

Meanwhile, in the case of $r \neq 0$, this problem is called as the moving infinite cylindrical source (MICS) and the analytical solution of this problem has not been obtained (Conti et.al, 2018). However, the authors assumed that the superposition of the MICS is possible as well the superposition of the infinite line source (ILS), the infinite cylindrical source (ICS), and the MILS (Katsura et.al, 2006). Then, the temperature field of MICS was calculated by the numerical model shown in

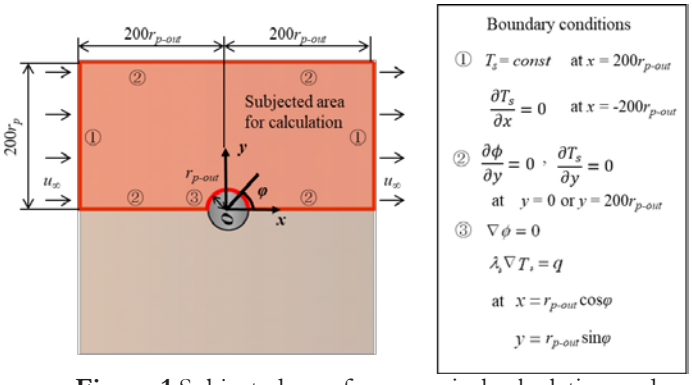

Figure 1 Subjected area for numerical calculation and boundary conditions

Figure 1 (Katsura et.al, 2006) and the result was compared to the temperature filed obtained by experiment with a thermal probe (Katsura et.al, 2006) and the analytical MILS model. The temperature fields indicated good agreement to each other.

However, the difference of temperature fields between MICS and MILS increases when the radius of cylindrical source becomes larger. On the other hand, it is difficult to apply the MILS for the calculation of underground temperature considering heat injection/extraction into/from GHEX with hourly variation as well the ILS. Therefore, in order to calculate the underground temperature considering heat injection/extraction into/from GHEX with hourly variation, the temperature at $r = r_{p-out}$ in the MICS is approximated by modifying the temperature at $r = r_{p-out}$ in the ICS, which is obtained by the analytical solution (Carslaw and Jaeger, 1959). If the modification coefficient C_c that can modify from the temperature at $r = r_{p-out}$ in the ICS to the temperature at $r = r_{p-out}$ in the MICS is assumed, the average temperature at $r = r_{p-out}$ with constant heat flux q in the MICS can expressed by the following equation.

$$\Delta T_{s-MICS}(r_{p-out}, t) = \Delta T_{s-ICS}(r_{p-out}, t) C_c = \frac{1}{\pi^2 r_{p-out} \lambda_s} q I(r_{p-out}, t) C_c \quad (6)$$

Now,

$$I(r,t) = \int_0^\infty (1 - e^{-a_s \beta^2 t}) \frac{J_0(\beta r) Y_1(\beta r_{p-out}) - Y_0(\beta r) J_1(\beta r_{p-out})}{u^2 [J_1^2(\beta r_{p-out}) + Y_1^2(\beta r_{p-out})]} d\beta$$

If $u_\infty = 0$, $C_c = 1$ and Equation (6) is the same as the analytical solution of the ICS. In addition, if we introduce the dimensionless quantities $t^*_{p-out} = at/{r_{p-out}}^2$, $r^*_{p-out} = r_{p-out}/r_{p-out} = 1$, and $T^*_{s-ICS}(1, t^*_{p-out}) = 2\pi\lambda_s \Delta T_{s-ICS}(r_{p-out}, t)/q$ ($\Delta T_{s-ICS}(r_{p-out}, t) = \frac{q}{\pi^2 r_{p-out,i} \lambda_s} I(r_{p-out,i}, t)$), Equation (6) is translated as the following equation. Then, the modification coefficient can be organized by using the dimensionless parameters $r^*_{p-out} = 1$, $R^*_{p-out} = U r^*_{p-out}/a_s$, and $F_O = U^2 t/a_s$ as shown in Equation (7).

$$T^*_{s-MICS}(1, t^*_{p-out}) = T^*_{s-ICS}(1, t^*_{p-out}) C^*_C(1, R^*_{p-out}, F_O) \quad (7)$$

The modification coefficient $C^*_C(1, R^*_{p-out}, F_O)$ is obtained by comparing $T^*_{s-ICS}(1, t^*_{p-out})$ and $T^*_{s-MICS}(1, t^*_{p-out})$. Here, $T^*_{s-MICS}(1, t^*_{p-out})$ is calculated by the numerical model introduced above. After the comparison, $C^*_C(1, R^*_{p-out}, F_O)$ is approximated as the function of $1, R^*_{p-out}$, and F_O.

$$C^*_C(1, R^*_{p-out}, F_O) \cong f(1, R^*_{p-out}, F_O) \quad (8)$$

Calculation of underground temperature considering heat injection/extraction into/from multiple GHEXs with hourly variation and groundwater advection

Figure 2 shows the multiple GHEXs buried in a random layout. The ground is regarded as an infinite medium and superposition of the temperature field in space is applied. Thus, in the case where m GHEXs are placed underground as shown in Figure 2, the soil temperature change on the surface of the certain GHEX can be calculated using the following equation.

$$\Delta T_{s,i}(r_{p-out,i}, t) = \Delta T_{s,i,i}(r_{p-out,i}, t) + \sum_{j=1}^{m} \Delta T_{s,i,j}(r_{d,i,j}, t) \quad (9)$$

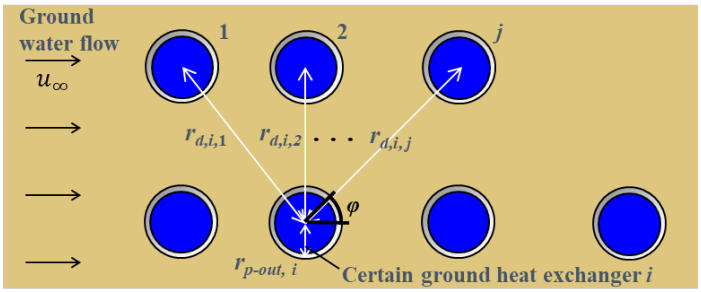

Figure 2 Multiple GHEXs buried in a random layout

Where the subscript *i* indicates the GHEX under consideration, *j* indicates a neighboring GHEX, and $j \neq i$. The first term on the right side shows the change in temperature due to the heat injection/extraction of the GHEX under consideration and the second term is the temperature change due to the heat injection/extraction of the neighboring GHEXs. When the free velocity u_∞ is zero, the temperature change in the first term on the right side of can be calculated from the following equation, applying the principle of superposition based on the solution of MICS and Duhamel's theorem.

$$\Delta T_{s,i,i}\left(r_{p-out,i},t\right)=\frac{1}{\pi^2 r_{p-out,i}\lambda_s}\int_0^t q_i(\tau)\frac{\partial I(r_{p-out,i},t-\tau)C_c}{\partial t}d\tau \tag{10}$$

$q_i(\tau)$ is the heat injection/extraction into/from the certain GHEX*i* at time $t=\tau$, and $\frac{1}{\pi^2 r_{p-out,i}\lambda_s}q_i(\tau)\frac{\partial I(r_{p-out,i},t-\tau)}{\partial t}$ indicates the amount of temperature change at the surface of the certain GHEX*i* caused by the heat injection/extraction at time $t = \tau$. Here, if the heat injection/extraction from the surface of the underground heat exchanger is considered to occur in a step-wise manner, as shown in Figure 10, Equation (10) can be simplified as in Equation (11) (Li et.al, 2015).

$$\Delta T_{s,i,i}\left(r_{p-out,i},t\right)\cong\frac{1}{\pi^2 r_{p-out,i}\lambda_s}\sum_{l=1}^{n}q_{l,i}I\left(r_{p-out,i},t-t_{l-1}\right)-I\left(r_{p-out,i},t-t_l\right) \tag{11}$$

Here, $q_{l,i}$ is the average quantity of heat injection/extraction from the considered GHEX*i* in the interval Δt_l. By introducing the dimensionless quantities $t^*_{p-out}=at/{r_{p-out}}^2$, $r^*_{p-out}=r_{p-out}/r_{p-out}=1$, and $T^*_{s-ICS}\left(1,t^*_{p-out}\right)=2\pi\lambda_s\Delta T_{s-ICS}\left(r_{p-out},t\right)/q_l$ ($\Delta T_{s-ICS}\left(r_{p-out},t\right)=\frac{q_l}{\pi^2 r_{p-out,i}\lambda_s}I\left(r_{p-out,i},t\right)$), Equation (11) can be translated to the following equation (Katsura et. al, 2018).

$$\Delta T_{s,i,i}\left(r_{p-out,i},t\right)\cong\frac{1}{2\pi\lambda_s}\sum_{l=1}^{n}q_{l,i}\left\{T^*_{s-ICS}\left(1,t^*_{p-out}-t^*_{p-out,l-1}\right)-T^*_{s-ICS}\left(1,t^*_{p-out}-t^*_{p-out,l}\right)\right\} \tag{12}$$

If the free velocity u_∞ is not zero, the temperature change $\Delta T_{s,i,i}\left(r_{p-out,i},t\right)$ can be calculated by changing from $T^*_{s-ICS}\left(1,t^*_{p-out}-t^*_{p-out,l}\right)$ to $T^*_{s-MICS}\left(1,t^*_{p-out}-t^*_{p-out,l}\right)$ in Equation (13) and substituting Equation (8). The equation is,

$$\begin{aligned}\Delta T_{s,i,i}\left(r_{p-out,i},t\right)&\cong\frac{1}{2\pi\lambda_s}\sum_{l=1}^{n}q_{l,i}\left\{T^*_{s-MICS}\left(1,t^*_{p-out}-t^*_{p-out,l-1}\right)-T^*_{s-MICS}\left(1,t^*_{p-out}-t^*_{p-out,l}\right)\right\}\\&\cong\frac{1}{2\pi\lambda_s}\sum_{l=1}^{n}q_{l,i}\left\{T^*_{s-ICS}\left(1,t^*_{p-out}-t^*_{p-out,l-1}\right)C^*_C\left(1,R^*_{p-out},F_{O,l-1}\right)-T^*_{s-ICS}\left(1,t^*_{p-out}-t^*_{p-out,l}\right)C^*_C\left(1,R^*_{p-out},F_{O,l}\right)\right\}\end{aligned} \tag{13}$$

Here, $F_{O,l}=U^2t_l/a_s$ and $F_{O,l-1}=U^2t_{l-1}/a_s$.

Next, the second term on the right side of Equation (9) which denotes the temperature change due to the extraction and injection of heat of the neighboring GHEX *j* is calculated from the following equation, applying the MILS analysis solution and the principle of superposition.

$$\Delta T_{s,i,j}\left(r_{d,i,j},t\right)=\int_0^t q_i(\tau)\frac{\partial\Delta T_{s-MILS}\left(r_{d,i,j},t-\tau\right)}{\partial\tau}d\tau \tag{14}$$

Here, $\Delta T_{s-MILS}\left(r_{d,i,j},t\right)$ can be obtained as the following equation if $r^2_{d,i,j}=\sqrt{x^2+y^2}$ and $\beta=4a_s(t-t')/r^2_{d,i,j}$ are substituted in Equation (5).

$$\Delta T_{s-MILS}\left(r_{d,i,j},t\right)=\frac{1}{4\pi\lambda_s}\exp\left(\frac{Ur_{d,i,j}}{2a_s}\cos\varphi\right)\int_0^{\frac{4a_st}{r^2_{d,i,j}}}\frac{1}{\beta}\exp\left(-\frac{1}{\beta}-\frac{U^2r^2_{d,i,j}\beta}{16a_s^2}\right)d\beta \tag{15}$$

The note φ in Equation (15) is polar angle, which is indicated in Figure 9. As in the case of Equation (4), if the heat injection

from the GHEX surface is considered to occur in a step-wise manner, Equation (15) can be rewritten as a simpler equation in the following manner.

$$\Delta T_{s,i,j}(r_{d,i,j},t) \cong \sum_{l=1}^{n} q_l \left\{\Delta T_{s-MILS}(r_{d,i,j},t-t_{l-1}) - \Delta T_{s-MILS}(r_{d,i,j},t-t_l)\right\} \quad (16)$$

Also, if the dimensionless quantities $t_d^* = a_s t/r_d^2$, $R_d^* = U r_d/a_s$, and $T_{s-MLS}^*(R_d^*,t^*) = 2\pi\lambda_s \Delta T_{s-MILS}(r_d,t)/q_l$ are adopted, Equation (16) is translated to the following equation.

$$\Delta T_{s,i,j}(r_{d,i,j},t) \cong \frac{1}{2\pi\lambda_s}\sum_{l=1}^{n} q_l \left\{T_{s-MILS}^*(R_{d,i,j}^*, t_{d,i,j}^* - t_{d,i,j,l-1}^*) - T_{s-MILS}^*(R_{d,i,j}^*, t_{d,i,j}^* - t_{d,i,j,l}^*)\right\} \quad (17)$$

Here,

$$T_{s-MILS}^*(R_{d,i,j}^*, t_{d,i,j}^*) = \frac{1}{2}\exp\left(\frac{R_{d,i,j}^*}{2}\cos\varphi\right)\int_0^{4t_{d,i,j}^*}\frac{1}{\beta}\exp\left(-\frac{1}{\beta}-\frac{R_{d,i,j}^{*2}\beta}{16}\right)d\beta \quad (18)$$

CALCULATION OF TEMPERATURE INSIDE GHEX

The heat carrier fluid in the GHEX is regarded as a lumped parameter system and the heat balance equation in the infinitesimal time dt is considered. The change in the heat capacity inside the GHEX can be thought as the sum of the heat input from the outside and the heat transferred from the ground. Hence the following expression holds.

$$c_{pf}\rho_f V_f \frac{dT_f}{dt} = c_{pf}\rho_f G_f(T_{pin} - T_{pout}) + K_{p-out}A_{p-out}(T_s(r_{p-out,}t) - T_f) \quad (19)$$

K_{p-out} in Equation (19) is the overall heat transfer coefficient based on the outer surface area from the GHEX to the heat carrier fluid and A_{p-out} is the outer surface area of the GHEX. Having determined q_l for each instant from the formula $q = K_{p-out}A_{p-out}(T_s(r_{p-out,}t) - T_f)/L_p$ and if the external surface temperature of the GHEX $T_s(r_{p-out,}t) = T_{s0} + \Delta T_s(r_{p-out},t)$ is calculated using the method previously described in this paper, the temperature of inside GHEX and the underground temperature can be evaluated.

In order to calculate the overall heat transfer coefficient of the GHEX, the Boundary Elemental Method (BEM) was applied (Nagano et.al, 2006). If the the thermal resistance R_b is calculated by BEM, the overall heat transfer coefficient K_{p-out} is obtained by usng R_b (Nagano et.al, 2006).

$$K_{p-out} = \frac{A_{U-out}}{\left\{A_{U-out}R_b + A_{p-out}r_{U-out}\left(\frac{1}{\lambda_U}\ln\frac{r_{U-out}}{r_{U-in}} + \frac{1}{r_{U-in}\alpha_f}\right)\right\}} \quad (20)$$

A_{U-out} is the external area of the U-tube, and r_{U-out} and r_{U-in} are the external and internal radius of the U-tube, respectively. Further, λ_U is the thermal conductivity of the U-tube, and α_f is the convection heat transfer rate, which can be calculated by the method presented in the previous paper (Nagano et.al, 2006).

CALCULATION OF TEMPERATURES CONSIDERING MULTIPLE GEOLOGICAL LAYERS

Figure 3 illustrates the multiple GHEXs buried in the ground with multiple geological layers. It is assumed that the heat transfer between the ground layers can be ignored. If the temperature changes on the surface of certain GHEX at every layer can be independently calculated, the temperature change at the layer *k* is expressed by using the following equation.

$$\Delta T_{s,i,k}(r_{p-out,i},t) = \Delta T_{s,i,i,k}(r_{p-out,i},t) + \sum_{j=1}^{m}\Delta T_{s,i,j,k}(r_{d,i,j},t) \quad (21)$$

The temperature changes $\Delta T_{s,i,i,k}(r_{p-out,i},t)$ and $\Delta T_{s,i,j,k}(r_{d,i,j},t)$ can be calculated as well as the calculation method previously explained.

The temperature of heat carrier fluid at each section in the GHEX are also independently calculated. The heat balance equation of heat carrier fluid in the supply pipe at the layer *k* (the section number *k*) in Figure 11 is expressed by the following equation.

$$c_{pf}\rho_f V_{f,k}\frac{dT_{f,k}}{dt} = c_{pf}\rho_f G_f\left(T_{pin,k} - T_{pout,k}\right) + \frac{K_{p-out}A_{p-out}}{2}\left(T_{s,k}(r_{p-out},t) - T_{f,k}\right) \quad (22)$$

Also, the heat balance equation of heat carrier fluid in the return pipe at the layer *k* (the section number 2n+1-*k*) in Figure 3 can be given as the following.

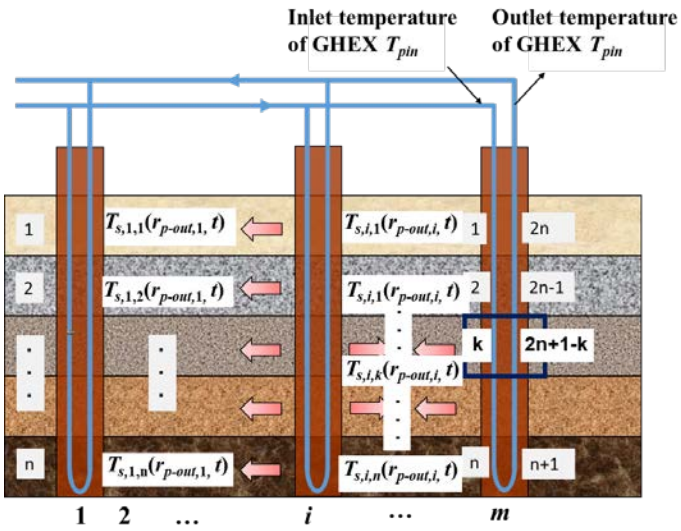

Figure 3 GHEXs buried in the ground with multiple geological layers

$$c_{pf}\rho_f V_{f,2n+1-k}\frac{dT_{f,2n+1-k}}{dt} = c_{pf}\rho_f G_f\left(T_{pin,2n+1-k} - T_{pout,2n+1-k}\right) + \frac{K_{p-out}A_{p-out}}{2}\left(T_{s,2n+1-k}(r_{p-out},t) - T_{f,2n+1-k}\right) \quad (23)$$

The heat injection rate at the layer *k* q_k is calculated by using the following equation.

$$q_k = -\pi r_{p-out}\left\{K_{p-out}\left(T_{s,k}(r_{p-out},t) - T_{f,k}\right) + K_{p-out}\left(T_{s,k}(r_{p-out},t) - T_{f,2n+1-k}\right)\right\} \quad (24)$$

EXAMPLE OF PERFORMANCE PREDICTION OF GROUND SOURCE HEAT PUMP SYSTEM

Calculation conditions

Considering the case of a GSHP system affected by the groundwater flow installed in an office building in Akita prefecture, Japan, the temperature change in the GSHP system was predicted. The calculation conditions are shown in Figure 4. The GSHP unit with the heating and cooling output of around 30 kW is connected to 4 borehole GHEXs with 100 m depth. The underground temperature and the effective thermal conductivity without groundwater flow were given as 12.0 °C and 2.0 W/(m・K), respectively. The three types of geological conditions shown in Figure 5 were provided. CASE A is the single geological layer without groundwater flow. CASE B is the double geological layers and the upper layer have the groundwater flow with the velocity of 1000 m/year. CASE C is the single layer with the groundwater flow and the velocity is 1000 m/year. The hourly thermal load shown in Figure 6 was assigned every hour and the external surface temperature of the GHEX $T_s(r_{p-out},t) = T_{s0} + \Delta T_s(r_{p-out},t)$ and the inlet temperature in the primary side of GSHP unit T_{1in} were calculated (Nagano et.al, 2006).

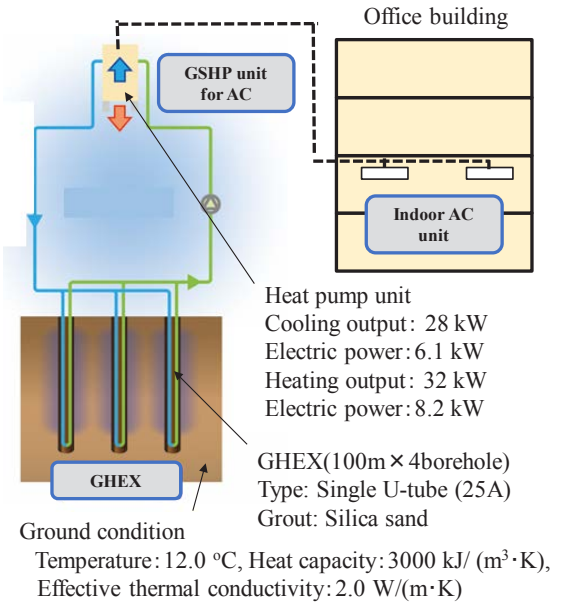

Figure 4 GSHP system installed in office building

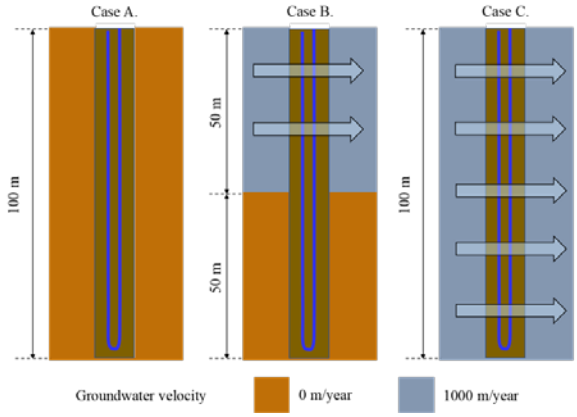

Figure 5 Conditions of geological layer

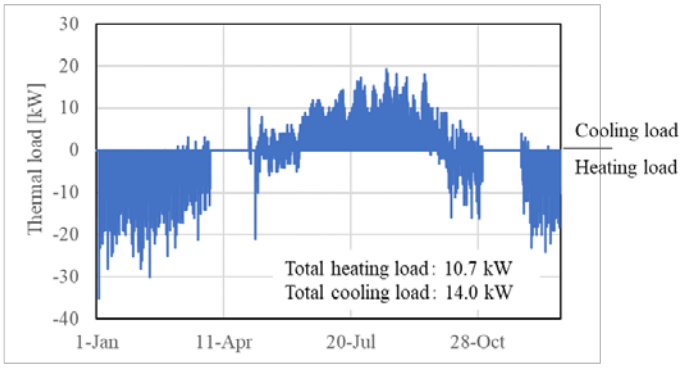

Figure 6 Hourly thermal load in annual

Result and discussions

Figure 7 compares the hourly variations of $T_s(r_{p-out},t)$. In CASE A, the temperature $T_s(r_{p-out},t)$ is around 8 °C at the minimum and around 20 °C at the maximum. On the other hand, the temperature $T_s(r_{p-out},t)$ in CASE C ranges from 10 °C to 14 °C. The reason is that the temperature change occurred by heat injection/extraction into/from GHEX is smaller when the groundwater flow is generated. The temperature $T_s(r_{p-out},t)$ at upper layer in CASE B is almost the same as the temperature $T_s(r_{p-out},t)$ in CASE C and the temperature change of $T_s(r_{p-out},t)$ at bottom layer in CASE B is alike the temperature change of $T_s(r_{p-out},t)$ in CASE A. Also, the hourly variations of $T_s(r_{p-out},t)$ in the representative period (Aug. 18 ~ Aug. 19) are shown in Figure 8. The temperature $T_s(r_{p-out},t)$ at upper layer in CASE B and $T_s(r_{p-out},t)$ in CASE C decrease to 12 °C, which is the initial ground temperature, if the GSHP system is not operated. This is due to the effect of groundwater advection. Finally, Figure 9 shows the hourly variation of T_{1in}.

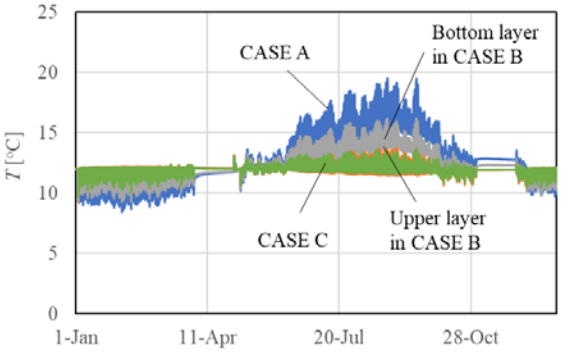

Figure 7 Hourly variation of $T_s(r_{p-out},t)$ in annual

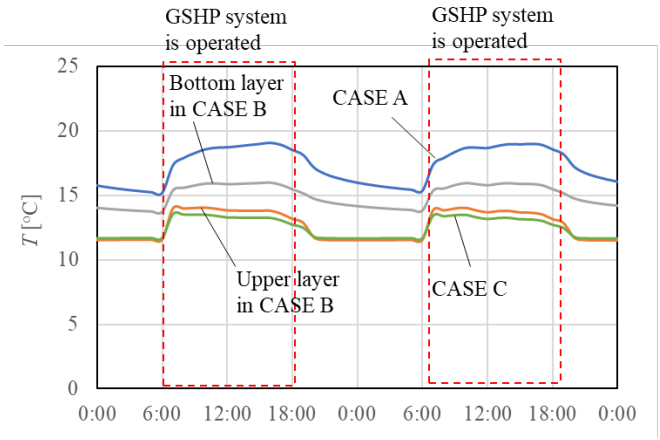

Figure 8 Hourly variation of $T_s(r_{p-out},t)$ in the representative period (Aug. 18 ~ Aug. 19)

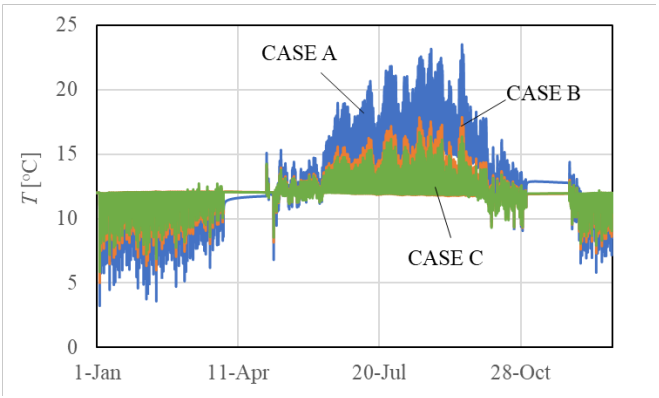

Figure 9 Hourly variation of T_{1in} in annual

The temperature variation of T_{1in} is also smaller when the groundwater flow is generated. Then, the temperature variation is smaller when the thickness of layer in which the groundwater flow is generated becomes larger. From this result, it seems that the GSHP system can be operated even if the number of GHEXs is reduced in CASE B and CASE C. Therefore, it is indicated that the total length of GHEX can be reduced by considering the groundwater flow in the design of GSHP system.

CONCLUSION

1) It is shown that the heat transfer in the porous media with Darcy flow surrounding cylinder can be expressed by applying the MICS and the MILS if the radius of cylinder is small. In addition, in order to calculate the MICS solution in short time, the method in which the modification coefficient is multiplied to the ICS analytical solution.

2) The calculation method of the underground temperature that can consider the heat injection/extraction into/from the GHEXs was introduced. The method applies the superposition of the MICS solution and the MILS solution.

3) Considering the case of a GSHP system installed in an office building, the conditions of geological layer and groundwater velocity were changed and the temperature changes of the ground and the heat carrier fluid in the primary side were calculated. The result shows that the temperature changes of the ground with groundwater flow is smaller than the temperature changes of the ground without groundwater flow. Therefore, it is indicated that the total length of GHEX can be reduced by considering the groundwater flow in the design of GSHP system.

ACKNOWLEDGMENTS

This study is based on results obtained from the project "Renewable energy heat utilization technology development," commissioned by the Japan national agency New Energy and Industrial Technology Development Organization (NEDO).

NOMENCLATURE

A = Area (m^2)
a = Thermal diffusivity (m^2/s)
C_c = Modification coefficient (-)
C_C^* = Non-dimensional modification coefficient (-)
c_p = Specific heat (J/(kg. K))
F_O = Non-dimensional number ($= U^2 t/a$) (-)
G = Flow rate (m^3/s)
h = Hydraulic head (m)
J_x = xth-order Bessel function of first kind (-)
K = Overall heat transfer coefficient (W/(m^2. K))
k = Hydraulic conductivity (m/s)
L = Length (m)
n = Number of time step (-)
Q = Thermal load, heat injection (W)
q = Heat injection rate per length (W/m)
R^* = Non-dimensional number ($= Ur/a$) (-)
R = Thermal resistance (m^2. K/W)
r = Radius (m)
r^* = Non-dimensional distance ($= r/r_{p-out}$) (-)
T = Temperature (°C)
T^* = Non-dimensional temperature ($= 2\pi\lambda\Delta T/q$) (-)
t = Time (s) or (h)
t^* = Non-dimensional time (Fourier number) ($= at/r$) (-)
U = Effective heat transport velocity ($= (uc_w\rho_w)/(c_s\rho_s)$) (m/s)
u = Groundwater velocity (m/s)
V = Volume (m^3)
x = x coordinate (m)
Y_x = xth-order Bessel function of second kind (-)
y = y coordinate (m)
α = Convection heat transfer coefficient (W/(m^2. K))
β = Characteristic value (-)
λ = Thermal conductivity (W/(m.K))
ρ = Density (kg/m^3)
φ = Angle coordinate (rad)
ϕ = Velocity potential (m^2/s)
τ = Parameter relating to time (s) or (h)
τ* = Non-dimensional parameter relating to time (-)

Subscripts

b = Borehole
d = Distance
f = Heat carrier fluid
i = Certain GHEX
j = Neighboring GHEX
k = Number of ground layer
l = Code number of approximate rectangular step load
m = Number of GHEX
n = Number of time step
p = GHEX
pin, pout = Inlet/Outlet of GHEX
p-out = Outside of GHEX
s = Soil
s0 = Soil initial
s-ICS = Solution of ICS problem
s-MICS = Solution of MICS problem
s-MLCS = Solution of MLCS problem
U = U-tube
w = Water in soil

REFERENCES

Abramowitz, M. and Stegun, I.: Hand book of Mathematical Functions 7th Edition, Dover Publications, New York, p.1046, 1970.

Bruce R. Munson, D. F. Young, T. H. Okiishi, W. W. Huebsch : Fundamentals of Fluied Mechanics, sixth ed., Johon Wiley & Sons, Inc, Hoboken, 2009

Carslaw H.S. and J. C. Jaeger: Conduction of Heat in Solid, Oxford Unversity Press, 1959.

Conti. P, D. Testi, W. Grassi : Transient forced convection from an infinite cylindrical heat source in a saturated Darcian porous medium, International Journal of Heat and Mass Transfer 117, pp.154-166, 2018.

Diao. N, Q. Li, Z. Fang : Heat Transfer in Ground Heat Exchangers with Groundwater Advection, International Journal of Thermal Sciences 43, pp.1203-1211, 2004.

Gehlin. S., G. Hellström : Influence on Thermal Response Test by Groundwater Flow in Vertical Fractures in Hard Rock, Renewable Energy 28, pp.2221-2238, 2003.

Hantush, M. S.: Analysis of data from pumping tests in leaky aquifers, Transactions American Geophysical Union 37, pp.702–714, 1956.

Henry, T. F. and Foree, E. G.: Dispersion modeling in time and two dimensions, Journal of the Environmental Engineering Division 10, pp.1131–1147, 1979.

Katsura T., K. Nagano, S. Takeda, K. Shimakura: Heat transfer experiment in the ground with ground water advection, Proceeding of 10th international conference of energy strorage Ecostock, Galloway, New Jersey, 2006.

Katsura T., K. Nagano, S. Takeda, Y. Nakamura: An investigation on relation between ground water advection and thermal response by the thermal probe method, Transactions of the Society of Heating, Air-conditioning and Sanitary Engineering of Japan, No.112, pp.51-60, 2006 (In Japanese).

Katsura T., K. Nagano, S. Takeda, Y. Nakamura: Method of calculation of the ground temperature with ground water flow and its application, Transactions of the Society of Heating, Air-conditioning and Sanitary Engineering of Japan, No.115, pp.9-18, 2006 (In Japanese).

Katsura T., K. Nagano, Y. Sakata, T. Higashitani: A Design and Simulation Tool for Ground Source Heat Pump System and Borehole Thermal Storage System, Proceeding of 14th international conference of energy strorage Enerstock, Adana, Turkey, 2018.

Li S., Kefeng Dong, Jinyong Wang, Xiaosong Zhang: Long term coupled simulation for ground source heat pump and underground heat exchangers, Energy and buildings 106, pp.13–22, 2015.

Molina-Giraldo.N, P. Blum, K. Zhu, P. Bayer, Z. Fang : A moving finite line source model to simulate borehole heat exchangers with groundwater advection, International Journal of Thermal Sciences 50, pp.2506-2513, 2011.

Nagano K., T. Katsura and S. Takeda: Development of a Design and Performance Prediction Tool for the Ground Source Heat Pump System, Applied Thermal Engineering, Volume 26, Issues 14-15, pp.1578-1592, 2006.

[This page has been intentionally left blank]

IGSHPA SWEDEN
2018 Research Conference

DOI: 10.22488/okstate.18.000016

A Full-scale Model to Predict Borehole Fluid Temperature with Groundwater Advection

Tengfei Cui **Shanshan Cai*** **Haijin Guo** **Ting Huang**

ABSTRACT

Ground source heat pump (GSHP) system is one of the major techniques that utilize shallow geothermal energy and borehole heat exchangers (BHEs) is the key component in GSHP system. Although most proposed analytical models for the thermal analysis of vertical BHEs take into account of the effects of either groundwater flow or axial heat conduction in the soil, the time scale of heat transfer in the BHEs is not well treated. In this study, an analytical full-scale model was developed to efficiently include the effects of the coupled transient heat transfer in the borehole, the axial heat conduction along the borehole and the effect of horizontal flow of groundwater. Results derived from the new model were compared with solutions of other traditional analytical and numerical models with the same configuration. The impacts of axial heat transfer and groundwater flow on the thermal response in the full time scale were also analyzed based on the proposed model.

INTRODUCTION

Ground source heat pump (GSHP) system is one of the major techniques that utilize shallow geothermal energy and borehole heat exchangers (BHEs) is the key component in the GSHP system (Somogyi, et al. 2017). Compared to horizontal boreholes, the vertical configurations are widely used in both commercial and residential buildings due to compact occupied areas and stable soil temperatures among different seasons. In order to estimate the heat transfer of vertical BHEs, different numerical (Kim, et al. 2010; Saner, et al. 2010), analytical (Diao, et al. 2004; Li and Lai 2012) and combined models (Hellström 1991; Yavuzturk 1999) have been proposed in the current literature, among which analytical methods are preferred because of the simple expression and fast computation.

The heat transfer in the vertical BHEs would be affected by several factors, such as the underground thermal properties and the variable building loads over years. Generally, it is recommended to consider the heat transfer procedure in two separated regions. One region is the space out of the borehole, where the heat transfer is usually treated as a transient process due to the fact that the heat exchanger is surrounded in a semi-infinite medium. The infinite line-source (ILS) model, finite line-source (FLS) model and the cylindrical source model are normally considered in this region (Zeng, et al. 2002). Compared to the other two methods, FLS model is more often used to include the effect of axial heat conduction along the borehole. The other region is the one in the borehole, which is filled with grouting material and U-shaped tube(s) with circulating medium. In the current literature, this region can be analyzed as steady state (including quasi steady state) due to the high aspect ratio (length/diameter ≈ 150m/0.1m for example) and the low thermal capacity compared to the surroundings. Treating the U-shaped tube as a single pipe with equivalent diameter in 1-D is one of the simplest expressions. In order to include thermal influence between legs of U-shaped tube, researchers (Hellström 1991; Claesson and Hellström 2011) further developed different 2-D

Shanshan Cai (shanshc@hust.edu.cn) is an assistant professor of Energy and Power Engineering in Huazhong University of Science and Technology.

models based on tube, researchers (Hellström 1991; Claesson and Hellström 2011) further developed different 2-D models based on the line-source assumption and multipole method, respectively. A 3-D quasi steady state model was also proposed to include the effect of varied fluid temperature along the depth of the borehole (Diao, et al. 2004).

However, it would result in some issues by treating the heat transfer procedure in two separated regions. According to some researchers' work, the traditional line-source models would be valid for $t \geq 5r_b^2/a$, which is around 4 to 8 hours for a typical borehole (Eskilson and Claesson 1988). Therefore, the conventional line-source models are inappropriate for the short-term energy analysis of GSHPs. Although some analytical solutions are available to predict the short-term response of BHEs, most of them are based on the assumption of "equivalent-diameter", which simplifies the complicated geometry of the borehole to one composite region enclosed in a hollow cylinder (Javed 2011; Javed and Claesson 2011). This simplification makes it impossible to include the transient effect of both the grouting material and the fluid circulating in the U-shaped tube. With the same assumption, a full-scale model is proposed to cover a wide time range from few minutes to several decades (Javed 2011), but there exists a gap between the temperature profiles derived from the short- and long-term solutions and an arbitrary temperature shift is required at the "breaking time". Li (Li, et al. 2014) developed another full-scale model based on the idea of "matching asymptotic expansion" and this model is able to simulate the thermal response by considering different structural parameters and physical properties in the borehole. However, all these full-scale models do not take into account of the groundwater impact. Several researches indicate that in most cases, the impact of groundwater flow on the heat transfer of BHEs cannot be neglected. Groundwater flow promotes the heat transfer between the BHEs and surrounding, and in some cases, this enhancement may allow 16% savings on the initial cost (Capozza, et al. 2013).

Although most proposed analytical models for the thermal analysis of vertical BHEs take into account of the effects of either groundwater flow or axial heat conduction in the soil, the time scale of heat transfer in the BHEs is not well treated. Therefore, in this paper, a new analytical full-scale model is developed to efficiently include the effects of the coupled transient heat transfer in the borehole, the axial heat conduction along the borehole and the horizontal flow of groundwater.

FUNDAMENTAL THEORY

This section provides a general review on the models that will be used as basis of the improved model. The schematic of vertical BHEs with groundwater flow is shown in Fig. 1. The assumptions are summarized as follows: i) the underground is homogeneous and composed of saturated soil with constant properties; ii) the surface temperature of the ground is constant; iii) the groundwater flows uniformly along x-axis with Darcy velocity u_d. In porous medium with groundwater flow, the 2-D heat transfer between the BHEs and the soil is mainly in the form of heat conduction and convection, as expressed in Eq. (1) (Nield and Bejan 2006).

$$\rho C_p \frac{\partial T}{\partial t} + u_d (\rho C_p)_w \frac{\partial T}{\partial x} - k\left(\frac{\partial^2 T}{\partial x^2} + \frac{\partial^2 T}{\partial y^2}\right) = 0 \quad (1)$$

Where T represents the average temperature of the porous medium; t is the operation time; k is the bulk thermal conductivity, and ρC_p represents the volumetric heat capacity of the porous medium. If η is the soil porosity,

the bulk properties can be expressed as Eq.(2).

$$k = \eta k_f + (1-\eta)k_s, \quad \rho C_p = \eta(\rho C_p)_f + (1-\eta)(\rho C_p)_s, \; a = k/\rho C_p \tag{2}$$

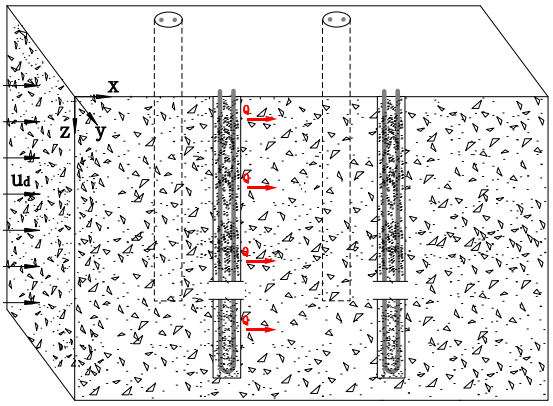

Fig. 1. Schematic of the vertical BHEs with groundwater flow (Q is the heating and cooling loads)

In the field application, the diameter of the borehole ranges from 0.1 to 0.2m and the depth normally varies from 40 to 200m. The aspect ratio between the depth and the diameter of the borehole is high and the borehole can be considered as a line heat source. According to the infinite line-source (ILS) model, the G-function at $r = r_b$ due to a unit-step load is shown in Eq. (3) (Eskilson and Claesson 1988).

$$G_{ILS}(t) = \frac{1}{4\pi k}\int_{\frac{r_b^2}{4at}}^{\infty} \frac{\exp(-u)}{u} du = \frac{1}{4\pi k} E_1\left(\frac{r_b^2}{4at}\right) \tag{3}$$

Where u is an integral variable; E_1 is an exponential integral function. In many cases the heating loads are not in balance with the cooling loads on a year-round basis, and the excessive load will accumulate in the ground and thus the effect of the heat transfer on the ground surface should be taken into account. Research showed that after 1.6 years, the ILS model would produce large error due to the neglect on the axial heat conduction of the borehole (Philippe, et al. 2009), and this would increase the length of BHEs by 15% during the initial design (Marcotte, et al. 2010). This limitation can be addressed by the finite line-source (FLS) model, which is derived from the method of images of heat sources. The G-function at $r = r_b$ due to a unit-step load can be expressed by Equation (4) (Zeng, et al. 2002).

$$G_{FLS}(t) = \frac{1}{4\pi Hk}\int_0^{\mathrm{H}} dz \int_0^{\mathrm{H}} \left[\frac{erfc\left(\frac{\sqrt{r_b^2+(z-l)^2}}{2\sqrt{at}}\right)}{\sqrt{r_b^2+(z-l)^2}} - \frac{erfc\left(\frac{\sqrt{r_b^2+(z+l)^2}}{2\sqrt{at}}\right)}{\sqrt{r_b^2+(z+l)^2}} \right] dl \tag{4}$$

Where l and z denote the integral variables, and $erfc(x)$ is the complementary error function. It should be noted that both ILS and FLS models are based on the assumptions of steady heat conduction in borehole. Therefore, they cannot be used directly for short time-step analysis in vertical BHEs. As a substitute, the composite-medium line-source (CMLS) theory (Li and Lai 2012) has been proposed to include the transient thermal process in the borehole and to further investigate the effect caused by the difference in the thermal properties of the ground and the backfilling material. As indicated in Fig. 2, the U-shaped tube is treated as two

infinite heating lines, and the wall temperature of the U-shaped tube is considered as characteristic temperature of the model and this value is the average of temperatures at points A and B. The short-term G-function for BHEs with single U-shaped tube is defined in Equations (5) and (6) (Li, et al. 2014; Yang and Li 2014).

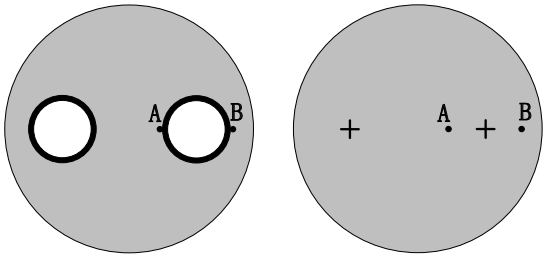

Fig. 2. The schematic of CMFL model for single U-shaped tube in the borehole

$$G_{CMLS}(t) = \frac{1}{2\pi k_b}\sum_{n=-\infty}^{+\infty}\int_0^{+\infty}[1-exp(-u^2 a_b t)]\times\frac{J_n(ur')(\varphi g-\psi f)[J_n(ur_A)+J_n(ur_B)]}{2u(\varphi^2+\psi^2)}du \quad (5)$$

$$\varphi = a^*k^*J_n(ur_b)J_n'(a^*u)-J_n'(ur_b)J_n(a^*u) \quad (6a) \qquad \psi = a^*k^*J_n(ur_b)Y_n'(a^*u)-J_n'(ur_b)Y_n(a^*u) \quad (6b)$$

$$f = a^*k^*Y_n(ur_b)J_n'(a^*u)-Y_n'(ur_b)J_n(a^*u) \quad (6c) \qquad g = a^*k^*Y_n(ur_b)Y_n'(a^*u)-Y_n'(ur_b)Y_n(a^*u) \quad (6d)$$

Where $a^* = \sqrt{a_b/a}$ and $k^* = k/k_b$ are the dimensionless variables; r' is the radius position of the heat line-sources (Fig. 2); r_A and r_B are the radius coordinates of points A and B respectively; u is the integral variable.

In the cases with groundwater flow, when neglect the effects of thermal dispersion, moving infinite line heat source (MILS) and moving finite line heat source (MFLS) models are the two main methods that take into account of the groundwater effect. (Chiasson and Connell 2011) examines two other analytical solutions for the heat transfer characteristics around closed-loop borehole heat exchangers in significant groundwater flow and proposes a model could account for the effects of thermal dispersion with groundwater advection. In MILS model, by considering the dimensionless parameters (*Pe* and *Fo*) and defining the integral average temperature of a circle with given radius, the G-function at $r = r_b$ due to a unit-step load is given in Eq. (7) (Diao, et al. 2004).

$$G_{MILS}(t) = \frac{1}{4\pi k}\int_0^{\pi}\left\{exp\left[\frac{Pe}{2}R'cos(\varphi)\right]\int_0^{Pe^2Fo/4}\frac{1}{\psi}exp\left[-\psi-\frac{Pe^2R'^2}{16\psi}\right]d\psi\right\}d\varphi \quad (7)$$

Where the reference length for non-dimensional parameters is *H*, $R' = \sqrt{x^2+y^2}/H$, $R = \sqrt{R'^2+(Z-Z')^2}$, $Z = z/H$, $Z' = z'/H$ are the dimensionless parameter; ψ is the integral variable. By considering the impact of the axial heat transfer in BHEs, MFLS model was developed with the G-function shown in Eqs. (8) and (9) (Molina-Giraldo, et al. 2011). Eq. (8) can be solved directly using numerical integral method, or it can be calculated by the simplified method given in the reference (Lamarche and Beauchamp 2007).

$$G_{MFLS}(t) = \frac{1}{4\pi k}\int_0^1 dZ\int_0^{\pi}\left\{2exp\left[\frac{Pe}{2}R'cos(\varphi)\right]\left[\int_0^1 f(R,Fo,Pe)\,dZ'-\int_{-1}^0 f(R,Fo,Pe)\,dZ'\right]\right\}d\varphi \quad (8)$$

$$f(R,Fo,Pe) = \frac{1}{4R}\left[exp\left(-\frac{Pe}{2}R\right)erfc\left(\frac{R-PeFo}{2\sqrt{Fo}}\right)+exp\left(\frac{Pe}{2}R\right)erfc\left(\frac{R+PeFo}{2\sqrt{Fo}}\right)\right] \quad (9)$$

IMPROVED FULL-SCALE ANALYTICAL MODEL

Fig.3 indicates the temperature profiles in one single borehole predicted by CMLS, ILS, FLS and MFLS

models. The time scale ranges from 0.5 min to 95 years and it can be roughly divided into two subintervals by a specific transition time t_b. This transition time is related to the structure of the borehole and it can be estimated by following a scaling relation $t_b \approx (2r_b)^2/a_b$ (Li and Lai 2015). The time scale is divided into short-term (0-5 hours) and medium-/long-term (>5 hours). When there is no groundwater flow or the effect of water flow can be neglected, another transition time $t_H \approx 70\ days$ (estimated from Fig.3) is used and t_H is related to the length of the borehole. It should be noted that these transition times are pre-required in the current full-scale models and the solutions are derived by shifting the line source solutions at an appropriate "breaking time".

As reviewed in the previous section, the traditional FLS model is able to be used in the mid-/long-term analysis and CMLS model is preferred in the short-term without considering the groundwater effect. Both MILS and MFLS models include the advection effect, but they would only be appropriate for the long-term. Therefore, a combination of CMLS and MFLS models would be able to include the effects of full time scale and advection caused by the water flow. By following a similar idea of "matching asymptotic expansion" proposed by other researchers (Li, et al. 2014 Javed 2011), the G-function of an improved CMLS-MFLS model is expressed as Eq. (10), where $G_{CMLS}(t)$, $G_{MFLS}(t)$ and $G_{MILS}(t)$ can be determined from Eqs. (5) to (9). When there is no effect of groundwater flow, the G-function Eq. (10) can also be written as the Eq. (11). It should be noted that different from other full-scale models, the transition times are not required to determine the improved G-function.

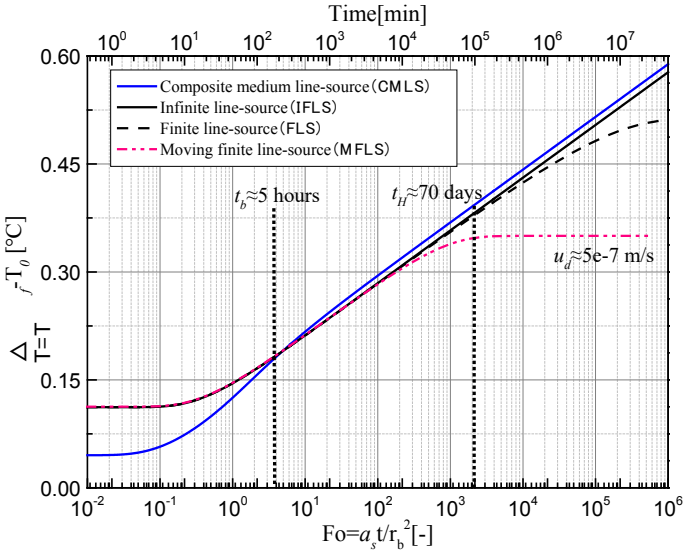

Fig.3. Temperature response of the circulating fluid in a borehole due to a unit-step thermal load, which is the solution of various analytical models (detailed input parameters are provided in Table 1)

$$G_{CMLS-MFLS}(t) = G_{CMLS}(t) + G_{MFLS}(t) - G_{MILS}(t) = \frac{1}{2\pi k_b}\sum_{n=-\infty}^{+\infty}\int_0^{+\infty}[1-exp(-u^2 a_b t)]\times$$

$$\frac{J_n(ur')(\varphi g-\psi f)[J_n(ur_A)+J_n(ur_B)]}{2u(\varphi^2+\psi^2)}du + \frac{1}{4\pi k}\left\{\int_0^1 dZ\int_0^{\pi}\left\{2exp\left[\frac{Pe}{2}R'cos(\varphi)\right]\int_{-1}^{1} f(R,Fo,Pe)\,dZ'\right\}d\varphi - \right. \quad (10)$$

$$\left.\int_0^{\pi}\left\{exp\left[\frac{Pe}{2}R'cos(\varphi)\right]\int_0^{Pe^2Fo/4}\frac{1}{\psi}exp\left[-\psi-\frac{Pe^2R'^2}{16\psi}\right]d\psi\right\}\right\}$$

$$G_{CMLS-MFLS}(t) = G_{CMLS}(t) + G_{FLS}(t) - G_{ILS}(t) = \frac{1}{2\pi k_b}\sum_{n=-\infty}^{+\infty}\int_0^{+\infty}[1 - exp(-u^2 a_b t)] \times$$

$$\frac{J_n(ur')(\varphi g - \psi f)[J_n(ur_A) + J_n(ur_B)]}{2u(\varphi^2+\psi^2)}du + \frac{1}{4\pi Hk}\int_0^{\mathrm{H}} dz \int_0^{\mathrm{H}} \left[\frac{erfc\left(\frac{\sqrt{r_b^2+(z-l)^2}}{2\sqrt{at}}\right)}{\sqrt{r_b^2+(z-l)^2}} - \frac{erfc\left(\frac{\sqrt{r_b^2+(z+l)^2}}{2\sqrt{at}}\right)}{\sqrt{r_b^2+(z+l)^2}}\right] dl - \frac{1}{4\pi k} E_1\left(\frac{r_b^2}{4at}\right) \quad (11)$$

The temperature of the circulating fluid due to a unit-step heating/cooling load can be obtained as Eq. (12).

$$T_f(t) - T_{s,0} = q_l\left[G_{CMLS-MFLS}(t) + R_p\right] \quad (12)$$

Where q_l is the heat flux per unit length, $R_p = R'_{conv} + R'_{cond}$ is the U-shaped pipe thermal resistance, $R'_{conv} = 1/(4\pi r_o h)$ is the convective resistance and $R'_{cond} = ln(r_o/r_i)/(4\pi k_p)$ is the conductive resistance of the U-shaped tube. The other important thing need to declare is that the steady-state borehole thermal resistance $R_b = R'_{conv} + R'_{cond} + R'_b = R_p + R'_b$ is used in the section, where R'_b is the thermal resistance of the grout. According to the literature (Lamarche, et al. 2010), R'_b is best predicted by the analytical solution derived from multipole method, and this expression is included in the CMLS-MFLS model and other formulates.

MODEL VALIDATION AND DISCUSSION

Numerical solutions by finite difference method or finite element method are commonly used to solve heat conduction problems. It is more flexible to deal with complicated geometries or other complexities such as the case of compound medium. In this section, a 2-D model was built to simulate the transient behavior of the thermal response in the actual U-shaped tube, which is normally in the short and medium time scale. Because the axial heat conduction has a significant effect only in a long time scale, the axial heat transfer is not considered and the solutions would be used to validate the new analytical solution developed in the previous section.

Fig. 4 indicates the 2-D mesh used in the finite element simulations. Constant heat flux (0.5W/m) were applied uniformly on the exterior surfaces of the two inner tubes. The infinite domain was replaced by a finite region with a large radius (10m), and the initial temperatures of both the soil and the outer boundaries were assumed as constant (15°C). The characteristic temperature of the tube walls equal to the average temperature of the circle as shown in the figure. Table 1 lists the physical properties of the medium and the operating conditions of the unsteady heat transfer procedure.

Fig.5 compares the predicted fluid temperature rise obtained from both analytical and numerical models. It is observed that the improved full-scale model (CMLS-MFLS) matched best with the numerical solutions in the short- and medium-term. The temperature rises also followed the variation trend of FLS model in the long-term. It should be noted that the traditional line-source models required to shift the temperature response after the transition time t_b. Therefore, the solution of the proposed CMLS-MFLS model would not rely on the transition time and could predict the temperature profile of the fluid in the tube of the borehole in the entire time scale.

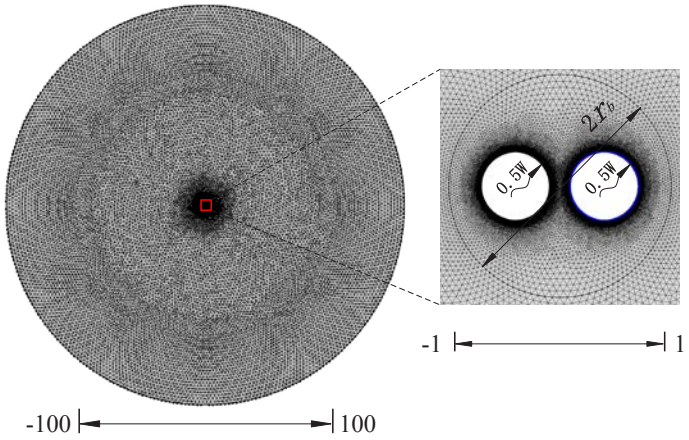

Fig. 4. Computation mesh used in the finite element simulations (without the U-shaped tube); the scale at the bottom indicates a non-dimensional distance based on the borehole radius

Table 1. Physical properties, and operating conditions of single U-tube BHEs models

Properties	Values	Properties	Values
q_l	1W/m	r_b	0.065m
k_p	0.42W/(mK)	H	100m
a	$1.33 \times 10^{-6}\mathrm{m}^2/\mathrm{s}$	x_U	$0.026m$
a_b	$4.84 \times 10^{-7}\mathrm{m}^2/\mathrm{s}$	r_i	0.017m
T_0	15℃	r_o	0.02m

Fig. 6 compares the thermal response curves derived with groundwater flow. Similar to the previous findings, the proposed CMLS-MFLS model could better predict the temperature rise in the short-term than the traditional MFLS model. In order to further investigate the impact of water flow on the thermal response, both CMLS-MFLS and CMLS-MILS models were compared at different flow rates. Results showed that the differences of fluid temperature obtained from moving finite and infinite line-source models were gradually decrease with the velocity increased. When Pe was higher than 20, the solutions derived from CMLS-MFLS and CMLS-MILS were almost overlapped, which indicated that the effect of axial heat transfer was weakened by the enhanced convection and the axial heat conduction in the borehole could almost be neglected. However, when Pe was less than 10, the results temperature rises predicted by CMLS-MFLS almost matched with the results in FLS, which indicated that the effect of groundwater could be neglected, and the axial heat conduction in the borehole would be the main factor to affect the long-term response.

CONCLUSION

A new full-scale CMLS-MFLS model, which could account for the entire time scale and the effect of groundwater flow, was proposed in this paper to predict the thermal response of a single, vertical BHEs. The analytical solution was validated by a numerical solution and compared with other typical analytical models. The analytical solutions of the proposed model remained simple in the expression and were convenient to use in the design of BHEs. The effect of axial heat loss and underground water flow were analyzed based on the proposed model. It was observed that when Pe was high (>20 in this study), the axial heat loss had a minor impact on the thermal response and could almost be neglected. When Pe was low (<10 in this study), the axial heat loss would be

the main factor in the long-term response and the advection effect could be neglected.

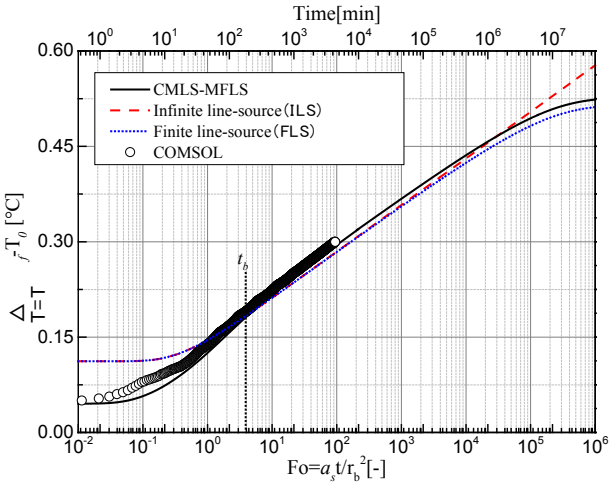

Fig.5. Validation of the new CMLS-MFLS model with a finite element method when Pe=0

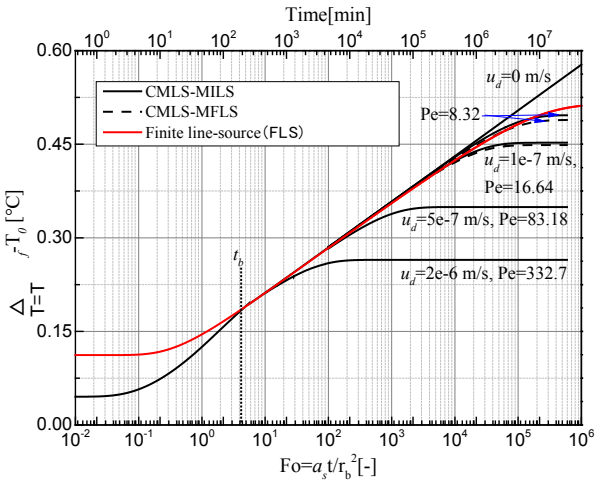

Fig. 6. Thermal response curves of CMLS-MFLS model at different groundwater flow rates

ACKNOWLEDGMENTS

The authors would like to thank and acknowledge Natural Science Foundation Grant No. 51706078 and Hubei Natural Science Foundation Grant No. 2017CFB131 for funding and supporting this work. The authors would also give special thanks to Dr. Min Li for providing the original simulation codes of CMLS model and Dr. Zhenhua Chai for his tremendous help on the mathematics.

NOMENCLATURE

Fo	=	Fourier number, $Fo = atH^{-2}$ (-)	q_l	=	heat flux per unit length (Wm^{-1})
Pe	=	Peclet number, $Pe = v_T Ha^{-1}$ (-)	a	=	thermal diffusivity $a = k\rho^{-1}C_p^{-1}$ ($m^2 s^{-1}$)
Pr	=	Prandtl number, $Pr = va^{-1}$ (-)	u	=	velocity (ms^{-1})
Re	=	Reynolds number, $Re = ur_i v^{-1}$ (-)	H	=	borehole vertical length, (m)
h	=	convective heat transfer coefficients ($Wm^{-2}K^{-1}$)	G	=	G function (-)
T	=	temperature (K)	v_T	=	effective heat transfer rate, (ms^{-1})
t	=	time (s)	J_n	=	Bessel functions of first kind of order n (-)
k	=	conductivity ($Wm^{-1}K^{-1}$)	Y_n	=	Bessel functions of second kind of order n (-)
R	=	unit length borehole resistance (mKW^{-1})	r	=	Radius coordinates, (m)
C_p	=	specific heat ($Jkg^{-1}K^{-1}$)	x, y, z	=	Cartesian coordinates (m)

Greek letters

φ	=	angle with x-axis (rad)	η	=	ground porosity (-)
ρ	=	density (kgm^{-3})			

Subscripts and superscripts

I	=	internal pipe	*s*	=	solid	*U*	=	shank spacing
b	=	grout	*p*	=	pipe	′	=	dimensionless
f	=	fluid	*o*	=	external pipe	*d*	=	Darcy

REFERENCES

Capozza, A. and M.D. Carli, et al. 2013. *Investigations on the influence of aquifers on the ground temperature in ground-source heat pump operation*. Applied Energy 107:350-363.

Chiasson, A. and A.O. Connell. 2011. *New analytical solution for sizing vertical borehole ground heat exchangers in environments with significant groundwater flow: parameter estimation from thermal response test data*. Hvac & R Research 17:1000-1011.

Claesson, J. and G. Hellström. 2011. *Multipole method to calculate borehole thermal resistances in a borehole heat exchanger*. Hvac & R Research 17:895-911.

Diao, N. and Q. Li, et al. 2004. *Heat transfer in ground heat exchangers with groundwater advection*. International Journal of Thermal Sciences 43:1203-1211.

Diao, N.R. and H.Y. Zeng, et al. 2004. *Improvement in modeling of heat transfer in vertical ground heat exchangers*. Hvac & R Research 10:459-470.

Eskilson, P. and J. Claesson. 1988. *Simulation model for thermally interacting heat extraction boreholes*. Numerical Heat Transfer Applications 13:149-165.

Hellström, G. 1991. *Ground heat storage: thermal analyses of duct storage systems*. Department of Mathematical Physics University of Lund, Sweden.

Javed, S. 2011. *An analytical method to calculate borehole fluid temperatures for time-scales from minutes to decades*. ASHRAE Transactions 117:279-288.

Javed, S. and J. Claesson. 2011. *New analytical and numerical solutions for the short-term analysis of vertical ground heat exchangers*. ASHRAE Transactions 117:3-12.

Kim, E.J. and J.J. Roux, et al. 2010. *Numerical modelling of geothermal vertical heat exchangers for the short time analysis using the state model size reduction technique*. Applied Thermal Engineering 30:706-714.

Lamarche, L. and B. Beauchamp. 2007. *A new contribution to the finite line-source model for geothermal boreholes*. Energy & Buildings 39:188-198.

Lamarche, L. and S. Kajl, et al. 2010. *A review of methods to evaluate borehole thermal resistances in geothermal heat-pump systems*. Geothermics 39:187–200.

Li, M. and A.C.K. Lai. 2012. *New temperature response functions (g functions) for pile and borehole ground heat exchangers based on composite-medium line-source theory*. Energy 38:255-263.

Li, M. and A.C.K. Lai. 2015. *Review of analytical models for heat transfer by vertical ground heat exchangers (ghes): a perspective of time and space scales*. Applied Energy 151:178-191.

Li, M. and P. Li, et al. 2014. *Full-scale temperature response function (g-function) for heat transfer by borehole ground heat exchangers (ghes) from sub-hour to decades*. Applied Energy 136:197 - 205.

Marcotte, D. and P. Pasquier, et al. 2010. *The importance of axial effects for borehole design of geothermal heat-pump systems*. Renewable Energy 35:763-770.

Molina-Giraldo, N. and P. Blum, et al. 2011. *A moving finite line source model to simulate borehole heat exchangers with groundwater advection*. International Journal of Thermal Sciences 50:2506-2513.

Nield, D.A. and A. Bejan. 2006. Convection in porous media. Springer.

Philippe, M. and M. Bernier, et al. 2009. *Validity ranges of three analytical solutions to heat transfer in the vicinity of single boreholes*. Geothermics 38:407-413.

Saner, D. and R. Juraske, et al. 2010. *Is it only co_2 that matters? A life cycle perspective on shallow geothermal systems*. Renewable & Sustainable Energy Reviews 14:1798-1813.

Somogyi, V. and V. Sebestyén, et al. 2017. *Scientific achievements and regulation of shallow geothermal systems in six European*

countries – a review. Renewable & Sustainable Energy Reviews 68:934-952.

Yang, Y. and M. Li. 2014. *Short-time performance of composite-medium line-source model for predicting responses of ground heat exchangers with single u-shaped tube*. International Journal of Thermal Sciences 82:130 - 137.

Yavuzturk, C. 1999. *Modeling of vertical ground loop heat exchangers for ground source heat pump systems*. Oklahoma State University, Stillwater, Oklahoma, U.S.A.

Zeng, H.Y. and N.R. Diao, et al. 2002. *A finite line-source model for boreholes in geothermal heat exchangers*. Heat Transfer-Asian Research 31:558-567.

IGSHPA SWEDEN
2018 Research Conference

DOI: 10.22488/okstate.18.000023

Soil thermal conductivity from early TRT logs using an active hybrid optic fibre system

Antonio Galgaro **Philippe Pasquier** **Luca Schenato**
Matteo Cultrera **Giorgia Dalla Santa***

ABSTRACT

At the Molinella test site in Italy, a monitoring well has been equipped with a hybrid active optical fibre cable down to the depth of 100 m sealed with geothermal grouting. The cored borehole provided a full stratigraphic sequence of unconsolidated alluvial deposits. The cored material has been classified from a geotechnical point of view, and the thermal parameters of the most relevant lithologies have been directly measured. Active heating of the optical fibre cable has been provided by a constant heating power injected through copper wires contained within the cable structure. This way, not only the equivalent thermal conductivity of the entire stratigraphy but also the thermal conductivity at a spatial resolution of 1 m have been obtained. For each investigated layer, the thermal conductivity obtained from the distributed temperature measurements and the ones acquired using direct measurements are interpreted and compared.

INTRODUCTION

Ground Source Heat Pumps (GSHP) are well-established systems for building conditioning, thanks to their high energy efficiency (Lucia et al., 2017). The closed-loop ground borehole heat exchanger (BHE) is the most widely used configuration for heating and cooling purposes (Sarbu and Sebarchievici, 2014). One of the most relevant elements in the design phase of GSHP systems is the knowledge of the thermal parameters of the geological materials crossed by the BHE; hence, the local thermal exchange capacity can be evaluated to finally calculate the required total borehole length. An overestimation or an underestimation of the thermal exchange capacity of the ground could strongly affect the installation and running costs of the ground heat exchanger as well as the energetic efficiency of the whole heating and cooling system over the years.

The local thermal exchange capacity can be obtained in several ways (Vieira et al., 2017); (I) by assuming the thermal parameters reported in literature for each sediment (VDI 4640, 2010); (II) by measuring thermal conductivity and capacity directly on the materials cored on-site (Popov et al., 1999; Tarnawski et al., 2013; Dalla Santa et al., 2017); (III) from the data acquired by a Thermal Response Tests (TRT) performed on site. The method (I) requires the availability of a detailed stratigraphic sequence for the installation site for which the evaluation could be incorrect because the thermal properties of a specific soil can vary greatly and differ from the ones reported in literature due to the variability of the geological conditions (consolidation status, moisture content and saturation, compaction level, etc.) as well as to the sediment's mineralogical composition. The (II) method requires the coring of the well and the

Antonio Galgaro (antonio.galgaro@unipd.it) is a professor of Geothermal Systems at Geosciences Department of Università degli Studi di Padova.
Philippe Pasquier (philippe.pasquier@polymtl.ca) is a professor of geological engineering at Polytechnique Montréal (Canada).
Luca Schenato (luca.schenato@cnr.it) is a researcher of the Research Institute for Geo-Hydrological Protection at the National Research Council.
Matteo Cultrera (matteo.cultrera@gmail.com) is a research fellow at the Geosciences Department of Università degli Studi di Padova (Italy).
Giorgia Dalla Santa (giorgia.dallasanta@unipd.it, *corresponding author*) is a research fellow at the Civil, Environmental And Architectural Engineering (ICEA) Department and at the Department of Geosciences of Università degli Studi di Padova (Italy).

sampling of each deposit to be measured directly. Moreover, the direct measurement of the samples thermal properties could be affected by some scale effects and neglects the contribution of the advection heat transfer processes in the aquifers.

Among the three methods, only the TRT-based one provides the undisturbed temperature of the ground and an equivalent thermal conductivity of the system, which is affected by the entire stratigraphy sequence, the local hydrogeological conditions as well as by the borehole thermal behaviour (heat-carrier fluid, pipes and sealing grout). A TRT is carried out by injecting/extracting heat to/from the BHE at a constant power and measuring the thermal response of the ground (Gehlin and Spitler, 2001). The system and the testing procedure were established by the American Society of Heating, Refrigerating and Air-Conditioning Engineers (ASHRAE) (Gehlin and Nordell, 2003).
Conventional TRT performed on closed-loop ground heat exchangers requires the use of a specific TRT unit and the procedure is time-consuming and, therefore, expensive.

Hence, with the purpose of evaluating the ground thermal properties at a lower cost and with a higher spatial and temporal resolution, the Distributed Thermal Response Test (DTRT) has been recently developed (Vieira et al., 2017). This new technique is performed by means of a hybrid cable integrating some copper wires and a bundle of fibre optics, sealed into the well (see fig.2a, fig. 2c). The DTRT allows the measurement of the vertical ground temperature distribution along the entire length of the borehole with high spatial and temporal resolution.
A hybrid optical fibre cable has been sealed into a borehole down to the depth of 100 m in the field laboratory of Molinella (Italy) with the purpose of testing the DTRT. The thermal conductivity data (related to the most relevant lithologies) directly measured by means of a portable device on the cored samples, combined with a geotechnical classification of the cored deposits, have been compared to the interpretation of the DTRT temperature profile obtained along the well with a spatial resolution of 1 meter after a very short (about 5 hours) heating period. This paper introduces the preliminary results and shows that the data acquired from the DTRT are able to identify the thermal conductivity profile and the geological layers variability. Therefore, by means of DTRT a significant reduction of the ground thermal testing time and – consequently – of the costs of the overall investigations can be expected.

METHODS

The test site

The test site is located in Molinella, between the city of Ferrara and Bologna in the Po Plain (Galgaro et al., 2017), which is the largest alluvial plain in Western Europe (Fig. 1a). The geological setting of the site is typical of lowland areas, consisting of unconsolidated sediments.

The 100m deep well coring of the test site has been collected in specific catalogue boxes. During the coring, the water table was 1.5m below the ground level. The geotechnical classification of the deposits provided the complete local stratigraphy of unconsolidated fluvial sediments. The lithological sequence can be described as a dominantly horizontally layered structure, typical of a quaternary floodplain deposition environment, dominated by silt and silty clay deposits alternated with thin sandy layers, as shown in Fig.1b. Recent studies have highlighted that these kinds of sediments can display settlements and permeability alterations when exposed to significant temperature variations (Dalla Santa et al., 2016a and 2016b; Dalla Santa et al., 2018). No aquifers with significant water flow have been detected, due to the very low permeability of the deposits and to the very low hydraulic gradient.

Direct thermal properties measurements on samples

For the main recognized layers, the thermal properties (conductivity and capacity) have been directly measured on the collected core samples by a hand–held instrument ISOMET 2114-Thermal properties analyzer (Isomet, 2017) which applies a transient heat transfer by means of a probe placed in direct contact with the tested sediment. The probe contains both a resistor used as a heat source and a temperature sensor. The temperature response generated by each material to the transient heating signal induced by the electrical heater is recorded and analyzed, hence obtaining

the thermal properties of the sample. The ISOMET measuring error declared by the producer is about 10 %. The procedure followed to perform the measurement follows ASTM standard recommendations (ASTM standard, 2008).
The sedimentary sequence of the Molinella test site is reported in Galgaro et al. (2017) and Zarrella et al. (2017), while the measured values of thermal conductivity are reported in Fig. 4b. The measurements were performed on site, soon after the coring, to maintain the sediments natural water content.

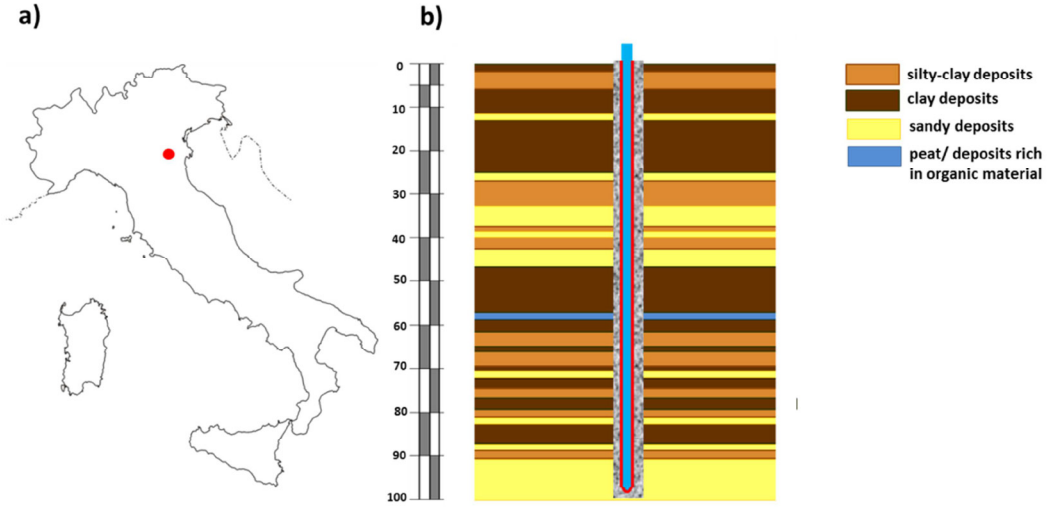

Figure 1 a) The position of the Molinella test site in Italy and b) The schematic geological sequence.

The DTRT with hybrid optical fibre cable

After the drilling, a hybrid fibre optic cable composed of 4 copper wires and one bundle of 5 optical fibres has been sealed into the well with thermally enhanced grout with a thermal conductivity of 1.7 W/mK. Fig. 2 reports a schematic representation of the device and some pictures of the installation procedure.
The DTRT has been performed by heating the ground by means of the current injected into the copper wires (i.e. Joule effect), while the vertical ground temperature distribution has been measured by the optical fibres. The use of the optic fibre cable allows the acquisition of temperature profile along the entire length of the borehole, due to the signal emitted into the fibre and backscatterd through the acquisition system being sensitive to temperature, thus exploiting the Raman scattering occurring in optical fibres (Schenato, 2017). The working principle is quite simple; when an optical pulse is injected into a fibre, three signals are generated (I) the Rayleigh backscattered signal at the same wavelength of the input light, (II) the Stokes component at a longer wavelength, and (III) the anti-Stokes component at a shorter wavelength. In particular, only the anti-Stokes signal intensity is temperature-dependent (approximately 0.8%/K at room temperature), while the Stokes is not. The ratio between the two intensities is, therefore, a measurement of the temperature at which the backscattered signals have been generated.
The use of Distributed Temperature Sensing (DTS) in thermal response testing allows measurements of high spatial (0.2-5m), temporal (1-10 min) and temperature (0.1-0.5K) resolution (Selker et al., 2006; Vieira et al., 2017). In this work, to perform the DTRT we used a commercial DTS interrogator by AP Sensing with sampling interval of 0.5 m, spatial resolution of 1m and a temperature repeatability of few tenths of a Kelvin degree.
The DTS has been firstly used without heating in order to collect the undisturbed temperature of the soil, that was around 14-15°C. Then, the thermal solicitation of the well and the surrounding ground has been provided by injecting

into the copper wires an almost constant heating power of 2630 W for about 5 hours. The heating power is assumed to be constant along the cable for its entire length (equal to 218 m).

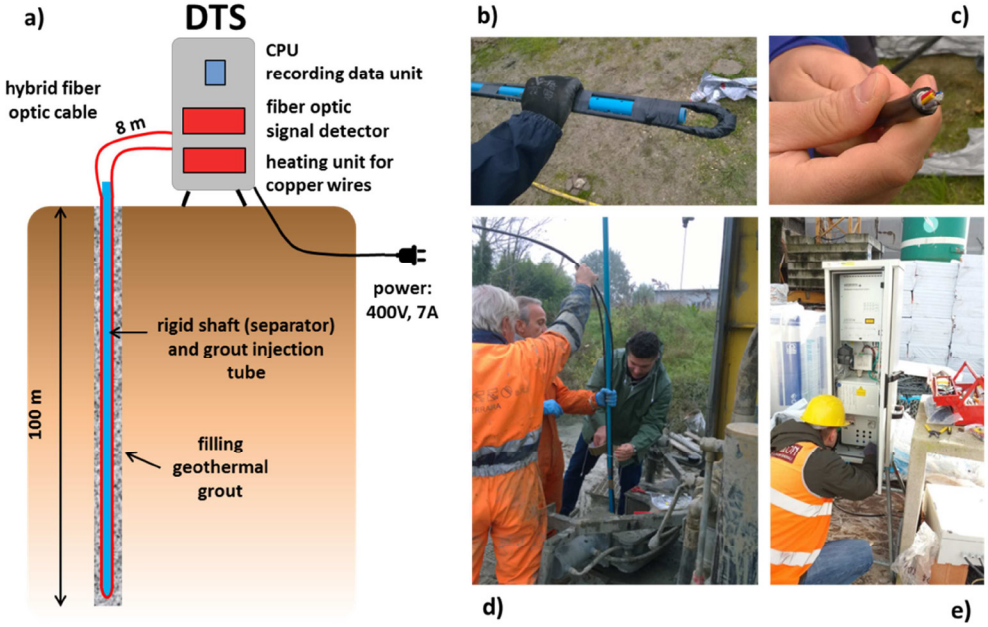

Figure 2 (a) A schematic representation of the DTS and some pictures of the installation procedure: (b) detail of the hybrid cable U-loop to be installed at the bottom of the well to protect the cable; c) section of the hybrid fibre optic cable with the copper wires and the bundle of optic fibres; d) installation procedure, with the hybrid fibre optic cable clamped to a rigid shaft before the installation; e) the Distributed Temperature Sensing interrogator during the test.

During the DTRT, the temperature along the fibre optic cable has been recorded every two minutes during the heating period and the subsequent 4 days, to measure the recovery thermal phase of the ground. At the end of the 5-hour heating test, the profile temperature was almost constant for the entire profile (around 25°C). During the subsequent recovery phase, the temperature measured at different depths cooled down at different rates, depending on the thermal properties of the surrounding deposits.

Given that the hybrid fiber optic cable was deployed in the well in a looped configuration (duplexed), both the heating than the measuring systems consist in two parallel lines.

From the DTRT data analysis the effective thermal conductivity of the surrounding ground can be inferred, allowing differentiating layers characterized by different thermal behaviour and, therefore, different geological conditions.

The raw temperature data, staked in time to form a 2D-dataset, have been numerically filtered to reduce the noise using 2D-wavelet transform. This approach benefits the effectiveness of 2D image processing and it allows for improved signal-to-noise ratio in both dimensions, i.e., time and space, simultaneously. A more rigorous approach would consist in using the algorithm directly to the Stokes and Anti-Stokes signals intensity (Soto et al., 2016) but here it was not applicable as they were not available.

Fig. 3 shows a comparison of the raw and denoised data for a given trace and for the temporal evolution at a given depth. One can observe that, during the cooling phase, the temperature oscillates over time with amplitude of few tenths of °C. A similar fluctuation is present at all depth and its origin is under investigation.

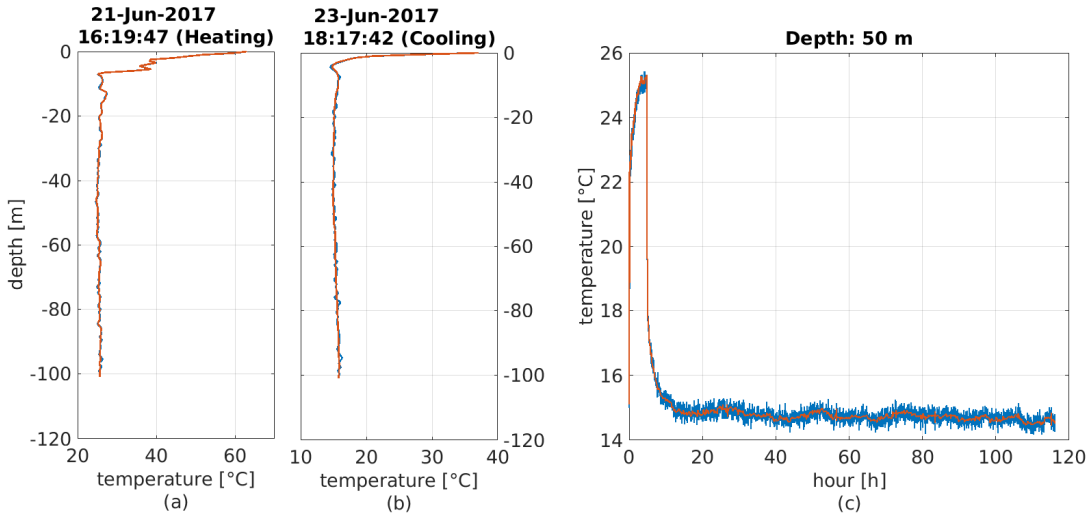

Figure 3 Raw data (blue) are compared with the denoised data (red curve) obtained by filtering with a biorthogonal wavelet. (a) Distributed temperature profile measured on June 21, 2017, 16:19:47 during the heating phase. (b) Distributed temperature profile measured on June 23, 2017, 18:17:42 during the cooling phase. (b) Temporal evolution of the temperature at 50 m of depth, during the heating and cooling phases.

The analytical method

TRTs performed on closed-loop ground heat exchangers are usually analyzed by the first-order approximation of the Infinite Line-Source model (Ingersoll et al, 1954). The traditional TRT interpretation strategy consists in fitting a linear regression model to the late average temperature data of the circulating fluid over time, after stimulating the soil with a thermal power approximately constant for a period of time long enough to ensure that the system will reach a thermal equilibrium. Being the obtained slope of the linear regression - that is the derivative of the mean temperature - related to the heating power and to the thermal properties of the surrounding ground, the method provides the value of the equivalent ground thermal conductivity (Gehlin and Spitler, 2001).
We used the same interpretation method to analyze the high spatial resolution temperature data acquired during the DTRT, by fitting a linear regression to the last part of temperature data measured at each depth along the cable, in order to infer the thermal conductivity of the surrounding deposit (see Fig.4a). Due to the U-loop shape of the hybrid cable, each ground layer is heated by two wires thermally interacting with each other.

The spatial superposition principle and Infinite Line-Source model can be used to interpret a TRT when two heat sources of infinite length, each emitting a heating power q, are close to each other. Using the first-order approximation of the Infinite Line-Source model to represent the temperature change around the heating wires allows to express the mean temperature measured by the optical fibres at a depth z through (Gehlin and Spitler, 2001):

$$T(z,t) = T_0(z) + qR_w + \sum_{i=1}^{n} \frac{q}{4\pi\lambda(z)} \left(\ln\left(\frac{4\alpha t}{r_i^2}\right) - \gamma \right) \qquad (1)$$

Reorganizing the previous equation to highlight the link between the natural logarithm of time and the thermal conductivity λ measured at a depth z leads to:

$$T(z) = T_0(z) + qR_w + \frac{2q}{4\pi\lambda(z)}\ln(t) + \frac{q}{4\pi\lambda(z)}\sum_{i=1}^{n}\left(\ln\left(\frac{4\alpha}{r_i^2}\right) - \gamma\right) \quad (2)$$

Finally, the thermal conductivity is provided for a case with two interacting heat sources by

$$\lambda(z) = \frac{q}{2\pi m(z)} \quad (3)$$

where *m(z)* is the regression coefficient obtained by a linear regression when using the logarithm of time as the regressor and the mean temperature measured by the two optical fibres as the dependent variable. By applying this procedure, we interpret the 200 temperature signals (one every 0.5 m) acquired during the DTRT.

RESULTS

The early heating phase has been analysed with the analytical method described previously and applied to the denoised signals for every depth. From the registered variation of temperature along time, the thermal conductivity of the surrounding deposit has been inferred; Fig. 4a illustrates an example of the regression fit to one of the 200 experimental traces obtained during the DTRT. The thermal conductivity values calculated every 0.5 m were assembled together to provide the entire vertical profile illustrated in Fig. 4b. For comparison, Fig. 4b also shows the thermal conductivity data obtained from the measurements performed directly on the cored samples (represented with the red circles) and the stratigraphy. The following comments should be made:

1. The spatial resolution of the DTS interrogator (1 m), is twice the distance among sensing points (0.5m). Hence, the thermal conductivity value inferred for each measurement point is correspondingly averaged over 1m fiber optic cable.
2. On the other side, the values of thermal conductivity of each lithological layer have been obtained from the experimental measurements performed on site on the core in the halfway point of each recognized layer.
3. The DTRT was performed during very hot days at the end of June with a mean external air temperature of 30°C, while the drilling and direct measurements on the samples were performed during a rainfall-heavy period of November soon after the drilling of the well.

While the thermal conductivities directly measured follow the stratigraphy succession (with higher values for sandy deposits and lower values for the cohesive ones), the profile obtained from the DTRT shows less concordance. It could be ascribed to the fact that the DTRT integrates a larger ground volume and performs a vertical spatial average of the signal including many influencing factors along the borehole.
For the shallower layers (less than 12 m), the difference between the two series is higher and the profiles even seem inverted; this could be a consequence of different humidity conditions of the geological materials due to external factors such as air temperature and solar heating/dehydration. In the deeper deposits the thermal conductivity shows less variability.
The vertical dotted lines in Fig. 4b) represent the mean values for the thermal conductivity obtained with the DTRT (in blue, 1.47 W/mK) and with the direct measurements (in red) (equal to 1.30 W/mK, calculated as the average of λ corresponding to each deposit weighted on the deposit thickness). The difference can be ascribed to scale effects such as the difference in the volume of soil involved in the thermal process used for the evaluation (Low et al., 2015). Due to the very short heating time, the volume of ground involved in the measurements is limited (less than 50cm from the borehole wall). For this reason, also the penetration of the grout injected to seal the well in the geological formations may have affected the measurements.

In addition, the values directly measured on the core may be underestimated with respect to the effective thermal conductivity on site because of the sample disturbance due to the loss in confining pressure after the sample was extracted, given that the higher the state of consolidation, the higher the thermal conductivity. In Fig4b, the green pointed lines represent the global values of λ obtained from a traditional TRT performed in a well with the same length at the same tests site by using different interpretation methods (as described in Zarrella et al, 2017). Both of the mean values presented in this paper are within the traditional TRT results.

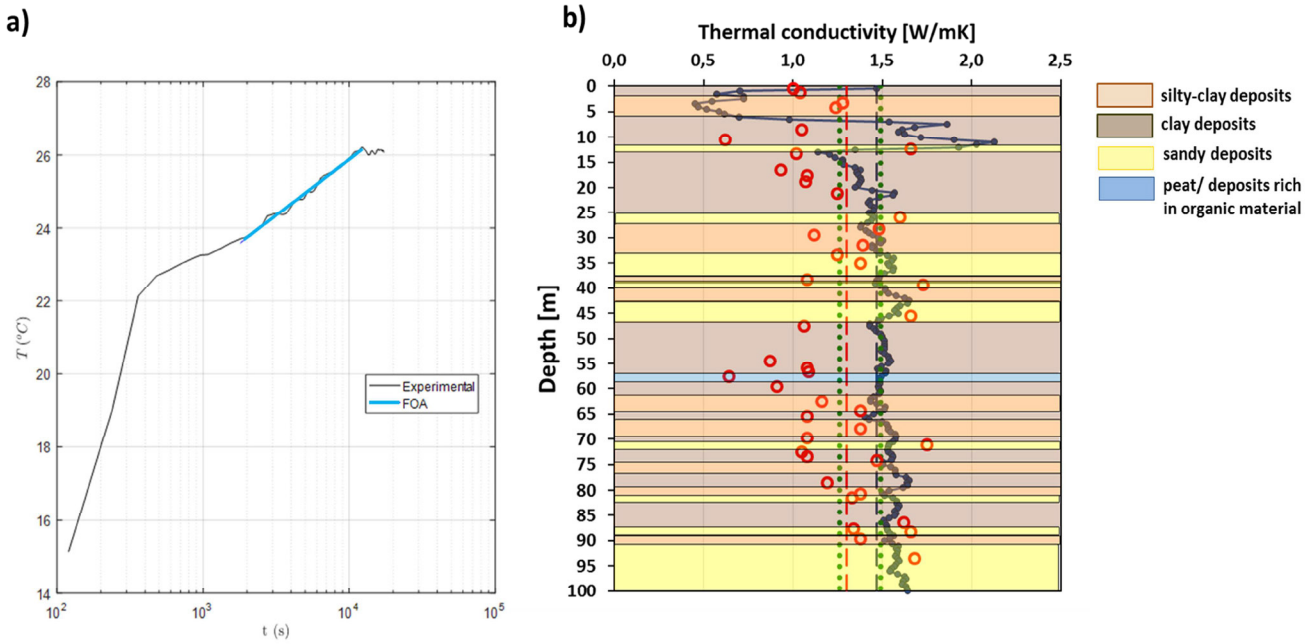

Figure 4 a) An example of fitting of the experimental data obtained from DTS used to calculate the thermal conductivity of each measurement point to determine the thermal behaviour of the surrounding sediments; b) The comparison between the thermal conductivity values obtained by analysing the DTRT data from the fibre optic cable (blue line) and the ones directly measured on the samples (red circles). The stratigraphy is represented by colours as described in the legend.

CONCLUSIONS

The results obtained highlight the potentiality of DTRT to estimate the vertical profile of thermal conductivity at low cost and not just a global value. While the thermal conductivities directly measured follow the stratigraphy succession (with higher values for sandy deposits and lower values for the cohesive ones), the profile obtained from the DTRT shows less concordance. It could be due to scale effects, to the vertical spatial average of the signal performed by the DTRT and to the penetration of grout into the deposits. In the shallower layers the outcomes are affected by external influences, while the results appear to be more stable in the deeper deposits.

Additional tests with longer heating periods performed in different seasonal conditions and in different geological conditions have been planned to provide new data and observations about the influence of some of the aforementioned perturbing factors.

Further development of the analysis method, currently on-going, will allow the interpretation of the recovery phase and the evaluation of the relationship between the stratigraphic units and the thermal conductivity measured by the DTRT.

ACKNOWLEDGMENTS

The coring of the well has been funded by the "Cheap-GSHPs" project that has received funding from the *European Union's Horizon 2020 research and innovation programme* under grant agreement No.657982. The authors wish to thank *Hydra srl -Hydraulic tools and Drilling Machines* (Molinella (Bo) - Italy) for providing the test field and their aid in the execution of the experimental measurements. The geotechnical classification of the deposits has been carried out in the Laboratory of Department ICEA at the University of Padova. Finally, Andrew Gambardello and Mattia Donà (technical officer of the ICEA Department – Geotechnical Engineering Laboratory) are gratefully acknowledged for performing the experimental tests.

NOMENCLATURE

α	=	Thermal diffusivity (m^2/s)
γ	=	Euler's constant (-)
λ	=	Thermal conductivity (W/mK)
q	=	Heating power per unit lenght(W/m)
r	=	Distance for the heat source (m)
R_w	=	Wire resistance (mK/W)
T	=	Temperature (K)
T_0	=	Initial temperature (K)
z	=	Depth (m)

Subscripts

0	=	initial
w	=	wire

REFERENCES

ASTM International. Standard Test Method for Determination of Thermal Conductivity of Soil and Soft Rock by Thermal Needle Probe Procedure. 2000. ASTM D5334–14 ASTM International: West Conshohocken, PA, USA.

Dalla Santa, G., Galgaro, A., Tateo, F. and S. Cola. 2016. *Induced Thermal Compaction in Cohesive Sediments around a Borehole Heat Exchanger: Laboratory Tests on the Effect of Pore Water Salinity*. Environmental Earth Sciences, 75(3): 1-11. doi: 10.1007/s12665-015-4952-z.

Dalla Santa, G., Galgaro, A., Tateo, F. and S. Cola. 2016. *Modified Compressibility of Cohesive Sediments Induced by Thermal Anomalies due to a Borehole Heat Exchanger*. Engineering Geology 202 :143-152. doi: 10.1016/j.enggeo.2016.01.011.

Dalla Santa, G., Peron, F., Galgaro, A., Cultrera, M., Bertermann, D., Mueller, J. and A. Bernardi. 2017. *Laboratory Measurements of Gravel Thermal Conductivity: an Update Methodological Approach*. Energy Procedia 125:671-677. doi: 10.1016/ j.egypro.2017.08.287.

Dalla Santa, G., Cola, S., Secco, M., Tateo, F., Sassi, R., and A. Galgaro. 2018. *Multiscale analysis of freeze–thaw effects induced by ground heat exchangers on permeability of silty clays*. Géotechnique, 1-11. Doi: 10.1680/jgeot.16.P.313

Galgaro, A., Dalla Santa, G., Cultrera, M., Bertermann, D., Mueller, J., De Carli, M., ... and A Bernardi. 2017. *EU Project "Cheap-GSHPs": The Geoexchange Field Laboratory*. Energy Procedia 125: 511-519. doi: 10.1016/j.egypro.2017.08.175.

Gehlin, S. and J. D., Spitler. 2001. *Thermal Response Test - State of the Art*. Report IEA - ECES.

Gehlin S. and B. Nordell 2003. *Determining Unidsturbed Ground Temperature for Thermal Response Test*. ASHRAE 2003 Winter Meet. CD, Chicago, IL; United States.

Ingersoll, L., Zobel, O., Ingersoll, A. 1954. Heat Conduction with Engineering, Geological and Other Applications. New York, USA: McGraw-Hill.

Isomet. *Portable Heat Transfer Analyser*. Available online: http://appliedp.com/produkty/isomet/(accessed on 29 November 2017).

Low, J.E., Loveridge, F.A., Powrie, W. and D. Nicholson. 2015. *A comparison of laboratory and in situ methods to determine soil thermal conductivity for energy foundations and other ground heat exchanger applications*. Acta geotechnica, 10(2):209-218.

Lucia, U., Simonetti, M., Chiesa, G. and G. Grisolia. 2017. G*round-source Pump System for Heating and Cooling: Review and Thermodynamic Approach*. Renewable and Sustainable Energy Reviews 70: 867–874.

Popov, Y.A., Pribnow, D.F.C., Sass, J.H., Williams, C.F. and H. Burkhardt. 1999. *Characterization of rock thermal conductivity by high-resolution optical scanning.* Geothermics 28:253–276.

Sarbu, L. and C. Sebarchievici. 2014. General Review of Ground-Source Heat Pump Systems for Heating and Cooling of Buildings. Energy and Buildings 70: 441–454.

Selker, J.S., Thévenaz, L., Huwald, H., Mallet, A., Luxemburg, W., Van De Giesen, N. ... and M.B. Parlange. 2006. *Distributed fiber-optic temperature sensing for hydrologic systems*. Water Resources Research, 42(12).

Schenato, L. 2017. A review of distributed fibre optic sensors for Geo-Hydrological applications. Applied Sciences 7(9), 896; doi:10.3390/app7090896

Soto, M., Ramìrez J. A. and Thévenaz, L. 2016. Intensifying the response of distributed optical fibre sensors using 2D and 3D image restoration. Nature Communications 7:10870. doi:10.1038/ncomms10870.

Tarnawski, V.R.., McCombie, M.L., Momose, T., Sakaguchi, I. and W.H., Leong. 2013. *Thermal Conductivity of Standard Sands. Part III. Full Range of Saturation*. International Journal of Thermophysics 34: 1130–1147.

Verein Deutscher Ingenieure-VDI. VDI 4640 Part 1. In Thermal Use of the Underground: Fundamentals, Approvals, Environmental Aspects; Verein Deutscher Ingenieure: Düsseldorf, Germany, 2010

Vieira, A., Alberdi-Pagola, M., Christodoulides, P., Javed, S., Loveridge, F., Nguyen, F., ... and G. V. Lysebetten. 2017. *Characterisation of Ground Thermal and Thermo-Mechanical Behaviour for Shallow Geothermal Energy Applications*. Energies 10(12): 2044.

Zarrella, A., Emmi, G., Graci, S., De Carli, M., Cultrera, M., Dalla Santa, G., Galgaro, A., Bertermann, D., Mueller, J. Pockelé, L., Mezzasalma, G., Righini, D., Psyk, M. and A. Bernardi. 2017. *Thermal Response Testing Results of Different Types of 2 Borehole Heat Exchangers: an Analysis and 3 Comparison of Interpretation Methods*. Energies 10, 801. doi:10.3390/en10060801.

[This page has been intentionally left blank]

IGSHPA SWEDEN
2018 Research Conference

DOI: 10.22488/okstate.18.000027

Temperature profile measurements – easy, cheap and informative

Henrik Holmberg **Randi Kalskin Ramstad** **Mari Helen Riise**

ABSTRACT

Regular thermal response tests (TRT) are routinely performed to get data for sizing larger installations with borehole heat exchangers. The effective borehole thermal conductivity and the effective borehole thermal resistance are the two main parameters determined with the test, in addition, the undisturbed temperature of the borehole is determined, most often by measuring the temperature of the collector fluid during circulation before startup of the test.

The undisturbed temperature of the borehole can also be determined from the vertical temperature profile in the borehole. Such temperature profiles are easily obtained with manual measurements using a probe in one of the collector pipes.

In addition to an accurate measurement of the undisturbed temperature, the vertical temperature profile can be interpreted to find e.g. water bearing fractures, thermal pollution from nearby buildings and variations in geology. Temperature profile measurements after the TRT is performed can be used as an indicator of groundwater flow in the borehole that might affect the results from the response test and the performance of the borehole (Liebel 2012).

This paper presents data from temperature profile measurements performed in single boreholes and in borehole fields in Norway. The profiles are measured before (undisturbed temperature) and after TRTs on boreholes ranging between 50 to 500 m. Based on the data, cases where the temperature profiles have been used to indicate variations in geology, water bearing fractures and variations in temperatures within neighboring boreholes are presented. Together with thermal conductivity values from laboratory measurements on rock samples, the profiles are also used to explain the results from TRTs affected by groundwater flow. Temperature profile measurements from several boreholes within single borehole fields also show significant differences important for the design of the GSHP system. As a conclusion, it is shown that the regular measurement of temperature profiles is an easy and cost effective method to gain knowledge and insight beyond that of a standard response test. It is therefore recommended to measure the undisturbed temperature profile of all boreholes in a GSHP as a regular part of the documentation and as a basis for design of GSHP systems.

INTRODUCTION

Thermal response tests (TRTs) are routinely performed to determine the effective thermal conductivity of the ground (λ_{eff}) and the effective borehole thermal resistance (R_b), together with the undisturbed temperature of the ground, these are the key parameters when sizing borehole fields for ground source heat pump systems (GSHP). While the method is robust and widely used (Sanner et al. 2013) it is usually only for lager GSHP installations with more than 12-15 boreholes that TRTs are performed due to the cost involved, and for most of these larger installation

Henrik Holmberg (henrik.holmberg@asplanviak.no) has a PhD in heat transfer and is an adviser at Asplan Viak AS.
Randi Kalskin Ramstad (randi.kalskin.ramstad@ntnu.no) is a associate Professor at the department of geoscience and petroleum at the Norwegian University of Science and Technology, (randi.kalskin.ramstad@asplanviak.no) and is an adviser (hourly basis) at Asplan Viak AS.
Mari Helen Riise (MariHelen.Riise@asplanviak.no) has a master of science in hydrogeology and is an adviser at Asplan Viak AS.

only one test is performed. When performing a TRT, the undisturbed temperature of the borehole is determined either by measuring the temperature of the collector fluid during circulation before startup of the test, or by measuring the vertical temperature profile in the borehole by using a probe in one of the collector pipes (Gehlin and Nordell 2003).

In addition to an accurate measurement of the undisturbed temperature, the vertical temperature profile can be interpreted to find e.g. water bearing fractures, thermal pollution from nearby buildings and variations in geology. Temperature profile measurements after the TRT is performed can be used as an indicator of groundwater flow in the borehole that might affect the results from the response test and the performance of the borehole (Liebel 2012).

In contrast to the TRTs, the temperature profile measurements are simple and inexpensive, and can therefore be performed on several boreholes to complement the results from the TRT. This has also been pointed out in Raymond et al. 2016.

The temperature profile in the borehole can also be determined using distributed temperature sensing (DTS) with fiberoptic cable as described in detail in Acuna (2013). While these measurements are promising, the high cost of the measurement equipment limits the use of DTS for many GSHP installations.

Since 2011, Asplan Viak AS has analyzed 100 + TRTs performed in Norway. The borehole depths range between 50 to 500 m and are analyzed according to Gehlin (2002) and Signorelli (2004 and 2007). In addition to the standard TRT procedure, which usually follows the guidelines established by the Swedish Geoenergycentrum (2015), the vertical temperature profiles in the boreholes are routinely measured before, and in most cases, also after the test is performed.

The locations of the analyzed TRTs are shown in figure 1 where blue dots are TRTs accompanied by temperature profile measurements and red dots are TRTs without temperature profile. In the cases without temperature profile, the undisturbed temperature of the borehole is determined by measuring the temperature of the circulated collector fluid before the TRT is initiated.

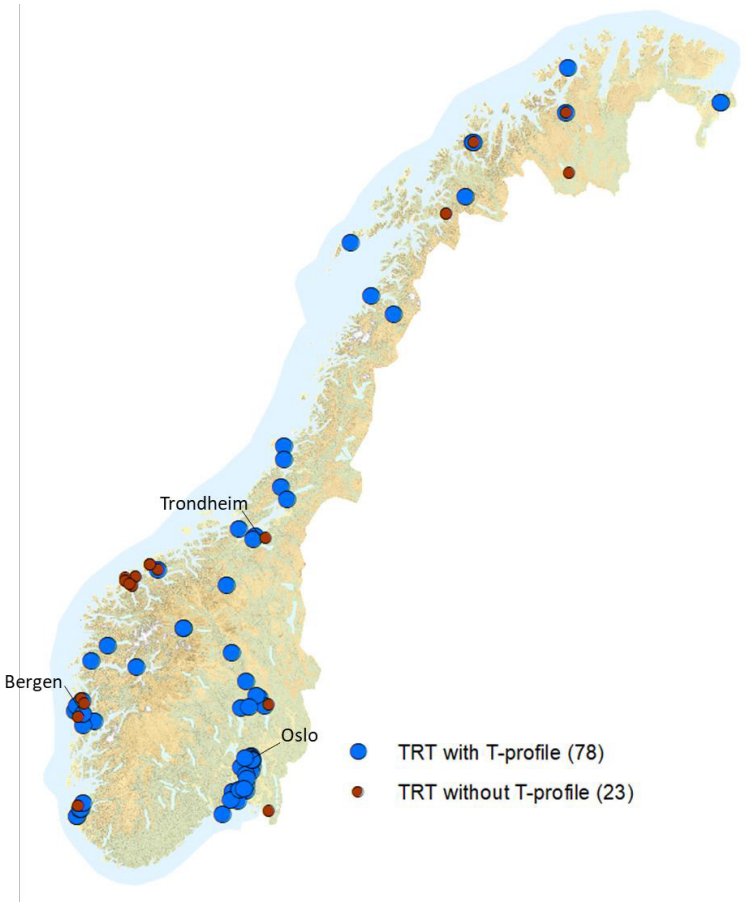

Figure 1. Location of most of the thermal response tests analyzed by Asplan Viak in Norway since 2011.

The aim of the present paper is to present data from temperature profile measurements and to demonstrate the usefulness of the temperature profiles for interpretation of TRT results and for the design of ground source heat pump systems (GSHP).

Specific cases have been selected to demonstrate the usefulness of the temperature profiles. Based on the data, cases were the temperature profiles have been used to indicate variations in geology, water bearing fractures and variations in temperatures within neighboring boreholes are presented. Together with thermal conductivity values from laboratory measurements on rock samples, the profiles are also used to explain the results from TRTs affected by groundwater flow. Therefore, the presented study can be regarded as an extension of the PhD-work of Liebel (2012).

METHODOLOGY

Temperature profiles presented in the present paper have been measured during the construction phase of GSHP installations. Measurements are usually performed by the drilling company and reported back to the consultant for sizing and documentation of the borehole heat exchangers (BHEs).

Undisturbed temperature profiles are measured after the borehole has rested a minimum of 3 days after the drilling is completed, in most cases the profile is measured after 5 to 7 days. When measuring the temperature profile there should not be any drilling in the area near to the borehole as this can disturb the measurements.

The temperature is measured inside one of the collector pipes with a probe, commonly of the type 110 from hydrotechnik GMBH. Such temperature probes have an accuracy of <0.1 K and a resolution of 0.1 K. This is a manual procedure were the value is noted for each 5^{th} to 10^{th} meter, at each step, the probe is held still until the temperature has stabilized. For a 250 m borehole, this takes about 30 - 40 minutes. Measurements are either performed from top to bottom, or from bottom to top. Provided that care is taken when performing the measurements, both measurement directions give the same results. When measuring from bottom to top, the probe is first lowered to the bottom of the borehole and then held still a few minutes until the temperature has stabilized before starting the measurements. This measurement direction is often more practical since it distributes the work involved with winding up the temperature probe.

For most cases, temperature measurements with a 5 m resolution is enough to capture effects such as groundwater movement in a 200 – 300 m borehole. For short boreholes (e.g. 50 m) is it natural to use a shorter measurement interval of about 2 m.

The temperature profiles after the TRT are measured while the temperature in the borehole is recovering. To avoid the rapid temperature changes directly after the TRT, the temperature should be measured after a few hours (Heiko et al. 2011). Due to practical considerations, the temperature profile is usually measured about 1- 5 hours after the heating period of the TRT is finished.

The temperature measurements presented in the present paper are derived from a series of GSHP projects involving several companies and with different temperature probes. While the measurements are expected to be influenced by the different operators, the temperature profiles are accurate enough to determine the undisturbed temperature of the borehole and to identify factors that are of importance for the BHE sizing and the interpretation of the TRT results.

The measurements are presented without any kind of post processing or corrections, e.g. as suggested in Raymond et al. 2016 for the rise of the collector fluid due to the added volume of the temperature probe.

TRT results presented in the paper are based on tests performed with a heating period of 72 hours, the tests are analyzed according to Gehlin (2002) and Signorelli (2004 and 2007).

THERMAL CONDUCTIVITY OF ROCKS BASED ON MINERALOGICAL COMPOSITION

Laboratory measurements on rock samples from the larger Oslo area, Norway, shows a variation in thermal conductivity typically from 2 to 4 W/m·K (Ramstad et al. 2014) representing the mineralogical composition and

layering effects (foliation) on dry rock samples. The thermal conductivity is highest in rock types with a high content of quartz and parallel to the foliation of the rock. The rock types covered in the study above represent many of the most common rock types in Norway and thus gives a good basis of what to expect for the different rock types considering heat transfer with conduction only.

The geology at the TRT-site is usually determined by maps from the Geological Survey of Norway and supported by observations from detailed driller's logs, and observations from drilling cuttings. In cases where the TRT-measurements deviates significantly from the expected value it has to be determined whether the results are affected by groundwater flow. In these cases, the temperature profiles measured before and after the TRT provide valuable information, often in combination with observations from the driller's log.

WATER BEARING FRACTURES AND GROUNDWATER FLOW

Boreholes are often intersected by water bearing fractures and fracture zones. In some cases, this affects the performance of the borehole and the result of the thermal response test. Most often, this is observed as an unrealistic high value of effective thermal conductivity. As noted by e.g. Sanner (2007) and Liebel (2012) fractures and zones with cold water that intersects the borehole are easily identified in the temperature profile measured after the TRT. In most cases the fractures only affects a limited part of the borehole and therefore have little or no influence on the effective thermal conductivity as determined from a TRT. It is first when there is a groundwater flow vertically and along the collector in the borehole (e.g. between two fracture zones) that a significant contribution to the measured effective thermal conductivity can be seen. In these cases, the groundwater flow is pressure driven, typically with highest water pressure in the lower fracture and lowest pressure in the upper fracture. Pressure driven groundwater flow can often be observed in the undisturbed temperature profile as sections of the borehole where the temperature is constant (deviates from the conductive temperature profile). A groundwater flow can also be induced by the TRT itself due to density differences caused by different temperatures in the groundwater surrounding the collectors, also known as the thermosiphon-effect as described e.g. by Gehlin et al. 2003.

Pressure driven vertical circulation of water in the borehole

Undisturbed temperature profiles from two separate borehole fields in Norway are shown in figure 2 and figure 4. The profiles are selected to illustrate the influence from pressure driven vertical groundwater flow in the boreholes. The temperature profiles shown in figure 2 are from Vensmoen borehole field in Northern Norway, and are to a different degree affected by vertical groundwater flow. The profiles were measured in August 2016.

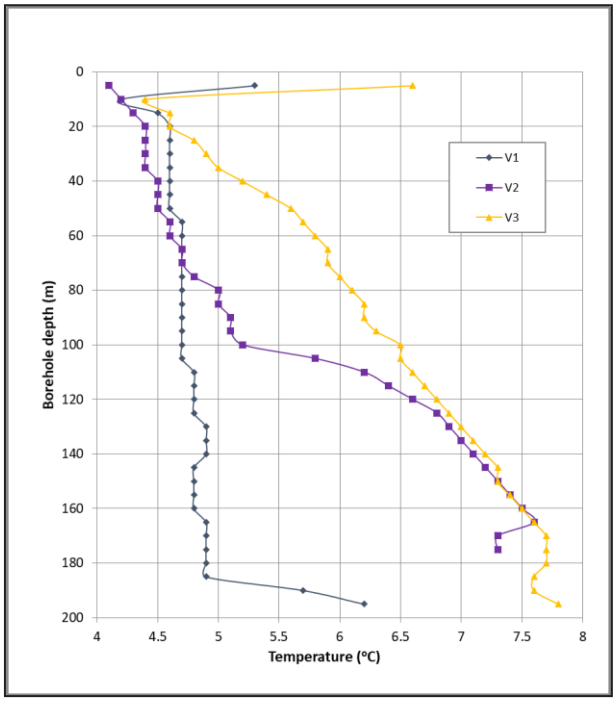

Figure 2. Undisturbed temperature profiles from Vensmoen borehole field, Nordland county in Norway. TRT performed in V1 yielded an λ_{eff} of about 60 W/ m·K. Temperature profiles V1 and V2 are affected by groundwater circulation while V3 is showing a conductive behavior. The profiles were measured in 2016.

In the first profile (V1), groundwater flows vertically along almost the entire length of the borehole (from around 185 m to ca. 15 m depth). Also in the second profile (V2), the upper 100 m of the borehole is affected by groundwater flow, while the third profile (V3) shows an almost ideal conductive profile for almost the entire borehole depth. The geology at the site is mapped as marble by the Geological Survey of Norway (NGU). It is not unusual that boreholes drilled in marble intersects large water bearing fracture zones and even caves (so-called karst) where the rock has dissolved. Borehole V1 (which was also the first borehole to be drilled) likely intersects such a karst with water at a higher pressure. A standard 72 hour TRT performed in borehole V1 in 2013 yielded a very high λ_{eff} of around 60 W/m·K. The unusually high λ_{eff} (even for TRTs affected by groundwater flow) can only be explained by a large vertical flow rate in the borehole. The temperature profiles measured before and after the TRT are shown in figure 3. The temperature profile that was measured 20-30 minutes after the test was finished resembles the undisturbed profile measured before the test.

It can also be noted that the undisturbed temperature profile measured in 2013, before the TRT, is about 0.8 K warmer than the temperature profile measured in 2016.

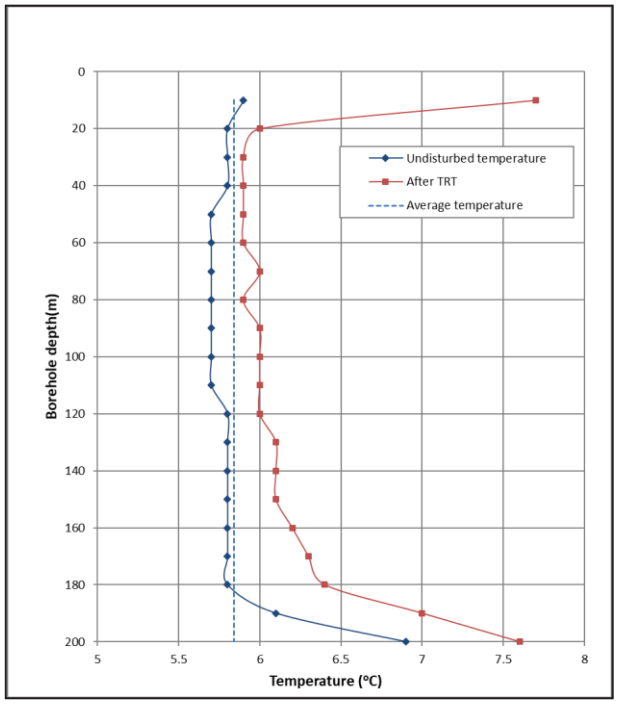

Figure 3. Measured temperature profile before and after the TRT in the test-borehole at Vensmoen, Nordland county, Norway

While no further TRT was performed in the project, a test performed in V2 would likely also give a rather high λ_{eff}, while a test performed in V3 would yield a more representative value for the thermal conductivity of the rock type on site reflecting the mineralogical composition only.

The temperature profiles shown in figure 4 are from Skjåk borehole field, in Norway, the first profile (S1) represents the undisturbed temperature in the first borehole drilled. The near constant temperature between 35 m to about 100 m indicates vertical flow of groundwater. A 72 h TRT performed in the borehole resulted in an unrealistically high thermal conductivity of 6.8 W/m·K. It was therefore concluded that the result was affected by the observed vertical groundwater flow. At a later stage in the project, observations from detailed driller's logs (water yield, observed fractures etc.) were used to select candidate boreholes for temperature profile measurements. A second 72 h TRT was then performed in the borehole with the least affected profile (profile S2 in figure 4). This test resulted in an λ_{eff} of 2.8 W/m·K which is more representative for the geology at the site which was mapped as granitic gneiss and migmatite by the Geological Survey of Norway (NGU).

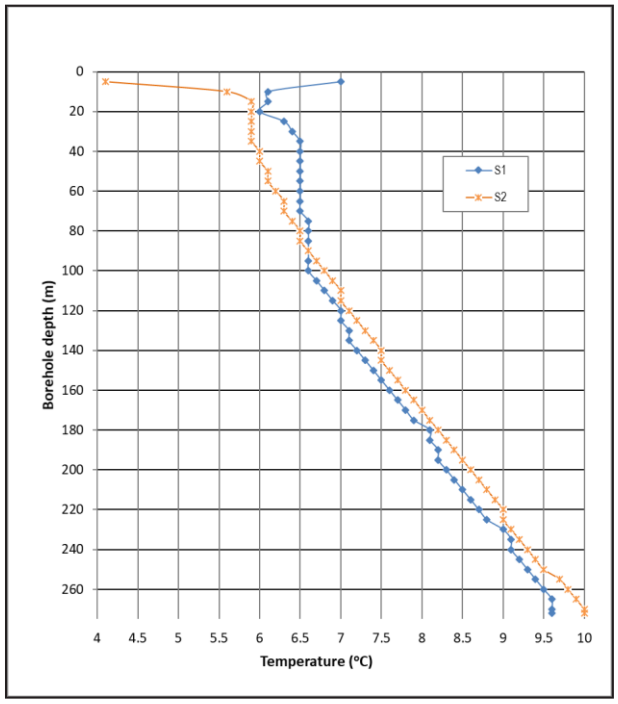

Figure 4. Temperature profiles from Skjåk borehole field, Oppland county, Norway. TRTs yielded an λ_{eff} = 6.8 W/ m·k in S1 and λ_{eff} =2.8 W/ m·k in S2.

Water-bearing fractures and induced water flow (thermosiphon effect)

Water-bearing fractures (where water crosses the borehole) are usually not visible in the undisturbed temperature profile, but can easily be identified in the temperature profiles measured after a TRT, as shown in figure 5 and figure 7. While showing as a distinct feature in the temperature profile, these fractures usually have little effect on the effective thermal conductivity (λ_{eff}) measured for a standard borehole (200 m – 300 m) since only a limited part of the borehole is affected. Temperature profiles measured before and after a TRT in a borehole with a single distinct fracture are shown in figure 5. The fracture, which was also observed in the drillers log at about 63 m, is clearly visible in the temperature profile measured 3 hours after the TRT. In this case the 72 hour TRT resulted in an λ_{eff} of 3.1 W/m·K which is a likely value for the rock type at the site, the influence of the groundwater passing through the borehole at about 60-70 m depth is therefore assumed to be limited.

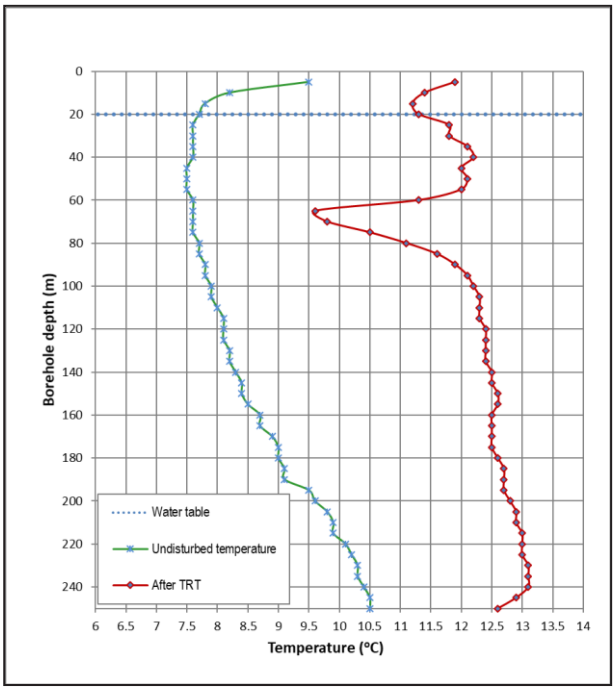

Figure 5. Temperature profiles before and 3 hours after TRT performed at Hovli, Oppland county, Norway. A single water-bearing fracture is observed after the TRT.

It seems that for groundwater to have significant effect on the results from the TRT there either has to be a vertical flow of water along the collector in the borehole or a larger amount of fractures and fracture zones intersecting the borehole. A vertical groundwater flow can also be induced by the TRT where added heat causes a thermosiphon effect, the phenomena is nicely described in Gehlin et al. 2003. In essence, the temperature increase causes the water to rise in the borehole; the warmed water leaves the borehole through fractures in the upper part of the borehole while cold water enters the borehole in fractures lower down. The result is an increase in λ_{eff} as measured by the TRT. Figure 6 show the development of λ_{eff} throughout a 72 hour TRT performed in a borehole in Skoppum, Norway. The borehole was intersected by two distinct fractures. The increase in λ_{eff} throughout the test indicates that the test is affected by the thermosiphon effect. The temperature profiles measured before and after the TRT are shown in figure 7.

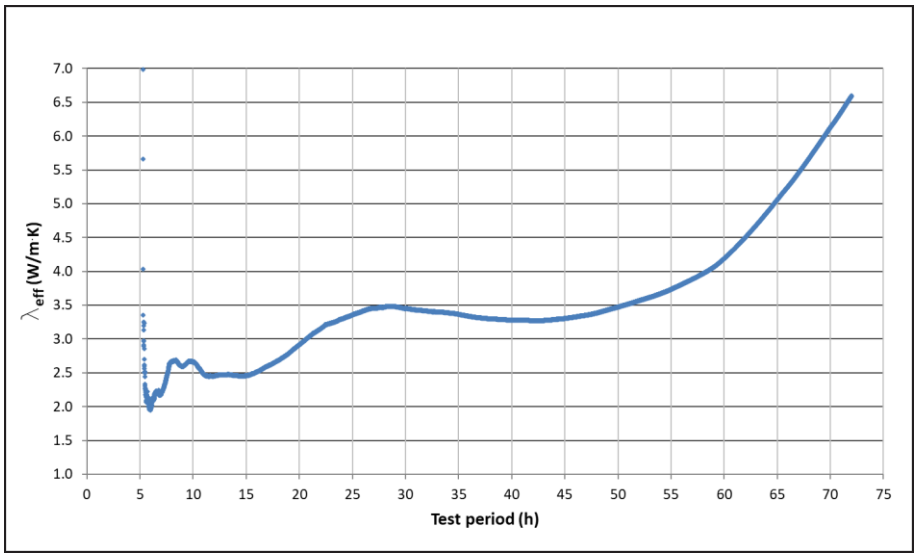

Figure 6. Development of λ_{eff} during a TRT performed in a borehole in Skoppum, Vestfold county, Norway. The test, which was influenced by the thermosiphon effect, is evaluated according to Signorelli (2007).

The undisturbed temperature profile in figure 7 is a near ideal conductive profile with a geothermal gradient of about 0.022 K/m which is high with respect to Norwegian conditions. The undisturbed temperature profile was measured one week after the drilling was finished. In the temperature profile measured 3 hours after the TRT (which was clearly affected by groundwater flow), two distinct fractures can be observed at about 30 m and 140 m depth. The fracture at about 30 m depth could also be interpreted as a reflection of the undisturbed temperature gradient in the borehole. Since the temperature profile was measured shortly after the TRT finished, it is, however, evident that the sudden temperature change is caused by groundwater flow. In the bottom of the borehole the temperature profile after the test crosses the undisturbed temperature, this might be a measurement error caused by the measurement procedure where the temperature probe is lowered to the bottom of the borehole before starting the measurements. The temperature profiles shown in figure 8 are from a second TRT, successfully performed in a neighboring borehole. The undisturbed temperature profile is measured on week after the borehole was drilled and the temperature profile after the test was measured 2 hours after the 72 hour TRT finished. This test yielded an λ_{eff} of 2.3 W/m·K, this is a low value, but it is not unlikely for the geology at the site which according to the Geological Survey of Norway (NGU) is mapped as rhomb porphyry. Laboratory measurements of rhomb porphyry presented in Ramstad et al. (2014) show a median thermal conductivity of 2.3 W/ m·K.

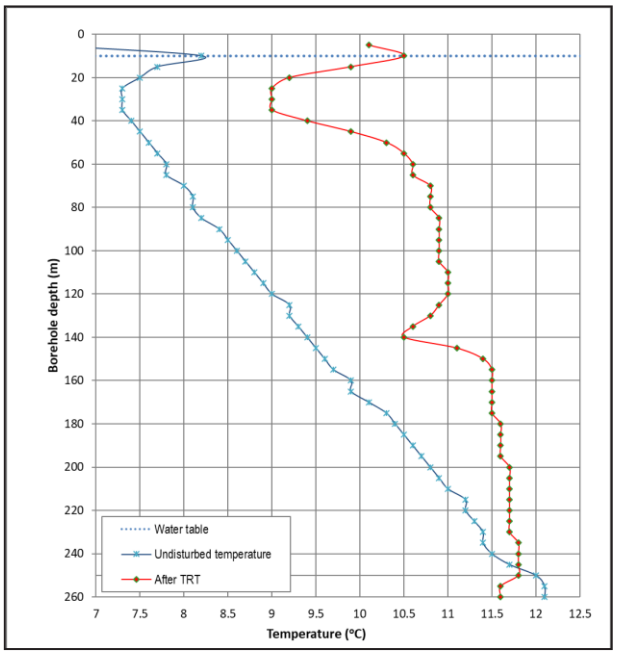

Figure 7. Temperature profiles before and after TRT performed in Skoppum, Vestfold county, Norway. Two distinct water-bearing fractures are observed at about 30 m respective 140 m depth.

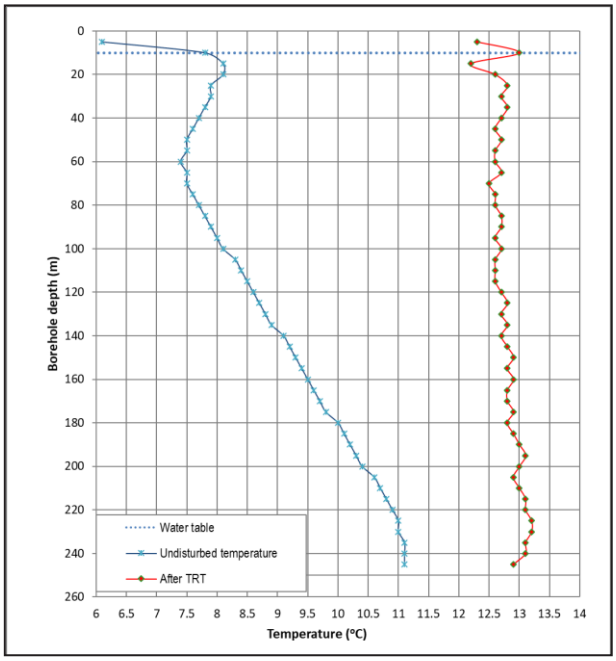

Figure 8. Temperature profiles before and after the second TRT (neighboring borehole for the borehole tested in figure 6 and figure 7) performed in Skoppum, Vestfold county, Norway.

It has been observed that pressure driven vertical ground water flow can be identified from the undisturbed temperature profiles measured before a TRT. Temperature profiles therefore provide an easy method to avoid tests that are affected by groundwater flow.

It is more difficult to avoid tests that are affected by induced ground water flow (thermosiphon effect); the undisturbed temperature profiles provide no information about groundwater flow horizontal to the borehole, e.g. fractures. These are, however, easily identified from the temperature profiles measured after the TRT. In addition, the induced thermosiphon effect shows as an increasing λ_{eff} throughout the test. The thermosiphon effect is more pronounced using higher specific heat effect during the test.

In most cases, the temperature profile measured after the test shows a conductive behavior (as in figure 8) and can be used to indicate that the test is successful and unaffected by ground water flow.

Temperatures within neighboring boreholes

When sizing a borehole field, the undisturbed temperature (as usually determined from the test borehole) is an important parameter, which have a large influence on the number of boreholes and the total amount of borehole meters drilled. The undisturbed temperature is usually determined either by measuring the temperature in the borehole (with a probe) or by measuring the temperature of the circulated collector fluid before the TRT is initiated.
The undisturbed temperature of the borehole can be affected by e.g. groundwater flow and thermal pollution from buildings, in addition, the undisturbed temperature reflects the deviation of the borehole, which is usually not measured. Here we present temperature profile measurements performed for two separate borehole fields. Figure 9 shows undisturbed temperature profiles from 13 boreholes at Vensmoen, in Nordland county, Norway. The boreholes were drilled on two parallel lines; about half of the boreholes, forming one of the lines, were drilled with a deviation, while the rest of the boreholes were drilled vertically. Temperature measurements were performed 5 days after the last borehole was completed. In this case, vertical circulation of groundwater and borehole deviation is thought to be the main cause of the variations in undisturbed temperature. Most of the boreholes stopped at about 165 m to 190 m due to high groundwater yields. Excluding the test borehole which had an average temperature of 4.8°C, the average temperature of the boreholes (in the depth range 20 m to 150 m) is between 5.08°C and 6.31°C with an arithmetic average of 5.81°C.

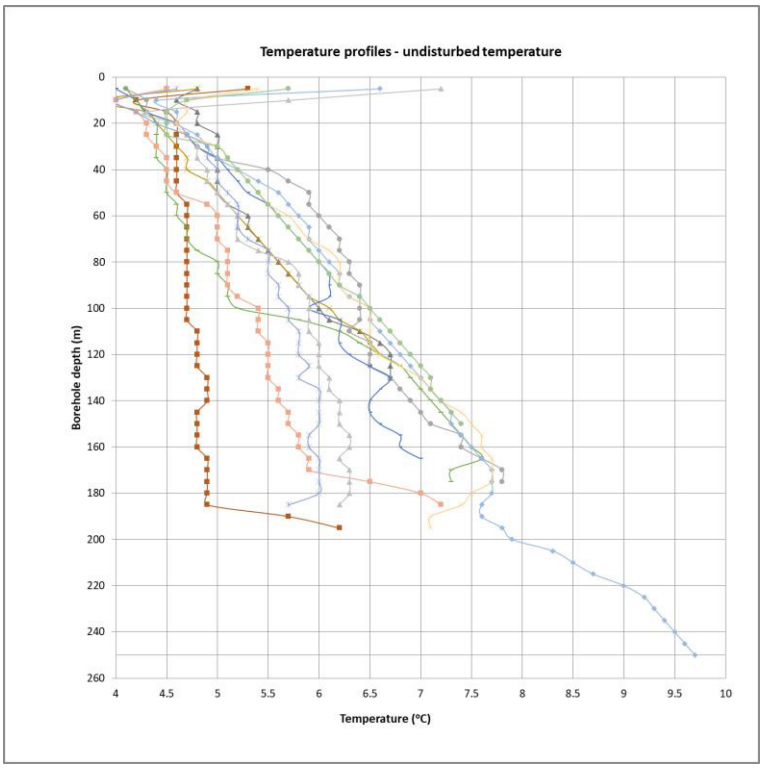

Figure 9. Undisturbed temperatures measured in 13 neighboring boreholes at Vensmoen, Nordland county, Norway.

The undisturbed temperature profiles measured from 18 neighboring boreholes at Revetal in Norway are shown in figure 10. The boreholes were drilled through several fracture zones, causing minor collapse in 8 of the boreholes. The boreholes had a well yield ranging between 30 000 l h^{-1} to 50 000 l h^{-1} and hydraulic connection was observed between about half of the boreholes. Due to high groundwater yields, most of the boreholes did not reach the target depth of 250 m. The temperature profiles were measured with a 10 m interval and the measurements were performed 5 days after the last borehole was completed. There are no direct signs of vertical groundwater flow in the boreholes but most of the boreholes intersected a large number of fractures and zones with fractured rock. The average temperature of the boreholes (in the depth range 10 m to 180 m) is between 9.07 °C and 10.57 °C with an arithmetic average of 9.62 °C. Although the boreholes were drilled on three lines parallel to an existing building, there are no obvious signs of thermal pollution in the temperature profiles. Though uncertain, the variation in temperature is more likely caused by a combination of groundwater flow and borehole deviation.

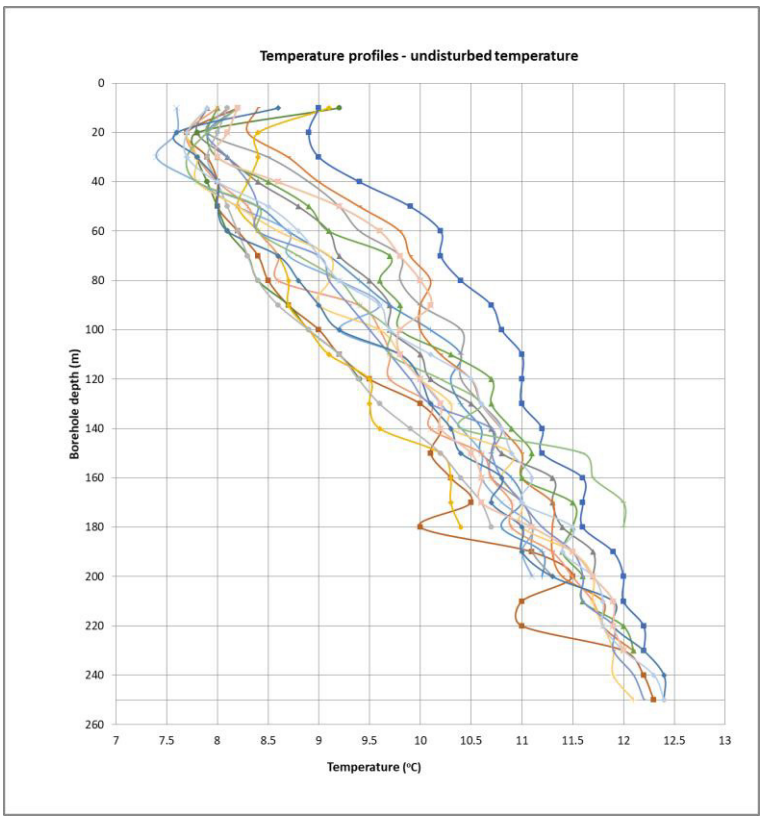

Figure 10. Undisturbed temperature profiles measured in 18 neighboring boreholes, Revetal, Vestfold county, Norway.

As seen in figure 9 and figure 10, the undisturbed temperature can vary significantly within neighboring boreholes. Therefore, the undisturbed temperature obtained either from circulation of collector fluid or from a single temperature profile, might in some cases not be representative for the undisturbed temperature of the borehole field. The temperature profile does, however, provide valuable information about e.g. groundwater flow and thermal pollution that can be used to estimate how representative the measured undisturbed temperature is. Temperature profile measurements can thereafter be performed during the progress of the project to validate that the determined undisturbed temperature is representative for the borehole field. By routinely measuring the undisturbed temperature profiles of all boreholes in a GSHP installation, it is possible to document that the installation is correctly sized.

DISCUSSION & CONCLUSIONS

Temperature profile measurements can be very useful for the planning of a TRT, the analysis of the test result, and finally, the sizing of the GSHP installation. By using temperature profiles actively to select suitable boreholes for TRTs, the risk for tests that are influenced by groundwater flow can be reduced.

As shown in the present paper and as also stated in Heiko et al. 2011, the temperature profiles measured before and after a TRT are an important supplement to the data required for sizing of a GSHP system. For each TRT, the plausibility of the calculated effective thermal conductivity has to be judged based on observations from the drillers log, the geology at the site (as determined on site or mapped by the geological survey), the test data from the TRT and the temperature profiles (preferably from both before and after the test).

Having a temperature profile that indicates conductive heat transfer both before and after the TRT is performed, is a good indicator that the results from the TRT are reliable.

It is shown that the undisturbed temperature can vary between neighboring boreholes. The cause of these variations is uncertain, but can be related to e.g. groundwater flow and borehole deviation. Temperature variations can also be caused by thermal pollution from buildings. The undisturbed temperature from one single borehole might in some cases not be representative for the borehole field.

While being far less detailed than e.g. DTS measurements (Acuna 2013) and in some cases less accurate due to the manual measurements procedure, which is prone to be affected by the operator, the big advantages of the temperature profile measurements are that they are cheap and easy. In many cases and due to minimal financial resources, these simple temperature profile measurements will be the only documentation for the undisturbed and "start-temperature" of the boreholes and the surrounding bedrock.

By routinely measuring the undisturbed temperature profiles of all boreholes in a GSHP installation, it is possible to document that the installation is correctly sized. This also makes the follow up of the GSHP in operation easier.

The strength of the method is the amount of data generated by the measurements. This contributes to a better understanding of the thermal behavior of the ground and the importance of groundwater flow in water bearing fractures in crystalline bedrock.

Further improvements would be to complement the temperature profiles with measurements of the borehole deviation or at least the borehole depth e.g. using a pressure sensor as in Raymond et al. 2016. For more complex GSHP installations with heating and cooling, the DTS measurements are recommended. DTS measurements will give a more detailed understanding of the heat production and behavior along the borehole profile, the influence of groundwater flow included.

ACKNOWLEDGMENTS

Temperature profile measurements have been made available through cooperation with:
Østlandet Brønn og Energiboring AS, Båsum Boring Trøndelag AS and Brustugun Brønnboring AS

REFERENCES

Acuña. J. (2013) Distributed thermal response tests – New insights on U-pipe and Coaxial heat exchangers in groundwater –filled boreholes. Jose Acuña. Doctoral thesis KTH, Sweden.

Gehlin. S. (2002) Thermal response test – Method development and evaluation. Doctoral thesis, Luleå University of Technology.

Gehlin. S., G. Hellström., B. Nordell. (2003) Influence on thermal response test by thermosiphon effect. Renewable energy v 28 nr 14.

Liebel. Heiko T., K. Huber., B. S. Frengstad., R. K. Ramstad., B. Brattli. (2011) Temperature footprint of a thermal response test can help to reveal thermogeological information. Norges geologiske undersøkelse Bulletin, 451, pp 20-31.

Liebel. Heiko T. (2012) Influence of Groundwater on Measurements of Thermal Properties in Fractured Aquifers. Doctoral thesis NTNU, Norway.

Randi. K. Ramstad., K. Midttømme., H.T. Liebel., B.S.Frengstad., B.Willemoes-Wissing. (2014) Thermal conductivity map of the Oslo region based on thermal diffusivity measurements of rock core samples. Bull Eng Geol Environ 2014.

Raymond. J., L. Lamarche., M. Malo. (2016) Extending thermal response test assessments with inverse numerical modeling of temperature profiles measured in ground heat exchangers. Renewable Energy v. 99, page 614-621.

Riktlinjer för termisk responstest (TRT) – Svenskt Geoenergicentrum 2015, http://media.geoenergicentrum.se/2015/11/0_Riktlinjer-f%C3%B6r-Termisk-Responstest_2015.pdf

Sanner. Burkhard.,G. Hellström., J.D.Spitler., S.Gelin. (2013) More than 15 years of mobile thermal response test- a summary of experiences and prospects. Proceedings EGC 2013.

Sanner. Burkhard., E. Mands., M. Sauer., E. Grundmann. (2007) Technology, development status, and routine application of thermal response tests. Proceedings European Geothermal Congress 2007.

Signorelli. S.(2004) Geoscientific investigations for the use of shallow low-enthalpy systems. Dissertation ETH No. 15519.

Signorelli. S., S. Bassetti., D. Pahud., T. Kohl. (2007) Numerical evaluation of thermal response tests. Geothermics, Volume 36, Issue 2, page 141-166.

IGSHPA SWEDEN 2018 Research Conference

DOI: 10.22488/okstate.18.000012

A Randomly Fractal Approach to Calculate the Thermal Conductivity of Moist Soil

Shanshan Cai* **Boxiong Zhang** **Tengfei Cui** **Haijin Guo** **Ting Huang**

ABSTRACT

Ground coupled heat pump (GCHP) is an energy saving technology that uses the shallow geothermal energy for the building heating and refrigeration systems. An optimized design of ground heat exchangers (GHEs) is the key to minimize the installation fee of GCHP systems. The effective thermal conductivity of soil is an important input parameter in the design of GHEs. This paper proposed a randomly fractal approach to predict the effective thermal conductivity of soil-like materials (quartz sand). The fractal Monte-Carlo method combined with the Quartet Structure Generation Set (QSGS) method was used to reconstruct the random structure of the soil-like materials. Lattice Boltzmann method (LBM) was further applied to the complicated porous structure and compute the effective thermal conductivity. The simulation results were compared to the findings from experiments and other similar models. The impacts of porosity, fractal dimension, size ratio and accumulation structure on the effective thermal conductivity were also analyzed in detail.

INTRODUCTION

Ground coupled heat pump (GCHPs) system is an energy saving technology that utilizes the ground as a steady heating or cooling source. The ground heat exchangers (GHEs) are the key components of GCHPs with high installation fee. A proper design of the GHEs would efficiently improve the performance and decrease the overall cost of the entire system. During the design stage of GHEs, the effective thermal conductivity of soil is an important input parameter to predict the heat transfer between boreholes and the ambient soil. From current literature, the effective thermal conductivity are mainly derived from four types of methods, which are field-testing, empirical correlations [3-5], theoretical modeling [6, 7] and geostatistical simulation. In most GSHP design tools, the effective thermal conductivity are either directly input by considering the findings from field-testing or calculated from empirical correlations with porosity and moisture content. However, from field-testing, it is observed that the measured effective thermal conductivity of moist soil varies differently even at the same location and the neglect of such variations might lead to inappropriate designs; from modelling, most of the models highly depend on the empirical coefficients and other fictitious parameters without physical meanings. A more general form is preferred to

Shanshan Cai (shanshc@hust.edu.cn) is an assistant professor of Energy and Power Engineering in Huazhong University of Science and Technology.

better predict the variations of the effective thermal conductivity or the heat transfer in the moist soil.

Porosity, thermal conductivity of different phases, size distribution and the pack geometry are some structure related parameters and may affect the effective thermal conductivity of soil-like materials (soil, sand and clay etc.) [1, 2], but such impacts are barely considered in the estimation of the effective thermal conductivity. Experimental and modelling study on the impacts of these structure related parameters would help improve the prediction accuracy of heat transfer belowground. Fractal theory provide a possible way to correlate these structure related parameters [8] with the effective thermal conductivity in porous medium. The fractal models of Sierpinski carpets and sponges are the most simple forms to include structure related parameters during heat transfer analysis [9]. A more realistic structure of soil is required to further investigate the impacts of structural parameters on the effective thermal conductivity of soil. One possible reconstruction technique is to combine the fractal theory with random reconstruction methods, such as Monte-Carlo method [10, 11]. Due to the complex geometries in the realistic structure, it would be difficult to solve the heat and mass transfer by the normally used finite volume or finite element methods. Lattice Boltzmann method (LBM) is a promising mesoscopic method to deal with complex boundaries and has been successfully applied in numerous studies [12-15] of heat and mass transfer in soil-like materials.

Therefore, in this study, a more realistic structure of soil-like materials would be reconstructed by a combined method of MC (Monte-Carlo) [10] and QSGS (Quartet Structure Generation Set) [16], and the effective thermal conductivity of the reconstructed moist soil-like materials would be calculated by LBM algorithm. The factors that would affect the thermal conductivity are analyzed in detail.

NUMERICAL METHOD

Basic concepts

Water film: water accumulates as a layer and covers the exterior surface of the particle, see Figure 1a.

Water bridge: water accumulate locally and form a connection between two particles, see Figure 1a.

Thermal bridge: preferential thermal path with low thermal resistance, see Figure 1a.

Fractal dimension: a characteristic parameter in fractal theory; in this study, it represents the mass proportion of particles in small size, see Figure 1b and c.

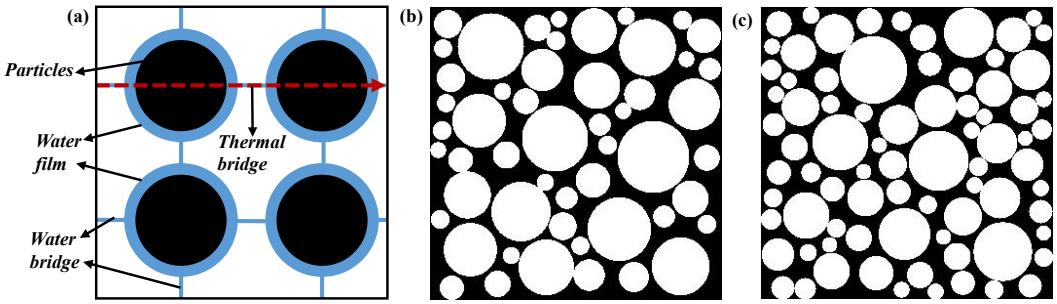

Figure 1. Schematics of (a): water film, water bridge and thermal bridge; (b) and (c): reconstructed soil-like materials when the fractal dimension is 1.1 and 1.7 with the same size ratio and porosity (black - air, white - solids)

Governing equations

In the following analysis, it is assumed that: i) the thermal conductivity of solid is constant; ii) the convective and radiative heat transfer is neglected due to the porous geometry and the low temperature; iii) there are no internal heat sources or body forces; iv) there is no phase change phenomenon; v) heat transfer is two-dimensional. The governing equations are shown in Equations (1) to (3) [16]. The effective thermal conductivity could be calculated by Equation (4).

$$\left(\rho C_p\right)_{a/s/w}\left(\frac{\partial T}{\partial t}\right) = k_{a/s/w}\nabla^2 T \quad (1)$$

$$T_{a,int} = T_{s,int} = T_{w,int} \quad (2)$$

$$k_a \left.\frac{\partial T}{\partial t}\right|_{a,int} = k_s \left.\frac{\partial T}{\partial t}\right|_{s,int} = k_w \left.\frac{\partial T}{\partial t}\right|_{w,int} \quad (3)$$

$$k_{eff} = \frac{L \cdot \int q \ dA}{\Delta T \cdot \int dA} \quad (4)$$

Reconstruction method

In order to better investigate the impacts of structures on the effective thermal conductivity of moist samples, the geometries are reconstructed by a combined methods of MC (Monte-Carlo) [10] and QSGS (Quartet Structure Generation Set) [16]. MC method is preferred to generate main solid particles in the fractal scale (Equation (5), where λ_i is the radius of the i_{th} particles, R_i is the i_{th} random number ranged from 0 to 1) [8], while QSGS method is added to generate the remains, so the geometries could be more connective (Figure 2b). The reconstruction procedure is summarized in Figure 2a. The generation of water phase would follow the formation of water bridges (when the degree of saturation is lower than 30% [17]) and water films, as shown in Figure 2c, d and e.

$$\lambda_i = \frac{\lambda_{min}}{(1-R_i)^{1/D_f}} = \left(\frac{\lambda_{min}}{\lambda_{max}}\right)\frac{\lambda_{max}}{(1-R_i)^{1/D_f}} \quad (5)$$

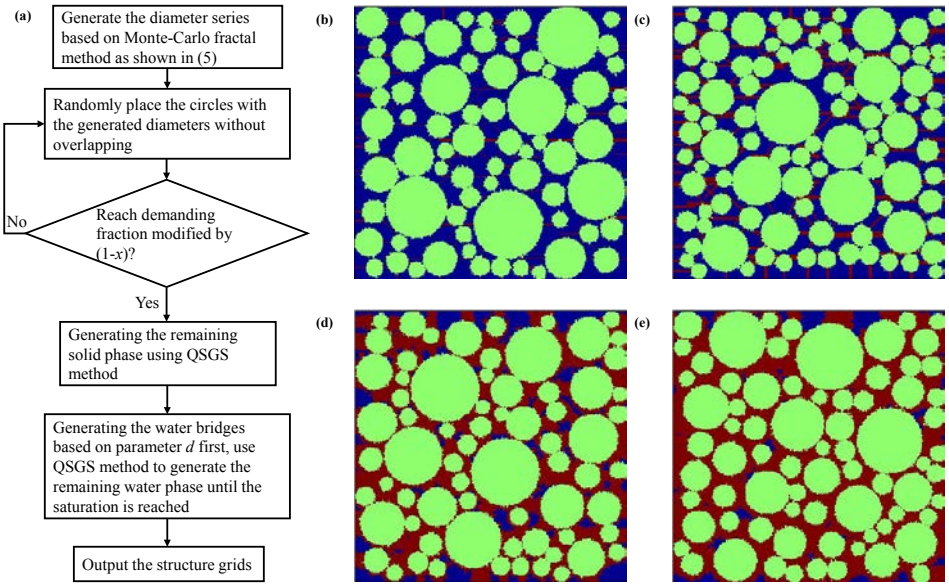

Figure 2. (a) Reconstruction procedures; (b) when the degree of saturation is 0.05; (c) when the degree of saturation is 0.25; (d) when the degree of saturation is 0.5; (e) when the degree of saturation is 0.9 (blue - air, green - solids, red - water)

LBM algorithm

DnQm series are the most commonly used LBM models, and the subscript "n" stands for the dimension of the problem, while the subscript "m" stands for the quantity of the discrete velocities. Due to the relatively large geometry scale of soil-like materials, D2Q5 is selected because of the acceptable accuracy and computation time. Compared to the multiple-relaxation-time (MRT) collision operator (more time consuming) and the single-relaxation-time (SRT) collision operator (less accurate), a twin-relaxation-time (TRT) collision operator is selected because of the accuracy and stability [18, 19]. For conduction problem, the temperature evolution equation with TRT collision operator for D2Q5 could be given in Equation (6) [18].

$$g_i(\vec{r}+\vec{e}_i\delta_t, t+\delta_t) - g_i(\vec{r},t) = -\omega^+\delta_t\left(g_i^+(\vec{r},t) - g_i^{eq+}(\vec{r},t)\right) - \omega^-\delta_t\left(g_i^-(\vec{r},t) - g_i^{eq-}(\vec{r},t)\right) \quad (6)$$

the subscript "i" represents the discrete directions. The equilibrium population function, the symmetric part and anti-symmetric part of the populations including equilibrium populations could be obtained from Equations (7) to (9).

$$g_i^{eq}(\vec{r},t) = \begin{cases} 0, & i=0 \\ T/6, & i=1\sim4 \end{cases} \quad (7)$$

$$g_i^+(\vec{r},t) = \left(g_i(\vec{r},t) + g_j(\vec{r},t)\right)/2 \quad (8)$$

$$g_i^-(\vec{r},t) = \left(g_i(\vec{r},t) + g_j(\vec{r},t)\right)/2 \quad (9)$$

$$1/\omega^-{}_{a/s/w} = 3\,k_{a/s/w}/\left(\left(\rho C_p\right)_{a/s/w}\cdot c^2\delta t\right) + 0.5 \quad (10)$$

where the subscript "j" represents the opposite discrete direction of direction "i". Since energy is conserved in the governing equations, the collision parameter related to the thermal diffusivity is the anti-symmetric one and can be obtained from Equation (10). To assure the temperature and heat flux continuity constrain at interfaces, the volumetric heat capacity (ρC_p) of different phases are assumed to be the same value [20]. c is the lattice constant which equals to δ_x/δ_t, and δ_x is the lattice length step which is commonly set as 1. Once the anti-symmetric collision parameter is determined, the symmetric collision parameter can be computed from Equation (11). The fields of temperature and heat flux can be derived from Equations (12) and (13) [21]. The boundary conditions are specula reflection form for the insulated boundaries and non-equilibrium bounce back form for the isothermal boundaries [22].

$$\Lambda = \left(\frac{1}{\omega^+_{a/s/w}} - 0.5\right)\left(\frac{1}{\omega^-_{a/s/w}} - 0.5\right) \quad (11)$$

$$T(\vec{r},t) = \sum_i g_i(\vec{r},t) \quad (12)$$

$$Q(\vec{r},t) = \sum_i \left(\vec{e}_i g_i(\vec{r},t)\right)\cdot\left(1 - 0.5\omega^-_{a/s/w}\right) \quad (13)$$

$$\vec{e_i} = \begin{cases} (0,0), i=0 \\ (\cos\theta_i, \sin\theta_i)c, \theta_i = (i-1)\pi/2 \end{cases}, i=1\sim4 \quad (14)$$

where Λ is a magic parameter [18]; it affects the stability and the accuracy of the calculation and this magic parameter is assigned 1/6 in this study [23]. $Q(\vec{r},t)$ is the heat flux vector and $\vec{e_i}$ is the discrete velocity of the i_{th} direction and is given in Equation (14).

MODEL VALIDATION

The proposed LBM model is validated by two basic two-phase (air-solid) conjugate heat transfer models (named the series and the parallel models). The thermal conductivity of air (k_1) is set as 0.026W/m-K and the higher

thermal conductivity of solid (k_2) is set as a multiple of k_1. The size of the grids is 200 by 200. The collision parameter of air phase, which is correlated to the thermal diffusivity, is assigned 1.2 based on the comparison with the theory results and this value remains constant in this study. The comparisons between analytical and numerical results derived from the D2Q5 model combined with TRT collision operator are shown in Table 1. It shows that all the relative deviations are lower than 0.5% even when there is a large difference between the values of k_1 and k_2, which is accurate enough for this study. It should be noted that the relative deviations could be further decreased by adjusting the collision parameters.

Table 1. Comparisons between analytical and numerical results

k_1: k_2	Series model			Parallel model		
	Analytical (W/m-K)	Numerical (W/m-K)	Deviations (%)	Analytical (W/m-K)	Numerical (W/m-K)	Deviations (%)
1:5	0.043333	0.043468	0.311831	0.078000	0.078378	0.484423
1:10	0.047273	0.047503	0.487672	0.143000	0.143683	0.477902
1:100	0.051485	0.051736	0.487682	1.313000	1.318126	0.390404
1:1000	0.051948	0.052030	0.157215	13.013000	13.021614	0.100976

RESULTS AND DISCUSSIONS

Comparisons between experimental and simulated results

Quartz sand was selected as the test material and the experimental results of four groups of moist samples (Table 2) were derived by using a thermal conductivity probe. The test procedures followed the standard ASTM D5334-14 and the uncertainty of the thermal probe is $\pm$12% (see the error bars in Figure 3). In order to further investigate the impacts of structural parameters on the thermal conductivity of sand, these four moist samples were varied in porosity, fractal dimension and size ratio. Considering the fact that higher size ratio required less fine grids, grid independency tests was required to minimize the error caused by the accuracy of grids.

Table 2. Structural parameters of four experimental groups

Group No.	Porosity	Fractal Dimension	Size Ratio	Solid Thermal Conductivity
1	0.393	1.7	1:5	1.5W/m-K
2	0.452	1.7	1:5	
3	0.393	1.7	1:23	
4	0.393	1.1	1:23	

The comparisons between the simulation and experimental results with corresponding uncertainty range are indicated in Figure 3. It should be noted that the simulation results were the average values derived from more than 10 randomly reconstructed geometries with the same structural parameters and the experimental results were the average values derived from three locations and three times measurements in each location. From the plot, it was observed that generally the experimental results increased rapidly when the degree of saturation was low (20% in Group 1 and 3,

16% in Group 2 and 32% in Group 4) and then slowed down as the degree of saturation increased. This might be explained by the fact that water bridges among adjacent particles tend to provide preferential thermal paths due to the higher thermal conductivity of solid phase than that of water and air. As the degree of saturation increased, water film started to form and grow, but the impact were less than that of the formally formed thermal path.

Compared to the experimental results, the simulation values indicated similar asymptotic trends. However, the simulation results were 5% to 60% lower than the experimental results and the deviations reached the maximum when the degree of saturation ranged from 10% to 30%. There are four possible reasons to explain such differences. First, the simulated moisture distribution might still be deviated from experimental cases and the regeneration of water distribution should be considered based on the theory of hydromechanics. Second, instead of regular circles, the shape of particles would be random polygon, which could be easier to form water bridges. Third, it was observed that cracks exist in the solid particles of quartz sand, which may lead to a variation on the solid thermal conductivity if water diffuse into the solid particles with small cracks; fourth, when the degree of saturation is low, the heating element in the thermal probe would result in water evaporation and moisture redistribution, which could lead to higher values of test results.

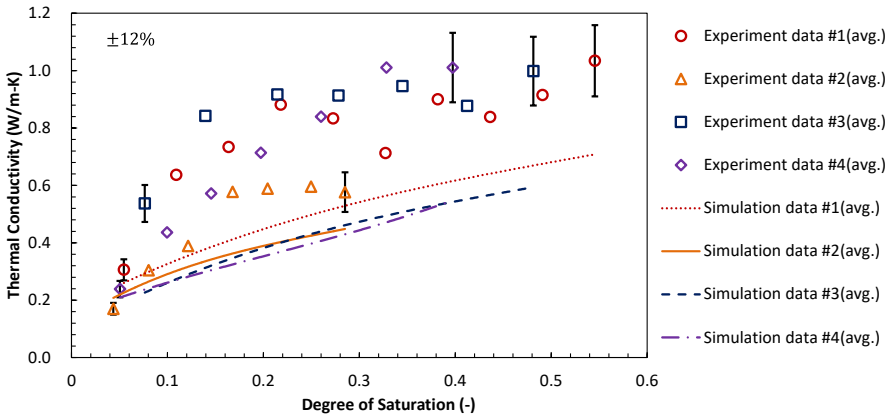

Figure 3. Comparisons between simulation and experimental results with corresponding uncertainty range

Impacts of structural parameters

The impacts of structural parameters on the effective thermal conductivity are indicated in Figure 3. Group 1 and 2 were samples with different porosity. Both experimental and simulated results showed that the values derived in group 1 were always higher than those in group 2 at the same degree of saturation. Therefore, it was verified that porosity would be a dominant factor during the prediction of the effective thermal conductivity of soil-like materials. Group 3 and 4 were samples with different fractal dimensions. Both the experimental and simulated results indicated faster increasing rates in samples with higher fractal dimension (more small size particles). Therefore, the particle size distributions might affect the effective thermal conductivity at low moisture region because it may change the presence of water bridges and would heavily affect thermal path. Group 1 and 3 were samples with different size ratios. The experimental results showed that the thermal conductivity of group 1 were slightly lower than that of

group 3. This was because more conductive thermal bridges were formed among particles with large size differences (small particles filled in the gaps among large particles). However, the simulated values showed opposite conclusion and the thermal conductivity of group 1 were much higher than that of group 3. Such difference might come from the reconstruction stage. The small particles were not only filled in the narrow gaps, but also suspended in the wide space formed among large particles, which deviated from the real cases. Therefore, the impact of size ratio on the effective thermal conductivity still need to be further investigated.

Impact of randomness in accumulation structures

Due to the randomness, the samples would form different accumulation structures even with identical parameters (porosity, fractal dimension and size ratio). Minor differences in the accumulation pattern of particles would vary the effective thermal conductivity of the moist composite. Figure 4 illustrates the uncertainty caused by different accumulation structures. The uncertainty bands were derived from the computation based on more than ten accumulation structures which were randomly generated with identical parameters. It seemed that the uncertainty reached the maximum (ranged from -11.5% to 24.7% based on the average value) when the degree of saturation varied between 20% to 25% and then the uncertainty started to decrease. If all the four groups are considered, then the uncertainty ranges from -25.0% to 40.0%. This was because the variations in accumulation structures would lead to different contact conditions (including both the contact thermal resistance and the formation of water bridges) which might significantly affect heat transfer. The impacts of contact conditions gradually reduced after the fully generation of water bridges. Therefore, the uncertainty bands observed from the plot decreased with the amount of water increased. Quantify the variations caused by the accumulation structures would help explain the results derived from field testing and improve the prediction of ground heat transfer.

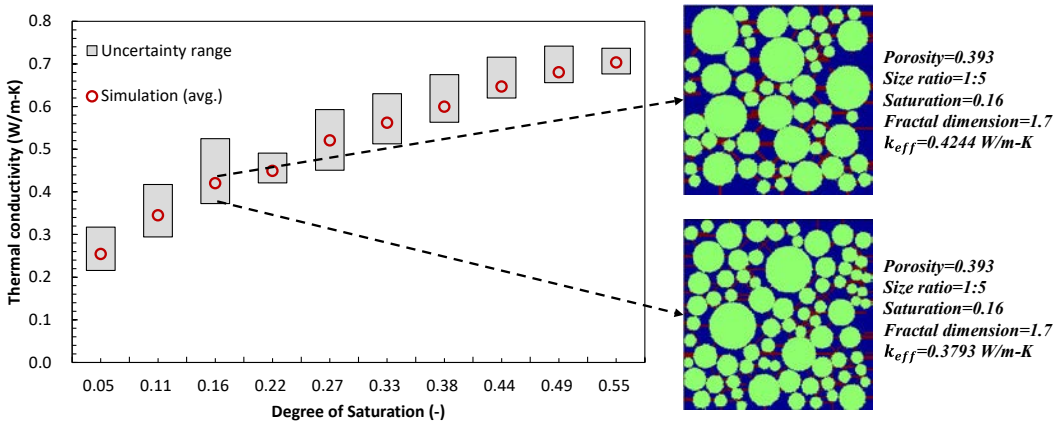

Figure 4. Uncertainty caused by the differences in the accumulation structures

Comparison among similar models

The proposed approach were also compared to other similar prediction models [3, 24] as indicated in Figure 5. The standard deviation is 0.016 for Chen's model, 0.078 for the proposed model and 0.130 for Tong's model.

Considering the entire range, Chen's model matched best with the experimental results: the deviations were within 16% when the degree of saturation is higher than 25%. The deviation reached over 25% in the proposed model and over 30% in Tong's model. However, when the degree of saturation is lower than 6%, Chen's model would overestimate the effective thermal conductivity by 41.8%, Tong's model reached the smallest deviation of 9.1% and the proposed model had a deviation of 16.9%. It should be noted that Chen's model is an empirical correlation, which is highly restricted to the test conditions and materials. The proposed model still require further improvements by including the theory of hydromechanics during the reconstruction of water distributions..

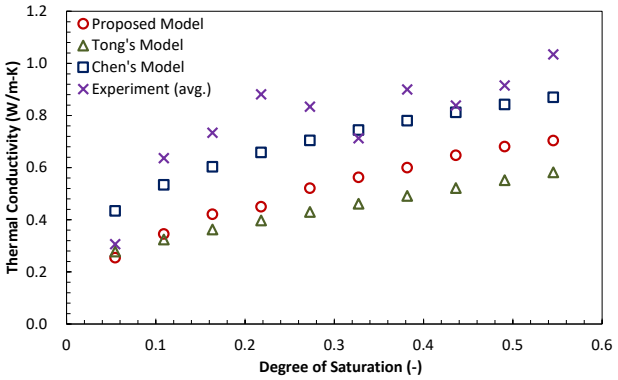

Model	Type	Input Parameters
Chen's model	Empirical model	Porosity, degree of saturation and two empirical parameters
Tong's model	Numerical model	Porosity and degree of saturation
Proposed model	Numerical model	Porosity, fractal dimension, size ratio and degree of saturation

Figure 5. Comparisons among similar models

CONCLUSIONS

This paper proposed a randomly fractal approach to predict the effective thermal conductivity of moist soil-like materials and further investigate the impact parameters. Three main findings are summarized as follows:

(1) Results showed that the proposed model could indicate similar asymptotic trends as the experimental findings, but at lower increasing rates in the low moisture region. Such deviations were possibly caused by the inappropriate moisture distributions reconstructed. Compared to other models, the proposed approach has the potential to reflect more fundamental mechanism of the heat transfer in the soil-like materials with moist.

(2) Porosity is verified as the dominant parameter on the effective thermal conductivity of moist soil-like materials. Fractal dimension would more affect heat transfer in the low moisture region: higher fractal dimension represents samples with more small size particles and behaves more conductive with the same amount of moisture. Size ratio would also affect the thermal conductivity and materials with larger size ratio seem to behave more conductive. However, the effect of size ratio still needs to be further verified.

(3) Randomness in the accumulation structures affect the contact conditions among particles and could lead to uncertainties varying from -25.0% to 40.0% of the average values. Such uncertainty bands were observed to reach the maximum with 20% to 25% degree of saturation and then decrease with the amount of water. Quantify the variations caused by the accumulation structures would help explain the results from field testing and improve the prediction of ground heat transfer.

ACKNOWLEDGEMENT

The authors would like to thank and acknowledge Natural Science Foundation Grant No. 51706078 and Hubei Natural Science Foundation Grant No. 2017CFB131 for funding and supporting this work.

NOMENCLATURE

Variables		$\vec{r}$	The location vector	**Superscripts and subscripts**	
A	Heat transfer area	T	Temperature	$+$	symmetric part
c	Lattice constant	t	Time	$-$	anti-symmetric part
D_f	Fractal dimension	**Greek symbols**		eq	equilibrium populations
$\overrightarrow{e_i}$	Discrete velocity	ΔT	Temperature difference over L	a	air
$g_i(\vec{r},t)$	Population function of temperature	δ_t	Time step	s	solid
k	Thermal conductivity	δ_x	Lattice length	w	water
L	Thickness	Λ	Magic parameter	eff	effective parameters
$Q(\vec{r},t)$	Heat flux vector	λ	Particle radius	int	interface
q	Heat flux density	ρC_p	Volumetric heat capacity	max	Maximum value
R	Random number ranged from 0 to 1	ω	The collision parameter	min	Minimum value

REFERENCES:

[1] Y. Dong, J.S. McCartney, N. Lu. Critical Review of Thermal Conductivity Models for Unsaturated Soils. Geotechnical and Geological Engineering, 2 (2015) 207-221.

[2] N. Zhang, Z. Wang. Review of soil thermal conductivity and predictive models. International Journal of Thermal Sciences, (2017) 172-183.

[3] S.X. Chen. Thermal conductivity of sands. Heat and Mass Transfer, 10 (2008) 1241-1246.

[4] V. Balland, P.A. Arp. Modeling soil thermal conductivities over a wide range of conditions. Journal of Environmental Engineering and Science, 6 (2005) 549-558.

[5] Z. Wang, F. Wang, Z. Ma, X. Wang, X. Wu. Research of heat and moisture transfer influence on the characteristics of the ground heat pump exchangers in unsaturated soil. Energy and Buildings, (2016) 140-149.

[6] A. Alrtimi, M. Rouainia, S. Haigh. Thermal conductivity of a sandy soil. Applied Thermal Engineering, (2016) 551-560.

[7] V.R. Tarnawski, W.H. Leong, F. Gori, G.D. Buchan, J. Sundberg. Inter-particle contact heat transfer in soil systems at moderate temperatures. International Journal of Energy Research, 15 (2002) 1345-1358.

[8] A.H. Thompson, A.J. Katz, C.E. Krohn. The microgeometry and transport properties of sedimentary rock. Advances in Physics, 5 (1987) 625-694.

[9] P. Lehmann, M. St Hli, A. Papritz, A. Gygi, H. Flühler. A Fractal Approach to Model Soil Structure and to Calculate Thermal Conductivity of Soils. 3 (2003) 313-332.

[10] B. Yu, M. Zou, Y. Feng. Permeability of fractal porous media by Monte Carlo simulations. International Journal of Heat and Mass Transfer, 13 (2005) 2787-2794.

[11] Y. Ju, J. Zheng, M. Epstein, L. Sudak, J. Wang, X. Zhao. 3D numerical reconstruction of well-connected porous structure of rock using fractal algorithms. Computer Methods in Applied Mechanics and Engineering, (2014) 212-226.

[12] X. Zhang, L.K. Deeks, A. Glyn Bengough, J.W. Crawford, I.M. Young. Determination of soil hydraulic conductivity with the lattice Boltzmann method and soil thin-section technique. Journal of Hydrology, 1-4 (2005) 59-70.

[13] F. Khan, F. Enzmann, M. Kersten, A. Wiegmann, K. Steiner. 3D simulation of the permeability tensor in a soil aggregate on basis of nanotomographic imaging and LBE solver. Journal of Soils and Sediments, 1 (2012) 86-96.

[14] H. Fan, H. Zheng. MRT-LBM-based numerical simulation of seepage flow through fractal fracture networks. Science China Technological Sciences, 12 (2013) 3115-3122.

[15] X. Zhang, J.W. Crawford, I.M. Young. A Lattice Boltzmann model for simulating water flow at pore scale in unsaturated soils. Journal of Hydrology, (2016) 152-160.

[16] M. Wang, J. Wang, N. Pan, S. Chen. Mesoscopic predictions of the effective thermal conductivity for microscale random porous media. Phys Rev E Stat Nonlin Soft Matter Phys, 3 Pt 2 (2007) 36702.

[17] Yu Mingzhi, Fan Xuejing, Hu Aijuan. Experimental study and mechanism analysis of liquid morphologies in particle packing porous medium[J]. CIESC Journal, 2015,66(7):2450-2455.

[18] I. Ginzburg, F. Verhaeghe, D. D'Humieres. Two-relaxation-time Lattice Boltzmann scheme: about parametrization, velocity, pressure and mixed boundary conditions. Communications in Computational Physics, 2 (2008) 427-478.

[19] I. Ginzburg, F. Verhaeghe, D. D'Humieres. Study of Simple Hydrodynamic Solutions with the Two-Relaxation-Times Lattice Boltzmann Scheme. Communications in Computational Physics, 3 (2008) 519-581.

[20] X. Chen, P. Han. A note on the solution of conjugate heat transfer problems using SIMPLE-like algorithms. International Journal of Heat and Fluid Flow, 4 (2000) 463-467.

[21] A. D'Orazio, M. Corcione, G.P. Celata. Application to natural convection enclosed flows of a lattice Boltzmann BGK model coupled with a general purpose thermal boundary condition. International Journal of Thermal Sciences, 6 (2004) 575-586.

[22] Q. Zou, X. He. On pressure and velocity flow boundary conditions for the lattice Boltzmann BGK model. Physics of Fluids, 6 (1997) 1591-1598.

[23] T. Krüger, H. Kusumaatmaja, A. Kuzmin, O. Shardt, G. Silva, E.M. Viggen. The Lattice Boltzmann Method: Principles and Practice. Switzerland: Springer International Publishing, 2017.

[24] F. Tong, L. Jing, R.W. Zimmerman. An effective thermal conductivity model of geological porous media for coupled thermo-hydro-mechanical systems with multiphase flow. International Journal of Rock Mechanics and Mining Sciences, 8 (2009) 1358-1369.

IGSHPA SWEDEN
2018 Research Conference

DOI: 10.22488/okstate.18.000037

Development of a thermal conductivity map of Stockholm

Malin Malmberg
Erwan Gloaguen
José Acuña
Jasmin Raymond
Claes Mellqvist
Lorenzo Perozzi
Gerhard Schwarz

ABSTRACT

New methods have been suggested to spatially extend in situ thermal response test (TRT) assessments based on geostatistical analysis. These methods can be used to determine a stochastic distribution of the subsurface thermal conductivity beyond the test borehole on larger scales by interpolating the data with geostatistics, including sequential Gaussian simulations (SGS) used in the present study. This paper presents a simulated thermal conductivity map for Greater Stockholm in Sweden, based on the SGS method with input data from in situ measurements (TRT and DTRT). The geology of Stockholm is used as a background raster in the simulations, based on bedrock maps from the Geological Survey of Sweden (SGU). The resulting maps are compared with a point map of punctual ground thermal conductivity of Greater Stockholm earlier derived by SGU, compiled from laboratory data that were obtained by thermal conductivity scanning and modal analysis of surface rock specimens of the area.

INTRODUCTION

All ground source heat pump (GSHP) installations in Sweden deliver together around 15 TWh of heat per year and constitute the third largest renewable energy source in the country. When designing larger GSHP systems, consisting of multiple boreholes, it is today a usual practice to perform an in situ Thermal Response Test (TRT) to assess the thermal conditions of the ground. TRT assessments give, among others, a measure of the effective thermal conductivity of the subsurface. A research group in Japan (Fujii et.al. 2006) suggested a method to improve TRT and measure the thermal conductivity of the rock along the borehole depth using optical fiber cables. The method was further used in Sweden by KTH researchers (Acuña, 2013), within the Effsys2 and Effsys+ research program and was named Distributed Thermal Response Test (DTRT).

Knowing the thermal conductivity allows for a more detailed evaluation of parameters such as the number of boreholes, their depth and the distance between the boreholes, and thereby facilitating to optimize the system. However, TRTs are spatially limited to the location of the borehole with a test radius of about 1 to 2 m (3.3 to 6.6 ft).

The use of geostatistical methods was suggested by Raymond et.al. (2017) with the objective of spatially extending TRT assessments beyond the test borehole on an urban district scale. The method, relying on stochastic simulations, has been performed in Greater Stockholm, Sweden, to map the subsurface thermal conductivity of the region based on the TRT and DTRT measurements from the company Bengt Dahlgren Geoenergi. Similar methodology has been used as for the first application of the method made in the St. Lawrence Lowlands geological provinces of Canada (Lorenzo et. al. 2016; Raymond et.al. 2017), with a few improvements. The bedrock map to be found in the

Malin Malmberg (malin.malmberg@bengtdahlgren.se) is a civil engineer at Bengt Dahlgren Geoenergi, Jasmin Raymond and Erwan Glaugen are proffessors at Institut national de la recherche scientifique, Lorenzo Perozzi is a postdoctoral fellow at Institut national de la recheche scientifique, Claes Mellqvist is geologist and Gerhard Schwarz is a geophysicist at the Geological Survey of Sweden and José Acuña is GSHP specialist at Bengt Dahlgren Geoenergi and researcher at KTH Royal Institute of Technology.

Geological Survey of Sweden (SGU) database (SGU, 2018) is used in the simulations as a background raster to account for the geology of the area. It should be emphasized, as pointed out by Raymond et al. (2017), that the method does not replace TRTs, but it can be an alternative to anticipate TRTs reducing uncertainty in geothermal feasibility studies.

Based on the available TRT and DTRT data measured in situ, the resulting map partly reflects bulk thermal conductivity of the subsurface on the macro scale. A map of the ground thermal conductivity of the Greater Stockholm earlier developed by SGU (Schwarz et al. 2010, Erlström et al. 2016) and an upgraded version (SGU, unpublished) primarily describes the micro-scale. The SGU map was compiled from laboratory data that were obtained by the method of thermal conductivity scanning (TCS: Popov et al. 1999) and modal analysis of surface rock specimen in the area to evaluate mineralogy and calculate thermal conductivity according to the volume faction of minerals. Schwarz et al. (2010) classified the thermal conductivity of the bedrock in five groups, from 2.5 to >4.5 W m^{-1} K^{-1} (1.4 to > 2.6 Btu hr^{-1} ft^{-1} $°F^{-1}$), based on the bedrock map (scale: 1:50 000) of the Stockholm region (Persson et al. 2001).

The map obtained from geostatistical simulations based on in situ thermal conductivity data (macro scale) and the map earlier derived by SGU drawn from TCS and modal data are compared and their features are discussed.

METHODOLOGY

The subsurface thermal conductivity was initially evaluated in situ with TRTs or DTRTs. For this project TRT and DTRT results have been used from ongoing installations in the Stockholm area and being performed by Bengt Dahlgren AB. Fifteen tests (TRT and DTRTs) have been completed by Bengt Dahlgren AB by the time this study was done. These were performed in the Stockholm region and are the ground for the work presented in this paper. All tests have been carried out under controlled conditions with a known and constant water flow and heat injection rate, as recommended by national and international best practices. The power is supplied to the boreholes through the heat carrier fluid circulated in the BHE with a constant flow rate. The effective thermal conductivity of the ground and the borehole resistance was determined from the continuous measurements of the temperature of the circulating fluid at the inlet and outlet of the collector.

The rock thermal conductivity map was achieved with interpolation using sequential Gaussian simulations (SGS: Goovaerts 1997). A Cartesian grid over the study area (527 km^2; 130 224 acres) was initially created to divide the area in 53 000 cells with a cell size of 100 × 100 m (328 × 328 ft). When performing the SGS algorithm, a random path visiting all the cells is created, as illustrated in Figure 1. Cells containing known thermal conductivity data from in situ TRTs are considered static. Along the random path, new cells are selected and assigned interpolated simulated value estimated by simple kriging under Gaussian hypothesis. The simulated values are then used as conditioning data. The map data are complete when all cells have been visited once and the algorithm assures the simulations to be spatially correlated. For one set of input parameters, multiple realizations can be generated by using different random paths and random seeds (Figure 1).

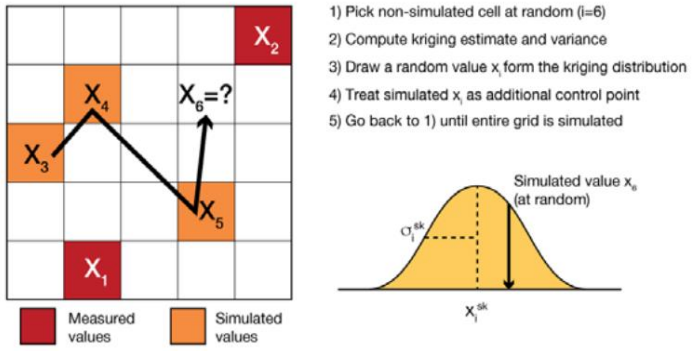

Figure 1 Schematic illustration of the SGS algorithm used to simulate the distribution of host rock thermal conductivity (Perozzi et al. 2016).

The SGS is a variogram based algorithm. The variogram informs about the spatial variability of the studied data and their distance correlation. As a limited amount of static data (in situ TRT assessments) was used for the simulations in this project, it was difficult to calculate the variogram and to know how the data correlates with distance. Hence three different variogram models were used. The three different variogram models (Table 1) have been consequently used to obtain a spectrum of potential variance of the subsurface thermal conductivity in the studied area: ordinary variance, extreme variance and smooth variance. The different variograms were created by changing the range, which corresponds to the maximal distance where a correlation can be observed of the studied variable. The maps can, however, be updated when a relevant amount of new measured data will be collected.

The assumptions made was that Scenario 1, with the "ordinary variance", is the scenario with the highest probability to describe the spatial variability in the area, while Scenario 3, with a very smooth variance has a lower probability as the geology is not expected to be continuous with distance. The different scenarios were hence indirectly weighted by performing a larger number of realizations for Scenario 1 and fewer for Scenario 3. An exponential model and an azimuth angle of 110° (defining an anisotropy ellipsoid) were used in all three scenarios. The azimuth angle was chosen owing to the geological structures observed in the northern part of the studied area (Figure 2).

Table 1. The Three Variogram Models Used for The Geostatistical Simulations

Parameter	Scenario 1 (ordinary variance)	Scenario 2 (extreme variance)	Scenario 3 (smooth variance)
Model	Exponential	Exponential	Exponential
Range 1 [m] (ft)	10 000 (32 808)	5 000 (16 504)	15 000 (49 212)
Range 2 [m] (ft)	6 000 (19 685)	3 000 (9 842)	10 000 (32 808)
Azimuth [degrees]	110	110	110
# of realizations	500	300	200

The bedrock geology in the Stockholm region mainly consists of intrusive granitic rock and a metamorphic metagraywacke of sedimentary origin. Based on the bedrock geology, regions were created dividing the lithologies in the two groups: granitic rocks and metagraywacke (Figure 2). Triangular distributions of the thermal conductivity of granite and metagreywacke were assigned to reproduce the characteristics to the region. The thermal conductivity for granite varies between 2.9-4.2 W m^{-1} K^{-1} (1.7-2.4 Btu hr^{-1} ft^{-1} °F^{-1}) with a mean value of about 3.5 W m^{-1} K^{-1} (2.0 Btu hr^{-1} ft^{-1} °F^{-1}) (Nordell 1994). The thermal conductivity specified for the triangular distribution of the granitic rocks in the area was averaged to a value of 3.5 W m^{-1} K^{-1} (2.0 Btu hr^{-1} ft^{-1} °F^{-1}), assuming a range of 2.0 - 4.5 W m^{-1} K^{-1} (1.2-2.6 Btu hr^{-1} ft^{-1} °F^{-1}). The average for the metagreywacke was taken as 3.0 W m^{-1} K^{-1} (1.7 Btu hr^{-1} ft^{-1} °F^{-1}) with a range of 1.5 - 4.0 W m^{-1} K^{-1} (0.9-2.3 Btu hr^{-1} ft^{-1} °F^{-1}). The simulations were performed within the region with respect to the

triangular distributions. Hence, two simulations were required, one for granitic rocks and one for metagreywacke, which were later merged together. A moving average was calculated as a postsimulation within a 200 m width using spatial filtering to smooth edging effects between the regions (Figure 2; white areas).

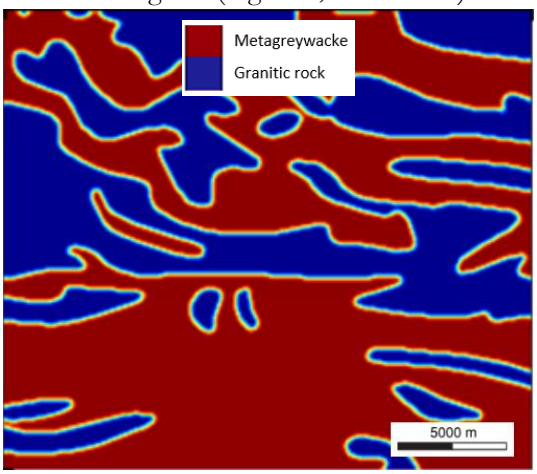

Figure 2 Grouped lithologies, metagraywacke and granitic rocks, used for the SGS in the studied region of Greater Stockholm (21.5 × 24.5 km).

In total, 1 000 realizations were simulated, considering indirect weighting of the three scenarios. Scenario 1, Scenario 2 and Scenario 3 were assigned 500, 300 and 200 realizations, respectively (Table 1). The result obtained is 1 000 equiprobable maps showing the distribution of the host rock thermal conductivity. Based on these, the total mean and total variance was calculated.

Finally, the generated maps were compared to those produced by the Geological Survey of Sweden (SGU). These maps were compiled from laboratory data obtained by thermal conductivity scanning (TCS: Popov et al. 1999) and modal analysis of surface rock specimens of the area.

RESULTS

The geostatistical method described above was used to spatially extend the thermal conductivity of the subsurface host rock in a 527 km² (130 224 acres) area of Greater Stockholm (Figure 3a). The results are shown in 53 000 pixels, each covering 100 × 100 m (328 × 328 ft). One thousand equiprobable realizations have been produced, divided as three scenarios with three different variances. Figure 3b, 3c and 3d show the result of single stochastic realizations of scenarios 1, 2 and 3, respectively. Figure 3e and 3f present the mean and the standard deviation of the 1 000 realizations, respectively. It can be noticed that for all scenarios, and for the mean of the 1 000 realizations, the thermal conductivity is higher in the areas associated to granitic rock, especially in the northern regions. This is due to the bedrock geology which was used as a background raster in the simulations. There is also a higher number of values of high thermal conductivity in the northern areas from the static in situ TRT measurements. Comparing the three single realizations in Figure 3b, 3c and 3d (Scenarios 1, 2 and 3), it can be observed that the result is smoothest for Scenario 3, while the variance is highest for Scenario 2, a result of the different ranges applied for the variograms in each Scenario (Table 1). One single value affects the neighboring cells in the SGS depending on the chosen range for the variogram.

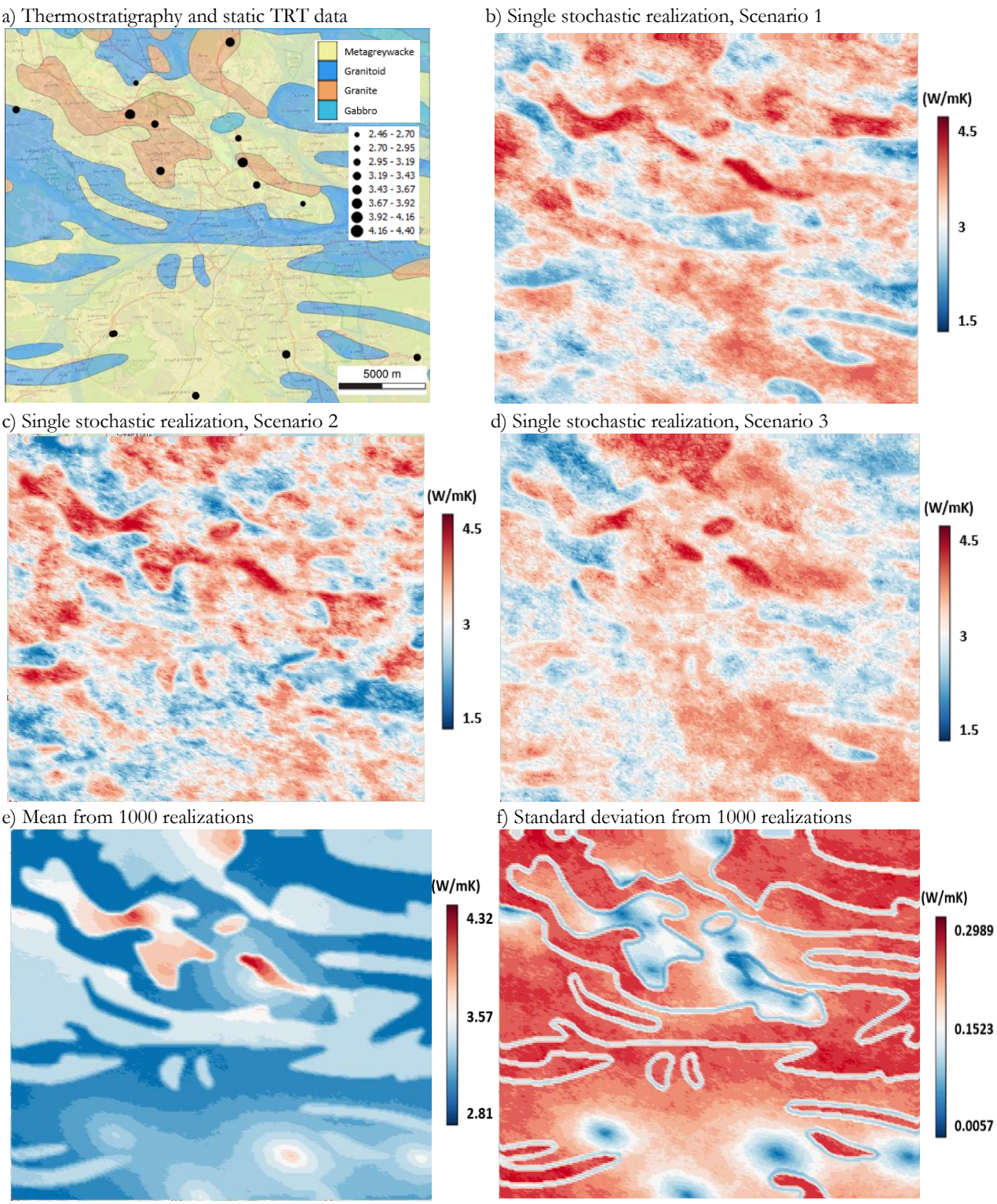

Figure 3 Sequential Gaussian simulations of the bedrock thermal conductivity in Greater Stockholm (21.5 × 24.5 km).

Results of an earlier map developed by SGU (unpublished) is shown in Figure 4. The map was originally prepared for the Greater Stockholm area (2500 km²) but was cropped to the area considered for the geostatistical simulations to allow a direct comparison for this study (527 km²; 130 224 acres). The point map shows data resulting from laboratory TCS evaluation and modal analysis of rock samples. The map includes a classification of the subsurface host rock from 2.4 to ≥4.5 W m^{-1} K^{-1} (1.4 to >2.6 Btu hr^{-1} ft^{-1} °F^{-1}) divided as five groups or thermal subunits. The range of the classes is based on the bedrock map over the Stockholm region showing the mineral distribution in the area (Persson et al. 2001).

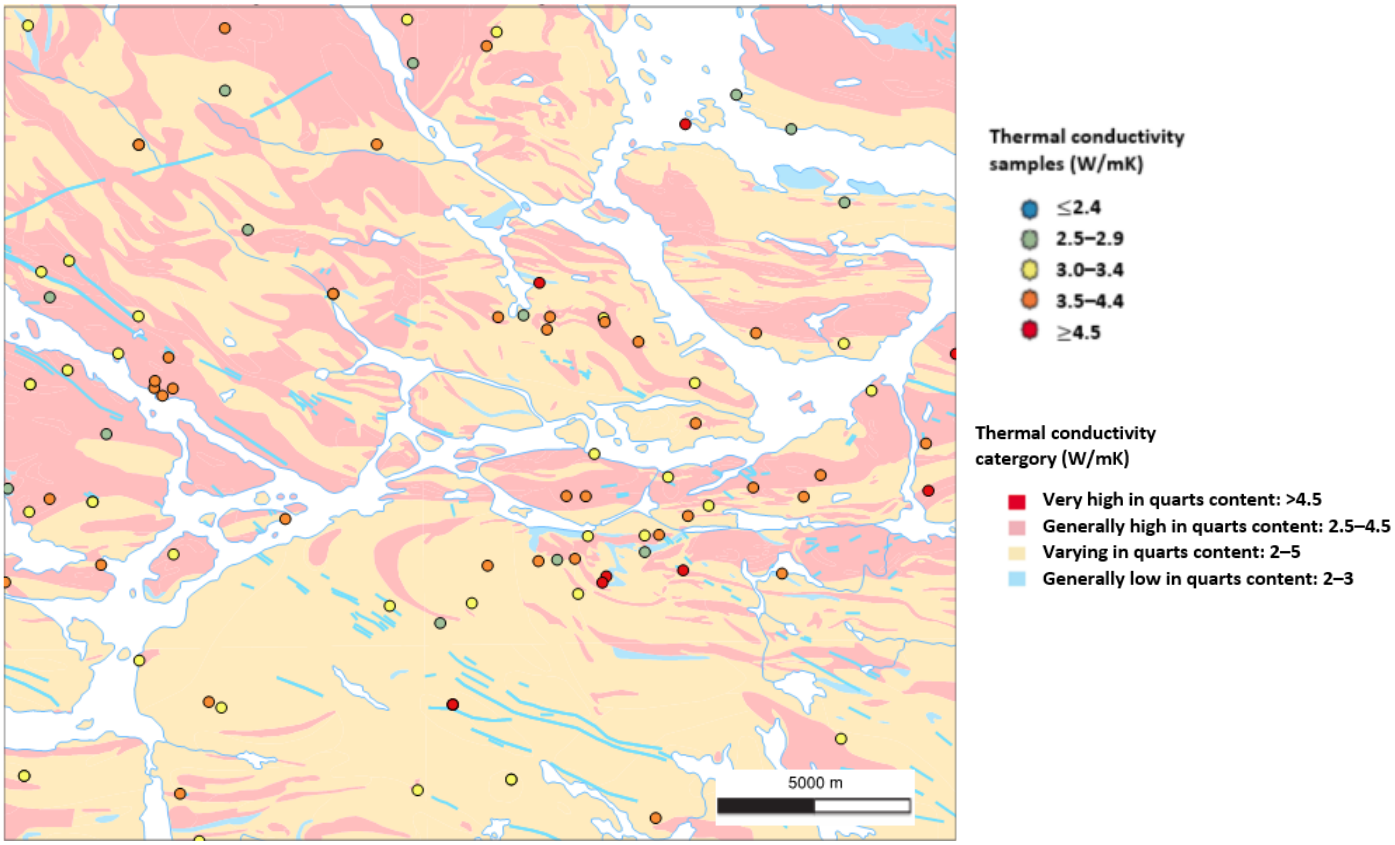

Figure 4 Point map of bedrock thermal conductivity in Greater Stockholm (21.5 × 24.5 km) evaluated from laboratory analysis by SGU (unpublished data) and plotted over thermal conductivity groups based on the geological map of Persson et al. (2001).

DISCUSSION

The resulting geostatistical map from Scenario 1 (Figure 3b), assumed to be the scenario with the highest probability to explain the spatial variance in the area, has been combined with the SGU thermal conductivity point map (Figure 4) to allow comparison (Figure 5). The range for the thermal conductivity differ between the two maps when comparing Figure 4 and Figure 5. This is because the triangular distributions of the thermal conductivity of granite and metagreywacke assigned for the two categories and used for the geostatistical simulations (Figure 5) differ from the geological categories used for the SGU map (Figure 4). Some correlations can be seen, regardless of this factor, when comparing areas with high and low thermal conductivity. Higher values are observed in the north of the map compared to the southern parts.

Factors affecting the field scale mapping with in situ assessments, such as groundwater flow, permeability and structural deformation of the bedrock can influence the resulting thermal conductivity distribution, which was not considered to develop the SGU point map. Results illustrated by the SGU map are micro-scale variations based on thermal conductivity data measured directly on rock samples or calculated from mineral composition determined under the microscope. The SGU data include important information regarding the mineralogy and distribution of different rock types and is based on a large quantity of laboratory analysis available at SGU. In situ TRTs, on the other hand, result in the effective thermal conductivity, which includes the impact of external factors - although TRT analysis is normally performed assuming heat transfer by conduction only. Thereby, a TRT result does not present the thermal conductivity of a specific rock sample but a mean or bulk value including many influencing factors along an entire borehole, though the effective rock volume is limited. Further work has to be done to adequately compare in situ TRTs with laboratory measurements and evaluate the field scale effects that is associated to the maps.

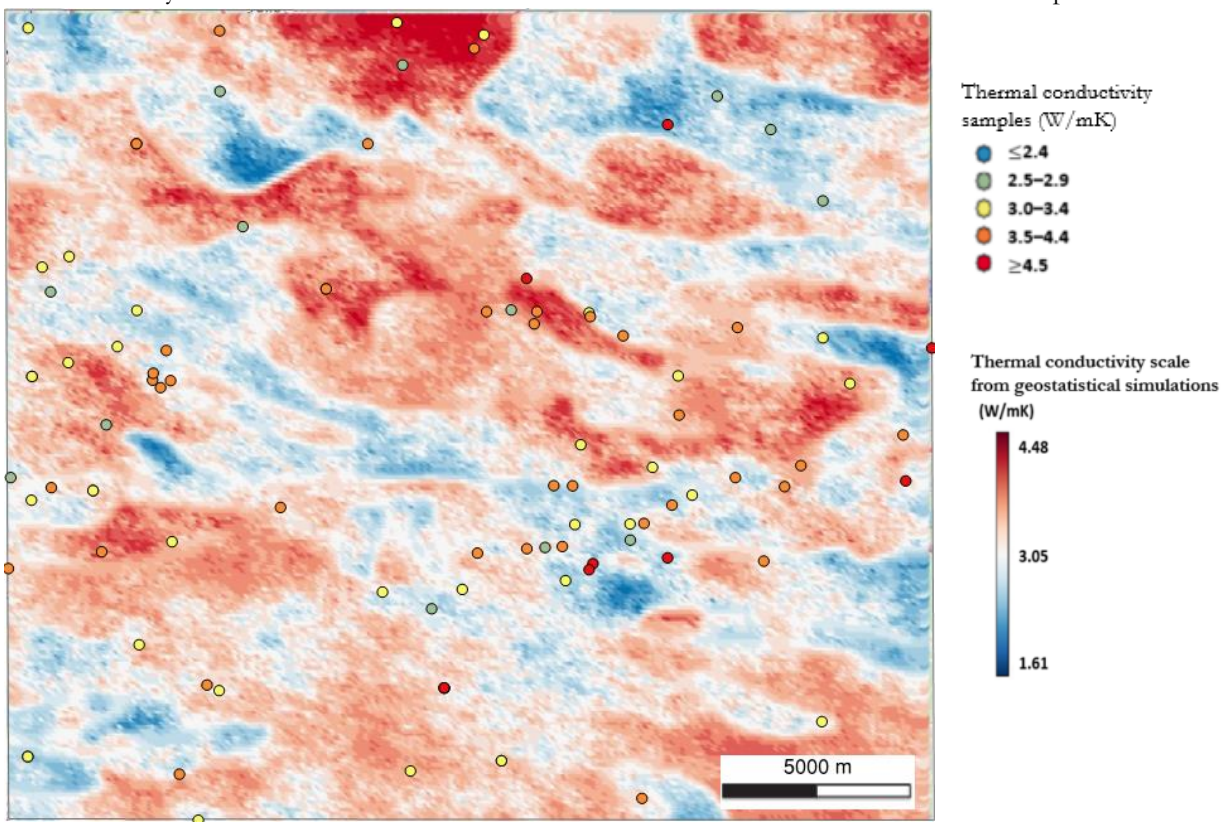

Figure 5 Combined bedrock thermal conductivity map of Greater Stockholm (21.5 × 24.5 km) with superposition of a SGS realization based on in situ TRTs (scenario 1) as transparent on top of the point map derived from SGU laboratory analysis (Schwarz et al. 2010, SGU, unpublished).

CONCLUSIONS

An attempt to map the distribution of subsurface thermal conductivity is presented in this study for the Stockholm region, based on geostatistical simulations using the methodology suggested by Raymond et al. (2017). The proposed method was improved by using the bedrock geological map available from SGU as a background information for the SGS simulations of TRT data. In a separate study, SGU had earlier developed a point map from laboratory analysis of surface rock samples evaluated with TCS and modal analysis over the Greater Stockholm (Schwarz et al. 2010).

In situ TRTs and the analyses of hand specimens are spatially limited to individual boreholes and rock samples, respectively. This is a limitation for the GSHP industry as repeating TRTs or outcropping bedrock accessible for collecting samples are required. Using interpolation methods from geographically unevenly distributed TRTs or hand specimen samples to illustrate variations in the bedrock can help to picture large-scale distribution of thermal conductivity but may not be adequate to identify its local heterogeneities. Thermal conductivity is linked to microscopic variation of mineral content observed in rock specimens, but also to macro effects, like, e.g., the groundwater flowing in the bedrock. Both mapping approach, from geostatistical simulations and modal and TCS analysis, are based on the geology of Stockholm available from SGU. The final projections are thereby considering the different boundaries of the bedrock distribution.

The two map types were derived from different approaches and map scales that could be combined to improve the quality and reliability of the maps. The classification made by SGU for the thermal conductivity for different regions could be used as a background raster for new geostatistical simulations. In addition, an increased number of TCS and modal data would enable calibration of the mineral distribution and additional information could be gained addressing field scale effects of thermal conductivity measurement.

In this paper, three variogram scenarios for thousand realizations obtained from the geostatistical simulations were presented. Some maps could show an equiprobable higher difference in thermal conductivity to the map developed by SGU, while other show a lower difference. Comparing the three different scenarios presented in Figure 3 (b, c and d) changes in the variogram model result in different map variances. An increased number of TRT data could improve the variogram model used for the geostatistical simulations which would increase the reliability of the maps.

Subscripts

DTRT = Distributed thermal response test
GSHP = Ground source heat pump
SGS = Sequential Gaussian Simulation
TCS = Thermal conductivity scanning
TRT = Thermal response test

REFERENCES

Acuña, J. 2013. *Distributed thermal response tests – New insights on U-pipe and Coaxial heat exchangers in groundwater-fi lled boreholes*. KTH Royal Institute of Technology, Division of Applied Thermodynamic and Refrigeration, Stockholm.

Erlström, M., C. Mellqvist, G. Schwarz, M. Gustafsson and P. Dahlqvist. 2016. *Geologisk information för geoenergianläggningar: en översikt*. Sveriges geologiska undersökning, SGU rapport 2016:16, 56 p.

Fujii, H., H. Okubo and R. Itoi. 2006. *Thermal Response Tests Using Optical Fiber Thermometers*. GRC Transactions 30: 545–51.

Geological Survey of Sweden, SGU. 2018. *Berggrund 1:1 miljon*. https://www.sgu.se/produkter/geologiska-data/vara-data-per-amnesomrade/berggrundsgeologiska-data/berggrund-11-miljon/

Goovaerts, P. 1997. *Geostatistics for Natural Resources Evaluation*. New York, USA: Oxford University Press.

Nordell, "Borehole heat store design optimization," Luleå University of Technology, Luleå, 1994.

Perozzi, L., J. Raymond, S. Asselin, E. Gloaguen, M. Malo and C. Bégin. 2016. *Simulation géostatistique de la conductivité thermique: Application à une région de La communauté métropolitaine de Montréal*. Quebec City, Canada: Institut national de la recherche scientifique - Centre Eau Terre Environnement, R1663, http://espace.inrs.ca/3374/1/R001663.pdf.

Persson, L., Sträng, M. & Antal, I. 2001. *Bedrock map 10I Stockholm, scale 1:100 000*. Sveriges geologiska undersökning Ba 60.

Popov, Y.A., Pribnow, D.F.C., Sass, J.H., Williams, C.F. & Burkhardt, H. 1999. *Characterization of rock thermal conductivity by high-resolution optical scanning*. Geothermics 28, 253–276.

Raymond, J., M. Malo, L. Lamarche, L. Perozzi, E. Gloaguen, C. Bégin. 2017. *New methods to spatially extendd thermal response test assessments*. IGSHPA Technical/Research Conference and Expo. Denver, United States: 256-265. March 14-16.

Schwarz, G., Göransson, M., Tunholm, B. & Förster, A. 2010. *Mapping thermal conductivity of the Swedish bedrock*. 29th Nordic Geological Winter Meeting, Oslo. NGF abstracts and proceedings 1, s. 177.

IGSHPA SWEDEN 2018 Research Conference

DOI: 10.22488/okstate.18.000024

Underground thermal energy storage in subarctic climates: a feasibility study conducted in Kuujjuaq (QC, Canada)

Nicolò Giordano **Inès Kanzari** **Mafalda M. Miranda**

Chrystel Dezayes **Jasmin Raymond**

ABSTRACT

Underground thermal energy storage can provide space and water heating and has been used in temperate climates so far. A step forward is to evaluate the efficiency and viability in arctic to subarctic environments, where rather low ground and air temperatures can make the design of such systems difficult. The present contribution describes the design of an underground storage system in Kuujjuaq (Québec, Canada) to heat the drinking water distributed in the town. The system was designed and modeled with TRNSYS and a parametric study was carried out to improve its efficiency based on 5-year simulations. The 20% of the 425 MWh annual demand can be satisfied by a solar collector area of 500 m² coupled to a 10,000 m³ underground storage through two short term tanks. Further improvements could be adopted to reach the target of 50% energy from the underground store.

INTRODUCTION

Kuujjuaq is the regional capital of Nunavik, the Québec territory standing north of 55th parallel. Nunavik inhabitants amount to around 12,300, Kuujjuaq being the most populated village with 2375 people. All the villages rely on fossil fuels to produce both electricity and heat. Power plants fueled by diesel provide electricity with production prices ranging between 0.5 and 1.1 USD/kWh, with Kuujjuaq standing near the average at 0.6 USD/kWh, while in the other parts of Québec on-grid and off-grid production costs about 0.02 and 0.3 USD/kWh, respectively (Hydro-Québec, 2011). Space heating (SH) and domestic hot water (DHW) in Nunavik are commonly achieved autonomously in each building equipped with furnaces. The subsidized cost of diesel in Nunavik was on the order of 1.6 USD/liter in 2015 and a common diesel furnace with 80% efficiency provides space heating with a cost of 0.19 USD/kWh (Belzile et al., 2017). Energy production and utilization appear critical in Nunavik. New developments to cover the energy needs of these communities are needed to diminish the high economic costs and environmental impact, as well as reducing fuel transportation in these hostile and fragile environments up north.

Renewable energy offers an opportunity to use local resources and detailed studies are being carried out in Northern Québec to evaluate the potential of geothermal technologies as a tool to meet the objectives of the action plan for sustainable development and reduce the greenhouse gas emissions (MDDELCC, 2012). The feasibility of exploiting both deep and shallow geothermal resources is being evaluated to provide heat for SH and DHW in Nunavik through enhanced geothermal systems and deep borehole heat exchangers (BHE; Miranda et al., 2018), as well as ground source heat pumps (GSHP) and borehole thermal energy storage systems (BTES). Underground storage systems, further described in this study, are a mature technology (Schmidt et al. 2004; Xu et al., 2014; Cabeza,

Nicolò Giordano (nicolo.giordano@ete.inrs.ca) is a post-doc fellow, Inès Kanzari is a master student, Mafalda M. Miranda is a PhD student and Jasmin Raymond is a Professor: they all work at the Institut national de la recherche scientifique – Centre Eau Terre Environnement (INRS-ETE) in Québec City, Canada. They are also members of the Centre d'études nordiques (CEN). Chrystel Dezayes is a research fellow at the Bureau de Recherches Géologiques et Minières (BRGM) in Orléans, France.

2015; Sibbitt et al., 2012) that can help solar thermal energy to be exploited throughout the whole heating season. Solar fraction (solar energy to total need ratio) can be easily higher than 50% and in some cases it was demonstrated to reach up more than 90% (Flynn and Sirén, 2015; Gao et al., 2015). Despite several demonstrations throughout the world in different climate contexts, to the best of our knowledge, a BTES system has not been tested in subarctic environment yet, where the SH demand is characterized by more than 8000 HDD_{18} as in Kuujjuaq (Governement of Canada, 2018).

The Kativik Regional Government, an administrative authority in Nunavik dealing with northern infrastructure, pointed out the drinking water facility in Kuujjuaq to be an important target for the community to reduce the use of fossil fuels. Currently the water is withdrawn from the Stewart Lake and heated on site by diesel furnaces to prevent freezing along the underground pipeline toward a reservoir building in the village. Here, the water is collected by tanker trucks and hence distributed to each house. A rough estimate shows that the cost of water heating amounts to about 80,000 USD/year (truck diesel consumption excluded). The scope of this contribution is to design a BTES system to partially cover the pumping station's heating needs. Transient simulations with TRNSYS (Klein et al., 2017) have been carried out to optimize the system and anticipate its thermal behavior in the Kuujjuaq climate setting.

GEOGRAPHICAL AND GEOLOGICAL SETTING

Kuujjuaq (58.10°N, -68.42°E) is the main Inuit village in Nunavik among the 14 First Nations communities placed along the coasts of the Ungava peninsula, surrounded by the Hudson Bay (W), the Hudson Strait (N) and the Ungava Bay (E; Fig. 1). Kuujjuaq shows a subarctic climate with average annual air temperature of -5.8 °C and 8520 HDD_{18}. Mean solar radiation from May to September is 4.5 kWh/m²d and mean temperature from October to April is -14 °C (1981-2010 Normals, Governement of Canada, 2018). A temperature increasing trend is nevertheless clear from 1990 (-7 °C) to 2010 (-3.5 °C; Fortier et al., 2011). The presence of discontinuous but widespread permafrost is reported in the region (Allard and Lemay, 2012) and it strongly depends on the local geological conditions (Lemieux et al., 2016).

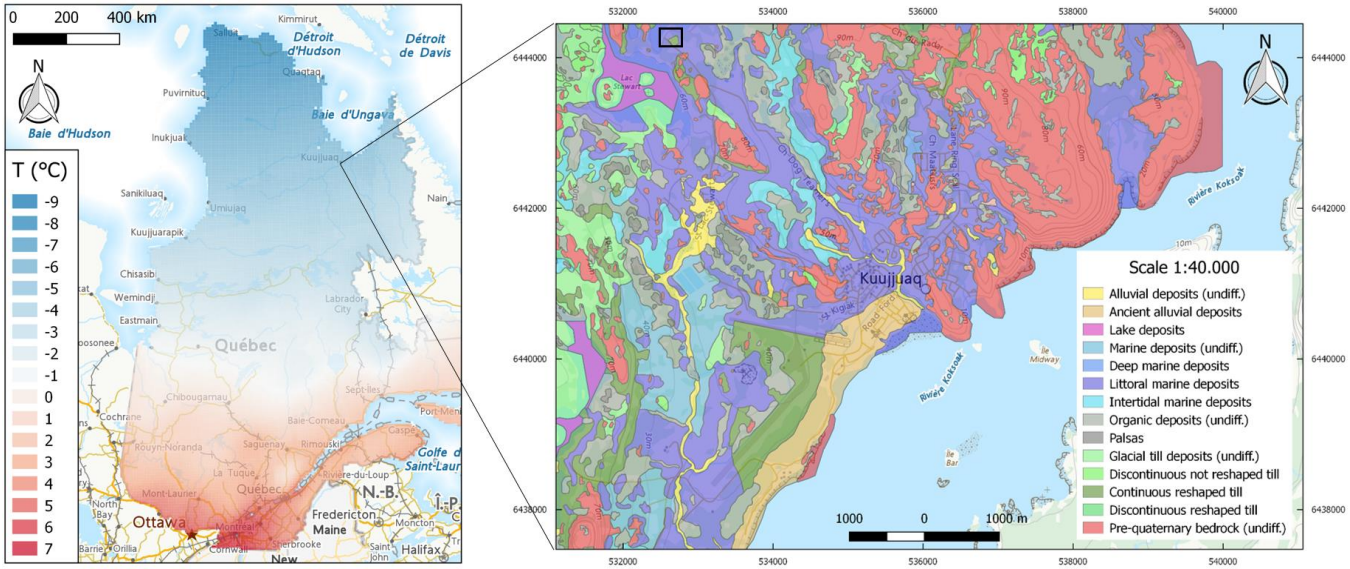

Figure 1 Geographical and geological setting of the examined area (modified from Fortier et al., 2011). The left map shows the average annual air temperature. The black rectangle in the right map highlights the study area. (Coordinate system NAD83/UTM Zone 19N).

The study area is located in the west part of the Southeastern Churchill Province (Simard et al., 2013 and references therein). The quaternary sediments mainly consist of littoral and pre-littoral sediments alternating to intertidal deposits related to different cycles of transgression and regression of the Iberville Sea (Fortier et al., 2011). Glacial till deposits often cover bedrock outcrops and it is common to find them underlying the marine sediments. Alluvial coarse-grained materials are only found along the small streams of two valleys with streams flowing toward the Kosoak River. A field campaign was carried out in Kuujjuaq in the summer 2017. Surveys involved rocks and quaternary sediments samples collection, temperature logs in wells, in situ hydraulic conductivity tests and electrical resistivity tomography (ERT) investigations. A detailed description of these field surveys is reported in Giordano et al. (2017) and Miranda et al. (2018); only the most important results for the aim of this contribution are described here.

The two ERT lines carried out on the site of the pumping station showed saturated marine deposits overlying glacial till sediments on the top of the bedrock (Giordano et al., 2017), whose presence is highlighted south of the examined area (Fig. 1). Local evidence of frozen ground was not identified by the ERT (investigation depth 20 m), even if the groundwater temperature was measured around 1 °C away from surface water bodies. The proximity of the Stewart Lake, the coarse-grained sands and the groundwater advection contribute together to locally prevent freezing in this unit, that is not affected by permafrost. The thermal properties of the quaternary sediments were measured in the lab with a needle probe (Raymond et al., 2017). The saturated marine deposits have a thermal conductivity of 1.5 W/mK and a heat capacity of 3.0 MJ/m^{3}K (Giordano et al., 2017).

The BTES system was therefore designed to be hosted in the saturated marine sediments, providing an optimal storage medium with moderate to low heat transfer characteristics. The local groundwater flow was also investigated during the field activities because it plays a critical role in the evaluation of the heat losses by advection (Diersch et al., 2011; Nguyen et al., 2017). However, it is not presented and developed further on in this paper because it is believed to deserve a detailed analysis beyond the scope of this first study.

MATERIALS AND METHODS

The pumping station at the Stewart Lake withdraws water from the lake all year long and in winter the temperature is almost constant at around 4 °C. Before being pumped in the pipeline at a flow rate of 36 m^3/h, the water is heated up to around 7 °C to prevent freezing during its 4.8 km way down to the village. Currently, the heating system is fed by two diesel boilers with a nominal capacity of 100 kW. It was assumed that the plant works 16 h/d for 7 months (October to April) and thus requires approximately 1525 GJ (425 MWh). The system was designed according to the guidelines of Pahud (2000), that define collector area, short-term and ground storage volumes depending on the heating loads of the final user. According to these guidelines, the annual heat demand of the pumping station can be covered by 2.4 m^2 of solar panels per MWh. The idea presented here is to cover 50% of the demand (210 MWh) and thus around 500 m^2 of total solar surface would be necessary.

The ground storage strongly depends on the thermal and hydraulic properties of the underground. In this perspective, the reference ground storage has been designed having 100 boreholes with a single U-pipe to a depth of 30 m, divided in 20 series of 5 BHE hydraulically connected in parallel, in a cylindrical shape disposition with 3 m spacing (~22,000 m^3, radius 15 m, shape factor (*SF*) equal to 1). Considering heat conduction as the only governing mechanism, an increase of the ground temperature by 10, 20 or 30 °C would allow to store 660, 1320 and 1980 GJ, respectively. To achieve the target of 760 GJ, the plant is expected to raise the temperature of the entire underground storage volume by at least 19, 23 or 29 °C considering a storage efficiency of 60%, 50% or 40%, respectively.

The solar and BTES loops are coupled together through a cylindrical short-term storage tank (STST) and the heat carrier fluid (HCF) consists of a mixture of water and 50% vol. of propylene glycol (minimal working temperature -30 °C) to prevent freezing. The water withdrawn from the lake passes within the STST through a coiled immersed heat exchanger (HX), as proposed by Rad et al. (2017), in order to heat the water in the winter. The last part of the whole system (Fig. 2) consists of a back-up auxiliary diesel boiler (capacity 80 kW) to raise the water temperature up to the target 7 °C, in order to satisfy the remaining 50% of the demand not covered by the BTES.

The system charges the ground from May to September and retrieves the energy from October to April. For simplicity, the water withdrawn from the lake is considered to be at 4 °C all year long and the flow rate of the water distribution network runs 24 h/d per 7 months at 2/3 of the actual flow (24 m³/h). During the charge phase, the solar collectors produce energy that is sent to the underground storage via the STST and the BHEs distribute the heat from the center to the outer zones of the storage volume. In the discharge, thermal energy is extracted from the BTES, with the HCF flowing from outer to inner zones, and transferred to the tank while the solar loop is not working.

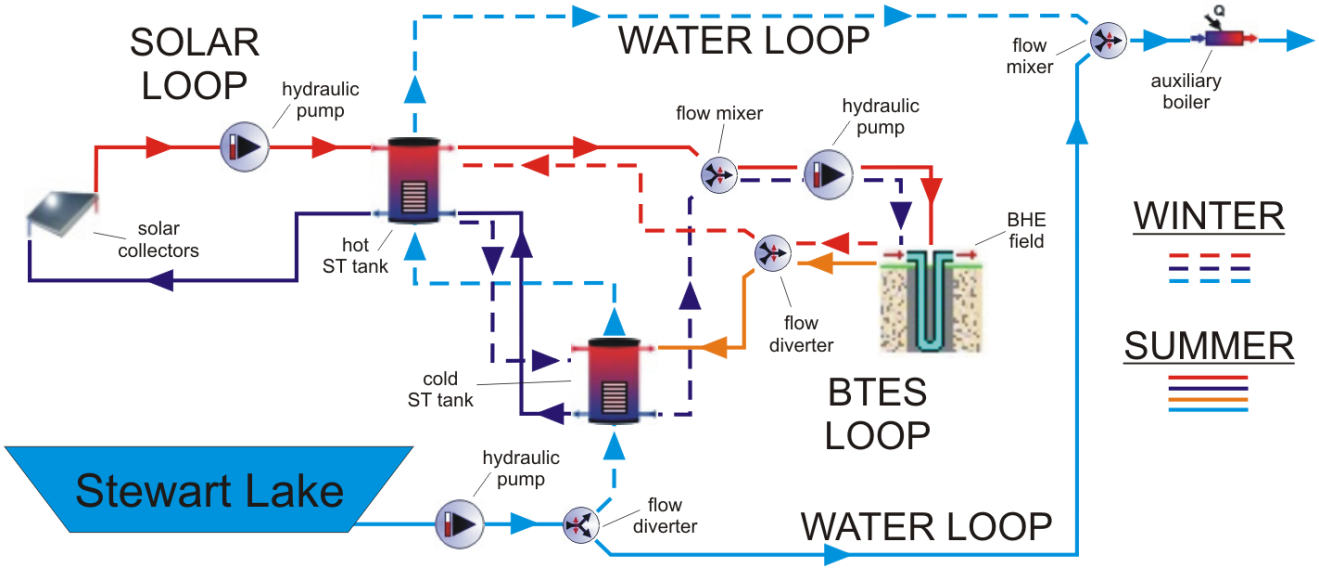

Figure 2 Sketch of the BTES system as designed in scenarios 2 and 3. Light blue color refers to the water loop; red, orange and dark blue gives an idea of the HCF relative temperature throughout the circuit.

TRNSYS MODEL

TRNSYS is a commercial simulation modular environment that allows the transient modeling of complex energy systems (Klein et al., 2017). Several different components (Types) are individually solved by single systems of equations and then coupled together to achieve the final outputs required by the user. The code has been widely adopted to simulate underground thermal energy storage systems in the last 20 years (e.g. Pahud, 2000; Diersch et al., 2011; Sibbitt et al., 2012; Terziotti et al., 2012; Flynn and Sirén, 2015; Rad and Fung, 2016), using the duct ground heat storage (DST) model developed by Hellström (1989) to simulate BHE operation. The DST is a cylindrical shaped storage volume with a vertical symmetry axis where the BHEs are assumed to be uniformly placed. Convective heat transfer in the ducts and conductive heat transfer in the ground are simulated together to output the whole ground temperature, where three different problems are solved numerically with the finite difference method in the ground (global and local temperature) and analytically in the BHE pipes (steady state problem). The total temperature is achieved by the superposition of the three parts as to ensure a fast and accurate simulation tool (Hellström, 1989).

The whole BTES system described in Fig. 2 was implemented in TRNSYS 18. The main Types used are:

- Type 557a is the currently available type to model the ground storage through the DST. Ten radial regions and ten vertical regions were adopted for the finite difference simulation. The boreholes are conventional 152 mm size with single U-pipe (d_0 = 32 mm). A 1-m top insulation layer (λ = 0.05 W/mK) and 0 °C as undisturbed ground temperature were assigned to the model;
- Type 534 was chosen to simulate the STST, a vertical cylindrical storage tank with immersed HX giving the

needed flexibility on the number of inlets and outlets (up to 10), number and type of immersed HX (up to 5) and number of nodes (up to 20) to increase the model complexity and consider water stratification. A 5 m height tank with volume of 100 m^3 was chosen, two inlets and outlets were selected to connect the solar and BTES loops; one coiled heat exchanger (d_i = 50 cm, λ_{HX} = 40 W/mK) hosts the water distribution loop and twenty nodes provide high accuracy to the simulation;

- Type 1b was chosen for the solar panels. It simulates a flat-plate solar collector with quadratic efficiency, a_0 = 0.8, a_1 = 13 kJ/hm^2K and a_2 = 0.05 kJ/hm^2K^2. The total collector area is 500 m^2, divided in 125 series of 4 collectors and specific flow rate of around 50 l/sm^2;
- Type 6 was selected to simulate the auxiliary diesel boiler with a maximum heating power of 80 kW and a target outlet temperature of 7 °C;
- Typical meteorological year (Type 15) from the Kuujjuaq airport weather station was selected to provide crucial input weather data to the solar panels and the storage volume.

Table 1. Features of the different scenarios

	SC1	SC2	SC3	SC4	SC5
Number of ST tanks (-)	1	2	2	2	2
BTES volume (m^3)	22,000	22,000	9500	9500	9500
BHE spacing (m)	3	3	2	2	2
SF (-)	1	1	1.5	1.5	1.5
Use of second ST tank (-)	-	Charge + discharge	Charge + discharge	Discharge	Discharge
Pre-heating period (y)	0	0	0	0	1
Preheating *T* (°C)	-	-	-	-	10

The features described above characterize the base model that was implemented to simulate the dynamic behavior of the system for five years, interchanging charge and discharge phases. A parametric study was then carried out to optimize the system, mainly focusing on the characteristics of the BTES volume and related parameters. Five different scenarios (SC) were created by modifying one parameter at each step (Tab. 1), but keeping the changes made in the previous scenario in order to aim at a performance increase from SC1 to SC5. A second ST tank (same volume) was added in SC2 to improve the stratification and decrease the BTES inlet temperature. SC3 is a case with a higher storage shape factor (1.5 vs. 1.0) while, in SC4, the second tank was used during the discharge phase only. A 1-year preheating period was finally tested in SC 5 to raise the ground temperature by 10 °C.

RESULTS

The simulation results generally show the system to progressively provide more energy to the drinking water network from the first to the fifth year, showing a transient condition before reaching an equilibrium. This is clearly highlighted is terms of temperature at the center of the BTES volume in Fig. 3, where it is evident that the time necessary to reach a steady state between injection and extraction strongly depends on the system's characteristics. The underground temperature in SC 1 rises from 0 °C to about 13-14 °C at the end of the first injection phase. Then, the maximum value increases each year reaching about 22 °C in the fifth, but clearly not being the equilibrium yet. SC3 takes advantage of a smaller volume (less than half of SC1, see Tab. 1) and reaches more than 20 °C already at the end of the first charge year. The maximum in the last year is 3-4 °C higher than SC1, meaning that an equilibrium is almost reached between years four and five. SC5 is almost immediately at a steady state, showing that a 10 °C preheating is sufficient to make the system working properly. It is also clear that SC3 and SC5 tend toward a balanced heat exchange with the underground when compared to SC1, as highlighted by the temperature decrease in the discharge phase that is almost comparable with the increase during the system charge (Fig. 3). This is related to a

smaller subsurface volume involved in heat exchanges, but also to the use of a second tank that, as we discuss later on, enables to extract more energy by keeping the BTES inlet temperature low. The temperature difference between center and edges of the volume is roughly constant throughout the five years of simulation, ranging between 3 and 4 °C at the peak of the charge and 0 and 1 °C (almost no difference) at the end of the discharge for SC3 and SC5. The scenario SC1 shows smaller values in the charge (2 °C) and higher in the discharge (1 °C) owing to a bigger volume involved.

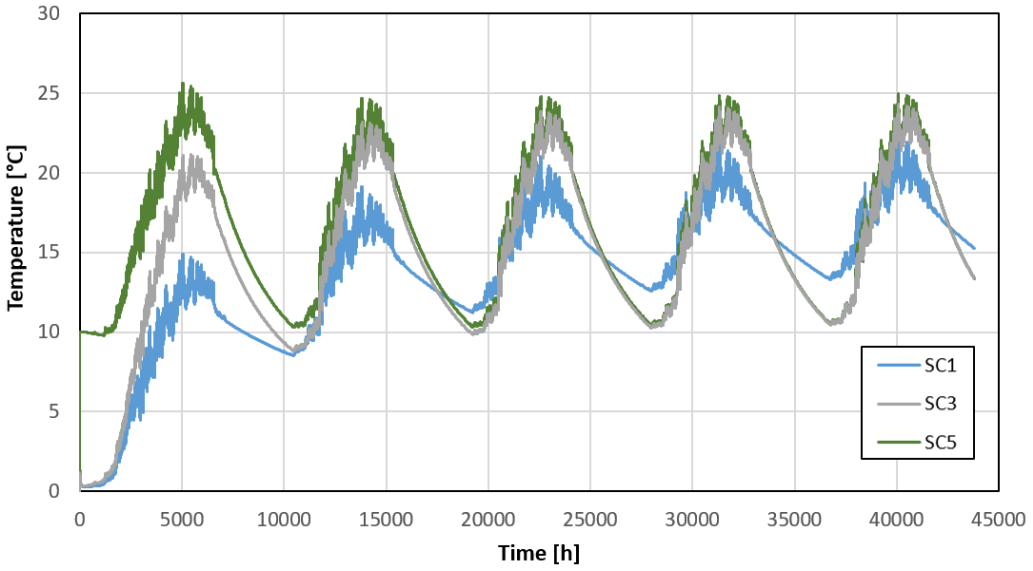

Figure 3 Temperature at the center of the BTES system for 5 years of simulation of scenarios 1, 3 and 5. SC2 and SC4 present trends similar to SC1 and SC3 respectively. They were not added to the graph to make the understanding clearer.

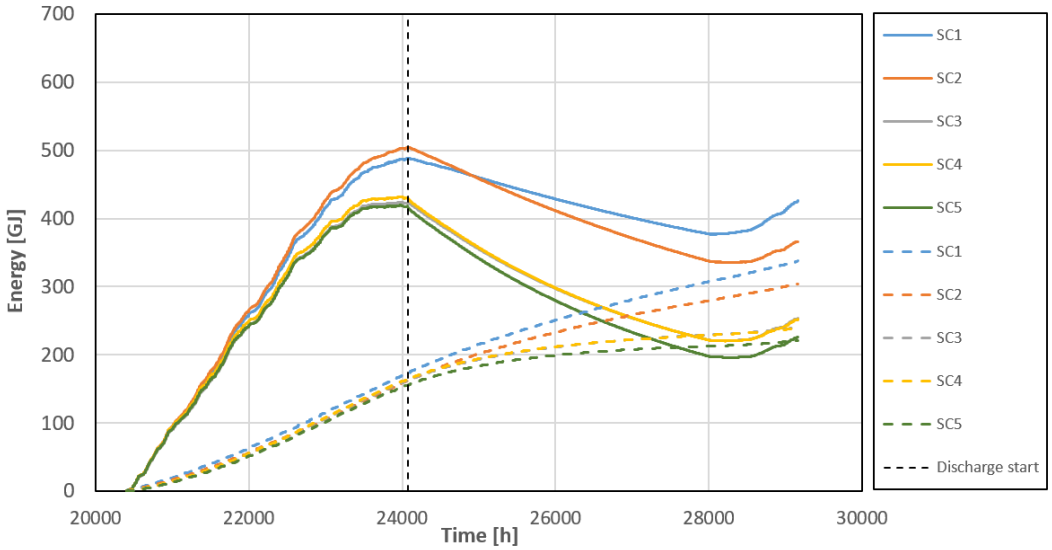

Figure 4 Normalized energy balance for the different scenarios in the third year. Continuous lines indicate the energy injection or extraction while dashed lines indicate the total energy losses.

A comparison among the energy injected and extracted was done by subtracting the value at the beginning of the period under exam as a normalization useful to highlight the differences among the five scenarios (Fig. 4). The systems conceived in SC1 and SC2 are able to inject about 16% and 21% more energy than the others, but they struggle to retrieve that energy in the winter. Indeed, only 22% and 32% of those amounts are recovered at the end of the discharge and almost 380 and 340 GJ each year are not used, making the whole storage systems not exploited at their full capacity. In any case, it is worth noticing that the addition of a second ST tank to the system significantly improves the performance, with SC2 injecting 3% more heat and retrieving 53 GJ more (+50%). This is possible because the second tank manages to keep the BTES inlet temperature 1.5 to 2 °C lower than the case with just one tank (SC1). Another important improvement is achieved by halving the underground storage volume, that is to say by reducing the spacing between the BHEs and thus increasing the *SF*. The storage of SC3 collects less (-17%) and loses more energy than SC2, but it clearly recovers the total amount of net energy available (injected - losses) and generates a valid balance between injection and extraction. Further modifications implemented in SC4 and SC5 do not provide significant better performance, the efficiency of the storage volume being just 5% better in SC5. The idea of using the cold tank only in the winter does not allow to further reduce the BTES inlet temperature: SC3 and SC4 are perfectly superimposed in the discharge period (Fig. 4) and give similar values in Tab. 2. The preheating period that differentiates SC4 and SC5 only helps to reach an earlier equilibrium, but the 1% better recovery highlighted in the third year would not really economically justify the preheating, during which the system would not provide energy. The total heat losses shown in Fig. 4 mostly occur through sides and bottom of the underground storage volume, while losses toward the atmosphere are negligible because of the top insulation layer at low conductivity. It is clear that this trend is similar to all the scenarios during the charge. On the other hand, a marked difference between SC1/SC2 and SC3/SC4/SC5 is observed. Losses are smaller in the first group and similar to those of the charge phase; in the second group, losses keep occurring in the discharge phase but represent less than 20% of the total heat lost. This happens because the storage volume is half that of SC1 and SC2 and the energy can be recovered more easily.

Table 2. Energy balances for the third year of BTES operation

	Underground Charge			Underground Discharge		Total Energy	
	Injected (GJ)	Lost (GJ)	Lost (%)	Extracted (GJ)	Recovered (%)	Aux. boiler (MWh)	BTES (%)
SC1	486	178	36.7	105	21.7	51	11.8
SC2	501	167	33.3	158	31.6	73	16.9
SC3	417	167	39.9	190	45.7	82	19.0
SC4	420	168	40.0	194	46.2	83	19.2
SC5	407	159	39.1	204	50.1	86	20.0

Scenarios 3 to 5 ended up to cover 19 to 20% of the total energy demand necessary to heat up the water at the pumping station (Tab. 2), providing 61 to 68% more energy with respect to the base case SC1. A better view of the amount of energy provided by the auxiliary system to reach the target of 7 °C is shown in Fig. 5 for the third year of the four most interesting scenarios (SC3 gives the same results of SC4 as shown in Fig. 4). The average heating load supplied by the diesel boiler is around 75 kW in SC1, where the water is going out of the STST at a maximum temperature of 4.4 °C at the beginning of the discharge phase and then stabilizes at 4.3 °C. The water is heated up to a maximum of 4.6 °C and a stable value of 4.4 °C when a second tank is added to the system, with a maximum load of 70 kW. The flow of water through the first "cold" tank provides nearly the same temperature increase generated in SC1. The water is heated up to a maximum of 5.0 °C in SC4 and SC5 to cover around 25% of the demand for almost a month (more than 600 h). Close to springtime, the auxiliary loads are basically the same as in SC2.

It is indeed worth noticing the negative trend of the water temperature that tends to stabilize and increase toward the end of the discharge near 27,500 h and vice versa for the heating loads. This temperature trend is sharper

in scenarios with two STST. A consistent observation is also clear in Fig. 4, where the negative trend of the energy curve switches to positive for the last 1000 h of discharge simulation. This happens because the average temperature in the hot tank increases with the restart of the solar production, supplying energy together with the BTES. Kuujjuaq actually receives high daily solar radiation in March (3.2 kWh/m²d) and April (5 kWh/m²d), which are however listed fourth and fifth as the coldest months, with mean air temperature of about -17 °C and -10 °C. As a comparison, August and September have solar radiation of 3.9 and 2.3 kWh/m²d and mean air temperature of 7 °C and 3 °C, respectively.

Finally, the target of covering 50% of the drinking water network energy demand has not been achieved yet, but some improvements were achieved through the optimization of the system (from 12 to 20% of the demand satisfied). The most important technical adjustments were the addition of a second ST tank, in order to keep the BTES inlet temperature as low as possible during the discharge, and the decrease of the spacing between the BHEs from 3 to 2 m. The latter actually decreased the nominal storage capacity of the underground, but it was shown to be critical in the ability of the system to retrieve the energy (+20%) because of the low ground thermal conductivity at the site. The performance of the whole system can be further improved by adding a second immersed HX in each tank in order to extract a larger amount of the energy available in the STST, adding a HX on the solar loop side in order to use a less viscous and more effective HCF with 25% vol. glycol in the BTES and STST or choosing more efficient solar panels.

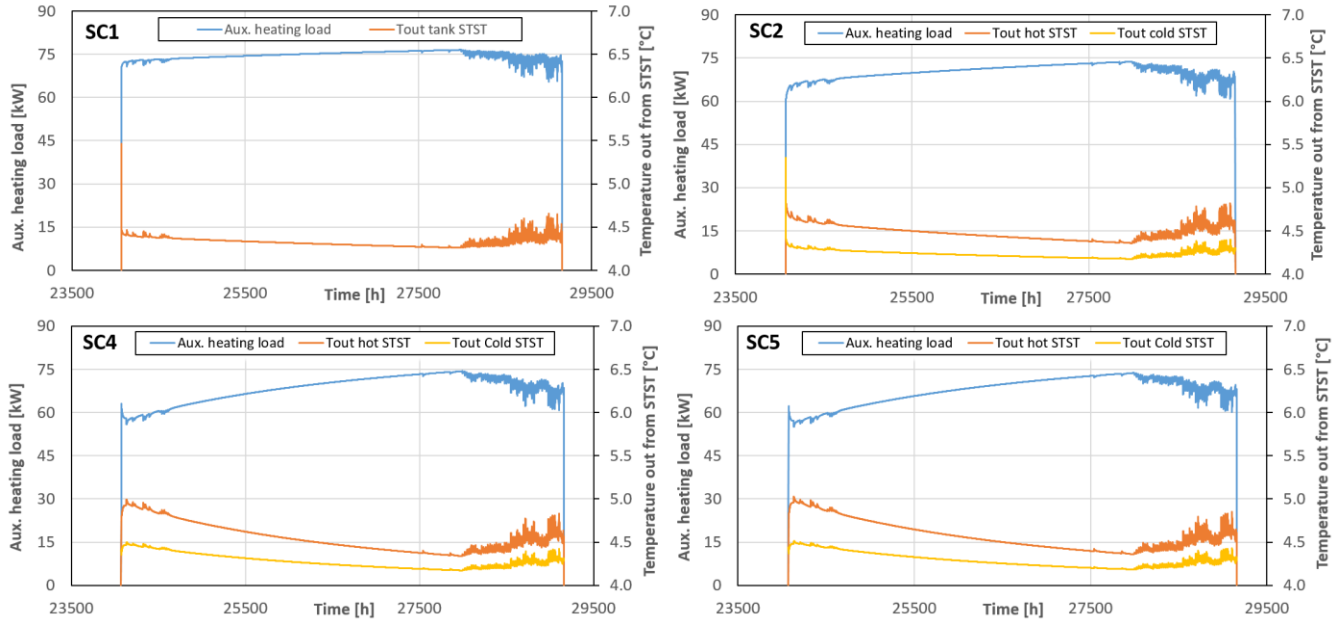

Figure 5 Heating loads provided by the auxiliary system compared to the temperature of the drinking water loop after passing through the cold and hot tanks. Discharge phase at the end of the third year (same period as in Fig. 4).

CONCLUSIONS

The present contribution showed a feasibility study for the construction of an underground storage system in Kuujjuaq, an Inuit village characterized by a subarctic environment with underground temperature near 0 °C. After developing a geological conceptual model based on the results of various field activities, a BTES system was designed and implemented in TRNSYS to run five-year simulations and vary different characteristics to increase the efficiency of the storage volume.

Even if improvements were achieved through the optimization of the system and other improvements can be further undertaken, it is clear that the guidelines of Pahud (2000) adopted to desing the system (Pahud, 2000) are not valid for this subarctic climatic context. The guidelines are valid for Swiss conditions, but were adopted because they are useful to define the relative amounts of collector area, short-term and ground storage. However, the collector area should be increased to account for the smaller solar radiation and the low annual air temperature, the latter significantly influencing the thermal collectors' efficiency. To this regard, specific studies are anticipated to propose similar rules for subarctic to arctic climates.

Moreover, the performance of small diameter ground heat exchangers will be evaluated (e.g. d_{BHE} = 76 mm and d_o = 27 mm) in order to exploit drilling technology available in Kuujjuaq and avoid onerous shipping from the south. The performance of the underground storage has been studied through the DST module in TRNSYS, which does not take into account the groundwater flow advection. The code FEFLOW (Diersch, 2014) will be used to better estimate the heat losses under groundwater advection. Different types of parallel and series connections and geometrical dispositions of the boreholes will be tested to limit the losses due to advection, hence to enhance the heat extraction during the winter.

ACKNOWLEDGMENTS

The authors would like to thank the Institut Nordique du Québec (INQ) that supports these research activities through the *Chaire de recherche sur le potential géothermique du Nord* awarded to Jasmin Raymond and the Labex DRIIHM for supporting the activity of Chrystel Dezayes. The *Fonds de recherche nature et technologies* through the sustainable mining development program and the *Observatoire Homme Milieu Nunavik* have additionally contributed to this research.

NOMENCLATURE

a_0 a_1 a_2	=	Efficiency intercept (-), slope (kJ/hm²K) and curvature (kJ/hm²K²)
d_{BHE}	=	Borehole diameter (mm)
d_o	=	Outer pipe diameter (mm)
d_i	=	Internal pipe diameter (mm)
HDD_{18}	=	Heating degree days below 18°C (°C)
λ	=	Thermal conductivity (W/mK)
SF	=	Shape factor, height/diameter (-)
T	=	Temperature (°C)

ABBREVIATIONS

BHE	=	Borehole heat exchanger
BTES	=	Borehole thermal energy storage
DHW	=	Domestic hot water
DST	=	Duct ground heat storage model developed by Hellström (1989)
ERT	=	Electrical resistivity tomography
HX	=	Heat exchanger
HCF	=	Heat carrier fluid
SH	=	Space heating
ST	=	Short term
STST	=	Short term storage tank
USD	=	U.S. Dollars

REFERENCES

Allard, M., Lemay, M. 2012. *Nunavik and Nunatsiavut: from science to policy: an integrated regional impact study (IRIS) of climate change and modernization*. ArcticNet, Quebec City, QC, 303 p.

Belzile, P., F-A. Comeau, J. Raymond and L. Lamarche. 2017. *Revue technologique: efficacité énergétique et énergies renouvelables au nord du Québec*. INRS, Centre Eau Terre Environnement, Quebec City, QC, Research Report R1716, 37 p.

Cabeza, L.F. 2015. Advances in thermal energy storage systems – methods and applications. Cambridge, UK: Woodhead Publishing Series in Energy.

Diersch, H.-J.G., D. Bauer, W. Heidemann, W. Rühaak, and P. Schätzl. 2011. *Finite element modeling of borehole heat exchanger systems Part 2. Numerical simulation*. Computers & Geosciences, 37(8): 1136-1147.

Diersch, H.J.G. 2014. FEFLOW: Finite element modeling of flow, mass and heat transport in porous and fractured media. Berlin, Germany: Springer.

Flynn, C. and K. Sirén. 2015. *Influence of location and design on the performance of a solar district heating system equipped with borehole seasonal storage*. Renewable Energy, 81: 377-388.

Fortier, R., M. Allard, J-M. Lemieux, R. Therrien, J. Molson and D. Fortier. 2011. *Cartographie des dépôts quaternaires des villages nordiques de Whapmagoostui-Kuujjuarapik, Umiujaq, Salluit et Kuujjuaq*. Rapport de synthèse de la phase I, Ministère du Développement Durable, de l'Environnement et des Parcs du Québec, Québec City, GM 65971, 122 p.

Gao, L., J. Zhao and Z. Tang. 2015. *A review on borehole seasonal solar thermal energy storage*. Energy Procedia, 70: 209-218.

Giordano, N., I. Kanzari, M.M. Miranda, C. Dezayes and J. Raymond. 2017. *Shallow geothermal resource assessments for the northern community of Kuujjuaq, Québec, Canada*. IGCP636 Annual Meeting, Santiago de Chile, Chile, 1-3.

Governement of Canada. 2018. http://climate.weather.gc.ca/climate_normals/index_e.html accessed in January 2018.

Hellström, G. 1989. Ground heat storage model: manual for computer code. Lund, Sweden: Department of Mathematical Physics, University of Lund.

Hydro-Québec. 2011. *Réseaux autonomes, portrait d'ensemble et perspectives d'avenir*. Demande R-3776, HQD-13, 35 p.

Klein, S.A., W.A. Beckman, J.W. Mitchell et al. 2017. TRNSYS 18: A Transient System Simulation Program. Solar Energy Laboratory, University of Wisconsin, Madison, USA, http://sel.me.wisc.edu/trnsys.

Lemieux, J-M., R. Fortier, M-C. Talbot-Poulin, J. Molson, R. Therrien, M. Ouellet, D. Banville, M. Cochand and R. Murray. 2016. *Groundwater occurrence in cold environments: examples from Nunavik, Canada*. Hydrogeology Journal, 24: 1497-1513.

MDDELCC - Ministère du développement durable, environnement et lutte contre les changements climatiques. 2012. *Plan d'action sur les changements climatiques 2013 – 2020*.

Miranda, M.M., C. Dezayes, N. Giordano, I. Kanzari, J. Raymond and J. Carvalho. 2018. *Fracture Network Characterization as input for Geothermal Energy Research: Preliminary data from Kuujjuaq, Northern Québec, Canada*. 43rd Stanford Geothermal Workshop, February 12-14, Stanford, United States, SGP-TR-213.

Nguyen, A., P. Pasquier and D. Marcotte. 2017. *Borehole thermal energy storage systems under the influence of groundwater flow and time-varying surface temperature*. Geothermics, 66: 110-118.

Pahud, D. 2000. *Central solar heating plants with seasonal duct storage and short-term water storage*. Solar Energy, 69(6): 495-509.

Rad, F.M. and A.S. Fung. 2016. *Solar community heating and cooling system with borehole thermal energy storage – Review of systems*. Renewable and Sustainable Energy Reviews, 60: 1550-1561.

Rad, F.M., A.S. Fung and M.A. Rosen. 2017. *An integrated model for designing a solar community heating system with borehole thermal storage*. Energy for Sustainable Development, 36: 6-15.

Raymond, J., F-A. Comeau, M. Malo, D. Blessent and I.J. López Sánchez. 2017. *The geothermal open laboratory: a free space to measure thermal and hydraulic properties of geological materials*. IGCP636 Annual Meeting, Santiago de Chile, Chile, 1-3.

Schmidt, T., D. Mangold and H. Müller-Steinhagen. 2004. *Central solar heating plants with seasonal storage in Germany*. Solar Energy 76: 165-174.

Sibbitt, B., D. McClenahan, R. Djebbar, J. Thornton, B. Wong, J. Carriere and J. Kokko. 2012. *The performance of a high solar fraction seasonal storage district heating system – five years of operation*. Energy Procedia, 30: 856-865.

Simard, M., I. Lafrance, H. Hammouche and C. Legouix. 2013. Géologie de la région de Kuujjuaq et de la baie d'Ungava (SRNC 24J, 24K). Québec, Canada: Gouvernement du Québec.

Terziotti, L.T., M.L. Sweet and J.T. McLeskey Jr. 2012. *Modeling seasonal solar thermal energy storage in a large urban residential building using TRNSYS 16*. Energy and Buildings, 45: 28-31.

Xu, J., R.Z. Wang and Y. Li. 2014. *A review of available technologies for seasonal thermal energy storage*. Solar Energy, 103: 610-638.

IGSHPA SWEDEN 2018 Research Conference

DOI: 10.22488/okstate.18.000029

Geothermal Storage Integration into Supermarket's CO_2 Refrigeration System

Mazyar Karampour, Samer Sawalha, Carlos Mateu-Royo, Jörgen Rogstam

ABSTRACT

This paper investigates the integration of geothermal storage into the state-of-the-art CO_2 trans-critical booster systems. The objective is to evaluate the impact on energy efficiency of this integration. Three scenarios of integration are studied including stand-alone and integrated supermarket building systems. The results show that for a stand-alone supermarket, heat recovery from the CO_2 system should be prioritized over extracting heat from the ground, which can be done either by an extra evaporator in the CO_2 system or by a separate ground source heat pump. In the case of supermarket integration with a nearby district heating consumer, geothermal storage integration with extra evaporator in the CO_2 refrigeration system can reduce the total annual running cost of the two buildings by 20-30%. The determining factors on profitability of geothermal storage integration are the heating demand of the supermarket and possibilities of coupling its heating system to another nearby consumer. This integration is beneficial if the full efficient heat recovery capacity of the CO_2 system is not sufficient to provide the entire demands.

1. INTRODUCTION

Supermarkets are the most energy intensive commercial buildings where the refrigeration system is their largest energy user (Karampour et al., 2016). They are also the largest consumers in Europe of high GWP refrigerants; about 35% of Europe HFC consumption (SKM Enviros, 2012). These two factors put the environmentally-friendly and energy-efficient supermarket refrigeration solutions as one of the priorities on climate change mitigation policies. CO_2 trans-critical refrigeration systems for supermarkets are seen as a solution that fulfills the environmental requirements; therefore, they have been introduced, installed and spread in mainly the relatively cold regions of Europe and the world with more than 15,000 systems as of November 2017 (Chasserot, 2017).

A potential improvement which has been less covered in the literature is the integration of geothermal storage into the CO_2 state-of-the-art system. The potential advantage of this integration is that the ground can be used as a heat sink to provide sub-cooling for the CO_2 system in summer and as a heat source in the winter for the heat pumping function of the CO_2 refrigeration system or via a separate Ground Source Heat Pump (GSHP).

As the number of CO_2 systems and integration of geothermal storage are increasing in Scandinavian supermarkets, it is necessary to discuss the advantages and limitations of this integration more in details. In section 2 of this paper the studied systems are described and three different scenarios of geothermal storage integration are presented in section 3.

2. SYSTEM DESCRIPTION

The reference system in this study is state-of-the-art (SotA) CO_2 trans-critical booster system which is presented by the black lines in the schematic in Figure 1. This system is abbreviated as CO_2 SotA hereinafter. The features of this

Mazyar Karampour (mazyar.karampour@energy.kth.se), **Samer Sawalha** (samer.sawalha@energy.kth.se) and **Carlos Mateu-Royo** from Royal Institute of Technology (KTH), Energy Technology Department, Brinellvägen 68, 100 44, Stockholm, Sweden.
Carlos Mateu-Royo (mateuc@uji.es) also from ISTENER Research Group, Department of Mechanical Engineering and Construction, University Jaume I, Campus de Riu Sec s/n, E-12071 Castellón de la Plana,Spain.
Jörgen Rogstam from (jorgen.rogstam@ekanalys.se) Energi & Kylanalys AB, Varuvägen 9, Älvsjö 125 30, Sweden

system have been discussed in details by the authors in previous research (Karampour and Sawalha, 2018). The CO_2 SotA system takes the advantage of flooded evaporation to run at high evaporation temperatures and uses parallel compression to compress the flash gas vapour. It has been shown that these features decrease the refrigeration annual energy use (AEU) of the standard CO_2 booster system by 15%. The CO_2 SotA system also integrates space heating, tap water heating, and air conditioning functions into the refrigeration system. The energy efficiency of providing heating and air conditioning demands by CO_2 SotA are either higher or comparable to efficient alternative solutions, which further decreases the overall AEU for refrigeration, heating, and air conditioning. The air conditioning and tap water heating are not included in this study, and heat recovery is done only for space heating, which is the major heating demand in supermarkets.

A feature which hasn't been evaluated in scientific publications but applied in some supermarkets, mainly in Scandinavia, is the geothermal storage integration. The design concept is to use the ground as a heat sink in summer and a heat source in winter. The schematic of a CO_2 SotA system and its integrated geothermal storage is shown in Figure 1-left. The geothermal integrated lines are highlighted by green colour. The geothermal sub-cooler is located after the gas cooler and provides sub-cooling in the warm summertime. The heat is stored in the ground during this season and an extra evaporator (Geothermal Heat Extractor in Figure 1) is used to extract the heat from the ground during winter. The extracted heat is then "pumped" by the compressors to provide heat in the heat recovery de-superheater.

As shown in Figure 1-left, the extracted heat can be added at P_{MT} level and compressed by high stage compressors or it can be added at P_{rec} level and processed by parallel compressors. In the case of heat extraction at P_{rec} level, the expansion valve before the extractor evaporator is fully open and the exit line is connected to the parallel compressor. Both methods of extracting at P_{MT} or P_{rec} level have been applied in field installations in Sweden and studied in this paper.

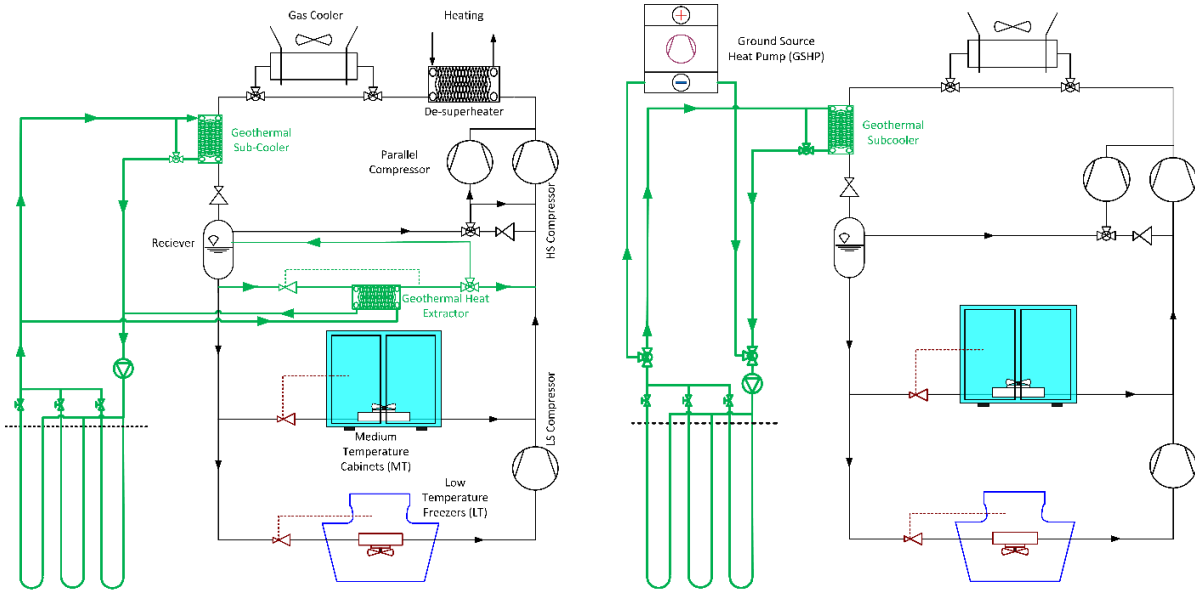

Figure 1: Schematic of a state-of-the-art CO_2 booster system and integrated geothermal storage, the later is highlighted by green (left), Hybrid geothermal solution, refrigeration system sub-cooling in summer, heat source for GSHP in winter (right)

Another option to extract and use the stored heat from the ground in winter is by running the CO_2 system in floating condensing mode, i.e. lowest pressure possible, and use a separate ground source heat pump (GSHP) to provide the supermarket's heating demands. Schematic of this system, called "hybrid" in this paper, is shown in Figure 1-right. This system is also studied in this paper.

3. RESEARCH SCENARIOS

The objective of the paper is to study three research scenarios, these are visualized in Figure 2:

S1- Comparing the annual energy use (AEU) of a stand-alone supermarket using CO_2 system (S1a) versus geothermal storage integrated CO_2 system (S1b).

S2- Comparing AEU of "separate systems of supermarket and a neighbor consumer of district heating energy" (S2a) versus "integrated systems of supermarket, the neighbor consumer and geothermal storage" (S2b). In the later, the entire heating demand of the neighbor is provided by heat recovery from the CO_2 system in winter. Ground also provides sub-cooling for CO_2 system in summer.

S3- Comparing AEU of a stand-alone supermarket using CO_2 system (S3a) versus a "hybrid solution of sub-cooling CO_2 system by ground in summer, and extracting heat from the ground by GSHP in winter (S3b).

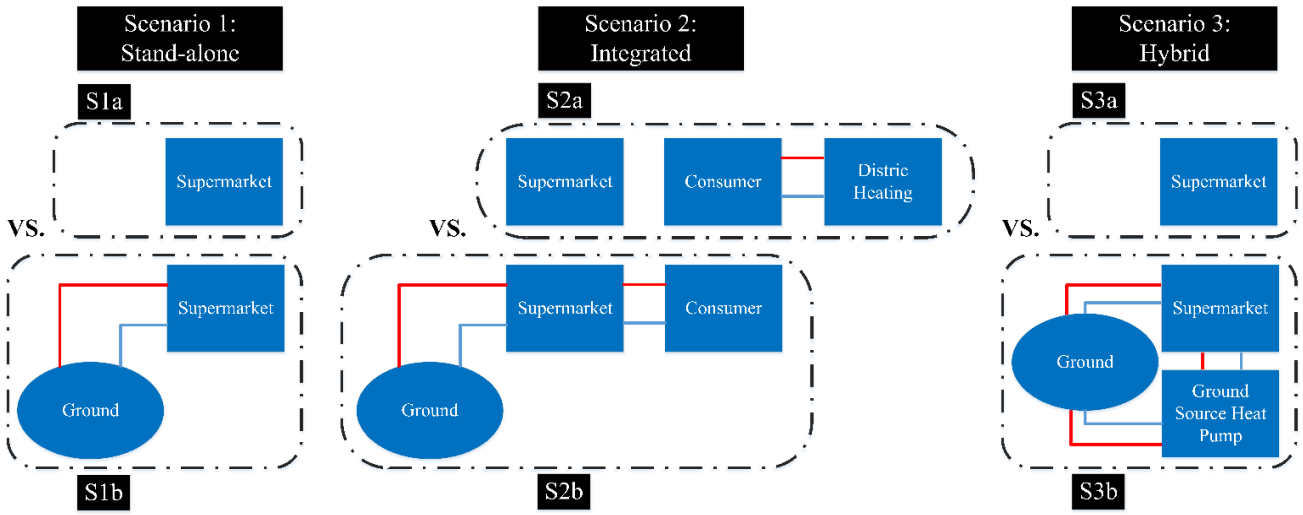

Figure 2: An illustration of the studied scenarios

4. MODELLING DETAILS

4.1 Boundary conditions and assumptions

4.1.1 Thermal Loads

Medium temperature cooling demand is assumed to be 200 kW at 35°C and decreases linearly to 100 kW at 10°C, below which the demand remains constant. Low temperature cooling demand is rather constant through the entire year and assumed to be 35 kW. Medium and low stage evaporation temperatures of the CO_2 SotA are -4°C and -29°C, respectively.

The heating demand is obtained by the program CyberMart for a medium-sized supermarket in Sweden. CyberMart is a tool to calculate the annual energy demand and use of different refrigeration, heating and air conditioning systems in supermarkets. Detailed description and calculation procedure of the program can be found in the Doctoral Thesis by Arias (Arias, 2005).

The main heating demand in supermarkets is space heating and it starts at the set-point of 10°C ambient temperature. Based on CyberMart calculations, the heating demand is estimated to be 40 kW at 10°C ambient temperature and increases linearly to 190 kW at -20°C ambient temperature. Water return temperature from the heating system is assumed to be 30°C. 5K approach temperature is assumed between the water return temperature and the refrigerant in the condenser of the separate GSHP, or the de-superheater..

4.1.2 Control strategy

The system runs in the floating condensing mode in the summer. It follows the ambient temperature in sub-critical condition with an approach temperature of 7K. It follows an optimum discharge pressure control for max *COP* in super-critical conditions with an approach temperature of 3K. The optimum pressure $P_{opt,\,ga}$ [bar] is a function of the gas cooler exit temperature $T_{gc,\,exit}$ [°C], as follows:

$$P_{opt,gc} = 2.7 * T_{gc,exit} - 6 \quad (1)$$

The heat recovery control strategy in winter follows the recommendations presented by Sawalha (2013). In brief, the recommendation consists of a stepwise control strategy; the first step is to regulate the gas cooler pressure P_{gc} and run the gas cooler fans with highest speed to maintain gas cooler exit temperature $T_{gc,\,exit}$ as low as possible with a minimum value of 5°C. The second step is to fix the gas cooler pressure at a maximum value for high efficiency P_{gc} and decrease the gas cooler capacity by reducing the fans speed. The third step is to fully by-pass the gas cooler. Due to the sharp drop in system efficiency the system should never go beyond the third step. If more heat is required, the fourth step is to extract the heat from the ground.

The heating season is called winter operation mode and it starts at ambient temperatures lower than 10°C. The rest is called summer operation mode. Temperature-bin hours of Stockholm is used as the studied climate.

4.1.3 Geothermal storage and GSHP hybrid solution

Modelling simulations for the ground heat exchanger have been done for Stockholm conditions, therefore the ground properties used for the borehole design are rock thermal conductivity of 3.1 $W.m^{-1}.K^{-1}$., volumetric heat capacity 2.16 $MJ.m^{-3}\cdot K^{-1}$ and ground surface temperature 6.6 ºC (Acuña, 2013).

As the most conventional GSHP secondary fluid in Europe (Ignatowicz et al., 2017), an aqueous ethanol solution of 24% weight concentration is used as the heat-carrier fluid for geothermal loops. It has a freezing temperature of -14.6 ºC; however, its operating temperature T_f [°C] is restricted to be within the range of -5°C and +20°C. The flow rate is 0.5 l/s per borehole, which is constant during all the operation time. The borehole uses single U-tube heat exchangers and their depth is selected to vary within the 150-200m range. The pump power is assumed to be 5% of the GSHP compressor electricity use. The GSHP uses R07C as the working fluid, with a heating capacity of 200 kW. The evaporator has a capacity of 80 kW. Both evaporator and condenser have 5K approach temperature with their heat exchanging fluids. The condensation temperature is fixed to 35°C (i.e. fixed 30°C water return temperature from the heating system), which is similar boundary conditions to CO_2 heat recovery de-superheater. The evaporator has an approach temperature of 5K with the secondary fluid and 10K internal super-heating.

4.2 Energy efficiency calculations

A computer model in EES (Engineering Equation Solver) software (Klein, 2015) is used to analyze the performance of the CO_2 SotA and GSHP systems. The calculations of cooling and heating loads have been explained comprehensive in authors previous research (Karampour and Sawalha, 2018) (Karampour and Sawalha, 2017).

The total electricity use $\dot{E}_{tot}$ [kW] of the system is calculated based on Eq. (2):

$$\dot{E}_{tot} = \dot{E}_{MT} + \dot{E}_{LT} + \dot{E}_{PC} + \dot{E}_{fan} + \dot{E}_{geo,pump} \quad (2)$$

where $\dot{E}_{MT}$, $\dot{E}_{LT}$, and $\dot{E}_{PC}$ [kW] are the electricity use of three compressor units. These are calculated based on overall efficiency of the compressors, extracted from manufacturer's data. $\dot{E}_{fan}$ [kW] is the electricity use of gas cooler fans. $\dot{E}_{fan}$ is estimated to be 3% of the heat rejected in the gas cooler $\dot{Q}_{gc}$ [kW]. $\dot{E}_{geo,pump}$ is the pump electricity use to circulate the secondary fluid. It is estimated that it is about 5% of the extra evaporator capacity in winter or geo sub-cooler in summer.

Heat recovery COP (COP_{HR}) of the CO_2 SotA system is defined as:

$$COP_{HR} = \frac{\dot{Q}_{HR}}{(\dot{E}_{tot} - \dot{E}_{tot,fc})} \quad (3)$$

$\dot{Q}_{HR}$ [kW] is the amount of recovered heat, $\dot{E}_{tot}$ [kW] is the total electricity use calculated from equation (2), and $\dot{E}_{tot,fc}$ [kW] is the amount of electricity use if the system was not controlled for heat recovery and was run in floating condensing mode with minimum condensing pressure in winter.

Annual energy use AEU [MWh] is calculated using the following equation:

$$AEU = \sum_{i=1}^{n} (\dot{E}_{tot,i} \cdot f_i) \quad (4)$$

where $\dot{E}_{tot}$ [kW] is the total electricity use calculated from equation (2), n is the number of temperature-bin hours, and f is the frequency, i.e. number of hours, of each temperature bin.

The calculations on the geothermal storage and its borehole field design are done using Earth Energy Designer (EED) software (Hellström and Sanner, 1994).

The monthly heat stored (summer sub-cooling) and heat extracted (winter heat pumping) are input to the EED software. The first estimation in EED is based on an assumed constant amount of sub-cooing in EES. Using the defined secondary fluid temperature range, the software calculates the optimized geometry and fluid temperature as a function of time of the year. This function is correlated to ambient temperature and used as a new variable sub-cooling amount in the EES code. EES calculates again the amount of ground loads in winter and summer. This iterative calculation between EES and EED is repeated to find a good match between EES and EED results.

5. RESULTS AND DISCUSSIONS

5.1 S1-Stand-alone Supermarket

The 1st scenario is to compare CO_2 refrigeration system without (S1a) and with (S1b) geothermal connection in a stand-alone supermarket. Eight system design cases have been calculated in this scenario:

- CO_2 SotA (reference): the system has no geothermal connection and heat recovery from its de-superheater is used to provide the space heating demand in the supermarket building.

- Sub-cooling in the summer (SC summer): the CO_2 system uses ground as heat sink in summer to sub-cool the refrigerant exiting the gas cooler.

- Sub-cooling in the summer (SC summer) and heat extraction in winter: The studied six cases include three cases of heat extraction at P_{MT} level, and three at P_{rec} level. The extra evaporator $\dot{Q}_{ex}$ [kW] is studied for sizes of 40, 80 and 120 kW. These values are selected to be a reasonable capacity able to be provided by the installed compressors; no additional compressors are needed. Summer sub-cooling is also studied in all these six cases for a reasonable range of up to 15K sub-cooling, this results in a sub-cooling design capacity of about 60 kW.

The AEU and AEU decrease, compared to the reference case (CO_2 SotA – no geothermal), of these eight cases are shown in Figure 3. As can be seen in Figure 3, geothermal sub-cooling can provide about 3.5% AEU saving. However, this is not an economically feasible solution since there is no heat extraction in winter time; no earth thermal de-charging, and a large number of boreholes are required to keep the earth energy balance. The savings for the later six cases are less than 3%, the reason that AEU saving changes from 3.5% (only sub-cooling) to less than 3% (sub-cooling and heat extraction) is that winter heat recovery in the geothermally integrated CO_2 system is less efficient than the stand-alone CO_2 system.

To understand why heat recovery in the integrated solution is less efficient than the stand-alone CO_2 system, COP_{HR} of the CO_2 refrigeration system without geothermal connection (COP_{HR}) is compared to the heating COP of the geothermal heat extraction only ($COP_{HR,ex}$) and shown in Figure 4. $COP_{HR,ex}$ is defined as the amount of recovered heat (by the addition of extra heat source) over the amount of extra electricity use in compressors. In COP_{HR} the geothermal heat extraction is assumed to be switched off while in $COP_{HR,ex}$ the heating demand is provide primarily by heat extraction from the ground, and the remaining demand is provided by heat recovery from the refrigeration system. For $COP_{HR,ex}$ the sole effect of the geothermal heat extraction is calculated.

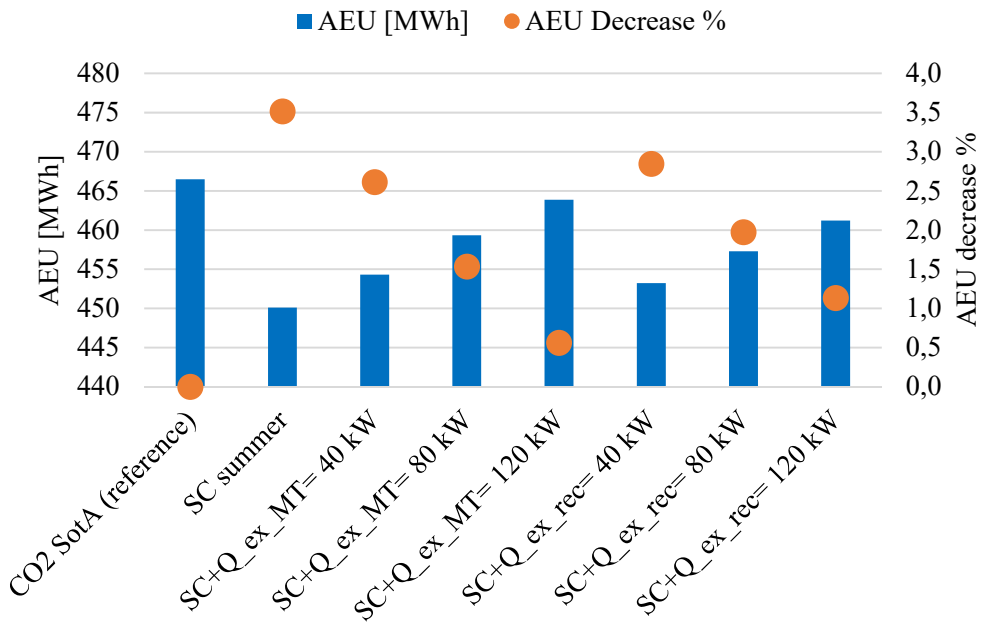

Figure 3: Annual Energy Use and Savings for S1 design cases

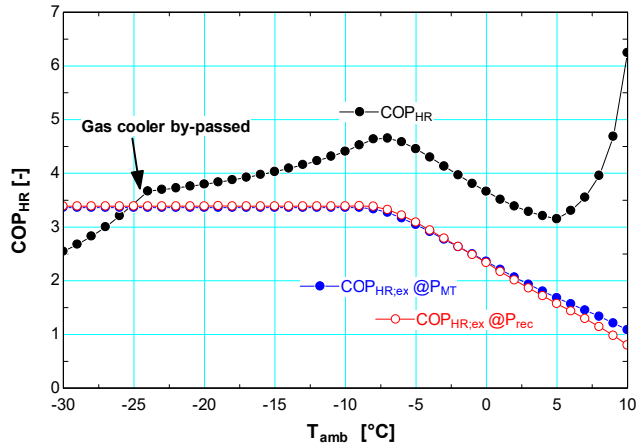

Figure 4: Heat recovery COPs for CO_2 stand-alone and CO2 ground-coupled systems

It can be observed that $COP_{HR,ex}$ is low at relatively high outdoor temperatures (i.e. heating loads) where the system operates in the sub-critical region and small amount of heat is recovered from the de-superheater. COP_{HR} is higher than $COP_{HR,ex}$ for most of the calculated range of ambient temperatures. It should be pointed out that the system is not expected to operate for many hours at very low outdoor temperatures; however, the range has been extended in this analysis to quite low outdoor temperatures in order to increase the heating demand in the building and show the limits of the refrigeration system to recover heat. $COP_{HR,ex}$ is only higher than COP_{HR} when the gas cooler is fully by-passed. This is the point where further increase in the discharge pressure beyond the maximum value for high efficiency results in sharp drop in COP_{HR} (i.e. fourth step in the control strategy explain in section 4.1.2).

The results plotted in Figure 4 means that heat extraction from the ground should be activated only when the gas cooler is fully by-passed; quite low outdoor temperatures and/or very high heating demand. In an average size

supermarket in Sweden, which has been assumed in this study, the refrigeration load in the supermarket is able to cover the space heating demand with relatively high COP for outdoor temperatures higher than -24°C; i.e. no need for heat extraction from the ground.

5.2 S2-Integrated Supermarket

The 2nd scenario is to compare "separate supermarket and district heating consumer" systems (S2a) with "integrated supermarket, consumer, and geothermal storage" systems (S2b) in two nearby supermarket and consumer buildings. This case is seen frequently, for example, when the supermarket is located inside a larger shopping mall. The consumer is assumed to have the same heating demand profile as the supermarket. Since the nature of heating and electricity are different, the separate and integrated solutions are compared based on the annual running cost spent on purchasing energy carriers. Two scenarios for energy prices are compared: (I) rather high electricity price and low district heating price, and (II) low electricity price and high district heating price. The numbers are based on prices on the Swedish market. The results of the comparison are shown in Figure 5.

As can be seen in the figure, depending on the energy prices, the integrated solution can offer about 20-30% of annual running cost savings. This integrated solution can offer lower heating prices for the consumer and provides some profits to the supermarket due to the winter time heating sale and summer time sub-cooling. This saving is the justified cost which should be compared with the cost of geothermal storage and systems integration. In the following sub-section, first, the borehole heat exchanger is designed for this integrated solution. Second, based on the energy and geothermal storage costs, the payback time for this integration concept is calculated.

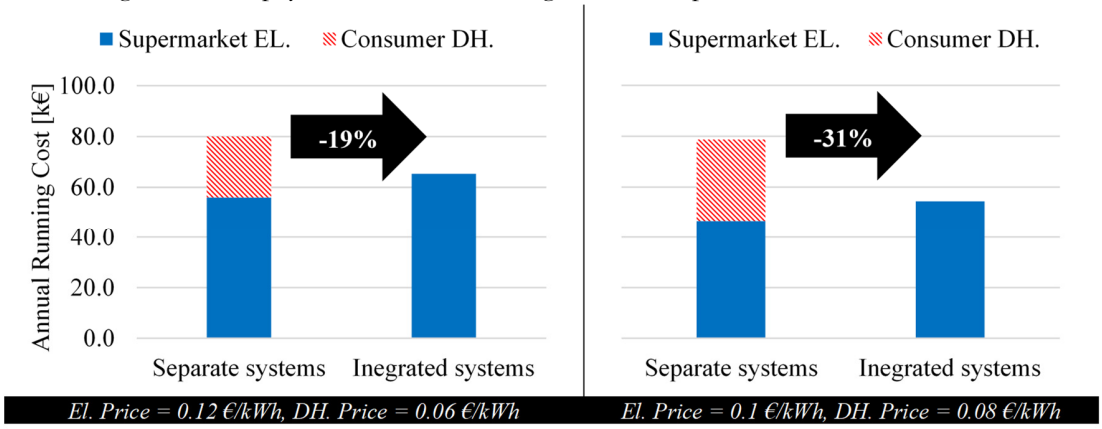

Figure 5: Separate and integrated systems annual running cost [thousand Euros]

Borehole design

In this section, the borehole field for the above-mentioned integrated solution is designed. The results of secondary fluid temperature T_f [°C] and specific heat extraction rate [W.m^{-1}] fluctuations for a 15-year lifetime of the energy system solution are shown in Figure 6-left. The minus values for the extraction rate means heat injection to the ground in summer. In addition to these variables, the secondary fluid temperatures at peak maximum and minimum loads are shown. As seen, T_f varies within the design criteria of -5°C to +20°C. This has been achieved by optimizing the geometry of the borehole field. The calculated number of boreholes to have reasonable ground energy balance is 12, in a 3*4 rectangular arrangement, with 10m spacing and about 159m deep. This results in a total length of 1908 meters. The total cost of borehole drilling and the U-tube heat exchanger is about 25 €/m in Sweden. This means that the total cost for the desired borehole heat exchanger is 47.700 €. This value can be compared with the amount of annual running cost saving, presented in the previous section, to calculate the payback time.

The payback time for different energy price ratios (electricity to heating) compared to the geothermal storage cost is shown in Figure 6-right. The three electricity prices considered are 0.1, 0.12 and 0.14 €.kWh^{-1} and the three heating

prices are 0.06, 0.08 and 0.1 €.kWh^{-1}. This forms nine combinations. According to some communications with supermarkets owners, a payback time of three years is a reasonable value for investments like the proposed solution. The energy price "ratios" for Sweden is presently within the range of 1.2-1.7. This implies that geothermal storage integration is a solution with reasonable payback time for present energy prices.

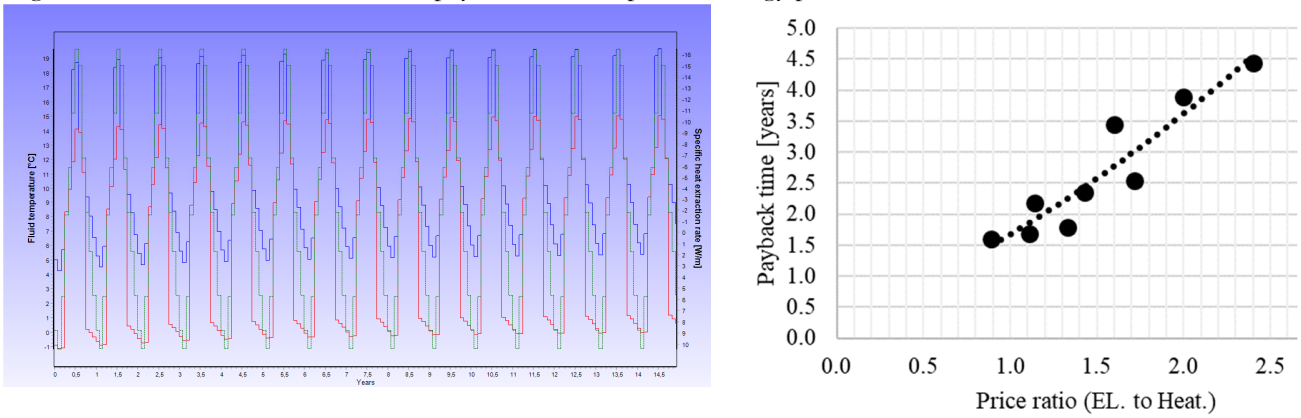

Figure 6: Secondary fluid temperature and heat extraction fluctuations (left), Payback time for different energy price ratios (right)

5.3 S3-Hybrid solution

The 3rd research scenario is to compare "CO_2" (S3a) and "hybrid CO_2 + GSHP" (S3b) systems. As mentioned earlier, the entire supermarket heating demand is provided by heat recovery from the CO_2 system in a stand-alone supermarket. However, the heat demand in the supermarket with the hybrid solution is provided by the GSHP. The ground is the heat source for GSHP in winter and heat sink for CO_2 sub-cooler in summer. Similar to section 5.2, EED and EES calculations are used to evaluate AEU and to size borehole field. The results of the comparison are shown in Figure 7. The hybrid system consumes about 8% less electricity than the stand-alone CO_2 system in summer, thanks to the geothermal sub-cooling. On the other hand, the winter energy use of the stand-alone system is 5% less than the hybrid system. These energy use decrease in summer and increase in winter counter balance, and the hybrid system is only 2% more efficient than the stand-alone CO_2 system annually.

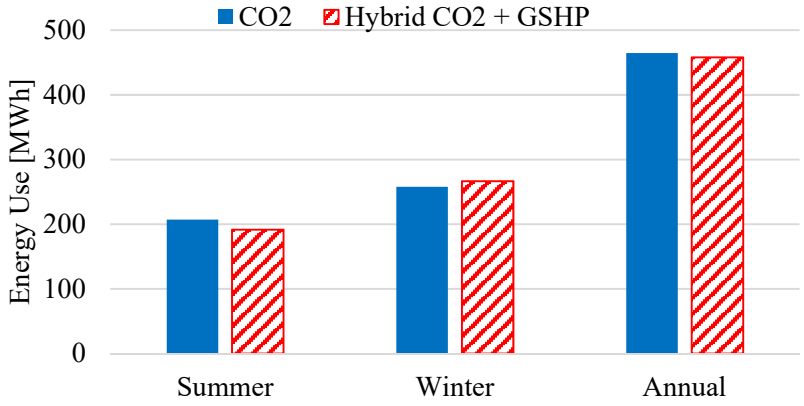

Figure 7: Energy use of stand-alone CO_2 vs hybrid system solutions

Borehole field design for GSHP has been done similar to section 5.2 procedure. Since the entire heat is provided by GSHP, the calculations show that the winter load on the ground has a higher order of magnitude than the summer heat injection load. This results in a total number of 24 boreholes required which is much higher compared to a CO_2 system, where heat recovery is prioritized to heat extraction. This large number of boreholes are required to guarantee

thermally balanced ground over the lifetime of the system. The payback time for such a large bore field is estimated to be more than 7-8 years since, in addition to the borehole drilling and pipe heat exchanger costs, a large heat pump is required to be purchased. To sum up, integration of ground source heat pump and CO_2 system does is not economically favorable over the stand-alone CO_2 system.

6. CONCLUSION

This paper investigates the advantages and challenges of geothermal storage integration into a state-of-the-art CO_2 supermarket refrigeration system. Three different integration scenarios are studied.

The 1st scenario study results indicate that heat recovery from a stand-alone CO_2 SotA system is more efficient than providing part of the heating demand by using an extra heat source, here, the ground. It has been shown that using this option is beneficial only when the gas cooler is fully by-passed. This is added as the ultimate step in a previously-presented stepwise heat recovery control strategy.

The 2nd scenario study results show that annual running cost of two separate supermarket and district heating consumer can be decreased by 20-30% if the systems are coupled, geothermal storage is applied and supermarket provides heating for the consumer. A parametric study shows that with the current energy and borehole drilling prices, the integrated solution can be applied with a payback time of less than 3 years.

The 3rd scenario study on the hybrid solution of the CO_2 system and a separate GSHP, shows that about 2% of the AEU can be saved compared to stand-alone CO_2 system. However, the demand for a large borehole field makes the payback time very long and the solution not economically feasible.

To conclude, geothermal storage integration into CO_2 supermarket refrigeration system doesn't have a significant impact in the case of a stand-alone supermarket. However, in the case of an integrated supermarket with a neighbor building/facility, geothermal storage integration can contribute to significant running cost savings compared to separate systems running costs. The application of a separate GSHP is also not recommended as long as heat can be recovered from the CO_2 system efficiently.

7. REFERENCES

Acuña, J., 2013. Distributed Thermal Response Tests: New Insights on U-pipe and Coaxial Heat Exchangers in Groundwater-filled Borehole (Doctoral Thesis). Royal institute of technology (KTH), Stockholm, Sweden.

Arias, J., 2005. Energy usage in supermarkets-modelling and field measurements (Doctoral Thesis). Royal institute of technology (KTH), Stockholm, Sweden.

Chasserot, M., 2017. Global Natural Refrigerant Trends.

Hellström, G., Sanner, B., 1994. Earth Energy Designer: software for dimensioning of deep bore holes for heat extraction., in: Calorstock. Presented at the 6th International Conference on Thermal Energy Storage, Espoo, Finland, pp. 195–202.

Ignatowicz, M., Melinder, Å., Palm, B., 2017. Properties of different ethyl alcohol based secondary fluids used for GSHP in Europe and USA. Presented at the IGSHPA Technical/Research Conference and Expo, Denver, USA.

Karampour, M., Sawalha, S., 2018. State-of-the-art integrated CO2 refrigeration system for supermarkets: A comparative analysis. Int. J. Refrig. 86, 239–257. https://doi.org/10.1016/j.ijrefrig.2017.11.006

Karampour, M., Sawalha, S., 2017. Energy efficiency evaluation of integrated CO2 trans-critical system in supermarkets: A field measurements and modelling analysis. Int. J. Refrig. 82, 470–486. https://doi.org/10.1016/j.ijrefrig.2017.06.002

Karampour, M., Sawalha, S., Arias, J., 2016. D2.2 Eco-friendly Supermarkets-an overview, H2020 Project SuperSmart, Grant Agreement No 696076, Retrieved 11.11.2016 from: http://www.supersmart-supermarket.info/downloads/.

Klein, S.A., 2015. Engineering Equation Solver (EES) V9, F-chart software, Madison, USA, www.fchart.com.

Sawalha, S., 2013. Investigation of heat recovery in CO2 trans-critical solution for supermarket refrigeration. Int. J. Refrig. 36, 145–156. https://doi.org/10.1016/j.ijrefrig.2012.10.020

SKM Enviros, 2012. Phase down of HFC consumption in the EU-Assessment of implications for the RAC sector, retrieved from: http://www.epeeglobal.org/refrigerants/epee-studies/skm-enviros-study/.

[This page has been intentionally left blank]

IGSHPA SWEDEN 2018 Research Conference

DOI: 10.22488/okstate.18.000003

Financial Assessment of Ground Source Heat Pump Systems against Other Selected Heating and Cooling Systems for Australian Conditions

G. Riyan Aditya **Olga Mikhaylova** **Guillermo A. Narsilio**
Ian W. Johnston

ABSTRACT

Ground source heat pump (GSHP) systems can provide cost-effective space heating and cooling for buildings while using less fossil fuel compared to many conventional systems. Despite these benefits, they typically have higher upfront costs and longer payback periods than other heating and cooling systems. These costs are often seen as potential roadblocks for property owners to install GSHP systems over conventional systems. The financial attractiveness of GSHP systems can be increased by adopting a hybrid ground source heat pump (HGSHP) system where GSHP systems provide the baseload thermal energy with the balance provided by conventional systems. This paper assesses the lifetime costs of GSHP and HGSHP systems designed for seven major cities in Australia and compares these costs with the lifetime costs of conventional systems. The results indicate that adopting HGSHP systems in Australian climatic conditions (from tropical to cool temperate) and under current Australian installation and fuel costs can lower the normalised lifetime costs of heating and cooling compared to adopting a GSHP or a conventional system only for the same applications.

INTRODUCTION

In Australia, electricity is used for space heating and cooling of many buildings. The Australian Bureau of Statistics (2014) reported that for residential heating, 38% of residents use electricity and 30% use gas, while for cooling 49% residents use an electrical air conditioner. Most of the electricity in the country is generated from coal and gas, which are traditionally low cost and reliable energy sources. However, burning these fuels to generate electricity leads to high greenhouse gas (GHG) emissions. Gas is also used directly in furnaces for heating which also contributes significantly to the overall GHG emissions.

To achieve long-term environmental sustainability, electricity and gas consumption needs to be reduced. Ground Source Heat Pump (GSHP) technology can contribute to this reduction because GSHP systems typically have higher coefficients of performance (CoP) compared to conventional heating and cooling systems. For example, GSHP systems have been reported to have a CoP between 3 to 5 (Bloom and Tinjum, 2016; Liu and Spitler, 2014; Lu et al., 2017; Michopoulos et al., 2007; Trillat-Berdal et al., 2006). Conventional heating and cooling systems, such as a reverse cycle air conditioners (RCAC, Air Source Heat Pump Systems), typically have a CoP of 2 to 4 (Huang, 2015; Liu and Spitler, 2014; Lu et al., 2017; Self et al., 2013; Wu, 2009). Other conventional systems which use electricity and gas to provide heating operate at a CoP of less than 1 and unable to provide cooling. Hence, GSHP systems are

G. Riyan Aditya (gregorius.aditya@unimelb.edu.au) is a PhD Candidate at the University of Melbourne, Olga Mikhaylova is a Geotechnical Engineer at Golder Associates Pty Ltd, Guillermo A. Narsilio is an Associate Professor at the University of Melbourne and Ian W. Johnston is a Professorial Fellow at the University of Melbourne

typically deemed to provide cost-effective heating and cooling to buildings while using less fossil fuels than most conventional systems.

Despite their efficiencies, property owners find it difficult to adopt GSHP systems due to their higher upfront costs and longer payback periods (Karytsas and Choropanitis, 2017; Lu et al., 2017). One strategy to reduce these costs and payback periods is to utilise hybrid ground source heat pump (HGSHP) systems, whereby GSHPs provide the baseload thermal energy to buildings with the balance provided by other, usually conventional, systems during particularly hot and cold periods of the year. These systems take advantage of the relatively low installation costs of conventional systems and the relatively low operating costs of GSHP systems to make HGSHP systems attractive financially (Alavy et al., 2013; Mikhaylova et al., 2016; Nguyen et al., 2014). Several recent studies investigated the optimum sizing strategy for HGSHP systems by adjusting the *shave factor* of the systems. The shave factor is defined as the proportion of the total heating or cooling peak load provided by the GSHP (Alavy et al., 2013; Mikhaylova et al., 2016; Nguyen et al., 2014). The most optimum configurations of hybrid systems are the ones that result in the lowest net present values over the lifetime of the systems.

This study assesses the lifetime costs of GSHP and HGSHP systems for seven major cities in Australia (see Table 1) and compare them with lifetime costs of conventional systems. Each of these Australian cities has significantly different climatic conditions, and hence, energy needs. To compare HGSHP systems with other heating and cooling options, the hybrids are optimised using extensions of previously published optimisation methods discussed in Alavy et al. (2013) and Mikhaylova et al. (2016).

DATA AND METHODOLOGY

Climatic conditions and thermal loads

This study covers a wide range of climatic conditions, which vary from a tropical climate in the north to a cool temperate climate in the south. The hourly outside air temperature (OAT) data based on the typical meteorological year is retrieved for all the chosen cities from Meteonorm (2017). These hourly OATs are used to estimate the undisturbed ground temperature (Tg) at shallow depths in each city. Tg is assumed as the average annual OAT plus 2°C as described in IGSHPA (2009).The heating and cooling loads in each city were calculated based on the bin method by IGSHPA (2009) with a balance point of 17.5°C. This study assumes all buildings are residential with a peak load of 10 kW. For simplicity, the effect of humidity in cooling operations is disregarded in this paper. Table 1 presents an overview of the input parameters and the peak heating and cooling load for each city.

Table 1. Locations, design temperatures and peak heating and cooling loads

	Lat (deg)	Long (deg)	t_{dh} (°C)	t_{dc}(°C)	Tg (°C)	Qh / Qc (kW)
Adelaide	34.9 °S	138.6 °E	5.9	33.9	18.7	7.1 / 10.0
Brisbane	27.5 °S	153.0 °E	7.3	30.0	22.2	8.2 /10.0
Cairns	16.9 °S	145.8 °E	14.9	32.0	26.5	1.8 / 10.0
Hobart	42.9 °S	147.3 °E	3.4	25.2	12.9	10.0 / 5.5
Melbourne	37.8 °S	145.0 °E	5.6	31.9	16.5	8.3 / 10.0
Perth	32.0 °S	115.9 °E	5.6	34.2	19.9	7.1 /10.0
Sydney	33.9 °S	151.2 °E	7.9	28.6	20.1	8.6 / 10.0

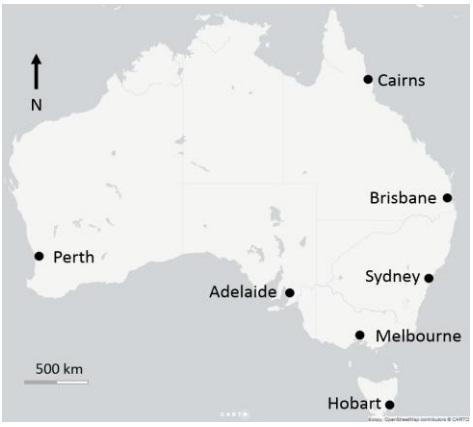

Notation: t_{dh} = heating design temperature, t_{dc} = cooling design temperature, Tg = estimated ground temperature at shallow depth. Qh or Qc = estimated peak heating / cooling loads

Heating and cooling options

The most common heating and cooling systems used in Australia are considered herein as conventional alternatives for GSHP systems. As such, the following options with their assumed CoPs are compared:

(1) Heating and cooling by an RCAC (CoP 2.5);
(2) Heating with a gas furnace (CoP 0.9) and cooling by an RCAC (CoP 2.5);
(3) Heating and cooling by GSHP (CoP 4);
(4) Heating and cooling by HGSHP system (HGSHP1) with a GSHP (CoP 4) and an RCAC (CoP 2.5); and
(5) Heating and cooling by HGSHP system (HGSHP2) with a GSHP (CoP 4), a gas furnace (CoP 0.9) for heating and an RCAC (CoP 2.5) for cooling.

This study considers only vertical ground heat exchangers (GHEs), where the required GHE length for the GSHP and HGSHP systems are calculated using the ASHRAE design approach shown in Equation 1 (Philippe et al., 2010).

$$L_{GHE} = \frac{q_h R_b + q_y R_{10y} + q_m R_{1m} + q_h R_{6h}}{T_m - \left(T_g + T_p\right)} \quad (1)$$

Table 2 summarises most design parameters employed, including those used in Equation 1. To simplify the comparison between different locations, the same ground conditions (but not T_g) and GHE geometry are assumed in all sites.

Financial Assessment

Installation costs, inflation rates and discount rates for electricity and gas, and life spans of the systems are kept constant for all locations for simplicity. These parameters are based on the work by Lu et al. (2017) and are shown in Table 3. In particular, it has been assumed that the life spans of GSHP systems are 20 years. The life spans of both RCAC and gas boilers are assumed to be 10 years each. This means that both systems will need to be replaced once over the 20 years design life. It is assumed that the replacement costs of the RCAC and gas boilers are the same as their original prices because the yearly price increase of the equipment is aligned with the discount rate. Since a 10 kW system is relatively small, maintenance cost is not included in the analysis. All the financial analysis are conducted in Australian dollars (A$), which at present is around US$ 0.79.

The operating cost for the heating and cooling systems are calculated based on the current retail prices of electricity and gas in the cities studied. These prices are taken from the major energy retailers (Aurora Energy, 2017; Origin Energy, 2017; Synergy, 2017) and shown in Table 4 below. Whenever possible, the prices have been calculated based on the weighted price average during peak, off-peak and shoulder periods. It is important to note that the operating cost of the circulation pumps is assumed negligible for these small residential buildings.

Based on the above inputs, the Net Present Costs (NPC) were calculated for each of the heating and cooling option in the seven cities considered using Equation 2.

$$NPC = \sum \frac{C_t}{(1+r)^t} \quad (2)$$

where C_t represents the cash outflow at time t which can be a capital cost or an operating cost. This cost at time t will be discounted back at interest rate r over the 20 year design life of the system. The NPC calculated here represents the present value of all outgoing cash flows during installation, operation, replacement (if necessary) over 20 years.

Table 2. Parameters used for sizing of GHEs

Design parameter (units)	Description	Value
q_h, q_m, q_y (kW)	Peak hourly, monthly average and yearly average ground loads	Calculated based on building thermal demand, heating and cooling shave factors, and COP of GSHP
R_b (mK/W)	Effective thermal resistance of the borehole, calculated based on the multipole method (Hellström, 1991)	0.103
λ (W/mK)	Thermal conductivity of ground. It is used to calculate R_{6h}, $R_{1m,}$ and R_{10y} below based on the cylindrical heat source solution proposed by Carslaw and Jaeger (1959)	2.5
R_{6h} (mK/W)	Effective thermal resistance of the ground to 6 hours of ground load	0.106
R_{1m} (mK/W)	Effective thermal resistance of the ground to 1 month of ground load	0.146
R_{10y} (mK/W)	Effective thermal resistance of the ground to 10 years of ground load	0.153
Tg (°C)	Undisturbed ground temperature at shallow depths	Listed in Table 1
T_{m_c} (°C)	Mean GHE fluid temperature in cooling operation	32.2 (= 90 °F, chosen value)
T_{m_h} (°C)	Mean GHE fluid temperature in heating operation	4 (= 40 °F, chosen value)
T_p (°C)	Temperature penalty	0 (GHE is thermally independent)

Table 3: Parameters used for financial assessment

Parameter (units)	Value	Note
Cost of drilling (A$/m)	80	Borehole installation
Cost of GSHP (A$/kW)	2,000	Equipment and installation of the system
Cost of RCAC (A$/kW)	1,000	Equipment and installation of the system
Cost of gas boiler (A$/kW)	500	Equipment and installation of the system
Electricity inflation rate (%)	6.2	
Gas inflation rate (%)	6.14	
Discount rate, r (%)	3.5	
Life span of GSHP system (years)	20	
Life span of RCAC and boiler (years)	10	
Replacement of RCAC and gas furnace	Every 10 years	
Design life (years)	20	

Table 4: Electricity and gas price considered

Cities	Electricity price (c/kWh)	Gas price (c/kWh)
Adelaide	31.3	13.0
Brisbane	22.0	10.6
Cairns	22.0	10.6
Hobart	20.2	12.6
Melbourne	27.6	9.4
Perth	27.2	10.3
Sydney	23.8	12.6

RESULTS AND DISCUSSIONS

Annual thermal demands

The calculated annual thermal demands for a 10 kW system run continuously in all the cities are shown in Figure 1. As expected, the annual thermal demand is highly correlated with the climatic conditions in each city presented in Table 1. For example, the results indicate that Hobart and Melbourne are heating dominant while the rest of the cities are cooling dominant. Perth is the city which has the most balanced heating and cooling thermal demands amongst all the cities considered. Since the demand for heating in Cairns is minor, less than 0.2 MWh, this study assumes that heating is not required in this city.

Net operating costs of GSHP and conventional systems

The computed NPCs for GSHP and conventional systems are shown in Figure 2. The NPCs are broken down into the components associated with mechanical plant costs, GHE installation costs, and operating costs. Since heating is not needed in Cairns, only one conventional system (RCAC) is considered in this city.

The capital cost component of GSHP systems (plant and GHE costs) are always higher than conventional systems due to the GHE cost components of the system. The GHE length in each city is determined by the unique thermal load pattern as well as the undisturbed ground temperature. The calculated GHE length varies from 200 m in Melbourne to 600 m in Cairns as shown in Figure 2 below. In Cairns, additional GHE length is required to allow heat dispersion to the ground without compromising a GSHP system's efficiency in this highly cooling dominant climate.

Figure 2 also shows that the operating costs of GSHP systems are always lower compared to conventional systems in the same location. From the same figure, operating cost components represent the largest shares of the NPCs of most systems in all locations even after accounting for the high GHE installation costs.

In all locations except in Cairns, the GSHP systems are the cheapest heating and cooling options compared to the conventional systems. The distinct results for Cairns are due to the high GHE lengths needed as discussed above. This means that the financial benefits generated from the lower operating cost from using GSHP systems over 20 years design life are not enough to offset the high GHE installation cost in this city.

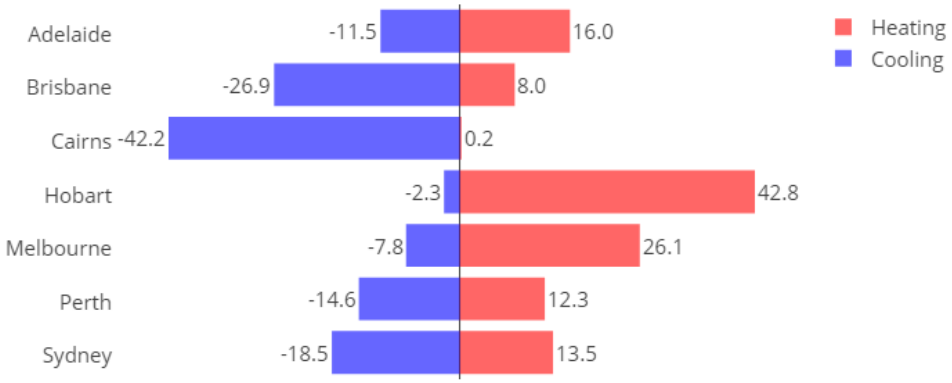

Figure 1 Annual heating and cooling demands **in MWh** of a typical 10 kW system. Negative values indicate cooling

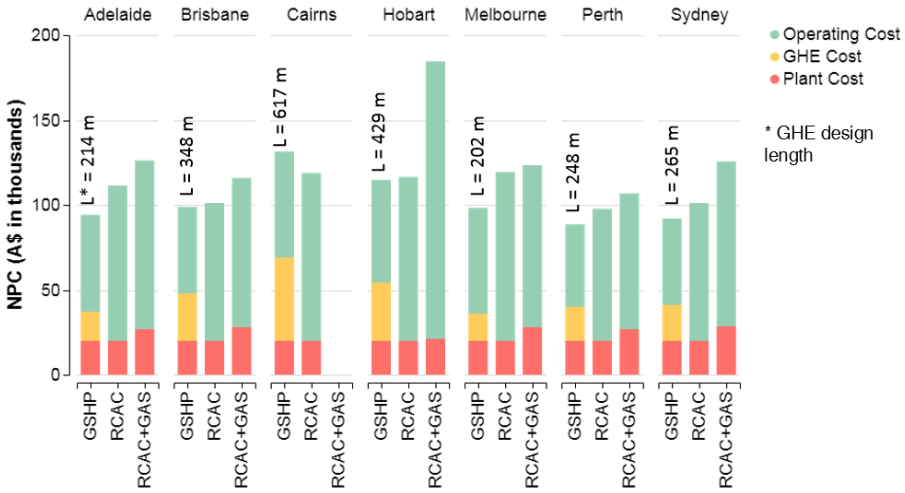

Figure 2 NPC **in A$** for GSHP and conventional systems

Hybrid ground source heat pump systems

The previous section has demonstrated that GSHP systems generally have lower NPCs compared to conventional systems. However, their high upfront capital costs can make GSHP systems a less desirable heating and cooling option in Australia. The financial attractiveness of GSHP systems can be increased by adopting hybrid ground source heat pump (HGSHP) systems. In such systems, GSHPs provide the baseload thermal energy to buildings which are topped up by conventional systems during the hotter and colder days of the year. An example of this is shown in Figure 3 below where if a GSHP system in Sydney is sized to provide 50% of peak heating and cooling load (a 50% shave factor giving 4.3 kW and 5.0 kW peak load), the GSHP systems can meet around 83% of the annual thermal energy requirements. Note that contrary to the northern hemisphere, winter in Australia occurs in mid-year.

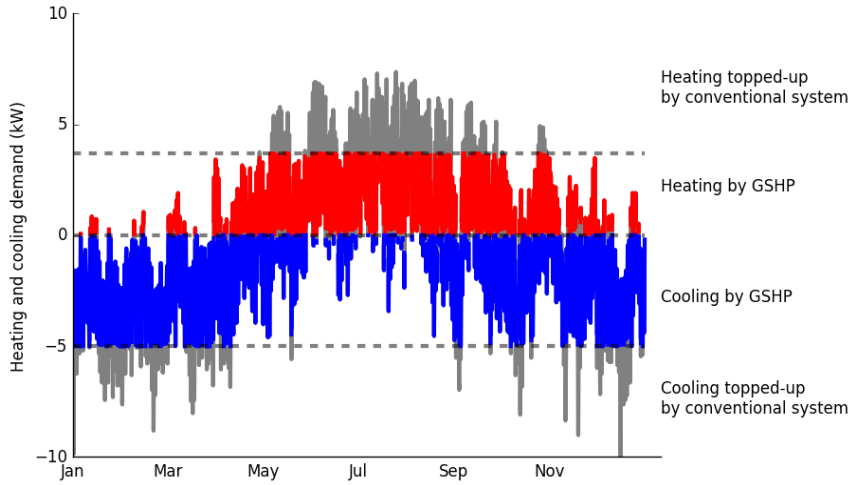

Figure 3 An example of a HGSHP in Sydney sized to meet 50% of peak heating and cooling power demands

This section explores financial benefits of HGSHP systems that are sized to achieve minimum NPC of these systems over 20 years life span. The optimisation of the HGSHP systems performed using the method described in Mikhaylova et al. (2016). The NPC is further normalised by the total amount of thermal energy provided to the buildings over 20 years to allow comparisons between the cities, which is expressed as the Total Normalised Cost (TNC) in A$/MWh.

$$TNC = \frac{NPC}{Total\ thermal\ energy\ provided\ by\ the\ system} \quad (3)$$

Two HGSHP systems are considered here, where HGSHP1 is a combination of GSHP and RCAC systems, while HGSHP2 is a combination of GSHP, RCAC, and gas furnace systems. For each HGSHP system, the TNC is calculated for heating and cooling shave factors from 0% to 100% with a step size of 2%. In these calculations, it is assumed that all input parameters are the same as stated in Table 2 to Table 4 and no additional costs arising from the complexity of installing hybrid systems over conventional systems since these costs could be minor for residential installations. This assumption may need to be revised for larger, more complex control of commercial systems.

As an example, Figure 4 presents the TNCs for HGSHP1 and HGSHP2 in Sydney. The bottom left corner of the plots represents 0% shave factor or, effectively, a conventional system. The top right corner of the plots represents a 100% shave factor or, effectively, a GSHP system. The points in between represent the calculated TNC

for different shave factor combinations of the HGSHP systems, where the TNCs are represented by contour lines. The lowest TNC is identified in the plot to indicate the most cost-effective shave factor combination for a HGSHP system where the system costs the least for a given amount of thermal energy produced. As discussed earlier, Sydney has a relatively balanced climate with a similar amount of heating and cooling energy required for a typical residential building. For this reason, both shave factors considerably influence the TNCs.

From Figure 4, the lowest TNC for HGSHP1 in Sydney is A$136/MWh where the GSHP system is designed to provide 62% and 54% of the peak heating and cooling power demands respectively (Figure 4a). This enables the GSHP system to meet around 88% of the thermal demand. For the same city, the lowest TNC for HGSHP2 is A$140/MWh, where the GSHP system is designed to provide 90% and 78% of the peak heating and cooling power demands respectively (Figure 4b). This enables the GSHP system to meet around 98% of the thermal demand. The plots in Figure 4 demonstrates that it is important to optimise HGSHP system sizing to maximise return on investment.

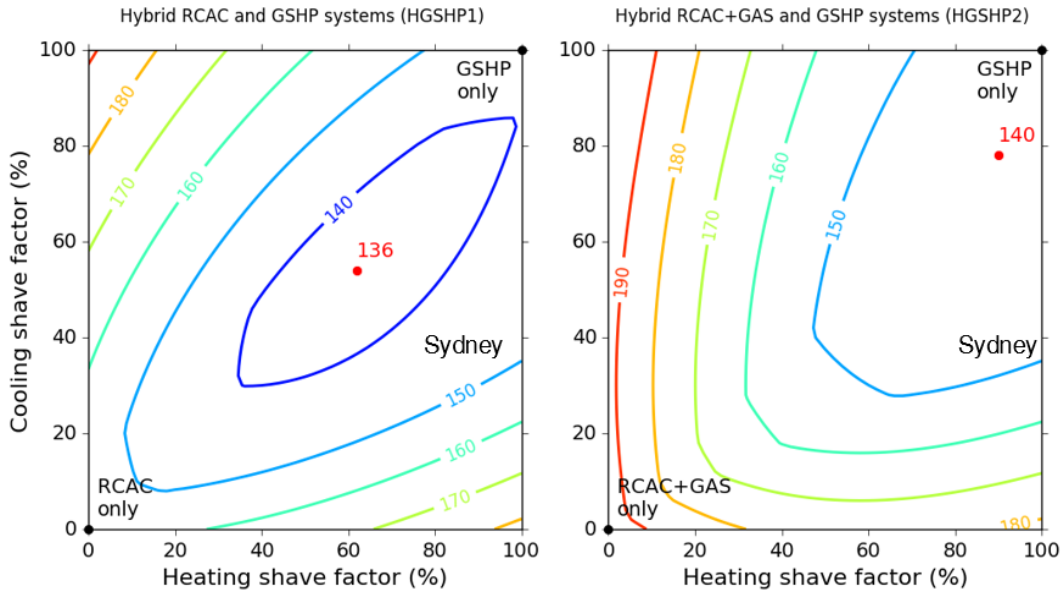

Figure 4 TNC values **in A$/MWh** of HGSHP1 (a) and HGSHP2 (b) systems for Sydney.

Figure 5 summarises the TNC calculations for all five heating and cooling options in the seven cities considered. For HGSHP systems, the TNCs values of optimised configurations (the lowest TNC) are shown. The figure also presents the TNC values normalised with respect to the TNC of GSHP systems in each city, shown as values above each column. A normalised TNC of 1 represents the TNC for GSHP systems in each city. If a normalised value of TNC is more than 1, the system's TNC is higher than the TNC of a GSHP system in the same city and vice versa.

The TNC for GSHP systems varies from A$127/MWh in Hobart to A$171/MWh in Adelaide. This suggests that 1 MWh of thermal energy supplied by a GSHP system over 20 years is the cheapest in Hobart and the most expensive in Adelaide. These results directly correlate with the unit costs of electricity in these cities (Table 4). Overall, the TNCs of GSHP systems are lower compared to conventional systems, in all cases except in Cairns.

For all locations, the TNC for both types of HGSHP systems are 1 to 10% lower than the TNCs of GSHP systems, which means that the hybrid systems are more financially beneficial than GSHP systems. However, the benefits may be relatively minor. Another observation is that the capital costs of hybrid systems are lower than the capital costs of GSHP systems, which is mainly due to the reduction in the required GHE length. This means that

hybrid systems can be more attractive than GSHP systems due to lower required initial investments which can be the primary motivation to install HGSHP systems over GSHP systems for some home owners.

In comparison to conventional systems, HGSHP systems can reduce TNC by up to 40% as shown by the HGSHP2 system in Hobart. It is important to note that unlike the GSHP system, a HGSHP system in Cairns has a lower TNC than a conventional system, where the TNC for HGSHP1 in Cairns is A$138/MWh compared to A$140/MWh for a conventional system. In this case, the hybrid system needs to be sized to meet 24% of the cooling peak load, assuming that the system does not require any heating in Cairns.

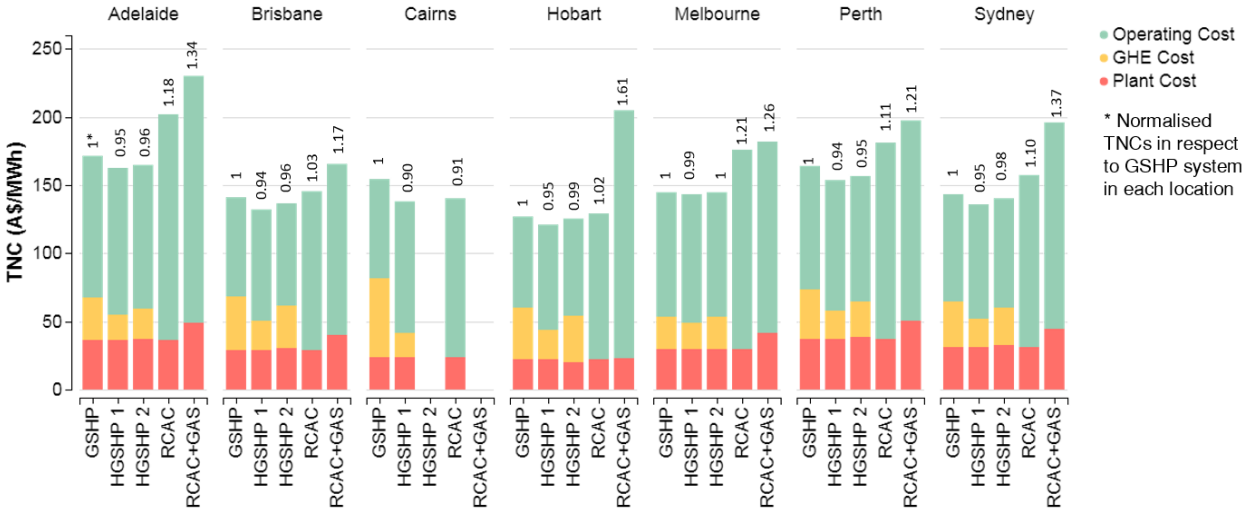

Figure 5 Lowest TNC in **A$/MWh** comparisons between HGSHP1, HGSHP2, GSHP and conventional systems

CONCLUSION

This paper has shown that ground source heat pump (GSHP) systems can have lower net present costs compared to conventional systems even with the high installation costs of the systems in Australia. Although for the specific cases considered, hybrid systems were only marginally cheaper than GSHP systems, they appear to have the potential to further reduce lifetime costs, particularly in cooling dominated climates. However, further detailed and/or sensitivity analyses are necessary. In a hybrid ground source heat pump (HGSHP) model, the GSHP systems provide the baseload thermal energy to buildings, which is topped up by conventional systems during the hotter and colder days of the year.

HGSHP systems can be more attractive than GSHP systems due to lower required initial investments. However, HGSHP systems need to be sized to maximise the financial investment return. This can be a complicated process where designers need to consider the climatic conditions, as well as the energy prices in the locations where the system is being installed. Adopting a HGSHP system in Australia can reduce the total normalised cost over 20 years life span of the systems by up to 10% and 62% compared to an equivalent sized GSHP and conventional systems respectively depending on location. With the wide range of climatic conditions considered, the new insights developed may be transferable to other parts of the world with similar climatic conditions.

ACKNOWLEDGMENTS

The authors appreciate the support of the Australian Research Council, The Victorian Government and The University of Melbourne.

REFERENCES

Alavy, M., Nguyen, H. V., Leong, W. H. & Dworkin, S. B., 2013, A methodology and computerized approach for optimizing hybrid ground source heat pump system design, *Renewable Energy* 57:404-412.

Aurora Energy, 2017, Energy and Gas Prices, See https://www.auroraenergy.com.au/your-home (accessed July 2017).

Australian Bureau of Statistics, 2014, 602.0.55.001 - Environmental Issues: Energy Use and Conservation, Mar 2014.

Bloom, E. F. & Tinjum, J. M., 2016, Fully Instrumented Life-Cycle Analyses for a Residential Geo-Exchange System, *Geo-Chicago 2016*, pp. 114-124.

Carslaw, H. S. & Jaeger, J. C., 1959, Conduction of heat in solids, *Oxford: Clarendon Press, 1959, 2nd ed.*

Hellström, G., 1991, Ground heat storage: thermal analyses of duct storage systems, Department of Mathematical Physics, Lund Univ.

Huang, S., 2015, Energy performance evaluation and optimisation of ground source heat pump systems, University of Wollongong.

IGSHPA, 2009, Ground Source Heat Pump Residential and Light Commercial Design and Installation Guide, Oklahoma State University, Stillwater, OK, USA.

Karytsas, S. & Choropanitis, I., 2017, Barriers against and actions towards renewable energy technologies diffusion: A Principal Component Analysis for residential ground source heat pump (GSHP) systems, *Renewable and Sustainable Energy Reviews* 78:252-271.

Liu, X. & Spitler, J., 2014, Performance of HVAC Systems at ASHRAE HQ, *ASHRAE Journal* 56(12):12.

Lu, Q., Narsilio, G. A., Aditya, G. R. & Johnston, I. W., 2017, Economic analysis of vertical ground source heat pump systems in Melbourne, *Energy* 125:107-117.

Meteonorm, 2017, Typical Meteorological Year, See http://www.meteonorm.com/ (accessed June 2017).

Michopoulos, A., Bozis, D., Kikidis, P., Papakostas, K. & Kyriakis, N., 2007, Three-years operation experience of a ground source heat pump system in Northern Greece, *Energy and Buildings* 39(3):328-334.

Mikhaylova, O., Choudhary, R., Soga, K. & Johnston, I. W., 2016, Benefits and optimisation of district hybrid ground source heat pump systems. In Energy Geotechnics.) CRC Press, pp. 535-541.

Nguyen, H. V., Law, Y. L. E., Alavy, M., Walsh, P. R., Leong, W. H. & Dworkin, S. B., 2014, An analysis of the factors affecting hybrid ground-source heat pump installation potential in North America, *Applied Energy* 125:28-38.

Origin Energy, 2017, Electricity and gas prices, See https://www.originenergy.com.au/for-home.html (accessed July 2017).

Philippe, M., Michel Bernier PhD, P. & Marchio, D., 2010, Sizing calculation spreadsheet: Vertical geothermal borefields, *ASHRAE Journal* 52(7):20.

Self, S. J., Reddy, B. V. & Rosen, M. A., 2013, Geothermal heat pump systems: Status review and comparison with other heating options, *Applied Energy* 101:341-348.

Synergy, 2017, Electricity and Gas Prices, See https://www.synergy.net.au/ (accessed July 2017).

Trillat-Berdal, V., Souyri, B. & Fraisse, G., 2006, Experimental study of a ground-coupled heat pump combined with thermal solar collectors, *Energy and Buildings* 38(12):1477-1484.

Wu, R., 2009, Energy efficiency technologies–air source heat pump vs. ground source heat pump, *Journal of Sustainable Development* 2(2):14.

[This page has been intentionally left blank]

IGSHPA SWEDEN
2018 Research Conference

DOI: 10.22488/okstate.18.000014

Seasonal performance assessment of a Dual Source Heat Pump system for heating, cooling and domestic hot water production

Antonio Cazorla-Marín **Carla Montagud** **José M. Corberán**
Javier Marchante-Avellaneda

ABSTRACT

In order to contribute to a global CO_2 emissions reduction in 2020, the increase in the use of highly efficient heat pumps for heating, cooling and domestic hot water production in buildings is very recommendable. In this direction, Ground Source Heat Pump (GSHP) systems are generally recognized as one of the most energy-efficient compared to air source heat pump systems. However, this strongly depends on the temperature evolution of the air and the ground during the year, which also depends on the geographical location of the system. Therefore, an optimal system from the energy point of view apparently would be the one that is able to switch from one source to the other in order to operate the heat pump with the highest efficiency.

In this context, a new Dual Source Heat Pump (DSHP) unit for heating, cooling and production of domestic hot water, was developed and manufactured in the framework of a H2020 European project called GEOTeCH (Geothermal Technology for €conomic Cooling and Heating). This paper presents the assessment of such a DSHP in different representative locations around Europe. For this purpose, an integrated system model in TRNSYS was developed to assess its performance for different thermal demand profiles obtained for the same building under different conditions.

INTRODUCTION

Achieving Europe's 2020 and 2050 targets on greenhouse gas emissions, will not only require a reduction in the energy demand, but also a more efficient energy use and a higher contribution of renewable energy technologies (European Technology Platform on Renewable Heating and Cooling 2013). Looking at the final global energy use, buildings are responsible for almost a third of the total amount (IEA 2011), becoming a very important source of CO_2 emissions. Particularly, in the European Union, buildings account for 40% of total energy use; and fairly half of this energy use corresponds to heating and cooling systems. Therefore, the introduction of highly efficient, reliable and affordable renewable heating and cooling systems in Europe becomes key to achieve on time the European Union's energy and climate objectives. This will mean the first step for a future decarbonisation in Europe. Ground source heat pump (GSHP) systems could positively contribute to this objective, as they are a renewable and efficient alternative to other conventional systems such as boilers that still imply the use of fossil fuels. However, they are still not competitive in terms of cost, especially in the South of Europe where the market of GSHP systems has not taken off yet. A strong

Antonio Cazorla-Marín (ancamar4@upvnet.upv.es), Carla Montagud, José Miguel Corberán and Javier Marchante-Avellaneda work at I.U.I.I.E. Universitat Politècnica de València

effort was made during the last years in order to improve their cost effectiveness. One of the most commonly used solutions consists of combining different types of sources into a hybrid energy system. An example can be found in the Geot€ch project 'GEOthermal Technology for economic Cooling and Heating' (European Commision 2015), a four year's duration project funded by the European commission within the H2020 program. One of the aims of the Geot€ch project is to develop system solutions that make the best use of hybrid heat pump and control technologies so that efficient replicable and comparative low cost"plug and play" whole systems for heating, cooling and domestic hot water (DHW), can be offered to the housing and small building market sectors. One of the core components of such 'plug and play' systems consists of an innovative dual source heat pump (DSHP), which is capable of making optimal use of ground or air environmental heat sources according to operating and climate conditions. For instance, it could happen that the air is a more advantageous source for the production of domestic hot water during the summer compared to the ground. Analogously, at the end of the winter after a long heat extraction period from the ground, the daily variation of the air temperature could make it more advantageous as a source compared to the ground. This innovative DSHP is a variable capacity (inverter compressor) reversible heat pump operating with R32 as refrigerant, with a nominal heating capacity of 8 kW and a constructive solution 'plug&play'. Further details of the heat pump design and operation can be found in (Corberán, et al. 2018). Thanks to the use of this innovative heat pump and the development of appropriate control strategies, not only the seasonal performance can be optimized but also the final cost of the installation can be reduced due to a lower amount of heat exchanged with the ground source heat exchanger (GSHE), and thus the need for less boreholes, reducing the investment cost significantly. This was highlighted in (Corberán, et al. 2018), where a first energy assessment was carried out for an office building located in the Netherlands. Results proved that the DSHP system would be able to reach a similar efficiency than the same unit operating as a GSHP, with half the ground source heat exchanger area needed, leading to a reduction in the investment cost up to 30%. This paper presents the energy assessment of the DSHP integrated system for heating, cooling and DHW production in an institutional type of building existing at the Universitat Politècnica de València, in Spain, which was constructed in the 1970s. This specific building was compeletely modelled in TRNSYS and validated against experimental data as a part of a GSHP system model of an existing installation that provides heating and cooling to several offices inside the building (Ruiz-Calvo, et al. 2017). The existing GSHP installation was built in the framework of the GeoCool project (European Commision 2003) and it was refurbished and optimized in the framework of the Ground-Med project (European Commision 2009). This is the main reason why it was the building considered for the energy assessement presented in this study. However, it should be noted that the DSHP analyzed is meant not only for renovation but also for new buildings. In order to carry out the assessment of such a DSHP system for the same type of building in different representative locations around Europe, the European regulation EU Reg. 811/2013 for energy labelling of space heaters, was considered. In such regulation, three reference locations are identified for colder, average and warmer climate conditions: Helsinki (Finland), Strasbourg (France) and Athens (Greece) respectively.However, the thermal demand of the building is not only affected by the climate conditions but also by the type of construction considered which is also influenced not only by the location but also by the age of the building. In order to account for this in the TRNSYS simulations carried out for the assessment, the building typology data base from the IEE European Project TABULA (Typology Approach for Building Stock Energy Assessment) (IEE 2009a) was considered for each of the representative locations considered in the energy assessment. This data base includes different building typologies for 13 European countries. Each national typology consists of a classification scheme grouping buildings according to their size, age and further parameters and a set of exemplary buildings representing the building types.

METHODOLOGY

Integrated system model in TRNSYS

A complete dynamic model was developed in TRNSYS. The model includes all the integrated system components: building thermal load, heat pump, ground loop including the GSHE, space heating and cooling (User

loop) and DHW hydraulic loops, all with their respective components such as pipes, circulation pumps, buffer tank and DHW tank. In order to model the control and operation of the system, a PID was included to set the frequency of the heat pump compressor, as well as other controllers to vary the frequency of the circulation pumps, and to control the temperature setpoint and on/off of the heat pump). A previous stage of this model was presented and analysed in (Corberán, et al. 2017) and (Ruiz-Calvo, et al. 2017). The model was prepared in a modular way, so that it allowed modifiying and adapting the components to different installations, as well as easily testing different optimization and control strategies. Regarding the heat pump, it consists of the innovative DSHP developed in the Geot€ch project. The DSHP system is capable of operating in eleven different operating modes, which are presented in Table 1.

Table 1. Heat pump and system operating modes (Corberán, et al. 2017)

	Condenser	Evaporator	Operating mode
SUMMER	Air	User	M1-Summer Air
	Ground	User	M2-Summer Ground
	--	--	M10-Free cooling
	DHW	User	M3-DHW User
	DHW	Air	M6-DHW Air
	DHW	Ground	M8-DHW Ground
	DHW	Air	M11-Free-cooling + DHW Air
WINTER	User	Air	M4-Winter Air
	User	Ground	M5-Winter Ground
	DHW	Air	M7-DHW Air
	DHW	Ground	M9-DHW Ground

As shown in Table 1, the DSHP is able to provide heating, cooling and DHW using two different sources (air or ground). Furthermore, when the return temperature from the ground loop is low enough to meet the thermal cooling demand, the system is able to work in free-cooling mode. For that purpose, the system includes an extra free-cooling heat exchanger. Additionally, in summer operating conditions, the DHSP is able to use the waste heat in the condenser to heat up the water in the DHW tank. This happens when there is both the need of cooling and DHW production and the operating mode M3-DHW User is used. This operating mode is also called by the DSHP manufacturer 'Full Recovery' operating mode. The DSHP was experimentally tested in the framework of the Geot€ch project under the different operating modes shown in Table 1. As the heat pump is the core of the system, a very accurate model is needed in order to make a fair assessment of its performance. Therefore, the authors decided to make their own TRNSYS type for modelling the heat pump. This way, the heat pump was modelled as a black box with polynomial correlations able to reproduce the heat pump performance under different operating conditions. It will depend not only on the source and load inlet temperature (Te_i and Tc_i, for the evaporator and condenser, respectively), but also on many other operating variables, such as the compressor frequency (f_{comp}), temperature difference in each heat exchanger (dTe and dTc) and fan frequency (f_{fan}). The correlations were tuned to experimental measurements and the influence of the variation of each operating variable was modelled with a maximum deviation of 5%. A detailed explanation of the DSHP model can be found in (Corberán, et al. 2017). Equations (1)–(3) provide the heat pump performance for the Winter Ground operating mode (M5), where $\dot{Q}_{cond}$ is the condenser capacity, $\dot{Q}_{evap}$ is the evaporator capacity, and $\dot{W}_{comp}$ is the compressor power input.

$$\dot{Q}_{cond} = f_{comp} \cdot (C_0 + C_1 \cdot Te_i + C_2 \cdot Tc_i + C_3 \cdot Te_i \cdot Tc_i + C_4 \cdot Te_i^2 + C_5 \cdot dTe + C_6 \cdot dTc + C_7 \cdot Te_i \cdot dTe + C_8 \cdot Tc_i \cdot dTc) \quad (1)$$

$$\dot{Q}_{evap} = f_{comp} \cdot (C_0 + C_1 \cdot Te_i + C_2 \cdot Tc_i + C_3 \cdot Te_i \cdot Tc_i + C_4 \cdot Te_i^2 + C_5 \cdot dTe + C_6 \cdot dTc + C_7 \cdot Te_i \cdot dTe + C_8 \cdot Tc_i \cdot dTc) \quad (2)$$

$$\dot{W}_{comp} = f_{comp} \cdot \left(C_0 + C_1 \cdot Te_i^2 + C_2 \cdot Tc_i^2 + C_3 \cdot dTe + C_4 \cdot dTc + C_5 \cdot Te_i \cdot dTe + C_6 \cdot f_{comp} \cdot Te_i + C_7 \cdot f_{comp} \cdot Tc_i + C_8 \cdot f_{comp}^2 \cdot Te_i \cdot Tc_i + C_9 \cdot f_{comp} \cdot dTe + C_{10} \cdot \frac{1}{f_{comp}} \right) \quad (3)$$

When the heat pump is operating with the air, the same polynomials were found to be adequate with the substitution of the temperature difference in the source heat exchanger, which is related to the brine flow rate in the ground mode, by the fan frequency.

Selection of the source/sink

In order to increase the seasonal performance of the system, it is key that the heat pump works under the most favourable conditions (air or ground source). For this purpose, a differential controller with hysteresis was implemented also to provide it with a stable type of control. Figure 1 shows this selection of the most favourable source (the colder in cooling mode and the hotter in heating and DHW mode).

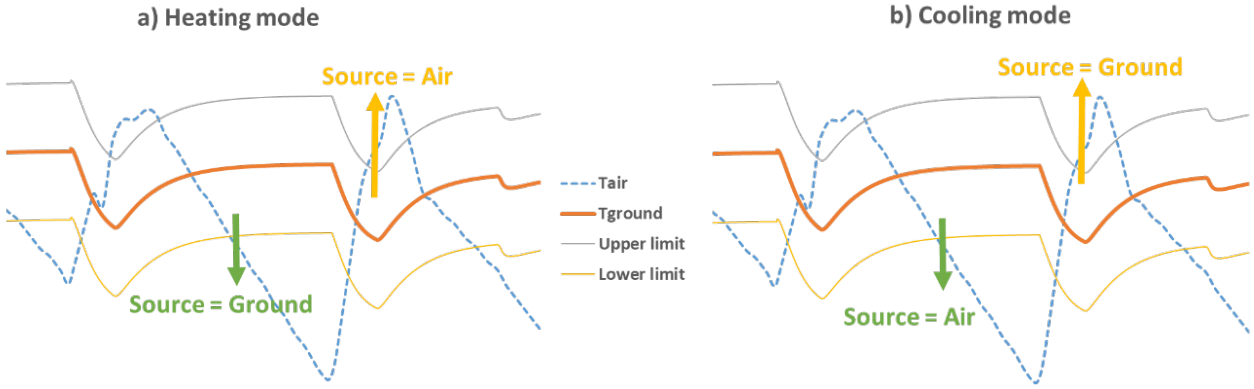

Figure 1 Selection of the source depending on the air and ground temperature: a) heating mode; b) cooling mode.

System performance indicators

The Seasonal Performance Factor (SPF) of the system was considered as the energy performance indicator for the energy assessment. The definition considered is the same as the one identified as SPF4 in the SEPEMO-build "SEasonal PErformance factor and MOnitoring for heat pump systems in the building sector" project (IEE 2009b).

$$SPF4 = \frac{\int_0^t (\dot{Q}_{USER} + \dot{Q}_{DHW}) \cdot dt}{\int_0^t (\dot{W}_{HP} + \dot{W}_{FAN} + \dot{W}_{BHE} + \dot{W}_{BACKUP} + \dot{W}_{USER} + \dot{W}_{DHW}) \cdot dt} \quad (4)$$

where $\dot{Q}$ is the useful heat in the user loop ($\dot{Q}_{USER}$) or DHW loop ($\dot{Q}_{DHW}$), and $\dot{W}$ is the power consumption of each of the components existing in the system (heat pump $\dot{W}_{HP}$, fan $\dot{W}_{FAN}$, borehole heat exchanger (BHE) circulation pump $\dot{W}_{BHE}$, user circulation pump $\dot{W}_{USER}$ and DHW circulation pump $\dot{W}_{DHW}$), including the back-up system electrical consumption $\dot{W}_{BACKUP}$ in case that there is any. The energy assessment will be carried out for one year of operation. So, the integration period will correspond to one year. Additionally, and in order to compare the use of the ground/air under different conditions, the amount of thermal energy provided by the heat pump in the different operating modes will be calculated.

System assessment in different locations

Building typology and thermal load calculation.

The thermal demand to be met by the system is modeled as a thermal load profile based on the building of the Applied Thermodynamics department of the Universitat Politècnica de València, in Spain. The building was built in the 70's. The air conditioned area (250 m^2 in total) corresponds to some of the department offices located on the second floor of the building. In order to compare the DSHP system operating under different climatological conditions, the thermal demand of this building has specifically been calculated for three different locations in Europe: Stockholm (Sweden), Strasbourg (France) and Athens (Greece) for the same type of building modelled in TRNSYS. These three locations were selected in order to follow the European regulation EU Reg. 811/2013 for energy labelling of space heaters. However, no data was available for Finland in the TABULA project. Alternatively, building construction information was found for Sweden. So, the authors decided to select Stockholm as the European city that stands for 'colder' climate conditions instead of Helsinki which is the city identified in the EU Reg. 811/2013. The reason for selecting Stockholm is that Sweden is a bordering country of Finland and the climate conditions are similar: the maximum, minimum and average temperatures in Helsinki are 24°C, -21°C and 4.7°C, respectively, while in the case of Stockholm, they are 28°C, -20°C and 5.3°C. Thanks to the building typology webtool provided by the TABULA project, it was possible to check the global heat transfer coefficient per unit area (U value expressed in (W/(m^2·K)) for the same type of building and the same construction year, in the three different European cities selected. According to the nomenclature used in the TABULA project data base, these U values were checked for the case of the existing building located in Valencia (Spain) and constructed in the 70's. It was found that they corresponded to a wall type Wall 1 (existing state) and a window type Window 1(usual refurbishment). Therefore, the U values considered correspond to Wall 1 and Window 1 type respectively for each one of the three cities identified in this study. Table 2 shows these values both for the building's envelope and the windows. As previously stated, the building considered in this study was previously modelled in TRNSYS, based on real data of occupancy, as a part of a GSHP system model of an existing installation with a total surface of around 250 m^2. The heating capacity of the installed heat pump is around 17 kW so, in order to adapt the thermal demand to the nominal capacity of the DSHP (8 kW) analysed in this research work for the different types of locations, only a 30% of the surface of the offices (around 75 m^2) was considered. Then, in order to account for the different types of construction existing in each location for the same type and same age of building, the U value of the building's envelope and windows were introduced in the building TRNSYS model, keeping the rest of the building parameters constant. The TRNSYS building model, adapted to the different locations by changing the U-values, was simulated for a whole year under the corresponding weather conditions, obtaining the required thermal loads in order to maintain the comfort conditions inside the conditioned area. Table 2 shows the peak heating and cooling demand of the whole year, together with the seasonal and yearly thermal demand required. Finally, the climatic weather data was considered for each different city extracted from the weather database Meteonorm (Meteotest 1981) and simulated in TRNSYS for a year. Table 3 shows the maximum, minimum and average ambient temperatures for each city considered in the study.

Table 2. Thermal parameters in the different locations

Location	Athens	Strasbourg	Stockholm
U building envelope/windows (W/m^{2}K)	2.2/3.20	0.78/1.40	0.41/0.9
Peak heating/cooling (kW)	6.1/4.8	9.2/2.1	11.7/0
Heating/cooling demand (kWh)	3565/3262	7766/514	11491/0
Yearly thermal demand (kWh)	6827	8280	11491
Summer period	02/05 - 22/10	18/06 - 10/09	-

Moreover, another parameter that is specific for each city and that will affect the performance of the installation is the

type of soil. Table 3 shows the main thermal properties of the soil that will affect the ground source heat exchanger performance in each location.

Table 3. Locations parameters

Location	Athens	Strasbourg	Stockholm
Maximum/Minimum/Average ambient temperature (°C)	38/0/17.6	32/(-11)/9.8	28/(-20)/5.3
Ground thermal conductivity (W/(m·K))	3.75	1	3.75
Ground volumetric thermal capacitance (kJ/(m^3·K))	1250	1250	1250

The values of the ground thermal properties appearing in Table 3 were obtained as a result of the work carried out in the framework of the GEOT€CH project (Tinti, et al. 2018), considering the thickness of the sediment layers existing in each location and the thermal properties of sediments and bedrock.

Operation parameters. The DSHP system performance has been analysed for three cities in Europe: Strasbourg (average climate), Athens (warmer climate) and Stockholm (colder climate). For this purpose, the integrated system model in TRNSYS has been adapted to the different locations, but keeping the same installation. Therefore, all the components and the main control parameters of the systems are the same for the three locations:

- Schedules: building climate conditioning: from 6 a.m. to 10 p.m., DHW production: 4 a.m. to 6 a.m.
- Comfort temperature in the offices: 23 °C, both for heating and cooling.
- Occupancy of the building, based on the real schedule of the professors that work in the offices.
- DHW demand: profile corresponding to an office of five people (equivalent to the occupancy of those five offices considered for the calculation of the thermal demand of the building).
- BHEs field: Four coaxial BHEs, 50 meters deep each. The borehole field was dimensioned for that location with the highest thermal load and it was kept the same for the three locations.
- Same components size: heat pump (nominal capacity 8 kW), hydraulic loops, buffer tank (150 litres), DHW tank (300 litres), circulation pumps.
- The temperature of the water supply is a function of the annual average ambient temperature: 20% larger in summer conditions and 20% lower in winter conditions.

In addition, the main parameters of the system that will vary from one location to the other are the thermal load profile, the heating (winter) and cooling (summer) period, the ambient temperature and the ground thermal properties, due to differences in the climatological and geological conditions of the locations. These main differences are summarized in Table 2 and Table 3.

ASSESSMENT RESULTS

In order to assess the behavior of the DSHP system operating under different climatic conditions, the integrated system model in TRNSYS has been adapted to the three cities (Athens, Strasbourg and Stockholm). For this purpose, the thermal demand of the building in each location has been considered, as well as the climatic and geological characteristics of each site, summarized in Table 2 and Table3. An annual simulation was carried out for each location, with a time step of 1 minute. The total thermal energy provided by the system was calculated for each operating mode, as well as the SPF4. Figure 2 shows the thermal energy provided by the heat pump in each different operating mode as a percentage of the total energy provided by the heat pump all over the year for every location. The total thermal energy provided by the heat pump in each location is shown in Table 4 for building climate conditioning (M1-M5 and M10), and DHW production (M6-M9). From Figure 2, it can be extracted that the most used source/sink in Athens is the ground (95%). Due to the warm climate, the ground is most of the time more favourable for providing both heating and cooling to the building, because the ground temperature is closer to the comfort temperature (average return temperature from the ground is 17.8 °C) than the air temperature. Here, the use of the heat pump for providing heating and cooling is quite balanced (51% of heating and 43% of cooling of the total energy provided), compared to the other

locations, where the heating is the prevailing operating mode. Regarding Strasbourg, it has a very low cooling demand, and it can be met by the free-cooling loop (6% of the total energy), this happens due to the mild summer and the low return temperatures from the ground. The energy provided using the air as a source is the 27% of the total energy. In the case of Stockholm, as it has no cooling demand, all the energy provided by the heat pump is used to provide heating and DHW during the winter, and only DHW during the summer. The most used source is the ground (78%).

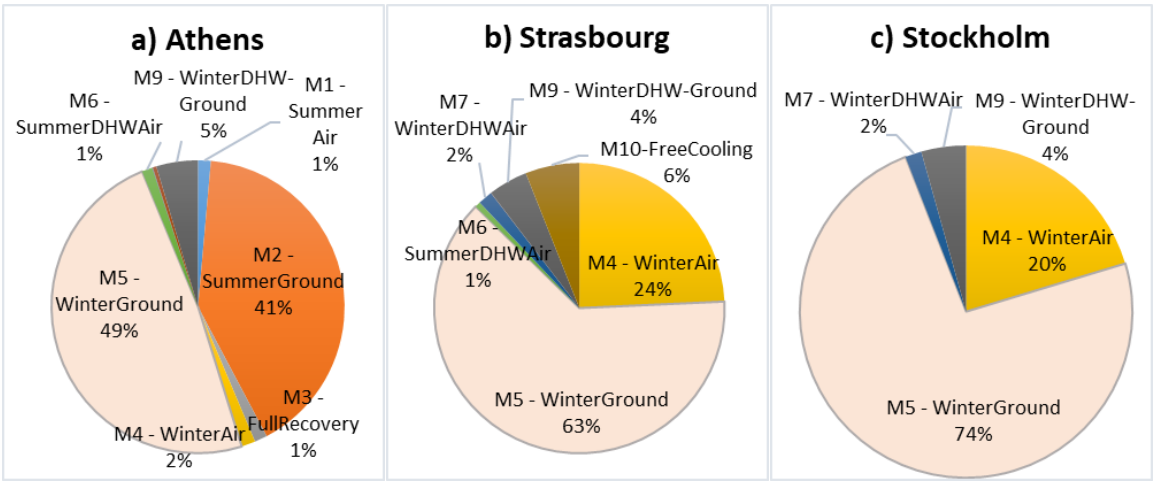

Figure 2 Percentage of the thermal energy provided by the heat pump in the different operating modes for each location: a) Athens; b) Strasbourg; c) Stockholm.

Table 4. Total energy and fluid return temperature from the ground

Location	Athens	Strasbourg	Stockholm
Total building climate conditioning / DHW energy (kWh)	7344 / 488	8913 / 634	12243 / 772
Maximum/Minimum/Average return temperature from the ground (°C)	25.1/10.3/17.8	15.1/(-4.4)/6.6	10.6/(-3.8)/3.5

It can be seen in Table 4 that the energy provided to the user for the building climate conditioning of the building by the heat pump and free-cooling heat exchanger is around a 7% higher than the yearly thermal demand shown in Table 2. This difference is due to the thermal losses in the pipes and the buffer tank. Regarding the DHW energy provided by the heat pump, it is higher in the colder locations, mainly due the colder water coming from the net to the tank. In Table 4 it is also possible to see the influence of the ground properties in the fluid temperature coming from the ground, the minimum return temperature is lower in Strasbourg (-4.4°C) than in Stockholm (-3.8°C), despite the fact that Stockholm has a colder climate. This is due to the low ground thermal conductivity in Strasbourg (1 W/(m·K)), which makes the local ground temperature decrease to a higher degree due to a lower heat transfer effectiveness in the ground source heat exchanger. Regarding the SPF4, it was calculated for each location and it is shown in Figure 3.

Figure 3 System Seasonal Performance Factor (SPF4) for the three locations

As shown in Figure 3, SPF4 values are rather low compared to standard GSHP systems already existing in the market. This is mainly because the DSHP considered in this study, is still a prototype that works with an innovative refrigerant (R32) for which the compressor available in the market is not optimized yet, leading to a lower performance.

As described in (Corberán, et al. 2018), the DSHP prototype has a better performance in cooling mode than in heating mode (up to 40% better SPF4 in the case of Amsterdam) . In the case of Athens, the SPF4 in summer operating conditions shown in Figure 3 is around a 50% higher than that of winter conditions. Regarding the performance during the summer season in Strasbourg, the heat pump system provides air conditioning only by free-cooling, but also produces a higher fraction of DHW, leading to a lower summer SPF4. Concerning the SPF4 in winter, it is higher in Athens (3.4), mainly due to the use of the ground as a source and the higher return temperature from the ground than in the other locations. In Strasbourg and Stockholm, the SPF4 is quite similar, due to the fact that their operating mode share (M4/M5) is similar and the return temperatures from the ground are also similar. Taking a look at the results, it could be concluded that the higher the number of hours that the system runs in heating mode and for DHW production, the more similar will be the yearly SPF4 to the one corresponding to winter conditions. As the heat pump performance is less efficient in heating mode than in cooling mode, the SPF4 will be lower for heating dominated areas. Given that Athens is the location with a higher cooling demand, it is expected that the yearly SPF4 is the largest as shown in Figure 3. Regarding the dual source concept, it is concluded that the use of a DSHP is not recommended for warmer locations like Athens, where the heat pump works most of the time using the ground, as it is a more favourable source/sink. However, in colder locations like Strasbourg or Stockholm, the air is used for more than 20% of the energy production, so the use of a DSHP could lead to a reduction in the BHEs size and then, a lower investment.

CONCLUSION

An energy assessment of a dual source heat pump (DSHP) system was carried out with the help of an integrated system model in TRNSYS for the same type of building located at three different locations in Europe: Athens (warm climate), Strasbourg (average climate) and Stockholm (cold climate). The studied DSHP was developed in the GEOTeCH European project with the aim of selecting the most favorable source/sink (air or ground) depending on their temperatures and leading to a reduction in the size of the BHE field needed with a consequent reduction in the initial cost of the installation. A yearly simulation of the system operation was carried out in TRNSYS for each location and the main performance indicators were calculated. It was concluded that the higher the running hours in heating mode and for DHW production, the lower the yearly performance factor (SPF4) of the system. Therefore, the SPF4 will be lower for heating dominated areas. Given that Athens is the location with a higher cooling demand, the yearly SPF4 obtained was the largest taking values up to 25% larger than that of the other heating dominated areas like Strasbourg and Stockholm. Regarding the use of the air or ground as a source, it was concluded that the use of a DSHP is not recommended for cooling dominated areas like Athens (warm climate), as the air is only used to provide a 4% of the total thermal energy demand. On the other hand, in the case of Strasbourg and Stockholm (average and cold climate), the air is used as a source to provide more than 20% of the thermal energy demand. Therefore, the use of a DSHP will be an attractive alternative compared to a standard ground source heat pump in this type of climatic conditions (average and cold climate), as it would allow taking advantage of the two sources, leading to a smaller size of the BHE field needed and a consequent lower investment.

ACKNOWLEDGMENTS

The present work has been supported by the European Community Horizon 2020 Program for European Research and Technological Development (2014-2020) inside the framework of the project 656889 – GEOTeCH (Geothermal Technology for Economic Cooling and Heating), by the Generalitat Valenciana inside the program "Ayudas para la contratación de personal investigador en formación de carácter predoctoral (ACIF/2016/131)" and by the Ministerio de Educación, Cultura y Derporte inside the program "Formación de Profesorado Universitario (FPU15/03476)".

REFERENCES

Corberán JM, Cazorla A, Marchante J, Montagud C and Masip X. 2017. *Modelling and energy analysis of a dual source heat pump system in an office building*. 16th International Conference on Sustainable Energy Technologies – SET 2017. Bologna, Italy. July 17-20.

Corberán, J. M., Cazorla-Marin A., Marchante-Avellaneda, J. and Montagud, C. 2018. *Dual Source Heat Pump, a High Efficiency and Cost-Effective Alternative for Heating, Cooling and DHW Production*. International Journal of Low-Carbon Technologies. Available online at: https://doi.org/10.1093/ijlct/cty008.

European Commision. 2003. GeoCool (Geothermal Heat Pump for Cooling and Heating along European Coastal Areas) (EU 5th Framework Programme, NNE5-2001-00847). Available online at: http://cordis.europa.eu/project/rcn/86940_en.html.

European Commision. 2009. GROUND-MED (Advanced Ground Source Heat Pump Systems for Heating and Cooling in Mediterranean climate) (TREN/FP7EN/218895). Available online at: http://groundmed.eu/.

European Commision. 2015. GEOTeCH (Geothermal Technology for €conomic Cooling and Heating) (H2020-LCE-2014-2, GEOTeCH-656889). Available online at: http://www.geotech-project.eu/.

European Technology Platform on Renewable Heating and Cooling. 2013. Strategic Research and Innovation Agenda for Renewable Heating & Cooling. Secretariat of the RHC-Platform, Brussels.

IEA. 2011. Technology Roadmap: Energy-Efficient Buildings: Heating and Cooling Equipment. Technical report. Paris, France. IEA Publications.

IEE. 2009a. TABULA (Typology Approach for Building Stock Energy Assessment). Available online at: http://episcope.eu/iee-project/tabula/.

IEE. 2009b. SEPEMO-Build (SEasonal PErformance Factor and MOnitoring for Heat Pump Systems in the Building Sector). (IEE/08/776/SI2.529222). Available online at: http://sepemo.ehpa.org/.

Meteotest. 1981. Meteonorm. Available online at: http://www.meteonorm.com.

Ruiz-Calvo, F., Montagud, C., Cazorla-Marín, A. and Corberán, J.M. 2017. *Development and Experimental Validation of a TRNSYS Dynamic Tool for Design and Energy Optimization of Ground Source Heat Pump Systems*. Energies 10: 1510.

Tinti, F., Kasmaee, S., Elkarmoty, M., Bonduà, S. and Bortolotti, V. 2018. *Suitability Evaluation of Specific Shallow Geothermal Technologies Using a GIS-Based Multi Criteria Decision Analysis Implementing the Analytic Hierarchic Process*. Energies 11(2): 457-478. Available online at: http://www.mdpi.com/1996-1073/11/2/457.

[This page has been intentionally left blank]

IGSHPA SWEDEN 2018 Research Conference

DOI: 10.22488/okstate.18.000048

Comparison of Two Simplified Approaches for Ground Temperature Estimations in Australia

Lu Xing Cuncun Mao Zhou Yu Olga Mikhaylova Pingfang Hu

ABSTRACT

Developing an accurate and practical method for ground temperature estimations are critical for the ground source heat pump system design and energy calculation procedures. In Australia, Baggs' method is a common procedure for ground temperatures predictions as a function of depth and time of year. Xing and Spitler developed a new procedure for ground temperature estimations for engineering applications at 4112 sites worldwide. This new procedure considers the variations of surface cover conditions (bare soil, vegetated, asphalt or concrete), effects of snow cover and soil freezing or melting. These important factors, which significantly affect the ground temperature results accuracy either are neglected or are simplified in Baggs' method. In this paper, we selected 6 sites in Australia which belongs to two climates: warm climates and arid or dry summer climates. Xing and Spitler's method and Baggs' method are used respectively to calculate the ground temperatures at depths of 10cm, 20cm, 50cm and 100cm. Calculation results of two methods are both compared to the 3-14 years of measurement results at the 6 sites and validation results are discussed and investigated. Results demonstrate the Xing and Spitler's method averaged root mean square error (RMSE) is 2.2°C of the 6 sites; Baggs' method averaged RMSE is 3.4°C of the 6 sites. This paper presents a new and improved procedure for ground temperature estimations in Australia. It enables a more accurate design of the ground heat exchangers so as to reduce the capital cost of the installed ground source heat pump systems.

Key words: Ground source heat pump system Ground temperatures World wide dataset

INTRODUCTION

Estimations of undisturbed ground temperatures are quite important and are required in building design load calculations, building energy calculations, ground heat exchangers design and energy analyses of district heating and cooling systems. As house envelopes become better insulated and tighter, the heat transfer to/from the foundation becomes more important. Although losses to the ground are currently neglected for cooling load calculations, it is possible that it will be advantageous to include the heat loss in the future. Beyond foundation heat transfer, undisturbed ground temperatures are also used in the design of vertical and horizontal ground heat exchangers and district heating and cooling systems.

Dr. Lu Xing (lxing@hust.edu.cn) is an assistant professor of Energy & Power Engineering; Prof. Pingfang Hu (pingfanghu@hust.edu.cn) is of Environmental Science & Engineering, Huazhong University of Sci. & Tech., China
Dr. Olga Mikhalova (olga.mikhaylova@unimelb.edu.au) is a research fellow of Geotechnical Engineering, University of Melbourne, Australia

Although the soil temperature predictions in the subsurface are of great importance for design of ground heat exchangers in the GSHP system, soil temperature data available for engineering applications are limited. There are two types of approaches used for estimating ground temperature: numerical method and analytical method. Numerical models account for such phenomena such as moisture transport, soil freezing or melting, snow cover at the ground surface, but these models are computationally intensive and time consuming. Analytical models require less computational time and are thus more convenient for engineering applications.

In the United States, the commonly used analytical approach is the one-harmonic model first proposed by Fourier (1822, as cited by Narasimhan 2010). The model relies on three parameters - annual average ground temperature, annual amplitude of ground temperature at the surface and the phase angle to estimate the ground temperatures. The average undisturbed ground temperature and annual amplitude of surface temperature variation are read from very small maps for the continental US (Figure 17 of Chapter 34 of the 2011 ASHRAE Handbook - HVAC Applications) or North America (Figure 13 of Chapter 18 of the 2013 ASHRAE Handbook - Fundamentals). ASHRAE published a district heating manual (ASHRAE 2013b) which also uses one-harmonic model to estimate the undisturbed ground temperatures. This is done for all 5564 weather stations world-wide listed in Chapter 14 of 2009 ASHRAE Handbook - Fundamentals. More details of the commonly used method in the U.S. are given in Xing and Spitler (2016b).

Xing and Spitler developed a new procedure – two harmonic model for ground temperature estimations at 4112 stations world-wide (Xing et al. 2016). The model mainly depends on five parameters: annual average ground temperature, two temperature amplitude, two phase lags. Xing and Spitler utilized world-wide measured weather data and a numerical model to calculate ground temperatures; the calculated results are used for generating the five parameters of the two harmonic model. The new procedure considers various surface cover conditions, such as asphalt, concrete, vegetated, etc. It considers snow cover and soil freezing or melting effects.

We used Xing and Spitler procedure, ASHRAE Handbook procedure and ASHRAE district heating manual procedure to predict ground temperatures at 19 sites located in three climates in the U.S.: warm climates, snow climates and arid or dry summer climates. The predicted ground temperatures are compared to the measured results; mean root mean square error (RMSEs) of 19 sites are summarized. It is found that the using Xing and Spitler procedure is 1.4°C, ASHRAE Handbook procedure and ASHRAE district heating manual procedure RMSEs are 2.6°C and 2.5°C respectively. The study results of the 19 sites in the U.S. shows that previous ASHRAE procedures work well in warm climates, the model accuracy obviously drops in the cold climates and arid or dry summer climates.

In order to demonstrate the undisturbed ground temperature estimations is a key factor which greatly affects the design length of the ground heat exchanger piping in the in ground source heat pump (GSHP) systems, consequently, the system cost. Xing et al. (2017) presents the impact of Xing and Spitler model development on the horizontal ground heat exchanger (HGHX) design. 12 geographically diverse sites in United States with three different HGHX configurations were studied. For each site, HGHX design length using the Xing and Spitler model estimated ground temperatures as inputs are compared to design results based on measured ground temperatures; the calculated HGHX design length percentage error are within ±18.9%. The calculated HGHX design length percentage error using previous common methods for ground temperature estimations in United States are much higher which are within ±38.3% and ±57.7% respectively.

Since ground temperature estimations are critical for design of ground heat exchangers in the GSHP systems, in this paper, we studied the widely applied model of ground temperature prediction in Australia - Baggs' model (1982) and compared it to Xing and Spitler method. The Baggs' formula depends on 3 parameters: annual average ground

temperature, the soil surface temperature amplitude, and the phase angle. To obtain the annual average ground temperature, Baggs developed a map that shows the geographical distribution of a temperature differential which relates annual average ground temperature to annual average air temperature. The map was developed which used long-term ground temperature records from 20 sample sites scattered throughout 5 states of Australia. Baggs' method assumes the ground is either bare soil or covered by vegetation, it doesn't consider other ground surface conditions such as covered by concrete or asphalt etc. It neglects the snow cover, rainfall and soil freezing and melting effects and assumes there is a simplified differential correlation between the ground temperatures and the air temperatures.

Both Xing and Spitler's method and Baggs' method are developed procedures for ground temperature estimations; Baggs' method is built based on more simplified assumptions than Xing and Spitler's method. In this paper, we evaluated two methods' performances basesd on case study results. 6 sites located in 2 climates: arid or dry summer climates and warm climates in Australia are chosen for the case study. The soil temperatures at depths of 10cm, 20cm, 50cm and 100cm are calculated respectively using the Xing and Spitler's method and Baggs' method. The results were compared with the 3-14 year measurements at the 6 sites to analyze the accuracy of the two methods.

METHODOLOGIES

6 sites in Australia have been chosen for the parametric study. These sites belong to 2 climates: warm climates and arid or dry summer climates. The geographical names and climate zones of the chosen sites are shown in Table 1, the geographical locations are shown in Figure 1.

Measured weather data and measured ground temperature data are obtained from the Australian Bureau of Meteorology website: http://www.bom.gov.au. There are 284 temperature-monitoring sites, these data have been screened according to the different monitoring quality of each site (monitoring duration, monitoring frequency, monitoring accuracy, monitoring depth) and 6 sites are finally chosen.

Table 1. Six Parametric Study Sites in Australia

Climate zone	States	Site name	Köppen-Geiger Climate type	Latitude and longitude (° , °)
Arid or dry summer climates	Queensland	Longreach aero	Bsh	-23.43,144.28
	Western Australia	Geraldton airport	Csa	-28.80.114.70
		Perth airport	Csa	-31.93,115.95
	South Australia	Adelaide (Kent town)	Csb	-34.92,138.62
Warm climates	New South Wales	Wagga wagga amo	Cfa	-35.17,147.45
		Canberra airport	Cfb	-35.30,149.20

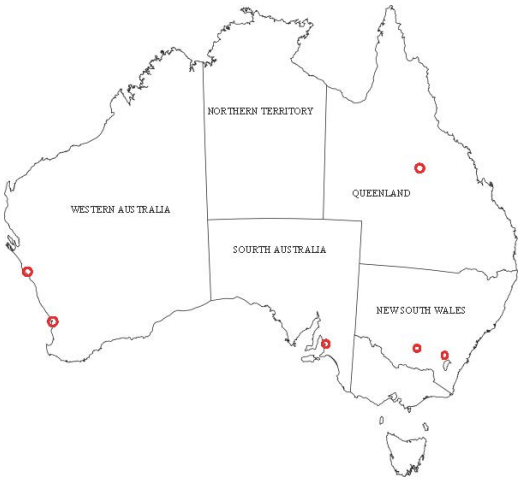

Figure 1 Six parametric study sites in Australia

Xing and Spitler's method

Xing and Spitler developed a two-harmonic analytical model that considers variations of ground cover conditions, the effects of snow cover, soil freezing and melting. The model depends on five parameters: annual average ground temperature, two temperature amplitudes, two phase lags. In Equation 1, these five parameter values are estimated using the computed results from a numerical model (Xing and Spitler 2016a, Xing and Spitler 2016b, Xing et al. 2016). The inputs to the numerical models are weather files including air temperatures, solar radiation, relative humidity, wind speed, rainfall, dew point temperature:

$$T_s(z,\ t) = T_{s,avg} - \sum_{n=1}^{2} e^{-z\sqrt{\frac{n\pi}{\alpha_s t_p}}} \cdot T_{s,amplitude,n} \cos\left[\frac{2\pi n}{t_p}(t - PL_n) - z\sqrt{\frac{n\pi}{\alpha_s t_p}}\right] \quad (1)$$

Where:

$T_s(z,t)$ is the undisturbed soil temperature at the depth of and time of the year, in ℃ or ℉;

z is the soil depth, in m or ft;

t is the time of year, starting from January 1st, in days;

t_p is the period of soil temperature cycle (365), in days;

α_s is the soil diffusivity, in m2/day or ft2/day;

$T_{s,avg}$ is the annual average ground temperature, in ℃ or ℉;

$T_{s,amplitude,n}$ is the nth order temperature amplitude, when n=1, it is the annual temperature amplitude at the ground surface, equal to half of the difference between the maximum and minimum monthly average temperatures at the ground surface in a year, in ℃ or ℉;

PL_n is the nth phase lag of the ground temperature cycle, in days.

Baggs' method

Baggs revised the Labs's model for ground temperature estimations (1982) by considering the variation of vegetation covers into the model, as shown in Equation 2. Equation 2 relies on five parameters k_v, $T_{a,avg}$, $\Delta T_{s,a}$, $T_{a,amplitude,1}$ and PL_1 to predict ground temperatures. Baggs found that at 10 meters depth, there was a certain mathematical relationship between annual average ground temperature and annual average air temperature. He presented a map for $\Delta T_{s,a}$ according to the data of 20 sample sites scattered throughout 5 states of Australia:

$$T_s(z,\ t) = \left(T_{a,avg} \pm \Delta T_{s,a}\right) + 1.07 k_v T_{a,amplitude,1} e^{-0.00316 z\sqrt{\frac{1}{\alpha_s}}} \times$$
$$\cos\left[\frac{2\pi}{365}\left(t - PL_1 - 0.1834 z\sqrt{\frac{1}{\alpha_s}}\right)\right] \quad (2)$$

Where:

$\Delta T_{s,a}$ is the difference of annual average ground temperature and annual average air temperature, in ℃ or ℉;

$T_{a,avg} \pm \Delta T_{s,a}$ is the annual average ground temperature, in ℃;

k_v is the vegetation coefficient, $k_v = 1$ for bare ground, $k_v = 0.22$ for year-round full vegetation cover;

$T_{a,amplitude,1}$ is the half of difference of the maximum monthly average air temperature and the minimum monthly average air temperature, in K or ℉;

PL_1 is the phase of air temperature wave, number of days in which the annual maximum air temperature, in days.

RESULTS AND DISCUSSION

The five Xing and Spitler' method parameters: annual average soil surface temperature, two temperature amplitudes and two phase angles for the six sites are presented in Table 2. The five Baggs' method parameters are shown in Table 3.

Xing and Spitler's model results and Baggs' model results at the depths of 10cm, 20cm, 50cm and 100cm are calculated. The calculated results are compared with the measured ground temperatures of 3-14 years in 6 sites, model RMSEs at 10cm, 100cm and averaged model RMSEs of four depths are calculated and presented in Figures 2, 3 and 4. The RMSE results are grouped into two climates: arid or dry summer climates, warm climates. Results demonstrate the Xing and Spitler's method averaged RMSE is 2.2°C of the 6 sites; Baggs' method averaged RMSE is 3.4°C of the 6 sites.

Table 2. Xing and Spitler' Method Parameters

Climate zone	Site	$T_{s,avg}$ (℃)	$T_{s,amplitude,1}$ (℃)	PL_1 (day)	$T_{s,amplitude,2}$ (℃)	PL_2 (day)
Arid or dry summer climates	Longreach aero	29.0	-8.1	7.9	1.2	7.9
	Geraldton airport	23.5	-6.3	23.4	0.2	34.7
	Perth airport	21.6	-7.3	20.8	0.1	8.9
	Adelaide (Kent town)	20.9	-7.9	19.9	-0.8	58.4
Warm climates	Wagga wagga amo	17.3	-7.3	23.7	0.3	0.9
	Canberra airport	16.1	-7.7	22.8	0.4	1.4

Table 3. Baggs' Method Parameters

Climate type	Site	$T_{s,avg}$ (℃)	$T_{a,amplitude,1}$ (℃)	PL_1 (day)	$T_{s,avg}=T_{a,avg}+\Delta T_{s,a}$		k_v
					$T_{a,avg}$	$\Delta T_{s,a}$	
Arid or dry summer climates	Longreach aero	26.9	7.8	362.0	23.9	3.0	1.0
	Geraldton airport	21.7	5.5	25.0	18.2	3.5	1.0
	Perth airport	21.5	5.5	57.0	18.0	3.5	1.0
	Adelaide (Kent town)	19.5	6.5	44.0	17.0	2.5	1.0
Warm climates	Wagga wagga amo	15.9	8.3	4.0	15.1	0.8	1.0
	Canberra airport	13.2	7.4	4.0	12.8	0.4	1.0

As shown in Figure 2, Xing and Spitler model RMSEs at 10cm depths are within 1.3-3.2°C, Baggs model RMSEs are within 2.4-4.5°C, about 0.4-2.4°C differences in RMSEs for different sites. Xing and Spitler consider variation of vegetation covers, effects of snow cover and soil freezing or melting. Baggs' method is developed based on relatively simplified assumptions. The value of $\Delta T_{s,a}$ in the Baggs' formula is semi-empirical. It is read from a map developed only based on the data of 20 sample sites scattered throughout five states of Australia. Moreover, Baggs method relies on the value of k_v associated with the given map of $\Delta T_{s,a}$, the value is set to 1.0 by default which means the surface coverage of all areas is bare soil, this may cause errors in the calculation results.

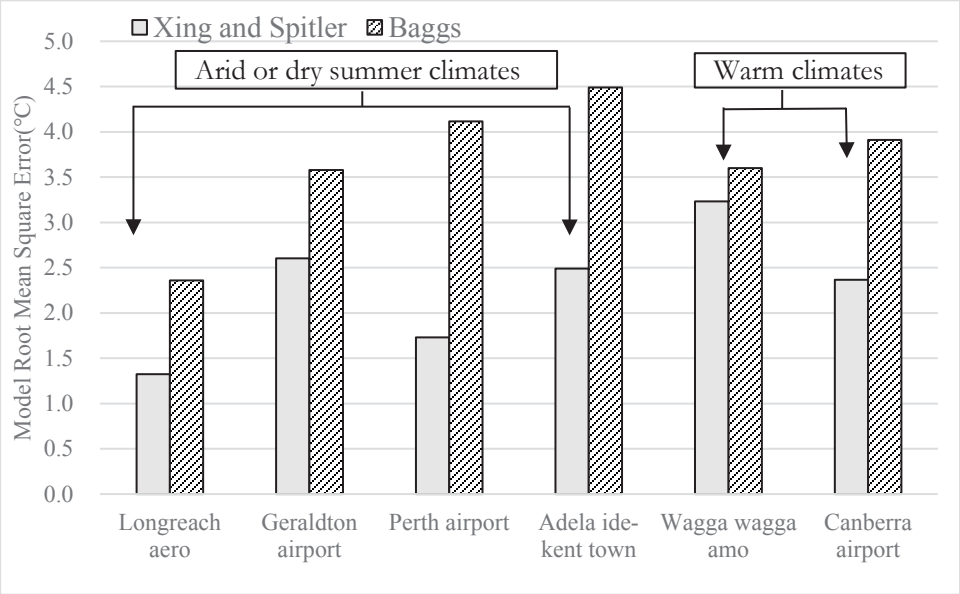

Figure 2 Xing and Spitler's method and Baggs' method RMSEs at 10cm depths for 6 sites

Similar results could be observed in Figures 3 and 4. In Figure 3, Xing and Spitler model RMSEs at 100cm depths are within 1.6-3.3°C, Baggs model RMSEs are within 1.2-3.7°C, about 0.2-1.7°C differences in RMSEs for different sites. In Figure 4, Xing and Spitler model' average RMSEs at 6 sites are within 1.6-3.9°C, Baggs model RMSEs are within 1.8-3.9°C, about 0.2-2.1°C differences in RMSEs. There is one site Wagga wagga amo located in New South Wales states and warm climates has a relatively higher RMSEs. We checked the vegetation coverage in the area but found that this does not explain this phenomenon. We speculate that this may be related to the actual surface coverage of the area, such as the length of the local vegetation. More detailed reasons need to be studied later.

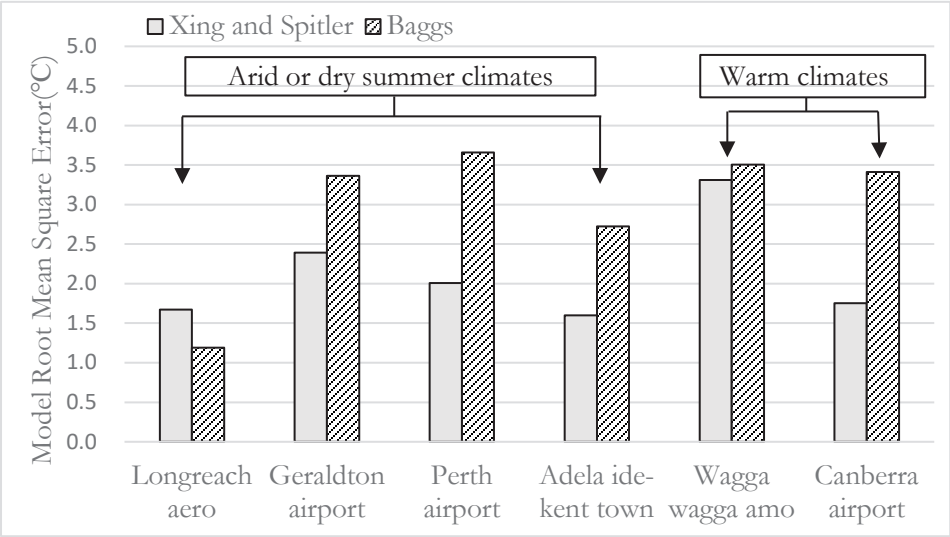

Figure 3 Xing and Spitler's method and Baggs' method RMSEs at 100cm depths for 6 sites

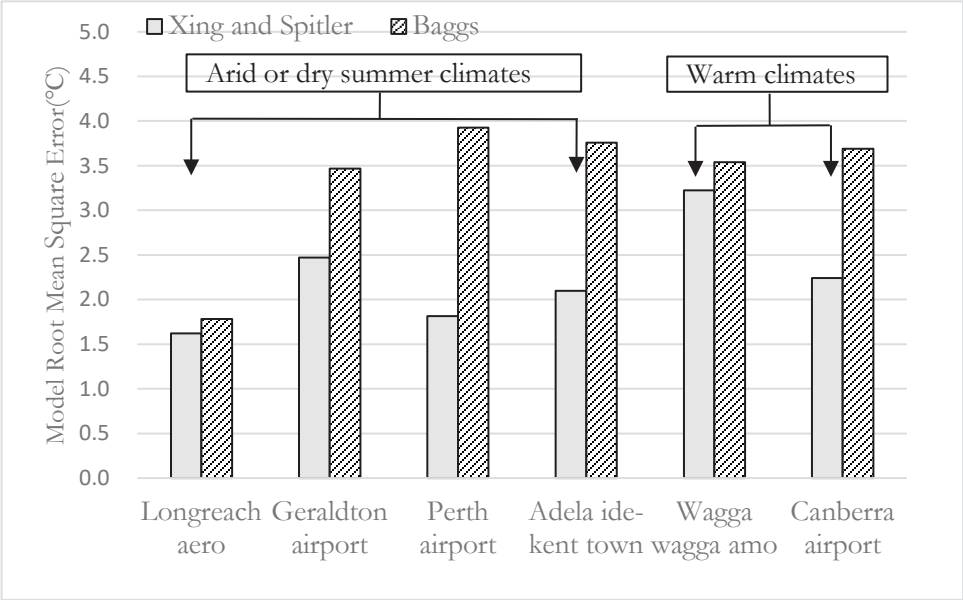

Figure 4 Xing and Spitler's method and Baggs' method averaged RMSEs at four depths for 6 sites

CONCLUSION

In this paper, two simplified approaches – Xing and Spitler's method, Baggs' method of ground temperatures estimations have been studied. 6 sites located in two climates in Australia: arid or dry summer climates and warm climates have been chosen for the validation and comparison study. The ground temperatures at 10cm, 20cm, 50cm and 100cm depths are calculated utilizing Xing and Spitler's method and Baggs' method. The simulation results are compared with the measured temperature and RMSEs are summarized. It is found that averaged RMSEs of Xing and Spitler's method at four depths is 2.2°C of the 6 sites; averaged RMSEs of Baggs' method at four depths is 3.4°C of the 6 sites. The Xing and Spitler's method considers variation of vegetation covers, effects of snow cover and soil freezing or melting. Baggs model is developed based on simplified assumptions. The value of $\Delta T_{s,a}$ in the Baggs' formula is semi-empirical, based on a map developed according to the data of 20 sample sites scattered throughout five states of Australia. Moreover, the value of k_v associated with the given map of $\Delta T_{s,a}$ is set to 1.0 by default which means the surface coverage of all areas is bare soil, this may cause higher errors in the calculation results.

ACKNOWLEDGMENTS

The authors of this publication gratefully acknowledge Dr. Jeffrey D. Spitler, regent professor from Mechanical and Aerospace Engineering, Oklahoma State University, United States for his support in this research.

REFERENCES

ASHRAE. 2011. ASHRAE Handbook-Heating Ventilating and Air Conditioning Applications. *Atlanta: ASHRAE*.

ASHRAE. 2013a. ASHRAE Handbook-Fundamentals. *Atlanta: ASHRAE*.

ASHRAE. 2013b. District Heating Guide. *Atlana: ASHRAE*.

Fourier, J. 1822. Theorie Analytique de la Chaleur (print in English in 1878, Analytical Theory of Heat). *Paries: Firmin Diot Pere et Fils*.

Baggs, S. 1982. Remote Prediction of Ground Temperature in Australian Soils and Mapping its Distribution. *Solar Energy*. 351-366

Labs, K. 1982. Regional analysis of ground and above-ground climate conclusion. Underground Space 7. 37-65.

Xing, L. and J. D. Spitler. 2016a. Prediction of undisturbed ground temperature using analytical and numerical modeling. Part Ⅰ: Model development and experimental validation. *Science and Technology for the Built Environment*. 787-808.

Xing, L. and J. D. Spitler. 2016b. Prediction of undisturbed ground temperature using analytical and numerical modeling. Part Ⅱ: Methodology for developing a world-wide dataset. *Science and Technology for the Built Environment*. 809-825.

Xing, L. J. D. Spitler and Arkasama Bandyopadhyay. 2016. Prediction of undisturbed ground temperature using analytical and numerical modeling. Part Ⅲ: Experimental validation of a world-wide dataset. *Science and Technology for the Built Environment*. 826-842.

Xing, L., J. D. Spitler, L.H. Li and P.F. Hu. 2016. A model for ground temperature estimations and its impact on horizontal ground heat exchanger design. *IGSHPA Technical/Research Conference and Expo* Denver March 14-16.

IGSHPA SWEDEN 2018 Research Conference

DOI: 10.22488/okstate.18.000041

A virtual borehole for thermal response test unit calibration: Test facility and concept development

Parham Eslami Nejad **Messaoud Badache** **Alexia Corcoran** **Michel Bernier**

ABSTRACT

Precise calculation of the borehole length requires good estimation of the ground thermal conductivity. In practice, the ground thermal conductivity is measured in-situ at a specific location using what is referred to as a thermal response test (TRT) unit. This paper presents a novel virtual borehole (VB) concept for calibrating TRT units. The VB replaces a real borehole with an above-ground compact heat exchanger and a chiller unit to mimic the thermal behavior of the ground with a user-set virtual ground thermal conductivity. In an attempt to develop the VB concept, three control scenarios are examined to emulate the ground thermal response for different thermal conductivity values. A test bench was built at the CanmetENERGY-Varennes research laboratory to validate the VB concept experimentally. A test is performed to calibrate a commercially available TRT unit for a thermal conductivity value of 3 W m^{-1} K^{-1}. The TRT unit connected to the VB reported a value of 3.18 W m^{-1} K^{-1} representing a 6% error.

INTRODUCTION

Ground source heat pump (GSHP) systems are receiving significant interests due to energy efficiency. However, to design them correctly, thermal properties of the ground where the ground heat exchangers (GHE) are installed, must be estimated precisely. Ground thermal conductivity (k), borehole thermal resistance and the undisturbed ground temperature (UGT) are among the most important parameters for design and are commonly estimated from in-situ thermal response tests (TRT) (Gehlin 1998). During a TRT, a constant and known thermal load is injected into the GHE and accurate measurements of the time history of the inlet and outlet fluid temperatures are recorded. The ground thermal conductivity is then deduced from these measured values.

Thermal response tests include the measuring period and the subsequent data analysis. The latter requires a relatively precise GHE mathematical model. The accuracy of the model has a major impact on the thermal conductivity value reported by the TRT units.

Different models have been used to evaluate the experimental data obtained from TRTs. Most models are based on either analytical approaches or numerical methods. Complete reviews of various analytical and numerical models have recently been presented (Rees 2016; Spitler and Gehlin 2015). In brief, the modeling of the GHE has undergone many improvements since it was first suggested in 1983 by Mogensen (Mogensen 1983). Starting from the infinite line source (ILS) model (Sharqawy, et al. 2009), the infinite cylinder source (ICS) model (Eskilson 1986), the finite line source (FLS) model (Bandos, et al. 2011) going to more complex two and three-dimensional numerical models by Bozzoli, et al. (2011) and Marcotte and Pasquier (2008). TRT result analysis is based on the ILS and ICS

Parham Eslami Neajad (parham.eslaminejad@canada.ca) and Messaoud Badache are research scientists at CanmetENERGY Natural Resources Canada. Alexia Corcoran was an intern at CanmetENRGY during this study and a graduate student at Polytechnique Montréal. Michel Bernier is a professor in the Mechanical Engineering Department at Polytechnique Montréal.

models that represent relatively simple and rapid methods for estimating the ground thermal properties. However, numerical approaches are more accurate and can capture more complex phenomena in the ground, such as ground water movement and variable heat injection and fluid mass flow rates. For instance, Bandos, et al. (2011) proposed a correction method to account for heat losses to the ambient, Sass and Lehr (2011) account for ground water advection while other studies (Beier and Smith 2003; Choi and Ooka 2015) improved the analysis by using multi-injection rate thermal response tests.

Concerning the TRT unit itself, significant improvements have been achieved since the design proposed by Mogensen (1983) including mobile TRT units allowing both heat injection and extraction. Some TRT units deviate from the standard approach and use different measurement techniques to perform a TRT. For instance, Raymond, et al. (2015) proposed to use a heating cable without supplying any flow to the GHE; Witte, et al. (2000a) proposed a telemetry system; Acuña and Palm (2013) used a distributed ground temperature measurement technique using optical fiber; and Rohner, et al. (2005) proposed downhole measurements using light submersible wireless probes.

Although research and development on TRT units has evolved significantly, conventional TRT units are still widely used in the industry. Individual measurements (temperature, flow rate, power input) inside the TRT unit are often calibrated. There has also been past attempts to perform round-robin testing of some TRT units. However, there is no method to calibrate a particular unit as a whole, including the data analaysis. The virtual borehole concept presented here proposes to simulate the behavior of a ground heat exchanger to calibrate TRT devices with user-selected ground thermal conductivities.

VIRTUAL BOREHOLE CONCEPT

In a TRT unit, several measuring devices are used to collect the required data including fluid mass flow rate and inlet and outlet fluid temperatures to the borehole. These data are typically used in conjunction with a one-dimensional heat transfer model (ILS for example) for evaluating the thermal conductivity of the ground. Both measurements and result interpretation introduce uncertainties in the process.

The VB proposed here is shown in Figure 1. It consists of a compact heat exchanger and a cooling unit. The TRT unit to be calibrated is connected to the VB as it would be to a borehole in an in-situ TRT. The chiller and compact heat exchanger are carefully controlled using a pre-defined control scenario to mimic the thermal behavior of the ground heat exchanger. In other words, the VB creates a thermal condition for the TRT unit to react thermally just like if it were connected to a real borehole located in a medium with a known ground thermal conductivity.

The control unit reduces the mass flow rate (using a 3-way mixing valve) or/and increases the temperature of the cooling loop to increase the average temperature of the heating loop (on the TRT side) over time exactly as it would happen during a real test. The thermal conductivity value interpreted by the TRT unit is then compared against the value set by the control unit.

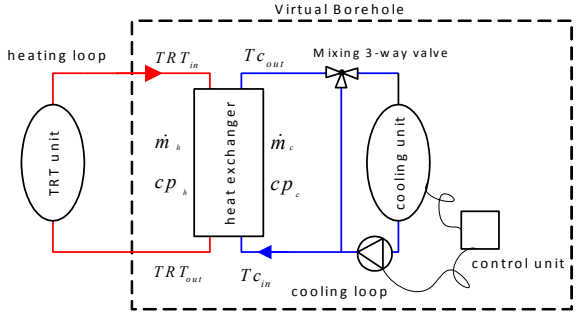

Figure 1: Virtual Borehole (VB)

GOVERNING EQUATIONS

The heat exchanger shown in Figure 1 is thermally insulated. Thus, it is assumed that the amount of heat injected from the heating loop is equal to the amount of heat removed by the cooling loop. It is further assumed that the rate of heat injection and mass flow rate of the TRT unit are constant.

Heating loop

The heat exchange rate on the heating side of the VB is calculated using the following equation.

$$q_{TRT} = \dot{m}_h \times cp_h \times \underbrace{\left(TRT_{in}(t) - TRT_{out}(t)\right)}_{\Delta T_{TRT}} \xrightarrow{\dot{m}_h \text{ and } q_{TRT} \approx \text{const}} \Delta T_{TRT} \approx const \quad (1)$$

where $TRT_{in}(t)$ and $TRT_{out}(t)$ are, respectively, the fluid temperatures at the inlet and outlet of the heat exchanger in the heating loop, $\dot{m}_h$ and cp_h are the mass flow rate and specific heat of the fluid circulating inside the heating loop, and q_{TRT} is the amount of heat injected into the heat exchanger by the TRT unit.

Cooling loop

The heat exchange rate on the cooling side of the VB is calculated using the following equation.

$$q_{cooling} = \dot{m}_c(t) \times cp_c \times \left(TC_{out}(t) - TC_{in}(t)\right) \quad (2)$$

where $TC_{in}(t)$ and $TC_{out}(t)$ are, respectively, the fluid temperatures at the inlet and outlet of the heat exchanger in the cooling loop, and $\dot{m}_c$ and cp_c are the mass flow rate and specific heat of the fluid circulating inside the cooling loop. Given that heat losses from the compact heat exchanger are negligible:

$$q_{TRT} = q_{cooling} = q \quad (3)$$

Heat exchanger

Any type of heat exchanger can be used between the cooling unit and the TRT device as long as it can be precisely modeled using either an analytical model or an experimentaly-derived performance map. In the present study, a plate heat exchanger is used and it's efficiency is quantified experimentally for different test conditions. Based on the effectiveness-NTU method, the heat transfer rate from the heat exchanger is given by:

$$q = \varepsilon \times (\dot{m} \times cp)_{\min} \times (TRT_{in} - TC_{in})$$
$$(\dot{m} \times cp)_{\min} = (\dot{m} \times cp)_h \quad (4)$$

It is assumed that the fluids in both loops are the same (pure water) and that the minimum fluid capacity ($\dot{m} \times cp$) always occurs in the cooling loop.

Borehole model

A so-called TRC (Thermal Resistance Capacitance) model developed in the TRNSYS environment is used to generate the time evolution of TRT_{in} in equation 4. The transient behavior inside the borehole is modeled using a resistance-capacitance approach (Godefroy and Bernier, 2014) while the analytical solution of the infinite cylinder source is used on the outside of the borehole. The TRC model used in the present study has been validated by comparison with the results of a thermal response test (Chiasson and O'Connell 2011). In this validation, the model reproduced the measured fluid temperatures with an average deviation of 0.12 °C.

CONTROL SCENARIOS AND PRELIMINARY CALCULATIONS

Depending on the control scenario used, either the mass flow rate, the fluid temperatures or both can be varied to mimic the thermal response of the ground. In this paper, three senarios are presented.

Scenario #1: Constant $\dot{m}_c$

In this scenario, the fluid mass flow rate in the cooling loop remains essentially constant. Therefore, the heat exchanger efficiency variation is negligible. However, marginal changes in the fluid specific heat and heat exchanger efficiency due to temperature changes can still be taken into account for calculating TC_{in}. The value of TRT_{in} calculated using the borehole model is substituted in Equation (4). Therefore, the time evolution of TC_{in} is simply calculated as follows:

$$TC_{in}(t) = TRT_{in}(t) - \frac{q}{\varepsilon \times (\dot{m} \times cp)_c} \quad (5)$$

The calculated TC_{in} profile (Equation 5) is given to the control unit in order to be reproduced using the chiller. Since this control scenario is less complicated to implement, it is used later in this paper.

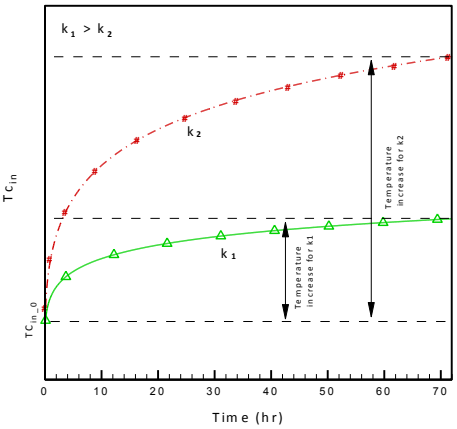

Figure 2: Qualitative change in TC_{in} for scenario #1

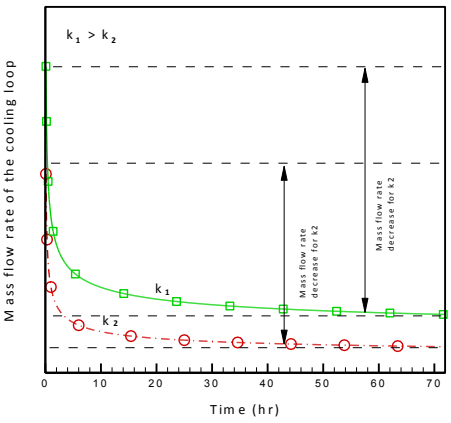

Figure 3: Qualitative change in cooling loop mass flow rate for scenario #2

Figure 2 presents the qualitative change in TC_{in} required to reproduce the ground thermal response under constant heat injection by the TRT unit for two thermal conductivity values k_1 and k_2 (k_1>k_2). The temperature increase range presented in the figure depends on the heat injection rate, borehole dimensions, preset ground thermal properties, heat exchanger performance and mass flow rate of the cooling loop. As shown in figure 2, high ground thermal conductivities lead to smaller TC_{in} increases. Also, during the first 10 hours, the TC_{in} increase is steep for both thermal conductivities. This rate of increase has to be handled by the control unit.

Scenario #2: Constant TC_{in}

For the second scenario, it is assumed that the chiller and control unit are able to supply a constant fluid temperature at the inlet of the compact heat exchanger during the test. However, the mass flow rate of the fluid in the cooling loop ($\dot{m}_c$) has to be reduced over time (and is always lower than the one in the heating loop) to increase the mean temperature of the heating loop under the constant heat injection rate of the TRT unit. This scenario is more complex to handle experimentally as the reduction in the mass flow rate is relatively steep. Furthermore, the compact heat exchanger efficiency changes during the test because of flow rate changes. These efficiency variations have to be evaluated beforehand in a separate test. Similar to scenario #1, the calculated TRT_{in} profile supplied by the borehole model is substituted in Equation (4). An iterative approach is used to calculate the fluid mass flow rate of the cooling loop at every time step based on TRT_{in} and the heat exchanger efficiency variation with time:

$$(\dot{m} \times cp)_c(t) = \frac{q}{(TRT_{in}(t) - TC_{in}) \times \varepsilon(t)} \quad (6)$$

$$TC_{in} = \text{constant}$$

The time evolution of $(\dot{m} \times c_p)_c$ (Equation 6) and the constant value of TC_{in} are reproduced by the control unit by acting on the chiller and the 3-way valve. Assuming that the fluid specific heat remains constant during the test, Figure 3 presents the qualitative evolution of the fluid mass flow rate of the cooling loop required to reproduce the ground thermal response for two thermal conductivity values k_1 and k_2 ($k_1 > k_2$). The mass flow rate change in the first few hours is relatively steep and the control unit might have difficulties in following this trend. The range of the mass flow rate reduction depends on the heat injection rate, borehole dimensions, preset ground thermal properties and heat exchanger performance.

Scenario #3: Hybrid

A "Hybrid" scenario can be envisioned to diminish the relatively steep temperature and mass flow rate variations in scenario #1 and #2 occuring at the beginning of the test. In scenario#3, either the temperature or the mass flow rate of the cooling loop changes linearly for a certain period of time (t_0) and then remains constant throughout the rest of the test. With this approach, the other parameter (e.g. temperature if the mass flow varies linearly) changes less steeply and the increase/decrease range is less significant. Decrease patterns other than the linear one used here could also be selected to facilitate the control of the other parameter.

$$(\dot{m} \times cp)_c(t) = \frac{q}{(TRT_{in}(t) - TC_{in}(t)) \times \varepsilon(t)} \quad (7a)$$

$$TC_{in}(t) = \begin{cases} at + b & t < t_0 \quad (a \text{ and } b \text{ are arbitrary parameters}) \\ \text{constant} & t \geq t_0 \end{cases}$$

or

$$TC_{in}(t) = TRT_{in}(t) - \frac{q}{\varepsilon(t) \times (\dot{m} \times cp)_c(t)} \quad (7b)$$

$$(\dot{m} \times cp)_c(t) = \begin{cases} ct + d & t < t_0 \quad (c \text{ and } d \text{ are arbitrary parameters}) \\ \text{constant} & t \geq t_0 \end{cases}$$

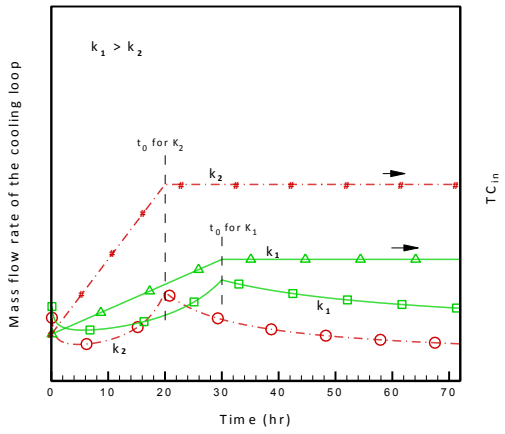

Figure 4: Qualitative change in $\dot{m}_c$ for scenario #3 under linear TC_{in} increase

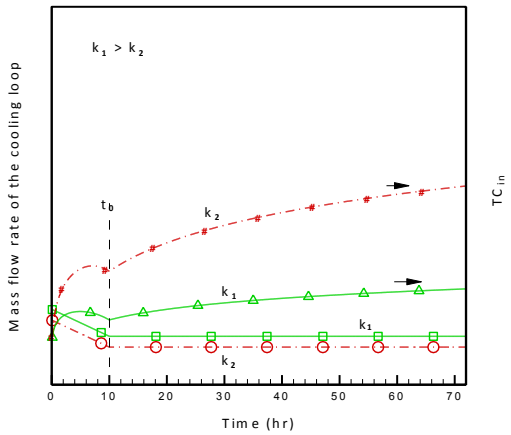

Figure 5: Qualitative change in TC_{in} for scenario #3 under linear $\dot{m}_c$ decrease

Similar to the other scenarios, the time evolution of $(\dot{m}_c \times c_p)$ and the time evolution of TC_{in} (Equation 7a and 7b) are given and reproduced by the chiller and the control unit. Figure 4 and Figure 5 present the qualitative time

evolution of $\dot{m}_c$ and TC_{in} for two cases: Linear TC_{in} increase (Figure 4) and linear mass flow rate decrease (Figure 5). The change in the TC_{in} and $\dot{m}_c$ values at the beginning of the test is not as sharp as those presented in Figures 2 and 3, respectively. Therefore, as shown in Figures 4 and 5, scenario #3 results in lower range variations of parameters than scenario #1 and #2 which might facilitate the operation of the control unit.

EXPERIMENTAL SETUP AND TEST PROCEDURE

Experimental setup

A VB test bench was built at the CanmetENERGY-Varennes research laboratory. The complete system is presented schematically in Figure 6. The main components of this facility include: a commercially-available TRT unit (4 kW heating capacity), a plate heat exchanger (PHE) and a chiller unit. The test facility is fully equipped with different measuring devices including temperature sensors (RTDs and thermopiles) and flow meters. As shown in Figure 6, four RTD probes measure the inlet and outlet temperatures to the PHE (TRT_{in}, TRT_{out}, TC_{in} and TC_{out}). Two thermopiles are also used to measure the temperature differences for each water loop. Loop flow rates ($\dot{m}_h$ and $\dot{m}_c$) are measured using Coriolis mass flowmeters. Specifications of the devices and measuring instruments used on the test bench are listed in Table 1. Data are recorded using a conventional data acquisition system.

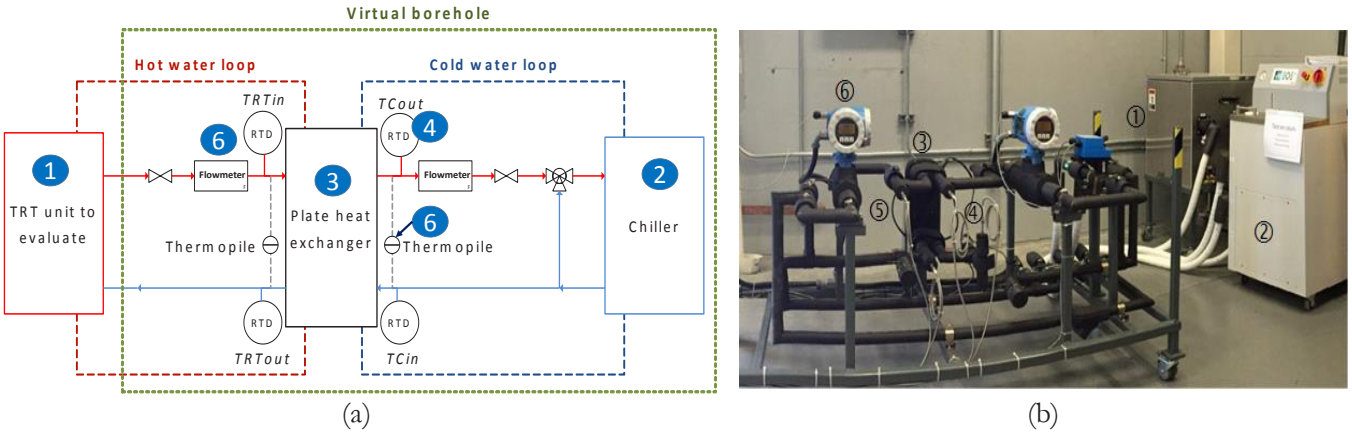

Figure 6: Virtual borehole test bench

Test procedure

As indicated earlier, the test bench is operated based on Scenario #1. The VB sequences of operation are:

- Step 1: Use the TRC model to calculate TRT_{in} as a function of time for a given set of borehole dimensions, preset ground properties, heat injection rate and TRT mass flow rate.
- Step 2: Calculate the TC_{in} evolution (Equation 5) to be reproduced by the chiller and the control unit. In this step, TC_{in} is calculated beforehand according to the plate heat exchanger efficiency, the mass flow rate of the cooling loop and the calculated TRT_{in}.
- Step 3: Set the temperature in the cooling loop by controlling the chiller outlet water temperature to follow precisely the pre-calculated TC_{in}. This is accomplished using a control unit integrated within the chiller.
- Step 4: Start both the TRT unit and the chiller. Then, the TRT loop measures the mean temperature in the heating loop (TRT_m).
- Step 5: Compare the thermal conductivity value reported by the TRT with the one selected by the user on the VB unit.

Table 1. Devices and measuring instruments used in the VB test bench

Items	Numbers (Figure 6)	Function	Technical specification	Uncertainty
TRT unit	①	Heat injection and water pumping in the hot water loop	4 kW heating capacity	
Chiller	②	Heat extraction and water pumping in the cold water loop	5 kW cooling capacity at 0 °C	
PHE	③	Heat transfer area	0.74 m^2	
RTD	④	Temperature measurement	Pt100	±0.2
Thermopile	⑤	Temperature differential measurement		
Flowmeter	⑥	Mass flow measurement	Coriolis flowmeter	±0.2%

TRT UNIT CALIBRATION

In this section, a commercially available TRT unit is evaluated by the VB test bench. The VB is set to reproduce a ground thermal conductivity of 3.0 $Wm^{-1}K^{-1}$. The parameters used for the test are shown in Table 2. The heat exchanger efficiency was evaluated experimentally according to the TC_{in} temperature range of the test and the mass flow rates. A heat injection rate of 4 kW is used in the TRC model simulation since this value is used by the TRT unit.

The time evolution of the mean fluid temperatures on the TRT side and the chiller outlet water temperature (TC_{in}) are obtained from the TRC model and from the heat exchanger model, respectively. To start the test, the flowrates are set to 0.2 kg/s in both loops, the calculated TC_{in} profile (Figure 7) is set on the chiller and then the TRT unit heat injection (4 kW) is started.

Table 2. Parameters used for the TRT unit calibration

		Test
	Injected heat (W)	4000
Hypothetical borehole dimensions and ground and grout thermal properties	Borehole length (m)	80
	Borehole diameter (m)	0.089
	Pipe outer diameter (m)	0.0267
	Pipe inner diameter (m)	0.0218
	Shank spacing (m)	0.0137
	Ground thermal conductivity ($W\,m^{-1}\,K^{-1}$)	3.0
	Ground thermal capacitance ($kJ\,m^{-3}\,K^{-1}$)	2415
	Grout thermal conductivity ($W\,m^{-1}\,K^{-1}$)	1.73
	Grout thermal capacitance ($kJ\,m^{-3}\,K^{-1}$)	1500
	Pipe thermal conductivity ($W\,m^{-1}\,K^{-1}$)	0.43
	Undisturbed ground temperature (°C)	10
	Experimentally calculated heat exchanger efficiency (-)	0.60
	Cooling and heating loops mass flow rates (kg/s)	0.2

Figure 7 presents the time evolution of the TC_{in} calculated using the plate heat exchanger model and the values reproduced using the chiller. It is shown that the chiller is able to reproduce TC_{in} with very good precision.

Figure 8 shows the time evolutions of the measured TRT_m on the VB and the corresponding value predicted by the TRC model for a ground thermal conductivity of 3.0 $Wm^{-1}K^{-1}$. As shown in Figure 8, the time evolution of TRT_m obtained on the virtual borehole is very similar to that given by the TRC model. The maximum deviation between the curves is 0.4°C and the mean deviation is 0.07°C. The maximum deviation occurs 6 minutes after the start of the test when the rate of change in the chiller outlet temperature is the highest. After that, the temperature of the hot water

loop approaches the one predicted by the TRC model and the gap between the curves decreases.

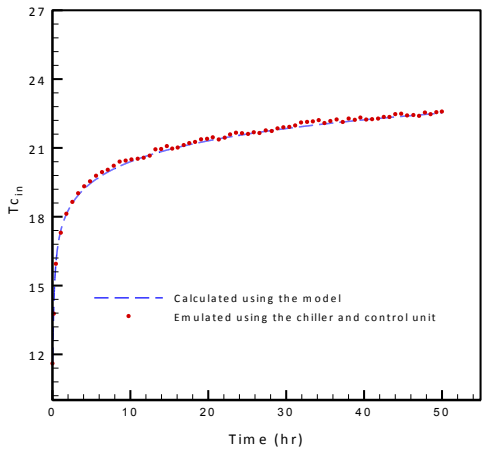

Figure 7: Calculated and measured TC_{in}

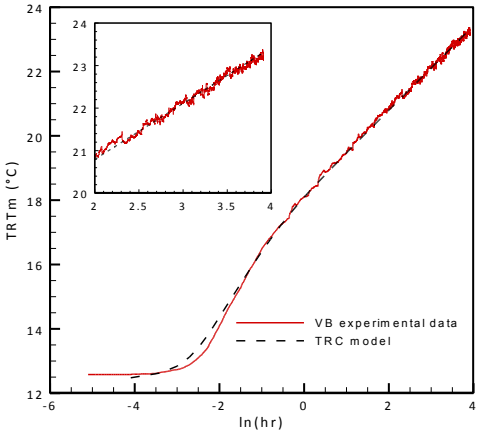

Figure 8: Comparison between the measured values of TRT_m and the ones predicted by the TRC model for k = 3.0 W m^{-1} K^{-1}

Based on this experiment, the VB is able to successfully reproduce the ground thermal behavior calculated by the TRC model for ground thermal conductivities of 3.0 W.m^{-1}.K^{-1}. An uncertainty analysis was also performed to quantify the uncertainty of the ground thermal conductivity simulated by the VB. For the test presented in this paper, the uncertainity is ±0.005 W.m^{-1}.K^{-1} This uncertainty corresponds to a relative error of ±0.2% confirming that the VB can accurately reproduce the ground thermal response.

The TRT unit connected to the virtual borehole includes measuring instruments and a data acquisition system that records temperature, flow, current and voltage measurements. The data recorded in the TRT unit is exported to an analysis software that uses the infinite line source method to calculate the ground thermal conductivity. For the tests performed on the virtual borehole, this software calculates a thermal conductivity of 3.18 W.m^{-1}.K^{-1} for the 3.0 W.m^{-1}.K^{-1} test. This corresponds to a difference of 6%.

CONCLUSION

In this paper, the concept of using a virtual borehole (VB) to calibrate TRT units is presented. The VB consists of a plate heat exchanger, a water loop cooled by a chiller and a control algorithm, which mimic the thermal behaviour of ground heat exchangers by using a TRC model. The TRT unit is connected to the VB as it would in a real geothermal borehole. In this paper, the VB is used to simulate a ground thermal conductivity of 3.0 W.m^{-1}.K^{-1}. For this test, there is a good agreement between the time evolution of TRT_m obtained using the VB and the one calculated by the TRC model of the borehole. A commercially-available TRT unit is then tested with the VB. The TRT unit reported a thermal conductivity of 3.18 Wm^{-1}K^{-1} while the VB had a preset value of 3.0 ± 0.005 Wm^{-1}K^{-1}. This corresponds to a 6% difference. The VB concept could be a valuable tool to calibrate TRT units for various groud conditions. However, additional work is necessary to characterize the heat exchanger for the complete range of flowrates that are likely to be used during tests.

ACKNOWLEDGMENTS

This work was financially supported by the Energy Innovation Program (Natural Resources Canada).

REFERENCES

Acuña, J. and B. Palm. 2013. *Distributed thermal response tests on pipe-in-pipe borehole heat exchangers*. Applied Energy 109: 312–320. http://doi.org/10.1016/j.apenergy.2013.01.024

Bandos, T. V, Á. Montero, P. Fernández de Córdoba, and J. F. Urchueguía. 2011. *Improving parameter estimates obtained from thermal response tests: Effect of ambient air temperature variations*. Geothermics 40(2): 136–143. http://doi.org/http://dx.doi.org/10.1016/j.geothermics.2011.02.003

Beier, R. A. and M. D. Smith. 2003. *Removing variable heat rate effects from borehole tests*. In ASHRAE Transactions 109 (2): 463–474. Retrieved from https://www.scopus.com/inward/record.uri?eid=2-s2.0-0242543986&partnerID=40&md5=1dc68415f6a4714ce828cdf1a620a1cc

Bozzoli, F., G. Pagliarini, S. Rainieri,. and L . Schiavi. 2011. *Estimation of soil and grout thermal properties through a two-step parameter estimation procedure applied to TRT (thermal response test data)*. Energy 36(2): 839–846.

Chiasson, A., A. O'Connell. 2011. *New analytical solution for sizing vertical borehole ground heat exchangers in environments with significant groundwater flow: Parameter estimation from thermal response test data.* HVAC&R Res. 17, 1000–1011. doi:10.1080/10789669.2011.609926.

Choi, W. and R. Ooka. 2015 . *Interpretation of disturbed data in thermal response tests using the infinite line source model and numerical parameter estimation method.* Applied Energy 148: 476–488. http://doi.org/10.1016/j.apenergy.2015.03.097

Eskilson, P. 1986 . *Thermal analysis of heat extraction boreholes*. Univ. Lund, 22.

Gehlin, S., 1998. *Thermal Response Test: method development and evaluation*. Thesis, Luleå University of Technology, ISSN 1402-1544 ; 2002:39.

Godefroy, V., M. Bernier. 2014. *A simple model to account for thermal capacity in boreholes.* In 11th IEA Heat Pump Conference 2014.

Marcotte, D. and P. Pasquier. 2008 . *On the estimation of thermal resistance in borehole thermal conductivity test*, 33: 2407–2415. http://doi.org/10.1016/j.renene.2008.01.021

Mogensen, P. 1983 . *Fluid to duct wall heat transfer in duct system heat storages*. Document-Swedish Council for Building Research (16): 652–657.

Raymond, J., L. Lamarche and M. Malo. 2015. *Field demonstration of a first thermal response test with a low power source.* Applied Energy 147: 30–39. http://doi.org/10.1016/j.apenergy.2015.01.117

Rees, S. J. 2016. Advances in Ground-Source Heat Pump Systems. Duxford, UK: Woodhead Publishing.

Rohner, E., L. Rybach and U. Schärli. 2005. *A new, small, wireless instrument to determine ground thermal conductivity in-situ for borehole heat exchanger design*. In Proceedings World Geothermal Congress.

Sass, I. and C. Lehr. 2011. *Improvements on the thermal response test evaluation applying the cylinder source theory*. In Proceedings of the 36th Workshop on Geothermal Reservoir Engineering.

Sharqawy, M. H., S. Said, E. Mokheimer, M.A. Habib, H.M. Badr and N.A. Al-Shayea. 2009 . *First in situ determination of the ground thermal conductivity for borehole heat exchanger applications in Saudi Arabia.* Renewable Energy 34(10): 2218–2223. http://doi.org/10.1016/j.renene.2009.03.003

Spitler, J. D. and S. E. A. Gehlin. 2015. *Thermal response testing for ground source heat pump systems—An historical review.* Renewable and Sustainable Energy Reviews 50(0): 1125-1137.

Witte, H. J. L., S. Kalma, S.and A.J. Van Gelder. 2000a. *In-situ Thermal Conductivity Testing: The Dutch Perspective* (Part 1). The Source 13(3): 3–5.

[This page has been intentionally left blank]

IGSHPA SWEDEN
2018 Research Conference

DOI: 10.22488/okstate.18.000039

The Newton-Raphson Method Applied to the Time-Superposed ILS for Parameter Estimation in Thermal Response Tests

Willem Mazzotti **Husni Firmansyah** **José Acuña**
Milan Stokuca **Björn Palm**

ABSTRACT

Thermal Response Testing is now a well-known and widely-used method allowing the determination of the local thermal or geometrical properties of a Borehole Heat Exchanger (BHE), those properties being critical in the design of GSHP systems. The analysis of TRTs is an inverse problem that has commonly been solved using an approximation of the ILS solution. To do this, however, the heat rate during a TRT must be kept constant, or least be non time-correlated, during the test, which is a challenging constraint. Applying temporal superposition to the ILS model is a way to account for varying power, although it requires the use of an optimization algorithm to minimize the error between a parametrized model and experimental values.

In this paper, the Newton-Raphson method is applied to the time-superposed ILS for parameter estimation in TRTs. The parameter estimation is limited to the effective thermal conductivity and the effective borehole resistance. Analytical expressions of the first and second derivatives of the objective function, chosen as the sum of quadratic differences, are proposed, allowing to readily inverse of the Hessian matrix and speed the convergence process.

The method is tried for 9 different TRTs, 2 of which are reference datasets used for validation of the method (Beier et al., 2010). Differences between estimated and reference thermal conductivities are of 3.4% and 0.4% for the first and second reference TRTs, respectively. The method is shown to be stable and consistent: for each of the 9 TRTs, 11 realizations are performed with different initial values. Convergence is reached in all cases and all realizations lead to the same final values for a given TRT.

The proposed convergence method is about 70% to 90% faster than the Nelder-Mead simplex and require about 8 times less iterations in average. The convergence speed varies between 0.3 to 13.6 s with an average of 3.7 s for all TRTs.

INTRODUCTION

Thermal Response Testing is a well-known in-situ method used to determine the local effective thermal conductivity, λ^*, and effective borehole thermal resistance, R_b^*, both parameters being critical for the design of Ground-Source Heat Pump (GSHP) systems and/or Borehole Thermal Energy Storage (BTES). The Thermal Response Test (TRT) method for Borehole Heat Exchangers (BHEs) was introduced by Mogensen (1983) who discussed the experimental setup as well as the analysis procedure. The first TRT units were not specifically built to be transported and mobile units only appeared later (Eklöf & Gehlin, 1996). Today, most TRT rigs are built as mobile units (IEA ECES Annex 21, 2013). A more detailed description of the historical development of TRT units can be found in Spitler and Gehlin (2015). TRTs are now performed worldwide for both commercial and research purposes (IEA ECES Annex 21, 2013; Spitler & Gehlin, 2015; Witte, 2016; Zhang et al., 2014). Several developments of the TRT method have been undertaken since Mogensen's initial proposal, including:

Willem Mazzotti (willem.mazzotti@energy.kth.se) is a PhD candidate at the Royal Institute of Technology (KTH) and a consultant at the Swedish firm Bengt Dahlgren AB (willem.mazzotti@bengtdahlgren.se). Husni Firmansyah is a recently graduated student from the Royal Institute of Technology (KTH). Milan Stokuca is a consultant at Bengt Dahlgren AB. José Acuña is a PhD and researcher at the Royal Institute of Technology (KTH) as well as a manager in Bengt Dahlgren AB. Björn Palm is a professor at the Royal Institute of Technology (KTH).

- Distributed Thermal Response Tests (DTRTs) through the use of fiber optic cables (Acuña, 2013; Fujii et al., 2009; Radioti et al., 2018; Sakata et al., 2018), wireless sensors (Martos et al., 2010) or wired sensors (Acuña, 2008; Aranzabal et al., 2016; Yu et al., 2013)
- accounting for groundwater flow on the thermal response (Molina-Giraldo et al., 2011; Raymond et al., 2011; Rivera et al., 2015; Witte, 2007)
- using different methods to calculate the average fluid temperature (Beier, 2011; Beier et al., 2012; Beier & Spitler, 2016; Lamarche et al., 2017; Marcotte & Pasquier, 2008)
- modified control strategies or methodologies (Choi & Ooka, 2017; Raymond et al., 2015; Rolando, 2015; Rolando et al., 2017; Witte et al., 2002)
- estimation of uncertainties (Witte, 2013)
- definition of a criterion for the test duration (Poulsen & Alberdi-Pagola, 2015).

New approaches for the determination of ground thermal properties have also been initiated, see for instance Raymond et al. (2016) and Raymond et al. (2017).

The analysis method initially proposed by Mogensen (1983) entailed the use of the Infinite Line Source (ILS) solution (Carslaw & Jaeger, 1959; Ingersoll & Plass, 1948) to evaluate the change in average fluid temperature, such that

$$\Delta T = q\left(R_b^* + \frac{1}{4\pi\lambda^*}E_1\left(\frac{r_b^2}{4\alpha t}\right)\right) \quad (1)$$

The exponential integral term in eq.1 may be expressed as the series expansion $E_1(x) = -\gamma - \ln(x) - \sum_{i=1}^{\infty}\frac{(-x)^i}{i\cdot i!}$ (Abramowitz & Stegun, 1964). For relatively large values of time (small values of x), the higher order terms in the previous equation may be neglected, leading to

$$\Delta T = q\left(R_b^* + \frac{1}{4\pi\lambda^*}\left(\ln\left(\frac{4\alpha t}{r_b^2}\right) - \gamma\right)\right) \quad (2)$$

which allows the estimation of λ^* and R_b^* through linear regression. This method is referred to as ILS regression in the rest of this article. Note that the determination of R_b^* requires knowledge of r_b, α and the undisturbed temperature. Hellström (1991) reported a maximum error of 2% for approximation (2) for $t \geq 5r_b^2/\alpha$, which can be verified by computing the exponential integral and its approximation (2) at the given value.

The ILS model is used in more than 90% of TRTs, being by far the most common analysis method for such tests (IEA ECES Annex 21, 2013). This is likely inherent to the simplicity of the approximation shown in eq.2. However, this approximation requires having a heat rate that is, if not perfectly constant, non time-correlated. This may be hard to accomplish as noted in the literature (IEA ECES Annex 21, 2013; Spitler & Gehlin, 2015; Zhang et al., 2014). Beier and Smith (2003) propose a way to bypass this issue by using deconvolution in the Laplace domain. The method requires knowledge of the temperature change from time zero to infinity, thus extrapolation for large times must be performed since TRTs are finite in duration. Other authors have proposed experimental methods to keep the power as constant as possible, see for instance Witte et al. (2002), Rolando (2015) and Rolando et al. (2017). The ASHRAE guidelines for TRTs recommend power variations with a standard deviation lower than 1.5% of the average value (ASHRAE, 2011). Standard deviation is however not the best metrics for power variation in TRTs as information about a potential time correlation is lost. Time-correlated variations may lead to errors in the estimation of the thermal conductivity, even with variations respecting the ASHRAE criterion.

Another way to account for varying power is to apply temporal superposition, assuming the power under a TRT can be approximated as a piecewise constant function (see eq.4). This however precludes the use the ILS regression for

the determination of λ^* and R_b^*, and parameter estimation has to be employed; the exponential integral approximation (2) will moreover be less accurate as the higher order terms may become significant. The full series expansion is therefore preferred when applying superposition with the ILS model. As there is no straightforward way to determine any unknown parameter, those must be estimated through the minimization of an objective function, hence an optimization problem. Choi and Ooka (2015) propose a parameter estimation method using temporal superposition with the ILS coupled to a quasi-Newton optimization algorithm. Li and Lai (2012) estimate up to 8 parameters in TRTs using the infinite cylindrical source model coupled to a Levenberg–Marquardt and a trust region method.

Parameter estimation may also be performed with numerical models (Austin, 1998; Austin, Yavuzturk, & Spitler, 2000; Pasquier, 2015; Shonder & Beck, 1999; Wagner & Clauser, 2005). Jain (1999) compares up to 8 parameter estimation techniques coupled to a numerical model. The author finds that non-gradient based deterministic methods such as the Nelder-Mead simplex are faster for the considered numerical model. Numerical models are of interest as they can accurately reproduce the conditions of a TRT, hence allowing the estimation of many parameters in the model. The use of numerical models may however be computationally demanding and require case-specific adjustments. It may also be challenging to apply all of the obtained parameters during the design of the system for which the TRT is performed.

This work presents the application of the Newton-Raphson method to the time-superposed ILS for parameter estimation in TRTs. In contrast to previous studies with analytical models, the Hessian matrix is analytically determined here, meaning that an expression of the second order derivatives is analytically determined and used in the algorithm. As the estimated parameters are limited to R_b^* and λ^*, the inverse of the Hessian matrix can be readily determined, thereby increasing the convergence speed. The convergence method is compared to the Nelder-Mead algorithm (1965) and its reliability is tested. The proposed method is validated against two reference datasets (Beier et al., 2011) and applied to 7 different commercial TRTs.

METHODOLOGY

This section is organized as such: first, the general form of the Newton-Raphson method for estimation of multiple parameters is reminded; then, the analytical expressions of the Hessian matrix elements are derived; finally, some other features of the convergence method are presented as well as the TRT datasets used in this study.

Newton-Raphson method

The Newton-Raphson method is a well-known root-finding iterative method used in engineering problems. The method is gradient-based and may be use for optimization problems. The unscaled, univariate Newton-Raphson method may be expressed as $x_{n+1} = x_n - \frac{f(x_n)}{f'(x_n)}$ where f is the function which root is sought (Christensen & Bastien, 2016; Venkateshan & Swaminathan, 2014). For multiple variables, the Newton-Raphson method may be reformulated as $\boldsymbol{x}^{(n+1)} = \boldsymbol{x}^{(n)} - \boldsymbol{J}^{-1}(\boldsymbol{x}^{(n)})\boldsymbol{f}(\boldsymbol{x}^{(n)})$ where $\boldsymbol{J}$ is the Jacobian matrix of the vector function $\boldsymbol{f}$ (Alart, 1997; Christensen & Bastien, 2016). This may also be formulated as an unconstrained optimization problem by introducing an objective function, h, so that $\boldsymbol{\nabla} h = \boldsymbol{f}$, leading to

$$\boldsymbol{x}^{(n+1)} = \boldsymbol{x}^{(n)} - \boldsymbol{H}^{-1}(\boldsymbol{x}^{(n)})\boldsymbol{\nabla} h(\boldsymbol{x}^{(n)}) \tag{3}$$

where $\boldsymbol{H}$ is the Hessian matrix of the function h, that is the matrix of the second order derivatives of the function h (Keller, 2018; Pollock, 1999; Sieniutycz & Szwast, 2018). When the expression of the second order derivatives can be determined and the inverse of the Hessian matrix made readily available, the Newton-Raphson method can be more efficient as it requires less steps to converge. In this study, the inverse of the Hessian matrix is analytically determined. The Newton-Raphson method is referred to as N-R method below.

N-R applied to the time-superposed ILS: derivation of the inverse Hessian matrix

Temporal superposition may be expressed for any given step response function, called here g, to calculate the modelled temperature change. If the power is approximated as a piecewise constant function, this change in inlet-outlet average temperature (temperature response) may be written as

$$\Delta T_{mod}(t_i, \boldsymbol{x}) = (q * g)(t_N, \boldsymbol{x}) = \sum_{j=0}^{i-1} \Delta q_j \cdot g\left(t_i - t_{j-1}, \boldsymbol{x}\right) \tag{4}$$

The specific heat rate, q, is either calculated from the measured flow rate and temperature difference, as well as the secondary fluid thermal properties and the borehole active depth or from the electric power input. One wants to minimize the error between experimental and modelled values by varying the parameters sought for, represented here by the vector $\boldsymbol{x}$. The minimization of the error requires the definition of an objective function, chosen here as the sum of quadratic differences

$$h(\boldsymbol{x}) = \sum_{i=N_1}^{N_2} \left(\Delta T_{mod}(t_i, \boldsymbol{x}) - \Delta T_{exp}(t_i)\right)^2 \tag{5}$$

where N_1 and N_2 determine the optimization period. In this work, the ILS coupled to an effective resistance model is chosen as response function, leading to $g = R_b^* + \frac{1}{4\pi\lambda^*} E_1\left(\frac{r_b^2}{4\alpha t}\right)$. The choice of the ILS as well the limitation to λ^* and R_b^* is done in accordance with the state-of-the-art (IEA ECES Annex 21, 2013). It shall be noted that the ILS cannot accurately reproduce the heat transfer behavior of a borehole at short time steps. Improvements in both the model and the amount of estimated parameters are left to later investigations. To determine the Hessian matrix, 1st and 2nd order derivatives of the function h must be determined. The 1st order derivatives of h with respect to $\boldsymbol{x}$ can be expressed as

$$\frac{\partial h}{\partial x_m}(\boldsymbol{x}) = 2 \sum_{i=N_1}^{N_2} \left(\frac{\partial \Delta T_{mod,i}}{\partial x_m}(\boldsymbol{x}) \left(\Delta T_{mod,i}(\boldsymbol{x}) - \Delta T_{exp,i}\right) \right) \tag{6}$$

The partial derivatives of the modelled temperature response with respect to λ^* and R_b^* are $\frac{\partial \Delta T_{mod,i}}{\partial \lambda^*}(\boldsymbol{x}) = \frac{1}{4\pi\lambda^{*2}} \sum_{j=0}^{i-1} \Delta q_i \left(e^{-a_{i,j}} - E_1\left(a_{i,j}\right)\right)$ and $\frac{\partial \Delta T_{mod,i}}{\partial R_b^*}(\boldsymbol{x}) = \sum_{j=0}^{i-1} \Delta q_j = q(t_i) = q_i$, where $a_{i,j} = \frac{r_b^2}{4\alpha(t_i - t_j)}$ and is dependent on λ^* (and, thus, $\boldsymbol{x}$). After successive derivations, it can be shown that

$$\begin{cases} \dfrac{\partial^2 h}{\partial \lambda^{*2}}(\boldsymbol{x}) = \dfrac{1}{2\pi\lambda^{*3}} \displaystyle\sum_{i=N_1}^{N_2} \left[\begin{array}{c} \dfrac{1}{4\pi\lambda^*} \left(\displaystyle\sum_{j=0}^{i-1} \Delta q_j \left(e^{-a_{i,j}} - E_1\left(a_{i,j}\right)\right) \right)^2 + \\ \left(\Delta T_{mod,i}(\boldsymbol{x}) - \Delta T_{exp,i}\right) \displaystyle\sum_{j=0}^{i-1} \Delta q_j \left(e^{-a_{i,j}}\left(a_{i,j} - 3\right) - 2E_1\left(a_{i,j}\right)\right) \end{array} \right] \\ \dfrac{\partial^2 h}{\partial R_b^{*2}}(\boldsymbol{x}) = 2 \left(\displaystyle\sum_{i=N_1}^{N_2} q_i \right)^2 \\ \dfrac{\partial^2 h}{\partial R_b^* \partial \lambda^*}(\boldsymbol{x}) = \dfrac{\partial^2 h}{\partial \lambda^* \partial R_b^*}(\boldsymbol{x}) = \dfrac{1}{2\pi\lambda^{*2}} \displaystyle\sum_{i=N_1}^{N_2} q_i \sum_{j=0}^{i-1} \Delta q_j \left(e^{-a_{i,j}} - E_1\left(a_{i,j}\right)\right) \end{cases} \tag{7}$$

The two first terms in eq.7 are the diagonal elements of the Hessian matrix in eq.3, while the last term represents both non-diagonal elements, the matrix being symmetric. It should be noted that $\frac{\partial^2 h}{\partial {R_b^*}^2}$ is a constant and does therefore not need to be reevaluated at every iteration step. One may notice redundancies in the 3 equations in 7; this observation can be used to speed the computation of the derivatives. Given the previous developments, and since the Hessian matrix is a 2x2 matrix in this case, eq.3 may be expressed in matrix form as

$$\boldsymbol{x}^{(n+1)} = \boldsymbol{x}^{(n)} - \frac{1}{\frac{\partial^2 h}{\partial {\lambda^*}^2}\frac{\partial^2 h}{\partial {R_b^*}^2} - \left(\frac{\partial^2 h}{\partial R_b^* \partial \lambda^*}\right)^2} \begin{pmatrix} \frac{\partial^2 h}{\partial {R_b^*}^2} & -\frac{\partial^2 h}{\partial R_b^* \partial \lambda^*} \\ -\frac{\partial^2 h}{\partial R_b^* \partial \lambda^*} & \frac{\partial^2 h}{\partial {\lambda^*}^2} \end{pmatrix} \begin{pmatrix} \frac{\partial h}{\partial \lambda^*} \\ \frac{\partial h}{\partial R_b^*} \end{pmatrix} \quad (8)$$

This matricial form can be decomposed into two equations, one for each variable in $\boldsymbol{x}$, namely λ^* and R_b^*.

Note that the positive-definiteness of the Hessian matrix is not investigated here, which entails an accurate first guess for the iterative process (Pollock, 1999). Therefore, the commonly used ILS regression, based on eq.2, is applied to find initial values of λ^* and R_b^*.

Implementation of the algorithm

The algorithm has been implemented in both an Excel spreadsheet, through VBA (*Microsoft Excel*, 2016; *Microsoft Visual Basic for Applications*, 2012), and in MATLAB® (*MATLAB*, 2017). The Matlab code is planned to be openly distributed. All the results used in this work are generated using the Matlab code.

Relative convergence criteria for λ^* and R_b^* are set as 0.1% for both parameters. Moreover, if the number of iterations is a multiple of 20 or if $\lambda^* \notin [1; 10]$ W·m^{-1}·K^{-1} or $R_b^* \notin [0.005; 0.3]$ m·K·W^{-1}, the next set of values for λ^* and R_b^* is taken around 2 W·m^{-1}·K^{-1} and 0.05 m·K·W^{-1}, respectively, with random variations of 50 to 150%.

Used TRT data

Data from 7 different commercial TRTs and two reference TRT datasets (Beier et al., 2011) are used in this work.

For the commercial TRTs, the used units are as described in Kamarad (2012) for TRT-1 and as described in Olausson (2018) for the remaining TRTs. For the first TRT, data is recorded about every 30 seconds whereas data is averaged over a span of 10 minutes for the remaining TRTs. The power is calculated using the measured temperature difference, the measured flow rate and thermal properties derived from Melinder (2007). All boreholes are filled with groundwater.

The two reference TRT datasets are directly taken from Beier et al. (2011) and referred to as TRT-B1 and TRT-B2. The two TRTs are performed under controlled conditions in the same grouted borehole. The first is a "constant heat input rate test" with "variations well within the guidelines suggested by ASHRAE". The second TRT is an interrupted test having a power outage between 9 and 11 hours after start. For more details about the reference datasets, the readers are referred to Beier et al. (2011). These datasets are used to validate the ILS model coupled to the N-R algorithm.

The flow and heat rate (power) for all TRTs are reported in Figure 1 while fixed parameters are reported in Table 1. It should be noted that for TRT-B2, the undisturbed temperature is approximated as the return temperature after 3 min, which is the closest lower time bound to the residence time. This is done because data shows some heat injection already at the very start of the test; moreover, the initial fluid temperature is about 1.5 K lower than the temperature in the sand. Figure 1 highlights the difficulties in keeping of constant heat rates during TRTs.

RESULTS

Optimization process, consistency and stability

The optimization procedure converges for all TRTs with a number of iterations varying between 2 to 8. The optimization process for TRT-1 is displayed in Figure 2, which shows an enlarged (a) and a zoomed view (b) of the optimization domain.

To try the consistency and stability of the algorithm, different initial values are tried for all the TRTs. What is meant here with consistency and stability is the consistency in the obtained final values and the stability in the algorithm convergence. For each TRT, 10 randomly chosen initial vector values $\left(\lambda^{*(0)}, R_b^{*(0)}\right)$ in the range $[1; 10]$ W·m^{-1}·K^{-1} × $[0.005; 0.3]$ m·K·W^{-1} are tried together the N-R convergence algorithm. In total, 99 optimization procedures are run, including those with initial vectors obtained through the ILS regression. All optimization procedures converge and, for a given TRT, the results are the same independently of the initial values (maximum difference of 0.5%).This result is important as the existence of a valley of low values for the objective function has been pointed out in the literature (Jain, 1999; Marcotte & Pasquier, 2008; Spitler & Gehlin, 2015; Witte et al., 2002).

The validation of the time-superposed ILS model coupled with N-R algorithm is performed using the reference thermal conductivity and borehole thermal resistance provided in Beier et al. (2011). The results and reference values are presented in Table 2.

Table 1. TRT fixed parameters

Parameters	TRT-1	TRT-2	TRT-3	TRT-4	TRT-5	TRT-6	TRT-7	TRT-B 1	TRT-B2
Borehole diameter [m]	0.12	0.115	0.115	0.115	0.115	0.115	0.115	0.126	0.126
Active borehole length [m]	331.7	324.8	298.2	296.2	122	297.3	230.3	18.3	18.3
Optimization start [hrs]	65	21	25	17	17	45	27	10	40
Optimization stop [hrs]	119	66	70	117	75	80	62	51.5	50
T_0 [°C]	8.60	9.97	9.30	9.59	10.53	9.77	8.50	22.00	21.53

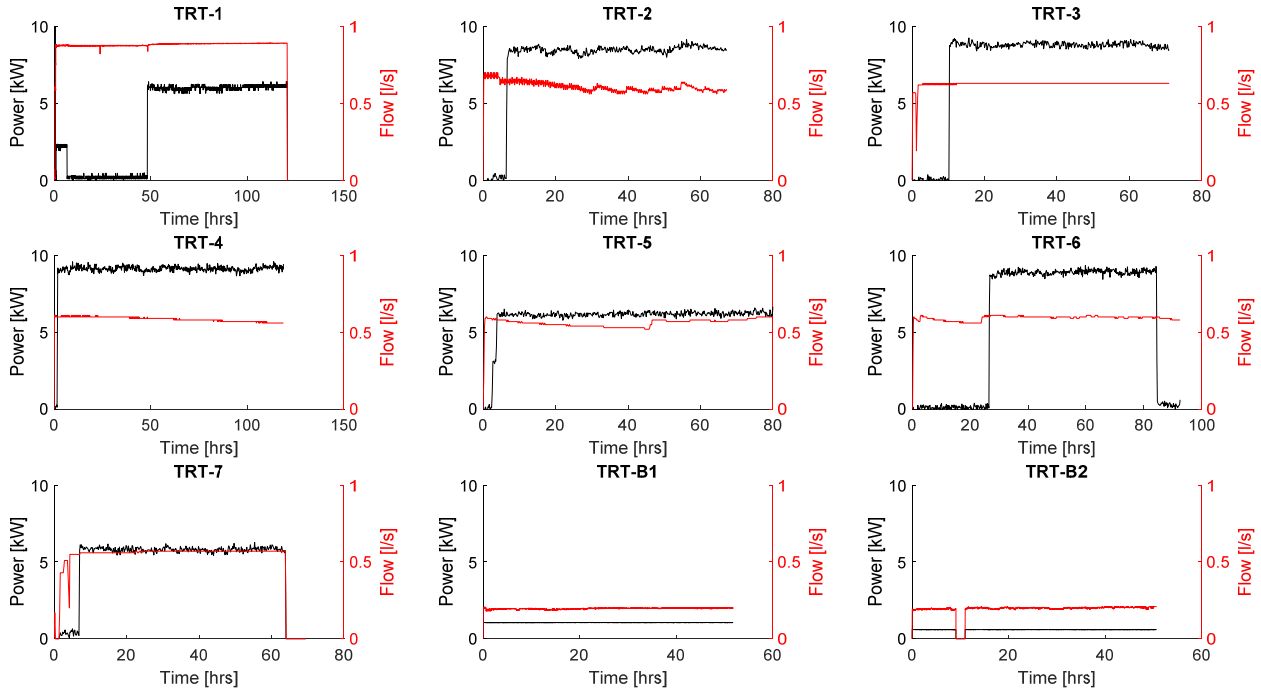

Figure 1. Power and flow rates during the 9 different TRTs used for this study

Comparison between the N-R and the Nelder-Mead algorithms

In order to evaluate the convergence speed of the N-R algorithm, the latter is compared with the Nelder-Mead algorithm (1965) as implemented in Matlab through the function *fminsearch*. The presented N-R method is always faster than the Nelder-Mead method with convergence durations between 70 to 92 % lower. In average, the Nelder-Mead method leads to about 8 times more iterations than the N-R method. This comforts the statement from Choi and Ooka (2015) that the Nelder-Mead simplex is not the most suitable method for ILS parameter estimation in TRTs.

The average convergence speed for all TRTs is of 3.7 s with the Newton-Raphson method (CPU: 2.60 GHz, RAM: 16 GB). The N-R and Nelder-Mead convergence speeds for each TRT are reported in Table 2, as well as the index of the last point (N_2) and number of points in the optimization period.

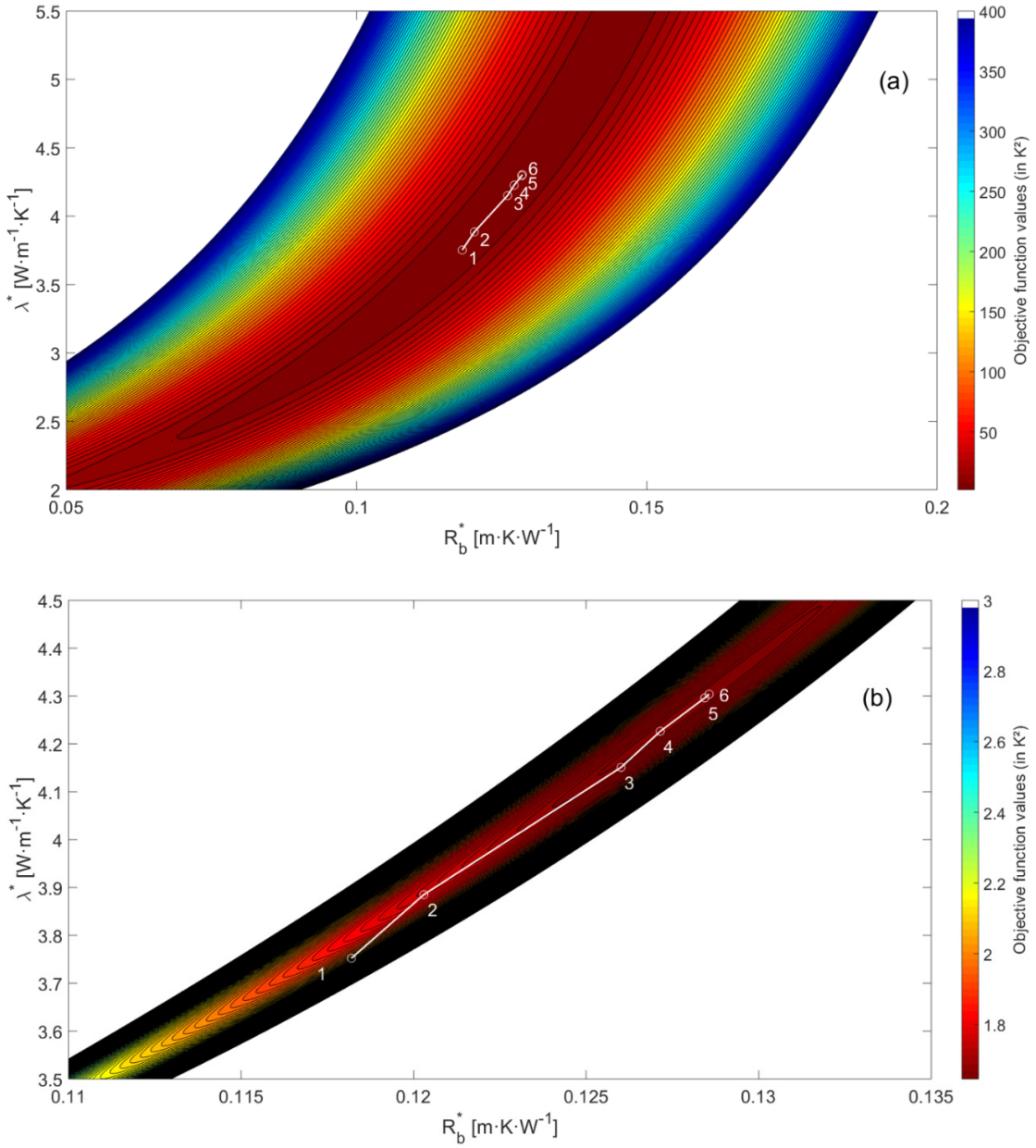

Figure 2. Optimization procedure for TRT-1: in an enlarged (a) and zoomed view (b) of the optimization domain.

Temperature response: models vs measurement

The obtained temperature responses are presented in Figure 3 against measured data for the 9 different TRTs. It can be observed that the time-superposed ILS generally overestimates the temperature response at the beginning of the heat injection. This is likely due to the quasi-steady-state assumption of the model that is not valid at early times. The overestimation seems to be more pronounced for grouted (TRT-B1-2) than water-filled boreholes (TRT-1-7). The agreement between the optimized and experimental responses is nonetheless good over the optimization periods with RMSEs no higher than 0.0765 K as can be seen in Table 2. This table also includes the initial (ILS regression) and final values obtained for each TRT using the N-R algorithm, as well as reference values of λ^* and R_b^* for TRT-B1 and TRT-B2 (Beier et al., 2011). For TRT-B1, the ILS regression and the time-superposed ILS show similar λ^* and R_b^* values that are slightly different from the reference values, although the difference between λ^* values is comprised within the 5% uncertainty of the independent measurement. For TRT-B2 however, the time-superposed ILS leads to a λ^* similar to the reference value whereas the ILS regression leads to a λ^*that is 7.8% higher than the reference value. The ILS regression nevertheless seems to give a slightly better estimation of R_b^* in TRT-B2 with a resulting value 1.1% higher than the reference against 1.7% lower for the time-superposed ILS.

For TRT 1 to 7, differences between the results obtained with the ILS regression and the time-superposed ILS may be observed although it is not possible to determine which value is closer to the true value.

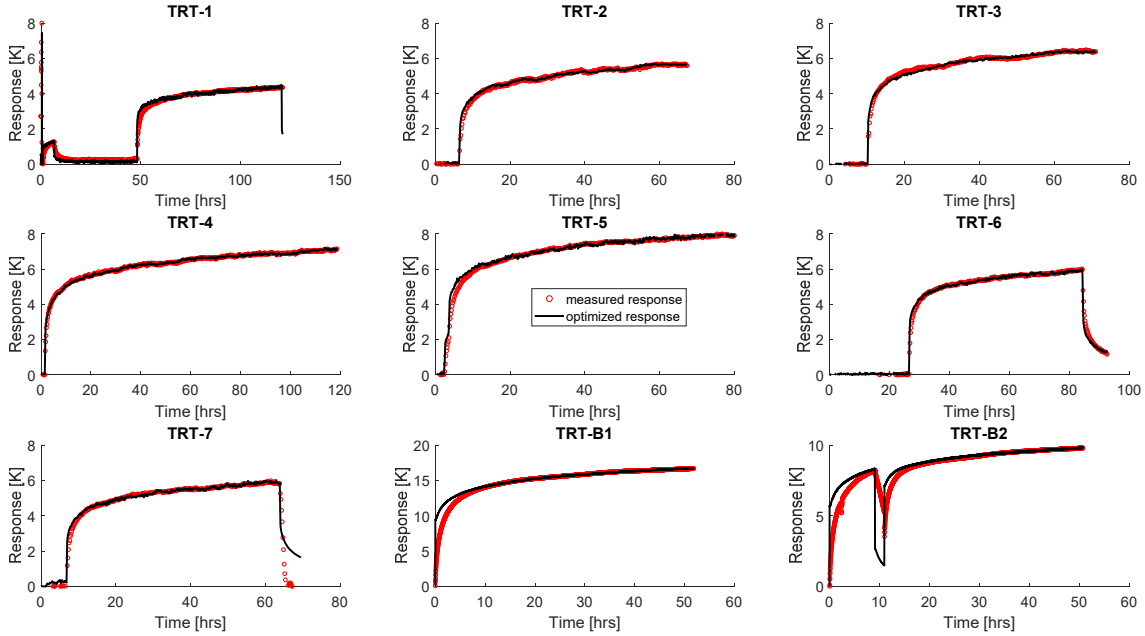

Figure 3. Measured and optimized thermal responses during the 9 TRTs used for this study

Table 2. TRT optimization results

Parameters		TRT-1	TRT-2	TRT-3	TRT-4	TRT-5	TRT-6	TRT-7	TRT-B1	TRT-B2
Newton-Raphson	λ^* [W·m^{-1}·K^{-1}]	4.30	3.18	3.05	3.08	5.12	4.26	2.92	2.92	2.83
	R_b^* [m·K·W^{-1}]	0.129	0.080	0.079	0.074	0.061	0.091	0.090	0.164	0.175
Reference values	λ^* [W·m^{-1}·K^{-1}]	-	-	-	-	-	-	-	2.82	2.82
	R_b^* [W·m^{-1}·K^{-1}]	-	-	-	-	-	-	-	0.173	0.178
ILS reg.	λ^* [W·m^{-1}·K^{-1}]	3.75	2.77	3.18	3.14	4.66	4.10	3.05	2.91	3.04
	R_b^* [W·m^{-1}·K^{-1}]	0.118	0.066	0.083	0.076	0.054	0.087	0.095	0.164	0.180
Time N-R [s]		4.8	0.3	0.3	0.5	0.7	0.4	0.3	13.6	12.7

Time Nelder-Mead [s]	24.7	1.6	1.5	5.4	2.4	1.6	1.2	158.3	78.7
Index of the last point (N_2)	1476	397	421	703	451	481	373	2816	3001
Number of points	620	271	271	601	349	211	211	2246	601
RMSE [K]	0.0516	0.0618	0.0707	0.0430	0.0765	0.0509	0.0591	0.0486	0.0306

CONCLUSION AND FUTURE WORK

This work presents the application of the Newton-Raphson optimization method to the time-superposed ILS for parameter estimation in TRTs. The time-superposed ILS is chosen so that non randomly-varying heat rates during TRTs can be considered, as opposed to the ILS regression. The ILS regression is nevertheless used to obtain the initial values for the Newton-Raphson procedure. The vector of estimated parameters is limited to λ^* and R_b^* and the inverse Hessian matrix is analytically determined, meaning that expressions of the second order derivatives of the sum of quadratic differences are proposed. The method is tested in 9 different TRTs, 2 of which are reference datasets used for validation of the method (Beier et al., 2010). For the first reference dataset, a constant heat rate TRT, the estimated λ^* and R_b^* are respectively 3.4% and 5.2% off the reference values. For the second, interrupted TRT, the differences drop to 0.4% and 1.7%, respectively.

The applied Newton-Raphson method is shown to be stable and consistent. For each of the 9 TRTs, 11 realizations are performed, 10 of which have randomly-picked initial values. Convergence is reached in all cases and all realizations lead to the same final values for a given TRT.

The proposed convergence method is about 70% to 90% faster than the Nelder-Mead simplex (1965) and require about 8 times less iterations in average. The convergence speed varies between 0.3 to 13.6 s with an average of 3.7 s for all TRTs.

The agreement between optimized and experimental responses is good with RMSEs no higher than 0.0765 K over the optimization periods. The time-superposed ILS overestimates the temperature response at the beginning of the TRTs, likely because of the quasi-steady-state assumption of the model, which is not valid at early times. The overestimation seems to be more pronounced for grouted than water-filled boreholes.

The developed optimization method could be further improved by including more parameters to be estimated, improving the convergence criterion, and adding constraints to the objective function.

ACKNOWLEDGMENTS

This work is financed by the Swedish Energy Agency through the EFFSYS Expand program. The authors thank all the sponsors involved in the project with a special mention to Bengt Dahlgren AB and Finspångs Brunnsborrning AB that provided TRT data and helped with the processing.

NOMENCLATURE

E_1 = Exponential integral (-)
g = Step response function (m·K·W^{-1})
$\boldsymbol{H}$ = Hessian matrix
h = Objective function (K^2)
$\boldsymbol{J}$ = Jacobian matrix
N = Number of points (-)
q = Specific heat load (W·m^{-1})
Δq = Step in specific heat load (W·m^{-1})
R = Borehole thermal resistance (m·K·W^{-1})
r = Borehole radius (m)
ΔT = Temperature response (K)
t = Time (s)
$\boldsymbol{x}$ = Parameter vector (bold) or symbolic variable
α = Thermal diffusivity (m^2·s^{-1})
γ = Euler–Mascheroni constant (-)
λ = Thermal conductivity (W·m^{-1}·K^{-1})

Superscripts /subscripts

* = Effective
$^{(k)}$ = kth iteration
$_{mod}$ = Model
$_{exp}$ = Experimental

REFERENCES

Abramowitz, M., & Stegun, I. A. (1964). Handbook of Mathematical Functions With Formulas, Graphs, and Mathematical Tables. United States Department of Commerce, National Bureau of Standards.

Acuña, J. (2008). Characterization and Temperature Measurement Techniques of Energy Wells for Heat Pumps (Licentiate Thesis). M. Sc. Thesis, KTH School of Industrial Engineering and Management Division of Applied Thermodynamic and Refrigeration, Stockholm, Sweden.

Acuña, J. (2013). Distributed thermal response tests: new insights on U-pipe and Coaxial heat exchangers in groundwater-filled boreholes (PhD Thesis). KTH Royal Institute of Technology, Stockholm.

Alart, P. P. (1997). Méthode de Newton généralisée en mécanique du contact. Journal de Mathématiques Pures et Appliquées, 76(1), 83–108. https://doi.org/10.1016/S0021-7824(97)89946-1

Aranzabal, N., Martos, J., Montero, Á., Monreal, L., Soret, J., Torres, J., & García-Olcina, R. (2016). Extraction of thermal characteristics of surrounding geological layers of a geothermal heat exchanger by 3D numerical simulations. Applied Thermal Engineering, 99, 92–102. https://doi.org/10.1016/j.applthermaleng.2015.12.109

ASHRAE. (2011). 2011 ASHRAE Handbook: HVAC Applications (SI Edition). Atlanta: ASHRAE. Retrieved from http://app.knovel.com/hotlink/toc/id:kpASHRAE61/2011-ashrae-handbook

Austin, W. A. (1998). *Development of an In-Situ System and Analysis Procedure for Measuring Ground Thermal Properties* (Master Thesis). Stillwater, Oklahoma: Oklahoma State University.

Austin, W. A., Yavuzturk, C., & Spitler, J. D. (2000). Development of an in-situ system for measuring ground thermal properties. ASHRAE Transactions, 106(1), 365–379.

Beier, R. A., & Smith, M. D. (2003). Removing variable heat rate effects from borehole tests (Vol. 109 PART 2, pp. 463–474). Presented at the ASHRAE Transactions.

Beier, R. A., Smith, M. D., & Spitler, J. D. (2011). Reference data sets for vertical borehole ground heat exchanger models and thermal response test analysis. Geothermics, 40(1), 79–85. https://doi.org/10.1016/j.geothermics.2010.12.007

Carslaw, H. S., & Jaeger, J. C. (1959). Conduction of heat in solids. Retrieved from http://adsabs.harvard.edu/abs/1959chs..book.....C

Choi, W., & Ooka, R. (2015). Interpretation of disturbed data in thermal response tests using the infinite line source model and numerical parameter estimation method. Applied Energy, 148, 476–488. https://doi.org/10.1016/j.apenergy.2015.03.097

Christensen, J., & Bastien, C. (2016). Chapter | three - Introduction to General Optimization Principles and Methods. In Nonlinear Optimization of Vehicle Safety Structures (pp. 107–168). Oxford: Butterworth-Heinemann. https://doi.org/10.1016/B978-0-12-417297-5.00003-1

Eklöf, C., & Gehlin, S. (1996). TED - a mobile equipment for thermal response test : testing and evaluation. Retrieved from http://urn.kb.se/resolve?urn=urn:nbn:se:ltu:diva-59091

Fujii, H., Okubo, H., Nishi, K., Itoi, R., Ohyama, K., & Shibata, K. (2009). An improved thermal response test for U-tube ground heat exchanger based on optical fiber thermometers. Geothermics, 38(4), 399–406. https://doi.org/10.1016/j.geothermics.2009.06.002

Hellström, G. (1991). Ground heat storage : thermal analyses of duct storage systems (PhD Thesis). Lund University, Lund, Sweden.

IEA ECES Annex 21. (2013). IEA ECES 2013 Annex21 Thermal Response Test Final Report. International Energy Agency. Retrieved from http://media.geoenergicentrum.se/2017/11/IEA_ECES_2013_Annex21_FinalReport.pdf

Ingersoll, L. R., & Plass, H. J. (1948). Theory of the ground pipe heat source for the heat pump. ASHVE Transactions, 54(7), 339–348.

Jain, N. K. (1999). *Parameter Estimation of Ground Thermal Properties* (Master Thesis). Oklahoma State University.

Kamarad, A. (2012). Design and construction of a mobile equipment for thermal response test in borehole heat exchangers. Retrieved from http://urn.kb.se/resolve?urn=urn:nbn:se:kth:diva-99558

Keller, A. A. (2018). Chapter 1 - Elements of Mathematical Optimization. In Mathematical Optimization Terminology (pp. 1–12). Academic Press. https://doi.org/10.1016/B978-0-12-805166-5.00001-0

Li, M., & Lai, A. C. K. (2012). Parameter estimation of in-situ thermal response tests for borehole ground heat exchangers. International Journal of Heat and Mass Transfer, 55(9), 2615–2624. https://doi.org/10.1016/j.ijheatmasstransfer.2011.12.033

Marcotte, D., & Pasquier, P. (2008). On the estimation of thermal resistance in borehole thermal conductivity test. Renewable Energy, 33(11), 2407–2415. https://doi.org/10.1016/j.renene.2008.01.021

MATLAB. (2017). (Version b). MathWorks.

Melinder, Å. (2007). Thermophysical Properties of Aqueous Solutions Used as Secondary Working Fluids (PhD Thesis). Retrieved from http://urn.kb.se/resolve?urn=urn:nbn:se:kth:diva-4406

Microsoft Excel. (2016). Microsoft Corporation.

Microsoft Visual Basic for Applications. (2012). (Version 7.1). Microsoft Corporation.

Mogensen, P. (1983). Fluid to duct wall heat transfer in duct system heat storages (pp. 652–657). Presented at the International conference on subsurface heat storage in theory and practice, Stockholm, Sweden: Swedish Council for Building Research.

Nelder, J. A., & Mead, R. (1965). A Simplex Method for Function Minimization. The Computer Journal, 7(4), 308–313. https://doi.org/10.1093/comjnl/7.4.308

Olausson, L. (2018). Construction and test of a new compact TRT equipment. Retrieved from http://urn.kb.se/resolve?urn=urn:nbn:se:kth:diva-226294

Pasquier, P. (2015). Stochastic interpretation of thermal response test with TRT-SInterp. Computers & Geosciences, 75(Supplement C), 73–87. https://doi.org/10.1016/j.cageo.2014.11.001

Pollock, D. S. G. (1999). Chapter 12 - Unconstrained Optimisation. In Handbook of Time Series Analysis, Signal Processing, and Dynamics (pp. 323–361). London: Academic Press. https://doi.org/10.1016/B978-012560990-6/50014-2

Poulsen, S. E., & Alberdi-Pagola, M. (2015). Interpretation of ongoing thermal response tests of vertical (BHE) borehole heat exchangers with predictive uncertainty based stopping criterion. Energy, 88, 157–167. https://doi.org/10.1016/j.energy.2015.03.133

Radioti, G., Cerfontaine, B., Charlier, R., & Nguyen, F. (2018). Experimental and numerical investigation of a long-duration Thermal Response Test: Borehole Heat Exchanger behaviour and thermal plume in the heterogeneous rock mass. Geothermics, 71, 245–258. https://doi.org/10.1016/j.geothermics.2017.10.001

Raymond, J., Lamarche, L., & Malo, M. (2016). Extending thermal response test assessments with inverse numerical modeling of temperature profiles measured in ground heat exchangers. Renewable Energy, 99, 614–621. https://doi.org/10.1016/j.renene.2016.07.005

Raymond, J., Malo, M., Lamarche, L., Lorenzo Perozzi, Gloaguen, E., & Begin, C. (2017). New Methods to Spatially Extend Thermal Response Test Assessments. http://dx.doi.org/10.22488/okstate.17.000519

Rolando, D. (2015, April). Modelling of temperature responsefactors and experimental techniques for borehole heat exchanger design in geothermal heat pump applications.pdf (PhD Thesis). University of Genova, Genova, Italy.

Rolando, D., Acuna, J., & Fossa, M. (2017). Heat Extraction Distributed Thermal Response Test: A Methodological Approach and In-situ Experiment. http://dx.doi.org/10.22488/okstate.17.000536

Sakata, Y., Katsura, T., & Nagano, K. (2018). Multilayer-concept thermal response test: Measurement and analysis methodologies with a case study. Geothermics, 71(Supplement C), 178–186. https://doi.org/10.1016/j.geothermics.2017.09.004

Shonder, J. A., & Beck, J. V. (1999). Determining Effective Soil Formation Thermal Properties from Field Data Using a Parameter Estimation Technique. ASHRAE Transactions, 105, 458–466.

Sieniutycz, S., & Szwast, Z. (2018). 1 - Outline of Classical Optimization Methods. In Optimizing Thermal, Chemical, and Environmental Systems (pp. 1–63). Elsevier. https://doi.org/10.1016/B978-0-12-813582-2.00001-X

Spitler, J. D., & Gehlin, S. E. A. (2015). Thermal response testing for ground source heat pump systems—An historical review. Renewable and Sustainable Energy Reviews, 50, 1125–1137. https://doi.org/10.1016/j.rser.2015.05.061

Venkateshan, S. P., & Swaminathan, P. (2014). Chapter 4 - Solution of Algebraic Equations. In Computational Methods in Engineering (pp. 155–201). Boston: Academic Press. https://doi.org/10.1016/B978-0-12-416702-5.50004-1

Wagner, R., & Clauser, C. (2005). Evaluating thermal response tests using parameter estimation for thermal conductivity and thermal capacity. Journal of Geophysics and Engineering, 2(4), 349. https://doi.org/10.1088/1742-2132/2/4/S08

Witte, H. J., Van Gelder, G. J., & Spitier, J. D. (2002). In situ measurement of ground thermal conductivity: a Dutch perspective. Ashrae Transactions, 108, 263.

Yu, X., Zhang, Y., Deng, N., Wang, J., Zhang, D., & Wang, J. (2013). Thermal response test and numerical analysis based on two models for ground-source heat pump system. Energy and Buildings, 66, 657–666. https://doi.org/10.1016/j.enbuild.2013.07.074

[This page has been intentionally left blank]

IGSHPA SWEDEN 2018 Research Conference

DOI: 10.22488/okstate.18.000021

Pulsated Thermal Response Test experiments and modelling for ground thermal property estimation

Marco Fossa **Davide Rolando** **Philippe Pasquier**

ABSTRACT

The Thermal Response Test (TRT) is a well known experimental technique for estimating both the ground thermal conductivity and the effective borehole heat exchangers (BHE) resistance in ground coupled heat pump (GCHP) applications. The usual experimental approach for the TRT measurements is to inject (and even extract) a constant heat rate in the ground while the carrier fluid is circulated inside a reference heat exchanger. In this paper the TRT approach is applied with reference to non constant heat rate condition during a several day measuring session at the SEB building site of the University of Genova, Italy. A constant heat injection has been operated for the first 100 hours of the experiment and then a series of 8 hour square pulses (on/off mode) have applied for about 11 days. The ground and BHE thermal properties have been here estimated according to different algorithms developed either at the University of Genova and Polytech Montreal, where either the ILS and FLS (Infinite and Finite Line Source) theories or a Resistance/Capacitance approach are implemented to reconstruct the measured temperature evolution from parameter estimation.

INTRODUCTION

The Thermal Response Test is an efficient measurement technique first proposed by P. Mogensen (1983) at the beginning of the 80' for inferring the ground thermal properties in ground source heat pump (GCHP) applications when borehole heat exchangers (BHE) are employed. As it is well known, during the test, heat carrier fluid temperature is measured at a pilot BHE and the experimental signal is compared to a predicted one when a given (constant) heat transfer rate is provided at the surface. This experimental technique is based on the assumption that the fluid resulting temperature depends on the undisturbed ground one and on a couple of thermal resistances, the (constant) BHE effective resistance and the (transient) ground one, as described by the Infinite Line Source (ILS, Carlaw and Jager, 1947, Ingersoll et al., 1954) model. After Mogensen, early contributions to the TRT technique are due to Gehlin in Sweden (Gehlin 1996), Austin (1998) in the US and Pahud and Matthey (2001) in Switzerland, at the end of the '90. After such experiences the method rapidly developed across the world until its most detailed versions, where multiple vertical measurements are carried out along the BHE for assessing the local ground properties (Distributed TRT at KTH Stockholm, e.g. Acuna et al. 2009).

When the TRT data are processed, a two resistance model is applied where the borehole resistance is conceived to be time invariant and the ground one is set to change in time as described by a suitable Temperature Response Factor (TRF) that from a mathematical point of view is able to describe heat conduction mechanism and provide the borehole periphery temperature evolution as a function of a proper Fourier number. The most popular TRF for TRT analyses is

Marco Fossa (marco.fossa@unige.it) is professor of Solar and Geothermal energy at the University of Genova, Italy. Davide Rolando is post-doctoral researcher at KTH Stockholm, Sweden and Philippe Pasquier is professor of geological engineering at Polytechnique Montreal, Canada

the ILS solution, but more sophisticated solutions can be chosen, including the Finite Line-Source model (FLS) (Eskilson 1987, Zeng, et al. 2002, Lamarche and Beauchamp 2007), the Moving Infinite Line-Source model (MILS) (Sutton et al. 2003), the Moving Finite Line-Source (MFLS) by Molina-Giraldo et al. (2011) or thermal resistance and capacity (TRC) model such as the one of Pasquier and Marcotte (2012, 2014).

The usual assumption related to the TRT experimental data reduction is related to the thermal conduction mechanism and to the absent (or negligible) effects due to the underground water advection. This assumption is usually not fully satisfied, since fractured rocks are often present and some groundwater displacement can be present and enhance the heat transfer from the borehole to the surrounding ground medium, as discussed for example by Gehlin & Hellstrom (2003) and Spitler & Gehlin (2015). If groundwater circulation is present the thermal conduction is hence reinforced by convection: in such cases a pure conduction modelling, in terms of moving line sources, demonstrated to be still efficient for describing the ground response to thermal pulses even under groundwater advection. In this sense the works by Sutton et al. (2003) on the MILS and that by Molina-Giraldo et al. (2011) on the MFLS clearly show how a conduction scheme can be efficiently applied for describing the BHE behaviour when groundwater is present.

This paper deals with a particular experimental condition where the heat rate at the heat carrier fluid is deliberately varied according to a series of on/off heat pulses able to resemble a real GCHP operating conditions. A dedicated equipment has been developed to this aim at the University of Genova which is able to very efficiently control the heat and flow rates either in constant or pulsated mode. The measurements carried out in particular refer to a constant heat injection for the first 100 hours of the experiment and to a series of 8 hour square pulses (on/off mode) that have been applied for the following 11 days.

Such Pulsated Thermal Response Test (PTRT) has been analysed with several interpretation models by two different inverse solution algorithms developed at the home universities of the Italian and Canadian authors of the present paper in order to estimate by parameter optimization the ground thermal properties and borehole characteristics, and compare their algorithms. The Italian approach is based on the temporal superposition of the ILS solution and to a cross check with respect to the MILS conditions (Fossa et. al, 2016). Alternatively, the Canadian approach used a convolution is the spectral domain (Marcotte and Pasquier 2008) to account for the heating power variation of the PTRT with the program TRT-SInterp (Pasquier 2015) to automatically calibrate the PTRT with the FLS model of Claesson and Javed (2011) and the TRC model of Pasquier and Marcotte (2012, 2014).

The measurements have been carried out in Italy, and the peculiar geological conditions with non negligible aquifer activity allows the use of either the ILS, MFLS, FLS and TRC models for measured data reduction. Finally, the experimental results and optimum search are presented in order to demonstrate the reliability and accuracy of the experimental apparatus and the parameters that can be estimated according the present modelling approaches.

EXPERIMENTAL APPARATUS AND MEASUREMENTS

In this paper, the TRT machine developed at Dime, University of Genova (Unige), has been employed for a pulsated TRT performed in Italy at Unige Savona Campus (44°18'04.6"N 8°27'02.9"E, Smart Energy Building SEB). The machine (Figure 2a) was developed in partnership with the Italian company Erde srl and it is equipped with a feedback control to manage either the flow rate or to the heat rate to the fluid. The heater section is constituted by three 3 kW electrical resistors controlled through a 3 phase angle power controller (TRIAC), with a control signal in the 0 to 10V range (Figure 2b). Analogue signals are provided by a D/A converter that communicates with Linux based microcomputer running a dedicated code. Control works according to a double PI (Proportional and Integral) algorithm and the PI parameters have been tuned following a Ziegler-Nichols [17] approach in dedicated laboratory tests. Temperature measurements are performed through PT1000 RTDs, calibrated to assure 0.1°C uncertainty. Mass flow rate and electrical power are available within 2% accuracy on reading thanks to proper instrumentation calibration performed at Dime.

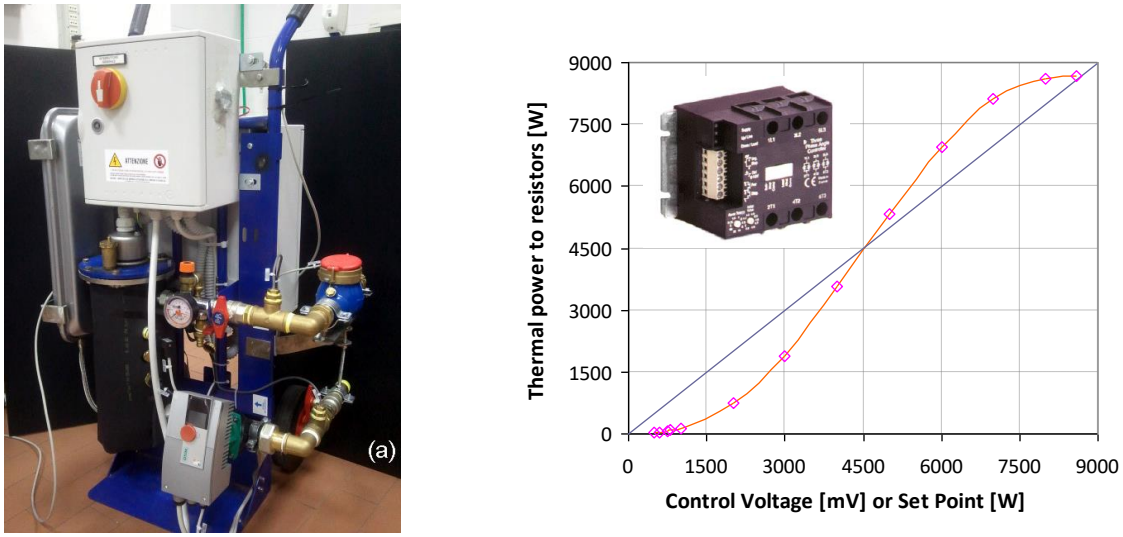

Figure 1 TRT machine developed at the University of Genova (a) and TRIAC power response vs control signal (b).

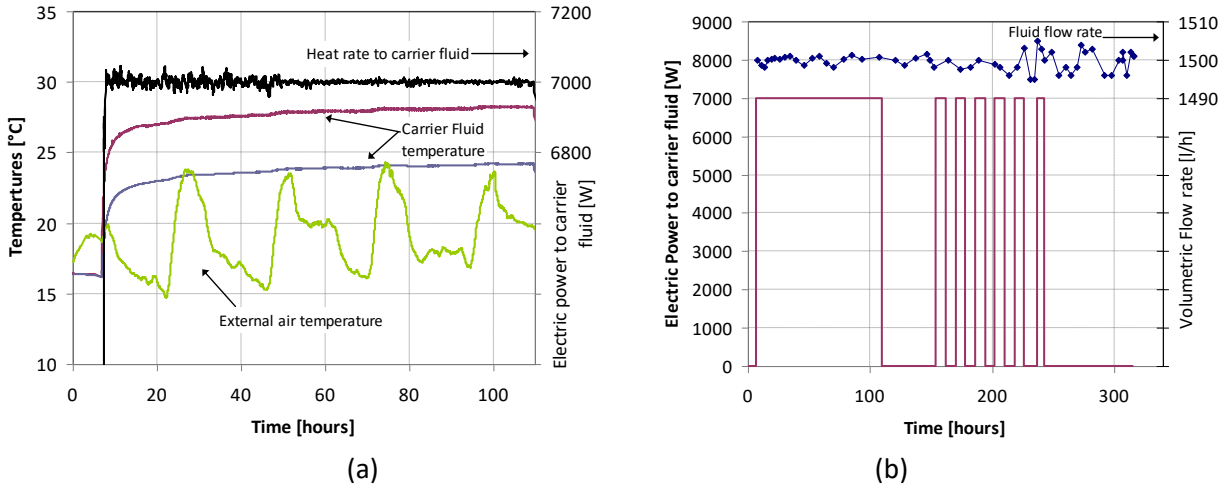

Figure 2 Temperature profiles during the first 100 hours of the pulsated TRT experiment (a), heat pulse sequence and carrier fluid flow rate vs time (b).

The measurements refer to an experimental campaign dated early November 2015. The pilot heat exchanger was 150 m deep grouted BHE, working with a single 40 mm U pipe. Grout nominal conductivity from manufacturer data was 2.0 W/m K. Geological surveys revealed that lithology is constituted by a top layer (20-25m deep) of alluvial material subjected to slow underwater movement and by fractured metamorphic formations. The measuring site is also close (70m) to the local creek which flows around the University Campus.

The TRT machine was shaded from the sunlight and surface pipes (about 2 m) properly insulated, but unusually hot conditions during the measurements slightly affected the carrier fluid temperatures, as can be noticed from the inspection of the fluid temperature records (Figure 2a). The TRT experiment lasted 12 days. The first 7 hours no heat rate was applied (undisturbed temperature measurements) and the following 100h a constant heat rate condition was set. From this instant on a series of heat pulses (heater off/on sequences) have been imposed: 45h (heating is off) then a series of 12 on and off cycles (8 hours each) and a final recovery period (power off) of about 60 h. In the heating

periods the heat transfer rate was set at 7000 W and the control was able to maintain a small 1.5% RMS variation irrespective of the daily supply voltage oscillations. The volumetric flow rate of water was maintained at 1500 liters/h, with 4 l/h RMS variation (Figure 2b) all along the test.

MODELLING THE HEAT TRANFER INSIDE THE GROUND MEDIUM

Interpretation with the ILS model

In GCHP modeling the Fourier conduction equation is very often the modeling approach according to which the variable ground temperatures are predicted when a vertical BHE is considered. As it is well known, the Fourier equation can be either refer to 1D or 2D temperature domains and different solutions arise from the related boundary conditions applied. The ILS model is probably the most successful scheme since it provides a simple but effective solution according to which when a constant heat transfer rate (per unit length $\dot{Q}'$) is applied to an extremely long linear source buried inside an infinite medium the ground temperature in space and time can be calculated according the well known relationship, here presented in terms of dimensionless excess temperature Γ :

$$\Gamma_{ILS} = \frac{T(r,\tau) - T_{gr,\infty}}{\dot{Q}'/2\pi k_{gr}} = \frac{1}{2} \int_{1/4Fo_r}^{\infty} \frac{e^{-\beta}}{\beta} d\beta = \frac{1}{2} E_1\left(1/4Fo_r\right) \tag{1}$$

Here above $T_{gr,\infty}$ is the initial and far field ground temperature, k_{gr} is the ground thermal conductivity, Fo_r is the Fourier number based on the radial distance from the line source, r. The Exponential Integral E_1 can be accurately approximated by its series expansions, as for example discussed by Fossa (2016). Similar solutions have been proposed for referring to heat sources finite in length, as discussed in the Introduction of this paper, but on the other hand it can be demonstrated (e.g. Fossa 2016) that in the short period, typically for $Fo_{rb}<10^4$, the ILS solution is accurate enough for TRT analysis purposes and it superposes very well to any FLS solution.

A slightly different problem is related to the presence of moving groundwater in the soil. Sutton et al. (2003) and later Molina Giraldo et al. (2011) demonstrated that the moving line source model, still based on the Fourier equation solution, is accurate enough for describing the heat transfer between a single BHE and the surrounding ground when groundwater circulation is present. Sutton et al. in particular described the MILS model, which allows the ground temperature excess to be calculated as a function of the source specific heat rate $\dot{Q}'$, the effective ground conductivity $k_{gr,eff}$ and the effective Peclet number ($Pe=w_{eff}\, r_b/\alpha_{gr,eff}$). All these *effective* properties depend either on the characteristics of the porous media and interstitial water. For the MILS, the resulting dimensionless temperature excess Γ is:

$$\Gamma_{MILS} = \frac{\left(T(r_b) - T_{gr,\infty}\right)}{\dot{Q}'/2\pi k_{gr,eff}} = \frac{\int_0^{\pi} \exp\left(\frac{Pe}{2}\cos(\vartheta)\right) d\vartheta}{2\pi} \int_{1/4Fo_{rb}}^{\infty} \frac{\exp\left(-\zeta - \frac{Pe^2}{16\xi}\right)}{\zeta} f\zeta \tag{2}$$

Molina Giraldo et al. (2011) demonstrated that the MFLS solution is very well approximated by its MILS counterpart for Fourier numbers corresponding to several months of time and that both solutions are in close agreement with 2D numerical solutions of conduction/convection problems in porous ground media with vertical heat exchangers.

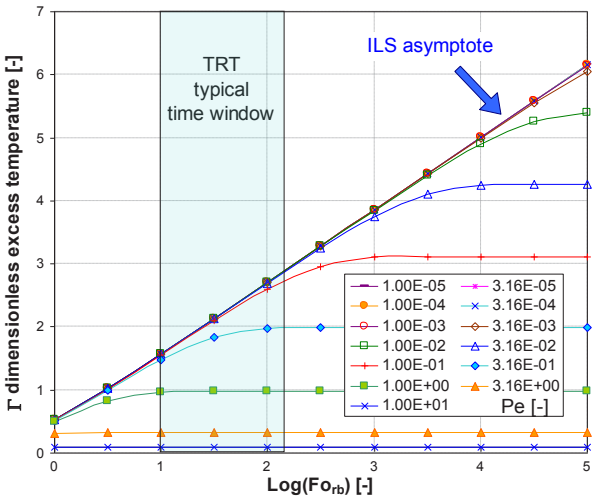

Figure 3. Dimensionless excess temperature Γ as a function of Fourier and Peclet numbers for the MILS solution. The TRT band shows the Pe values for ILS applicability to TRT measurements

Recently at Unige the proper and improper integrals of Eq. (2) have been solved and compared to the ILS profile (Eq. 1). Figure 3 shows this comparison in terms of ILS and MILS dimensionless temperature excess. The independent parameters are Fo_{eff} and Pe numbers. Figure 3 reveals that for Fourier numbers ranging from 10 to 100 (magnitude orders) the ILS solution is a good approximation of its MILS counterpart, provided that the Peclet number is sufficiently small (Pe < 0.02). Therefore, it has been decided to use the ILS model to interpret the PTRT since both solutions are similar for the duration of the PTRT.

Interpretation with the FLS model

Although for short TRT duration the ILS and FLS models have the same response, it has been decided to also interpret the PTRT with the FLS model and to observe if integration of the axial effects by the FLS model could lead to different thermal properties for this unusually long TRT. Using the formulation of Claesson and Javed (2011), the dimensionless excess temperature of the FLS model is given by:

$$\Gamma_{FLS} = \frac{1}{2} \int_{\frac{1}{\sqrt{4 r_b^2 Fo_r}}}^{\infty} e^{-r_b^2 s^2} \frac{Y(Hs, Ds)}{Hs^2} ds \tag{3}$$

with

$$Y(Hs, Ds) = 2\,\mathrm{ierf}(Hs) + 2\,\mathrm{ierf}(Hs + 2Ds) - \mathrm{ierf}(2Hs + 2Ds) - \mathrm{ierf}(2Ds) \tag{4}$$

and with

$$\mathrm{ierf}(X) = X\,\mathrm{erf}(X) - \frac{1}{\sqrt{\pi}}(1 - e^{-X^2}) \tag{5}$$

Interpretation with a TRC model

To verify if an advanced interpretation model accounting for the capacity of the borehole components could lead to a different set of parameters, the TRC model of Pasquier and Marcotte (2012, 2014) was also used to interpret the PTRT. The TRC model integrates the fluid advection within the vertical pipes, the geometry and thermal conductivity and capacity of each component (fluid, pipe, grout, and ground) through a network of interconnected thermal resistances (*R*) and capacities (*C*) chosen to ensure a high accuracy of the interpretation model. For a network of *n*

nodes, the model allows writing heat conservation at node *j* by

$$C_j \frac{dT_j}{dt} = \sum_{k=1}^{n_j} \frac{T_k - T_j}{R_k} \tag{6}$$

where n_j is the number of neighbouring nodes to node *j*. Assembling Eq. 6 for all nodes of the model leads to a stiff first-order differential equations system whose solution is obtained by numerical integration with the Haae wavelet method (Nguyen and Pasquier 2015).

PARAMETER ESTIMATION FROM TRT MEASUREMENTS

The interpretation of a TRT can be accomplished by formulating the parameter identification task as an inverse problem. The interpretation strategy then consists to minimize an objective function quantifying the misfit between the temperatures simulated by an interpretation model and the temperatures actually measured on the field. This interpretation method is now used frequently (Wagner and Clauser 2005; Marcotte and Pasquier 2008) and permits using interpretation models that incorporate directly significant variations of the heating power. The use of a more accurate interpretation model often leads to a more robust parameter identification.

For the ILS and FLS models, the evolution of the mean fluid temperature under the constraint of a variation of the heating power signal, as in a PTRT, can be formulated as a convolution product by

$$T_{f,ave}(\tau_N) = T_{gr,\infty} + \dot{Q}'_N R_{bhe} + \frac{1}{2\pi k_{gr}} \sum_{i=1}^{N} (\dot{Q}'_i - \dot{Q}'_{i-1})\, \Gamma\big(Fo(\tau_N - \tau_{i-1})\big) \tag{7}$$

where R_{bhe} is the equivalent borehole resistance and the index *i* refers to the time step index. From Eq.7, the optimization procedure consists to find the R_{bhe} and k_{gr} couple that minimizes the discrepancy between the experimental and modelled temperatures.

The procedure used with the ILS model is based on trial and error. Starting with initial guesses of k_{gr} and R_{bhe}, the simulated fluid temperatures are compared to the average fluid temperature $T_{f,ave}$ and the parameters are changed until an optimum solution is found. To interpret the PTRT with the FLS and TRC models, the program TRT-SInterp (Pasquier 2015) was used. The latter is dedicated to stochastic and deterministic interpretation of TRTs by optimization. Since its initial publication, the program has undergone constant improvements and now includes a graphical user interface to ease its use in the industry.

RESULTS AND DISCUSSION

The parameter recognition procedures adopted in this paper has been used with the ILS, FLS and TRC models to interpret the PTRT. The parameters found at the optimum along with the calibration statistics are summarized in Table 1. In addition, Figure 4 compares the experimental temperatures and the temperatures simulated by the various interpretation models used in this work with the parameters found at the optimum. The thermal conductivity values range from 6.17 to 6.25 W/mK. Although the values obtained are quite high, these results are in agreement with a

Table 1: Thermal parameters obtained after interpretation of the PTRT

Interpretation model	Thermal conductivity (W/mK)	Borehole Resistance (mK/W)	Mean error on predicted temperature (K)
ILS	6.25	0.122	0.10
FLS	6.17	0.131	0.11
TRC	6.24	0.128	0.16

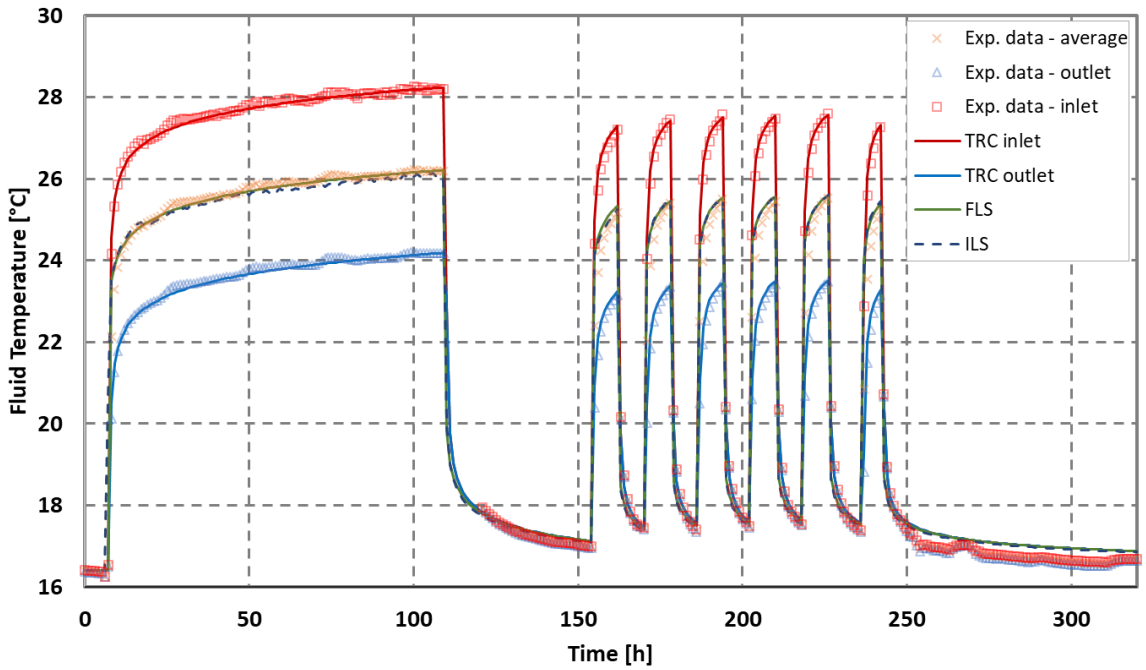

Figure 4. Comparion of the experimental temperatures with the ILS, FLS and TRC models used to interpret the PTRT.

value obtained independently on the same BHE in August 2015 by a private company having its own standard TRT unit and applying its own interpretation procedures. The thermal conductivity values have hence been ascribed to the particular local lithology, where the circulation of groundwater seems plausible. The reduced slope of alluvial plane (2.5%) and the estimated permeability of the top layer around 10^{-5} cm/s are finally compatible with Pe numbers related to the validity of ILS model to the present enhanced TRT analysis. However, at this point it is unclear if the high thermal conductivity observed is caused by a significant groundwater flow or is simply the expression of a highly conductive geological material.

It is reassuring to see similar thermal parameters, regardless of the interpretation model used. Indeed, the parameters found at the optimum differ than less than 1.3% for k_{gr} and 6.9% for R_{bbe}. For the interpretation of this specific PRTR, the variations observed are attributed mainly to the different convergence parameters used to control the optimization algorithms. It should be noted that this PTRT induced a narrow valley for the objective function in the parameter space that was sometimes a challenge for the optimization algorithms.

It should be noted that from the author's experience, obtaining borehole equivalent resistance with the ILS/FLS models that is so close to the one obtained with the TRC model is unusual. When interpreting a conventional TRT, the thermal conductivity obtained are quite similar but the borehole resistance provided by the TRC model is usually better identified. These results might indicate that performing a long PTRT can filter out the impact of the interpretation model on the interpretation outcome and improve the identification of R_{bbe}.

The thermal parameters found reproduce also quite well the experimental temperatures measured during the PTRT as seen in Figure 4. Indeed, the output of all three interpretation models adjust quite well the experimental temperatures. Note how the TRC model was slightly better at adjusting the peaks corresponding the each pulse, but this did not resulted in a significantly better adjustment from an overall statistic error. All three models are able to reproduce correctly also the long recovery phases, even if a closer inspection of numerical values would reveal discrepancies within tens of degree. A thermal contamination of the measurements or a significant groundwater flow could explain the inability of the models to fit the long recovery phases. However, for now this remains an open problem.

CONCLUSIONS

In this paper the measurements from a pulsated Thermal Response Test have been presented and discussed. In this particular experiment the heat rate at the carried fluid was deliberately varied according to a series of on/off heat pulses able to resemble a real GCHP operating conditions. A dedicated equipment has been developed to this aim at the University of Genova which is able to very efficiently control the heat and flow rates either in constant or pulsated mode. Such a Pulsated Thermal Response Test has been processed by 3 different inverse solution algorithms developed at the home universities of the Italian and Canadian authors of the present paper. The methods include the application of the temporal superposition techniques, the use of the ILS and FLS solutions for the semi-infinite ground medium and even a resistance/capacitance method (the TRC algorithm) able to take into consideration whole the inner borehole thermal network. Very similar thermal parameters have been estimated by the three algorithms: at convergence the results differ less than 1.3% for k_{gr} and 6.9% for R_{bhe}. Based on author's experience, a similar agreement on R_{bhe}. estimations between TRC and ILS/FLS models is pretty unusual. These results might indicate that performing a long PTRT can filter out the impact of the interpretation model on the interpretation outcome and improve the identification of borehole thermal resistance.

ACKNOWLEDGMENTS

Dime Dept. at University of Genova is greatful to MAVOCO Gmbh for the support provided in measurement data transfer via dedicated machine-to-machine protocol.

NOMENCLATURE

E_1	=	Exponential Integral solution (-)
Γ	=	temperature response factor (-)
Fo_r	=	radius based Fourier number (-)
Pe	=	Peclet number (-)
$\dot{Q}'$	=	specific heat rate (W/m)
α	=	ground thermal diffusivity (m^2/s)
C	=	thermal capacity (J/m^3K)
k_{gr}	=	ground thermal conductivity (W/mK)
H	=	borehole length (m)
r_b	=	borehole radius (m)
r	=	radial distance from the line source (m)
R_{bhe}	=	effective borehole resistance (mK/W)
τ	=	time (s)
T	=	temperature (K)
$T_{gr,\infty}$	=	initial temperature of the medium (°C)

SUBSCRIPTS

FLS	=	Finite Line Source
ILS	=	Infinite Line Source
MILS	=	Moving Infinite Line Source
eff	=	effective, as weighted average between soil and water properties

REFERENCES

Acuna J., P. Mogensen and B. Palm, 2009. *Distributed thermal response test on a U-pipe borehole heat exchanger*. In: 11th Int. Conf. on Energy Storage EFFSTOCK, Stockholm.

Austin, W A. 1998. *Development of an in situ system for measuring ground thermal properties*, PhD Thesis, Oklahoma State University.

Carslaw, H.S and J.C. Jaeger, 1947. Conduction of heat in solids. Claremore Press Oxford UK.

Claesson J. and S. Javed, 2011. *An Analytical Method to Calculate Borehole Fluid Temperatures for Time-scales from Minutes to Decades*. ASHRAE Transactions 117:279–288.

Eskilson P., 1987. *Thermal analysis of heat extraction boreholes*. Ph.D. Thesis, Lund University of Technology, Sweden.

Fossa M., A. Priarone, D. Rolando and F. Berti, 2016. *Borefield Design and Enhanced Thermal Response Test for the Energy Building of the University of Genova*, UIT Heat Transfer Conference, Ferrara, Italy.

Fossa, M., 2016. *Correct Design of Vertical BHE Systems Through the Improvement of the Ashrae Method*, Science and Technology for the Built Environment, 1-10

Gehlin, S., 1996. *Thermal response test method development and evaluation* Licentiate Thesis, Lulea University of Technology.

Gehlin, S.E.A. and G. Hellström, 2003. *Influence on Thermal Response Test by Groundwater Flow in Vertical Fractures in Hard Rock*. Renewable Energy 28: 2221-2238.

Hellström G., 1991. *Ground Heat Storage. Thermal Analysis of Duct Storage Systems. Part I Theory*. University of Lund, Sweden.

Ingersoll, L.R., O.J. Zobel and A.C. Ingersoll, 1954. Heat conduction with engineering, geological, and other applications. McGraw-Hill New York.

Lamarche, L. and B. Beauchamp, 2007. *A new contribution to the finite line-source model for geothermal boreholes*, Energy Build. 39: 188–198.

Marcotte D. and P. Pasquier, 2008. *On the estimation of thermal resistance in borehole thermal conductivity test*. Renewable Energy 33(11):2407-15.

Mogensen, P. 1983. *Fluid to duct wall heat transfer in duct system heat storages* Document-Swedish Council for Building Research 16: 652-657.

Molina-Giraldo N, P. Blum, K. Zhu, P. Bayer and Z. Fang, 2011. *A moving finite line source model to simulate borehole heat exchangers with groundwater advection*. International Journal of Thermal Sciences 50(12):2506-13.

Molina-Giraldo, N., P. Blum, K Zhu, P Bayer and Z Fang. 2011. *A moving finite line source model to simulate borehole heat exchangers with groundwater advection.* Int. J. Therm. Sci 50: 2506–2513.

Nguyen A and P. Pasquier, 2015. *An adaptive segmentation Haar wavelet method for solving thermal resistance and capacity models of ground heat exchangers*. Applied Thermal Engineering 89:70-9.

Pahud, D and B. Matthey, 2001. *Comparison of the thermal performance of double U-pipe borehole heat exchangers measured in situ*. Energy and buildings 33: 503-507.

Pasquier P, D. Marcotte, 2014. *Joint use of quasi-3D response model and spectral method to simulate borehole heat exchanger*. Geothermics. 51:281-99.

Pasquier P. and Marcotte D., 2012. *Short-term simulation of ground heat exchanger with an improved TRCM*. Renewable Energy 46:92-9.

Pasquier P., 2015. *Stochastic interpretation of thermal response test with TRT-SInterp*. Computers & Geosciences 75:73-87.

Spitler, J. D. and S. E. A. Gehlin, 2015. *Thermal response testing for ground source heat pump systems—An historical review*. Renewable and Sustainable Energy Reviews 50(0): 1125-1137.

Sutton, M.G., D.W. Nutter and R.J. Couvillion. 2003. *A ground resistance for vertical bore heat exchangers with groundwater flow*. J. Energy Resources. Technology 125(3): 183-189.

Wagner R, C. Clauser, 2005. Evaluating thermal response tests using parameter estimation for thermal conductivity and thermal capacity. Journal of Geophysics and Engineering 2(4):349-56.

Zeng H.Y., N.R. Diao and Z.H. Fang, 2002. *A Finite line-source model for boreholes in geothermal heat exchangers*, Heat Transfer-Asian Research, 31: 558-567.

Ziegler, J.G. and N.B. Nichols, 1942. Optimum settings for automatic controllers Transaction ASME 64 (11).

[This page has been intentionally left blank]

IGSHPA SWEDEN
2018 Research Conference

DOI: 10.22488/okstate.18.000040

Are shallow boreholes a suitable option for inter-seasonal ground heat storage for the small housing sector?

Carlos Naranjo-Mendoza **Richard M. Greenough** **Andrew J. Wright**

ABSTRACT

In recent years, various researchers have studied the performance of Solar Assisted Ground Source Heat Pump (SAGSHP) systems using borehole heat exchangers. However, the research conducted has been limited to conventional boreholes (30m to 150m depth), which are expensive and not suitable for the small housing sector. This paper reports an experimental analysis of a shallow SAGSHP system with inter-seasonal storage. The system, installed in Leicester UK, consists of seven photovoltaic-thermal (PVT) collectors connected in series with an array of 16 shallow boreholes (1.5 meters depth). Data regarding the energy fluxes involved in the soil-based thermal store have been monitored and analysed for one year. The results show that the shallow soil is able to serve as a storage medium to cover the heating demands of a near zero energy domestic building. However, it was noticed that in addition to the solar heat captured and stored in the soil, the system covers part of the heating demand from heat extracted from the soil surrounding the thermal store. During winter, the lowest temperature reached by the soil so far is 2 °C. Hence, no freezing problems have occurred in the soil. An analysis of the temperature variation of the ground storage under the system operation is also shown.

INTRODUCTION

Ground source heat pumps (GSHP) with vertical boreholes have been largely used as an alternative system to cover both cooling and heating thermal loads by using the ground as a renewable energy source or sink (Emmi et al. 2015). The main reason to use this technology is increasing the heat pump efficiency by having a more stable energy source or sink when compared to air source heat pumps (ASHP) (You et al. 2015). In fact, GSHP has been shown to be a very promising option when implemented in the early design of new buildings and in a climate where the thermal loads are balanced over the entire year (i.e. cooling and heating needs). However, in most climates the thermal loads are not balanced over the year and consequently GSHPs tend to lose efficiency in the long term (Wu et al. 2013). For instance, in heating dominated climates, the ground serves as a heat source, which mean that over the time the constant heat extraction from the ground will affect the natural ground temperature. Indeed, Zhu et al. (2015) show that the continued use of a GSHP decreased soil temperature by 0.185°C per year. This problem has been one of the main obstacles for the development of GSHP technologies (You et al. 2015). An option to deal with this problem might be to increase the borehole depth. However, this leads to an increase in the initial cost due to the need for large machinery for the drilling process (You et al. 2015). Therefore, storing heat in the ground from another heat source is an option that has been studied in recent years, solar energy being the most common of the external heat sources

Carlos Naranjo-Mendoza (carlos.naranjo@epn.edu.ec) is a researcher at the Departamento de Ingeniería Mecánica in Escuela Politécnica Nacional in Ecuador and PhD studet at IESD in De Montfort University in UK, Richard M. Greenough and Andrew J. Wright are Professors at IESD in De Montfort University in UK.

(Banjac 2015). This system is known as Solar Assisted Ground Source Heat Pump (SAGSHP) and it is claimed be a sustainable system that can maintain a highly efficient heat pump operation in the long term. The functioning principle of SAGSHP is that of inter-seasonal heat storage where heat collected in summer using a solar thermal collector is stored in the ground to be used by the GSHP during winter. The increase in the heat source temperature allow the system to have a higher efficiency and to compensate for the thermal imbalance of the ground (Zhai et al. 2011). Moreover, with the increase in the ground temperature, the required borehole length in the GSHP can be minimised as stated by Cao et al. (2014).

Regarding SAGSHP systems, both numerical (Emmi et al. 2015; Eslami-nejad and Bernier 2011; Chiasson and Yavuzturk 2003; Paiho et al. 2017) and experimental (Xi et al. 2011; Wang et al. 2010) studies are found in the literature. However, the application of this technology has been limited to large buildings due to the high cost of system installation, mainly related to drilling costs. Conventional boreholes in GSHP systems are installed at depths from 30m to 150m, which makes the technology unsuitable for domestic applications. On the other hand, shallow boreholes in GSHP have not been deeply studied, as the soil near to the surface is thermally disturbed so that a system installed at shallow depths will be inefficient. For a domestic application a shallow borehole system can be a potential alternative for conventional heating systems if the boreholes are installed at the foundation construction stage (Wright et al. 2014). Shallow boreholes at depths up to 5 meters installed at the same time as the building foundations might be an option for low energy housing in heating dominated climates.

This paper presents the preliminary results of an experimental study of a SAGSHP system, which has shallow vertical boreholes to cover the heating demands of a small dwelling. This research focuses on the energy flows to and from the shallow soil for a system that aims to store heat from solar energy in summer and use it in winter to cover heating demands. The system is evaluated under the climatic conditions of Leicester, UK during one year.

EXPERIMENTAL SET-UP

System configuration

The experimental project was conducted by the Institute of Energy and Sustainable Development (IESD), at De Montfort University (DMU) in Leicester, UK. The experiment was set-up to investigate whether shallow boreholes (1.5m deep and spaced 1.5m apart) can be a potential solution for SAGSHP systems in order to store enough energy in summer to cover heating demands in winter for the small domestic sector. The use of very shallow boreholes is the main innovation of this type of SAGSHP system. The reason for the choice of shallow boreholes is that they can be built very cheaply in the majority of locations without the need for expensive drilling equipment (Wright et al. 2014). In fact, the shallow boreholes of the experimental system were built using a simple fencepost auger mounted on a mini-excavator. The intention of this system is to be built during the construction stage of high efficiency buildings or buildings toward net zero energy as the footprint of the building above limits the number of boreholes and in consequence, the heat that can be stored. However, the SAGSHP of the present study was retrofitted to an unoccupied Victorian terrace owned by DMU. Although this building has been upgraded with loft insulation and double-glazing, it is draughty and has no solid wall insulation, hence it is a relatively inefficient building. Another difference between the intended application of the system and the current installation of this study is that the inter-seasonal ground thermal store (known as an 'earth energy bank', or EEB) could not be built within the foundations of the house. Instead, a thermal store of the same footprint was placed in an adjacent grass verge. The sides were reinforced with concrete (15cm) as if they were the footings for a new-build house and insulated at the edges and on top.

A system schematic is shown in Figure 1. As shown, the system consists mainly of three fluid loops. The solar loop, the ground loop and the heating loop (storage or radiant floor). In the solar loop, the fluid gains heat through seven solar-photovoltaic collectors (PVT) that transfer the heat to the fluid of the ground loop by means of a heat exchanger. Both, the solar loop and ground loop working fluids are a 30% glycol/water mix by volume. This

concentration rate is the recommended by the PVT manufacturers to avoid freezing problems under the weather conditions in the UK. The thermal efficiency of the PVTs is 67% and the aperture area of the collector is 1.5m². If the temperature at the outlet of PVT collectors is greater than the EEB temperature by 7°C then the solar loop pump is activated. The ground fluid passes through a series of 16 shallow U-tube boreholes (1.5m deep) transferring heat into the EEB. If the heat pump is not calling for heat at this point, then the fluid circulates and recharges the thermal store until the temperature difference between the EEB and the outlet of the PVT falls below 4°C, at which point the solar loop pump switches off. If the heat pump is calling for heat during solar generation, the fluid releases some heat to the heat pump evaporator and any surplus recharges the thermal store. If there is any heat demand when the solar loop is inactive, then the heat pump will circulate fluid around the ground loop and through the evaporator, which therefore extracts heat from the EEB. In this way, the EEB will lose the stored heat, which must be recharged whenever solar energy is available again.

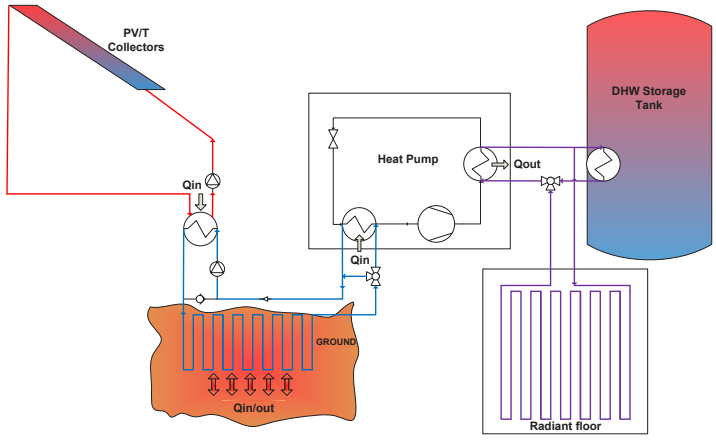

Figure 1 Schematic of the system configuration

The vertical ground heat exchanger (VGHE) consists of an array of 16 shallow boreholes in series (Figure 2). The EEB, which is used as a thermal store, has a dimension of 10m x 4m and is insulated on the top (20cm) and sides (10cm) as mentioned previously. The distance between each adjacent borehole is 1.5m except for distances between boreholes B1-B2, B10-B11 and B15-B16 (see Figure 2) which are separated 1m. The thermal properties of the soil were determined by a thermal response test conducted on site prior to construction of the EEB. The boreholes (15cm diameter) are filled with thermal grout (bentonite). The thermal properties of the soil and the working fluid are shown in Table 1. The heat pump heating capacity is 3kW, which is approximately enough to cover the heating needs of a well-insulated small dwelling in the UK. The heat pump stores the heat for DHW needs in a 200 litre cylinder.

Table 1. Soil and working fluid thermal properties

Type of soil/fluid	Wet clay	Glycol (30%)
Thermal conductivity	1.5 W/mK	---
Density	1800 kg/m³	1070 kg/m³
Specific Heat	1200 J/kgK	3768 J/kgK
Thermal diffusivity	6.94×10^{-7} m²/s	---

Monitoring system

The National Instruments cDAQ system (2016) is used to monitor the EEB and using 48 temperature sensors (PT1000) that are distributed at distances and depths of interest around the EEB. Calibrated resistance temperature detectors (RTD) are used for the temperature monitoring to minimise errors in the data due to the length of the wires from the monitoring point to the data logger. The margin of error in these measurements is ±0.3 °C. Figure 2 shows the location of the sensors (1 to 14) and Table 2 describes the depths of temperature monitoring of each sensor. The time scale of the monitored data is 15 minutes and data have been recorded since 04/06/2016. The fluid flow rate for the ground loop is also monitored. This parameter is key for analysing the energy flows from/to the EEB.

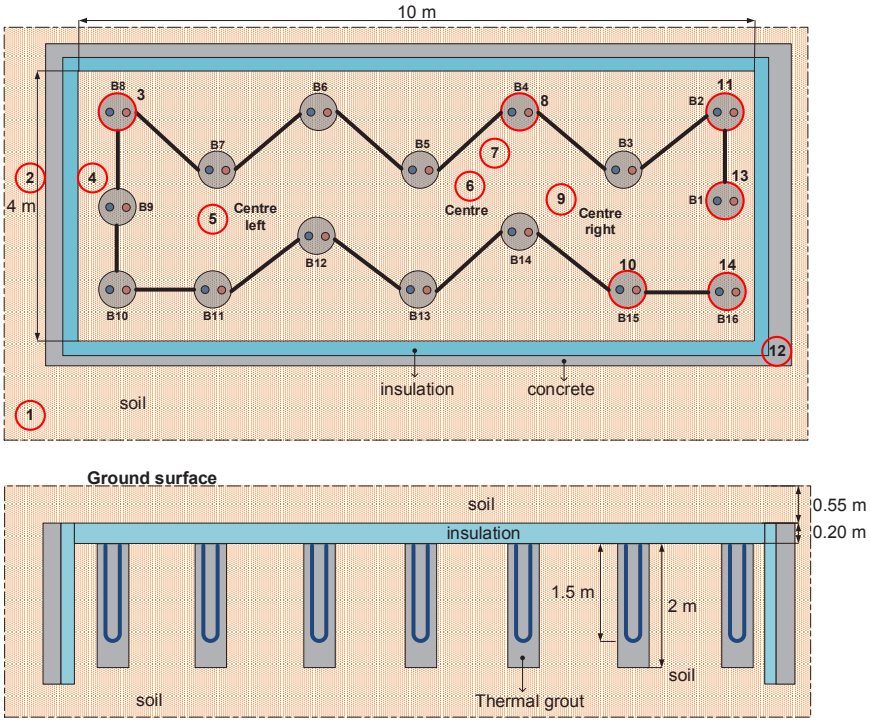

Figure 2 Vertical and horizontal cross-section view of the GHE with sensor location for the cDAQ system

Table 2. Sensors location and depth of measurement for the EEB

Sensors point	Location	Depth of measurement
1	Distant from EEB	0.75 m, 1.25 m, 1.75 m, 2.75 m
2	Just Outside EEB	0.75 m, 1.25 m, 1.75 m, 2.75 m
4	Just Inside EEB	0.75 m, 1.25 m, 1.75 m, 2.75 m
3, 8, 10, 11	Borehole wall (B8, B4, B15, B2)	0.75 m, 1.25 m, 1.75 m, 2.75 m
5, 6, 7, 9	Centre of the EEB	0.75 m, 1.25 m, 1.75 m, 2.75 m
12	Inside and outside the insulation	1.75 m
13	Inlet flow temperature	0.75 m
14	Outlet flow temperature	0.75 m

Weather data have also been monitored from a weather station located on the roof of the Gateway House Building on DMU campus (250m from the experimental SAGSHP installation). These data can be downloaded from the station itself in one-hour time steps. The measured variables include ambient temperature, relative humidity, wind speed, solar radiation (global and diffuse), precipitation, etc. Figure 3 shows the monthly solar insolation and ambient temperature from the actual data monitored from March 2016 to February 2017. These data provide a useful context for the study but were not necessary to analyse the performance of the EEB.

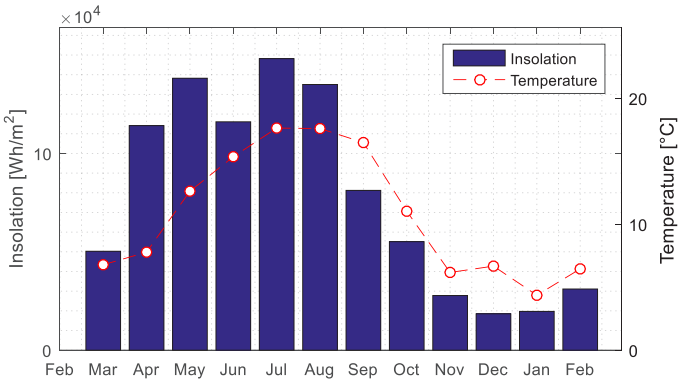

Figure 3 Monthly average ambient temperature and solar insolation from the monitored data

Earth Energy Bank heat flux

Using the data monitored, it is possible to determine the heat fluxes going to (heat stored) or taken from (heat removed) the EEB. Heat is stored mainly in summer when there is little heat demand from the building. During heat storage, the average soil temperature in the EEB is lower than the solar PVT outlet temperature. On the other hand, heat is removed from the EEB mainly in winter when there are large heating loads from the building and solar energy is not available. During the transition periods (Spring and Autumn) a combination of heat extraction and injection can be observed. The heat flux during storage or extraction can be calculated as follows (Equation 1):

$$Q_{gr} = \dot{m}_{ghe} \times c_p \times \left(T_{out_{EEB}} - T_{in_{EEB}}\right) \quad (1)$$

where, Q_{gr} (W) is the heat flux during storage (negative) or extraction (positive) from the EEB; $\dot{m}_{ghe}$ (kg/s) is the mass flow rate; c_p (kJ/kg°C) is the specific heat of the working fluid in the VGHE; $T_{out_{EEB}}$ (°C) is the VGHE outlet fluid temperature and $T_{in_{EEB}}$ (°C) is the VGHE inlet fluid temperature. The mass flow rate is determined from the monitored volumetric flow rate data multiplied by the glycol density. While it is true that the physical properties of fluids vary with temperature, from a practical point of view this variation can be ignored since it is less than 1.8% in the temperature ranges from 5°C to 50°C (Lemmon at al. 2005). Average values, corresponding to a fluid temperature of 26.7°C, have been used as thermal properties for the glycol.

RESULTS AND DISCUSSIONS

Heat flux throughout the Earth Energy Bank

The data used for the analysis of the energy balance correspond to the period from 04/06/2016 to 30/06/2017. As shown in Equation 1, the measured values of the EEB (vertical ground heat exchanger) inlet and outlet fluid temperature were combined with the measured mass flow rate of the fluid in the ground loop ($\dot{m}_{ghe}$) to calculate the amount of heat injected or extracted into or from the soil. Thus, Figure 4 shows the hourly values of the EEB inlet and outlet temperature. The figure shows that from June to September (summer), the heat injection process into the EEB takes place, whereas from November to February (winter) heat is mostly extracted. It is worth mentioning that the old heating system remained operative throughout test period, but in frost protection mode only. However, during January/February somebody tampered with the thermostat for the original system so that it provided space heating and the heat pump was not operating in the expected manner and the house was overheating. This explains why the fluid temperature in the EEB during this period did not go negative.

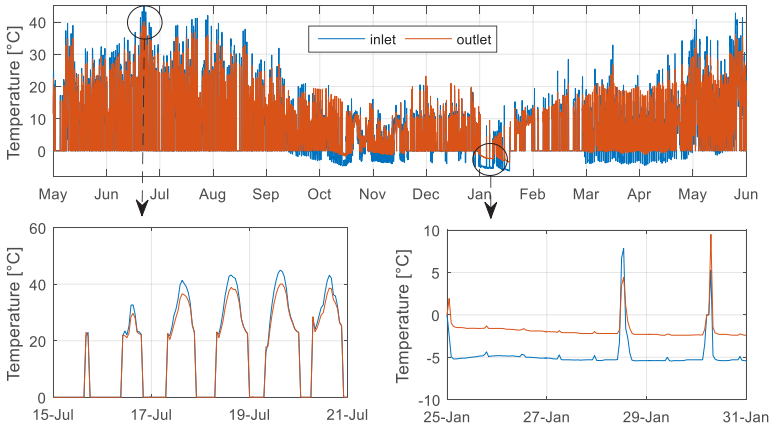

Figure 4 Inlet and Outlet fluid temperatures in the EEB

The analysed data correspond to a total of 9404 hours during which the ground loop pump was operating for 5964 hours (for either heat injection or extraction). Hence, to avoid erroneous heat flux readings, only the data in which the system was operating were analysed. In this context, Figure 5a shows the hourly heat flux (W) throughout the EEB. The heat injection rate (negative), predominant in summer, reaches peak values up to 5 kW, while the peak heat extraction rate (positive) is around 3 kW. This figure also shows that the heat injection is much more variable as it is governed by the solar energy availability. In addition, as seen in Figure 5a, heat extraction and heat injection can each occur in both summer and winter. Heat extraction in summer occurs when heating for domestic hot water (DHW) is required, while heat injection in winter occurs when there is solar energy available, typically on a mild, sunny day.

Figure 5b shows the total energy stored (negative) or extracted (positive) to/from the EEB. As can be seen, in the total balance there is more energy extracted than stored. This is logical due to the heating dominated climate in Leicester, UK. However, it is also important to mention that the extracted energy from the EEB is not only recovered by the solar energy injected by the system but also by the natural soil recovery. Since the bottom of the EEB is not insulated, in wintertime the EEB is partially replenished by the heat in the soil below. Hence, the heat extracted is both solar and geothermally sourced. Further research is needed in order to determine the amount of heat that the surrounding soil can transfer to the EEB during the whole year cycle. At present the cost-benefits of the side insulation are the subject of discussion and future analysis, and it may be that under some circumstances the benefits of heat retention in summer are outweighed by the reduction of heat gains from the surrounding soil in winter.

Earth Energy Bank thermal performance

In this section, we conduct an analysis of the thermal performance of the thermal store (EEB). Figure 6 shows the natural temperature variation of the soil (sensor 1) at different depths (0.75m, 1.25m, 1.75m and 2.75m). The natural recharging of the EEB from below occurs from late March to September, where the maximal temperature of the soil at 2.75m is slightly higher than 15°C. On the other hand, from late September to March the EEB soil is naturally discharging and the minimal soil temperature at 2.75 m is below 10°C. Hence, although the installation of the ground heat exchanger is at a maximum depth of 2.75 m, the annual temperature oscillation is around 5°C, which is small enough that it does not seriously reduce the performance of the heat pump.

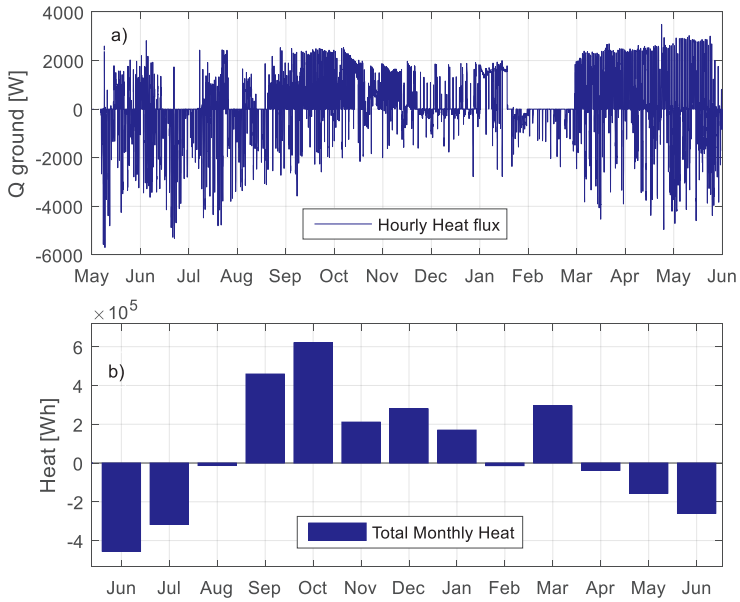

Figure 5 **a)** Hourly ground heat flux; **b)** Monthly ground heat

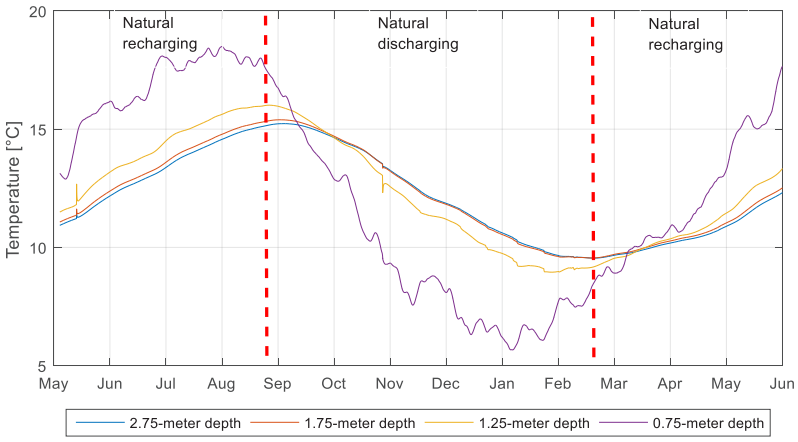

Figure 6 Natural soil temperature variation, sensor 1

Figure 7 shows the temperature variation of the EEB centre temperature (sensors 5, 6, 7 and 9) compared to the natural soil variation (sensor 1) at different depths. The regions of heat storage and extraction can be clearly seen. For example, at a depth of 1.25m, the EEB reaches a maximum temperature of 20°C which is about 5°C higher than the natural soil temperature at the same depth. In contrast, the lowest temperature of the EEB at the same depth is close to 2°C which is around 8°C lower than the natural soil at the same depth. These data show greater storage effects (ΔT) at mid-range depths, as expected. However, no conclusions about the long-term energy balance can be drawn yet, as this analysis must be performed using data collected over several years or through multi-year simulations.

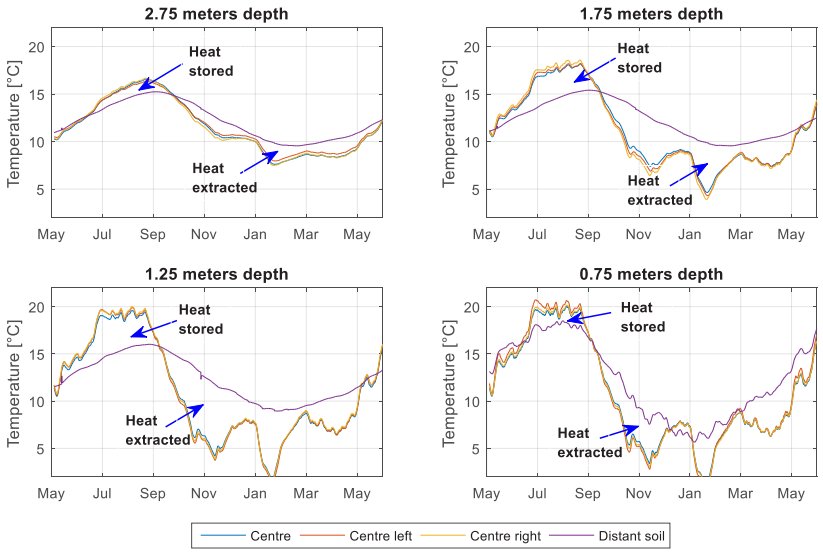

Figure 7 EEB and natural soil temperature variation

CONCLUSIONS

In this paper, the performance of an experimental SAGSHP with shallow boreholes for residential heating applications has been analysed. The system performance was studied from data collected over 13 months. The main innovation of this system is the use of a shallow (1.5 meter depth) vertical ground heat exchanger, which is used to seasonally store heat into a thermal store known as an earth energy bank (EEB). Although the system is small and it could not cover all the heating demands of the thermally inefficient test building, it is evident that the system can properly work to cover heating demands for a near net zero energy building. The use of long-term (inter-seasonal) heat storage as well as short-term (hot water tank) allow the system to cover heating loads during winter including peak heating loads. The total heat extracted during the whole period is higher than the total heat injected from solar energy. However, it was also evident that the soil in the EEB partially recovers heat from the surrounding soil below the EEB. Further research is needed to quantify this heat, which will help in the further optimisation of this shallow system. Regarding the performance of the EEB, during the heat extraction period, the EEB soil temperature drops to only 2°C. Without solar recharging, the temperature in the soil might easily reach temperatures below 0°C, freezing the soil and affecting the overall system efficiency.

ACKNOWLEDGMENTS

The authors of this publication gratefully acknowledge De Montfort University, Caplin Homes and Vaillant UK for their support in this research.

NOMENCLATURE

ΔT	temperature difference [°C]
$ASHP$	air source heat pump
COP	coefficient of performance
EEB	earth energy bank
GHE	ground heat exchanger
$GSHP$	ground source heat pump
PVT	photovoltaic thermal collector
Q	heat flux [W]
SA	solar assisted GSHP
T	temperature [°C]
c_p	specific heat [J/kg°C]
$\dot{m}$	mass flow rate [kg/s]

Subscripts

ghe	ground heat exchanger
in	inlet
out	outlet

REFERENCES

Banjac, Miloš. 2015. "Achieving Sustainable Work of the Heat Pump with the Support of an Underground Water Tank and Solar Collectors." *Energy and Buildings* 98 (July). Elsevier Ltd: 19–26. doi:10.1016/j.enbuild.2014.11.059.

Cao, Sunliang, Ala Hasan, and Kai Sirén. 2014. "Matching Analysis for on-Site Hybrid Renewable Energy Systems of Office Buildings with Extended Indices." *Applied Energy* 113 (January): 230–247. doi:10.1016/j.apenergy.2013.07.031.

Chiasson, Andrew D, and Cenk Yavuzturk. 2003. "Assessment of the Viability of Hybrid Geothermal Heat Pump Systems with Solar Thermal Collectors." *ASHRAE Transactions* 109 (2): 487–500.

Emmi, Giuseppe, Angelo Zarrella, Michele De Carli, and Antonio Galgaro. 2015. "An Analysis of Solar Assisted Ground Source Heat Pumps in Cold Climates." *Energy Conversion and Management* 106 (December): 660–675. doi:10.1016/j.enconman.2015.10.016.

Eslami-nejad, Parham, and Michel Bernier. 2011. "Coupling of Geothermal Heat Pumps with Thermal Solar Collectors Using Double U-Tube Boreholes with Two Independent Circuits." *Applied Thermal Engineering* 31 (14): 3066–3077. doi:10.1016/j.applthermaleng.2011.05.040.

Instrument, National. 2016. "LabVIEW System Design Software - National Instruments." *LabVIEW System Design Software - National Instruments*. http://www.ni.com/labview/.

Lemmon, E W, M O McLinden, and D G Friend. 2005. "Thermophysical Properties of Fluid Systems." *NIST Chemistry Webbook, NIST Standard Reference Database* 69.

Paiho, Satu, Ha Hoang, and Mari Hukkalainen. 2017. "Energy and Emission Analyses of Solar Assisted Local Energy Solutions with Seasonal Heat Storage in a Finnish Case District." *Renewable Energy* 107: 147–155. doi:10.1016/j.renene.2017.02.003.

Wang, Xiao, Maoyu Zheng, Wenyong Zhang, Shu Zhang, and Tao Yang. 2010. "Experimental Study of a Solar-Assisted Ground-Coupled Heat Pump System with Solar Seasonal Thermal Storage in Severe Cold Areas." *Energy and Buildings* 42 (11): 2104–2110. doi:10.1016/j.enbuild.2010.06.022.

Wright, Andrew J., Robin Talbot, and Michael Goddard. 2014. "The Solar House – a True Low Carbon Solution for 2016?" In *CIBSE ASHRAE Technical Symposium*, 3–4. http://www.cibse.org/symposium2014.

Wu, Wei, Baolong Wang, Tian You, Wenxing Shi, and Xianting Li. 2013. "A Potential Solution for Thermal Imbalance of Ground Source Heat Pump Systems in Cold Regions: Ground Source Absorption Heat Pump." *Renewable Energy* 59: 39–48. doi:10.1016/j.renene.2013.03.020.

Xi, Chen, Lu Lin, and Yang Hongxing. 2011. "Long Term Operation of a Solar Assisted Ground Coupled Heat Pump System for Space Heating and Domestic Hot Water." *Energy and Buildings* 43 (8). Elsevier B.V.: 1835–1844. doi:10.1016/j.enbuild.2011.03.033.

You, Tian, Wenxing Shi, Baolong Wang, Wei Wu, and Xianting Li. 2015. "A New Ground-Coupled Heat Pump System Integrated with a Multi-Mode Air-Source Heat Compensator to Eliminate Thermal Imbalance in Cold Regions." *Energy and Buildings* 107 (November): 103–112. doi:10.1016/j.enbuild.2015.08.006.

Zhai, X.Q., M. Qu, X. Yu, Y. Yang, and R.Z. Wang. 2011. "A Review for the Applications and Integrated Approaches of Ground-Coupled Heat Pump Systems." *Renewable and Sustainable Energy Reviews* 15 (6): 3133–3140. doi:10.1016/j.rser.2011.04.024.

Zhu, Neng, Jingmei Wang, and Long Liu. 2015. "Performance Evaluation before and after Solar Seasonal Storage Coupled with Ground Source Heat Pump." *Energy Conversion and Management* 103 (October): 924–933. doi:10.1016/j.enconman.2015.07.037.

IGSHPA SWEDEN 2018 Research Conference

DOI: 10.22488/okstate.18.000031

Thermal performance evaluation of horizontal spiral coil-type ground heat exchangers

Min-Jun kim **Seung-Rae Lee** **Hwan-Hui Lim**
Jun-Seo Jeon **Min-Seop Kim**

ABSTRACT

Geothermal energy has been widely used over the world instead of fossil fuel for environmental merits. A ground-source heat pump (GSHP) system utilizes a constant ground temperature to absorb heat during winter and to emit heat in summer. The GSHP system can be devieded into a closed type system and an open type system. The closed type system using a horizontal ground heat exchanger (HGHE) is relatively inexpensive and easy to install compared to the other types of systems. Among the types of HGHEs, since a horizontal spiral-coil type GHE has the advantageous arrangement for heat exchange between the heat exchanger and surrounding ground, it is the most effective type of the HGHE in terms of thermal performance. However, the thermal performance of a horizontal spiral-coil type GHE critically depends on its dimension which consists of the radius and pitch of a spiral, and thus it is important to accurately analyze how the radius and pitch affect the thermal performance of the horizontal spiral-coil type GHE. Therefore, this paper investigated the thermal performance of a horizontal spiral-coil type GHE according to its diverse shapes to suggest a beneficial design specification of the horizontal spiral-coil type GHE. In order to evaluate the thermal performance of the heat exchanger, a spiral-coil type HGHE was installed in a steel box of which the size was 5 m × 1 m × 1 m filled with dry Joomunjin standard sand, and a thermal response test (TRT) was conducted for 30 hours continuously. Besides, a numerical analysis was performed for its verification and a parametric study of the horizontal spiral-coil GHE using a numerical program which is based on a finite element method (FEM). As a result, in case that the pitch of the horizontal spiral-coil type GHE was more than 0.6 m, there was no more significant benefit in the thermal performance.

1. INTRODUCTION

Renewable energy has been widely used throughout the world as a substitute for fossil fuels due to its ecological advantages. Geothermal energy, one of the renewable energy types, has no environmental problems, and it can be used at any time regardless of a weather condition. The ground-source heat pump (GSHP) system utilizes a relatively constant ground temperature to discharge heat in summer and to obtain heat in winter for heating and cooling, respectively. The GSHP system can be divided into a closed type system and an open type system. The closed-type system can be vertical or horizontal, depending on the installation method. The vertical system uses vertically installed ground heat exchangers (GHEs) in which circulating fluid flows in the pipe embedded in the ground to a depth of 150~200 m. This system can demand high initial construction costs because of deep boreholes. The horizontal system can be used as an alternative

Min-Jun Kim is a doctor course student, Seung-Rae Lee (srlee@kaist.ac.kr) is a professor of civil and environmental engineering department at KAIST, Jun-Seo Jeon is a post Doctor, Hwan-Hui Lim is a master course student and Min-Seop Kim is a doctor course student there.

to the vertical system. Since GHEs in the horizontal system are installed at shallow depths of 1~3 m parallel to the ground surface, it does not need boring costs which are more expensive than excavation costs in the installation process of the horizontal system. However, despite the huge economic benefits of the horizontal system, it is not widely used in comparison with the vertical system due to a great deal of required land space in the HGHEs. As a solution to this problem, a horizontal spiral configuration can be optimized to minimize the installation area of GHE.

While previous studies regarding a horizontal spiral-coil type GHE showed its better efficient performance [1, 2], there have not been yet studies considering thermal performance according to a pitch variation. A coil pitch denotes the distance between the center of spiral rings, and it is a critical factor to determine the thermal performance of GHE. As shown in Fig 1., if the coil pitch is too small, the thermal performance efficiency decreases due to thermal interference while the large coil pitch is not advantageous for heat exchange with surrounding ground. Accordingly, it is important to decide an advantageous pitch in the design of a horizontal spiral-coil type GHE.

Thus, the thermal performance of a horizontal spiral-coil type GHE according to pitch variation through a numerical analysis was carried out in order to suggest a beneficial pitch of the horizontal spiral-coil type GHE.

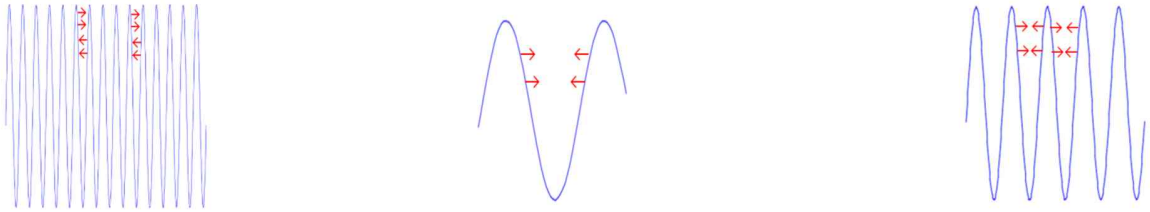

(a) Small pitch (b) Large pitch (c) Optimized pitch

Fig. 1 Concept of optimized pitch in horizontal spiral-coil type GHE

2. Laboratory thermal response test

2.1 Description

Prior to conducting a numerical analysis, a laboratory thermal response test (TRT) was performed to verify the reliability of the numerical analysis. Principle of the laboratory TRT is to monitor the circulating fluid temperatures of the inlet and outlet GHE and to measure the thermal performance of GHE or a nearby ground temperature change. In this study, for comparison of a thermal performance of the GHE, the heat exchange rate of the GHE was calculated by Eq. (1).

$$Q = \dot{m} C_p \triangle T = \dot{m} C_p (T_{in} - T_{out}) \quad (1)$$

where $\dot{m}$ refers to the flow rate of the fluid, C_p is the specific heat capacity at a constant pressure, T_{in} is the inlet temperature of the fluid, and T_{out} is the outlet temperature of the fluid.

2.2 Test prodedure

The laboratory TRT was conducted with the experimental setup including an electric heater with a circulating pump, a water tank, and a 4-m length spiral-coil shaped polybutylene (PB) heat exchanger. Table 1 show the TRT equipment and specification of the TRT equipment that was used in the test [3].

Table 1. Specification of the equipment for TRT

TRT equipment	Properties	Value
	Heater capacity (kW)	5
	Water Tank (L)	20
	Flow meter (lpm)	(SUS 304)
	Pump capacity (lpm)	2 ~ 20
	Sensor	RTD(pt-100) (accuracy : ± 0.01 ℃)

Besides, in the experiment, a 5m x 1m x 1m steel box filled with dry Joomunjin standard sand (Table 2) was also used to reflect the surrounding ground, while the TRT equipment was installed to supply the circulating water and constant power to the inside of the heat exchanger buried in the ground. The size of the steel box was determined by taking into account the compromise between the sufficiently small to be a lab-scale and large enough for released heat from the GHE not to be disturbed by the end of the box. As the thermal conductivity of the dry Joomunjin standard sand is very low, the volume is large enough for neglecting side effects [4].

Table 2. Properties of standard Joomunjin sand

Properties	Value
Uniformity Coefficient, C_u	2.06
Curvature Coefficient, C_c	1.05
Specific Gravity, G_s	2.65
Maximum Dry Density, γ_{dmax} (kg/m^3)	1617
Minimum Dry Density, γ_{dmim} (kg/m^3)	1349
Water Content, w (%)	0

The outer and inner diameters of the PB pipe were 20 mm and 16 mm, respectively. In order to measure the temperature change in the surrounding ground, resistance temperature detector (RTD) sensors were installed at 10 cm away from the edge of the GHE. The initial temperature of the Joomunjin sand was 17.5 °C. The thermal properties of materials and the test procedure are shown in Table 3 and Fig. 2, respectively.

(a) Composition of sample

(b) Spiral-coil type GHE setting

Fig. 2 Laboratory TRT process

Table 3. Thermal properties of experimental material

	Density (kg/m^3)	Thermal conductivity (W/mk)	Specific heat capacity (J/kgK)
Soil	1400	0.26	807
Circulating water	1000	0.6	4200
GHE(PB pipe)	955	0.39	525

The laboratory TRT was carried out continuously for 30 hours. In this study, a thermal performance test(TPT) in which the inlet temperature is constant could not be performed using the small-scale steel-box because the thermal conductivity of the sand was so low that the inlet temperature of the circulating water in the TPT could not be constantly maintained. Therefore, the TRTs were conducted with no heat injection, using only the power of the circulating pump, while the heat exchange rates were obtained using Eq. (1) in the same manner as when calculating the heat exchange rate in a TPT. The outlet temperature of the circulating water and the ground temperature change were measured to compare them with the results of numerical analysis.

3. Numerical study

3.1 Description

To investigate the heat transfer from the fluid flow inside of the GHE, heat exchanges between the soil, pipe and circulating fluid flow should be considered simultaneously in the analysis. In this study, a numerical analysis was conducted using a commercial program known as COMSOL Multiphysics 5.2a, which is based on a finite element method (FEM) [5]. The governing equation of the numerical analysis was based on the heat transfer in the ground as expressed in Eq. (2) [6]. Additionally the heat flow combined with the heat flow through pipe is the energy equation for an incompressible fluid flowing in a pipe as expressed in Eq. (3) [6].

$$-\lambda_i\left(\frac{\partial^2 T}{\partial x^2}+\frac{\partial^2 T}{\partial y^2}+\frac{\partial^2 T}{\partial z^2}\right)+\rho_i c_i\frac{\partial T}{\partial t}+q_i=0 \quad (i=x,y,z) \tag{2}$$

where λ_i denotes the thermal conductivity, T is the ground temperature, ρ_i is the density, c_i is the specific heat capacity and q_i is the internal heat generation.

$$\rho_f C_p A_p\frac{\partial T_f}{\partial t}+\rho_f C_p A_p u\cdot\nabla T_f=\nabla\cdot A_p\lambda_f\nabla T_f+f_D\frac{\rho A_p}{2d_h}|u|^3+Q+Q_{wall} \tag{3}$$

where ρ_f denotes the fluid density, C_p is the specific heat capacity at a constant pressure, A_p is the pipe cross section area, T_f is the fluid temperature, u is the tangential velocity of the fluid, and λ_f is the fluid thermal conductivity. In addition, f_D denotes the coefficient of friction, d_h is the average hydraulic diameter, and Q represents the heat injection. Friction loss effects was considered with Churchill's friction model, specification of the GHE (circular, diameter), Reynolds number, and surface roughness. The conduction of the fluid was also considered in the analysis by applying the thermal conductivity of the water. Finally, Q_{wall} denotes the external heat exchange through the pipe wall which arises from the temperature difference between the pipe wall and the inside of the pipe, and it can be calculated by Eq. (4).

$$Q_{wall}=(hZ)_{eff}(T_p-T_f) \tag{4}$$

where $(hZ)_{eff}$ represents the effective value of the heat transfer coefficient, Z is the wall perimeter of the pipe, T_p is the temperature at the pipe wall, and T_f is the fluid temperature in the pipe. For a circular tube, the effective hZ can be described by Eq. (5).

$$(hZ)_{eff} = \frac{2\pi}{\frac{1}{r_0 h_{\text{int}}} + \frac{1}{r_N h_{ext}} + \sum_{n=1}^{N}\left(\frac{\ln\frac{r_n}{r_{n-1}}}{\lambda_n}\right)} \tag{5}$$

where λ_n is the thermal conductivity of wall n, and r_n is the outer radius of wall n. Furthermore, h_{int} and h_{ext} represent the film heat transfer coefficients inside and outside of the tube, respectively. However, in this study, only internal film forced convection was considered in the numerical model because there is no convective heat transfer outside the pipe.

3.2 Validation

To verify the reliability of the numerical analysis program, a finite element model was developed under the same conditions as the laboratory test, and then the numerical analysis was performed. The adiabatic conditions were set to the outer edge of the geometry in COMSOL to take into account the side effects. It implies that the initial condition, boundary condition, material properties, geometry and analysis time of the numerical analysis were the same as those in the laboratory TRT. Fig. 3 compares the results of lab test and numerical analysis. In addition, Fig. 4 shows the difference of temperature between COMSOL and the laboratory TRT.

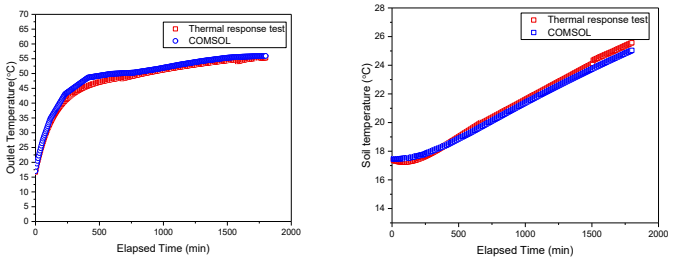

(a) Outlet temperature (b) Soil temperature

Fig. 3 Results of lab test and numerical analysis

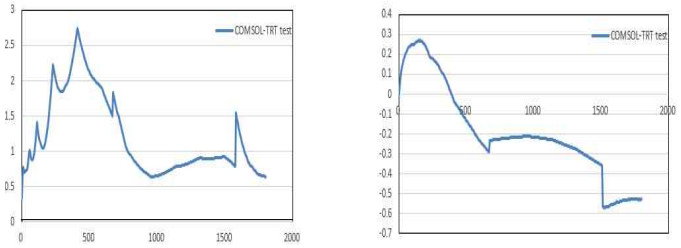

(a) Outlet temperature (b) Soil temperature

Fig. 4 Difference of temperature between COMSOL and TRT

As a result of a relative error analysis regarding the laboratory TRT and numerical analysis, the error range of the outlet fluid temperature and soil temperature were 5.9% and 2.3%, respectively. It can be seen that the numerical

modelling results validated the agreement with the experimental results.

3.3 Parametric study

Prior to a parametric study, installation depth, flow rate and ground thermal conductivity were selected as representative factors which influence the thermal performance of GHE. Table 4 summarizes the case set up for the parametric study.

Table 4. Case set up for parametric study

Case	Installation depth (m)	Flow rate (lpm)	Ground thermal conductivity (W/mk)	Pitch (for all cases)	
1	1.8	5.65	0.8		
2	1.8	5.65	1.1	0.1	0.7
3	1.8	8.45	0.8	0.2	0.8
4	1.8	8.45	1.1	0.3	0.9
5	2.5	5.65	0.8	0.4	1.0
6	2.5	5.65	1.1	0.5	1.1
7	2.5	8.45	0.8	0.6	1.2
8	2.5	8.45	1.1		

Numerical models were developed to conduct the parametric study. A cooling condition was assumed and analysis time was 120 hr, which took into consideration 5 working days per week in the summer. In addition, to consider the actual operation time of the GSHP, operating conditions were set to only operate the heat pump from 9 am to 8 pm, the time in which the cooling load occurs during the day. The intermittent operating conditions were described by ceasing the circulating water flow during the rest period, and setting the circulating water flow rate to simulate the operating period (Fig. 5).

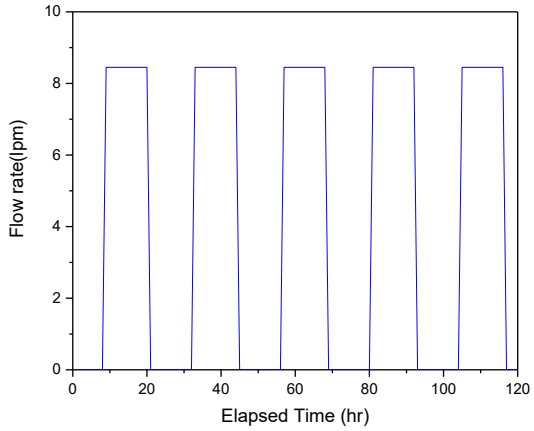

Fig. 5 Boundary condition in the case study

Furthermore, the inlet temperature of the heat exchanger, which is the entering water temperature (EWT) of the system, was set at 35.4 °C. The material of the heat exchanger was PB (Polybutylene), which is commonly used in GHEs, and the outer and inner diameters of the pipe were 20 mm and 16 mm, respectively. In this study, the total length of the horizontal spiral-coil GHE was kept constant at 40 m for all cases for comparison of thermal performance. Since the total length of the spiral heat exchanger is constant, a change in pitch or spiral diameter means that the horizontal

length of the spiral heat exchanger; that is, the required trench length, varies. Then, the numerical analysis was performed for all cases shown in Table 4 when the pitch varies from 0.1, 0.2 ⋯, to 1.2 m. Fig. 6 depicts the finite element model for the case study.

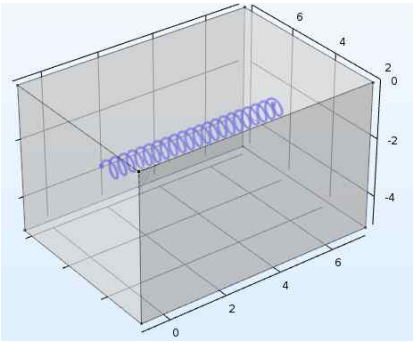

Fig. 6 Finite element model for the case study

4. Results and discussions

From the numerical analysis, the heat exchange rate of each case was obtained to compare the thermal performance according to the pitch variation. Fig. 7 compares the heat exchange rates of each case obtained by the parametric study when the pitch is 0.3 m. Fig. 8 indicates a representative result of the parametric study for the outlet fluid temperature.

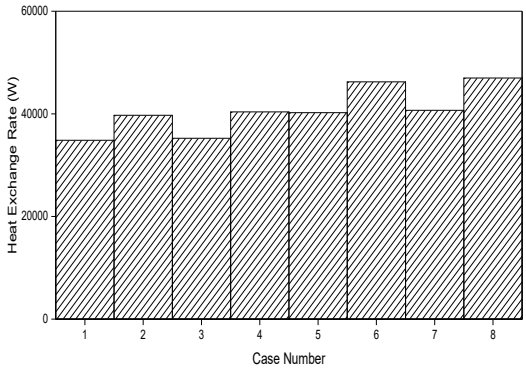

Fig. 7 Heat exchange rate obtained in the numerical study (p = 0.3 m)

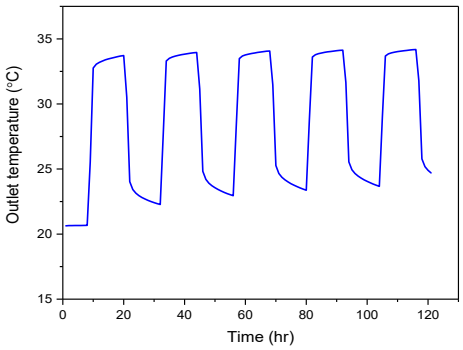

Fig. 8 Variation of outlet temperature in the numerical sudy

Fig. 9 illustrates graphs summarizing the thermal performance evaluation results of case 1 and case 8 according to the pitch variation.

As a result of the thermal performance evaluation according to the pitch variation, it was found that as the pitch becomes larger, the thermal performance gradually increased but it finally converged. As the pitch of the GHE increases, the heat exchange rate gradually increases up until a point where the effects of the pitch value become negligible and the influence of pitch on the heat exchange rate becomes insignificant.

In this work, a T-test with the assumption of equal variance, which is a statistical significance test, was performed to determine the interval in which the pitch value has no further effect on the heat exchange rate. The T-test is a statistical technique which determines whether the difference in the average of two groups is significant, and whether the factor affects the outcome. If the significance probability (P-value) obtained from the T-test results exceeds a significance level of 0.05, it can be said that there is no statistical significance, and thus it can be concluded that the factor has no effect on the result [7].

As a result of the T-test, it was confirmed that the pitch only had an effect on the heat exchange rate up to a value of 0.6 m and beyond this value the heat exchange rate was not varied in all cases (Table 5 and Table 6). This finding is observed because increasing the pitch gradually reduces the thermal interference effect between the spirals, until the pitch increases to 0.6 m. However, pitch values greater than 0.6 m had no effects on the heat exchange rate. The results are consistent regardless of other factors that affect the thermal performance.

Therefore, it can be concluded that when the pitch of the horizontal spiral heat exchanger is set to 0.6 m, an optimal thermal performance can be achieved with the minimal installation site for the horizontal spiral-coil GHE.

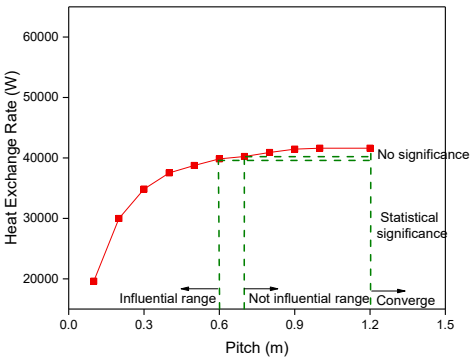

(a) Case 1

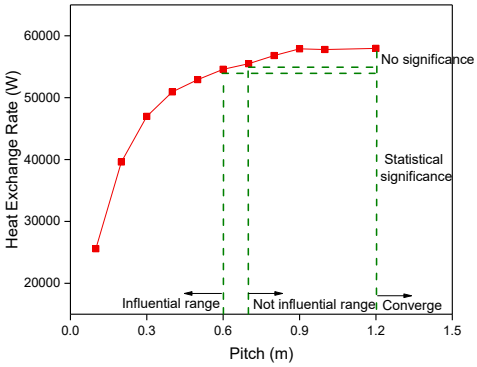

(b) Case 8

Fig. 9 Heat exchange rate according to the pitch variation
(For all cases the pitch vares from 0.1,0.2,…,to 1.2m)

Table 5. Result of a statistical T-test (p=0.6 m)

	Levene's Test for Equality of Variances		T-test for Equality of Means	
	F	Sig.	Sig. (2-tailed)	Std.Error Difference
Equal variances assumed	0.520	0.220	0.23	8.262
Equal variances not assumed			0.23	8.262

Table 6. Result of a statistical T-test (p=0.7 m)

	Levene's Test for Equality of Variances		T-test for Equality of Means	
	F	Sig.	Sig. (2-tailed)	Std.Error Difference
Equal variances assumed	0.962	0.329	0.153	17.910
Equal variances not assumed			0.153	17.910

5. CONCLUSION

In the present study, the thermal performance of horizontal spiral-coil GHEs according to the pitch was investigated. To achieve the goal, a parametric study was conducted using the commercial program COMSOL Multiphysics 5.2a, which is based on a FEM. Prior to a parametric study, the applicability of numerical program was validated by a laboratory TRT result. Then, the parametric study which took into consideration the pitch variation was conducted with regard to the diverse conditions. The conclusion of the study can be summarized as follows:

• Thermal performance of the horizontal spiral-coil GHE continuously increased with increasing pitch, but it was shown that the degree at which performance increases gradually reduces until the heat exchange rate converges.

• A T-test, a statistical significance analysis, was performed to determine a specific pitch value that no longer has an effect on the heat exchange rate, in addition to the results of each parameteric study. As a result, it was concluded that the pitch does not affect the thermal performance if the pitch exceeds 0.6 m. These same results were derived even when additional changes in the critical influence factors were taken into consideration.

6. ACKNOWLEDGMENTS

The research was supported by the Regional Development Research Program (17RDRP-B076564-04) by Ministry of Land, Infrastructure and Transport of Korean government and by the basic research project (2018021564) by the National Research Foundation of Korea and Ministry of Land, Infrastructure and Transport of Korean government.

7. REFERENCES

[1] Conedo, P.M., Conlangeo, G. and Starace, G. 2012. *CFD simulations of horizontal ground heat exchangers: A comparison among different configurations*, Applied Thermal Engineering, 33-34, 24-32.

[2] Kim, M.J., Lee, S.R., Seok, Y. and Go, G.H. 2016. *Thermal performance evaluation and parametric study of a horizontal ground heat exchanger*, Geothermics, 60, 134-143.

[3] Yoon, S., Lee, S.R. and Go, G.H. 2015. *Evaluation of thermal efficiency in different types of horizontal ground heat exchangers*, Energy and Buildings, 105, 100-105.

[4] Yoon, S., Lee, S.R. 2011. *Evaluation of heat transfer Characteristics in Soils by Application of Optical Fiber Sensors,* Korea Advanced Institute of Science and Technology, MS. Thesis.

[5] Comsol Inc. 2016. *Comsol multiphysics user's manual Ver. 5.2a*, USA.

[6] Incropera, F.P., Dewitt, D.P., Bergman, T.L. and Lavine A.S. 2007. *Fundamentals of Heat and Mass Transfer, (6th Edition)*, John Willey&Sons.

[7] Anthony, J.H. (2012) *Probability and Statistics for Engineers and Scientists, (4th Edition*), Thomson Brooks/Cole.

IGSHPA SWEDEN
2018 Research Conference

DOI: 10.22488/okstate.18.000008

Performance Analysis of a Single Underground Thermal Storage Borehole Using Phase Change Material

A. M. Bayomy Hiep V. Nguyen Jun Wang Seth B. Dworkin

ABSTRACT

Ground source heat pumps (GSHP) are used to provide both heating and cooling to a given system. These heat pumps transfer heat efficiently between the system and the ground. Despite this high efficiency, there has been a low adoption rate for GSHPs owing to limited usage in commercial structures and buildings primarily due to high installation costs, but also due to a lack of drilling space and unbalanced heating/cooling loads. Phase change materials (PCMs) can absorb, store and release large amounts of latent heat over a defined narrow temperature range while the material changes phase or state. The main goal of this paper is to be able to predict numerically the performance of a single borehole with the effect of implementing PCMs. In order to successfully proceed with the discussion, two main objectives for this paper are presented. The first objective is to establish a finite element model of a single borehole with accurate assumptions in order to achieve an accurate prediction over four years of operation for a GSHP. Then, the second objective of the paper is to investigate the effect of using PCM in the borehole of GSHP to help maintain a more stable ground temperature range. Two scenarios of different PCM volumes and melting temperatures are presented. It was found that the performance enhancement due to PCMs reaches up to 35% in monthly average COP. In addition, PCMs show great potential to smooth the ground thermal response.

INTRODUCTION

The utilization of efficient space heating and cooling systems has become rather urgent owing to the fact that 40% of the total energy consumption worldwide is attributed to space heating and cooling (De Ridder et al., 2011). Space heating and cooling has a high energy demand and has a significant impact on energy consumption. Thus, it has been necessary to find efficient alternatives to pre-existing methods for space heating and cooling in order to reduce energy consumption and greenhouse emission of such devices.

One possible solution to the problem of high energy consumption of space heating and cooling systems is through the adoption of ground source heat pumps (GSHPs). GSHPs utilize the ground as an infinite heat sink and heat source for both cooling and heating (Florides and Kalogirou, 2007). The efficiency of the heat pump lies in the fact that ground temperature at a particular depth remains nearly constant over the year. However, despite the prospective benefits of GSHPs, there are several limitations with the use of such systems. GSHPs

Ayman. M. Bayomy (ayman.bayomy@ryerson.ca) is a Postdoctoral Fellow at Ryerson University- Canada, Hiep V. Nguyen is a PhD candidate at Ryerson University- Canada, J. Wang is R&D Manager at McClymont and Rak Engineers Inc. and Seth B. Dworkin is an Associate Professor and Canada Research Chair at Ryerson University- Canada

are rather challenging to utilize due to possible lack of drilling space, imbalance in heating or cooling, and high installation costs of the system.

One of the main problems in utilizing the cooling process of GSHPs is that long-term heat addition to the ground may cause increases in ground temperature resulting in a detriment th the cooling efficiency of the GSHP for a single borehole (Hu et al., 2010). According to a study by Zheng (2013), it was found that changes in ground temperature were most noticeable in the region within 0.5 m of the borehole. These temperature changes were most noticeable during the first few years of operation, wherein changes in the temperature of the ground can lead to inefficient GSHP functioning due to insufficient temperature gradient (Zheng,, 2013), as well as ecological problems in the soil (Wu et al., 2014). However, it is possible to address this issue by ensuring that boreholes of GSHPs are separated by 6 m (ASHRAE, 2011). It is highly important that borehole field arrangements (i.e. the borehole array size) are taken into consideration as these arrangements can have a significant effect on the ground temperature and the overall performance of GSHPs.

Several models and studies have been done in order to properly determine the most feasible design for GSHPs. These models predict the performance of a single borehole, and in the process provide a model of how ground temperature changes with the operation of a GSHP. In the model by De Paepe and Willems (2001), they considered a three-dimensional numerical model wherein pure conduction was considered in the interaction between soil and other materials. In the model by Zhang et al., they considered a numerical model of heat transfer wherein the distance between boreholes and backfill material thermal conductivity were considered as the parameters in geothermal heat exchange (Zhang et al., 2015). Finally, in the numerical model designed by Law and Dworkin, it was found that the recommended distance of 6 m in between boreholes, as recommended by ASHRAE, does not always provide an effective means of avoiding thermal interactions between the boreholes of GSHPs (Law and Dworkin, 2016). Kuzmic, et al. (2016) conducted a 2-D model to study the heat transfer of hybrid system of GSHP and conventional HVAC. They noticed that the hybridization has a potential effect on ground temperature stability.

To the best of the authors' knowledge, the existing research on predicting the performance and efficiency of GSHPs is scarce and severely incomplete owing to the oversimplifications numerical models take into consideration. One such assumption leading to oversimplification is the consideration that only pure conduction occurs between the soil and boreholes, which then neglects the effect of convection. Furthermore, other models neglect the porous behaviour of soil, which can then affect the heat transfer models. In addition, models similarly neglect turbulent heat transfer inside the heat exchange system and, in the process, the models consider constant heat flux. These neglected factors can be taken into consideration by establishing a finite elements model of a single real borehole. This proposed model takes into consideration the turbulent heat transfer of the circulating fluid, along with load variation over time, as well as the actual heat flux profile inside the soil, and actual heat pump performance

A proposed technique in which the GSHPs may provide better efficiency is through the conversion of the geothermal heat exchanger from infinite volume to a finite volume of thermal storage material (TSM). This finite volume of TSM can then address problems in thermal interaction between boreholes, ground temperature changes, and land utilization. Land utilization can be further addressed through the implementation of phase change material (PCM) in the borehole.

PCMs are commonly used in thermal storage media, and have been long-recognized as both sustainable and environmentally-friendly (Baetens et al, 2010; Lin et al., 2014). PCMs are able to absorb, store and release large amounts of latent heat over a given defined narrow temperature range. It has been shown that PCM heat exchangers are able to achieve high thermal performance (Medrano et al., 2009; Rabin and Korin, 1996). PCMs

have been used in heat exchangers such as in double pipe copper tubes (Longeon et al., 2013), flat plate (Liu et al., 2014), and shell and tube heat exchangers (Hosseini et al., 2014; Trp et al., 2006).

The application of PCMs to GSHP systems can lead to the enhancement of the overall performance of the heating and cooling system through smoothening the abrupt heating and cooling waves generated from variations in building load of GSHPs. The ability of PCM to aid in increasing the efficiency of GSHPs can be attributed to the results by Wu and Li wherein PCMs were shown to have significantly better performance as compared to other backfilling materials used in geothermal heat exchange systems (Wu, 2008; Li, 2014). Similar results have been shown in studies by Lei and Zhu (2009), and Yang et al. (2014).

In this study, paraffin was utilized as PCM in ground heat exchange systems, wherein their effects on GSHPs were simulated over the span of four years. Paraffin was chosen as the PCM due to its high latent heat of 190 kJ/kg. With this latent heat over a defined narrow temperature range, the TSM layer can absorb and release large amounts of heat without causing significant ground temperature variation.

In the present study, two scenarios of implementing the PCMs (Paraffin) in the ground heat exchanger are simulated for four years of operation. The heat pump COP is evaluated over four years of operation for a balanced building. Section 2 presents the methodology, followed by the results and discussion in section 3. Finally, Section 4 highlights the findings obtained and the conclusions.

METHODOLOGY

The finite elements study consists of two main parts as follow:

1- Establishing a finite element model using COMSOl Multiphysics for a single borehole.
2- Investigating the effect of two different scenarios of the PCM's melting temperature and volume.

Building load

It is important to note that one of the assumptions made in creating the model in this study is that a balanced building load is considered, where in 8760 hours in a year, half is considered to utilize heating and the other half utilized cooling. Figure 1(a) illustrates hourly building load variation. The finite element model of this study simulates a single borehole. The building loads have been normalized to 3.5 kW (1 ton) maxima for both cooling and heating processes. This normalization is illustrated in Figure 1(b). Finally, taking into consideration this assumption, the borehole depth was estimated to be about 60-80 meters per ton heating and cooling.

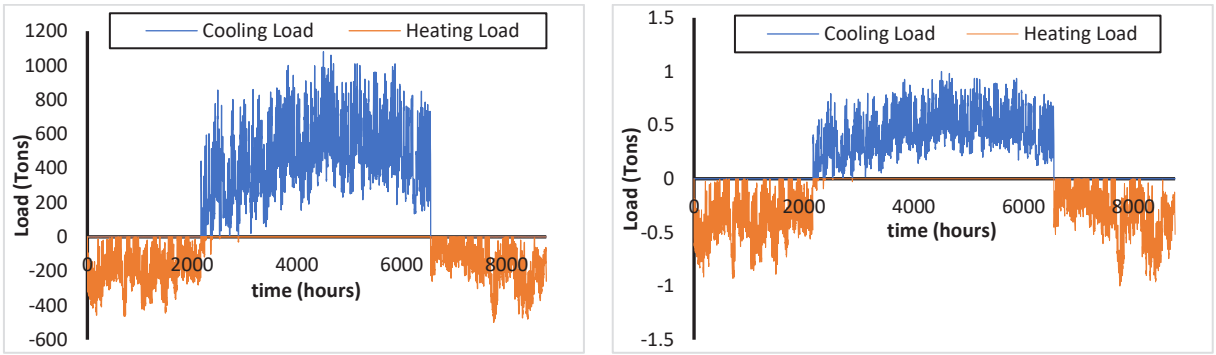

(a) Raw heating and cooling load values (b) Normalized building load profile to 1 ton

Figure 1 Building load variation for a balanced building

Heat pump performance

The heat pump used in the study is the 5T ClimateMaster Tranquility Water-to-Water Series Model TMW060. The heat pump was tested by the industrial partner, McClymont and Rak Engineers, Inc. The actual performance of the heat pump was evaluated to be 25% below the manufacturer specification for both heating and cooling. The actual performance of the heat pump was tested under load/source flow rate of 56.78 L/min (15 gpm) and load side EWT (Entering Water Temperature) of 38℃ for cooling and 15 ℃ for heating. Figure 2 shows the manufacturer and actual heat pump performance for heating and cooling.

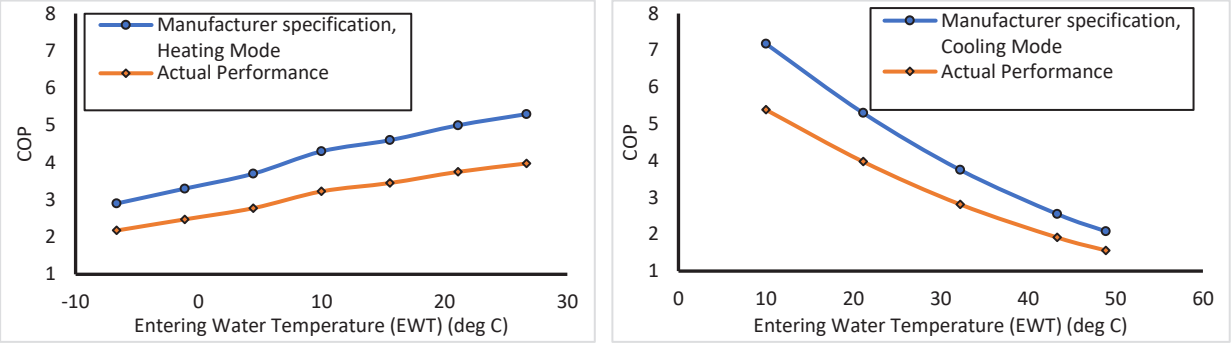

(a) Heat Pump performance for heating mode (b) Heat Pump performance for cooling mode

Figure 2 Actual and manufacturer specification for heat pump performance

Finite elements model description

In this study, the three-dimensional numerical model was created by using the finite elements techniques (COMSOL Multiphysics) for a single borehole of a GSHP, which is buried at a depth of 60 m. In addition, a U-loop heat exchanger (HEX) was placed at the center of the borehole, wherein this U-loop was characterized with outer and inner diameters given to be 42.2 mm and 34.0 mm, respectively. The separation distance of the U-loop HEX used in this study was 0.065 m. Figure 3(a) shows the two main layers which have been used to simulate material surrounding the U-loop. The layers consist of 0.1524 m of grout material layer, and 4 m of soil layer. Table 1 gives a summary of the thermal properties of each of the layers. It should be noted as well that a tetrahedral element was utilized in describing the numerical model, and an analysis of grid independence was conducted.

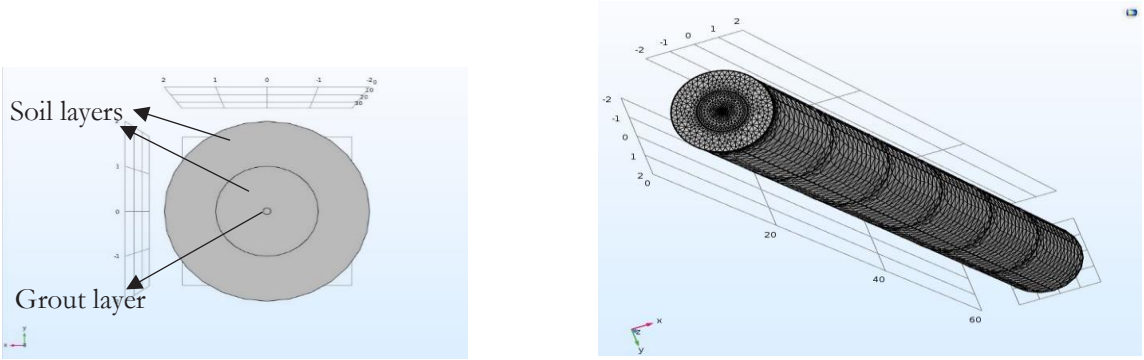

(a) (b)

Figure 3 Model geometry and meshing

Table 1. Layer properties

Material	Density (kg/m³)	Thermal Conductivity (W/m.K)	Specific heat (J/kg.K)
Soil	1900	2	1053
Grout	1700	0.7	1647

An assumption utilized with the present numerical model is that the ground water movement inside the soil is negligible, along with the assumption that both the grout material and soil are homogeneous with constant properties. From these assumptions, a system of governing equations to describe heat transfer inside both layers and in the U-loop HEX is obtained. The equations are given as:

$$(\rho_s c_{p_s}) \cdot \frac{\partial T}{\partial t} + \left(\rho_s c_{p_s}\right) U.\nabla T = \nabla.(k_s.\nabla T) \quad (1)$$

$$(\rho_l A\, c_{p_l}) \cdot \frac{\partial T}{\partial t} + \left(\rho.A.c_{p_l}\right) U.\nabla T = \nabla.(A.k_l.\nabla T) + \frac{1}{2} f.\frac{\rho A}{d} |u|u^2 \quad (2)$$

The turbulent Nusselt number inside the U loop HEX is obtained as follow:

$$Nu_D = 0.027\, Re_D{}^{4/5}.Pr^n \quad (3)$$

In the above equations ρ_s is density of solid layers *(e.g. soil or grout)*, c_{p_s} is specific heat of solid, U is the velocity field vector, T is the temperature, Ks is thermal conductivity of solid, ρ_l is liquid's density, c_{p_l} is liquid's specific heat, k_l is liquid's thermal conductivity, f is the friction factor of the U loop HEX tube, A is the cross section area of the U loop HEX tube, Nu_D is Nusselt number, Re_D is Reynolds number, Pr is Prandtl Number, and n is a constant given to be 0.4 for cooling and 0.3 for heating.

The procedure for formulating the finite element model is outlined in Figure 4. For every time step, the model obtains the value of the load and the outlet water temperature predicted from the borehole. These two parameters aid in evaluating the COP of the heat pump, and from here the amount of heat added or extracted by the heat pump is then calculated. Knowledge of this value aids in calculating the inlet water temperature of the borehole in the proceeding time step.

The convergence criterion at each iteration is set as follows: at every iteration, the average relative error of U and T are computed. These are obtained via the following relation:

$$R = \frac{1}{n\,.\,m} \sum_{i=1}^{i=m} \sum_{j=1}^{j=n} \left| \frac{(F_{i,j}^{s+1} - F_{i,j}^{s})}{F_{i,j}^{s+1}} \right| \quad (4)$$

where F represents one of the independent parameters, s represents the number of iterations, and (i, j) represent the x and y coordinates. The solution reached convergence when R was below 1×10-6 for each independent parameter.

The implementation of PCMs in the borehole is established through the use of two models. Both of these models utilize paraffin-filled pipes which are inserted around the U-loop HEX tube. Practically, PCM filled tubes will be inserted and arranged in the vicinity of the borehole HEX. The dimeter of each PCM tube was 34 mm. PCMs possess a transition temperature, the transition temperature of paraffin wax is about 4°C. The first model, herein referred to as Model (A), consists of 12 PCM filled pipes with thin PCM rectangular layers placed between the U-loop HEX legs.

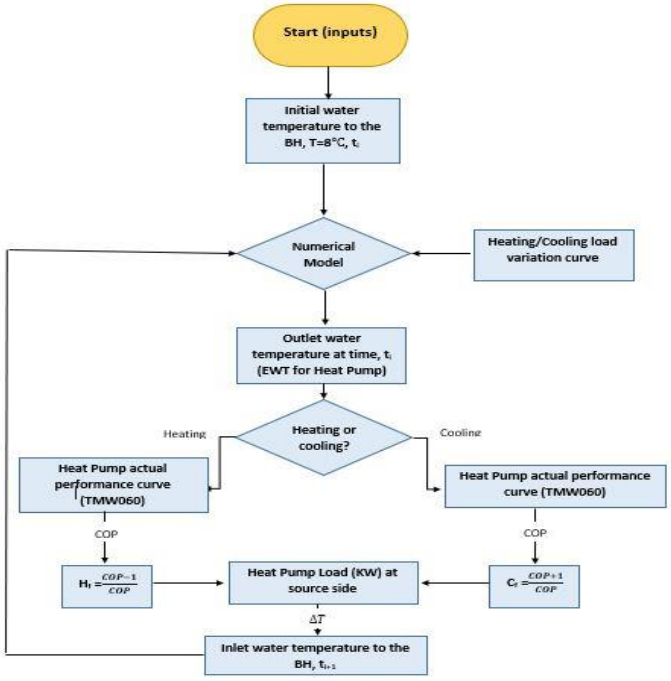

Figure 4 Algorithm procedure

The PCM has a melting temperature of 12℃. Conversely, the second model (Model (B)) is similar to model (A) but in addition has another 12 PCMs composed of filled pipes with a melting temperature of 2℃. Both of these models are illustrated in Figure 5, and the properties of the PCMs are summarized in Table 2. Paraffin wax is an organic PCM, so it is environmentally safe, reliable, less expensive, non-corrosive, more stable below 500 ℃, long-term freeze-melt cycles.

Other factors taken into consideration are the boundary conditions implemented in the model. Included in these boundary conditions are the fluid flow rate inside the U-loop, which is given to be 11.5 L/m (3 gpm). In addition, the outer and bottom portion of the soil layer surface is treated as by obtaining outward heat flux by considering the far field distance to be 30 m from the center of the borehole. Finally, the top portion of the borehole is treated to be an open boundary to the external environment, the temperature of which varies according to the session.

RESULTS AND DISCUSSION

In evaluating the results obtained from the model, it should be noted that the starting month of each year was set to be April. This means that each year begins with cooling demand followed by heating demand. It was found that the minimum COP for cooling is 2.3, while for heating it is 2.6 at the end of each session, where the ground temperature was found to either be colder after heating, or hotter after cooling. The same trend was observed for monthly average COP. Results are summarized in Figures 6 and 7. The temperature contours of the borehole at 30 m depth right after cooling and heating sessions in the fourth year of operation are visualized in Figure 8.

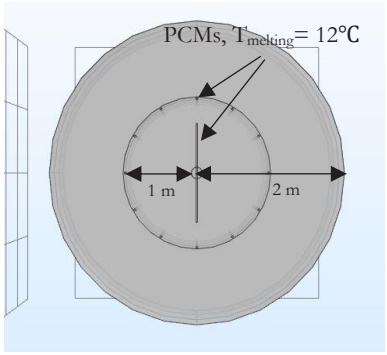

(a) Model (A)

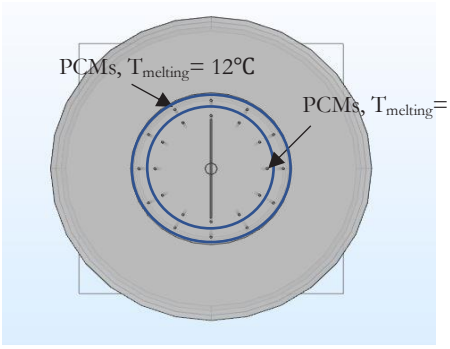

(b) Model (B)

Figure 5 Models with PCMs pipes

Table 1. PCMs properties

Paraffin	Properties
Density (kg/m³)	760 for liquid, 850 for solid
Thermal conductivity(W/m.K)	0.1
Heat capacity (J/kg.K)	2140
Latent heat (kJ/kg)	190
Melting temperature (℃)	0℃ – 35℃

In predicting the effect of the implementation of PCMs in the borehole, it was found that PCMs indeed provide smoothing to the ground thermal response. This smoothing is manifested by the behavior of COP variation with time. It was also found that the enhancement of the COP of model (A) in the daily average COP reaches up to 50%, while the monthly average COP was increased up to 35%. Moreover, the average enhancement percentage of model (A) over four years of operation was found to be 10 to 12%. Figure 9 shows the results outlined for model (A).

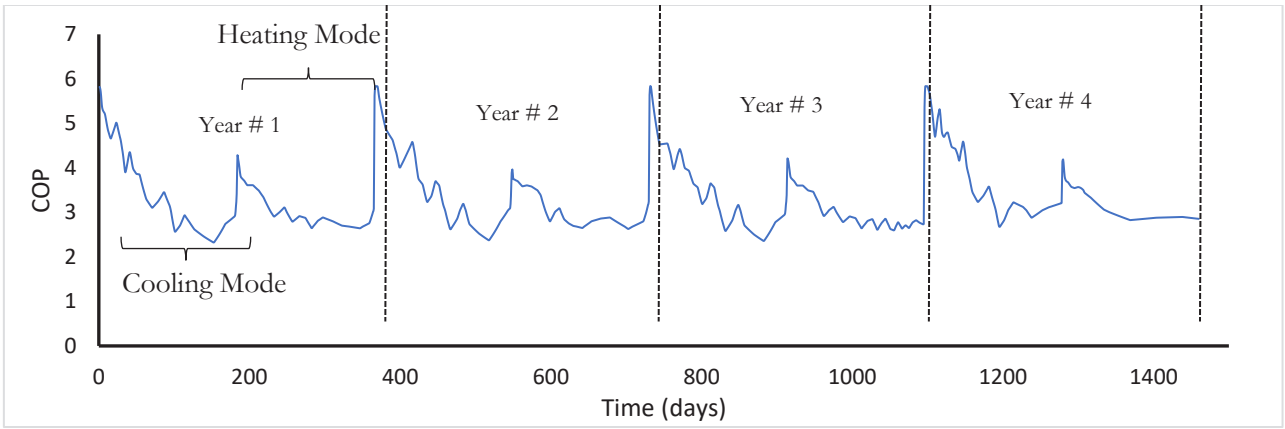

Figure 6 Daily average COP for 60m borehole without PCMs

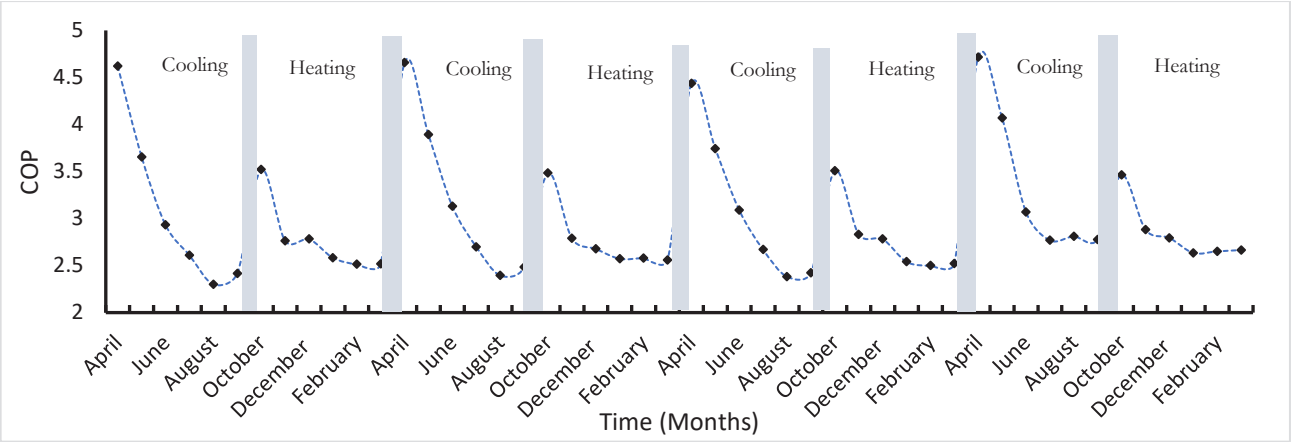

Figure 7 Monthly average COP for 60m borehole without PCMs

Figure 10 shows the daily average COP of model (B) compared to a 60 m borehole without PCMs. It was noted that the enhancement percentages reach up to 25% and 22% for daily and monthly average COP, respectively. Although the total volume of PCMs was larger in model (B) compared to model (A), the enhancement percentage achieved by model (A) was greater than that for model (B). This means that the PCM's volume is not the only factor that governs performance. PCM melting temperature as well as the location of the PCM with respect to the U-loop ground heat exchanger are also factors that effect on the performance of the system.

CONCLUSION

In this study, a finite element model was established in order to simulate a single borehole for a balanced building. The coefficient of performance of the GSHP was evaluated over four years of operation. Furthermore, the effect of using PCMs was investigated and it was found that the implementation of such material enhances the overall performance of the system by smoothing the sudden heating and cooling waves of the ground, which can be attributed to load variation. A possible extension of this model would be a way to optimize the volume, location, and melting point of PCMs, which could then aid in achieving the highest enhancement percentage as compared to existing GSHP boreholes without PCMs.

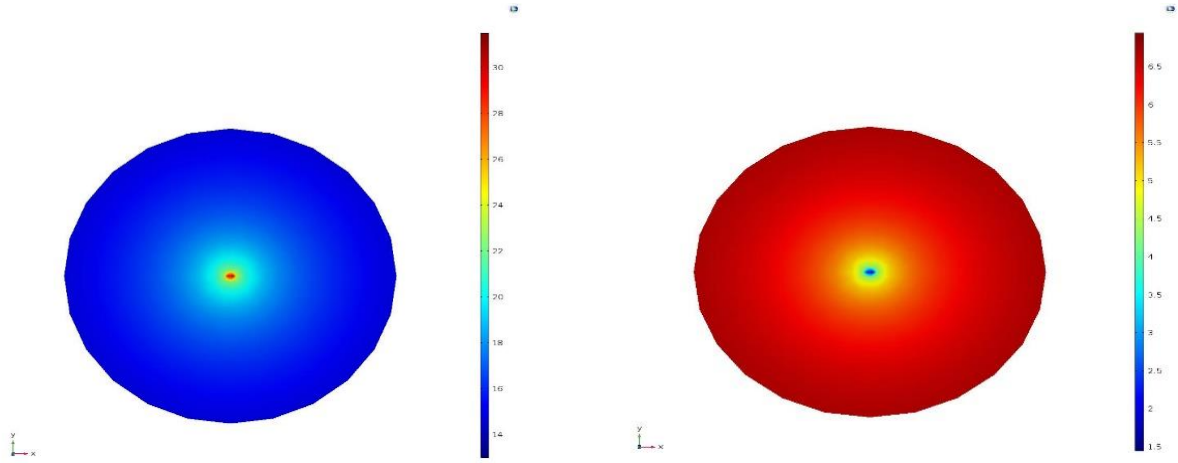

(a) Temperature contours at the end of cooling session

(b) Temperature contours at the end of heating session

Figure 8 Temperature contours at 30m depth on fourth year

8

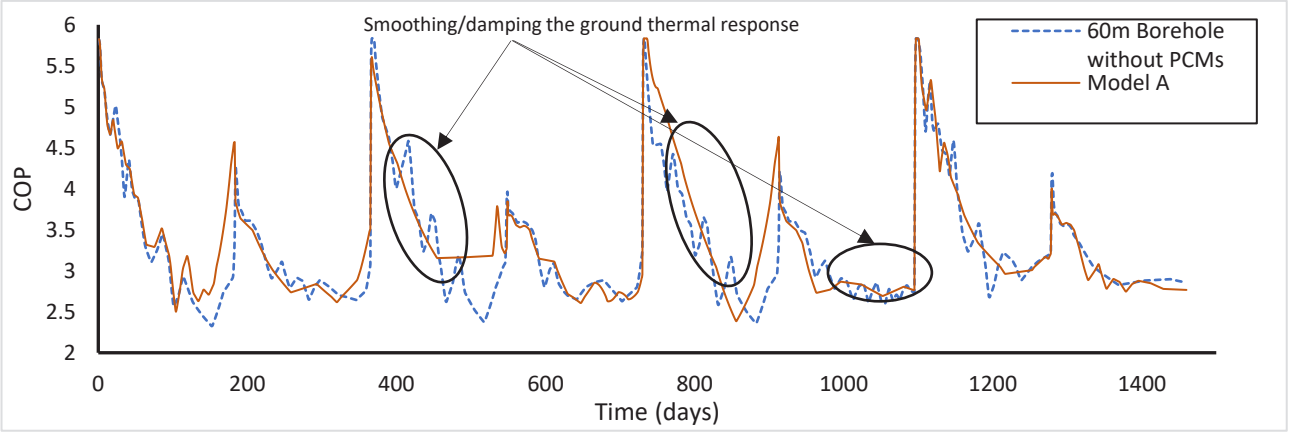

Figure 9 Daily average COP of model (A) and 60m depth borehole without PCMs

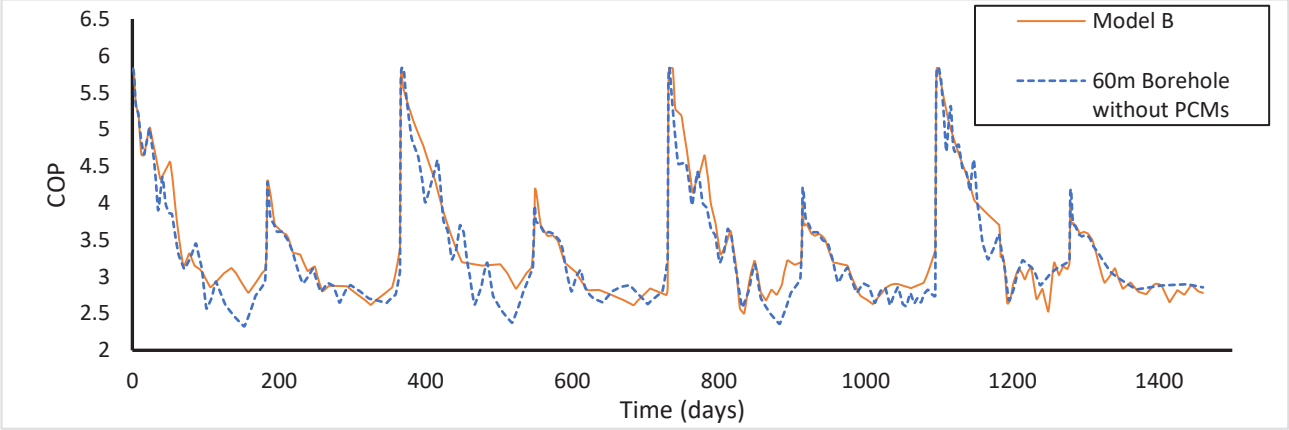

Figure 10 Daily average VOP of Model(b) and 60m depth borehole without PCMs

ACKNOWLEDGEMENTS

This research was undertaken, in part, thanks to funding from the Canada Research Chairs program. We would also like to acknowledge the Natural Sciences and Engineering Research Council of Canada, Ontario Centres of Excellence, and McClymont and Rak Engineers Inc. for financial support. Furthermore, we would like to thank Ladislav Rak of McClymont and Rak for data and helpful discussion.

REFERENCES

De Ridder, F., M. Diehl, G. Mulder, J. Desmedt, and J. Van Bael. 2011. An optimal control algorithm for borehole thermal energy storage systems. Energy & Buildings, 43(10), 2918-2925. 10.1016/j.enbuild.2011.07.015

Florides, G., and S. Kalogirou. 2007. Ground heat exchangers—A review of systems, models and applications. Renewable Energy, 32(15), 2461-2478. 10.1016/j.renene.2006.12.014

Hu, S., W. Song, Y. Zhang, D. Pan, T. Meng. 2010. Study of Cold/Hot Stacking Problem Based on Balance Storage of Ground Source Heat Pump. 2nd International Conference on Computer Engineering and Technology. Chengdu, China. April 16-18.

Li, S., W. Yang, and X. Zhang. 2009. Soil temperature distribution around a U-tube heat exchanger in a multi-function ground source heat pump system. Applied Thermal Engineering 29 (17): 3679-86.

Zheng, X. 2013. Long-term effects of ground source heat pumps on underground temperature. In: Proceedings of the COMSOL Conference.

Wu C., C. Hui, W. Wang, X. Li, and W. Fu. 2014. Characteristics of ground temperature and system performance for the intermittent operation of GSHP system. Environ, Energy And Sust Dev 2014:123–7.

Rybach, L., and W. Eugster. 2010. Sustainability aspects of geothermal heat pump operation, with experience from switzerland. Geothermics 39 (4): 365-9.

ASHRAE. 2011 ASHRAE Handbook-HVAC Systems and Equipment. SI ed. Atlanta: ASHRAE; 2011.

Tzaferis, A., D. Liparakis, M. Santamouris, and A. Argiriou. 1992. Analysis of the accuracy and sensitivity of eight models to predict the performance of earth-to-air heat exchangers. Energy & Buildings 18 (1): 35-43.

Bi, Y., L. Chen, and C. Wu. 2002. Ground heat exchanger temperature distribution analysis and experimental verification. Applied Thermal Engineering 22 (2): 183-9.

Mihalakakou, G., M. Santamouris, and D. Asimakopoulos. 1994. Modelling the thermal performance of earth-to-air heat exchangers. Solar Energy 53 (3): 301-5.

Bojic, M., N. Trifunovic, G. Papadakis, and S. Kyritsis. 1997. Numerical simulation, technical and economic evaluation of air-to-earth heat exchanger coupled to a building. Energy 22 (12): 1151-8.

De Paepe M, N. Willems. 2001. 3D unstructured modelling technique for ground-coupled air heat exchanger. In: Clima 2000/Napoli World Congress, Napoli, Italy. p. 15–8.

Zhang, W., H. Yang, L. Lu, and Z. Fang. 2015. Investigation on influential factors of engineering design of geothermal heat exchangers. Applied Thermal Engineering 84 : 310-9.

Law, Y. and S. Dworkin. 2016. Characterization of the effects of borehole configuration and interference with long term ground temperature modelling of ground source heat pumps.

Kuzmic, N., Y. Law, and S. Dworkin. 2016. Numerical heat transfer comparison study of hybrid and non-hybrid ground source heat pump systems. Applied Energy 165 : 919-29.

Longeon, M., A. Soupart, J. Fourmigue, A. Bruch, and P. Marty. 2013. Experimental and numerical study of annular PCM storage in the presence of natural convection. Applied Energy 112 (10): 175-1504.

Liu, Ming, M. Belusko, N. Steven Tay, and F. Bruno. 2014. Impact of the heat transfer fluid in a flat plate phase change thermal storage unit for concentrated solar tower plants. Solar Energy 101 : 220-31.

Hosseini, M., M. Rahimi, and R. Bahrampoury. 2014. Experimental and computational evolution of a shell and tube heat exchanger as a PCM thermal storage system. International Communications in Heat and Mass Transfer 50 : 128-36.

Trp, A., K. Lenic, and B. Frankovic. 2006. Analysis of the influence of operating conditions and geometric parameters on heat transfer in water-paraffin shell-and-tube latent thermal energy storage unit. Applied Thermal Engineering 26 (16): 1830-9.

Baetens, R., B. Jelle, and A. Gustavsen. 2010. Phase change materials for building applications: A state-of-the-art review. Energy & Buildings 42 (9): 1361-8.

Lin, W., Z. Ma, M. Sohel, and P. Cooper. 2014. Development and evaluation of a ceiling ventilation system enhanced by solar photovoltaic thermal collectors and phase change materials. Energy Conversion and Management 88 : 218-30.

Medrano, M., M. Yilmaz, M. Nogués, I. Martorell, J. Roca, and L. Cabeza. 2009. Experimental evaluation of commercial heat exchangers for use as PCM thermal storage systems. Applied Energy 86 (10): 2047-55.

Rabin, Y., E. Korin. 1996. Incorporation of phase change materials into a ground thermal energy storage system: theoretical study. J. Energy Res. Technol. 118. pp. 237–241.

Wu, C. 2008. Feasibility Analysis of the Ground Source Heat Pump Backfilled With Phase Change Materials. Tianjin University, Tianjin.

Li, Q. 2014. Study on Heat Transfer Characteristics of Phase Change Material Backfilling Ground Source Heat Pump. Donghua University, Shanghai.

Bottarelli, M., M. Bortoloni, and Y. Su. 2015. Heat transfer analysis of underground thermal energy storage in shallow trenches filled with encapsulated phase change materials. Applied Thermal Engineering 90 : 1044-51.

Lei, H. and N. Zhu. 2009. Analysis of phase change materials (PCMs) used for borehole fill materials. Geothermal Resources Council Annual Meeting 2009. Reno, USA. vol. 33. pp. 83–88.

Yang, W., L. Sun and X. Wu. 2014. Energy storage and heat transfer characteristics of ground heat exchanger with phase change backfill materials. Trans. Chinese Soc. Agric. Eng. (Trans. CSAE). vol. 30 (24). pp. 193–199.

COMSOL Multiphysics, retrieved from http://www.comsol.com/comsol-multiphysics, March, 2015.

[This page has been intentionally left blank]

IGSHPA SWEDEN
2018 Research Conference

DOI: 10.22488/okstate.18.000015

g-Functions for bore fields with mixed parallel and series connections considering axial fluid temperature variations

Massimo Cimmino

ABSTRACT

A semi-analytical method based on the finite line source (FLS) solution is presented to evaluate thermal response factors for geothermal bore fields with mixed series and parallel connections between boreholes. Each borehole in the bore field is modelled as a series of finite line source segments. The spatial and temporal superposition of the FLS solution for all pairs of segments in the bore field gives the total temperature change at the wall of the borehole segments. The axial variation of heat extraction rates is evaluated from the borehole wall temperatures using a steady-state analytical model of the fluid temperature variations inside the boreholes, considering the piping configuration to determine the inlet fluid temperature into a borehole from the inlet fluid temperature into the bore field. The concept of effective bore field thermal resistance is introduced to relate the arithmetic mean fluid temperature in a bore field, the average heat extraction rate per unit borehole length and a newly introduced effective borehole wall temperature. The g-function of a bore field with mixed series and parallel connections between boreholes is then defined from the effective borehole wall temperature, rather than the average borehole wall temperature.

INTRODUCTION

Simulation and design methods for geothermal systems often make use of thermal response factors – or g-functions. When superimposed in time, g-functions give the variation of ground temperatures due to varying heat extraction rates from the bore field. Originally, thermal response factors for bore fields were evaluated numerically (Eskilson, 1987). Since then, analytical methods based on the finite line source solution have been developed to evaluate g-functions (Zeng et al., 2002; Lamarche and Beauchamp, 2007; Claesson and Javed, 2011; Cimmino and Bernier, 2014; Lazzarotto, 2016). In analytical methods, boreholes are generally considered to be connected in parallel. Marcotte and Pasquier (2014) developed a method to account for piping connections between boreholes by including the borehole thermal resistance in their formulation. Their method, however, did not consider the axial variation of fluid temperatures, borehole wall temperatures and heat extraction rates. Previous work has shown that axial variation of heat extraction rates have an important impact on the long-term ground temperature variations (Cimmino and Bernier, 2014; Cimmino, 2015). The present paper represents improvements over previous works. In Cimmino (2015), g-functions were calculated for single U-tube boreholes connected in parallel. In Cimmino (2016), fluid and borehole wall temperature profiles were calculated for a single borehole with multiple U-tubes. In the present work, g-functions

Massimo Cimmino (massimo.cimmino@polymtl.ca) is an assistant professor in the Department of Mechanical Engineering, Polytechnique Montreal, Montreal, Quebec, Canada.

are calculated for boreholes – with potentially multiple U-tubes – in any configuration of parallel and series connections between boreholes. While series-connected boreholes are not common in ground-source heat pump systems, they are useful in ground thermal energy storage applications.

MATHEMATICAL MODEL

The g-function of a geothermal bore field gives the relation between the rate of heat extraction and the borehole wall temperature change:

$$\bar{T}_b(t_k) = T_0 - g(t_k)\frac{\bar{Q}'_b}{2\pi k_s} \quad (1)$$

where $\bar{T}_b$ is the average borehole wall temperature, T_0 is the undisturbed ground temperature, $\bar{Q}'_b$ is the average heat extraction rate per unit borehole length, k_s is the ground thermal conductivity and g is the g-function.

A field of 3 boreholes is presented in Figure 1. Each borehole i has a length L_i, is buried at a distance D_i from the ground surface, and is positioned at coordinates (x_i, y_i) on the ground surface. All boreholes have the same radius r_b. In the context of the present paper, boreholes may be connected in mixed configurations of series and parallel piping connections between boreholes. In Figure 1, the outlet of borehole 1 is connected to the inlet of borehole 2. The circuit composed of boreholes 1 and 2 is in parallel with borehole 3: fluid is fed at the inlet fluid temperature $T_{f,in}$ to boreholes 1 and 3 and the outlet fluid temperature of the bore field $T_{f,out}$ is the mix of the fluid exiting boreholes 2 and 3.

Thermal response factor with mixed inlet fluid temperature conditions

g-Functions are evaluated by simultaneously solving 3 sets of equations: (1) the superposition of the FLS solution, (2) the global energy balance, and (3) the fluid temperature variations inside boreholes.

Superposition of the finite line source solution. Each borehole i in the bore field is modelled as a series of $n_{q,i}$ borehole segments of equal length $L_i/n_{q,i}$. The temperature along any segment in the bore field is obtained by summing the temperature variations caused by all segments in the bore field. The spatial and temporal superpositions of the FLS solution is given by:

$$\boldsymbol{T_b}(t_k) = \boldsymbol{T_{b,0}}(t_k) - \boldsymbol{H}(\Delta t_k)\frac{\boldsymbol{Q'_b}(t_k)}{2\pi k_s} \quad (2)$$

$$\boldsymbol{T_{b,0}}(t_k) = T_0 - \sum_{p=1}^{k-1}\left[\boldsymbol{H}(t_k - t_{p-1}) - \boldsymbol{H}(t_k - t_p)\right]\boldsymbol{Q'_b}(t_p)/2\pi k_s \quad (3)$$

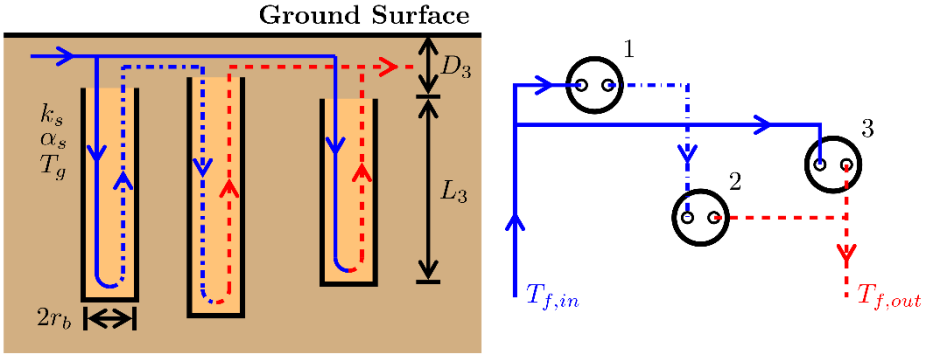

Figure 1 Boreholes in a mixed parallel-series configuration: side view (left) and top view (right)

where $\boldsymbol{T_b} = \begin{bmatrix} \boldsymbol{T_{b,1}^T} & \cdots & \boldsymbol{T_{b,N_b}^T} \end{bmatrix}^{\boldsymbol{T}}$ is a $N_q \times 1$ vector of the borehole wall temperatures along all segments of all boreholes, $\boldsymbol{T_{b,i}} = \begin{bmatrix} T_{b,i,1} & \cdots & T_{b,i,n_{q,i}} \end{bmatrix}^{\boldsymbol{T}}$ is a $n_{q,i} \times 1$ vector of the borehole wall temperatures along all segments of a borehole i, $\boldsymbol{T_{b,0}}(t_k)$ is a $N_q \times 1$ vector of the borehole wall temperatures along all segments of all boreholes assuming $\boldsymbol{Q'_b}(t_k) = 0$, $\boldsymbol{Q'_b} = \begin{bmatrix} \boldsymbol{Q_{b,1}^{\prime T}} & \cdots & \boldsymbol{Q_{b,N_b}^{\prime T}} \end{bmatrix}^{\boldsymbol{T}}$ is a $N_q \times 1$ vector of the heat extraction rates per borehole length along all segments of all boreholes, $\boldsymbol{Q'_{b,i}} = \begin{bmatrix} Q'_{b,i,1} & \cdots & Q'_{b,i,n_{q,i}} \end{bmatrix}^{\boldsymbol{T}}$ is a $n_{q,i} \times 1$ vector of the heat extraction rates per borehole length along all segments of a borehole i, $\boldsymbol{H}$ is a $N_q \times N_q$ matrix of segment-to-segment thermal response factors, $N_q = \sum_{i=1}^{N_b} n_{q,i}$ is the total number of segments in the bore field. The thermal response factor matrix is built from the FLS solution for all pairs of borehole segments. From Cimmino and Bernier (2014):

$$h_{ij,uv}(t_k) = \frac{1}{2L_{i,u}} \int_{1/\sqrt{4\alpha_s t_k}}^{\infty} \frac{1}{s^2} \exp\left(-d_{ij}^2 s^2\right) I_{FLS}(s) ds \tag{4}$$

$$\begin{aligned} I_{FLS}(s) = {} & \text{erfint}\left(\left(D_{i,u} - D_{j,v} + L_{i,u}\right)s\right) - \text{erfint}\left(\left(D_{i,u} - D_{j,v}\right)s\right) + \text{erfint}\left(\left(D_{i,u} - D_{j,v} - L_{j,v}\right)s\right) - \\ & \text{erfint}\left(\left(D_{i,u} - D_{j,v} + L_{i,u} - L_{j,v}\right)s\right) + \text{erfint}\left(\left(D_{i,u} + D_{j,v} + L_{i,u}\right)s\right) - \text{erfint}\left(\left(D_{i,u} + D_{j,v}\right)s\right) + \\ & \text{erfint}\left(\left(D_{i,u} + D_{j,v} + L_{j,v}\right)s\right) - \text{erfint}\left(\left(D_{i,u} + D_{j,v} + L_{i,u} + L_{j,v}\right)s\right) \end{aligned} \tag{5}$$

where $h_{ij,uv}$ is the segment-to-segment thermal response factor on segment u of borehole i from heat extraction at segment v of borehole j, $L_{i,u} = L_i/n_{q,i}$ is the length of segment u of borehole i, $D_{i,u} = D_i + (u-1)\,L_i/n_{q,i}$ is the buried depth of segment u of borehole i, d_{ij} is the distance between boreholes i and j, $d_{ii} = r_b$, α_s is the ground thermal diffusivity, and $\text{erfint}(x) = x \cdot \text{erf}(x) - \frac{1}{\sqrt{\pi}}(1 - \exp(-x^2))$ is the integral of the error function.

Global energy balance. The total heat extraction rate in the bore field is equal to the sum of the heat extraction rates along all segments of all boreholes:

$$\boldsymbol{L}\boldsymbol{Q'_b}(t_k) = Q_{b,tot} \tag{6}$$

where $\boldsymbol{L} = [\boldsymbol{L_1} \quad \cdots \quad \boldsymbol{L_{N_b}}]$ is a $1 \times N_q$ vector of the lengths of all segments of all boreholes, $\boldsymbol{L_i} = \begin{bmatrix} L_{i,1} & \cdots & L_{i,n_{q,i}} \end{bmatrix}$ is a $1 \times n_{q,i}$ vector of the lengths of all segments of borehole i and $Q_{b,tot}$ is the total heat extraction rate in the bore field. From Equation (1), for $Q_{b,tot} = 2\pi k_s L_{tot}$, the average borehole wall temperature is equal to the g-function of the bore field.

Fluid temperature variations. Assuming steady-state heat transfer between the fluid circulating in a borehole i and its borehole wall, the fluid temperature variations in the borehole are given by the following system of differential equations (Cimmino, 2016):

$$\frac{\partial \boldsymbol{T_{f,i}}}{\partial z}(z) = \boldsymbol{S_i}\boldsymbol{T_{f,i}}(z) - \boldsymbol{S_i}\boldsymbol{1}_{2n_{p,i}\times 1} T_{b,i}(z), \;\; 0 \le z \le L_i \tag{7}$$

where $\boldsymbol{T_{f,i}}$ is a $2n_{p,i} \times 1$ vector of fluid temperatures in each pipe of borehole i, and $\boldsymbol{S_i}$ is a $2n_{p,i} \times 2n_{p,i}$ built from the delta-circuit of internal thermal resistances in borehole i, considering the fluid mass flow rate inside the pipes. $n_{p,i}$ is the number of pipe pairs in borehole i. $\boldsymbol{1}_{2n_{p,i}\times 1}$ is a $2n_{p,i} \times 1$ matrix of ones.

The solution to the system of differential equations, assuming uniform borehole wall temperatures along the borehole segments, is given by:

$$\boldsymbol{T_{f,i}}(z) = \exp\mathrm{m}(\boldsymbol{S_i} z)\, \boldsymbol{T_{f,i}}(0) - \boldsymbol{F_i}(z)\boldsymbol{T_{b,i}} \tag{8}$$

$$\boldsymbol{F_i}(\mathrm{z}) = \begin{bmatrix} \boldsymbol{F_{i,1}}(\mathrm{z}) & \cdots & \boldsymbol{F_{i,n_{q,i}}}(\mathrm{z}) \end{bmatrix} \tag{9}$$

$$\boldsymbol{F_{i,u}}(\mathrm{z}) = \boldsymbol{S_i^{-1}} \left[\exp\mathrm{m}\left(\boldsymbol{S_i} \max\left(0, \mathrm{z} - \frac{(u-1)L_i}{n_{q,i}}\right)\right) - \exp\mathrm{m}\left(\boldsymbol{S_i} \max\left(0, \mathrm{z} - \frac{uL_i}{n_{q,i}}\right)\right)\right] \boldsymbol{S_i} \boldsymbol{1}_{2n_{p,i}\times 1} \tag{10}$$

where $\boldsymbol{F_i}$ is a $2n_{p,i} \times n_{q,i}$ matrix of coefficients and $\exp\mathrm{m}(\boldsymbol{X})$ is the matrix exponential.

For boreholes with any amount of U-tubes connected in series or in parallel, the outlet fluid temperature and the heat extraction rates along the borehole segments can be expressed in terms of the inlet fluid temperature and the borehole wall temperature along the borehole segments:

$$T_{f,out,i} = a_{out,i} T_{f,in,i} + \boldsymbol{b_{out,i}} \boldsymbol{T_{b,i}} \tag{11}$$

$$\boldsymbol{Q_{b,i}} = \boldsymbol{a_{Q,i}} T_{f,in,i} + \boldsymbol{b_{Q,i}} \boldsymbol{T_{b,i}} \tag{12}$$

where $T_{f,in,i}$ and $T_{f,out,i}$ are the inlet and outlet fluid temperatures of borehole i, $\boldsymbol{Q_{b,i}} = \begin{bmatrix} Q_{b,i,1} & \cdots & Q_{b,i,n_{q,i}} \end{bmatrix}^{\boldsymbol{T}}$ is a $n_{q,i} \times 1$ vector of the heat extraction rates along all segments of a borehole i, $a_{out,i}$ is a coefficient, and $\boldsymbol{b_{out,i}}$, $\boldsymbol{a_{Q,i}}$ and $\boldsymbol{b_{Q,i}}$ are $1 \times n_{q,i}$, $n_{q,i} \times 1$ and $n_{q,i} \times n_{q,i}$ vectors and matrices of coefficients. Expressions for the coefficients are given by Cimmino (2016).

By considering the connections between the boreholes in the bore field, Equations (11) and (12) can be rewritten in terms of the inlet fluid temperature into the bore field:

$$T_{f,out,i} = A_{out,i} T_{f,in} + \sum_{j \in P_i} \boldsymbol{B_{out,i,j}} \boldsymbol{T_{b,j}} \tag{13}$$

$$A_{out,i} = \prod_{k \in P_i} a_{out,k}\,, \quad \boldsymbol{B_{out,i,j}} = \left(\prod_{\substack{k \in P_i \\ k \notin P_j}} a_{out,k} \right) \boldsymbol{b_{out,j}} \tag{14}$$

where $T_{f,in}$ is the inlet fluid temperature into the bore field, $A_{out,i}$ is a coefficient, $\boldsymbol{B_{out,i,j}}$ is a $1 \times n_{q,i}$ vector of coefficients and P_i is the path from borehole i to the field inlet. The path P_i is the list of boreholes that connect the borehole i to the field inlet, starting from borehole i. As an example, the paths of the boreholes identified on Figure 1 are $P_1 = \{1\}$, $P_2 = \{2,1\}$ and $P_3 = \{3\}$. $\prod$ is the product operator, with $\prod_{k \in \{1,2,3\}} a_k = a_1 a_2 a_3$.

Coefficients for the heat extraction rates are obtained in the same manner:

$$\boldsymbol{Q_{b,i}} = \boldsymbol{A_{Q,i}} T_{f,in} + \sum_{j \in P_i} \boldsymbol{B_{Q,i,j}} \boldsymbol{T_{b,j}} \tag{15}$$

$$\boldsymbol{A_{Q,i}} = \boldsymbol{a_{Q,i}} \left(\prod_{\substack{k \in P_i \\ k \neq i}} a_{out,k} \right), \quad \boldsymbol{B_{Q,i,j}} = \left(\prod_{\substack{k \in P_i \\ k \notin P_j}} a_{out,k} \right) \boldsymbol{b_{Q,j}} \tag{16}$$

where $\boldsymbol{A_{Q,i}}$ is a $n_{q,i} \times 1$ vector of coefficients and $\boldsymbol{B_{Q,i,j}}$ is a $n_{q,i} \times n_{q,i}$ matrix of coefficients.

System of equations. Equations (2), (6) and (15) form a system of equations that relate the heat extraction rates along all segments of all boreholes, the borehole wall temperatures along all segments of all boreholes and the inlet fluid temperature into the bore field. The system of equation can be solved sequentially to evaluate the g-function of a bore

field at all times t_k. The system of equations is given by:

$$\begin{bmatrix} \boldsymbol{H}/2\pi k_s & -\boldsymbol{I}_{N_q} & \boldsymbol{0}_{N_q\times 1} \\ -\boldsymbol{I}_{N_q} & \boldsymbol{B_Q} & \boldsymbol{A_Q} \\ \boldsymbol{L} & \boldsymbol{0}_{1\times N_q} & \boldsymbol{0}_{1\times N_q} \end{bmatrix} \begin{bmatrix} \boldsymbol{Q_b'} \\ \boldsymbol{T_b} \\ T_{f,in} \end{bmatrix} = \begin{bmatrix} -\boldsymbol{T_{b,0}} \\ \boldsymbol{0}_{N_q\times 1} \\ Q_{b,tot} \end{bmatrix} \tag{17}$$

$$\boldsymbol{A_Q} = \begin{bmatrix} \boldsymbol{A}_{\boldsymbol{Q,1}}^{\boldsymbol{T}} & \cdots & \boldsymbol{A}_{\boldsymbol{Q,N_b}}^{\boldsymbol{T}} \end{bmatrix}^{\boldsymbol{T}},\ \boldsymbol{B_Q} = \begin{bmatrix} \boldsymbol{B_{Q,1,1}} & \cdots & \boldsymbol{B_{Q,N_b,1}} \\ \vdots & \ddots & \vdots \\ \boldsymbol{B_{Q,N_b,1}} & \cdots & \boldsymbol{B_{Q,N_b,N_b}} \end{bmatrix} \tag{18}$$

Effective borehole wall temperature

During simulation of ground-source heat pump systems, the mean fluid temperature in a borehole is commonly expressed in terms of the average borehole wall temperature and the effective borehole thermal resistance:

$$\bar{T}_f = \frac{1}{2}\left(T_{f,in} + T_{f,out}\right) = \bar{T}_b - \bar{Q}_b' R_b^* \tag{19}$$

where R_b^* is the effective borehole thermal resistance.

However, in bore fields that include series connections between boreholes, it is possible for the arithmetic mean fluid temperature in the field to be lower than the average borehole wall temperature during heat extraction. This makes Equation (19) impossible to apply in these cases and necessitates the introduction of the concept of effective borehole wall temperature to replace the average borehole wall temperature in the definition of the g-function. The effective borehole wall temperature will be defined from an effective bore field thermal resistance.

Effective borehole termal resistance. Based on the work of Hellström (1991), an effective borehole thermal resistance can be calculated by assuming a uniform temperature along the length of the borehole. Equations (11) and (12) are then simplified by considering the fluid temperature differences $\theta_{f,out,i} = T_{f,out,i} - \bar{T}_{b,i}$ and $\theta_{f,in,i} = T_{f,in,i} - \bar{T}_{b,i}$, where $\bar{T}_{b,i}$ is the uniform borehole wall temperature along borehole i:

$$\theta_{f,out,i} = a_{out,i}\theta_{f,in,i},\ \boldsymbol{Q_{b,i}} = \boldsymbol{a_{Q,i}}\theta_{f,in,i} \tag{20}$$

The effective borehole resistance is calculated based on the arithmetic mean fluid temperature:

$$R_{b,i}^* = -\frac{\bar{\theta}_{f,i}}{\bar{Q}_{b,i}'},\ \bar{\theta}_{f,i} = \frac{1}{2}\left(\theta_{f,in,i} + \theta_{f,out,i}\right),\ \bar{Q}_{b,i}' = \boldsymbol{1}_{1\times n_{q,i}}\boldsymbol{Q_{b,i}}/L_i \tag{21}$$

$$R_{b,i}^* = -\left(\frac{1+a_{out,i}}{\boldsymbol{1}_{1\times n_{q,i}}\boldsymbol{a_{Q,i}}}\right)\frac{L_i}{2} \tag{22}$$

Effective bore field termal resistance. The same process is applied to define an effective bore field termal resistance and an effective borehole wall temperature. The outlet fluid temperature difference from the bore field is obtained from an energy balance:

$$\theta_{f,out} = A_{out}\theta_{f,in},\ A_{out} = 1 + \boldsymbol{1}_{1\times N_q}\cdot\boldsymbol{A_Q}/\left(\dot{m}c_p\right) \tag{23}$$

The effective bore field termal resistance is then calculated based on the mean fluid temperature in the bore field:

$$R^*_{field} = -\left(\frac{1+A_{out}}{\mathbf{1}_{1\times N_q}\cdot \boldsymbol{A_Q}}\right)\frac{L_{tot}}{2},\ \bar{T}^*_b = \frac{1}{2}\left(T_{f,in}+T_{f,out}\right) + R^*_{field}\bar{Q}'_b \quad (24)$$

where R^*_{field} is the effective bore field thermal resistance and $\bar{T}^*_b$ is the effective borehole wall temperature. This temperature replaces the average borehole wall temperature to evaluate the g-function values.

RESULTS

The g-function of a field of 5 series-connected boreholes of unequal lengths is evaluated. All boreholes have a radius r_b = 0.075 m, are buried at a depth D = 4 m and are positioned on a straight line with an even spacing of 7.5 m. Each borehole contains a single U-tube with pipes of inner radius $r_{p,in}$ = 0.015 m and outter radius $r_{p,out}$ = 0.020 m, positioned symmetrically at a shank spacing of 0.050 m. The pipe thermal conductivity is k_p = 0.4 W/m-K, the grout thermal conductivity is k_g = 1.0 W/m-K, the ground thermal conductivity is k_s = 2.0 W/m-K and the ground thermal diffusivity is α_s = 10^{-6} m²/s. The fluid mass flow rate per borehole is $\dot{m}_f$ = 0.25 kg/s. The fluid specific heat capacity is 4000 J/kg-K, its density is 1015 kg/m³, its dynamic viscosity is 0.002 kg/m-s and its thermal conductivity is k_f = 0.5 W/m-K. The borehole lengths, starting from the borehole connected to the bore field inlet, are 75 m, 100 m, 125 m, 150 m and 75 m. The bore field characteristic time $t_s = \frac{\bar{L}^2}{9\alpha_s}$ is then 38.8 years.

The g-function of the series-connected boreholes and the temperature profiles at $\ln(t/t_s)$ = 4.35 (t = 3000 years) are shown on Figure 2. Each of the g-functions were calculated in 26 seconds. The calculation of the g-function involved the inversion of the matrix of Equation (17) at each of the 50 time steps. The matrix sizes were 61 × 61 and 121 × 121 for the uniform temperature and the mixed inlet temperature conditions, respectively. The g-function of the series-connected boreholes is less than the g-function using the uniform temperature condition: the g-function value is 9.53 at $\ln(t/t_s)$ = 4.35 while it is 10.61 using the uniform temperature condition. This merely means that the *effective* borehole wall temperature is lower. As shown on Figure 2 (right), temperature variations vary between boreholes: the maximum dimensionless temperature change is 13.23 for the borehole located at the bore field inlet. Due to the effective bore field thermal resistance being larger than the effective borehole thermal resistance, the variations of mean fluid temperature will be larger in the case of series-connected boreholes. On Figure 2 (right), the dimensionless inlet and outlet fluid temperatures are 16.27 and 9.67. The bore field thermal resistance is 0.274 m-K/W.

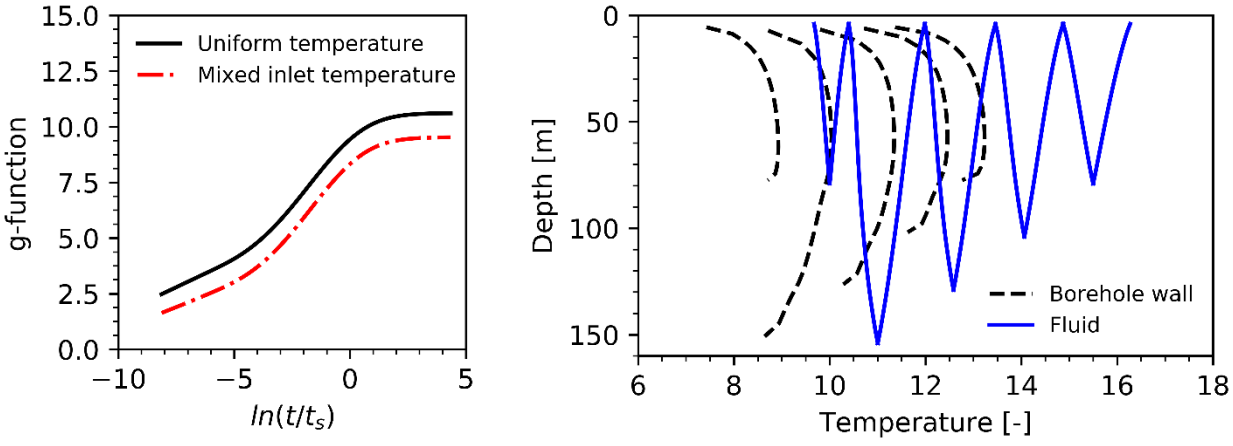

Figure 2 g-Function of 5 series-connected boreholes (left) and fluid and borehole wall temperatures at $\ln(t/t_s) = 4.35$ (right)

The effective bore field thermal resistance depends on both the bore field configuration and the fluid mass flow rate. Figure 3 shows the effective bore field thermal resistances of fields of 1, 3 and 5 series-connected boreholes at varying fluid mass flow rates. The thermal resistances are calculated for the same parameters as the previous example except the boreholes have equal lengths L = 150 m. The effective bore field thermal resistance increases when boreholes are connected in series and decreases at larger fluid mass flow rates. At $\dot{m}_f$ = 0.25 kg/s, the effective bore field thermal resistance is 0.141 m-K/W for a single borehole and 0.274 m-K/W for 5 series-connected boreholes. At a larger fluid mass flow rate $\dot{m}_f$ = 1.0 kg/s, the effective bore field thermal resistances are closer: 0.135 m-K/W and 0.145 m-K/W for the single borehole and 5 series-connected boreholes, respectively.

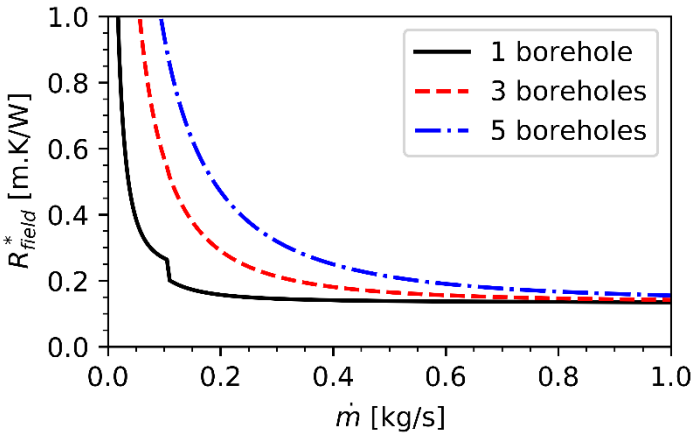

Figure 3 Effective bore field thermal resistance of series-connected boreholes

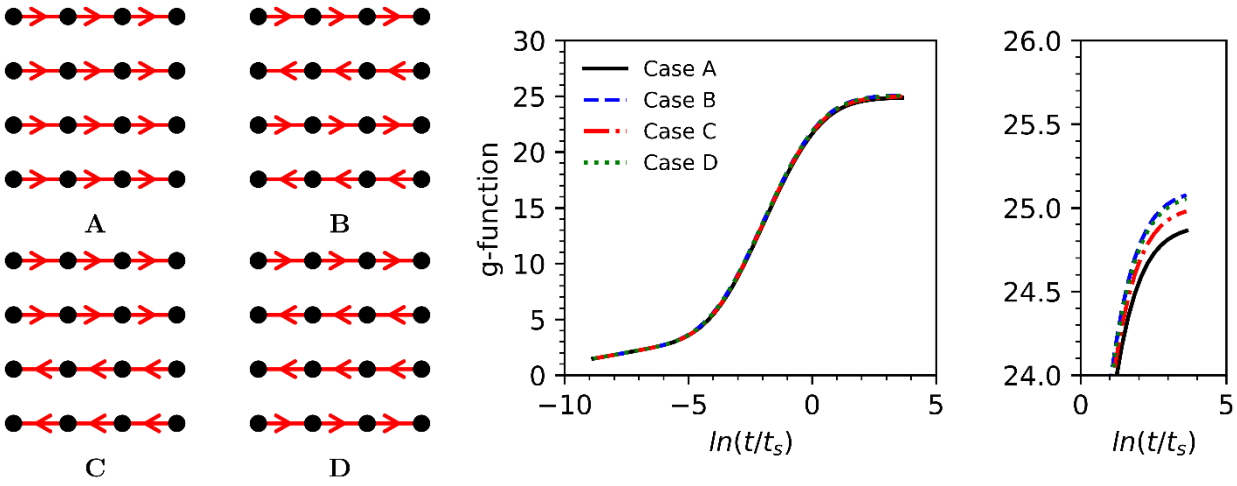

Figure 4 Field of 4 × 4 boreholes in mixed parallel-series configuration: piping network configurations (left), g-functions (center), and zoomed view (right)

g-Functions can be used to compare different piping configurations for the same bore field. Figure 4 shows the g-functions of 4 possible configurations of a field of 4 × 4 boreholes with 4 rows of 4 series-connected boreholes. The direction of flow in the rows is varied to evaluate its impact on the long-term temperature changes. All boreholes have the same length L = 150 m and receive the same fluid mass flow rate $\dot{m}_f$ = 0.25 kg/s. It is shown that the direction of flow has little effect on the g-function. The g-function curves are very close, with the g-function of Case A having the lowest value and the g-function of Case B having the largest value. At $\ln(t/t_s)$ = 3.63 (t = 3000 years), the g-function values for Cases A and B are 24.86 and 25.08, respectively. In all cases, the bore field thermal resistance is 0.307 m-K/W.

CONCLUSION

A semi-analytical method to evaluate the g-function of bore fields with mixed series and parallel connections between boreholes is presented. Since both the borehole wall and fluid temperatures vary between boreholes, the g-function needs to be defined based on the effective borehole wall temperature, rather than the average borehole wall temperature. The effective borehole wall temperature is in turn defined based on an effective bore field thermal resistance. The effective bore field thermal resistance is calculated by considering all boreholes to have the same uniform borehole wall temperature, equal to the effective borehole wall temperature. The method allows the evaluation of g-functions of bore field with any number of boreholes of potentially different sizes, at any position, and with any piping configuration connecting the boreholes. The source code for the evaluation of g-functions using this new method is available online (Cimmino 2018).

ACKNOWLEDGMENTS

The author received a start-up subsidy from the *Fonds de recherche du Québec – Nature et Technologie* (FRQNT).

NOMENCLATURE

α	=	Thermal diffusivity (m²/s)	n, N	=	Number, total number
a, b	=	Local coefficients	Q, Q'	=	Heat extraction rate (W, W/m)
A, B	=	Global coefficients	r	=	Radius (m)
D	=	Buried depth (m)	T	=	Temperature (K)
g	=	g-Function (-)	θ	=	Temperature difference (K)
h, H	=	Thermal response factors (-)	R^*	=	Effective resistance (m-K/W)
k	=	Thermal conductivity (W/m-K)	t	=	Time (s)
L	=	Length (m)			

Subscripts

0	=	No heat extraction	in, out	=	Inlet, outlet
b	=	Borehole	q	=	Borehole segment
f	=	Fluid	s	=	Ground
g	=	Grout			

REFERENCES

Cimmino, M. and M. Bernier. 2014. *A semi-analytical method to generate g-functions for geothermal bore fields*. International Journal of Heat and Mass Transfer 70(c): 641-650.

Cimmino, M. 2015. *The effects of borehole thermal resistances and fluid flow rate on the g-functions of geothermal bore fields*. International Journal of Heat and Mass Transfer 91: 1119-1127.

Cimmino, M. 2016. *Fluid and borehole wall temperature profiles in vertical geothermal boreholes with multiple U-tubes*. Renewable Energy 96, Part A: 137-147.

Cimmino, M. 2018. *MassimoCimmino/pygfunction V1.1.0*. Zenodo. doi:10.5281/zenodo.1195039.

Claesson, J. and S. Javed. 2011. *An analytical method to calculate borehole fluid temperatures for time-scales from minutes to decades*. ASHRAE Transactions 117(2): 279-288.

Eskilson, P., 1987. *Thermal Analysis of Heat Extraction Boreholes*. Thesis (PhD), PhD Thesis, University of Lund, Sweden.

Hellström, G. 1991. *Ground Heat Storage – Thermal Analyses of Duct Storage Systems – Theory*. PhD Thesis, University of Lund, Sweden.

Lamarche, L. and B. Beauchamp. 2007. *A new contribution to the finite line-source model for geothermal boreholes*. Energy and Buildings 39(2): 188-198.

Lazzarotto, A. 2016. *A methodology for the calculation of response functions for geothermal fields with arbitrarily oriented boreholes – Part 1*. Renewable Energy 86: 1380-1393.

Marcotte D. and Pasquier P. 2014. *Unit-response function for ground heat exchanger with parallel, series or mixed borehole arrangement*. Renewable Energy. 68: 14-18.

Zeng, H. Y., N. R. Diao and Z. H. Fang. 2002. *A finite line-source model for boreholes in geothermal heat exchangers*. Heat Transfer - Asian Research 31(7): 558-567.

[This page has been intentionally left blank]

IGSHPA SWEDEN 2018 Research Conference

DOI: 10.22488/okstate.18.000035

Understanding transient heat transfer in large-scale ground heat exchanger (GHE) matrices: Insights from high-resolution analytical solutions

Min Li **Cheng Zhou**

ABSTRACT

This paper reports on a set of high-resolution analytical solutions, which combines a composite-medium line-source solution, the conventional finite and infinite line-source solutions, and a quasi-3D model for fluid inside U-shaped tubes. This model extends our full-scale line-source model to deal with the thermal interaction between adjacent boreholes and the vertical variation in fluid temperature along U-shaped tubes. Based on this model, we analyze both hourly high-frequency temperature responses and long-term temperature evolution of GHEs clusters. The results indicate that 1) the heat capacity of backfilling material can heavily influence the prediction of temperature extrema and 2) the mainstream of heat flux within GHE matrices shifts gradually from the horizontal direction to the vertical direction due to the thermal interaction between GHEs. Finally, this paper suggests a two-borehole approach to approximating the average temperatures of large-scale GHEs matrices.

INTRODUCTION

Inspired by the urgent need for renewable energy, ground-coupled heat pumps (GCHPs) have been globally accepted and increasingly used in large-scale applications. For example, it is not uncommon in China to use GCHPs in buildings having heating and cooling areas greater than 1, 000 000 m^2. The design and operation of these large-scale systems require detailed knowledge of the heat transfer through ground heat exchangers (GHEs) matrices. A great challenge in the heat-transfer calculations of large-scale GHEs is the diverse time and space scales (Li and Lai 2015; Li, et al. 2016). As shown in Li and Lai (2015), four space scales ranging from several centimeters to hundreds of meters and eight time-scales ranging from minutes to decades can be important in the heat transfer of borehole GHEs. A successful model should provide an accurate and efficient approach to calculating the diverse-scale problem. From the perspective of accuracy, the heat transfer analysis should use a model of time resolution ranging from subhour to decades, corresponding to a length range from several centimeters to more than one hundred meters. From the efficient viewpoint, the analysis should tackle the complete spectrum of the time-length scales in an analytical way.

To meet the challenge in modeling GHEs, researchers have developed a vast number of analytical heat transfer models. Among them, conventional finite line-source models (FLS) appear to be the most suitable and efficient

Min Li (cnlimin78@gmail.com) is a professor and Cheng Zhou is a MSc student at Central South University.

this direction is relatively small, compared with the heat advection of the fluid. These equations consider both the horizontal thermal process through the plastic pipe wall and the vertical variation of the fluid temperature along the U-shaped pipes. The boundary conditions of Eqs. (1) and (2) are the temperature conditions on the ground surface ($z = 0$) and at the bottom of the borehole ($z = H$): $T_{f1}(t,0) = T_{f,in}$. $T_{f2}(t, H) = T_{f1}(t, H)$, where $T_{f,in}$ is the inlet temperature of GHEs. T_{p1} and T_{p2} in Eqs. (1) and (2) denote the average temperatures on the outer walls of the U-pipe legs (Fig. 1) and generally differ from each other. These temperatures vary linearly with the heat fluxes imposed on the pipe legs; but the average of T_{p1} and T_{p2} remains almost unchanged for a given total heat flux (Yang and Li 2014). For example, the average temperature in the case of 50%-50% assignment is identical to the case of 70%-30% assignment for a given total heat flux, because the increased wall temperature due to the increased flux is offset by the decreased wall temperature due to the decreased heat flux. Therefore, it appears to be acceptable to assume that the heat flux is assigned equally to each U-pipe leg, leading to $T_{p1} = T_{p2} = T_a$. Here T_a denotes the average temperature on the outer walls of U-pipe and can be approximated by the arithmetic mean of temperatures of positions A and B as labeled in Fig. 1 (Li and Lai 2012). Based on these assumptions and the boundary conditions, the solution to Eqs. (1) and (2) is (Polyanin and Zaitsev 2003)

$$T_{f,out}(t) = T_a(t) + \left[T_{f,in}(t) - T_a(t)\right]\exp(-2\eta) \tag{4}$$

where η is defined as $H/(c_p \dot{m} R_p)$, a quantity that have a similar implication as the number of transfer units (NTU) used in the heat exchanger literature. Eq. (4) is applicable only for single U-tube and parallel-connected double U-tubes. The similar idea is applicable to the case of series connected double U-tubes (or W-shaped tubes), and the outlet temperature response is (Ma, et al. 2015)

$$T_{f,out}(t) = T_a(t) + \left[T_{f,in}(t) - T_a(t)\right]\exp(-4\eta) \tag{5}$$

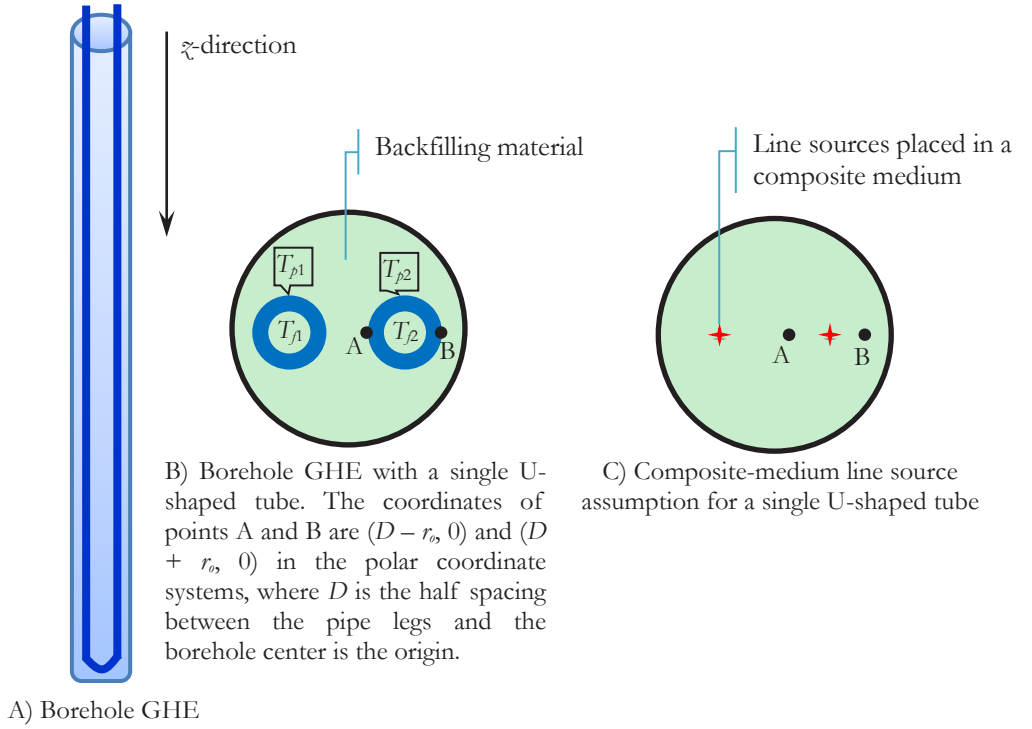

A) Borehole GHE

B) Borehole GHE with a single U-shaped tube. The coordinates of points A and B are ($D - r_o$, 0) and ($D + r_o$, 0) in the polar coordinate systems, where D is the half spacing between the pipe legs and the borehole center is the origin.

C) Composite-medium line source assumption for a single U-shaped tube

Figure 1 The line-source assumption and variable definitions used in the heat transfer model for U-shaped GHEs

The overall average temperature T_a in Eqs. (4) and (5) is unknown and needs to be determined. There are several approaches to determining T_a. The approach used here is by imposing a constant heat-flux boundary condition on the outer walls of U-shaped pipes because the heat flux can be determined using the heating/cooling loads and the COP of heat pumps. By this approach, T_a is the time-dependent average temperature on the U-pipe walls due to the given heat flux on the U-pipe walls; it can be determined using the theory of composite-medium line-source and the idea of matched asymptotic expansion as follows (Li, et al. 2014; Li and Lai 2012):

$$T_a = T_0 + q_l G(t) \tag{6}$$

G is the temperature response on the outer wall of the U-shaped pipes due to a unit step change in the heat flux (i.e., $q_l = 1$ in Eq. (6)), consisting of four temperature response functions as follows (Li, et al. 2014):

$$G(t) = G_i + G_o - G_m + \Delta G \tag{7}$$

Eq. (7) extended the full-scale line-source model by the additional term ΔG. Here, G_m is an infinite line-source solution for the temperature on the borehole wall. (Carslaw and Jaeger 1959):

$$G_m(t) = \frac{1}{4\pi k_s} \int_{r_b^2/4a_s t}^{\infty} \frac{\exp(-s)}{s} ds = \frac{1}{4\pi k_s} E_1\left(\frac{r_b^2}{4a_s t}\right) \tag{8}$$

G_o in Eq. (7) is a finite line-source solution for the temperature on the borehole wall. According to Claesson and Javed (2011), the expression for the mean temperature of the borehole wall can be

$$G_o(t) = \frac{1}{4\pi k_s} \int_{1/\sqrt{4a_s t}}^{\infty} \exp(-r_b^2 u^2) \frac{I(Hu, H_1 u)}{Hu^2} du \tag{9}$$

where I is a special function defined as follows:

$$I(x_1, x_2) = 2 \cdot \text{ierf}(x_1) + 2 \cdot \text{ierf}(x_1 + 2x_2) - \text{ierf}(2x_1 + 2x_2) - \text{ierf}(2x_2) \tag{10}$$

ierf(x) denotes integral of the error function erf(x):

$$\text{ierf}(x) = \int_0^x \text{erf}(s) ds = x \cdot \text{erf}(x) - \frac{1}{\sqrt{\pi}}\left[1 - \exp\left(-x^2\right)\right] \tag{11}$$

G_i is a composite-medium line-source solution to the average temperature on the outer walls of the U-shaped pipes. The key idea of the composite-medium line-source solution is that the legs of U-shaped tubes (not the borehole) are assumed as lines of heat sources placed in a cylindrical composite medium. Thus, it is possible to obtain the transient temperature field inside the borehole and the average temperature T_a. Readers can find more details about this model in the references (Li and Lai 2012; Li and Lai 2013; Yang and Li 2014). For single U-shaped tubes, G_i is

$$G_i(t) = \frac{1}{2\pi k_b} \sum_{i=-\infty}^{+\infty} \int_0^{+\infty} \left[1 - \exp(-u^2 a_b t)\right] \frac{J_{2i}(ur_A) + J_{2i}(ur_B)}{2} \frac{J_{2i}(ur')(\varphi g - \psi f)}{u(\varphi^2 + \psi^2)} du \tag{12}$$

For double U-shaped GHEs, the expression of G_i is

$$G_{\mathrm{i}}(t)=\frac{1}{2\pi k_{\mathrm{b}}}\sum_{i=-\infty}^{+\infty}\int_{0}^{+\infty}\left[1-\exp(-u^2a_{\mathrm{b}}t)\right]\frac{J_{4i}(ur_A)+J_{4i}(ur_B)}{2}\frac{J_{4i}(ur')(\varphi g-\psi f)}{u(\varphi^2+\psi^2)}du \quad (13)$$

where r_A and r_B are the radius coordinates of points A and B (see Fig. 1); functions φ, ψ, f, and g are defined as

$$\begin{cases}\varphi=akJ_n(ur_b)J_n'(aur_b)-J_n'(ur_b)J_n(aur_b)\\ \psi=akJ_n(ur_b)Y_n'(aur_b)-J_n'(ur_b)Y_n(aur_b)\\ f=akY_n(ur_b)J_n'(aur_b)-Y_n'(ur_b)J_n(aur_b)\\ g=akY_n(ur_b)Y_n'(aur_b)-Y_n'(ur_b)Y_n(aur_b)\end{cases} \quad (14)$$

where a and k are dimensionless variable $k=k_{\mathrm{s}}/k_{\mathrm{b}}$, $a=(a_{\mathrm{b}}/a_{\mathrm{s}})^{1/2}$; J_n' and Y_n' are the derivatives of J_n and Y_n; the order n is equal to $2i$ and $4i$ in Eqs. (12) and (13), respectively.

ΔG in Eq. (7) denotes the superimposed temperature response due to the thermal interaction between adjacent boreholes. Since the thermal interaction between boreholes is a mid- and long-term process (Li and Lai 2015), it should be calculated by the long-term solution, i.e., the finite line-source model (Claesson and Javed 2011):

$$\Delta G(t)=\frac{1}{4\pi k_s}\int_{1/\sqrt{4a_st}}^{\infty}\sum_{i=1,i\neq j}^{M}\exp\left(-B_{ij}^2u^2\right)\frac{I\left(Hu,H_1u\right)}{Hu^2}du \quad \left(j=1,2\cdots,M\right) \quad (15)$$

Eq. (15) is identical to Eq. (9) except that r_b is replaced by the distance between th ith borehole and the jth borehole under consideration, B_{ij}. The summation in Eq. (15) means the superposition of all thermal interaction from the adjacent GHEs. Furthermore, the mean temperature of a GHEs cluster can be approximated by the algebraic mean of all the M boreholes:

$$\Delta G(t)=\frac{1}{4\pi k_sM}\int_{1/\sqrt{4a_st}}^{\infty}\sum_{j=1}^{M}\sum_{i=1,i\neq j}^{M}\exp\left(-B_{ij}^2u^2\right)\frac{I\left(Hu,H_1u\right)}{Hu^2}du \quad (16)$$

In Eq. (16), the summation according to j is used to calculate the total temperature response of M borehole GHEs.

RESULTS AND DISCUSSION

High-frequency temperature responses

The short-time performance of the analytical models has been validated by comparing the theoretical model to a set of reference sandbox data and a numerical model in our previous work (Li and Lai 2013; Yang and Li 2014). Thus, this section only shows hourly high-frequency prediction. Fig. 2 shows the results of a simulation of a GHEs cluster by inputting a set of hypothetical hourly building loads. The temperature responses to the hourly loads were calculated by applying a conventional line-source model and the full-scale line-source model. Although the heat capacity of backfilling materials is small compared with that of the surrounding soil/rock, its influence on short-term and high-frequency responses is surprisingly significant (Fig. 2): 1) the hourly response given by the full-scale model oscillates with an amplitude clearly smaller than that given by the conventional line-source model; 2) the variation of the temperature responses yielded by the conventional model is entirely consistent with that of the hourly loads; but, the responses produced by the full-scale model do not always follow the pattern of the loads. These two discrepancies can be explained by the damping effect of the heat capacity of backfilling materials on the hourly high-frequency temperatures because the conventional model differs from the full-scale model only in that it ignores the influence of the heat capacity of backfilling materials. In fact, our previous study has illustrated that ignoring the heat capacity

within bores may lead to a discrepancy in short-term thermal resistance ranging from 26% to 55% (Li, et al. 2017).

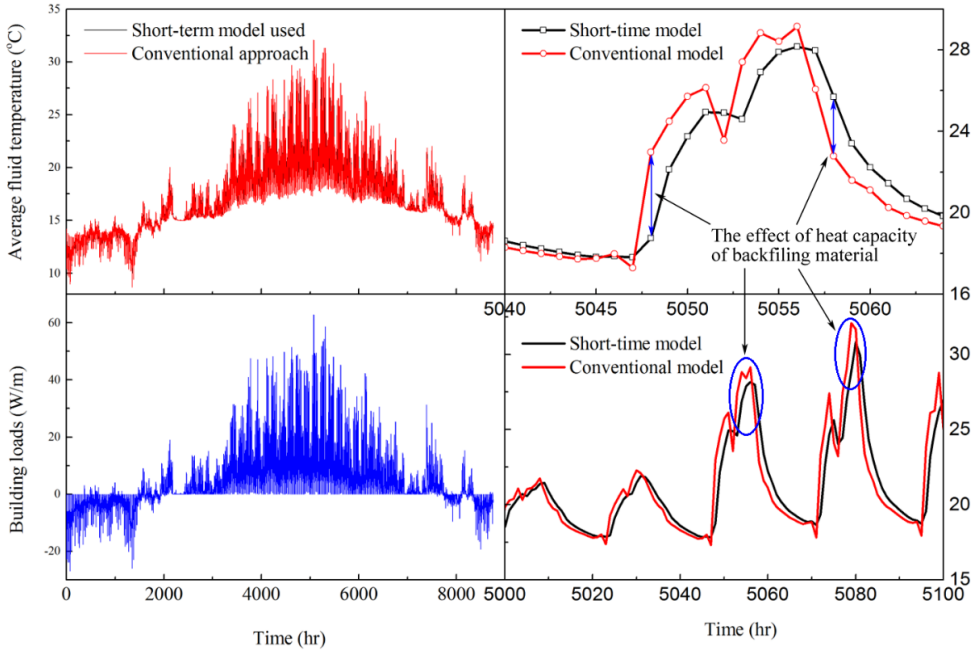

Figure 2 A case study assessing the performance of the full-scale line-source model in predicting high-frequency temperature responses (The conventional model consists of the finite line-source model and a 2-D model for effective borehole thermal resistance)

Long-term underground temperature evolution

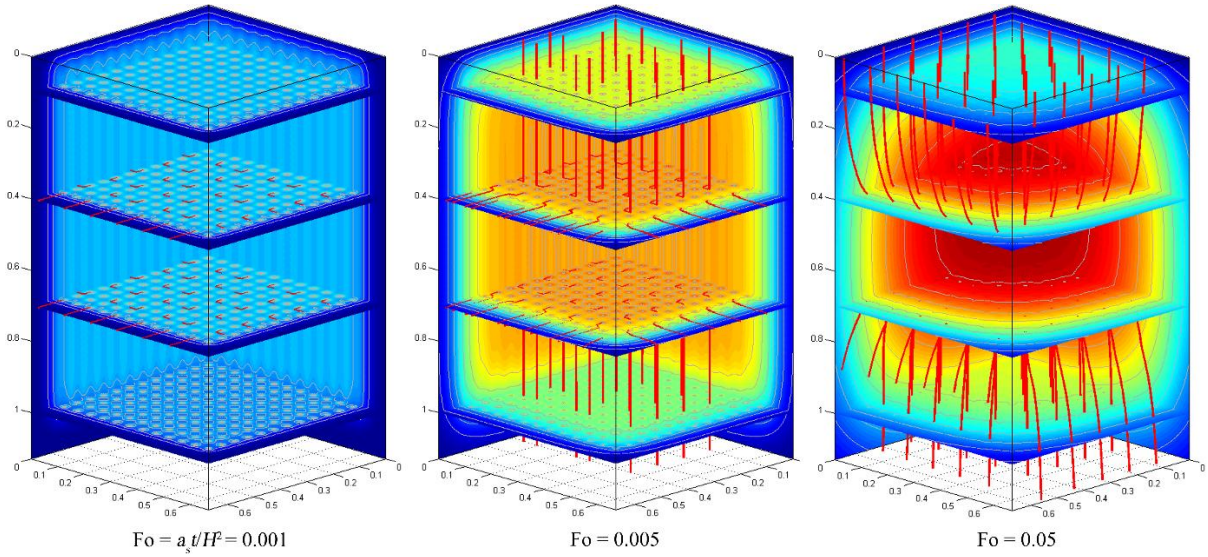

Figure 3 3D temperature and heat-flux fields within and around a GHE matrix (24×24 = 576) at three instants. The red lines represent heatlines that show the direction of heat flux.

It is necessary for long-term processes to address the thermal interaction between boreholes, which is involved in Eq. (7) using the principle of superposition (i.e., ΔG). Fig. 3 shows three snapshots of the 3D underground temperature and heat-flux fields calculated by the new model (576 bores). The heat-flux field is illustrated by the heatlines (the red lines in Fig. 3). A heatline is a vector line whose tangents everywhere coincide with the direction of the heat flux. An interesting observation following from Fig. 3 is that with time increasing the mainstream of the heat fluxes within the GHEs cluster shifts gradually from the horizontal direction to the vertical direction. Especially, the heat fluxes from the inner boreholes become totally vertical (e.g., Fo = $a_s t/H^2$ = 0.005 and 0.05). The shift in heat-flux directions is caused by the thermal interaction between boreholes and the increase in surrounding ground temperature, which blocks the horizontal transfer of heat. The shift also implies that load imbalance can cause a sharp increase in the mean temperature of large-scale GHE clusters. Moreover, for the purposes of ground heat storage (GHS), improving ground-surface insulation may be a viable means of improving storage efficiency.

Average temperature responses

For engineering applications, the most important variable should be the average temperature of GHEs clusters, which determines the overall efficiency of GCHP and GHS systems. The analytical model summarized here facilitates heat transfer calculation for large-scale engineering applications. Fig. 4 is one example, which presents a family of G curves for matrix arrangements of bores. While similar charts have been reported by other researchers (Claesson and Javed 2011), Fig. 4 is complementary to previous charts in providing G functions for extremely large clusters and applicable to time scales from minutes to decades.

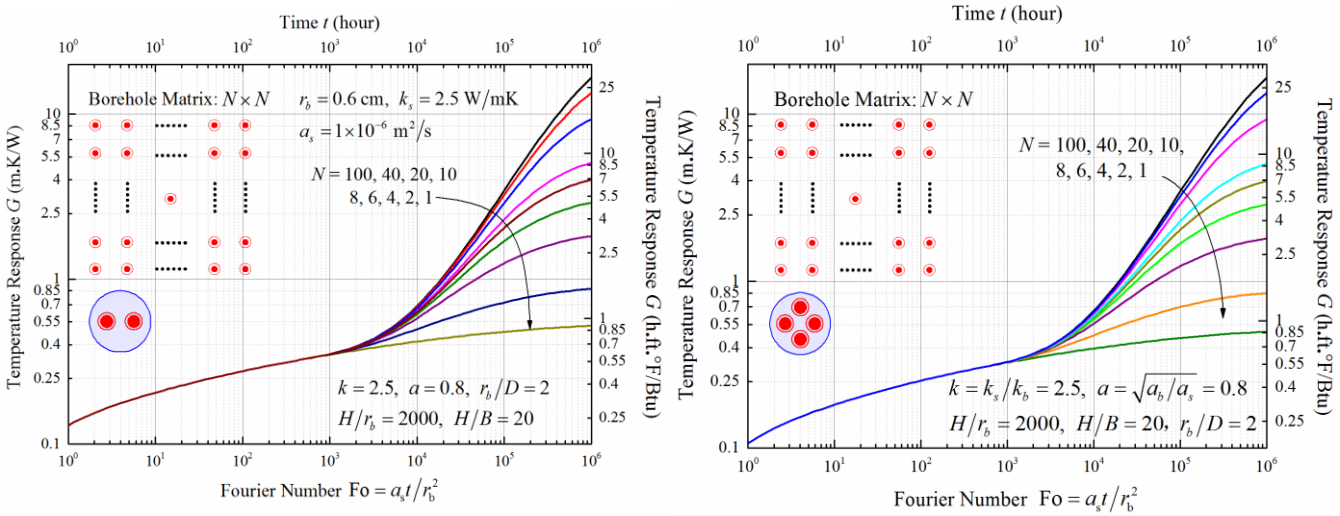

Figure 4 Time-dependent temperature response functions (G-functions) of U-shaped GHEs matrices: From 1 to 10,000 boreholes.

CONCLUSION

This paper reports on an analytical solutions to heat transfer of GHEs, which can predict temperature responses of GHE matrices from sub-hour to decades. The solution uses the inlet temperature, the flow rate of the fluid, and the initial ground temperature as the boundary/driven conditions for computing the outlet temperature of GHEs, reproducing the physical reality of the operation of GHEs and providing a very direct way of simulation. This feature enables the model to be an idea foundation for analysis, simulation, and design of large-scale GHE clusters.

NOMENCLATURE

α = Convective heat transfer coefficient (W/(m^2·℃))
η = Dimensionless variable
a = Thermal diffusivity (m^2/s)
c_p = Specific heat of the circulating fluid at constant pressure (J/(kg.℃))
G = G-function or time-dependent thermal resistance (℃·m/W)
H = Borehole depth (m)
J_i = The Bessel functions of the first kind of order i,
k = Thermal conductivity (W/(m.℃))
m = Mass flow rate (kg/s)
M = The number of boreholes in a GHEs cluster
q_l = Specific heat load (W/m)
r = Radius or radial coordinate (m)
R = Thermal resistance per unit length of bore (℃·m/W)
t = Time (s)
T = Temperature (℃)
Y_i = The Bessel functions of the second kind of order i
z = coordinate along borehole depth (m)

Subscripts

a = average
b = borehole or backfilling material
f = fluid
i = inner
in = inlet
m = mid
o = outer
out = outlet
p = pipe
s = soil or ground
0 = initial

REFERENCES

Carslaw, H.S., and J.C. Jaeger. 1959. *Conduction of heat in solids*. Oxford: Clarendon Press, 2nd ed.

Claesson, J., and S. Javed. 2011. *An analytical method to calculate borehole fluid temperatures for time-scales from minutes to decades*. ASHRAE Transactions 117(2): 279–288.

Hellstrom, G. 1991. Ground heat storage – thermal analysis of duct storage systems I. Theory. Lund, Sweden: University of Lund.

Li, M., and A.C.K. Lai. 2012. *New temperature response functions (G functions) for pile and borehole ground heat exchangers based on composite-medium line-source theory*. Energy 38: 255–263.

Li, M., and A.C.K. Lai. 2013. *Analytical Model for short-time responses of borehole ground heat exchangers: Model development and validation*. Applied Energy 104: 510–516.

Li M., P. Li, V. Chan, and A.C.K. Lai. 2014. *Full-scale temperature response function (G-function) for heat transfer by borehole ground heat exchangers (GHEs) from sub-hour to decades*. Applied Energy 136: 197–205.

Li, M., and A.C.K. Lai. 2015. *Review of analytical models for heat transfer by vertical ground heat exchangers (GHEs): A perspective of time and space scales*. Applied Energy 151: 178–191.

Li, M., K. Zhu, and Z. Fang. 2016. *Analytical methods for thermal analysis of vertical ground heat exchangers.* In S.J. Rees Advances in Ground-Source Heat Pump Systems. Duxford, UK: Elsevier/Woodhead Publishing.

Li, M., X.C. Zhuo, and G.S. Huang. 2017. *Improvements on the American Society of Heating, Refrigeration, and Air-Conditioning Engineers Handbook equations for sizing borehole ground heat exchangers.* Science and Technology for the Built Environment 23(8): 1267 – 1281.

Ma, W.W., M. Li, P. Li, and A.C.K. Lai. 2015. *New quasi-3D model for heat transfer in U-shaped GHEs (ground heat exchangers): Effective overall thermal resistance*. Energy 90: 578 – 587.

Polyanin, A.D. and V.F. Zaitsev. 2003. Handbook of exact solutions for ordinary differential equations. Boca Raton: Chapman & Hall/CRC, 2nd ed.

Yang, Y., and M. Li. 2014. *Short-time performance of composite-medium line-source model for predicting responses of ground heat exchangers with single U-shaped tube*. International Journal of Thermal Sciences 82: 130–137.

Zeng, H.Y., N.R. Diao, and Z.H. Fang. 2002. *A finite line-source model for boreholes in geothermal heat exchangers*. Heat Transfer—Asian Research 31: 558–567.

Zeng, H.Y., N.R. Diao, and Z.H. Fang. 2003. *Heat transfer analysis of boreholes in vertical ground heat exchangers*. International Journal of Heat and Mass Transfer 46(23): 4467–4481.

IGSHPA SWEDEN
2018 Research Conference

DOI: 10.22488/okstate.18.000006

Carbon dioxide evaporation process in direct expansion geothermal boreholes

Messaoud Badache
Zine Aidoun
Parham Eslami Nejad
Mohamed Ouzzane
Arash Bastani

ABSTRACT

Ground Heat Exchangers (GHE) play an important role in the performance of Ground Source Heat Pumps (GSHP). The impact is even more significant in direct expansion GSHP (DX-GSHP) systems as the refrigerant used in the heat pump also acts as the heat transfer fluid for the GHE. In this study, several experiments were carried out to investigate the performance of GHEs in a carbon dioxide (CO_2) DX-GSHP. The evaporation of CO_2 in the GHE was studied under various mass flow rates and number of active boreholes. For this purpose, a transcritical CO_2 DX-GSHP test facility was built and fully equipped at CanmetENERGY-Varennes research laboratory. It was found that a partial two-phase flow regime along the GHE decreases the performance compared to the full two-phase flow and it has to be avoided for more efficient DX-GSHP systems.

INTRODUCTION

The global climate change and urge for using energy efficient systems call for the development and implementation of emerging eco-friendly technologies for heating and cooling applications. This new tendency has motivated the scientific community to adapt natural refrigerants such as carbon dioxide (CO_2) in DX-GSHP. The use of transcritical CO_2 in DX-GSHP offers several opportunities for the cost reduction of the ground loop and makes these systems a promising environmentally friendly and energy efficient alternative compared to other heating equipment. In addition, CO2 is inexpensive to produce and has a relatively high vapour density as well as latent heat of evaporation. This and its working pressures allows for less refrigerant with small specific volume to be cycled than conventional refrigerants, achieving the same heating/cooling capacity and size reduction of the GHE as well as other system components.

One of the main components in transcritical CO_2 DX-GSHP systems is the GHE, as it is the component where heat transfer between the GSHP system and the soil occurs. GHE heat transfer performance is the key factor influencing the operation performance of the entire system.

At present, a relatively few studies is reported on DX-GSHP. The available theoretical researches have mainly focused on numerical methods to simulate the GHE and study the effect of different parameters on the system performance (Ghazizade and Ameri, 2018; Yuefen, et al. 2017; Mastrullo 2014; Austin and Sumathy, 2011, Eslami Nejad, et al. 2014, and Eslami Nejad, et al. 2018). The modeling of transient behavior of GHE and the surrounding

Messaoud Badache (Messaoud.badache@canada.ca) is a research scientist at Natural Resources Canada. Parham Eslami Nejad, Arash bastani, and Zine Aidoun are research scientists at Natural Resources Canada. Mohamed Ouzzane is a professor in Mechanical Engineering Department, Islamic university in Madinah, Saudi Arabia:

ground is somehow complex and only few transient models are available in the literature (Beauchamp, et al. 2013; Rousseau, et al. 2015; Eslami Nejad et al. 2015). Most of the experimental studies evaluated the whole system performance using typical refrigerants (Guo et al. 2012; Wang et al. 2009; Lenarduzzi and Bennet 1991 and Goulburn and Fearon 1978). Compared to other working refrigerants, CO_2 has been the least studied. Several studies were performed to establish some guides and improvements for the design of such systems (Mei and Baxter, 1990 and Wang, et al. 2013) while others focused on various GHE types (i.e, horizontal, vertical, spiral or inclined) in the heating and cooling mode (Johnson, 2002; Minea, 2003 and Goulburn 1983). Recently Badache, et al., 2018 experimentally investigated the overall system performance, phase change of CO_2 due to evaporation inside the ground heat exchanger and the effect of the number of boreholes on the system performance.

In the present work, several experiments were conducted to investigate the GHE performance using CO_2 as the working fluid. For this purpose, a transcritical CO_2 DX-GSHP test facility was built at CanmetENERGY-Varennes research laboratory. First, the profiles of the ground temperature and pressure drop through the boreholes are analysed. In the second step, the evaporation process taking place inside the heat exchanger and the related heat extraction performance were investigated for different number of active boreholes and the CO_2 mass flow rate per borehole.

DESCRIPTION OF THE EXPERIMENTAL SETUP AND TEST PROCEDURE

Experimental setup

Figure 1(a) schematically shows the single-stage transcritical CO_2 DX-GSHP test bench in heating mode. The main components of this test facility include a semi hermetic compressor (one ton nominal refrigeration capacity), the GHE, and a water loop for heat rejection from the gas cooler. An oil system consisting of a separator, a reservoir and a pressure regulating valve ensures adequate compressor lubrication while minimizes the amount of oil circulating in the whole cycle including the borehole. The test facility is fully equipped with different measuring devices including the pressure and temperature sensors and flowmeters. The system operates in three pressure levels namely high, intermediate, and low. The refrigerant (CO_2) is compressed to the high-pressure level (supercritical pressure) at point 2 with a corresponding temperature rise. Then, the high pressure-high temperature gas enters the gas cooler to heat water. After internal heat exchanger (IHE), CO_2 is expanded to the intermiddiate-pressure level of the cycle (point 5). The two-phase CO_2 enters the separator and the vapor portion is bypassed around the boreholes, while the liquid portion flows toward the boreholes. Then, CO_2 with low vapor quality enters the boreholes, mixes with the the bypass vapor at the outlet of the boreholes, becomes superheated in IHE, and enters the compressor to complete the cycle. Note, for all tests, the pressure of the separator was set to 36.45 bars, corresponding to 1.7 °C.

The GHE consists of four 30-meter vertical boreholes with single cooper U-tube arranges in a square pattern with a uniform spacing of 6.25 m. The boreholes dimensions and the grout filling material are listed in Table 1. Insitu thermal properties of the soil obtained from a thermal response test are given in Table 2. One of the boreholes was equipped with temperature sensors in diferent levels to present the temperature profile of CO_2 in both two legs of the U-pipe. Figure 1 (b) shows the location of those temperature sensors on the borehole.

Table 1. Borehole dimensions

Borehole	r_b			3.9
	U	ID	*cm*	0.64
		OD		0.8
	D	ID		0.48
		OD		0.64
	2D			2.3
	k_{grout}	$W/m/K$		0.8
	k_{pipe}			400
	Length	*m*		30

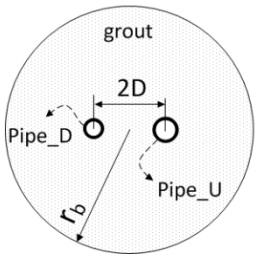

Table 2. Ground thermal properties

Ground	K_{ground}	$W/m/K$	2.65
	$(\rho c_p)_g$	$kJ/m^3/K$	2862
	UGT	*°C*	9.5

Test procedure

The system can be operated in two different modes; manual and automatic. The former is employed in the present work in which the opening position of the Expantion Valves (EVs) (installed before the inlet of the the boreholes) can be changed manually.

Each test started by adjusting the water temperature, the water mass flow rate, and the opening of the EVs. For each test, the same opening was fixed for all EVs involved. The temperature variation along the borehole is then recorded during the system operation. Note that the temperature measurements along the borehole were not taken directly on the CO_2 but at the surface of both U-tube legs. Other data are also recorded from the test that enable the actual borehole extraction to be calculated and the actual pressure drop and enough information to yield any time dependent characteristics of the heat pump performance.

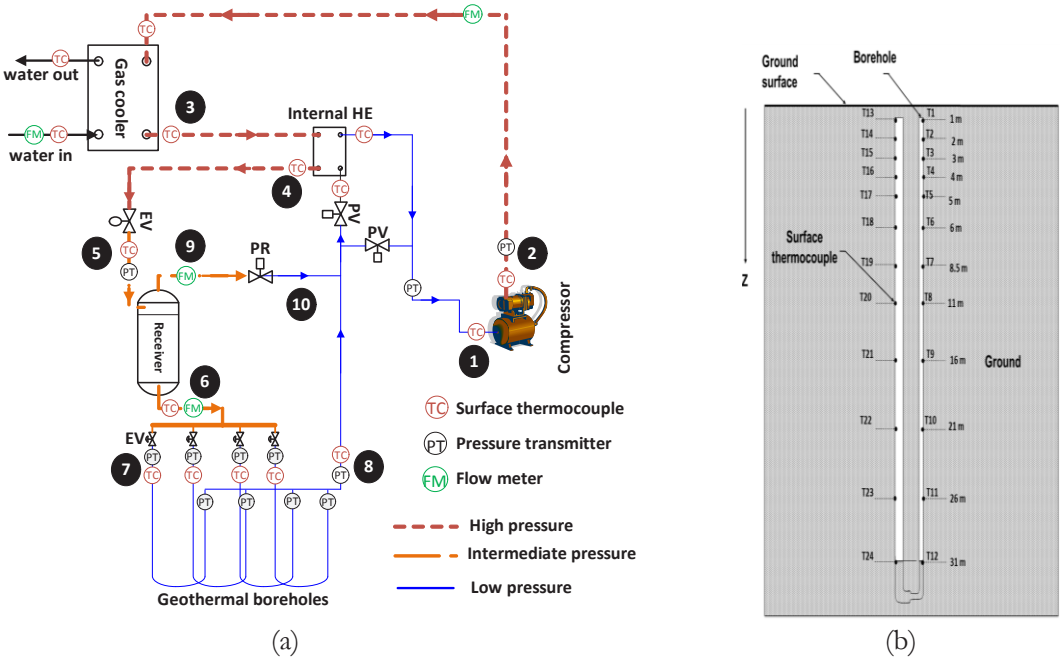

Figure 1. (a) Simplified schematic of the CO_2-DX-GSHP test facility; and (b) Position of the thermocouples in the GHE.

RESULTS AND DISCUSSION

For investigating the GHE performance and the evaporation process taking place in the GHE, the profiles of the ground temperature and pressure drop through the boreholes are first analysed in this section.

Ground temperature measurement

The temperature distribution in the ground significantly affects the performance of the GHE. The profiles of the ground temperature for three days (April 20th, September 2nd, and October 24th) are presented in Figure 2. The profiles of the April 20th and September 2nd (black dash lines) present the ground temperature before conducting the first test (i.e. before operation of the CO_2-DX-GSHP), thus they represent the far field ground temperature. For each profile, two different regions are observed; the shallow zone (up to 8 meters) and the deep zone (down to 31 meters). It can be seen that for the shallow zone, the ground temperature depends greatly on the seasonal weather conditions. In the deep zone, the ground temperature profile stays almost constant for both days, which corresponds to the undisturbed ground temperature (UGT). At the lower zone, the influence of the seasonal climate changes on the ground temperature is negligible. Note that the UGT values are in accordance with the value determined by the thermal response test, which is about 9.5 °C.

After running a number of tests, the ground temperature is expected to be disturbed as shown in the temperature profile of October 24th (blue dashed lines). It corresponds to the ground temperature in the vicinity of the borehole when the system was not operating. In fact, the actual ground temperature at the proximity of an active borehole is different than the far field temperature even at the time that the system is off. As can be seen in Figure 2, the deep zone temperature value is 1.5 °C less than that measured on April 20th and September 2nd.

An experimental estimates of soil temperature recovery after heat extraction test indicates that generally for the ground it took at least 8 hours for an adequate temperature recovery (i.e., to reach the profile in black). In consequence, a soil recovery time of 12 hours was scheduled before each test.

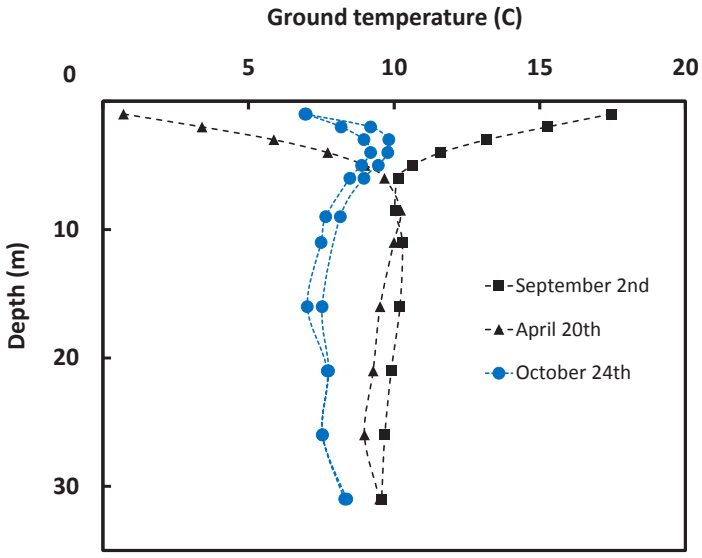

Figure 2. Measured ground temperature at different depths at Varennes for three days (April 20th, September 2nd, and October 24th).

Pressure drop through the boreholes

Refrigerant pressure drop inside boreholes influences the performance of a GHE. Significant reduction in the pressure of the refrigerant results in an inconsistent evaporation temperature in a GHE. Therefore, to investigate the evaporation process inside a GHE, the pressure drop in a borehole needs to be measured. Thus, for different openings of the EVs (40%, 20% and 10%) the pressures at the inlet and the outlet of the boreholes were messured as presented in Figure 3. The tests were conducted with $\dot{m}_w$ = 0.27 kg/s and $T_{w,in}$ = 35 °C. It can be seen that when the opening of the EVs decreases from 40% to 10%, the pressure in the borehole decreases. It is also observed that the pressure drop, ΔP (difference between CO_2 inlet and outlet pressure) along the boreholes is relatively small. Table 3 illustrates ΔP values for different openings of the EVs. The maximum measured pressure drop was less than 80 kPa (at 40% opening). In other openings of the EVs, the measured pressure drop is less than 40 kPa. The pressure drop has negligible effects on the evaporating pressure and therefore the evaporation temperature along the borehole remains almost constant.

Table 3. Pressure drop through the boreholes

Number of Boreholes	EVs Opening	Pin (kPa)	ΔP (kPa)
3	40%	3422	≤80
3	20%	3245	≤40
3	10%	3116	≤40

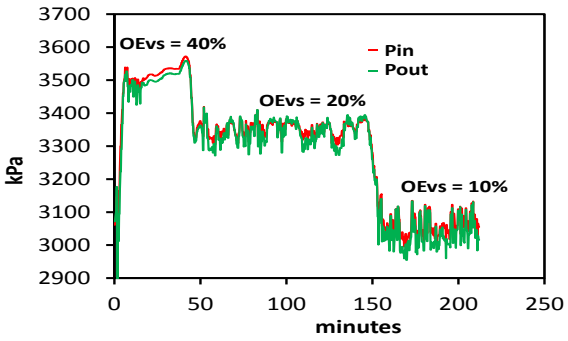

Figure 3. Inlet and outlet GHE pressure data

Phase change process in the GHE

The phase change process in the GHE was examined for the system working with different CO_2 mass flow rates ($\dot{m}_{CO2}$) and two different number of active boreholes (two and three boreholes).

Figure 4 illustrates temperature profile for three different CO_2 mass flow (1.46×10^{-3} kg/s, 2.21×10^{-3} kg/s and 2.58×10^{-3} kg/s) per borehole in a system operating with four active boreholes. Table 4 gives the tests conditions and the main results. For each mass flow rate, two temperature profiles are presented: one at the shutdown-period (recovered ground) and the other one during operation. As mentioned previously, the shutdown-period profile (black dash lines) illustrates the ground temperature at the vicinity of the borehole before it has been disturbed by the experiment. As the tests were conducted in different days of the year, the shallow ground temperatures are not identical. The blue solid lines present CO_2 temperature profile inside the borehole for a given mass flow rate. Arrows on the curves indicate the flow direction of CO_2 inside the pipe. In each profile, two regions can be distinguished: (a) two-phase region and (b) single-phase region. In the former region, CO_2 temperature remains constant due to the large amount of energy from the latent heat of vaporization, indicating that low pressure drop is maintained in the flow. The length of this region represents the length of complete evaporation, and it is equal to 10 m from the inlet of the first leg for case #1. However, it is equal to 40 m for the two other cases.

A comparison of cases #1 and #2 shows that the length of the two-phase region inside the borehole increased with the higher flow rate associated with large refrigerant quantities inside the GHE. This trend is not specific to CO_2 but general for all refrigerants. When comparing cases #2 and #3, however, the length of the two-phase region did not increase with higher flow rate (i.e, case #3). On the other hand, T_{evap} decreased due to the phase change process, compensating for the increase in the evaporation length. This result confirms our previous expectation meaning that

the phase change process depends on both T_{evap} and CO_2 mass flow rate. Note that it was not possible to perform the tests with variable T_{evap} (without changing the mass flow rate) in order to highlight its effect on phase change process in the GHE.

The single-phase region starts from the last point of the two-phase region and finishes at the end of the second leg. The temperature variation of CO_2 is more significant in case #1 due to the relatively low specific heat of single-phase CO_2. In this case, single-phase CO_2 fills the major part of the GHE. The CO_2 temperature increases from -2.5 °C to reach the UTG, which is the maximum temperature that can be reached, then, it decreases in the second leg due to the negative thermal interaction with the first leg as well as the cold soil temperature at the shallow depth. The borehole is less efficient in this case (case#1). The superheating, observed for the case #1 is 1 °C higher than that of case #2.

As it can be seen in table 4, the borehole extraction rate in case #3 shows a slight difference compared to case #2, while it is 43% higher than that of the case #1 in which the major part of the GHE is filled by single-phase CO_2. This means that a partial two-phase flow rather than a full two-phase flow regime along the U-tube length leads to lower borehole performance and it has to be avoided for more efficient DX-GSHP systems.

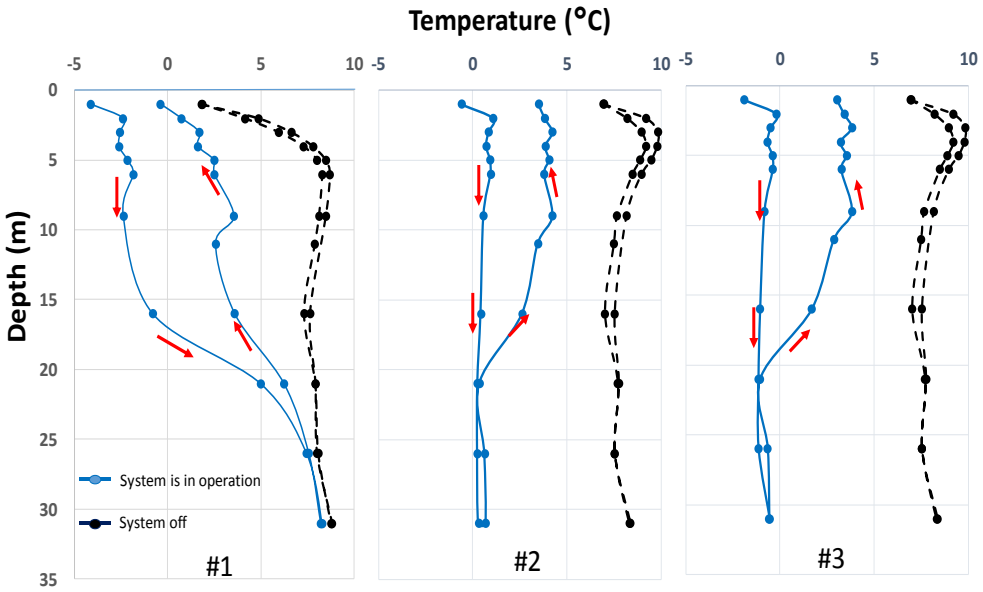

Figure 4. Pipe wall temperature variation along the borehole for different mass flow rates

Table 4. Tests conditions and results

Case Number	Number of Boreholes	Tw, in (°C)	CO_2 Gas bypass flow (kg/s)×10³	CO_2 total liquid flow (kg/s)×10³	CO_2 liquid flow/bor (kg/s)×10³	T_{evap} (°C)	Operation period (hours)	$Q_{GHE/\ bor}$ (kW)
1	4	35	11.90	5.86	1.46	-2.55	15	0.3
2	4	35	11.10	8.78	2.21	0.50	12	0.57
3	4	30	7.53	10.33	2.58	-1.2	2.5	0.59

Figure 5a and 5b presents the change of CO_2 fluid temperature profile for two different number of active boreholes. The water mass flow rate to the gas cooler was set to 0.25 kg/s during all the tests. Table 5 illustrates the main test conditions and results. Here again the solid lines show the pipe wall temperature profile representing the CO_2 flow temperature along the U-tube in three cases. Black dash lines represent the ground temperature profile

before starting the system. As shown in this figure, the temperature profiles show clearly the evaporation length, two-phase region with constant temperature (CO_2 quality < 1) and single-phase region.

Firstly, systems with three and two active boreholes show different CO_2 fluid temperature variation (single and two phase regions) along the borehole and different length for complete evaporation. Since the system with two active boreholes carries through a lower T_{evap} (-2.55 °C), higher mass flow rate (3.31×10^{-3} kg/s) of liquid CO_2 per borehole, this creates a larger temperature difference between the CO_2 and the ground. Consequently, it results in a longer length for complete evaporation (50 m) and higher $Q_{GHE/bor}$ compared to the case with three active boreholes. It means that employing more boreholes decreases the heat extracted per unit borehole due to lower CO_2 mass flow rate.

Secondly, in both profiles, the temperature increase in the single-phase region is marginal as the temperature of the surrounding material (grout) decreases due to the cold soil temperature at the shallow depth.

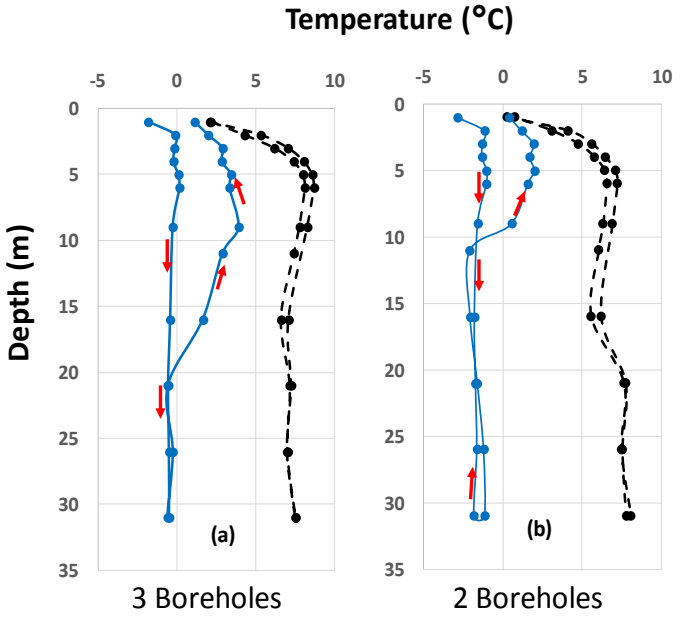

Figure 5. Pipe wall temperature variation for different number of active boreholes.

Table 5. Main test conditions and results

Number of Boreholes	CO_2 Gas bypass flow (kg/s)×10^3	CO_2 total liquid flow (kg/s)×10^3	CO_2 liquid flow/bor (kg/s)×10^3	T_{evap} (°C)	Operation period (hours)	$Q_{GHE/bor}$ (kW)
2	10.40	6.61	3.31	-2.55	15	0.66
3	10.70	8.64	2.88	-0.50	36	0.57

CONCLUSION

In this work, an experimental investigation was performed to analyze the evaporartion process of CO_2 in the GHE as well as its heat extraction performance for different CO_2 mass flow rates per borehole and number of active boreholes of the system. For this purpose, pressure drop through the boreholes and the ground temperature profiles (before and after running the tests) were first monitored and analyzed.

Results show that the evaporation process was completed in the first leg of the U-tube with insufficient CO_2 mass flow rate per borehole. Therefore, the single-phase CO_2 fills the major part of the GHE. Furthermore, single-

phase CO_2 temperature at the first leg of the U-tube increases to reach the ground temperature in some cases and it decreases in the second leg due to the thermal interaction with the first leg as well as the cold soil temperature at the shallow depth. It is concluded that a partial two-phase flow rather than a full two-phase flow regime along the U-tube length leads to lower borehole heat extraction rate and it has to be avoided for more efficient DX-GSHP systems design.

It is also shown that employing more boreholes decreases the heat extracted per unit borehole due to lower CO_2 mass flow rate. Nevertheless, increasing the number of GHEs over a certain limit may have a negative impact even on the system performance due to the borehole performance reduction as described in case with insufficient CO_2 mass flow rate.

ACKNOWLEDGMENTS

This work was financially supported by the Energy Innovation Program (Natural Resources Canada).

NOMENCLATURE

$\dot{m}$ = mass flow rate (kg/s)
Q = Specific heat load (W/m)
T = Temperature of the medium (°C)
P = Pressure
x = Vapour mass fraction quality
ΔP = Pressure drop through the boreholes (kPa)
OEV= Expansion valve opening

Subscripts

in = inlet
out = outlet
bor = Borehole
evap = *Evaporating*
w = *Water*

REFERENCES

Ghazizade-ahsaee, H. and M. Ameri. 2018. *Energy and exergy investigation of a carbon dioxide direct-expansion geothermal heat pump*. Applied Thermal Engineering *129*: 165-178, doi:10.1016/j.applthermaleng.2017.10.022.

Yuefen, G., C. Yongzhao and S. Nan. *Heat transfer performance of the underground CO2 pipe in the direct expansion ground source heat pump*. Energy Procedia 2017, 105, 4955-4962, doi:10.1016/j.egypro.2017.03.989.

Mastrullo, R, A.W. Mauro, L. Menna and G.P. Vanoli. *A model for a borehole heat exchanger working with CO2*. Energy Procedia 2014, 45: 635-644, doi:10.1016/j.egypro.2014.01.068.

Austin, B.T. and K. Sumathy. 2011. *Parametric study on the performance of a direct-expansion geothermal heat pump using carbon dioxide*. Applied Thermal Engineering (31): 3774-3782.

Eslami-Nejad, P. M. Ouzzane and Z. Aidoun. 2014. *Modeling of a two-phase CO_2-filled vertical borehole for geothermal heat pump applications*. Applied Energy (114): 611-620, doi:10.1016/j.apenergy.2013.10.028.

Eslami-Nejad, P., M. Badache, A. Bastani and Z. Aidoun. 2018. *Detailed Theoretical Characterization of a Transcritical CO2 Direct Expansion Ground Source Heat Pump Water Heater*. Energies. 11(2): 387. doi:10.3390/en11020387

Beauchamp, B., L. Lamarche and S. Kajl. 2013. *A numerical model of a U-tube vertical ground heat exchanger used as an evaporator*. J. Energy Power Engineering (7): 237-249.

Rousseau, C., J.C. Fannou, L. Lamarche, M. Ouzzane and S. Kajl. 2015. *Modeling and experimental validation of a transient direct expansion geothermal heat exchanger*. Geothermics (57): 95-103.

Eslami-Nejad, P., M. Ouzzane and Z. Aidoun. 2015. A *quasi-transient model of a transcritical carbon dioxide direct-expansion ground source heat pump for space and water heating*. Applied Thermal Engineering (91): 259-269, doi:10.1016/j.applthermaleng.2015.07.058.

Guo, Y., G. Zhang, J. Zhou, J. Wu and W. Shen. 2012. *A techno-economic comparison of a direct expansion ground-source and a secondary loop ground-coupled heat pump system for cooling in a residential building*.

Applied Thermal Engineering (35): 29-39.

Wang, X.C. Ma, and Y. Lu. 2009. *An experimental study of a direct expansion ground-coupled heat pump system in heating mode*. Int. J. Energy Res., 33, 1367-1383.

Lenarduzzi, F.J. and T. J. Bennett. Direct-expansion ground-source heat pump with spiral ground coil. Heating

mode. ASHRAE Trans. 1991, 1991, 902-908.

Goulburn, J.R. and J. Fearon. 1978. *Deep ground coil evaporators for heat pumps*. Applied Energy 4(4): 293-313, doi:10.1016/0306-2619(78)90028-4

Mei, V.C.and V.D. Baxter. *Experimental Analysis of Direct Expansion Ground Coupled Heat Pump Systems*; Oak Ridge Natl. Lab.: Oak Ridge, TN, USA, 1991.

Yang, W. 2013. *Experimental performance analysis of a direct-expansion ground source heat pump in Xiangtan*, China. Energy (59): 334-339, doi:10.1016/j.energy.2013.07.036.

Johnson, W.S. *Field tests of two residential direct exchange geothermal heat pumps/Discussion*. ASHRAE Trans. 2002, 108, 99.

Minea, V. *Combined radiant floor and forced air heating with direct expansion GSHP in a northern greenhouse*. In Proceedings of the 21st International Congress of Refrigeration, Washington, DC, USA, 17-22 August 2003.

Goulburn, J.R. and J. Fearon. 1983. *Domestic heat pump with deep hole ground source evaporator*. 2013. Applied Energy (14): 99-113.

Badache, M., M. Ouzzane, P. Eslami-Nejad, Z. Aidoun. 2018. *Experimental study of a carbon dioxide direct-expansion ground source heat pump* (CO2 DX-GSHP). Applied Thermal Engineering (130): 1480-1488 doi:10.1016/j.applthermaleng.2017.10.159.

[This page has been intentionally left blank]

IGSHPA SWEDEN 2018 Research Conference

DOI: 10.22488/okstate.18.000010

Dynamic modeling of flow boiling within plate heat exchangers for heat pump and refrigeration applications

Lennart Boese **Frank Opferkuch** **Julian Becker** **Michael Wensing**

ABSTRACT

Brazed Plate Heat Exchangers (BPHEs) are increasingly used as evaporators for refrigeration and heat pump applications. Detailed understanding of the underlying heat transfer phenomena is required for their effective design and use. The number of correlations which are suitable for modeling the dynamics of flow boiling within BPHEs is rather low compared to other evaporator types. In this paper some correlations that involve integral values of steam quality are evaluated for different sets of experimental data from literature. Modifications to the correlations are presented, which allow to predict the quasi-local heat transfer coefficient in each refrigerant cell. The cells equal finite volumes that are composed to a dynamic model of a BPHE acting as evaporator. Heat transfer coefficient and heat flow rate from simulation results are compared to those calculated from existing experimental data based on the same boundary conditions. The fine-tuned evaporator model is finally used to demonstrate effects of sudden load changes for the evaporator performance.

INTRODUCTION

More flexible operation strategies of heat pumps, which support and stabilize the electrical grid, will increase the number of startup procedures and load cycles. More transient states of the heat pump cycle come along with thermo-hydraulic effects in the evaporator making the control of the process more difficult. Brazed Plate Heat Exchangers (BPHEs) offer compactness and high efficiency at low unit costs and are becoming increasingly important for refrigeration applications. Due to their complex structure of flow guidance with up to 5 main flow patterns (Vakili-Farahani, et al. 2016) that can occur during the evaporation, high heat transfer coefficients can be achieved, but the underlying transport phenomena are difficult to describe and model. By means of elaborate dynamic simulation models, the design and control of heat exchangers can be optimized for both transient and stationary operating points and inefficient states with high values of superheat avoided. Longo and Gasparella (2007) showed for three different refrigerants that a value of evaporator superheat of 10 K lead up to 30 to 40 % reduction of the average heat transfer compared to when outlet vapor quality is around 0.8.

1. FLOW BOILING HEAT TRANSFER WITHIN PLATE HEAT EXCHANGERS

Unlike other physical phenomena, nucleate boiling heat transfer, which occurs within BPHEs, can yet not be described mathematically on the basis of the prevailing mechanisms, even if initial progress has already been made in

Lennart Boese (lennart.boese@th-nuernberg.de) is research associate, Frank Opferkuch is professor and Julian Becker is student researcher at Technische Hochschule Nürnberg Georg Simon Ohm. Michael Wensing is professor at Friedrich-Alexander-Universität Erlangen-Nürnberg.

this field (Dhir 2005). Until then, it is necessary to use empirical correlations, which provide estimations for the heat transfer coefficient (htc) as a function of thermodynamic state, variables that describe transport phenomena and other parameters. Correlations used by the manufacturers of BPHEs to describe heat transfer and pressure drop contain valuable empirical knowledge but are subject to secrecy and are unlikely to be published. Nevertheless, a considerable amount of correlations for evaporation in plate heat exchangers is available in the literature. In contrast to correlations for evaporation within other geometries, like tubes, there is still indistinction which of them will prove itself for larger amounts of evaporation data sets. A first approach is for example provided by Vakili-Farahani, et al. (2016), who apply correlations and measurement data crosswise and provide some statistical evaluation. However, the majority of the correlations and measurement provide only estimations of the average heat transfer coefficient, which can be used for calculation methods such as the Number of Transfer Units (NTU) or Log Mean Temperature Difference (LMTD). Eldeeb, et al. (2016) give a good overview of some of the most well-known correlations for evaporation and condensation in BPHEs.

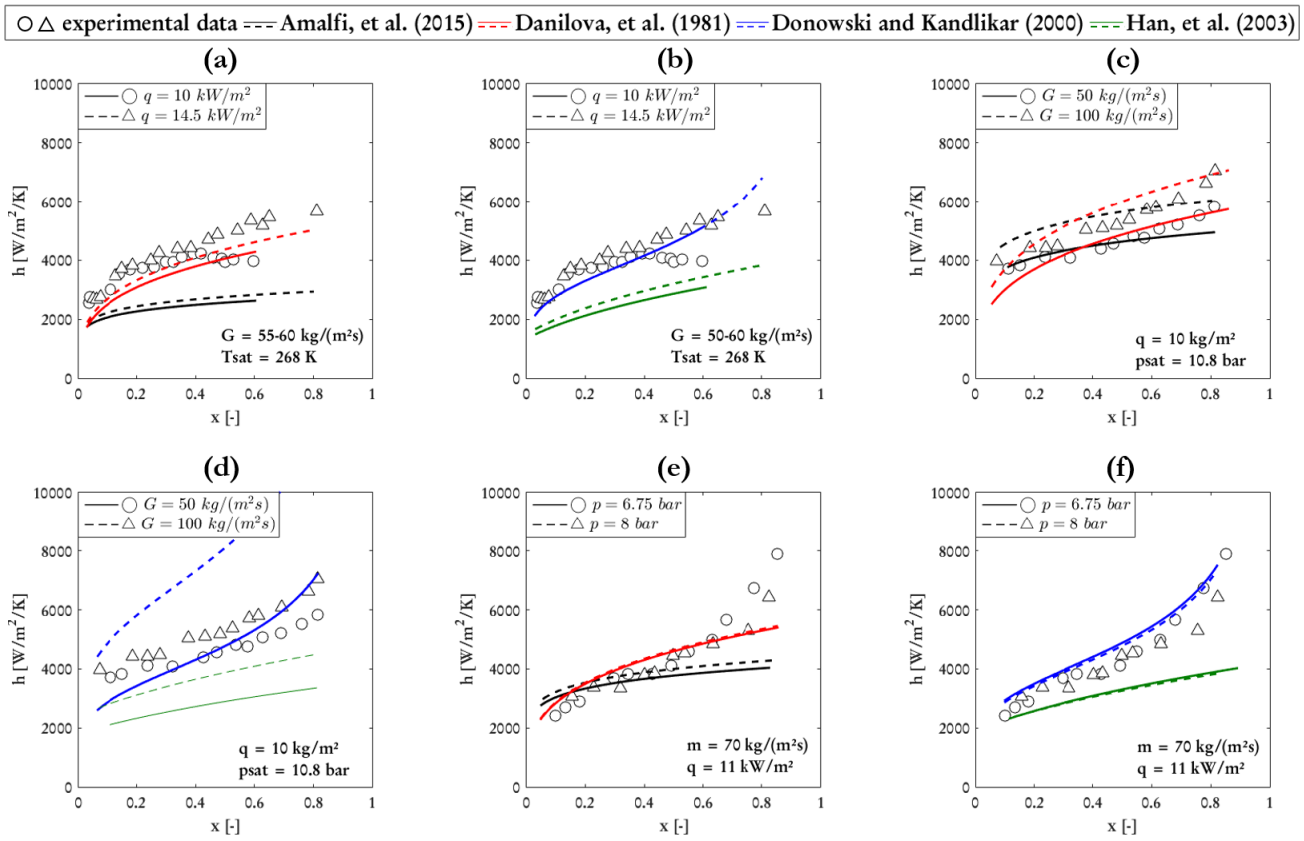

Figure 1 Comparison of correlations applied to experimental data from Djordjevic and Kabelac (2008) (a) and (b) for R134a, Hsieh and Lin (2002) (c) and (d) for R410A, Yan, et al. (1997) (e) and (f) for R134a.

1.1. Heat transfer correlations and experimental observations

Correlations developed for ammonia are not considered because of its significantly higher heat transfer

coefficient compared to the hfc refrigerants analyzed in this study. For the dynamic modeling of flow boiling with lengthwise discretization, only correlations that directly or indirectly consider steam quality as a variable are considered. Of these, the correlations from Amalfi, et al. (2015), Donowski and Kandlikar (2000), Danilova, et al. (1981) and Han, et al. (2003) are evaluated in this study. A general correlation for nucleate boiling by Cooper (1984) will be used later for comparison purposes. The Cooper correlation is independent of steam quality but is reported to estimate BPHE average htc well when multiplied with a factor of 1.5 (Palm and Claesson 2006) or 1.7 (Huang 2010).

Different sets of measurement data allow calculating the heat transfer coefficient for chevron type plate heat exchangers for diverse geometries and boundary conditions. Figure 1 shows different correlations applied to segments of measurement data taken from authors where the input quantities for the correlations were available. The following conclusions and the depictured data represent the majority of more extensive data while there is a minority of data that lead to ambiguous or contradictory results. While other parameters are held constant, one can observe the following trends:

1. heat transfer coefficient increases with increasing heat flux, (a) and (b)
2. low mass flux tends correlate with low heat transfer coefficients, (c) and (d)
3. effect of the higher evaporation temperature in (f) compared to (e) is inconclusive and might be dependent on steam quality

Furthermore higher values of chevron angles (referring to vertical axis) increase both pressure drop and heat transfer coefficients. A general-purpose BPHE evaporator model and suitable correlations should reproduce these main observations. Subsequently, the Han, et al. (2003) correlation is discarded since it gives constantly too low values of heat transfer coefficient or was not correctly implemented. The Donowski and Kandlikar (2000) correlation developed on the basis on the data set from Yan, et al. (1997) for R134a. Thus validity for other refrigerants might not be given and its high a sensitivity to mass flux is noticeable. By contrast, the Amalfi, et al. (2015) correlation was developed from 1903 heat transfer data points for multiple refrigerants, geometries and refrigerants.

1.2. Comparison and selection of applicable correlations for dynamic modeling

For those correlations involving steam quality, it should be noted that steam is usually considered with its mean value. Steam quality is difficult to measure directly. In the experimental data used to develop the empirical correlations it is mostly calculated from energy balances. Eq. (1) gives the definition how steam quality will be calculated for a control volume with refrigerant in vapor-liquid equilibrium. It is further assumed that no slip between the velocities of refrigerant gas and liquid occurs. This means that flow steam quality, which is the relation of mass flow rate of gas phase to total mass flow rate, is equal to the local steam quality of the control volume.

$$x = \frac{h - h_l}{h_g - h_l} \tag{1}$$

While some experiments focused on single plates, in other experiments entire heat exchangers with a small number of plates were tested. Thus, the average of the steam quality used for calculating the average heat transfer coefficients may be based on a wide range of steam quality between inlet and outlet. New approaches are e.g. presented by Djordjevic and Kabelac (2008), where the quasi-local htc is derived from temperature readings inside the plate heat exchanger. The later presented simulation model of the heat exchanger divides the path of evaporating refrigerant into discrete cells. This requires prediction methods for the quasi-local heat transfer coefficient dependent of the time-varying steam quality of the cell. Since no such correlations for plate heat exchangers were found in the literature, the above correlations are used for this approach. Because of this an unknown amount of inaccuracy must

be accepted and correlations may be used beyond their range of validity. This is encountered by the following piecewise definition of heat transfer coefficient dependent on local steam quality:

$$h_{tp} = \max(h_{sp}, h_{tp,corr}) \text{ for } 0 < x < 0.1 \quad (2)$$

$$h_{tp} = h_{tp,corr} \text{ for } 0.1 < x < x_{di} \quad (3)$$

$$h_{tp} = h_{tp,corr}\left\{-\sin\left[\frac{2\pi(x-1)}{(1-x_{di})}\right]\right\} + h_{sp}\left\{1+\sin\left[\frac{2\pi(x-1)}{(1-x_{di})}\right]\right\} \text{ for } x_{di} < x < 1 \quad (4)$$

Since the evaporation correlations do not map the heat transfer coefficients for single-phase fluid in the subcooled or superheated range, the correlation of Martin (2010) will be used in the later simulation for this range. The two-phase region of incipient evaporation with low steam quality might not be covered by some correlations or unrealistic low values of the heat transfer coefficient are returned. In this case the higher value of single-phase and two-phase heat transfer coefficients is used in the simulation model, see Eq. (2). This corresponds to the approach of Shah (1982) for the superposition of nucleate and convective boiling. However, it can be usually assumed that the refrigerant is in the two-phase state when leaving the expansion valve.

Wojtan, et al. (2005) present measurement data for the inception of dryout of refrigerant flow boiling in tubes. A strong decrease of heat transfer coefficient can be observed in the high quality region and the inception starting roughly between x = 0.7 and 0.9. For the proposed modification of heat transfer coefficient this is effect is modeled by a transition between two-phase htc and single-phase htc by means of a sine function, see Eq. (4). For the later simulation transition is assumed to start at x_{di} = 0.8. The Figure 2 (b) shows application of the methods to an exemplary curve of heat transfer coefficient over steam quality.

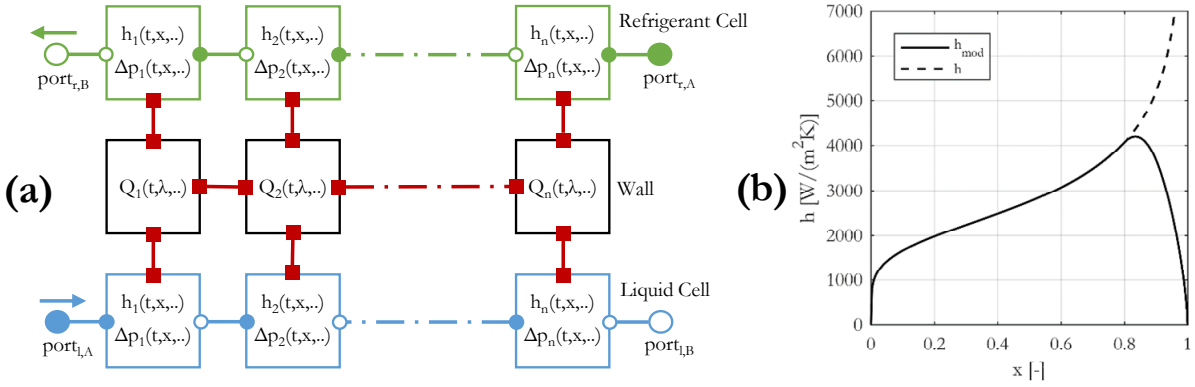

Figure 2 Structure of the heat exchanger model consisting of finite volume cells (a) and shape of heat transfer curve when modification is applied to Donowski and Kandlikar (2000) correlation (b).

2. EVAPORATOR MODEL AND SINGLE-PHASE RESULTS

The dynamic simulation model of the heat exchanger is programmed in the modeling language Modelica and taken from the component library *TIL* (Richter 2008; Schulze 2013) and slightly modified. The fluid channels are divided into *n* discrete cells along its length (z-coordinate) following a 1D upwind discretization scheme. The fundamental modeling of refrigerant or liquid cells remains unchanged as well as the finite volume approach, by which these cells are composed together with heat transfer and pressure drop equations and geometrical parameters to a

model of the heat exchanger. The energy balance, Eq. (5),for each refrigerant cell is formulated as the time derivative of specific enthalpy times cell mass which equals the sum of enthalpy streams entering/leaving the cell, heat flow and the time derivative of work by change in pressure. Two other fundamental equations come in addition: The continuity equation, Eq. (6), and momentum equation, Eq. (7), which is simplified by assuming the time derivative of the momentum and the difference between momentum at inlet and outlet to equal zero:

$$\frac{dh}{dt} = \frac{1}{M}\left[\dot{m}_A\left(h_A - h\right) + \dot{m}_B\left(h_B - h\right) + \dot{Q} + V \cdot \frac{dp}{dt}\right] \tag{5}$$

$$\dot{m}_A + \dot{m}_B = \left[\left(\frac{d\rho}{dh}\right)_p \frac{dh}{dt} + \left(\frac{d\rho}{dp}\right)_h \frac{dp}{dt}\right] A_{ch} \cdot l_z \tag{6}$$

$$p_A - p_B = \Delta p \tag{7}$$

The individual control volumes of the fluids and fluid wall are connected by equations in a bidirectional way, see Figure 2(a). Through object-oriented programming, the overall model of the heat exchanger can be easily integrated as a component for the later system simulation of a heat pump cycle.

Table 1. Geometrical Parameters of the modeled BPHE evaporator from Huang (2010)

Number of plates	$N_p = 24$	Overall heat transfer area	$A = 2.09\ m^2$
No. of refrigerant channels	$N_{ch,r} = 12$	Port-to-port channel length	$L_p = 519$ mm
No. of water channels	$N_{ch,w} = 11$	Effective channel length	$L_{eff} = 466$ mm
Channel width	$W = 180$ mm	Corrugation depth	$b = 2$ mm
Corrugation wavelength	$\lambda = 8.1$ mm	Enlargement factor	$\phi = 1.14$
Hydraulic diameter	$D_h = 2b/\phi = 3.51$ mm	Corrugation angle	$\beta = 28°$ or $60°$

Since in this study the accuracy of the heat transfer and the exact temperature profile was more important than a short simulation time, a high number of N = 30 cells was set for each primary, secondary fluid and wall. The fluid properties for each liquid or refrigerant cells are considered as integral values and are obtained from *REFPROP* (NIST 2015). Pressure losses on the secondary side are neglected and the effects of conduction and dispersion in the direction of fluid flow (z-coordinate) are ignored. The model BPHE consists of 24 chevron type plates in counter-flow arrangement. The relevant geometrical parameter are given in Table 1.

2.2. Single-Phase Heat Transfer Modeling

The modeling approach using the finite volume method is validated with single-phase heat transfer data from Huang (2010). Two correlations are used. The first correlation for the Nusselt number is based on a widespread approach using Reynolds to account for turbulence of flow and Prandtl number for the ratio of momentum diffusivity to thermal diffusivity. The exponent m and the factor C_1 are fitted to the measurement data:

$$Nu_{sp} = C_1 \cdot \mathrm{Re}^m \cdot \mathrm{Pr}^{0.33}\left(\frac{\mu}{\mu_{wall}}\right)^{0.17} \tag{8}$$

Correlation and fitting factors are taken from Huang (2010) and were obtained by fitting the correlation to data for the heating of cold water with the same BPHE which will later be used as evaporator. As an alternative approach, the correlation of Martin (2010) was implemented, which is also used for modeling the heating of subcooled liquid or

superheated steam. As expected, the results from experiment and simulation show good agreement for the correlation of Huang (2010) with a mean absolute error $|\delta|$ = 0.67 % for the cold side and $|\delta|$ = 2.79 % for the hot side. The unfitted correlation from Martin (2010) results in significantly higher deviations.

Table 3. Experimental conditions from Huang (2010) for water to water heat transfer

Chevron angle	No. of data points	Re_h	$T_{h,in}$ [°C]	Re_c	$T_{c,in}$ [°C]
28	22	510-560	55.0-56.0	280-1100	18.4-19.3
60	16	430-460	56.0-56.5	350-1030	18.3-19.1

2.3. Two-Phase Heat Transfer Modeling

For modeling the fluid flow on the side of the refrigerant (primary side), the following assumptions are additionally made. The influence of oil can significantly lower the heat transfer at high admixture (Spindler and Hahne 2009). In the following, it is neglected because it is unknown whether its influence is contained in experimental data sets or the correlations based upon them. Since measurement data are usually obtained under laboratory conditions, the influence of fouling is also neglected. The presented modified correlations for two-phase region are concatenated with the correlation of Martin (2010) that is used for the single-phase heat transfer. In the transition area around x=0 and x=1, the smooth transition function from *TIL* is used to improve the numerical stability of the simulation. The pressure losses on the refrigerant side are modeled as follows:

$$\Delta p = \Delta p_p + \Delta p_{fri} + \Delta p_{sta} \tag{9}$$

Pressure drops caused by the acceleration of the fluid during evaporation are neglected in a first approximation being comparatively low according to results from Amalfi (2016). The pressure loss at each inlet or outlet port is calculated according to Shah and Focke (1988):

$$\Delta p_p = 0.75 \cdot N_{pass} \cdot \frac{G_p^2}{2 \cdot \rho} \tag{10}$$

For modeling the friction pressure loss within the refrigerant channels the correlation of Amalfi, et al. (2015) is used. Maldistribution of refrigerant between the channels is not considered. Table 3 gives an overview of the boundary conditions of the evaluated experimental data. The complete measurement data sets for inlet temperature, volume flow and inlet pressure can be found at Huang (2010).

Table 3. Experimental conditions from Huang (2010)

Refrigerant	Chevron angle	No. of data points	$G_{z,w}$ [kg/(m²s)]	$T_{w,in}$ [°C]	$G_{z,r}$ [kg/(m²s)]	T_{sat} [°C]	q [kW/m²]
R134a	28	58	125-203	13.7-16.0	5.6-30.3	5.9-12.2	1.9-6.1
	60	59	124-203	13.8-15.9	5.8-27.0	7.8-10.6	3.8-6.4
R507A	28	22	200-204	16.3-16.6	16.0-29.8	7.8-10.6	3.8-6.4
	60	11	202-203	16.2-16.3	17.6-31.4	9.2-12.6	4.7-6.9

3. RESULTS AND DISCUSSION

Figure 3 displays a parity plot, comparing simulated and experimental heat transfer coefficients and heat flow in the case of refrigerant R134a and β=28 °. In addition to the correlations outlined above, the Huang (2010) correlation fitted to the measurement data is displayed. As expected, it shows a good match.

The results for the other data points are presented in Table 4. The modified Danilova, et al. (1981) (B) correlation shows the lowest overall deviation for the evaluated experimental data. The modified Cooper (1984) correlation (D) predicts the htc for R134a well but shows great deviations for R507A. The modified Amalfi, et al. (2015) (A) and Donowski and Kandlikar (2000) (C) have moderate prediction quality for the specific data evaluated.

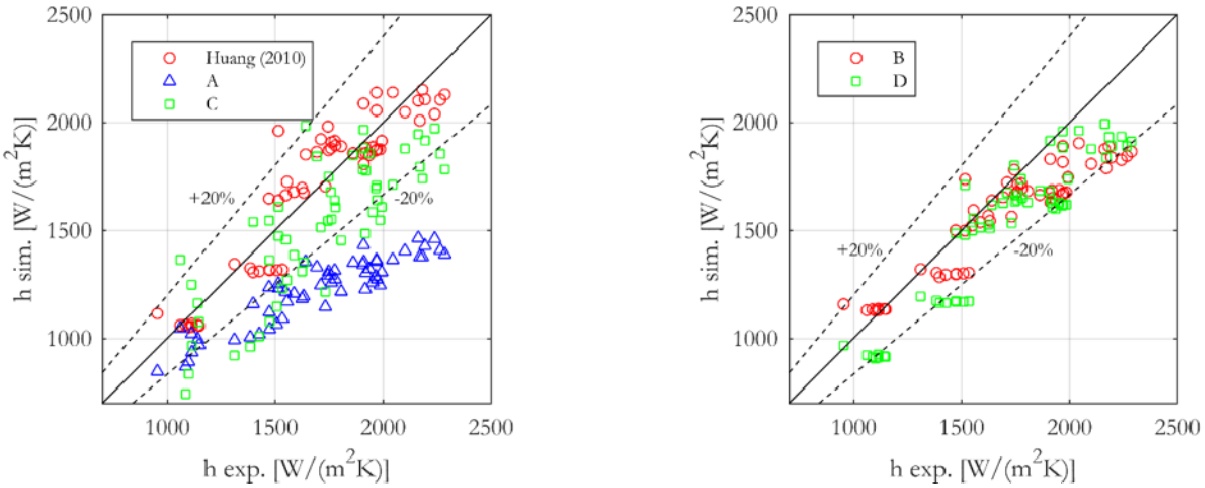

Figure 3 Comparison of experimental and simulated two-phase htc for flow boiling of R134a and chevron angle β=28°.

The experimental values of Huang (2010) were determined using the logarithmic mean temperature difference. The fluid properties used in his calculations were from ASHRAE Handbook 2005 at saturation temperature. Huang (2010) indicates an uncertainty of 7.6-8.6% for his calculated htc. According to Claesson (2005) the LMTD approach has to be modified when applied to a BPHE evaporator where htc is not constant along its length.

Table 4. Mean error δ and mean absolute error |δ| between correlation and simulation

Refrigerant	Chevron angle	Huang (2010)	A	B	C	D
R134a	28	|δ| = 6.9% δ = 0.6%	|δ| = 26.7% δ = -26.7%	|δ| = 8.5% δ = -6.4%	|δ| = 14.7% δ = -11.4%	|δ| =11.2% δ = -10.6%
	60	|δ| = 11.4% δ = -10.9%	|δ| = 11.4% δ = -10.9%	|δ| = 15% δ = -14.9%	|δ| = 20.5% δ = -20.2%	|δ| = 16.4% δ = -16.3 %
R507A	28	|δ| = 13.6% δ =3.5%	|δ| = 18.0% δ =14.2%	|δ| = 20.6% δ =17.3%	|δ| = 11.9% δ = 4.9%	|δ| = 74.3% δ =74.3%
	60	|δ| =12.9% δ =-7.6%	|δ| = 26.3% δ =19.86%	|δ| = 14.6% δ =2.2%	|δ| = 12.7% δ =-9.2%	|δ| = 56.4% δ =53.3%
Overall		|δ| = 10.1%	|δ| = 19.4%	|δ| = 13.3%	|δ| = 16.4%	|δ| = 25.8%

3.1. Dynamic Response of the Evaporator

Figure 4 shows the step response of the evaporator using the modified Danilova, et al. (1981) correlation. During the transient state change, the maxima of steam quality x and quasi-local heat transfer coefficient h move in the direction of refrigerant inlet. While the superheat at outlet SH increases from 5 to 10 K, the average heat transfer coefficient is reduced by 30.6 %. The presented model can be utilized for different purposes. Maintaining a high number of cells and fitting the model to experimental data, evaporation transients can be further identified by

implementing those thermo-hydraulic effects in the model that were neglected so far. By reducing the number of cells or switching to a moving boundary approach, simulation can be performed in real time and act as feedback for the control of refrigerant mass flow.

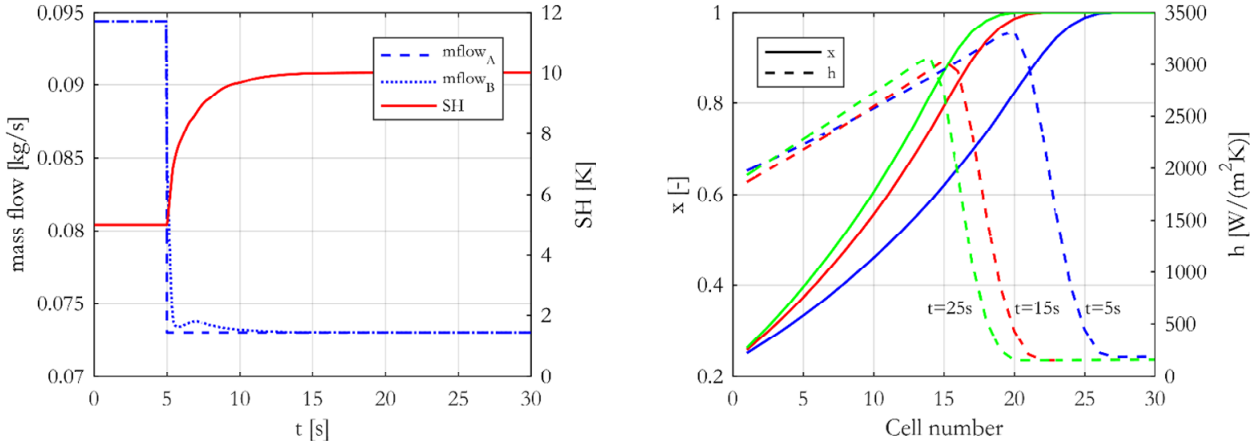

Figure 4 Step response of the evaporator after an instantaneous drop in mass flow by 23%.

CONCLUSION

Available correlations for flow boiling in BPHEs considering steam quality are comparatively evaluated on the basis of experimental data. After mathematical modifications and by concatenating single and two-phase correlations a quasi-local heat transfer coefficient for a lengthwise discretization scheme can be reproduced. The prediction method based on the Danilova, et al. (1981) correlation shows the best accordance with a given set of experimental boiling data from literature. Implementing this prediction method into a dynamic simulation model of a BPHE evaporator, the response to a step reduction in refrigerant mass flow can be demonstrated. The increase of superheat zone and reduction of average heat transfer coefficient follows the trends reported by Longo and Gasparella (2007) from experimental results. However, more experimental work is required to verify the modeling method and to evaluate suitable correlations for heat transfer of superheated refrigerants in BPHEs. Nevertheless, the presented approach can contribute to describe the dynamic behavior of heat pump cycles and be utilized for novel control strategies.

NOMENCLATURE

G	=	mass flux (kg/m²s)	h	=	heat transfer coefficient (W/m²K) or specific enthalpy (J/kg)		
l	=	length (m)	M	=	mass of control volume	$\dot{m}$	= mass flow (kg/s)
N_{pass}	=	number of passes in BPHE	p	=	pressure (Pa)	$\dot{Q}$	= heat flow rate (W)
ϱ	=	density (kg/m³)	V	=	volume of control volume	x	= vapor quality

Subscripts

A	=	inlet	B	=	outlet	ch	=	channel	c	=	cold side
$corr$	=	from correlation	di	=	dryout inception	fri	=	frictional	g	=	gas
h	=	hot side	l	=	liquid	p	=	port	r	=	refrigerant
sp	=	single-phase	sta	=	static	tp	=	two-phase	z	=	in z-direction

REFERENCES

Amalfi, R. L., F. Vakili-Farahani and J. R. Thome. 2015. *Flow boiling and frictional pressure gradients in plate heat exchangers. Part 2: Comparison of literature methods to database and new prediction methods.* International Journal of Refrigeration 65:185-203. DOI:10.1016/j.ijrefrig.2015.07.009

Amalfi, R. L. 2016. *Two-Phase Heat Transfer Mechanisms Within Plate Heat Exchangers: Experiments, Modeling and Simulations.* Doctoral dissertation. EPFL. DOI:10.5075/epfl-thesis-6856

Claesson, J. 2005. *Correction of logarithmic mean temperature difference in a compact brazed plate evaporator assuming heat flux governed flow boiling heat transfer coefficient.* International Journal of Refrigeration 28(4): 573-578. DOI:10.1016/j.ijrefrig.2004.09.011.

Cooper, M.G. 1984. *Heat flow rates in saturated nucleate pool boiling - A wide-ranging examination using reduced properties.* Adv. Heat Transfer 16:157-239. DOI: 10.1016/S0065-2717(08)70205-3

Danilova, G.N., V.M. Azarskov and B.B. Zemskov. 1981 *Teploobmen V Plastinchatihispariteljan Razichnole Geometri - Heat Transfer in Plate Evaporators of Different Geometry.* Kholod. Tek. 4: 25-31.

Dhir, V. K. *Mechanistic Prediction of Nucleate Boiling Heat Transfer–Achievable or a Hopeless Task?*. 2005. ASME J. Heat Transfer 128(1):1-12. DOI:10.1115/1.2136366.

Djordjevic, E. and S. Kabelac. 2008. *Flow boiling of R134a and ammonia in a plate heat exchanger.* International Journal of Heat and Mass Transfer 51(25–26):6235-6242. DOI:10.1016/j.ijheatmasstransfer.2008.01.042.

Donowski, V.D. and S. G. Kandlikar. 2000. *Correlating evaporation heat transfer coefficient of refrigerant R-134a in a plate heat exchanger.* Engineering Foundation Conference on Pool and Flow Boiling, Alaska.

Eldeeb, R., V. Aute and R. Radermacher. 2016. *A survey of correlations for heat transfer and pressure drop for evaporation and condensation in plate heat exchangers.* International Journal of Refrigeration 65: 12-26. DOI:10.1016/j.ijrefrig.2015.11.013.

Han, D. H., Lee, K. J. and Kim, Y. H. 2003. *Experiments on the characteristics of evaporation of R410A in brazed plate heat exchangers with different geometric configurations.* Appl. Therm. Eng. 23(10):1209-1225. DOI: 10.1016/S1359-4311(03)00061-9

Huang, J. 2010. *Performance analysis of plate heat exchangers used as refrigerant evaporators*. Doctoral dissertation.

Hsieh, Y. Y. and T. F. Lin. 2002. *Saturated flow boiling heat transfer and pressure drop of refrigerant R-410A in a vertical plate heat exchanger.* International Journal of Heat and Mass Transfer 45(5): 1033-1044. DOI:10.1016/S0017-9310(01)00219-8.

Longo, G.A. and A. Gasparella. 2007. *Heat transfer and pressure drop during HFC refrigerant vaporisation inside a brazed plate heat exchanger.* International Journal of Heat and Mass Transfer 50: 5194-5203. DOI:10.1016/j.ijheatmasstransfer.2007.07.001.

Martin, H. 2010. *N6 Pressure Drop and Heat Transfer in Plate Heat Exchangers.* In: VDI e. V. VDI Heat Atlas. Springer. Berlin, Heidelberg.

NIST. 2015. NIST Reference Fluid Thermodynamic and Transport Properties Database (REFPROP): Version 9.1.

Palm, B. and J. Claesson, 2006. *Plate heat exchangers: Calculation methods for single and two-phase flow.* Heat Transfer Eng. 27(4): 88-98.

Richter, C. 2008. *Proposal of New Object-Oriented Equation-Based Model Libraries for Thermodynamic Systems.* Doctoral dissertation. Technische Universitaet Braunschweig.

Vakili-Farahani, F., R. L. Amalfi and J. R. Thome. 2016. *Two-Phase Heat Transfer and Pressure Drop within Plate Heat Exchangers.* In J. R. Thome Encyclopedia of two-phase heat transfer and flow. New Jersey: World Scientific.

Schulze, C. 2013. *A Contribution to Numerically Efficient Modelling of Thermodynamic Systems.* Doctoral dissertation. Technische Universitaet Braunschweig.

Shah, M. M. 1982. *Chart correlation for saturated boiling heat transfer: equations and further study.* ASHRAE Trans 88: 185-196.

Shah, R. K. and W. W. Focke. 1988. *Plate Heat Exchangers and Their Design Theory.* In Heat Transfer Equipment Design. Washington, DC: Hemisphere Publishing.

Spindler, K. and E. Hahne. 2009. *The influence of oil on nucleate boiling heat transfer.* Heat Mass Transfer 45: 979-990.

Wojtan, L., T. Ursenbacher and J. R. Thome. 2005. *Investigation of flow boiling in horizontal tubes: Part II-Development of a new heat transfer model for stratified-wavy, dryout and mist flow regimes.* International Journal of Heat and Mass Transfer 48(14): 2970-2985. DOI:10.1016/j.ijheatmasstransfer.2004.12.013.

Yan, Y., T. Lin and B. Yang. 1997. *Evaporation Heat Transfer and Pressure Drop of Refrigerant R134a in a Plate Heat Exchanger.* ASME Turbo Expo: Power for Land, Sea, and Air, ASME 1997 Turbo Asia Conference. DOI:10.1115/97-AA-048.

[This page has been intentionally left blank]

IGSHPA SWEDEN
2018 Research Conference

DOI: 10.22488/okstate.18.000034

Model predictive control applied to residential self-assisted ground source heat pumps

Alex Laferrière **Massimo Cimmino**

ABSTRACT

The seasonal performance and feasibility of a "self-assisted" ground source heat pump system are examined. The system uses an electric heating element to inject heat into the ground and reduce peak energy demand by eliminating the need for auxiliary heating. Doing so allows for an undersized borehole to be used with a smaller penalty on peak power consumption. A simulation model for an energy efficient residential building in the Montreal area is implemented in the Modelica language. A model predictive control strategy with a week-long prediction horizon is applied to determine the optimal heat injection rate and timing for the electric heating element. The model uses an improved cell shifting load aggregation scheme for ground temperature predictions. On a borehole that is undersized by 16.7%, the self-assisted configuration with model predictive control reduces peak energy demand by 58% over a 5 year period, with an increase in total annual energy consumption of 2.8% when compared to an unassisted configuration.

INTRODUCTION

Ground source heat pump (GSHPs) systems are an increasingly popular method of heating and cooling residential buildings, in large part thanks to their low energy consumption. When used in cold climates, where yearly building heating demand can be significantly larger than the yearly building cooling demand, ground temperatures in the vicinity of the geothermal boreholes will gradually decrease. Low ground temperatures translate into low returning fluid temperatures from the geothermal boreholes and thus have a negative influence on the efficiency of GSHPs in heating operation. When there is a large heating demand for a sufficient amount of time, returning fluid temperatures may reach a lower threshold where the heat pump may no longer safely operate. In these cases, auxiliary heating (e.g. electric heating) is necessary to meet the building heating demand, creating a peak in the system's energy consumption and thereby hindering the competitiveness of GSHPs. Peak heating loads also create additional constraints on the design of geothermal systems by increasing the required borehole length at a great financial cost.

It is possible to assist GSHPs by implementing additional energy sources, which will recharge the ground thermal energy stores and raise ground temperatures. By strategically injecting heat into the ground from an auxiliary source, returning fluid temperatures may be kept above the lower operating limit, thus limiting the need for auxiliary heating at times of peak heating demand and reducing the penalty on undersized boreholes. A common strategy to assist GSHPs is to have solar thermal collectors coupled to the GSHPs. Among other methods of coupling solar energy to GSHPs, Han, et al. (2008) found improvements for systems in colder climates by using latent heat energy storage with an

Alex Laferrière is a Master's student and Massimo Cimmino (massimo.cimmino@polymtl.ca) is an assistant professor in the Department of Mechanical Engineering at Polytechnique Montréal, Montreal, Quebec, Canada.

additional ground circuit. Kjellsson, et al. (2010) tested different configurations with storage tanks connected to solar collectors and water heating systems. Eslami-nejad and Bernier (2011) found a substantial decrease in required borehole length by using an independent double U-tube configuration where solar heat is injected in a secondary circuit. More recently, Eslami Nejad, et al. (2017) proposed a new "self-assisted" heat pump configuration where the heat pump injects heat in a secondary ground loop prior to predicted peak heating loads which resulted in a decrease in peak power consumption with little increase in energy consumption.

A simulation model for a GSHP controlled using model predictive control (MPC) is developed to further study the feasibility of a modified "self-assisted" configuration for GSHPs operating in cold climates. Recent research has shown that different types of MPC can offer improved building energy performance compared to other control techniques – such as standard rule-based control laws – in a wide array of different applications (Afram and Janabi-Sharifi 2014; Oldewurtel, et al. 2012; Shaikh, et al. 2014).

Figure 1 shows a schematic of the modified self-assisted GSHP system used in this study. The system uses a single closed-loop vertical borehole coupled to a water-to-air single speed heat pump in a single-family house. An electric heating element at the point of fluid reentry into the borehole injects heat into the ground. The model predictive controller used in the simulation model uses future ambient temperatures to regulate this heating element. The controller minimizes the peak electrical consumption of the GSHP by determining the amount of heat to be injected into the ground and the optimal timing in which to do so. The use of MPC allows this optimization to be done while limiting the increase of the GSHP energy consumption due to the use of the electric heating element. The impact of the heat injection over a 5 year period is examined on an undersized borehole, and is also compared with the fully sized borehole. The simulation model (including the building, the heat pump, the borehole, the heating elements and the controllers) is constructed with components created using the Modelica language with the IBPSA library (Wetter, et al. 2015).

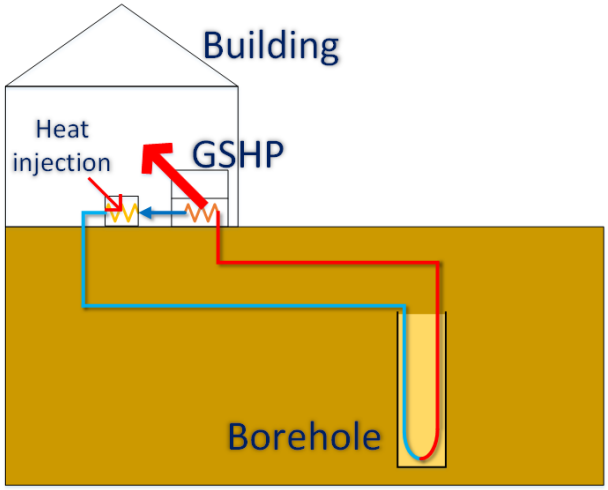

Figure 1 Self-assisted ground-source heat pump system

SIMULATION MODEL

Building Component

The building is modeled as a single zone building with thermal resistances defined by the NovoClimat building energy performance standard (Transition Énergétique Québec, 2017). This standard defines a set of minimum thermal resistances for the building's various surfaces as well as maximum air inflitration rate and refers to the local *ENERGY*

STAR standard for window UA values. Solar heat gains are neglected in the simulation model. The resulting total thermal resistance of the building to the exterior air is 0.00786 K/W. Occupancy-related heat gains are modeled by an average occupancy gain schedule proposed by Hendron (2005):

$$Q_{int} = Q_{max} * \begin{cases} 1 & 19{:}00 \le t \le 8{:}00 \\ 0.25 & 8{:}00 \le t \le 19{:}00 \end{cases} \quad (1)$$

The value used for maximum occupancy-related heat gains (Q_{max}), assuming an average of 2.5 occupants per residence, is 725 W and is evaluated following an ASHRAE (2013) method to estimate total residential heat gains.

$$Q_{max} = Q_{latent} + Q_{sensible} = 156 + 2.42(200\ \text{m}^2) + 34(2.5\ \text{occupants}) = 725\ \text{W} \quad (2)$$

Heat Pump Component

A simulation model for a fully reversible water-to-air heat pump is implemented. The source-side temperature dependence of the heating and cooling coefficient of performance (COP) and capacity is represented by second degree polynomial correlations. The correlation coefficients are evaluated by a fitting procedure on performance data from a commercial geothermal heat pump with a nominal capacity of 7.6 kW and a source-side nominal mass flow rate of 0.38 kg/s. This mass flow rate is assumed to be an average operational value at which the heat pump capacity and COP are evaluated. The entering air temperature is the indoor temperature, and its variations are considered to have negligible effect on the capacity or COP. The resulting capacity and COP curves are shown in Figure 2.

The heat pump in the present study can also operate at partial load, in which case the part load ratio (PLR) will be lower than 1 and will linearly impact the heat being added or substracted to the building air. When operating at partial load, a part load factor (PLF) is calculated to determine the resulting COP using the rational expression shown in Equation 3. The coefficients are those given by Henderson, et al. (1999) for what they describe as a "good AC" in regards to energy performance, with the same part load coefficients also being recommended for heating performance. The PLF's impact on the COP is shown in Equation 4.

$$\text{PLF} = \frac{\text{PLR}}{0.00988125 + 1.08033 \cdot \text{PLR} - 0.105267 \cdot \text{PLR}^2 + 0.0151403 \cdot \text{PLR}^3} \quad (3)$$

$$\text{COP}_{part\ load} = \min(1, \text{PLF} * \text{COP}_{full\ load}) \quad (4)$$

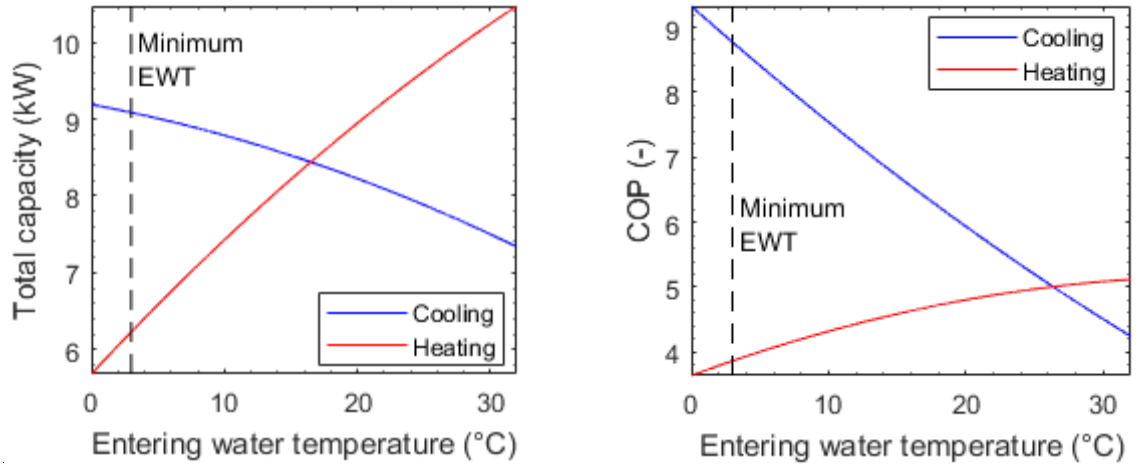

Figure 2 Source-side temperature dependence of heat pump capacity (left) and COP (right)

Using a PLR and a PLF in such a way means that the behaviour of the heat pump (including its on-off cycles) is represented as a mean operational value which globally accounts for performance losses that occur when turning the heat pump on or off. In the simulation model, the PLR applied to the heat pump is calculated at every time step according to the following procedure:

1. If the current indoor temperature is outside of the temperature setpoint interval (i.e. 21°C for heating and 25°C for cooling, with a ±0.25°C interval for both bounds) and the heat pump can operate at the current source-side entering water temperature, the heat pump operates at full capacity.
2. When the indoor temperature is within the set point range, the net building heat loss or gain is used to dertermine the required PLR (with a maximum of 1) and maintain the zone temperature constant.
3. If the heat pump is unable to adequately heat the building and the indoor temperature falls to 20°C, an auxiliary electric heating system is triggered and its average heating power is modulated to maintain the indoor temperature at the auxiliary set point of 20°C.

The activation of the auxiliary electric heating can be required when the heat pump's source-side inlet temperature falls below its lower limit of 3°C, which forces it to shut off. This limit ensures that, in heating mode, the leaving water temperature is always above 0°C. The maximum inlet temperature is 32.2°C. Whenever the inlet temperature falls below the minimum operating value, the heat pump is not turned on until the temperature has risen to at least 4.5°C.

Borefield Component

Component Parameters and Borehole Resistance. The component uses an external file containing a timeseries describing the borefield's thermal response factor as an input. This thermal response factor links the temperature change at the borehole wall with the ground heating load, and is applied between the borehole wall and the undisturbed ground. The heat transfer between the heat carrier fluid and the borehole wall is modeled using 10 evenly sized borehole segments. Each segment has the same borehole resistance between its local fluid temperature and the borehole wall temperature (the latter being the same for all 10 segments).

Improved Load Aggregation Scheme. To greatly reduce calculation times during simulations, a load aggregation scheme is used based on that of Claesson and Javed (2012). This scheme must however be adapted due to the way the Modelica solver handles events. During a simulation, the solver will attempt to determine when a conditional event is triggered and will automatically create additional time steps around the time of the event. This allows for conditional statements to be integrated very easily in the system, as there is no need to modify the solver's calculation time step to account for it. However, it also means that it is difficult to control the solver's time steps. Thus, modifications to the load aggregation scheme are proposed to handle the variable time steps. At every aggregation time step $t_k = t_{k-1} + \Delta t_{agg}$, temporal superposition is used to predict the borehole wall temperature at the next aggregation step, assuming no heat is extracted over the interval $t_k \leq t \leq t_{k+1}$. At every simulation time during this interval, the borehole wall temperature is evaluated by adding the contribution of heat transfered before and after the aggregation time t_k:

$$T_b(t) - T_g = \int_0^{t_k} Q(\tau)\frac{dh}{d\tau}(t-\tau)d\tau + \int_{t_k}^{t} Q(\tau)\frac{dh}{d\tau}(t-\tau)\mathrm{d}\tau$$
$$\Delta T_b(t) = \Delta T_b^*(t) + \Delta T_{b,q}(t) \qquad (5)$$

where T_b is the borehole wall temperature, T_g is the undisturbed ground temperature, Q is the heat extraction rate per unit borehole length and $h = g/2\pi k_s$ is the temperature response factor. g is the g-function proposed by Eskilson (1987), a dimensionless parameter to characterize the temporal change in the thermal response of a borefield.

The borehole wall temperature increase assuming no heat extraction ΔT_b^* can be rewritten for discrete aggregation time steps Δt_{agg} according to the load aggregation scheme of Claesson and Javed (2012). At the time corresponding to the next aggregation step t_{k+1}:

$$\Delta T_b^*(t_{k+1}) = \sum_{p=2}^{N_{agg}} \bar{Q}_p \cdot \Delta h(t_p) \tag{6}$$

where $\Delta h(t_p)$ is the thermal response factor increment from t_{p-1} to t_p, $\bar{Q}_p$ is the average heat transfer rate in aggregation cell p. An advantage of using Modelica is that expressions may explicitely use time derivatives of variables when building equations, as the time derivatives of all of the variables used in the system of equations are calculated numerically. In the absence of heat extraction during an interval $t_k \leq t \leq t_{k+1}$, it is assumed that the borehole wall temperature drop varies linearly between $\Delta T_b(t_k)$ and $\Delta T_b^*(t_{k+1})$. Additionally, it is assumed that the temperature response factor varies linearly between $t = 0$ and $t = \Delta t_{agg}$. The time derivative of the borehole wall temperature drop is thus given by:

$$\Delta \dot{T}_b(t) = \Delta \dot{T}_b^*(t) + \Delta \dot{T}_{b,q}(t) \tag{7}$$

$$\Delta \dot{T}_b(t) = \frac{\Delta T_b^*(t_{k+1}) - \Delta T_b(t_k)}{\Delta t_{agg}} + \frac{h(\Delta t_{agg})}{\Delta t_{agg}} Q(t) \tag{8}$$

The modified load aggregation scheme is validated using the asymmetrical synthetic load profile proposed by Pinel (2003) over a 20 year simulation. The synthetic heating profile is shown for a single year in Figure 3 (where a positive load value indicates heat injected in the ground). Figure 4 shows the resulting borehole wall temperature over 20 years assuming an undisturbed ground temperature of 0°C, while Figure 5 shows the absolute difference between the calculated borehole wall temperature and the exact value calculated by solving the temporal superposition in the spectral domain using fast Fourier transforms.

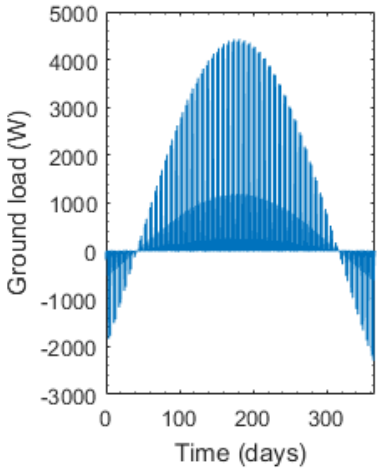

Figure 3 Synthetic load profile

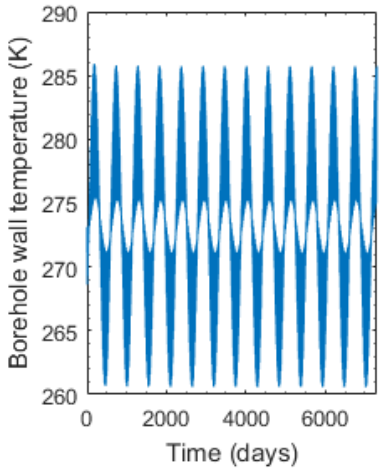

Figure 4 Borehole wall temperature

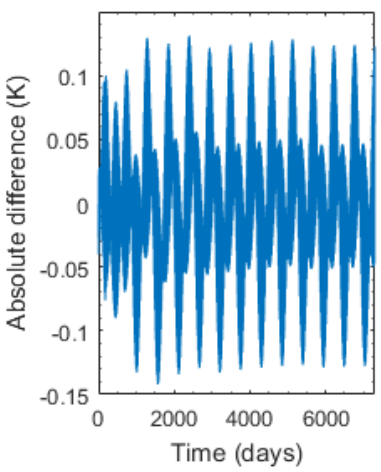

Figure 5 Absolute difference between new scheme and FFT solution

CONTROL STRATEGY

The complete Modelica model with all three major components described in the previous section as well as the necessary controllers is simulated and optimized using the JModelica platform. Every controller decision relies on a constant receding horizon of 7 days without any forecast errors. This receding horizon is chosen to ensure that the controller can see far enough ahead to appropriately inject heat in the ground and to account for weather forecasts with a one-week forecast horizon. The duration of each heat injection period (along with the frequency at which a new decision to inject heat or not is taken) is 24 hours, which is chosen as a compromise between computation times and the accuracy of results. Every day in the simulation, an optimization problem of 7 different values of heat injection rate (one value per day in the receding horizon) must therefore be solved, after which only the first optimized value is kept. Between different simulations, temperatures, controller states and the averaged heat transfer rates $\bar{Q}_p$ in Equation 6 must be initialized with the values at the end of the first day of the previous simulation. The simulation itself has a nominal time step of 1 hour, though as described previously, in practice this is a maximum time step in Modelica.

A quadratic cost function is developed to account for the tradeoff between peak power and energy consumption:

$$C = P^2 + \beta * E^2$$
$$\begin{Bmatrix} E = \int_0^t \left(P_{HP} + P_{aux} + P_{inj}\right)\mathrm{dt} \\ P = \max_{0 \le t' \le t} \left(P_{HP} + P_{aux} + P_{inj}\right) \end{Bmatrix} \quad (9)$$

The three subscripts *HP*, *aux* and *inj* represent the heat pump power input, the auxiliary electric heating power and the power of the electric heat injection element, respectively. The maximum of their sum thus gives the peak power consumption P (measured in W in the previous equation), while their integral gives the total energy consumption E (measured in kWh in the previous equation). The remaining term β is a parameter with a value of 1700. This value was chosen using a case study of a single week for which β was calculated with the goal of limiting the energy increase at 15% assuming the maximum peak power decrease (meaning that only the heat pump power is used) of 73.7% for that week. The optimization algorithm chosen to minimize this cost function is a particle swarm optimization, as this was found to have acceptable performance with a test case representing a single week while limiting the maximum number of function evaluations due to high computation times.

RESULTS

The simulation model and the control strategy shown previously are used on a residential building with a total floor area of 200 m² and a GSHP with a single U-tube. The borehole's physical characteristics are shown in Table 1.

Table 1. Borehole Characteristics

Parameter	Value
Ground thermal conductivity (W/m-K)	2
Ground thermal diffusivity (m²/s)	1e-06
Undisturbed ground temperature (°C)	10
Borehole radius (m)	0.075
Buried depth (m)	4
Cross-sectional borehole thermal resistance (m-K/W)	0.15

The basic configuration without any heat injection in the ground requires a borehole length of 198 meters to avoid the use of any auxiliary heating over the first 5 years of operation. To measure the impact of the proposed MPC strategy, a reduction of 16.7% to a length of 165 meters is attempted. Figures 6 and 7 compare the resulting total power consumption of the base configurations with those of the proposed assisted configuration. The power consumption values shown are time-averaged values which vary continuously throughout the simulation. Because of the load

aggregation procedure, no time step is ever longer than 1 hour.

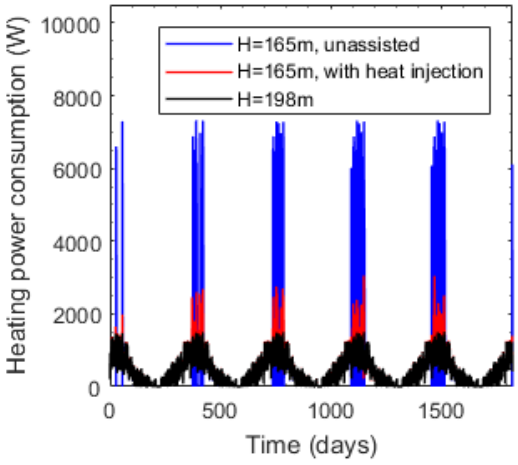

Figure 6 Power consumption over 5 years

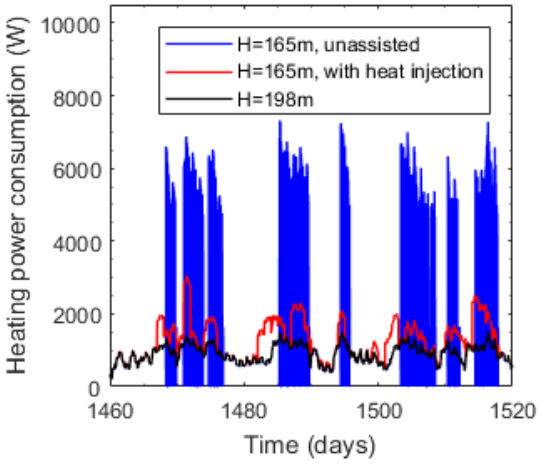

Figure 7 Power consumption during the 5th heating season

The total heating power consumption (the heat pump compressor when operating in heating mode as well as the auxiliary heating) thus increases substantially with the reduced borehole length when no thermal assistance is used, which is representative of the energy performance penalty associated with an undersized GSHP system. The new control strategy applied with the self-assisted GSHP over 5 years allows to greatly reduce this performance penalty with a minimal increase in total energy consumption. Specifically, results show a 58% reduction in the peak power consumption over 5 years and an increase of 2.8% in the total energy consumption over the 5th year compared to the undersized and unassisted configuration. Compared to the fully sized configuration, the 5th year energy consumption thus increases from 11% to 14%. The self-assisted GSHP completely eliminates the use of auxiliary electric heating over the first 5 years. Compared to the initial configuration with a depth of 198 meters, this means that the penalty on peak power consumption caused by the undersized borehole decreases from 488% to 204%. Detailed results are shown in Table 2.

Figure 8 shows the injection pattern over 5 years. The injection pattern found to be optimal by the controller involves beginning heat injection typically 3 or 4 days before the beginning of the peak period, with injection periods often coinciding with local peak loads. This behaviour is displayed in Figure 9, where the periods of auxiliary heating with the unassisted configuration are used to indicate the approximate location of peaks for the assisted configuration.

Table 2. Comparison of three configurations

Result	(units)	Base configuration (full size borehole)	Undersized borehole – unassisted	Undersized borehole – self-assisted
Borehole length	(m)	198	165	165
Peak total power usage over 5 years	(W)	1499	7320	3056
Peak total power usage increase relative to base config.	(-)	-	488%	204%
Peak heat pump usage over 5 years	(W)	1499	1640	1637
Peak aux. heating over 5 years	(W)	0	5687	0
Peak heat injection over 5 years	(W)	0	0	1662
Total energy consumption (5th year)	(kWh)	3532	3928	4039
Total energy consumption increase relative to base config. (5th year)	(-)	-	11%	14%

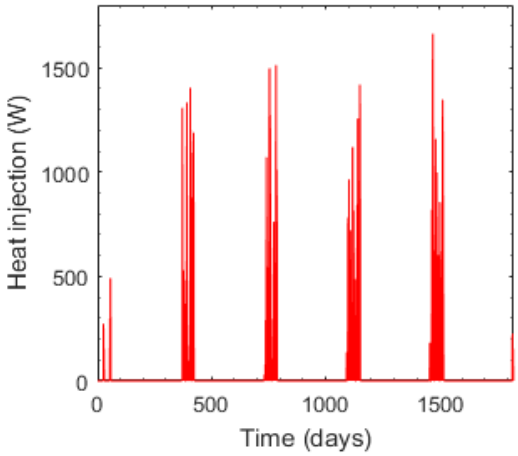

Figure 8 Heat injection over 5 years

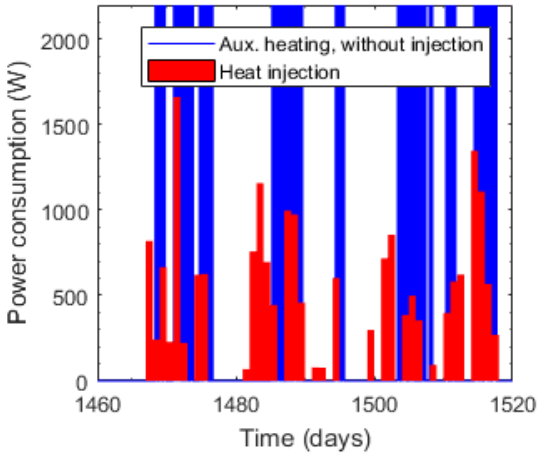

Figure 9 Heat injection during the 5th heating season

CONCLUSION

This study presents a control strategy for a residential self-assisted GSHP operating in a cold climate which aims to reduce peak power consumption while minimizing energy consumption, thereby reducing the penalty suffered by shorter boreholes with regards to their energy performance. To do so, a simulation model was developed in the Modelica language, which includes an improvement to a load-shifting aggregation scheme. A model predictive controller with a receding horizon of 7 days was used to optimize a heat injection pattern per day over a simulation period of 5 years. This controller was used with a borehole undersized by 16.7% and removed all auxiliary electric power usage. Total peak power consumption was reduced by 58% compared to the same borehole used without any thermal assistance. This reduction comes at a cost of an increased annual energy consumption of 2.8%.

These results indicate that self-assisted GSHPs offer potential to reduce required borehole lengths, thereby decreasing installation costs, which are an obstacle to the development of GSHPs. Future work will be required to quantify the impact of some of the assumptions made in the present study. The heat pump model will be modified to consider the dynamic operation of the system, rather than its time-averaged behavior. The borehole model will be modified to account for the short term heat transfer inside the borehole. As for the controller, future work will include the uncertainty of forecasted weather conditions in the MPC strategy. Furthermore, other MPC strategies, such as state space methods, will be considered for future use to reduce computation times.

ACKNOWLEDGMENTS

The second author received a start-up subsidy from the *Fonds de recherche du Québec – Nature et Technologie*.

NOMENCLATURE

COP	=	Coefficient of performance	Q, $\bar{Q}_p$	=	Heat transfer rate (W), instant and average
g	=	Borehole "g-function"	T_b	=	Borehole wall temperature (°C)
h	=	Borehole thermal response (m-K/W)	T_g	=	Ground temperature (°C)
k_s	=	Soil thermal conductivity (W/m-K)	Δh	=	Thermal response factor increment
PLF	=	Part load factor	Δt_{agg}	=	Aggregation time step (s)

REFERENCES

Afram, A. and Janabi-Sharifi, F. 2014. *Theory and applications of HVAC control systems – A review of model predictive control (MPC)*. Building and Environment(72): 343-355.

ASHRAE. 2013. *2013 ASHRAE Handbook – Fundamentals (SI Edition)*. American Society of Heating, Refrigeration, and Air Conditioning Engineers. Atlanta, GA.

Claesson, J. and Javed, S. 2012. *A load-aggregation method to calculate extraction temperatures of borehole heat exchangers*. ASHRAE Transactions 118(1): 530-539.

Eskilson, P. 1987. *Thermal analysis of heat extraction boreholes*, Ph.D. thesis, Lund University.

Eslami-nejad, P. and Bernier, M. 2011. *Coupling of geothermal heat pumps with thermal solar collectors using double U-tube boreholes with two independent circuits*. Applied Thermal Engineering 31(14-15): 3066-3077.

Eslami Nejad, P., Cimmino, M. and Hosatte-Ducassy, S. 2017. *Heat Pump Capacity Effects on Peak Electricity Consumption and Total Length of Self- and Solar-assisted Shallow Ground Heat Exchanger Networks*. IGSHPA Technical/Research Conference and Expo 2017. Denver, USA. March 14-16.

Han, Z., Zheng, M., Kong, F., Wang, F., Li, Z. and Bai, T. 2008. *Numerical simulation of solar assisted ground-source heat pump heating system with latent heat energy storage in severely cold area*. Applied Thermal Engineering 28(11-12): 1427-1436.

Henderson, H., Huang, Y. J. and Parker, D. 1999. *Residential Equipment Part Load Curves for Use in DOE-2*. Lawrence Berkeley National Laboratory Report 42175.

Hendron, R. 2005. *Building America Research Benchmark Definition, Version 3.1, Updated July 14, 2004*. National Renewable Energy Laboratory Report NREL/TP-550-36429.

Kjellsson, E., Hellström, G. and Perers, B. 2010. *Optimization of systems with the combination of ground-source heat pump and solar collectors in dwellings*. Energy 35(6): 2667-2673.

Oldewurtel, F., Parisio, A., Jones, C. N., Gyalistras, D., Gwerder, M., Stauch, V., Lehmann, B., and Morari, M. 2012. *Use of model predictive control and weather forecasts for energy efficient building climate control*. Energy and Buildings(45): 15-27.

Pinel, P. 2003. *Amélioration, validation et implantation d'un algorithme de calcul pour évaluer le transfert thermique dans les puits verticaux de systèmes de pompes à chaleur géothermiques,* M.A.Sc. thesis, École Polytechnique de Montréal.

Shaikh, P. H., Nor, N. B. M., Nallagownden, P., Elamvazuthi, I. and Ibrahim, T. 2014. *A review on optimized control systems for building energy and comfort management of smart sustainable buildings*. Renewable and Sustainable Energy Reviews(34): 409-429.

Transition Énergétique Québec. 2017. *Exigences techniques Novoclimat 2.0 - Maison et petit bâtiment multilogement*. Available online at: http://www.transitionenergetique.gouv.qc.ca/en/business-clientele/construction-residentielle/novoclimat-20/maisons/documents-techniques-et-formulaires/#

Wetter, M., Fuchs, M., Grozman, P., Helsen, L., Jorissen, F., Müller, D., Nytsch-Geusen, C, Picard, D., Sahlin, P., and Thorade, M. 2015. *IEA EBC annex 60 modelica library – an international collaboration to develop a free open-source model library for buildings and community energy systems*. 14th International Conference of the International Building Performance Simulation Association. Hyderabad, India. December 7-9.

[This page has been intentionally left blank]

IGSHPA SWEDEN 2018 Research Conference

DOI: 10.22488/okstate.18.000030

Development and Verification of Control System for Heat Recovery Ground Source Heat Pump System

Takao Katsura, PhD **Yutaka Shoji** **Yoshiki Miyashita**

Katsunori Nagano, PhD **Yasushi Nakamura, PhD**

ABSTRACT

An operation method and control system for heat recovery ground source heat pump (HR-GSHP) systems have been developed. By applying the operation method and control system, the heating and cooling output from the respective GSHP units can be controlled according to the operational condition. This maximizes the energy saving effect by operating the GSHP units without excess temperature change of the heat carrier fluid. In this paper, the outlines of HR-GSHP system and the importance of control system for the HR-GSHP systems were firstly explained. Next, the control system's configuration and the control methodology were explained. In addition, the operation of a HR-GSHP system with the control system, in which the control methodology had been installed, was verified by using the field test apparatus. As the result, it was confirmed that the above control methodologies were applicable.

INTRODUCTION

Ground source heat pump (GSHP) systems have gained attention in Japan since the ground thermal energy was defined as one of the renewable energies in 2009. In a period before and behind it, the research works to promote the installation of GSHP systems especially in the moderate climate region such as Tokyo were carried out. As the representative examples, developments of design method and operation system for hybrid GSHP systems combined with the cooling tower are mentioned (Katsura et.al, 2011, Katsura et.al, 2014). However, the number of GSHP systems installed in Japan is still smaller than other countries due to the higher installation cost for ground heat exchangers (GHEXs). Especially, there are few examples of large GSHP systems with a total heating or cooling capacity of more than several hundred kW.

The advantages of heat recovery GSHP (HR-GSHP) systems could potentially promote the installation of large GSHP systems. The HR-GSHP system has several types of GSHP units for different uses connected to the GHEXs in order to yield two types of heat recovery effects. The first type of heat recovery is the direct heat recovery effect obtained by operating several types of GSHP units, such as cooling and hot water supply, at the same time; this effect is the same as that of the conventional heat recovery heat pump system with the double-bundle condenser (ASHRAE handbook, 2008). The other type of heat recovery is the indirect heat recovery effect that utilizes underground thermal storage and is obtained by short-term alternate operation of several types of GSHP units. By utilizing these two heat recoveries, the HR-GSHP system can yield both of energy saving and drastic reduction of the total GHEX length. Therefore, the HR-GSHP system has a large potential for saving energy in large-scale complex buildings and industrial plants, which require both heating and cooling at the same time. The authors focused attention on this point and the design method for HR-GSHP systems applying the optimization method was established (Katsura et.al, 2017).

Takao Katsura (katsura@eng.hokudai.ac.jp) is an associate professor, Graduate School of Engineering, Hokkaido University.

In this paper, the control system for HR-GSHP systems is established. The HR-GSHP system has the GSHP units with the larger capacity compared to the total length of GHEXs because the direct heat recovery effect is expected. Thus, if the GSHP units operate with the maximum capacity under a situation where the direct heat recovery effect does not occur, the heat extraction or injection from GHEXs is not enough. Then, the temperature of heat carrier fluid decreases or increases excessively and the HR-GSHP system cannot be operated. Therefore, as shown in Figure 1 it is important to control the heat extraction or injection from the GSHP units when the multiple GSHP units are not operating for heating and cooling simultaneously. There are several research works related to the capacity control of GSHP units (Gao et.al, 2015) and the flow rate control of circulation pumps (Katsura et.al, 2011, Edward et.al, 2015) but no research works in which the capacity of GSHP units is controlled to prevent the excess variation of heat carrier fluid in the primary side of GSHP system. The authors firstly explain the outlines of control system. Also, the results of a verification of control operation using a field test apparatus are reported.

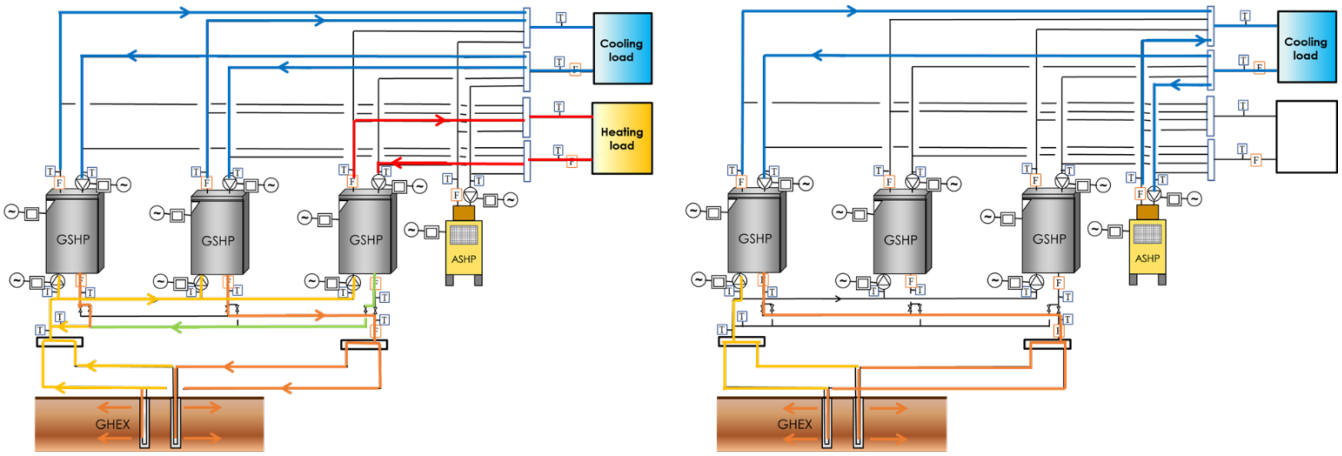

(a) Simultaneous both side operation for heating and cooling

(b) Single side operation

Figure 1 Changing HR-GSHP system operation

OUTLINES OF THE HR-GSHP SYSTEM AND THE CONTROL SYSTEM

Outline of HR-GSHP systems

Figure 1 shows a schematic diagram of HR-GSHP system, which is the control target. The HR-GSHP system has several types of GSHP units for different uses and the GSHP units are connected to the GHEXs. In the HR-GSHP system, the auxiliary heat source units such as the air source heat pump (ASHP) units, the absorption hot/cold water generators are equipped. In addition, the software and the PLC are installed to control the HR-GSHP system.

Control Method of HR-GSHP Systems

Figure 3 shows the flow chart of the control system for HR-GSHP systems. The PLC sends measurement data to the software, which carries out a simulation and determine the control parameters. The determined control parameters are sent to the PLC, which control the HR-GSHP system.

First, as shown in Figure 2(b), the authors introduce the control method in the case where the GSHP units are operated for either heating or cooling (Single side operation). In the case of Figure 2(b), The direct heat recovery effect cannot be expected; thus, the maximum output from GSHP units (Q_{g2hmax}, Q_{g2cmax}) in which the HR-GSHP system can operate continuously long term is determined with the software.

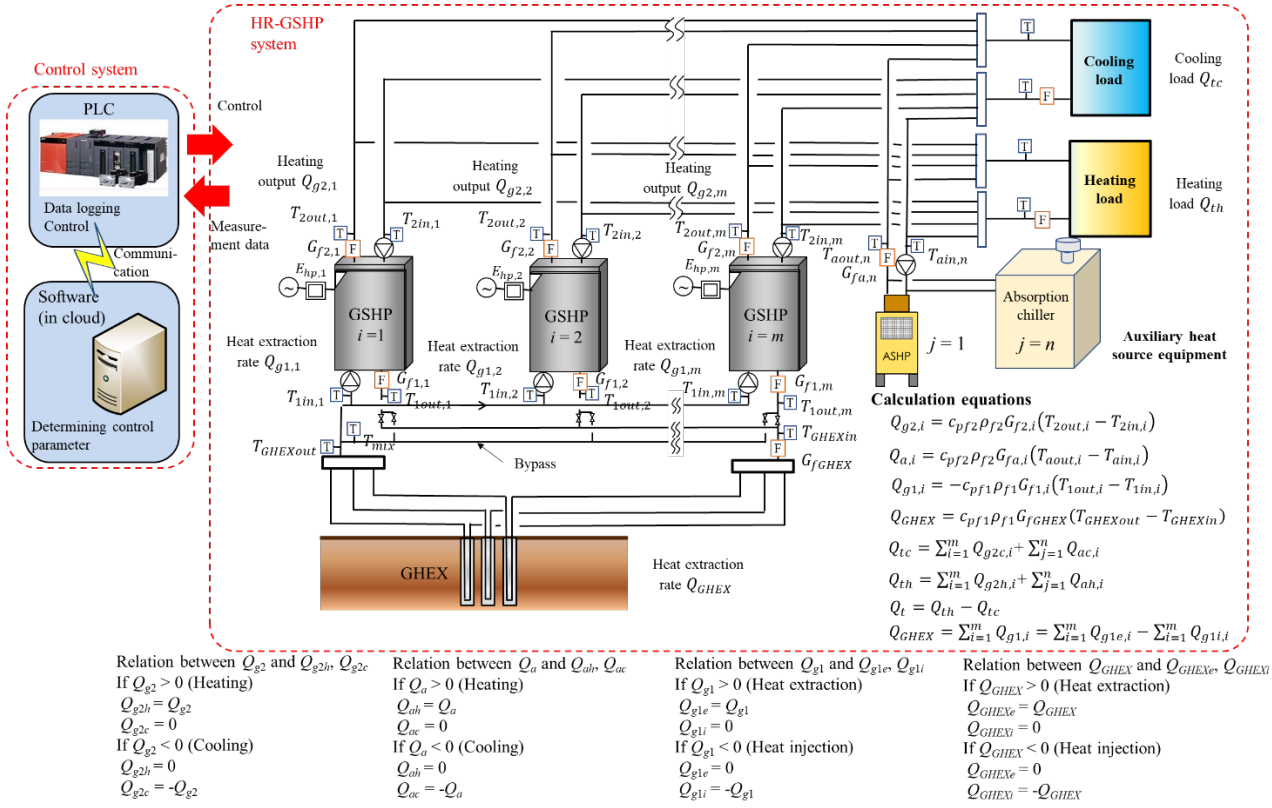

Figure 2 Schematic diagram of HR-GSHP system

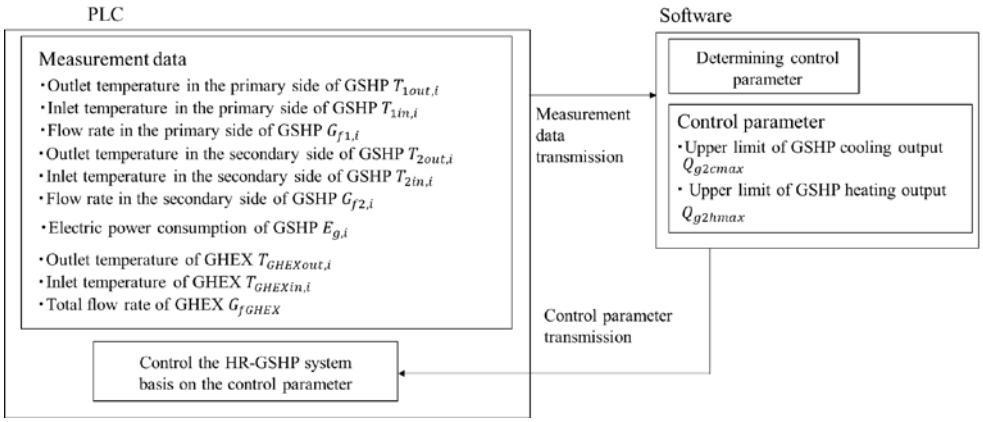

Figure 3 Flow chart of the control system for HR-GSHP system

Figure 4 shows the determination flow of Q_{g2hmax}, Q_{g2cmax}. Before determining Q_{g2hmax}, Q_{g2cmax}, the software estimates the apparent effective thermal conductivity of the ground by using the method introduce in the previous paper (Katsura et.al, 2014), the hourly load, and the heat pump coefficient of performance (COP), which are important parameters to carry out simulation. Subsequently, the simulation of HR-GSHP system are carried out and the temperature variation of heat carrier fluid considering the indirect heat recovery effect is predicted. Then, the simulation is repeated by changing Q_{g2hmax}, Q_{g2cmax} and Q_{g2hmax}, Q_{g2cmax} are determined in the condition that the temperature of heat carrier fluid is in the range of maximum and minimum set temperatures. Finally, the control parameters Q_{g2hmax}, Q_{g2cmax} are sent to the PLC. The process shown in Figure 4 is generally conducted every week (However, the period can be changed).

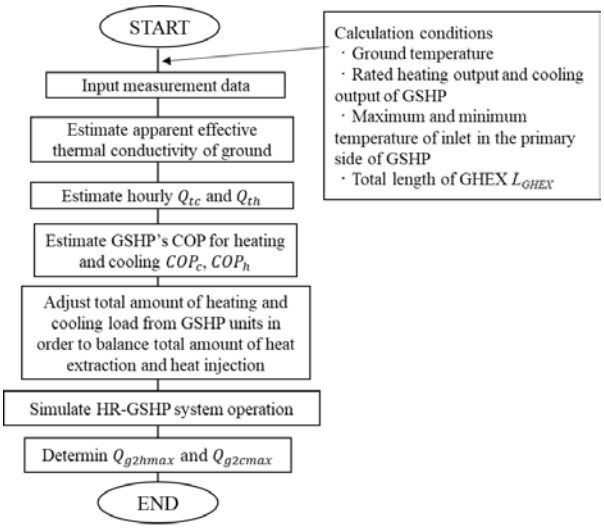

Figure 4 Flow chart for determining Q_{g2hmax}, Q_{g2cmax}

In the HR-GSHP system, the output from the GSHP units must be controlled depending on the determined Q_{g2hmax}, Q_{g2cmax}, and the auxiliary heat source units should be operated. Therefore, the authors introduce the base load control that can control the output from the GSHP units. The base load control keeps the output from the GSHP unit constant by adjusting the flow rate of cold/hot water from the heat source units in the HR-GSHP system that has two or more heat source units. Figure 5 shows the flow chart of base load control. In the HR-GSHP system with multiple heat source units, the secondary return temperature becomes the same; thus, the load is depending on the flow rate of each heat source unit. Therefore, the flow rate of each heat source unit is changed to distribute the load.

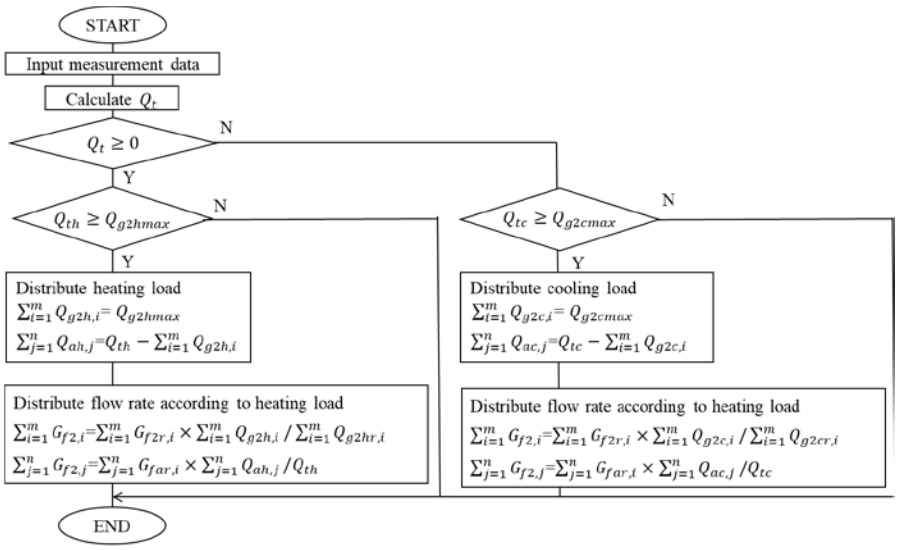

Figure 5 Flow chart of base load control

Next, as shown in Figure 2(a), the authors explain the control method in the case where the multiple GSHP units are simultaneously operated for both of heating and cooling (Both side operation). When the multiple GSHP units for heating and cooling are operated simultaneously, the maximum output Q_{g2hplc} and Q_{g2cplc} that considers simultaneous operation is calculated with the PLC as shown in Figure 6. Whether Q_{g2hplc} (or Q_{g2cplc}) exceed Q_{g2hmax} (or Q_{g2cmax}) is determined, and the output from the GSHP units is increased based on the result.

When the multiple GSHP units for heating and cooling are simultaneously operated, the total flow rate of the GSHP units might exceed the maximum flow rate of the GHEXs. To avoid such situation, the bypass system is installed in the primary side of the HR-GSHP system, as shown in Figure 2. In order to maximize the direct heat recovery effect, the flow rate in the bypass is adjusted so that $T_{mix} = T_{GHEXout}$. Then, the residual flow is sent to the GHEX. Here, the flow from each heat pump is adjusted indipendentely by controlling the revolution speed of circulation pump. And the revolution speed is controlled by adjusting the temperature difference between inlet and outlet of heat pump, which are $T_{1in,i}$ and $T_{1out,i}$ in Figure 2.

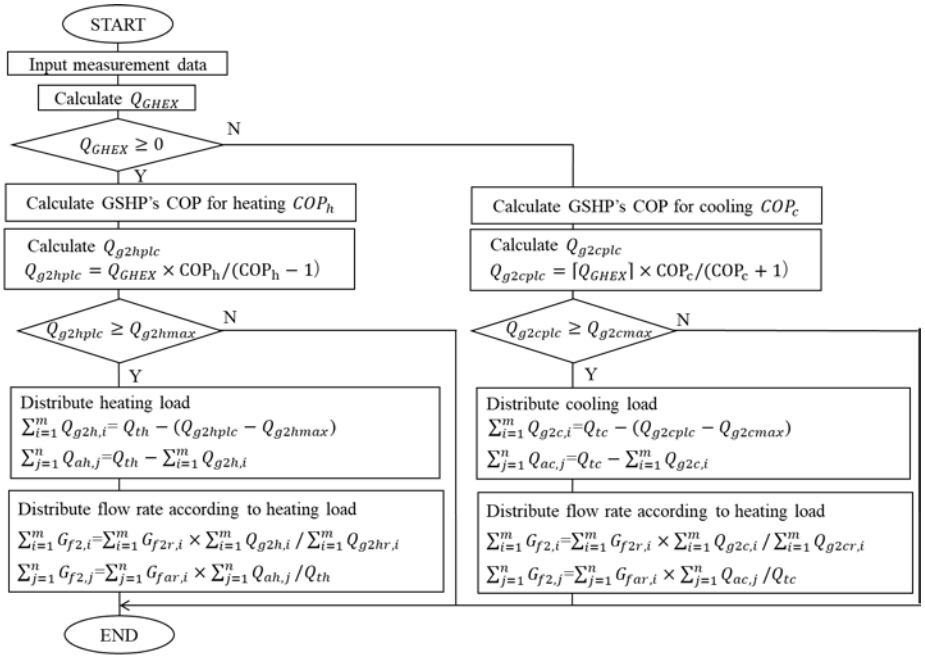

Figure 6 Flow chart of output control from GSHP units during simultaneous operation of multiple GSHP units

VERIFICATION OF CONTROL SYSTEM IN THE FIELD TEST

Outlines of Field Test Apparatus

In order to verify the control system, the experiment apparatus for the HR- GSHP system has been constructed in the field of Hokkaido University since 2016. Figure 7 shows the diagram of the field test apparatus. The field test apparatus consists of the GHEXs, the multiple GSHP units, the ASHP units as the auxiliary heat source units. The field test apparatus can cover the cooling and heating loads in the range of 0~30 kW by using the load imitation tank. The feature of the test apparatus is that the capacity of each GSHP unit is small but multiple GSHP units are installed. In addition, it is possible to give the excessive load conditions that would be difficult to execute in the real building. The PLC in the field test apparatus can communicate with the software in cloud and control the HR-GSHP system. The software can determine the control parameters Q_{g2hmax} , Q_{g2cmax} and send them to the PLC.

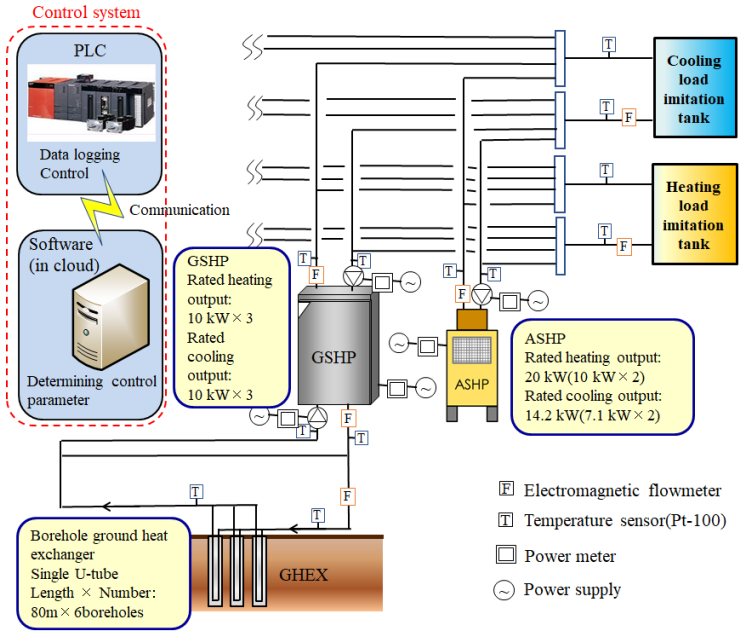

Figure 7 Diagram of the field experiment apparatus

Verification of Control System

The developed control system was verified by using the field test apparatus. The field test carried out on July 2017. Table 1 shows the test conditions for the control system.

Table 1 Test conditions for control system

	Verified control	Q_{th} [kW]	Q_{tc} [kW]	Q_{g2h} [kW]	Q_{g2c} [kW]	Q_{ah} [kW]	Q_{ch} [kW]
CASE1	Base load control	0.0	11.1	0.0	4.0	0.0	7.1
CASE2	Output control from GSHP units during simultaneous operation	16.0	10.0	16.0	10.0	0.0	0.0
CASE3	Output control from GSHP units during simultaneous operation + Base load control	10.0	16.0	10.0	10.0	0.0	6.0

First, the values of Q_{g2hmax}, Q_{g2cmax} were calculated as 4 kW by using the software and given as the conditions for CASE1 to CASE3. In CASE1, the base load control was verified, the cooling load of 11 kW was given as the imitation load. Based on Q_{g2cmax} = 4 kW, the control that retains the GSHP unit's cooling output as 4 kW and yields the ASHP unit's cooling output as 7 kW was verified. In CASE2, the output control from GSHP units during simultaneous operation, the cooling load of 10 kW and heating load of 16 kW were given as the imitation loads. And the simultaneous operation of the multiple GSHP units for heating and cooling in the HR-GSHP system was performed. However, in CASE2, the ASHP unit is not used because it was Q_{GHEX} >0 and $Q_{g2hplc} < Q_{g2hmax}$ in the flow shown in Figure 6. Next, in CASE3, both of the base load control and the output control was verified; the cooling load of 16 kW and heating load of 10 kW were given as the imitation load and the simultaneous operation of the multiple GSHP units for heating and cooling was performed as well as in CASE2. However, in CASE3, it becomes $Q_{GHEX} < 0$ and $Q_{g2hplc} \geq Q_{g2hmax}$ in the flow shown in Figure 6; thus, the output from the GSHP unit for cooling is controlled, and the remaining cooling load should be covered by the ASHP unit. In other words, in CASE3, the control that provides the simultaneous operation of the multiple GSHP units and retains the GSHP unit's cooling output was verified.

As the result of CASE1, Figure 8 shows the variations of flow rate of the cold water from the GSHP unit and the ASHP, and Figure 9 shows the variations of cooling output from the GSHP unit and ASHP unit. Figure 8 shows that the flow rate of the cold water from the GSHP unit was kept at 10 L/min and Figure 9 shows that the cooling output from the GSHP unit was kept at 4 kW. These results indicated that the flow rate control was occurring, and the cooling output from GSHP (Light blue curve in Figure 9) was controlled according to the maximum output Q_{g2hmax}. The cooling output from ASHP (Light green curve in Figure 9) was approximately 6 kW, which was slightly below 7.1 kW, but the load distribution was generally according to the control.

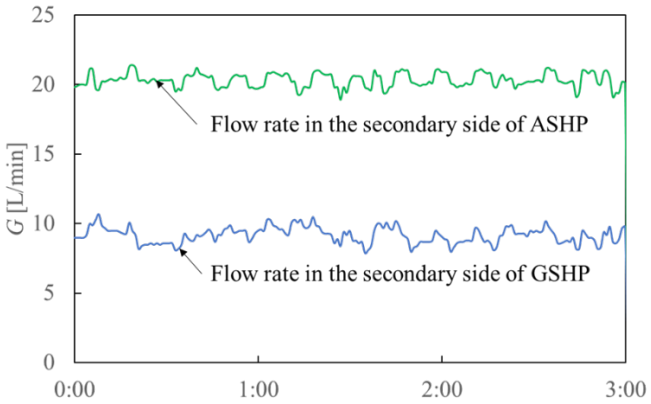

Figure 8 Variations of flow rate from GSHP unit and ASHP unit (CASE1)

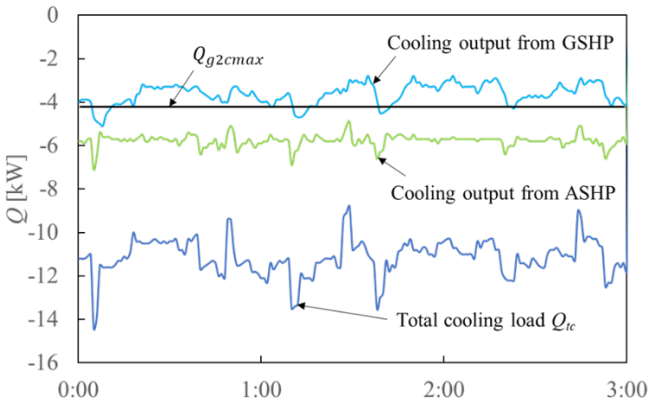

Figure 9 Variations of cooling output from GSHP unit and ASHP unit (CASE1)

Next, as the result of CASE2, Figure 10 shows the variations of heat extraction/injection rate from the GSHP unit and the GHEXs. Figure 10 also shows the variations of temperatures $T_{GHEXout}$ (Red curve) and T_{mix} (Right red curve), which are indicated in Figure 1. In addition, Figure 11 shows the variations of heating and cooling output from the GSHP units. Figure 10 indicated that it was almost $T_{mix} = T_{GHEXout}$. In addition, it was confirmed that the heat extraction and injection from the multiple heat pump units were cancelled each other with the bypass and the only excess heat extraction was exchanged in the ground. In addition, the heating (Red curve) and cooling output (Light blue curve) from the GSHP units became larger than the values of Q_{g2hmax}, Q_{g2cmax} when the simultaneous operation of the multiple GSHP units was performed.

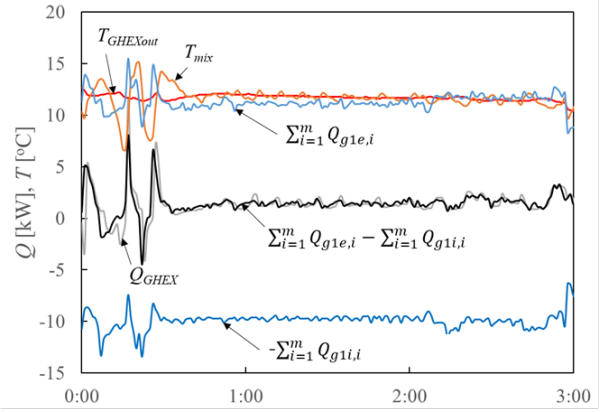

Figure 10 Variations of heat extraction/injection rate and temperatures (CASE2)

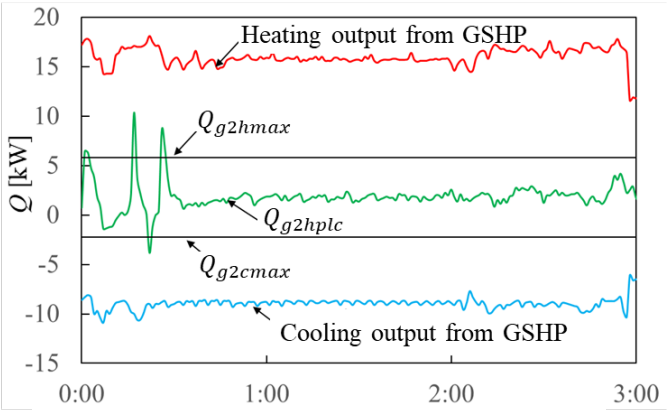

Figure 11 Variations of heating and cooling output from GSHP units (CASE2)

Furthermore, as a result of CASE3, Figure 12 shows the variations of heat extraction/injection rate and temperatures and Figure 13 shows the variations of heating and cooling output from the GSHP units and the ASHP unit. Figure 13 shows it was mostly $T_{mix} = T_{GHEXout}$ as well as in CASE2. Then, the heat extraction and injection from the multiple heat pump units were cancelled each other with the bypass, and the direct heat recovery effect was confirmed. In addition, the output from the GSHP unit for cooling was controlled, and the ASHP unit was operated as the auxiliary heat source unit. The cooling output from the GSHP unit (Light blue curve in Figure 13) and the ASHP unit (Light greem curve in Figure 13) were kept as 10 kW and 6 kW, respectively. This result indicated the cooling outputs were properly distributed with the control system.

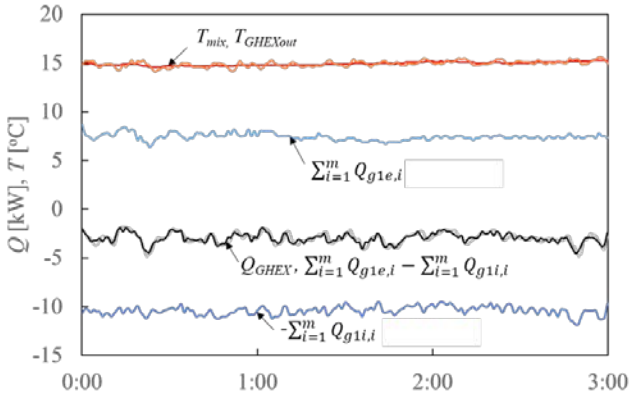

Figure 12 Variations of heat extraction/injection rate and temperatures (CASE3)

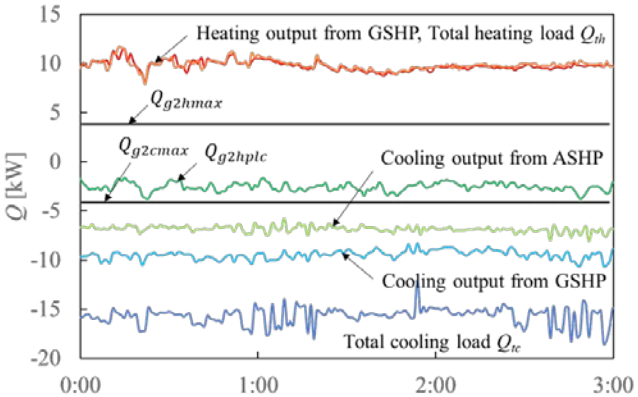

Figure 13 Variations of heating and cooling output from GSHP units and ASHP unit

CONCLUSION

1) The control system for HR-GSHP systems, which consisted of a PLC and software, was developed. The control methodology has the following features:

- A method for determining the maximum allowable output from the GSHP units in case where the GSHP units are operated for either heating or cooling.
- The control method limits the output from the GSHP units and operates the auxiliary heat source unit so that the maximum allowable output is not exceeded.
- The control method of output from the GSHP unit during simultaneous operation of the multiple GSHP units for both of heating and cooling.
- The bypass system in the primary side of the HR-GSHP system is controlled to maximize the direct heat recovery effect when GSHP units are simultaneously providing both of heating and cooling.

2) The operation of HR-GSHP system with the control system could be verified by using the field test apparatus. Therefore, the HR-GSHP system with the developed control system can drastically reduce the total length of GHEXs according to the heating and cooling supply and the initial cost although the initial investment cost is generated.

ACKNOWLEDGMENTS

This study is based on results obtained from the project "Renewable energy heat utilization technology development," commissioned by the Japan national agency New Energy and Industrial Technology Development Organization (NEDO).

NOMENCLATURE

c_p = Specific heat at constant pressure [kJ/kg/K]
E = Electric power consumption [kW]
G = Flow rate [m^3/s]
L = Length [m]
Q = Heat load, heat extraction [kW]
q' = Heat extraction rate per length and temperature difference [W/m/K]
T = Temperature [^oC]
ϱ = Density [kg/m^3]

Subscripts

1 = primary side of ground source heat pump
2 = secondary side of ground source heat pump
a = air source heat pump
ac = cooling operation of air source heat pump
ah = heating operation of air source heat pump
f = fluid
g = ground source heat pump
g1 = primary side of ground source heat pump
g1e = heat extraction from primary side of ground source heat pump
g1i = heat injection from primary side of ground source heat pump
g2 = secondary side of ground source heat pump
g2c = cooling operation of ground source heat pump
g2h = heating operation of ground source heat pump
GHEX = ground heat exchanger
GHEXe = heat extraction from the ground heat exchanger
GHEXi = heat injection from the ground heat exchanger
i, j = order
in = inlet
m, n = number
max = upper limit
mix = after mixing
out = outlet
plc = calculated by PLC
r = rated value
t = total
tc = total cooling output
te = total heating output

REFERENCES

ASHRAE. 2008, ASHRAE handbook 2008 HVAC Systems and Equipment. Chapter 8, 8.10

Edwards. K. C, D. P. Finn: Generalised water flow rate control strategy for optimal part load operation of ground source heat pump systems, Applied Energy, 150, pp. 50-60, 2015

Gao. J, G. Huang, X. Xu: Space temperature control of a GSHP-integrated air-conditioning system, Energy and Buildings, pp.127-136, 2015

Katsura. T, Y. Nakamura, K. Nagano: Development of a computer aided simulation program for the ground source heat pump system combined cooling tower and its application, Proceedings of 10th IEA Heat Pump Conference, Tokyo, 2011-5

Katsura. T, Y. Nakamura, K. Nagano: Experimental proof of seasonal performance of the ground source heat pump system applying variable water flow control and multi-split system, Proceedings of 10th IEA Heat Pump Conference, Tokyo, 2011-5

Katsura. T, Y. Nakamura, M. Hirata, Y. Matsuo：Performance Analysis and Operation Improvement of the Hybrid Ground Source Heat Pump System by Using Performance Prediction Tool, Proceedings of 11th IEA Heat Pump Conference 2014, Montoreal, 2014-5

Katsura. T, K. Nagano, Y. Nakamura：Investigation of a Design and Operation Method for a Heat Recovery Ground Source Heat Pump System, Proceedings of ASHRAE annual conference, Conference Paper, Long Beach, 2017-6

[This page has been intentionally left blank]

IGSHPA SWEDEN 2018 Research Conference

DOI: 10.22488/okstate.18.000047

Parameters optimization of ground source heat pump system combined energy consumption and economic analysis using Taguchi method

Yiwei Xie **Pingfang Hu** **Fei Lei**
Na Zhu **Lu Xing**

ABSTRACT

In order to obtain a high performance and low cost of ground source heat pump (GSHP) system, a methodology based on Taguchi method and analysis of variance (ANOVA) is used to optimize design parameters of GSHP systems. Eight parameters of GSHP system are selected as control factors to investigate effect on the system. Energy efficiency ratio (EER), coefficient of performance (COP), net annual value (NAV) and the average temperature rise (TEM) in soil of GSHP system are chosen as response factors to evaluate the system performance. A GSHP system model software is established by TRNSYS to calculate the EER, COP, NAV and TEM for 36 times repeatedly according to the L36 (2^2, 6^3) mixed level Taguchi orthogonal array. The result showed that the design outlet temperature of heat pump unit is the most important parameter for EER and COP, of which the contribution of significance are 41.88% and 88.12% respectively. While the number of U-Tubes per borehole has the major contribution (84.64%) for NAV and borehole spacing contribute most (45.42%) to TEM. The optimum EER, COP, NAV and TEM for the system with the optimized parameters combination are found to be 3.9355, 3.0339, CNY 106445 yuan and 2.362 ℃ respectively, which have been validated by confirmatory experiment. The utility concept has been used in this paper to find the optimum parameters combination with comprehensive consideration of all response factors (EER, COP, NAV and TEM) and the optimum combination we can get is A2 B1 C3 D1 E1 F3 G1 H3 with the response factors of 3.873, 3.023, 107212 yuan and 2.774 ℃ for EER, COP, NAV and TEM respectively.

INTRODUCTION

GSHP system is widely known for its high performance and low energy consumption despite the relatively high initial investment. Therefore, increasing the system's performance while minimizing initial investment is a major issue to promote GSHP widely. Mensah et al. (2017) carried out a numerical simulation on the optimum design of a closed loop vertical-type ground heat exchanger considering the building load and heat pump performance. Lubisa et al. (2011) considered thermodynamic analysis of a hybrid geothermal heat pump system and concluded that the performance of hybrid geothermal heat pump is superior to air-source heat pumps. Menberg et al. (2017) developed hybrid ground source heat pump system by reducing the power demand of the supply system, altering the temperature level of the supply system and reducing the space energy demand. There are many design parameters

Yiwei Xie (d201780873@hust.edu.cn) is a PhD student at University of Science and Technology, China. **Pingfang Hu (pingfanghu@163.com) is a professor** at University of Science and Technology, China.

in GSHP systems and the relationships among them are very complicated. (Li et al. 2014) Some design parameters significantly reduce the energy consumption and improve the financial performance of a GSHP project (Henault, et al 2016; Gabrielli and Bottarelli 2016). But these methods only considered the effect of single variable, which were usually selected according to the experience, to the system. Often several parameters are included in these study and they failed to consider the impact of multiple parameters on the global result. Therefore, a new method based on Taguchi to analyze the effect of multi-parameter is given in this paper. Taguchi method is one of design of experiment methods developed by Dr. Genechi Taguchi in 1940, which is an effective method to deal with the multi-parameter problem. It can conclude the influence of various parameters on the result by a series of designed experiments and estimate the optimal parameter combination at the parameter design stage.

Sholahudin and Hwataik (2016) used Taguchi method to identify significant inputs and reduce number of parameter for dynamic neural network model, which is used to predict the load of building. Song (2017) combined the Taguchi method and CFD simulation to improve the cooling effectiveness and efficiencies of data centers. Numerous studies have applied the Taguchi method to the parameters optimization of the GSHP system. (Sivasakthivel et al. 2014; Verma and Murugesan 2014 and Pandey et al. 2017)

Cervera-Vázquez (2016) optimize the global energy performance of GSHP system by putting forward a new experiment campaign for multistage heat pump units. Another paper of them (2016) make improvements on the basis of the original multistage GSHP system by combining circulation pumps frequency variation and building supply temperature compensation to satisfied the users' comfort while keep energy saving. Ruiz-Calvo (2016) gave an experiment analysis and performance evaluation of GSHPs, which can be used by researchers for model validation. Currently few studies considered the variation of the building load and dynamic energy consumption of the pump and heat pump units simultaneously for the parameters optimization of GSHP system.

This study is mainly to optimize the basic parameters combination of GSHPs with the maximum coefficient of performance (COP) and energy efficient ratio (EER) for heating and cooling mode while minimizing the net annual values (NAV) and the average temperature rise (TEM) in soil after operating for ten years. The dynamic hourly load and the variation of energy consumption for heat pump units and pump under the variation of load and flowrate are taken into consideration. A methodology based on Taguchi technology is proposed to find the optimum parameters combination for the GSHP system with EER, COP and NAV respectively. Then the ANOVA (analysis of variance) is utilized to analyze the influence of each parameter on the evaluation indexes quantitatively. Finally, the optimized evaluation has been made and confirmed by simulation.

MATHEMATICAL MODEL

1. Heat pump

The COP and heat pump capacity (Cap) are used to evaluate the heat pump model. The heat pump's COP in heating and cooling are given by Eq. (1) and Eq. (2).

$$COP_{heating} = \frac{Cap_{heating}}{P_{heating}} \quad (1)$$

$$COP_{cooling} = \frac{Cap_{cooling}}{P_{cooling}} \quad (2)$$

Where $Cap_{heating}$ and $Cap_{cooling}$ are the heat pump heating and cooling capacity at current conditions as shown in Eq. (3) and Eq. (4). $P_{heating}$ and $P_{cooling}$ are the power consumption by the heat pump in heating and cooling mode.

$$Cap_{cooling} = m_{load} \cdot Cp_{load}(T_{load,out} - T_{load,in}) \quad (3)$$

$$Cap_{heating} = m_{load} \cdot Cp_{load}(T_{load,in} - T_{load,out}) \quad (4)$$

Where m_{load} and Cp_{load} are the mass flow rate and the specific heat of the liquid on the load side of the heat pump. The performance of the heat pump model are illustrated as function of EST and ELT, which is entering source temperature and entering load temperature of the heat pump, in Figure 1, Figure 2, Figure 3 and Figure4 according to the manufacturer specification sheets. In this paper, some variables will be chosen as the control factor, such as heat pump outlet temperature and mass flowrate of both load and source side, which would significantly affect the value of EST and ELT when these factors on different levels. Therefore, this transient heat pump model can satisfied the need with the changing of control factors.

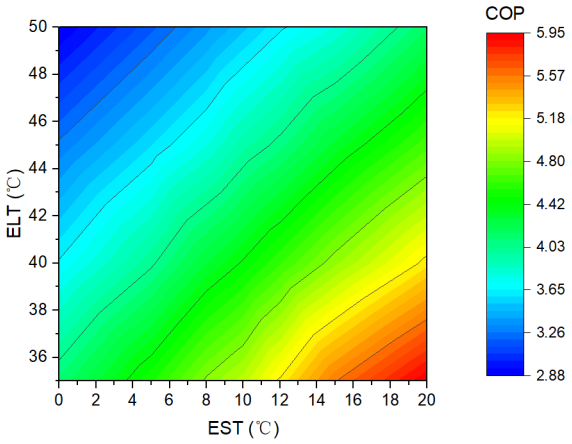

Figure 1 COP contour map in heating mode

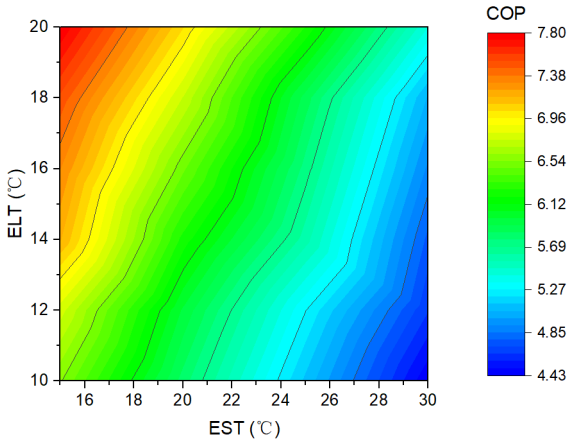

Figure 2 COP contour map in cooling mode

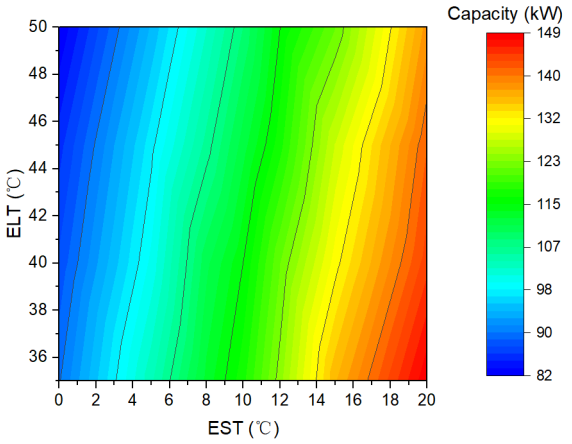

Figure 3 Heating capacity map of heat pump model

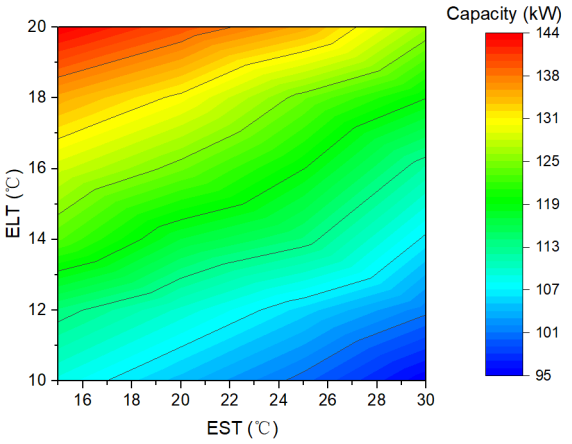

Figure 4 Cooling capacity map of heat pump model

2. Pump

In this article, we also consider the changing of the pump power consumption with the design control factors on different level, such as mass flowrate on both source and load side. The TP65-260/2 pump are chosen with the rated pump head 13.8 m, the rated power 3.75 kW and rated flowrate 55 m^3/h. The polynomial model of the pump are calculated by Eq. (5).

$$P = a_0 + a_1\left(\frac{m}{m_{rated}}\right) + a_2\left(\frac{m}{m_{rated}}\right)^2 + a_3\left(\frac{m}{m_{rated}}\right)^3 + \cdots \quad (5)$$

Where P is the power consumption of the pump and a_0, a_1, a_2, a_3 are the polynomial coefficients in pump

power curve. With m is the design flowrate and m_{rated} is the rated flowrate. Other effects of the pump such as pressure drop, temperature rise etc. are neglected.

3. EER and COP of the system

In the present analysis, the model of this GSHP system has been built in TRNSYS to calculate EER, COP and NAV in Figure 5. The equation of EER and COP are given by Eq. (6) and Eq. (7) respectively.

$$EER_{sys} = \frac{Q_{SC}}{\sum N_i + \sum N_j} \tag{6}$$

$$COP_{sys} = \frac{Q_{SH}}{\sum N_i + \sum N_j} \tag{7}$$

Where Ni is heat pump units accumulated power consumption and Nj is the pump accumulated power consumption include the source and user pump together during the season and the unit is kWh. Q_{SC} and Q_{SH} are the cumulative cooling and heating capacity of the GSHP system and the unit of it is kWh ,which are presented in Figure 6 with the red line is the heating energy demand and the blue line is the cooling demand.

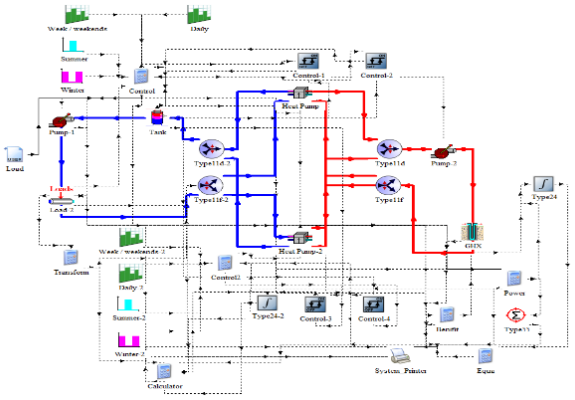

Figure 5 TRNSYS simulation model.

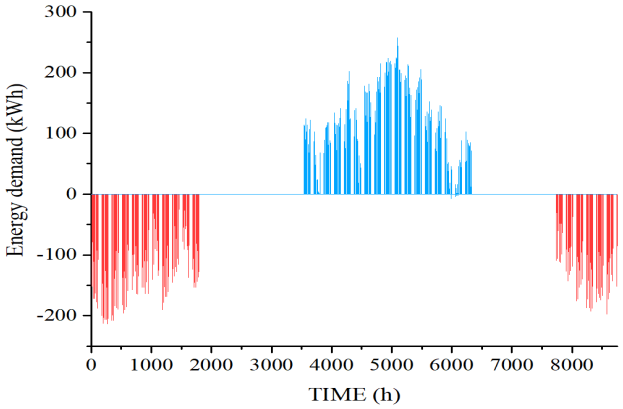

Figure 6 Energy demand of this building throughout year

4. NAV of the system

Net annual value (NAV) of the formula is calculated by Eq. (8).

$$NAV = C_r + C_m + (A/P, i, n) \cdot (C - R) \tag{8}$$

Where C is total initial investment and R is net residual value. R is calculated as $R=\varrho \cdot C$, where ϱ is residual rate chosen as 0.05. Cr is annual operating costs calculated as $C_r=\varepsilon \cdot C$, ε is a coefficient selected as 0.05. Cm is annual maintenance costs, (A/P, i, n) is capital recovery factor, which is calculated as $(A/P, i, n)=\frac{i}{1-(1+i)^{-n}}$. The formula of i is $i=\frac{u-f}{1+f}$ where i is the constant discount rate, u is the current discount rate and f is inflation rate. We consider the life of the pump, heat pump units are 10 and 20 years respectively with the life of GHX is 50 years. Electricity price is CNY 0.94 yuan/kWh. The cost of drilling and grout, the pipe cost are also included, for different type of GHX are summarized in the four columns on the left side of the Table 1. The right three columns of the Table 1 gives the cost of heat pump and pump we selected.

Table 1

Name	DN25	DN32	Unit	Name	Value	Unit
Single-U tube	95	98	yuan/m	**Heat pump**	600	yuan/kW
Double-U tube	100	105	yuan/m	**Pump**	13373	yuan/unit

SYSTEM DESCRIPTION

The schematic office building in Xi'an, China is presented in Figure 7. The area is 2557.8 m^2 and GSHP is used for heating and cooling. Both cooling and heating season are 120 days per year. The weekly operating time is from Monday to Friday and the daily operating time is from 8:00 am to 18:00 pm. The hourly load of this building for one specific years are presented in Figure 8. The blue points mean the hourly load of the building in cooling season and the red points mean the hourly load in heating season, which the maximum cooling load is 287 kW and the maximum heating load is 231 kW. Geothermal properties of soil are obtained from the TRT test. The thermal conductivity of soil is 1.78W/ (m·K) and the volume specific heat capacity of the soil 24820kJ/ (m^3·K). The initial average temperature of the soil 16.0℃. In the TRT test uncertainties are involved in the measurement of temperature, flowrate and power and the uncertainties are calculated by the method (Henk and Witte 2013): error in temperature ±0.2%, flowrate ±0.5%, power ±2%. The error of thermal conductivity and specific heat capacity that are combination error are calculated with the values of ±4.3% and ±14% respectively. Some basic parameters of ground heat exchanger (GHX) are pre-determined. The depth of GHX is 100 m, the diameter of the borehole is 0.14 m, the thermal conductivity of PE pipe is 0.49 W/ (mK) and the center distance of the pipes is 0.08 m.

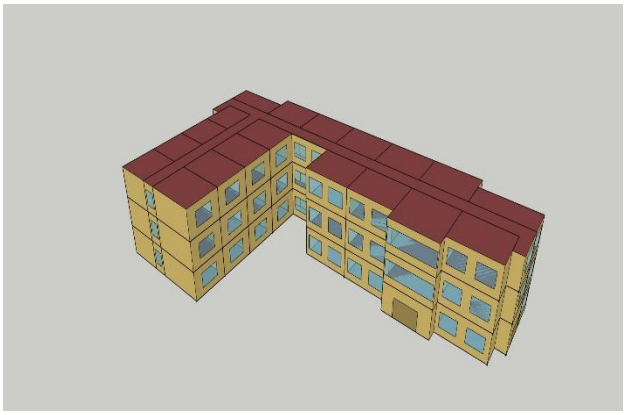

Figure 7 The office building model

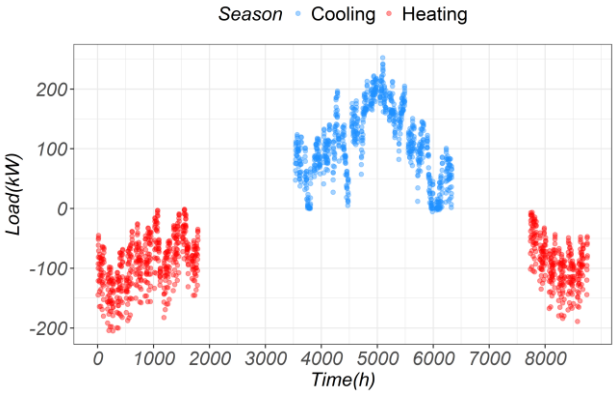

Figure 8 Building hourly load throughout year

METHODOLOGY

1. Taguchi technology

Taguchi optimization is an experimental technology, which uses orthogonal table to arrange fewer levels of combinations for experiments and uses these typical and representative experimental data to make statistical analysis on the role of factors. The main steps of this method are summarized as follows.

1. Definition the number of control parameters and levels. The choice of parameters and its levels are usually based on the previous studies and experiments. Here eight controlled parameters are selected, two of them have two levels and the others have three levels.
2. Design Taguchi orthogonal array (OA) and conduct the experiment. The OA is selected based on the controlled parameters and levels. With the help of this array can get the maximum information by conduction minimum number of experiments. For example, in this study, eight parameters with two parameter having two levels and six parameters having three levels, we need to conduct $2^2 \times 3^6 = 2916$ times experiments if we want to get the optimal parameters combination. It is so complex and time consuming to do this. Here only 36 times experiments are needed to conduct to get the maximum

information we need.

3. Analysis the result. In this studies, the signal-to-noise (S/N) ratios are used to analyze the response of the experiment trail and it can conclude the optimal parameters by using three functions: lower the better, higher the better and nominal the better. What's more, ANOVA is used to analyze the contribution of each parameters to the response factors and estimate the values of optimal response factor under the optimal controlled parameter combination.
4. Validation the result. This process is to validate the reliability of the model by comparing whether the error between the experimental value and the estimated value falls into the confidence interval or not. If the errors are outside the confidence the interval, it need return to the step 1 and redesign the parameters, which means the estimated model can't reflect on the optimal values.

2. Utility concept

Utility can be defined as the utilization of a product in response to the expectations of the customers/users which is widely used in manufacturing and quality engineering. (Prasad and Susanta, 2013) The performance parameters of utility are obtained by combining all the individual performance parameters such as EER, COP, NAV and TEM in this paper. Utility function can be expressed as Eq. (9):

$$\mathrm{U}(y_1, y_2, \dots, y_n) = \mathrm{f}(U_1(y_1), U_2(y_2), \dots, U_n(y_n)) \quad (9)$$

Where y is the performance parameters and the 'n' is the number of performance parameters. This article assumes that each factor is independent that means each response factors are not related to other factors, hence the utility function can be expressed as Eq. (10).

$$\mathrm{U}(y_1, y_2, \dots, y_n) = \sum_{j=1}^{n} U_j(y_j) \quad (10)$$

Priority basis can be calculated by defining the weighting coefficients of each response factor and setting weight coefficients in based on the relative importance of each distribution, which are usually obtained according to other studies or experience. The weighting coefficients has to satisfy the sum of them equal to 1. The weight coefficient are assigned equally to each parameters in this study (each response factors share the weighting coefficient of 0.25). The functions are represented as follow Eq. (11) and Eq. (12).

$$\mathrm{U}(y_1, y_2, \dots, y_n) = \sum_{j=1}^{n} w_j \cdot U_j(y_j) \quad (11)$$

$$P_j = A_j \times \log\left(\frac{y_j}{y_j'}\right) \text{ with } A_j = \frac{9}{\log\left(\frac{y_j^*}{y_j'}\right)} \quad (12)$$

Where the preference numbers are assumed to between 0 (representing the lowest performance value that can be accepted) and 9 (representing the highest performance). We can calculate the A value by defining the preference number as 9 so as to obtain a global optimum parameters combination. The y* is the optimum value of y_j that is the performance of the GSHP system (EER, COP, NAV and TEM) and y' is the minimum acceptable performance value. The overall utility is calculated as Eq. (13).

$$\mathrm{U} = \sum_{j=1}^{n} w_j \cdot P_j \quad (13)$$

The main purpose to apply the utility concept is to determine a global optimal parameters combination after considering the impact of various factors (EER, COP, NAV and TEM) of the GSHP system comprehensively. Figure 9 gives a detailed procedure for applying Taguchi technology and utility concept in this study, in which different phases and its logical relationship are listed.

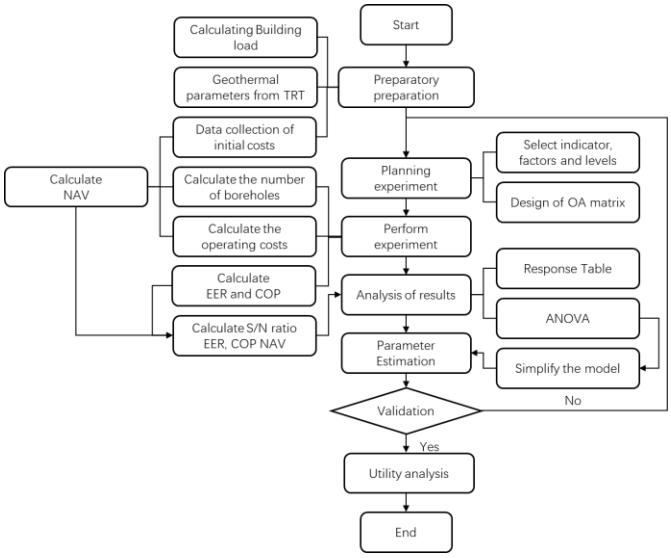

Figure 9 Flow chart for Taguchi procedure in this study

RESULTS AND DISCUSSION

In this study, eight important parameters of GSHPs had been chosen as the controlled factors in Taguchi orthogonal. They are: number of U-Tubes per bore (A), diameter of pipe (B), outlet load temperature in cooling mode (C), load side mass flow rate (D), source side mass flow rate (E), thermal conductivity of fill material (F), outlet load temperature in heating mode (G) and borehole spacing (H). Here the factors A and B have two levels because single-U and double-U are the most common type of boreholes and DN25 and DN32 are the most commonly used buried pipe diameter in China. Other factors are considered at three levels. The outlet load temperature in cooling mode and heating load (C and G) are 7 ℃ and 45 ℃ in the initial system design. We increase and decrease the levels of change by 1 ℃ around this initial design parameter and get the three levels of these parameters. The levels of mass flowrate (D and E) are obtained in same reason, which are around the initial design values with 37.5 m3/h and 42.5 m3/h. The levels of factor G is obtained because we choose three different fill material. The borehole spacing is initially designed in 5 m, which is commonly used in China, and 0.5 m is selected as a gap that the levels are around the 5 m. The values of these controlled factors at different level are presented in Table 2.

Table 2 . Control factors and their levels

Label	Factors	Level		
		1	2	3
A	**Number of U-Tubes per bore**	1	2	
B	**Diameter of pipe (m)**	0.025	0.032	
C	**Outlet load Temperature in cooling mode (℃)**	6	7	8
D	**Load side mass flow rate (m^3/h)**	35	37.5	40
E	**Source side mass flow rate (m^3/h)**	40	42.5	45
F	**Thermal conductivity of fill material (W/mK)**	1.56	1.95	2.27
G	**Outlet load temperature in heating mode (℃)**	44	45	46
H	**Borehole spacing (m)**	4.5	5	5.5

EER, COP, NAV and TEM are chosen as response factors to evaluate the performance of the GSHP system under the optimum parameters combinations. Among those response factors, EER and COP are beneficial in nature where higher values are preferred, and on the other hand, the low value of NAV and TEM are usually desired as it is a non-beneficial criterion. A total of 36 trials need to be implemented and a mixed level L_{36} (2^2, 3^6) orthogonal array has been selected for deciding the experimental layout and the parameters-level matrix trail runs presented in Table 3. It also gives the values of EER, COP, NAV and TEM calculating from TRNSYS and the signal to noise ratio (S/N ratio) for all 36-trail runs. In Taguchi design, signal-to-noise ratio is a measure of robustness used to identify control factors that reduce product or process variability by minimizing the effects of uncontrollable factors (noise factors).The S/N ratio of the EER and COP are calculated using the higher the better concept while the S/N ratio of the NAV and TEM are calculated by using the lower the better. The formulas are given in Eq. (14) and Eq. (15). The last column is the number of boreholes that are calculated according the geothermal parameters from TRT test and the controlled parameters we selected.

$$\text{Higher the better } S/N = -10log_{10}\left(\frac{1}{n}\sum_{i=1}^{n}\frac{1}{y_i^2}\right) \quad (14)$$

$$\text{Lower the better } S/N = -10log_{10}(\frac{1}{n}\sum_{i=1}^{n}y_i^2) \quad (15)$$

Attention that the indicators (EER, COP and its S/N ratio) are given with 3 decimals in Table 3. This is because the difference of EER and COP among the experiments is very small. Therefore, these indicators retain three decimal places will reflect on the difference among the experiments better and provide with more accurate results for ANOVA in the next step.

Table 3 . Taguchi L_{36} (2^2, 3^6) orthogonal array

Exn	A	B	C	D	E	F	G	H	EER	COP	NAV	TEM	S/N EER	S/N COP	S/N NAV	S/N TEM	No. B
1	1	1	1	1	1	1	1	1	3.837	3.022	115200	2.898	11.680	9.606	-101.229	-9.241	54
2	1	1	2	2	2	2	2	2	3.839	2.927	114281	2.698	11.683	9.329	-101.160	-8.621	50
3	1	1	3	3	3	3	3	3	3.842	2.865	113107	2.515	11.690	9.143	-101.070	-8.010	47
4	1	1	1	1	1	1	2	2	3.823	2.957	115381	2.653	11.648	9.417	-101.243	-8.476	53
5	1	1	2	2	2	2	3	3	3.807	2.874	113583	2.522	11.611	9.171	-101.106	-8.036	48
6	1	1	3	3	3	3	1	1	3.871	2.993	113691	2.963	11.756	9.523	-101.114	-9.434	49
7	1	1	1	1	2	3	1	2	3.817	3.017	113345	2.779	11.634	9.592	-101.088	-8.879	48
8	1	1	2	2	3	1	2	3	3.780	2.917	114627	2.452	11.550	9.299	-101.186	-7.792	51
9	1	1	3	3	1	2	3	1	3.911	2.883	114716	2.900	11.846	9.197	-101.192	-9.248	51
10	1	2	1	1	3	2	1	3	3.740	2.989	111047	2.646	11.458	9.512	-100.910	-8.452	45
11	1	2	2	2	1	3	2	1	3.825	2.948	110877	3.128	11.654	9.389	-100.897	-9.907	45
12	1	2	3	3	2	1	3	2	3.827	2.866	113991	2.716	11.657	9.146	-101.137	-8.679	49
13	1	2	1	2	3	1	3	2	3.748	2.863	114477	2.776	11.476	9.136	-101.174	-8.868	49
14	1	2	2	3	1	2	1	3	3.789	2.974	110885	2.624	11.570	9.467	-100.897	-8.378	45
15	1	2	3	1	2	3	2	1	3.874	2.951	112232	3.083	11.764	9.399	-101.002	-9.779	45
16	1	2	1	2	3	2	1	1	3.761	2.976	112867	3.113	11.506	9.473	-101.051	-9.863	47
17	1	2	2	3	1	3	2	2	3.816	2.935	112227	2.855	11.632	9.352	-101.002	-9.113	45
18	1	2	3	1	2	1	3	3	3.832	2.885	112452	2.528	11.669	9.203	-101.019	-8.057	47

19	2	1	1	2	1	3	3	3	3.777	2.895	108430	2.828	11.543	9.233	-100.703	-9.030	39
20	2	1	2	3	2	1	1	1	3.781	2.976	110397	3.181	11.552	9.472	-100.859	-10.05	44
21	2	1	3	1	3	2	2	2	3.862	2.949	108994	2.899	11.735	9.393	-100.748	-9.244	42
22	2	1	1	2	2	3	3	1	3.793	2.886	110356	3.284	11.579	9.207	-100.856	-10.33	41
23	2	1	2	3	3	1	1	2	3.765	2.960	110179	2.901	11.515	9.425	-100.842	-9.252	44
24	2	1	3	1	1	2	2	3	3.866	2.956	107491	2.731	11.744	9.415	-100.627	-8.725	40
25	2	1	1	3	2	1	2	3	3.722	2.910	109483	2.754	11.416	9.278	-100.787	-8.800	42
26	2	1	2	1	3	2	3	1	3.806	2.892	110292	3.217	11.609	9.224	-100.851	-10.15	42
27	2	1	3	2	1	3	1	2	3.901	3.024	108059	2.935	11.824	9.612	-100.673	-9.352	41
28	2	2	1	3	2	2	2	1	3.743	2.929	110486	3.353	11.464	9.334	-100.866	-10.508	40
29	2	2	2	1	3	3	3	2	3.787	2.895	110008	3.045	11.566	9.233	-100.828	-9.673	39
30	2	2	3	2	1	1	1	3	3.794	2.984	108366	2.763	11.582	9.496	-100.698	-8.829	40
31	2	2	1	3	3	3	2	3	3.695	2.909	108912	2.930	11.352	9.275	-100.741	-9.336	37
32	2	2	2	1	1	1	3	1	3.799	2.900	111028	3.240	11.593	9.248	-100.909	-10.21	42
33	2	2	3	2	2	2	1	2	3.833	2.988	108937	2.990	11.671	9.508	-100.744	-9.512	40
34	2	2	1	3	1	2	3	2	3.766	2.877	110316	3.058	11.518	9.179	-100.853	-9.710	40
35	2	2	2	1	2	3	1	3	3.764	2.991	107791	2.885	11.513	9.516	-100.652	-9.203	37
36	2	2	3	2	3	1	2	1	3.794	2.915	110890	2.683	11.582	9.293	-100.898	-8.571	38

The average response of S/N ratios for each level of eight parameters for EER, COP and NAV are summarized in Figure 10, Figure 11, Figure 12 and Figure 13. Figure 10 and Figure 11 shows the S/N variation with different levels for EER and COP. Compared with other factors having big change with the variation of the levels, factor G (outlet load temperature in heating mode) in Figure 10 shows little change with different levels, which illustrates this factor has small impact on EER. Low level of the factors A, B, D, E, H and high level of the factor C contribute to the higher S/N ratio of EER for the GSHP system. It is observed that the factor D, E, F have an obvious influence on the S/N ratio of COP for the system and lower the level of these three factors contribute to the higher COP in Figure 11. Figure 12 exhibits the S/N ratio variation for NAV and it is observed that the factor A has the biggest change on the variation of levels compared with other controlled factors. Figure 13 presents the S/N ratio of TEM, in which factor H has the biggest variation on different levels and the factor A followed by.

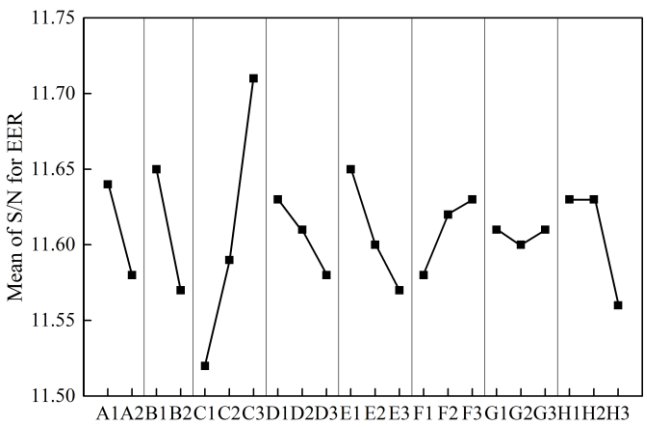

Figure 10 Mean of S/N for EER

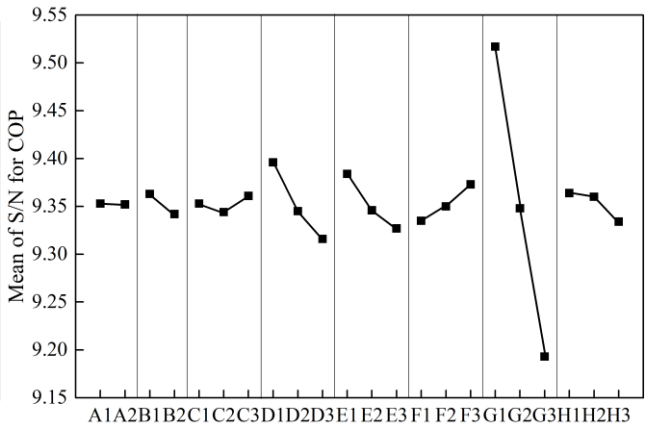

Figure 11 Mean of S/N for COP

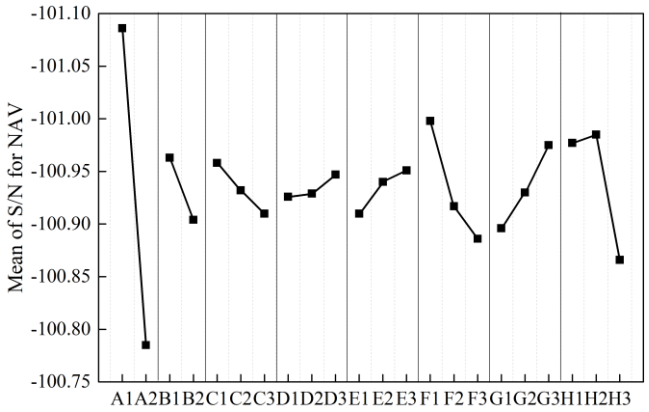

Figure 12 Mean of S/N for NAV

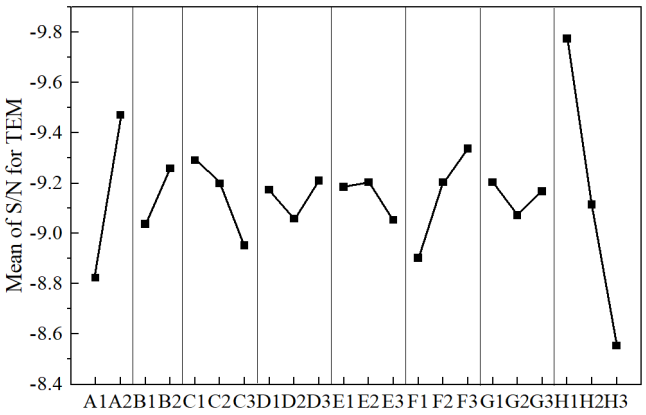

Figure 13 Mean of S/N for TEM

The best parameters combination of GSHPs can be determined by selecting the level with highest S/N ratio for EER and COP and with the lowest absolute value of S/N ratio for NAV. Hence the optimum control parameters levels are A1 (A at level 1), B1 (B at level 1), C3 (C at level 3), D1 (D at level 1), E1 (E at level 1), F3 (F at level 3), G3 (G at level 3), H1 (H at level 1) for EER and A1, B1, C3, D1, E1, F3, G1, H1 for COP. Following the best set of combination parameters for NAV is A2, B2, C3, D1, E1, F3, G1, H3. What's more, A1, B1, C3, D2, E3, F1, G2, H3 is the optimal parameters combination for TEM.

ANOVA ANALYSIS

We use ANOVA to estimate the relative importance of these control factors by calculating the percentage contribution of each parameter in overall response. Degree of freedom, sum of squares, mean of squares, F ratio, P value, percentage contribution and significance by different control factors are included in variance analysis Table 4-7. The aim of ANOVA is to analyze the importance of each factor to the result by verifying whether the testing statistics F ratio falls within the rejection region or not. The p-value is the minimum level of rejection of the null hypothesis. Sum of square (SS), degree of freedom, mean of square (MS) and F ratio have been calculated by using the Eq.(16) and Eq.(17).

$$SS=\left\{\begin{array}{c}(\text{sum of S/N ratio level I})^2\\ +(\text{sum of S/N ratio level II})^2\\ +(\text{sum of S/N ratio level III})^2\text{-C.F}\end{array}\right\} \quad (16)$$

$$\text{Correction factor(C.F)}=\frac{(\text{sum of S/N})^2}{N} \quad (17)$$

Where N is the total number of experiments and Degree of Freedom=level-1 Mean of square=$\frac{SS}{DOF}$ and F ratio=$\frac{\text{Mean of square}}{\text{Mean square error}}$.

Table 4. ANOVA for EER

Factors	Df	SS	MS	F	P	Contribution	Sig
A	1	0.035191	0.035191	197.68	0	13.62%	**
B	1	0.053564	0.053564	300.89	0	20.72%	**
C	2	0.216478	0.108239	608.02	0	41.88%	**
D	2	0.017403	0.008702	48.88	0	3.37%	**

E	2	0.045549	0.022775	127.93	0	8.81%	**
F	2	0.016703	0.008351	46.91	0	3.23%	**
G	2	0.000792	0.000396	2.23	0.133	0.15%	
H	2	0.042484	0.021242	119.32	0	8.22%	**
Error	21	0.003738	0.000178				
Total	35	0.431903				100.00%	

$F_{0.05}$ (1, 21) =4.32, $F_{0.01}$ (1, 21) =8.02, $F_{0.05}$ (2, 21) =3.47, $F_{0.01}$ (2, 21) =5.78

"*" represents the effect is significant, "**" represents the effect is extremely significant.

Table 5. ANOVA for COP

Factors	Df	SS	MS	F	P	Contribution	Sig
A	1	0.000005	0.000005	0.02	0.888	0.00%	
B	1	0.003942	0.003942	15.85	0.001	1.11%	
C	2	0.001689	0.000845	3.4	0.053	0.24%	
D	2	0.039791	0.019896	79.99	0	5.59%	*
E	2	0.020166	0.010083	40.54	0	2.83%	
F	2	0.008756	0.004378	17.6	0	1.23%	
G	2	0.627755	0.313877	1261.9	0	88.12%	**
H	2	0.006316	0.003158	12.7	0	0.89%	
Error	21	0.005223	0.000249				
Total	35	0.713645				100.00%	

Table 6. ANOVA for NAV

Factors	Df	SS	MS	F	P	Contribution	Sig
A	1	0.79342	0.793419	213.84	0	84.46%	**
B	1	0.03091	0.030912	8.33	0.009	3.29%	
C	2	0.01396	0.00698	1.88	0.177	0.74%	
D	2	0.00315	0.001577	0.42	0.659	0.17%	
E	2	0.01069	0.005347	1.44	0.259	0.57%	
F	2	0.08132	0.040658	10.96	0.001	4.33%	*
G	2	0.0372	0.018601	5.01	0.017	1.98%	
H	2	0.0838	0.041902	11.29	0	4.46%	*
Error	21	0.07792	0.00371				
Total	35	1.13238				100.00%	

Table 7. ANOVA for TEM

Factors	Df	SS	MS	F	P	Contribution	Sig
A	1	3.7696	3.7696	50.07	0	38.24%	**
B	1	0.4397	0.43975	5.84	0.025	4.46%	*
C	2	0.7311	0.36557	4.86	0.018	3.71%	*
D	2	0.1486	0.07432	0.99	0.389	0.76%	
E	2	0.1615	0.08075	1.07	0.36	0.82%	
F	2	1.1914	0.59568	7.91	0.003	6.04%	*
G	2	0.11	0.055	0.73	0.493	0.56%	
H	2	8.9549	4.47743	59.47	0	45.42%	**
Error	21	1.5809	0.07528				
Total	35	17.0878				100.00%	

It can be observed from Table 4 that almost all the factors except G (outlet load temperature in heating mode) have extremely significant effect on the EER and the higher to lower order percentage contribution of parameters can be arranged as CBAEHDF. The highest contribution comes from the outlet load temperature in cooling mode (C) with 41.88% followed by diameter of pipe (B) with 20.72% and number of U-Tubes per bore (A) with 13.62%. Table 5 shows the ANOVA results for COP of GSHP system, which indicate only load side mass flow rate (D) and outlet load temperature in heating mode (G) have a significant effect on COP. Among them, Factor G contributes the highest percentage of 88.12% and it has an extremely significant effect on the COP. Factor D is followed with the percentage of 5.59%. From this table the COP contributing parameters ranking can be obtain as GDEFBHCA. From the values shown in Table 6 for NAV, the important controlled factor are found to be the number of U-Tubes per bore (A), thermal conductivity of fill material (F) and borehole spacing (H). It can easily notice that the most important factor is the number of U-Tubes per bore (A) for NAV, which contributes 84.64%. Combined the results in previous step that the double U is favorable, we can conclude that the number of borehole in initial investment has a great impact on the NAV because Double U needs less borehole than the Single U when the building load is fixed. Factor H and F is followed with the percentage of 4.46% and 4.33%. The number of U-Tubes per bore (A) and borehole spacing (H) have an extremely significant effect on the average temperature rise of soil (TEM) with the contribution of 38.24% and 45.42% respectively as shown in Table 7. Factor D, E and G are the insignificant variables compared with the others.

It is worthy taking note of that the factors related to GHX having an extremely significant effect on EER become insignificant when considering the COP, such as the factor A, B, F and H. This is because that the design of the GHX is based on the cooling load in summer, which is higher than the heating load in winter when the power of the heat pump and pumps are considered. Therefore, the number of GHX is enough for cooling condition but much for heating condition, which leads to the effect that factors relevant to GHX are insignificant for COP.

CONFIRMATION TEST

1. Parameter Estimation

The first step for confirmation test is to estimate the optimal values of the indicators (EER, COP, NAV and TEM) and the mathematical model is given as Eq. (18).

$$\hat{y}_{opt} = \hat{\mu} + \hat{a}_i + \hat{b}_i + \hat{c}_i + \hat{d}_i + \hat{e}_i + \hat{f}_i + \hat{g}_i \tag{18}$$

With $\hat{\mu}=\bar{y}$, $\hat{a}_i=\overline{A}_i-\bar{y}$, $\hat{b}_i=\overline{B}_i-\bar{y}$, $\hat{c}_i=\overline{C}_i-\bar{y}$, $\hat{d}_i=\overline{D}_i-\bar{y}$, $\hat{e}_i=\overline{E}_i-\bar{y}$, $\hat{f}_i=\overline{F}_i-\bar{y}$, $\hat{g}_i=\overline{G}_i-\bar{y}$. Where $\bar{y}$ is the means of the entire response factor, $\overline{X}_i$ (X=A, B, C, D, E, F, G, H) represents the means of response factors on the different level selected and i is the levels of the factors. According to the ANOVA results from Table 4-7, the optimum response factors for EER, COP and NAV can be estimated under the optimum parameter combination selected previously. The insignificant factors can be neglected during the process of estimation so as to simplify the model. Confirmation test is carried out based on the estimated optimal response factors with the optimum parameter combination coming from Figure 10-13. Simultaneously, an interval estimation with 95% confidence interval is carried out to determine the range of these response factors. The confidence interval is given as Eq. (19):

$$\begin{cases} S_e' = S_e + \sum S_{in} \\ df_e' = df_e + \sum df_{in} \\ n_e = \frac{N}{1+\sum S_{sig}} \end{cases} \text{ and } (\hat{y}_{opt} - \sqrt{\frac{F_\alpha(1,df_e')S_e'}{n_e df_e'}}, \hat{y}_{opt} + \sqrt{\frac{F_\alpha(1,df_e')S_e'}{n_e df_e'}} \quad (19)$$

Where S_{in} is the sum of square (SS) of the insignificant factors, S_e is the mean square error, df_{in} is the degree of freedom of insignificant factors, N is the total number of test and S_{sig} is the sum of square (SS) of the significant factors. The interaction between parameters is not taken into consideration. The optimized EER, COP, NAV and TEM at the optimum parameters combination are estimated to be 3.936, 3.034, 106445 and 2.362 respectively. The confirm values for EER, COP ,NAV and TEM calculated by using TRNSYS software are falling within the region of interval estimates at 95% confidence and the predictive values are all fully close to the confirmed values (see Table 8). Therefore, the optimal response factors obtained from the model have been validated by confirmatory experiment using TRNSYS simulation.

Table 8 Confirmation

Response factors	df'	SSe'	ne'	Predictive value	Confidence interval	Confirmed value
EER	23	0.000894	2.769	3.936	(3.9278, 3.9433)	3.940
COP	31	0.005352	7.2	3.034	(3.0239, 3.0439)	3.031
NAV	30	28848374	6	106445	(105627, 107263)	106054
TEM	27	0.22105	6	2.308	(2.23221,2.384)	2.362

2. Utility analysis

From the result of Taguchi analysis, the optimum parameters combination for response factors are obtained respectively. In order to find out the global optimum parameters combination of this GSHP system from all the parameters combination, the utility concept method are use. The given response factor EER and COP need to be as higher as possible while NAV and TEM are the opposite. We use the parameter estimation model in previous steps to estimate performance (EER, COP, NAV and TEM) of all the parameters combinations for 2916 times and then calculate the U values of each combination. The optimum parameters levels combination for achieving maximum EER and COP while minimum NAV and TEM of this GSHP system are found to be A2 (double U), B1 (pipe diameter with 25mm), C3 (8℃ of the heat pump outlet temperature in cooling mode), D1 (the load side mass flowrate with 35 m^3/h), E1 (the source side mass flowrate with 35 m^3/h), F3 (thermal conductivity with 2.27 W/mK), G1 (44℃ of the heat pump outlet temperature in heating mode), H3 (borehole spacing for 5.5m). The optimum response factor (EER, COP, NAV and TEM) of this combination are 3.873, 3.023, 107212, 2.774 respectively with the utility values are calculated as 7.098.

CONCLUSION

In this study, the performance of the GSHP system has been analyzed using Taguchi method, ANOVA test model and utility concept. Eight parameters at mixed levels of operation for the GSHP system are considered. A TRNSYS model is developed to calculate the system EER, COP, NAV and TEM according to the design of Taguchi method. The optimum combination of parameters are obtained for EER, COP, NAV and TEM respectively. The significant effects of each control factor on the response factors for this GSHP system are quantified according to the result of ANOVA. The main findings are outlined as follows;

The optimum combination of the parameters for the GSHP system are selected by Taguchi method as A1 B1 C3 D1 E1 F3 G3 H1 for EER, A1 B1 C3 D1 E1 F3 G1 H1 for COP , A2 B2 C3 D1 E1 F3 G1 H3 for NAV and A1 B1 C3 D2 E3 F1 G2 H3 for TEM respectively. According to the result of ANOVA, the heat pump outlet temperature (factor C and factor G) are the most influencing (41.88% and 88.12% respectively) control factors of the system for EER and COP respectively while the number of U-Tubes per borehole (factor A) have the major contribution (84.64%) for NAV and borehole spacing (factor H) contribute most (45.42%) to TEM.

The optimum EER, COP, NAV and TEM of the GSHP system have been estimated with the optimized parameters combination, which are found to be 3.9355, 3.0339, CNY 106445 yuan and 2.36 ℃ respectively. The predicted value has been validated by the confirmed value computed from the TRNSYS software.

The utility concept combined the Taguchi method has been used in this paper to find the optimum parameters combination with comprehensive consideration of all response factors (EER, COP, NAV and TEM). After calculating the utility values, the optimum combination can we get is A2 B1 C3 D1 E1 F3 G1 H3 with the response factors of 3.873, 3.023,CNY 107212 yuan and 2.774 ℃ for EER, COP, NAV and TEM respectively.

ACKNOWLEDGMENTS

The authors would like to acknowledge the supports from the National Nature Science Foundation of China (No.51678262)

REFERENCES

Benjamin Hénault, Philippe Pasquier, Michael Kummert. 2016. Financial optimization and design of hybrid ground-coupled heat pump systems. Applied Thermal Engineering 93 (2016):72–82

F. Ruiz-Calvo, J. Cervera-Vázquez, C. Montagud*, J.M. Corberán. 2016. Reference data sets for validating and analyzing GSHP systems based on an eleven-year operation period. Geothermics 64 (2016) 538–550

J. Cervera-Vázquez, C. Montagud, J.M. Corberán. 2015. In situ optimization methodology for ground source heat pump systems: Upgrade to ensure user comfort. Energy and Buildings 109 (2015) 195–208.

J. Cervera-Vázquez, C. Montagud, J.M. Corberán. 2015. In situ optimization methodology for the water circulation pumps frequency of ground source heat pump systems: Analysis for multistage heat pump units. Energy and Buildings 88 (2015) 238–247.

Kathrin Menberg,Yeonsook Heo, Wonjun Choi, Ryoz oOoka, Ruchi Choudhary, Masanori Shukuya. 2017. Exergy analysis of a hybrid ground-source heat pump system, Applied Energy 204 (2017) 31–46.

Kwesi Mensah, Yong-Sung Jang, Jong Min Choi. 2017. Assessment of design strategies in a ground source heat pump system. Energy and Buildings 138 (2017) 301-308.

Laura Gabrielli, Michele Bottarelli. 2016. Financial and economic analysis for ground-coupled heat pumps using shallow ground heat exchangers. Sustainable Cities and Society 20 (2016):71–80.

Luthfi I. Lubis, Mehmet Kanoglu, Ibrahim Dincer, Marc A. Rosen. 2011. Thermodynamic analysis of a hybrid geothermal heat pump system, Geothermics 40 (2011) 233–238.

Navdeep Pandey, K. Murugesan, H.R. Thomas. 2017. Optimization of ground heat exchangers for space heating and cooling application using Taguchi method and utility concept. Applied Energy 190 (2017): 421-438.

Prasad Karande, Susanta Kumar Gauri, Shankar Chakraborty, 2013. Applications of utility concept and desirability function for materials selection. Materials and Design 45 (2013) 349–358.

Rongling Li, Ryozo Ooka, Masanori Shukuya. 2014. Theoretical analysis on ground source heat pump and air source heat pump systems by the concepts of cool and warm exergy, Energy and Buildings 75 (2014) 447–455.

S. Sholahudin, Hwataik Han. 2016. Simplified dynamic neural network model to predict heating load of a building using Taguchi method. Energy 115 (2016): 1672-1678.

T.Sivasakthivel, K.Murugesan, H.R.Thomas. 2014. Optimization of operating parameters of ground source heat pump system for space heating and cooling by Taguchi method and utility concept. Applied Energy 116 (2014):76-85.

Vikas Verma, K. Murugesan. 2014. Optimization of solar assisted ground source heat pump system for space heating application by Taguchi method and utility concept. Energy and Buildings 82 (2014) 296-309.

Zhihang Song. 2017. Studying the fan-assisted cooling using the Taguchi approach in open and closed data centers. International Journal of Heat and Mass Transfer 111 (2017): 593-601.

Henk J.L. Witte. 2013. Error analysis of thermal response tests. Applied Energy 109 (2013) 302–311.

[This page has been intentionally left blank]

IGSHPA SWEDEN 2018 Research Conference

DOI: 10.22488/okstate.18.000045

A Foundation Wall Heat Exchanger Model and Validation Study

Ida Shafagh **Simon Rees**

ABSTRACT

Making use of foundation substructural elements as ground heat exchangers is an attractive option for larger non-residential buildings. An alternative to Energy Piles is to use wall substructures – so called diaphragm or screen walls – with embedded pipes that are partly below ground and partly exposed to basement spaces. This paper will describe the development of a model of such a heat exchanger that uses a weighting factor approach known as Dynamic Thermal Networks (DTN). This approach allows for detailed representation of the wall section geometry and multiple boundary conditions. In this case thermal boundary conditions are applied at surfaces representing the adjacent ground and the semiexposed basement wall surface in addition to the pipe surface. The weighting factors for the model have been derived using a parametric numerical model that has been developed using the OpenFOAM library. Validation of the model has been carried out using data from an extended series of thermal response test (TRT) measurements at a full-scale diaphragm wall heat exchanger in Barcelona. In this paper, development of the model using the DTN approach will be briefly described along with the parametric numerical modelling approach used to derive the weighting factor data. Validation test procedures will be presented along with comparisons between the predicted and measured fluid temperatures and heat transfer rates. Given some uncertainty in the experimental thermal properties, the model was able to predict the dynamics of thermal response over a range of operating conditions with reasonable accuracy and using very modest computational resources.

INTRODUCTION

One of the grand challenges confronting the world today is to meet the growing demand for energy while addressing the environmental and climate impacts of fossil fuels consumptions. A large portion of energy consumptions in developed countries corresponds to heating of residential and commercial buildings (Pérez-Lombard et al., 2008). Exploitations of sustainable and renewable energy resources for direct use as thermal energy in such spaces can significantly reduce the need for conventional fuels and therefore decrease greenhouse gas emissions. To that end, geothermal energy represents an indispensable choice for its applicability in variable atmospheric conditions. Depending on its application geothermal energy can be extracted from deep or near surface reservoirs. Shallow geothermal energy is mainly used for the purpose of heating and cooling of buildings, referred to as its direct use. One important aspect of direct geothermal use is its applicability in almost all geographic locations (Lund et al., 2011).

To extract energy from the ground reinforced substructural elements equipped with heat exchanger pipes are used (Florides and Kalogirou, 2007). The ground works well as a heat exchanger since the underground temperature stays constant throughout the year and the ground temperature below 10m underground is not affected by the seasonal changes in outdoor air temperature (Droulia et al., 2009). Using substructures as heat exhchangers started in

Ida Shafagh (I.Shafagh@leeds.ac.uk) is postdoctoral research fellow and Simon Rees (S.J.Rees@leeds.ac.uk) is professor of building energy systems at the University of Leeds.

the 1980s, starting from ground-bearing slabs with the first adoption of diaphragm walls as heat exchangers being reported in 1996 in Austria and Switzerland (Brandl, 2006).

To date, numerious investigations into performance of thermos-active piles have been carried out (Esen and Inalli, 2009; Hepbasli et al., 2003; Li et al., 2006; Lim et al., 2007) while diaphragm wall heat exchangers (DWHE) are less researched (Rees, 2016). Brandl (2006) studied heat transfer in diaphragm walls applied in three main pilot projects including a rehabilitation centre, a traffic tunnel, and metro stations in addition to further smaller projects. Adam and Markiewicz (2009) performed finite element simulations to calculate heating and cooling performance of absorber elements such as diaphragm walls at different absorber distances. They reported that with larger distances the thermal power will decrease as well as the installation cost tending to an optimum. However, it was emphasized that their results are only valid for the studied case and may vary significantly for other geothermal systems while the method is applicable to any geothermal energy system installed in foundation elements. Xia et al. (2013) made the first attempt to experimentally investigate heat transfer performance of DWHEs and through comparison with borehole heat exchangers (BHE) revealed heat transfer characteristics of DWHEs and the factors influencing heat exchange rate in such geostructures. Sun et al. (2013) developed two-dimensional heat transfer models for DWHEs according to the structural features, i.e. over and under the excavation line, based on which a design model for such energy geostructures was proposed. Their models showed good agreement with numerical solutions and measured data.

Kürten et al. (2013) proposed a new numerical approach for the thermal analysis of DWHEs and verified their findings with laboratory tests. Bourne et al. (2016b) conducted numerical analysis to establish the heat exchange mechanisms in DWHEs, and reported that the main mechanism is between the air-void and wall rather than the ground. In another study Bourne-Webb et al. (2016a) identified communalities and differences between the methods used for evaluating BHEs and energy geostructures. Sterpi et al. (2017) investigated the energy performance and short and long term influence on the soil temperatures using finite element therml analysis. Furthermore, they carried out finite element thermo-mechnical analysis to highlight the wall geothecnical and structural response. Coletto and Sterpi (2016) used coupled thermo-mechanical analysis to study the heat transfer effects on the soil temperatures, the wall internal actions and the soil-structure interaction. Di Donna et al. (2016) used numerical simulation and statistical analysis to highlight the parameters governing energy efficiency in DWHEs. Soga and Rui (2016) summerised the current understanding on the performance of energy geostructures and discussed some design considerations. They suggested that more work is required to build confidence in the use of such substructure heat exchangers.

Major insights into heat transfer processes between DWHEs and their surrounding boundaries can be provided by monitoring temperature data from full-scale in-situ cases which conventionally is carried out using a thermal response test (TRT) for substructure heat exchangers. In the present work, a TRT apparatus that injects heat energy at a constant rate into one end of the loop and measures the outflow temperature at the other end is used to stimulate the heat exchanger and derive data for model validation. In contrast to a TRT we are not seeking to parametrically evaluate the ground or concrete thermal properties. To interprete such temperature data and evaluate temperature evolution in the circulating fluid as a function of time a suitable heat transfer mathematical model is required. Various mathematical models are inrtroduced for the analysis of heat exchange processes whithin a borehole heat exchanger and pile foundations, however, there are few models concerning DWHE due to their complexity. Temperature profiles predicated by the two-dimensional heat transfer model developed by Sun et al. (2013) show limited consistency with the experimental data but have been considered adequate by the authors. A thermal resistance model that takes rotational symmetry, number of pipes, and the spatial separation into account was presented and implemented into a finite difference code by Kurten et al. (2015). Their model does not consider seasonal fluctuation of the near surface temperature and the groundwater. In the present work, a combination of finite volume analysis and an approach known as dynamic thermal networks (DTN) proposed by Claesson (2002) and Wentzel (2005) is used for calculating dynamic conduction heat transfer in DWHEs. DTN is a response factor method that can provide efficient simulation of complex three-dimensional geometries such as DWHE with the basement, pipe and adjacent ground as temperature boundaries. To that end, the corresponding geometry of a DWHE is created and dicretized in

OpenFOAM (Weller et al., 1998). OpenFOAM was also employed to obtain the weighting factor series required as inputs to the DTN model. The experimental inlet temperature, ambient temperature, and the thermal properties of the ground and concrete were employed in the model to predict the outlet temperature of the DWHE over a period of 8 weeks. The method is verified against experimental data collected from an in-situ DWHE installation.

DIAPHRAGM WALL HEAT EXCHANGER (DWHE)

A schematic representation of a diaphragm wall equipped with heat exchanger pipes is illustrated in Figure 1-a and Figure 1-b. The wall depth varies depending on its application. High density polyethylene pipe (HDPE) or cross-linked polyethene (PEX) pipe is typically used to contain the heat exchange fluid in a closed loop. The pipes are installed by attachement to the reinforcement steel cage of the concrete wall closer to the side facing the ground. There are various possible layouts for arranging the pipe whithin the wall; the one shown in Figure 1 is a common configuration. Walls are typically constructed in panels depending on the practicalities of assembly and lifting and it is often convenient to arrange pipe circuits to be divided accordingly, with some consideration to available pipe lengths and limiting hycraulic pressure drops.

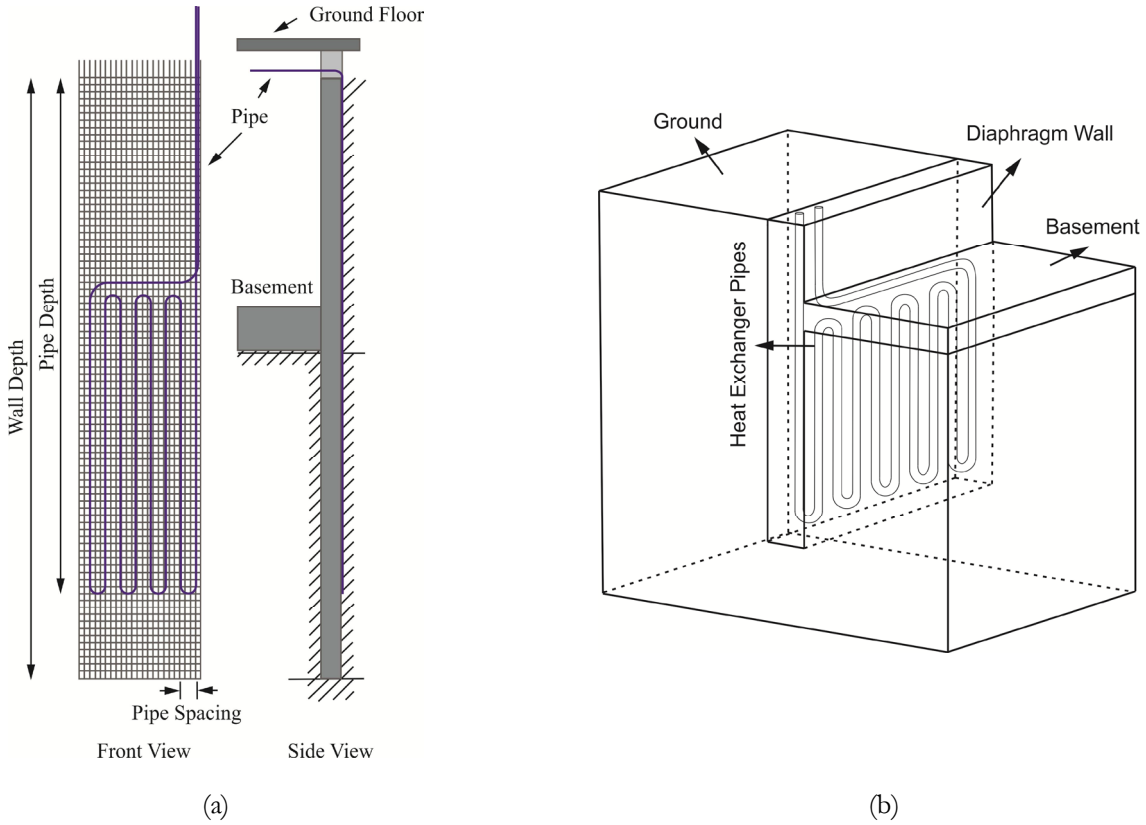

Figure 1 Schematic representation of a diaphragm wall heat exchanger and its surrounding boundaries.

HEAT TRANSFER MODEL

The DWHE studied here consists of a diaphragm wall of 17m depth and thickness of 0.6m embedded with a 93m long pipe cuircuit looped in veritical orientation (4 loops as shown in Figure 1). Pipe inner and outer diameters

are 21mm and 25mm, respectively. To simplify the calculations and considering the symmetric configuration of the wall an isolated section containing only one pipe is considered. The corresponding geometry was created and dicretized in OpenFOAM (Weller et al., 1998) using the respective blockMesh utility, as shown in Figure 2. This parametric mesh generation tool allows generation of meshes in an automatied manner. An additional utility was developed to allow generation of DWHE meshes from relatively few design parameters.

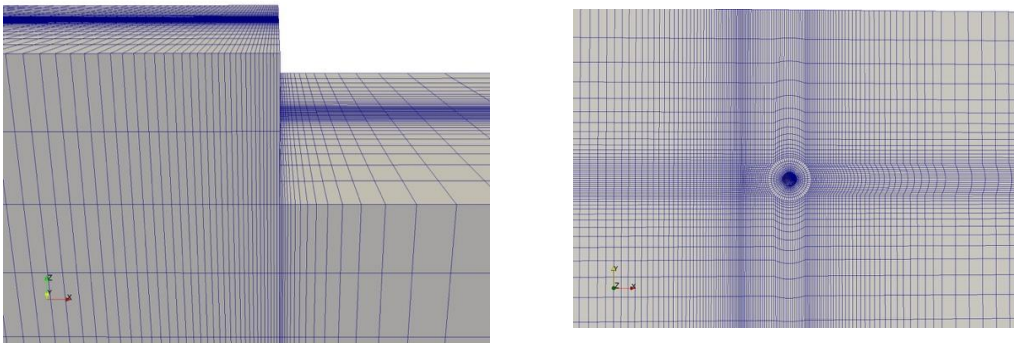

(a) (b)

Figure 2 The validation model numerical mesh showing the top of the wall (a) and the pipe (b).

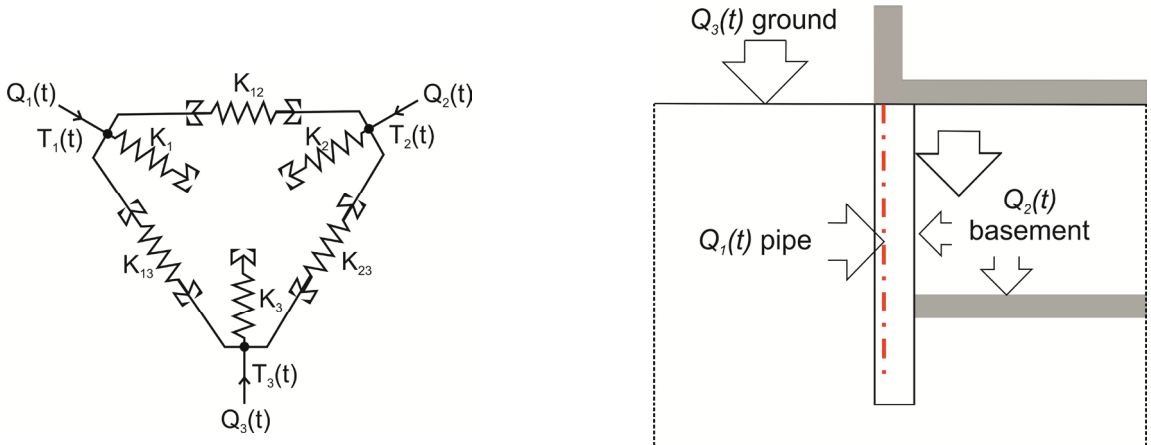

(a) (b)

Figure 3 A three-surface form of Dynamic Thermal Network showing the resistance and nodes (a) and the corresponding surfaces in a DTN representation of a DWHE problem (b).

For DTN calculations, the time-dependent thermal processes are represented as a network to describe the relationship between boundary temperatures and heat fluxes. This network includes a combination of admittive and transmittive heat paths and time-varying conductances that are characterized by a series of response factors (Figure

3-a). The method can be shown to be exact in both continuous and discrete forms and can be applied, in principle, to arbitrary geometries with heterogeneous thermal properties (Claesson, 2002; Rees and Fan, 2013; Wentzel, 2005). This makes the method very attractive for energy pile and DWHE problems. In such situations we are interested in specifying complex geometries with two sets of thermal properties (concrete and ground) and representing three boundary condtions: (1) the pipe surfaces, (2) the basement surface and (3) the upper gorund surface. The fluxes at these boundaries are denoted Q_1, Q_2 and Q_3 respectively as shown in Fig.3.

An essential feature of the DTN method is that fluxes at each surface are separated into transmittive and absorptive components. So that, using node 1 as an example, the transient heat balance equation is expressed as:

$$Q_1(t) = Q_{1a}(t) + Q_{12}(t) + Q_{13}(t) \tag{1}$$

where Q_{1a} is the absorbtive flux and Q_{12} and Q_{13} are the transmittive fluxes. Rather than these fluxes being functions of instantaneous node temperatures and conductances as in a steady-state network representation, the transient fluxes are experessed as functions of constant conductances and weighted average node temperatures so that for node 1:

$$Q_1(t) = K_1 \cdot \left[T_1(t) - \bar{T}_{1a}(t)\right] + K_{12} \cdot \left[\bar{T}_{12}(t) - \bar{T}_{21}(t)\right] + K_{13} \cdot \left[\bar{T}_{13}(t) - \bar{T}_{31}(t)\right] \tag{2}$$

where $T_1(t)$ is the current boundary temperature and $\bar{T}_{1a}(t)$ is the weighted average absorbtive temperature and $\bar{T}_{12}(t)$ and $\bar{T}_{13}(t)$ are the weighted mean transmittive temperatures. In discrete form these temperatures are expressed as summations of past temperatures multiplied by respective weighting factors as follows:

$$\bar{T}_{ia,n} = \sum_{\rho=1}^{\infty} \kappa_{ia,\rho} \cdot T_{i,n-\rho} \quad \text{and} \quad \bar{T}_{ij,n} = \sum_{\rho=0}^{\infty} \kappa_{ij,\rho} \cdot T_{i,n-\rho} \tag{3}$$

where $\kappa_{ia,\rho}$ is an absorptive weighting factor and $\kappa_{ij,\rho}$ is a discrete transmittive weighting factor in a finite series of such weighting factors. These weighted average temperatures are updated from one timestep to the next. This gives a heat balance equation for boundary 1 of the problem in the following form:

$$Q_{1,n} = \bar{K}_1 \cdot [T_{1,n} - \sum_{\rho=1}^{\rho_s} \kappa_{1a,\rho} T_{1,n-\rho}] + K_{12} \cdot \sum_{\rho=0}^{\rho_s} \kappa_{12,\rho} (T_{1,n-\rho} - T_{2,n-\rho}) + K_{13} \cdot \sum_{\rho=0}^{\rho_s} \kappa_{13,\rho} (T_{1,n-\rho} - T_{3,n-\rho}) \tag{4}$$

This equation is a computationally cheap summation of temperatures multiplied by weighting factors and so the model is very efficient. Some effort is required in deriving the sets of weighting factors, however, these can be conveniently derived by applying step-changes in temperatures at each boundary in turn. In our case we use the OpenFOAM numerical model described above to do this. The time-series fluxes from these calculations are then used to derive the weighting factors. Details of the process are desicribed in Wentzel (2005) and Rees and Fan (2013) along with detailed descriptions of the boundary condtion treatment for the pipe and exposed surfaces.

RESULTS AND DISCUSSIONS

Model validation has been attempted by making comparisons with experimental DWHE data over a period of 6 weeks and the results are displayed in Figure 4. The experimental testing program was conducted during the construction of a demonstration building in Barcelona. A series of heat rejection pulses were applied using thermal response test (TRT) equipment. In these experiments the inlet and outet fluid temperatures into and from the diaphragm wall were measured at 5 min intervals from 18th September to 30th October 2017. During the experiments the heat pump was switched on and off intermittently while the circulating pump ran continuously. Figure 4-a to Figure 4-c show the profile of the inlet, outlet, and ambient temperatures measured during the test as well as measured heat transfer rate. Predicated outlet temperature and heat trasnefr rate using the DTN DWHE model are also pesented. The wall dimensions and properties are detailed in Table 1. Three stages of measurements can be identified during this test series as shown in Figure 4. During the first stage, the pump ran for relatively longer hours before being switched off. The length of the cycles was reduced in stage two and are shorter again (2 hours) in stage three.

It was not possible to obtain independent measurements of concrete and ground thermal properties at the site. Consequently, we have investigated a range of property values (somewhat heuristically) to investigate the sensitivity of the model results. Accordingly, calculations using the DTN diaphragm wall model have been performed using thermal conductivity values ranging from 1.8–3.0 $Wm^{-1}K^{-1}$ for concrete and 0.6–2.0 $Wm^{-1}K^{-1}$ for the ground. In addition, volumetric heat capacity values of 1.6×10^{6}–3.75×10^{6} J $m^{-3}K^{-1}$ are examined for concrete while one single value of 1.6×10^{6} J $m^{-3}K^{-1}$ is used for ground. The results indicated that there is sensitivity to both the concrete and the ground thermal conductivities. Data from the shortest cycle periods was used to guide the choice of concrete properties as heat transfer variations are mostly limited to within the concrete in such conditions. Conversely, data from the longer cycles of heat rejection were more sensitive to ground thermal properties.

Table 1. DTN DWHE Model Parameters for the TRT Test Conditions

Model Parameters	Value	Units
Wall Depth	17.0	m
Pipe Depth	15.6	m
Basement Depth	6.5	m
Pipe outer diameter	25	mm
Pipe inner diameter	21	mm
Pipe horizontal spacing	0.40	m
Pipe circuit length	93.0	m
Number of loops	4	-
Pipe thermal conductivity	0.39	W $m^{-1}K^{-1}$
Fluid conductivity	0.625	W $m^{-1}K^{-1}$
Fluid specific heat	4178	J $kg^{-1}K^{-1}$
Fluid density	994.0	kg m^{-3}
Fluid viscosity	0.000714	Pa

Table 2. Thermal Properties of Concrete and Ground Used in Figure 2

Thermal Properties	Value	Units
Concrete thermal conductivity	2.25	W $m^{-1}K^{-1}$
Ground thermal conductivity	1.6	W $m^{-1}K^{-1}$
Concrete volumetric heat capacity	3.5×10^{6}	J $m^{-3}K^{-1}$
Ground volumetric heat capacity	1.6×10^{6}	J $m^{-3}K^{-1}$

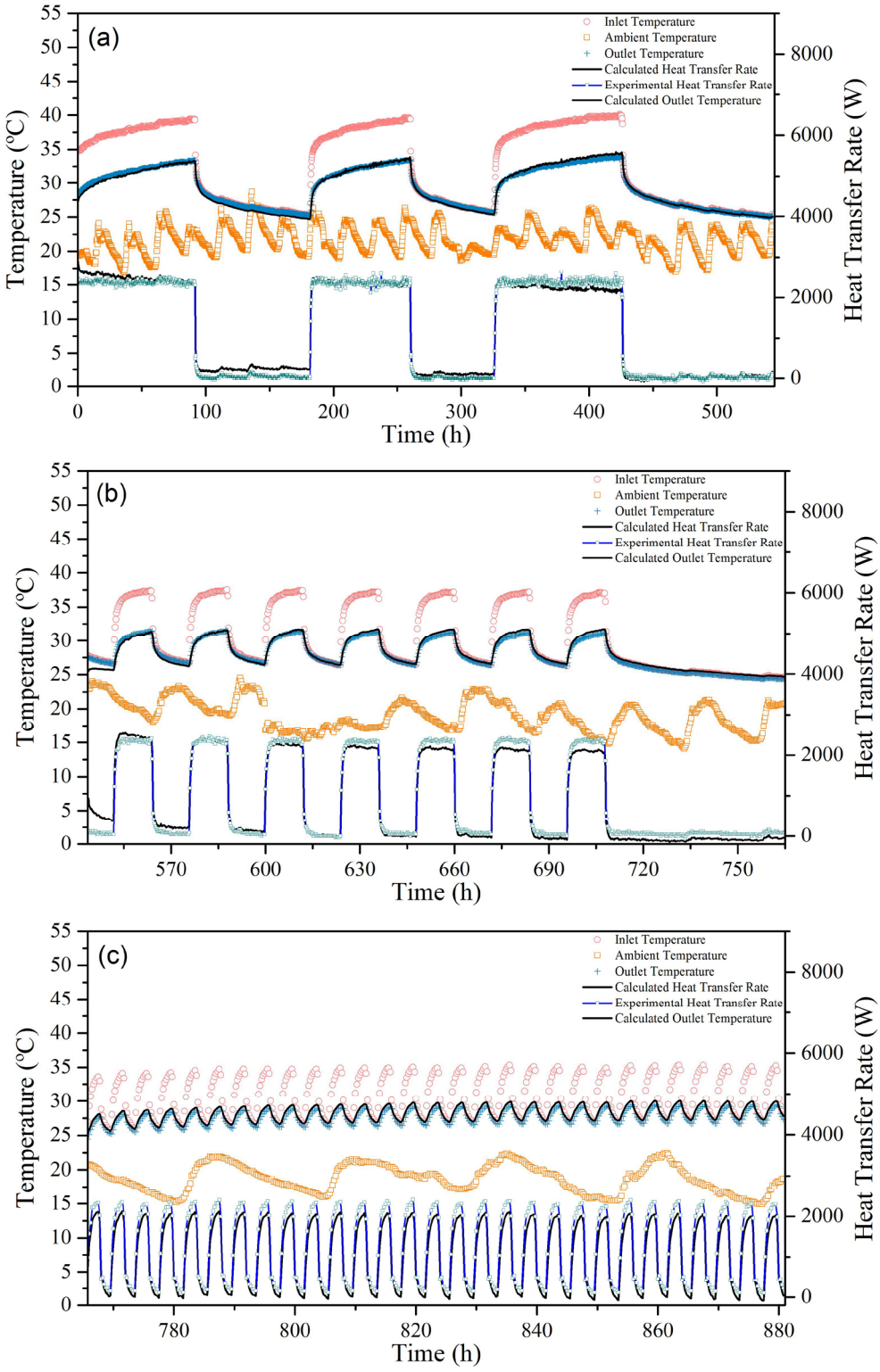

Figure 4 Hourly variations in measured temperatures and heat transfer rate compared with calculated data.

Calculated time series in Figure 4 represents the best fit with the experiments for which corresponding thermal properties of ground and concrete are shown in Table 2. Predicted outlet temperature and heat trasnefr rate follow the experiments closely over the operation period. The root mean square error (RMSE) between the calculated and measured outlet temperatures over the 6 weeks operation period is 0.4K which represents a good level of agreement for modelling purposes. Data in Table 2 indicates that the closest agreement is found with higher values of ground and concrete thermal conductivities and relatively high value of concrete volumetric heat capacity. We believe using values that are higher than that for plain concrete are justifyable in view of the significant level of reinforcement steel surrounding the pipes. In this model the wall thermal properties are effective or composite values for the wall material. The issue of the impact of the reinforcement on the nature of short timescale response is worthy of further investigation.

The validity of the DTN DWHE analogy to define heat transfer at the wall in the proposed model has been investigated by examining prediction of ground heat transfer over the operation period. The model compares favourably with the experimental data. The measured heat rejection over the whole period is 999.7 kWh and this compares with a predicted value of 988.7 kWh which corresponds to a 1.10% relative error and this seems an acceptable value. Completing calculations for the whole experimental data series required of the order of one minute of computing time.

CONCLUSIONS

A heat transfer model has been proposed that combines a numerical finite volume representation of a diaphragm wall heat exchanger and surrounding ground and basement boundaries and a Dynamic Thermal Network (DTN) representation derived from the numerical data. The model validation testing has been carried out using a thermal response test (TRT) approach over an extended period with different periods of cyclic operation. It has been shown that the results are sensitive to thermal property values of the ground and concrete. Values of effective thermal capacity were chosen at the upper end of the usual range and this seems justifyable in view of the large amount of reinforcement steel in the wall. The relative errors in outlet temperature between the DTN model and the measured data are no more than 0.4K for an operation period of about 880h. The levels of agreement in predicted dynamic performance are concluded to be more than satisfactory for heat exchanger design and TRT analysis purposes. The model is relatively efficient and so well suited to analysis of long-term performance analysis.

ACKNOWLEDGMENTS

This work was possible thanks to the research project H2020 GEOTeCH. GEOTeCH is co-funded by the European Community Horizon 2020 Program for European Research and Technological Development (2014–2020) and has received research funding from the European Union (www.geotech-project.eu) under grant agreement No. 656889. Experimental data was kindly provided by project partners Technalia, COMSA, and ARC BCN.

REFERENCES

Adam, D. and Markiewicz, R. 2009. *Energy from Earth-Coupled Structures, Foundations, Tunnels and Sewers*. Géotechnique. **59**(3), pp.229-236.

Bourne-Webb, P. et al. 2016a. *Analysis and Design Methods for Energy Geostructures*. Renewable and Sustainable Energy Reviews. **65**, pp.402-419.

Bourne-Webb, P.J. et al. 2016b. *Thermal and Mechanical Aspects of the Response of Embedded Retaining Walls Used as Shallow Geothermal Heat Exchangers*. Energy and Buildings. **125**, pp.130-141.

Brandl, H. 2006. *Energy Foundations and Other Thermo-Active Ground Structures*. Géotechnique. **56**(2), pp.81-122.

Claesson, J. 2002. *Dynamic Thermal Networks. Outlines of A General Theory*. In: Proceedings of the 6th Symposium on Building Physics in the Nordic Countries, Trondheim, Norway. pp.47-54.

Coletto, A. and Sterpi, D. 2016. *Structural and Geotechnical Effects of Thermal Loads in Energy Walls*. Procedia Engineering. **158**, pp.224-229.

Di Donna, A. et al. 2016. *Energy Performance of Diaphragm Walls Used as Heat Exchangers*. Geotechnical Engineering. **170**(GE3), pp.232-245.
Kürten, S. et al. 2015. *A new model for the description of the heat transfer for plane thermo-active geotechnical systems based on thermal resistances*. Acta Geotechnica. **10**(2), pp.219-229.
Rees, S.J. and Fan, D. 2013. *A Numerical Implementation of the Dynamic Thermal Network Method for Long Time Series Simulation of Conduction in Multi-dimensional Non-homogeneous Solids*. International Journal of Heat and Mass Transfer. **61**, pp.475-489.
Soga, K. and Rui, Y. 2016. *7 - Energy geostructures A2 - Rees, Simon J*. Advances in Ground-Source Heat Pump Systems. Woodhead Publishing, pp.185-221.
Sterpi, D. et al. 2017. *Investigation on the Behaviour of a Thermo-Active Diaphragm Wall by Thermo-Mechanical Analyses*. Geomechanics for Energy and the Environment. **9**, pp.1-20.
Sun, M. et al. 2013. *Heat Transfer Model and Design Method for Geothermal Heat Exchange Tubes in Diaphragm Walls*. Energy and Buildings. **61**, pp.250-259.
Weller, H.G. et al. 1998. *A Tensorial Approach to Computational Continuum Mechanics Using Object-oriented Techniques*. Computers in Physics. **12**(6), pp.620-631.
Wentzel, E.-L. 2005. *Thermal Modeling of Walls, Foundations and Whole Buildings Using Dynamic Thermal Networks*. thesis, Chalmers University of Technology.

[This page has been intentionally left blank]

IGSHPA SWEDEN
2018 Research Conference

DOI: 10.22488/okstate.18.000022

Numerical Simulation of Slinky-coil Ground Heat Exchangers Installed in Railway Tunnels

Hikari Fujii **Satoko Taniguchi** **Keisuke Ogai**

ABSTRACT

The use of horizontal ground heat exchangers (HGHEs) greatly reduces the initial cost of GSHP systems in comparison with vertical GHEs. Though the HGHEs are commonly used in North American countries, the installation number of the HGHEs is still few in European and Asian countries due to the limited land availability. The use of tunnels is one of the measures to promote the HGHEs because the tunnel walls are suitable for laying the HGHEs. In this research, analysis of operation data and numerical modeling were carried out in a GSHP system using Slinky-coil HGHEs installed in the basement of a railway tunnel in Tokyo. Through the interpretation of operation data, the stable energy efficiency of the system was confirmed, though the amount of heat disposal and extraction were not well-balanced in the GSHP system. A numerical simulation model of the HGHE was then developed based on the physical properties of ground and the design of the HGHEs. The simulation model was well-validated with the operation data and showed that 1) the GSHP system could maintain the initial heating and cooling capacity for 10 years and 2) the deeper installation of the HGHE is favorable to obtain higher COP.

INTRODUCTION

Today, vertical and horizontal ground heat exchangers (GHEs) are commonly used in ground source heat pump (GSHP) systems. Though horizontal ground heat exchangers (HGHEs) require large land space for installation, the installation cost of HGHEs are lower than that of vertical GHEs since the HGHEs can be installed using common excavation machines. For this reason, HGHEs are widely installed in USA and Canada, where more land space tends to be available than in European and Asian countries. Considering the low installation cost, the use of HGHE can improve the competitiveness of GSHP systems, in case the required surface land space is minimized.

Several researches have been carried out by European researchers in the last decade to use the underground space for HGHEs. Energy Geo-Structure (EGS) is a prefabricated panel containing horizontal heat exchangers inside which can be set on the walls of subway or railway tunnels (e.g., Bourne et al., 2016). Fordl et al. (2010) investigated the optimum design and installation method of EGS in the Brenner Base Tunnel in the Austrian Alps. Nicholson et al. (2013) studied in temperature performance and the stress distribution change with the operation of EGS in a subway tunnel in the U.K. Bourne-Webb et al. (2016) investigated the effect of the temperature, wind velocity in the tunnel and the thermal conductivity of the ground on the heat exchange performance in GSHP system with EGS using a FEM model. Barla et al. (2016) evaluated the energy saving and the environmental impact of EGS in a subway tunnel in Milan using a FEM model.

In Japan, GSHP systems using the tunnel walls for the installation of HGHEs are not introduced yet. In 2013, on the other hand, a GHSP system using HGHE installed in the basement of a railway tunnel was completed in Tokyo. Since the system uses only the basement of the tunnel, the construction procedure is less complicated and the impact on the tunnel wall strength is smaller than the sidewall installation. The system started the heating and cooling operations in July 2013 and the operation data have been recorded since then. In this research, the heat exchange

Hikari Fujii (fujii@mine.akita-u.ac.jp) is a professor of energy resource engineering at Akita University, Japan. Satoko Taniguchi and Keisuke Ogai are GSHP engineers at Mitsubishi Materials Techo Corporation, Japan.

performance, the load behavior and the ground temperature performance are evaluated based on the operation data. Then a numerical model of the HGHE and the surrounding ground is developed using a groundwater and thermal transport simulator, FEFLOW ver.7.0. The model is validated through a history matching with operation data and sensitivity studies are performed using the model to optimize the design and operation strategy of the HGHEs.

INFORMATION ON THE GSHP SYSTEM

The GSHP system using HGHEs was constructed in 2013 at Setagaya-Daita station in Tokyo. The station was relocated from land surface to underground to mitigate the traffic jams at railway crossings. Figure 1 shows the cross sectional view of the station. The passenger's platform is located in the B2 level (B2F), while express trains pass the B3 level (B3F). Five water-air heat pumps (cooling/heating capacity: 5.0 kW/5.2 kW, respectively) are installed in B2F to supply the warm and cool air to the passenger's waiting room on the platform.

The HGHEs are installed in the basement concrete of the B3F. The depth of HGHE from the surface of the basement and land surface are 1.9 m and 26.6 m, respectively. The HGHEs are Slinky coils of 0.8 m diameter and 0.6 m pitch using high-density polyethylene tubes of 24 mm/34 mm ID/OD. The thermal conductivity of the concrete is enhanced using SiO2-rich aggregates. The geology of the ground is loam and the thermal conductivity of ground and concrete were measured as 1.39 W/m/K and 2.34 W/m/K, respectively.

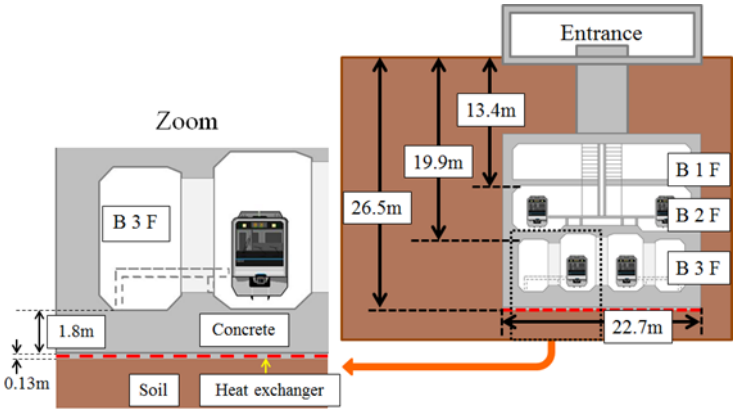

Figure 1 Cross sectional view of Setagaya-Daita Station.

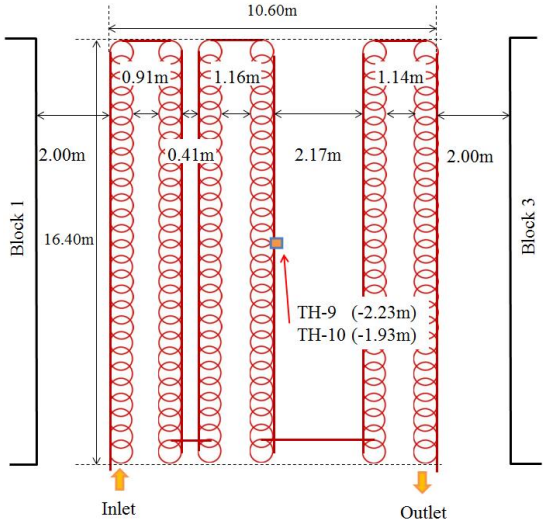

Figure 2 Layout of Slinky-coil GHEs

The HGHE fields are divided into 10 blocks each of which has a coil length of 100 m and pipe length of 500 m as shown in Figure 2; each heat pump is connected with two HGHE blocks. Water was used as the heat carrying fluid because there is no risk of freezing in the tunnel. In this research, Block No. 2 was chosen for the numerical modeling and the performance analysis since ground temperatures were measured only in this block. Two Pt100 temperature sensors were set in the central part of Block No.2, one at the depth pf GHE (TH-10) and one 0.3 m below the GHE (TH-9). The construction of the station was completed in the first half of 2013 and the operation of the GSHP system was started on July 3, 2013.

Figure 3 shows the temperature measured in B2F, the local ambient temperature and the inlet and outlet temperatures of heat medium in Block No. 2 from July 2013 to July 2015. As shown in Figure3, the cooling operation started when the temperature in B2F exceeded 25 ºC, while the heating operations were carried out when the temperature became below 17 ºC. The yearly-average operation days of cooling and heating in the two years were 99 days and 151 days, respectively, which are significantly shorter than the normal cooling (135 days) and heating periods

(161 days) in Tokyo. The shorter operation is explained by the stability of temperature in the tunnel in comparison with the ambient temperature. The daily operation hours of cooling and heating were 20 to 21 hours, which were much longer than the operation in buildings and houses, since the railway is operated from 5 A.M. to 1 A.M. The inlet temperature of heat medium to HGHE (outlet temperature of heat pumps) increased close to 40 ºC in the cooling periods, which is not favorable to maintain high COP (Coefficient of Performance), while the temperature was maintained above 10 ºC in each heating period.

Figure 4 shows the total heat exchange rate and COP of the heat pump in the same period. The average COP in the cooling and heating periods for two years were 4.65 and 3.05, respectively. In each period, the COP showed a steep decrease with the change of ground temperatures due to the long operation hours, low thermal conductivity of the ground and the lack of advection effects of groundwater flow in the concrete. The average heat exchange rates in the cooling and heating periods were calculated as 44.6kW, 14.9kW, respectively, which could cause the rise of ground temperature in long-term operations. The comparison of COP in the first year and the second year, however, did not show a major reduction since cooling periods are much shorter than the heating periods and the difference between the cumulative heat exchange rates in the cooling (6.34 MWh) and in the hearting periods (4.15 MWh) were 53%.

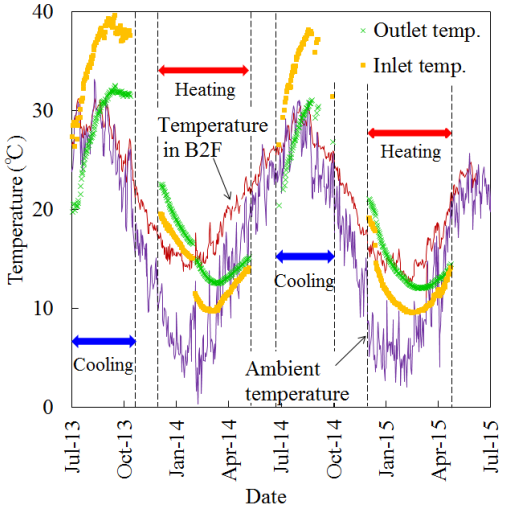

Figure 3 Measured temperature data in Block 2.

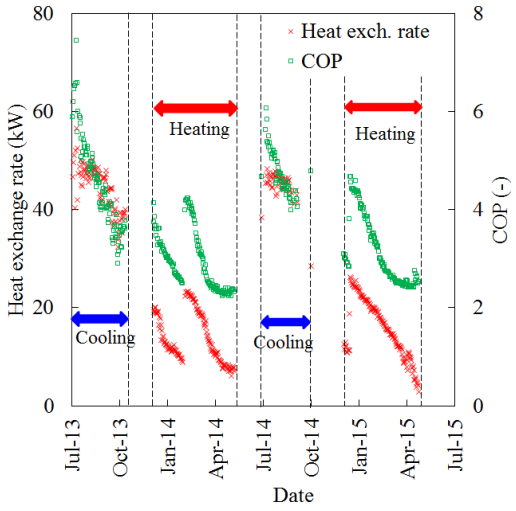

Figure 4 Measured COP performance.

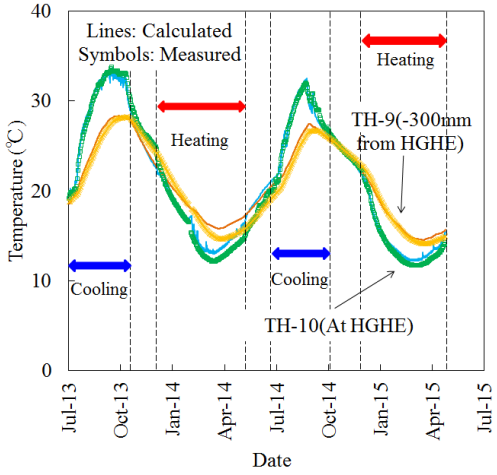

Figure 5 Measured and simulated ground temperatures in Block 2.

In Figure 5, the changes of measured ground temperature at the depth pf GHE (TH-10) and 0.3 m below the GHE (TH-9) are shown with symbols. The temperature at the depth of the GHE showed a significant change due to the operation of the heat pumps; maximum 33.7 ºC in cooling and minimum 11.7 ºC in heating. At the beginning of the cooling period in June 2014, the ground temperature showed a recovery to the original temperature, while the temperature did not recover to the original temperature at the beginning of the heating period in December 2013 and December 2014. This indicates that the disposed heat in the cooling operations is stored in the ground due to the large cumulative heat disposal rate, while the cold heat has been dissipated in the ground after the heating seasons.

NUMERICAL MODELING

For the prediction of the performance of the HGHEs, a 3D numerical model was constructed for the HGHE and the surrounding ground using a finite-element based groundwater and thermal transport simulator, FEFLOW ver.7.0 (Diersch, 2014). Figure 6 shows the grid system of the numerical model. The area surrounded by red lines shows the position of the HGHEs. The heat carrying fluid flows from the inlet to the outlet of the HGHE. At the center of the HGHE, observation points are set to output the ground temperatures at the depth of the position of TH-9 and TH-10. The width of the upper and lower peripheral area of the model is defined short because adjacent blocks are located in this direction, which allows the use of adiabatic boundary conditions due to symmetry. To the right and left side of the model, 50 m of blank blocks are defined to avoid the interference of boundaries. The number of layers and the finite elements of each layer are set as 25 and 7,216, respectively. As shown in Figure 7, the spiral HGHEs are modeled using a thin flat plate based on the modeling approach of Fujii et al. (2012). The thermal conductivity of the polyethylene pipe was set as 0.03 W/K/m based on the loop pitch of 0.6 m. The thickness of the flow path was defined as 0.0015 m, which gives the same traveling time of heat carrying fluid from inlet to outlet. The initial temperature of the entire ground was set as 17.9 ºC, which is 1.0 ºC higher than the annual mean temperature of Tokyo. The measured air temperature in the tunnel was used as the surface boundary condition, while the temperature at the bottom of the model was fixed at the initial temperature of 17.9 ºC. The thickness of the model was defined as 10 m to eliminate the effect of the bottom boundary condition.

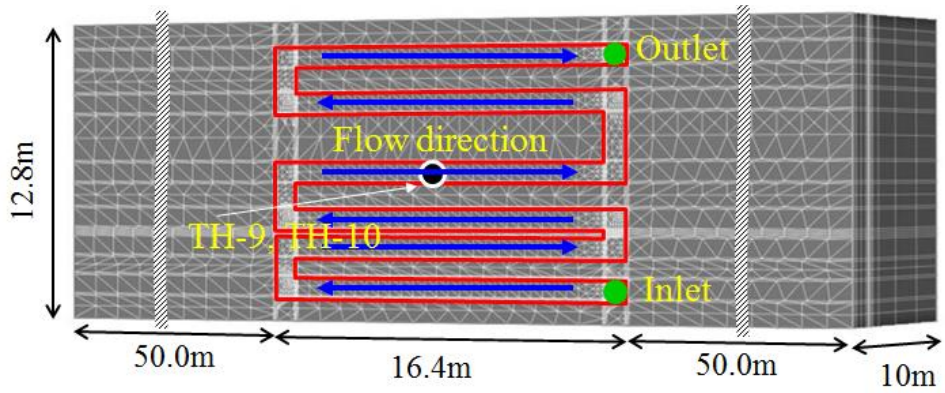

Figure 6 3D view of the numerical simulation model.

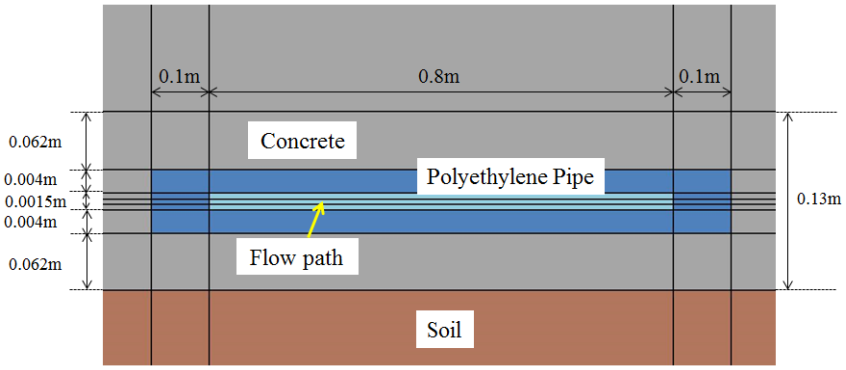

Figure 7 Treatment of Slinky-coils in the numerical model.

The model was run for the two years' cooling and heating operations, treating the inlet temperature as the input data. The model was validated through the history matching between the measured and simulated temperatures. The history matching results of ground temperatures is shown in Figure 5. Reasonably good agreement was obtained on the measured and simulated ground temperature except in the period between January and April, 2014. The reason of the disagreement was considered as the malfunction of data acquisition system during this period. The problem was fixed in April, 2014 and reasonable history matching results were obtained afterwards. The Root Square Mean Error (RSME) between the measured and simulated temperatures at TH-10 and TH-9 are 0.94 ºC and 0.85 ºC, respectively during the 2 years of operation. The RMSE is reduced to 0.82 ºC and 0.71 ºC, respectively, excluding the period between January and April, 2014. Figure 8 shows the measured and simulated outlet temperatures of heat medium. Though the matching results were poor between January and April, 2014 as mentioned above, good matching results were obtained for the rest of the cooling and heating periods. The RSME between the measured and simulated outlet temperatures are 0.71 ºC during the 2 years of operation excluding the period between January and April, 2014.

In the above history matching simulations, the validity of the numerical model was sufficiently demonstrated. The following section discusses the optimum design of the HGHEs using the validated numerical model.

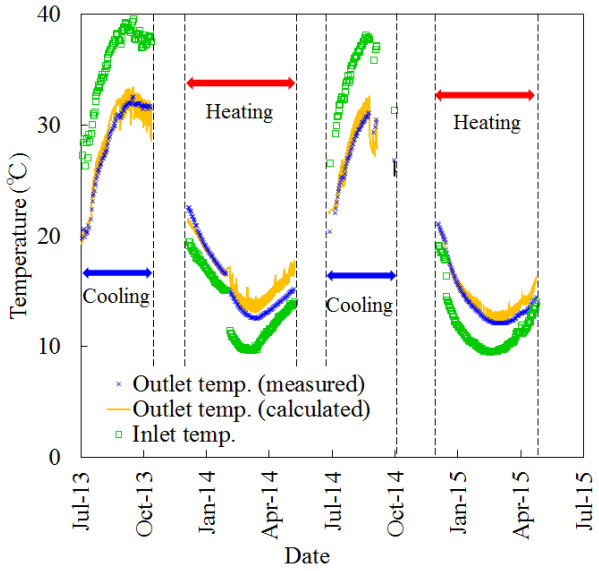

Figure 8 Measured and simulated outlet temperatures in Block 2.

SENSITIVITY STUDIES

In this section, sensitivity studies are performed using the numerical model to optimize the design and operation strategy of the GSHP system based on the long-term prediction. The heating period was fixed as 5 months, from November to April in each year, while the length of the cooling period was set as 2 months (July - August, Case 1) or 4 months (June - September, Case 2) in the prediction terms of 10 years. The size of the HGHE field was set equal to the Block No. 2 in the train station, though the influence of the adjacent block were not considered in the sensitivity study. The cooling and heating loads for the field were set as 4.46kW and 1.49kW, respectively, based on the actual operations. The total heat extraction rate of 1 year is calculated as 4.50MWh, while the rejection rate in the same period are 5.53MWh and 10.88MWh in Case1 and Case 2, respectively. The poor balance of heat exchange rate, especially in Case 2, could cause the increase of ground temperature and the reduction of COP in long-term operations.

Figure 9 shows the predicted outlet temperature of heat carrying fluid from the HGHE obtained in the simulation. In the first 2 years, the temperatures show a small drop in both cases, but they get stabilized for the rest of the simulation even in Case 2. This suggests that the HGHEs in the tunnel can maintain stable heat exchange performance even when the heat balance is not well maintained. The heat flow from the bottom of the HGHEs and the heat exchange at the surface of the tunnels will be the main energy source of temperature recovery during the periods between the cooling and heating seasons.

Figure 10 shows the contour map of the temperature in the ground at the depth of the HGHE in Case 2. The three figures show the temperature at the beginning of the heating periods in the (a) 1st, (b) 2nd and (c) 10th operation years, respectively. The central part of the figure shows the HGHE field. The comparison of the distribution in the first year and the second years indicates the temperature drop of about 1 ºC in the HGHE field, while the distribution in 10th years is quite similar to the one in the second year. These figures demonstrate the stable performance of the GSHP system using the tunnels even in the case of poor energy balance.

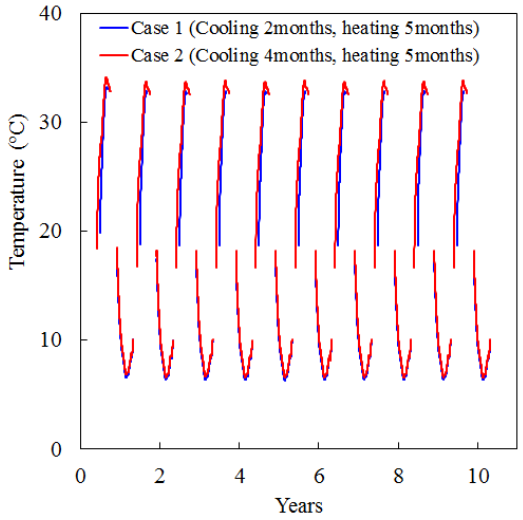

Figure 9 Prediction results of outlet temperature of heat carrying fluid in Case 1 and Case 2

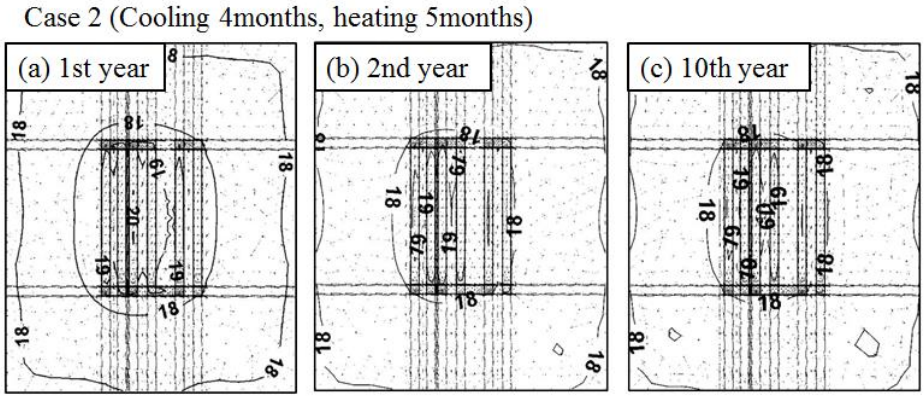

Figure 10 Contour maps of simulated temperatures at the depth of HGHEs at the beginning of the heating periods of (a) 1st, (b) 2nd and (c) 10th years.

Next, the effect of the burial depth of the HGHE was examined by changing the depth as 1 m, 2 m and 3 m below the surface of the tunnel. The heating period was fixed as 5 months from November to April and the cooling period was set as 4 months from June to September. Same heat exxhange rates were applied as used in Case 2. Figure 11 shows the season-averaged outlet temperature of the heat medium from the HGHE in each case. In all cases, the temperatures get stabilized within 3 years indicating the stabilization of the ground temperatures. In the cooling and heating operations, the difference in the heat medium temperature between the 1 m and 3 m were 1.4 ºC and 3.4 ºC. This suggests that the deeper installation of HGHE is more important in the heating operation than in the cooling operation. The difference can be explained by the difference in heat exchange rates in the cooling operation (25.7 W/m^2) and heating operations (8.6 W/m^2). In the cooling operation, larger heat exchange rate between the air and the ground is expected at the surface of the tunnel due to the larger heat exchange rate per unit area, while most of the heat is supplied from the ground when the HGHE is deep. In the case of heating operations, the small heat exchange rates increase the ratio of heat from the bottom, which clearly shows the effect of installation depth.

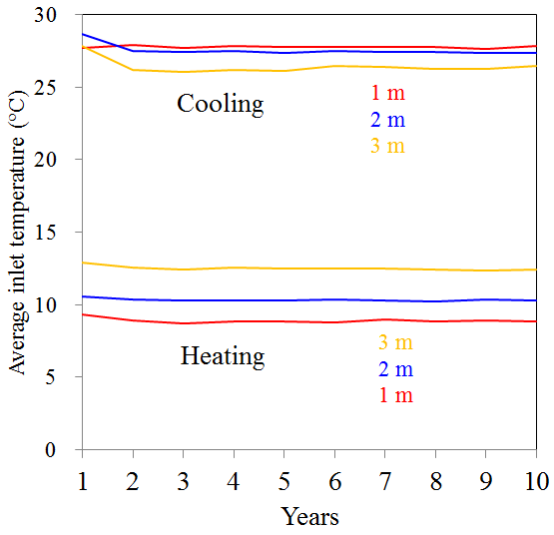

Figure 11 Simulated season-averaged temperature of heat medium at the outlet of HGHEs.

CONCLUSION

The interpretation of operation data and numerical modeling were carried out in a GSHP system using Slinky-coil HGHEs installed in the basement of a railway tunnel in Tokyo, Japan. The interpretation of the operation data for 2 years demonstrated the stable energy efficiency of the system, though the amount of heat release and extraction were not well balanced in the GSHP system. A numerical simulation model of the HGHE was then developed based on the physical properties of the ground and the design of the HGHEs. The model was well-validated using the monitored data during the heating and cooling operations. The sensitivity studies using the model showed that the GSHP system will maintain the initial heating and cooling capacity for 10 years and the deeper installation of the HGHE is preferable to obtain higher COP, especially in the heating operation.

ACKNOWLEDGMENTS

The authors would like to thank Odakyu Electric Railway Co., Ltd. for providing the operation data of the GSHP system. This work was partly supported by Grants-in-Aid for Scientific Research (B) (JP15H04223) from JSPS.

REFERENCES

Barla, M., Di Donna, A., Perino, A. 2016. *Application of energy tunnels to an urban environment*. Geothermics 61: 104-113.

Bourne-Webb, P., Freitas, T., Gonçalves, R. 2016. *Thermal and mechanical aspects of the response of embedded retaining walls used as shallow geothermal heat exchangers*. Energy and Buildings 125: 130-141.

Diersch, H.J.G. 2014. FEFLOW Finite Element Modeling of Flow, Mass and Heat Transport in Porous and Fractured Media. Springer, 996 p.

Frodl, S., Franzius, J., Bartl, T. (2010) *Design and construction of the tunnel geothermal system in Jenbach*. Geomechanics and Tunnelling, 3, 658-668.

Fujii, H., Nishi, K., Komaniwa, Y., Chou, N. 2012. *Numerical modeling of slinky-coil horizontal ground heat exchangers*. Geothermics 41: 55–62.

Nicholson, D.P., Chen, Q., Pillai, A., Chendorain, M. 2013. *Development in the thermal pile and thermal tunnel linings for city scale GSHP systems*. 38th Stanford Geothermal Workshop SGP-TR-198.

IGSHPA SWEDEN
2018 Research Conference

DOI: 10.22488/okstate.18.000019

Thermal Response Test experiments and modelling applied to shallow geothermal piles of different geometry

Marco Fossa **Fabio Minchio** **Davide Rolando**

ABSTRACT

Geothermal piles are structural elements that encountered interest in ground source heat pump (GCHP) applications thanks to the great potential in cost reduction compared to the traditional solutions based on borehole heat exchanger (BHE). In this paper a series of experimental results related to TRT measurements carried out on geopiles of different geometry is presented. These geostructures are reinforced concrete cylinders with diameter ranging from 0.6 to 1 m and depth of about 13m, with pipes either arranged as coils or multiple vertical U-tubes. The measurements show that the evolution of the fluid temperature in time cannot be properly described by the usual ILS (infinite line source) solution since the experimental temperature profiles do not gather along any line when represented as a function of the logarithm of the time. Starting from the above findings, measurements are here recast by calculating the temperature response factor of the different pipe arrangements by spatial superposition of base FLS (Finite Line Source) solutions. Finally, a recursive technique of parameter estimation based on a 2 resistance model is applied for calculating the effective BHE resistance and the ground/concrete thermal conductivity at minimum deviation between experimental and predicted temperature profiles.

INTRODUCTION

Geothermal piles (GP) are structural elements which can be employed in buildings for cooling and heating purposes once connected to a ground source heat pump (GCHP). The interest in such a ground heat exchanger is related to the great potential cost reduction compared to the traditional solutions based on borehole heat exchanger (BHE) or horizontal/trench shallow pipes. Inside foundation piles, the carrier fluid pipes can be arranged according to helix coils (Helix Heat Exchangers, HHE) or as a series of vertical U pipes along the pile periphery (U coil heat exchanger, UCHE): in both cases the pipes embrace a cylindrical volume that is typically filled with steel reinforced concrete. It is apparent from these preliminary considerations that the thermal response of GPs vertically buried into the ground cannot be properly described by those models that take into account "thin and long" heat sources, say the classical models for vertical BHE, including the Infinite Line Source ILS (Ingersoll et al. 1954) and the finite line source (FLS, Eskilson 1987, Zeng et al. 2002, Lamarche and Beauchamp 2007, Javed and Claesson 2011). In addition also the "thick" sources like the hollow long cylinders (ICS, Infinite Cylindrical Source) described by Carslaw and Jaeger (1947) and Ingersoll et al. (1954) are not suitable for describing the geopile heat interactions with the ground. The reasons for such discrepancies are all related to the GP geometry: GP in short in depth and the depth to diameter ratio H/D is the

Marco Fossa (marco.fossa@unige.it) is professor of Solar and Geothermal energy at the University of Genova, Italy. Davide Rolando is post-doctoral researcher at KTH Stockholm, Sweden and Fabio Minchio, PhD, is thermal Engineer at the 3F group located in Vicenza, Italy.

order of 20 to 100 (for BHEs is 1000 to 2000 typically), there is a meaningful heat transfer area at GP bottom (and even at its top), the thermal capacity of the concrete volume is much more important than the presence of grout and pipes in common BHEs.

The design of the GCHP system when coupled to structural heat exchangers is hence more complicated than in common applications and dedicated FEM models are usually employed for simulating the thermal response of the ground and concrete thermal elements. One of the first literature contribution in this sense is the one by Rabin and Korin (1996), who numerically solved the heat conduction problem where a series of thermally active rings were present. More recently a similar numerical approach has been applied by Dehgan et al. (2016) who performed a 3D simulation of a thermal domain where spiral coils are releasing heat into the GP.

From an analytical point of view, a group of Chinese researchers (Man et al. 2010-2011, Cui et al. 2011) developed a series of analytical solutions able to describe the temperature distribution in time and space models when a thin source is symmetrically located apart from the central axis of a cylinder. In this approach the inner cylindrical volume is "solid" with respect to the Carlslaw one. The proposed solutions refer to different geometries of the heat source, including the infinite and finite cylindrical surface and infinite and finite ring and helix source models.

The new "solid cylinder" models are a meaningful contribution to the GCHP science but they involve complex integral solutions that cannot be easily applied as an engineering approach to ground heat exchanger design. For this reason (and for geometry flexibility), a simple hybrid method has been proposed in the last IGSHPA conference for generating custom temperature response factors (TRF) for GP related applications based on the superposition of the single point source (SPS) solution (Fossa et al. 2017). The problem of the application of a proper temperature response factor to GP temperature dynamics is again complex when the ground properties have to be estimated from temperature response test (TRT) data from measurements on the carrier fluid circulating inside a geopile. Loweridge et al. (2014a, 2014b) provided an extensive discussion on analytical model limitations for GP related applications and presented recommendations for TRT data analysis depending on GP geometry and test duration.

In this paper a series of experimental results related to TRT measurements carried out on geopiles of different geometry is presented. The geostructures are reinforced concrete cylinders with diameter ranging from 0.6 to 1 m and depth of about 14m, with pipes either arranged as coils or vertical U-tubes.

The evolution of the fluid temperature in time clearly showed how the ILS (infinite line source) model cannot efficiently describe the temperature profiles that are characterized in these experiments by peculiar non-linear trends as a function of the logarithm of time. Starting from the above findings, measurements have been recast by calculating the temperature response factor of the different pipe arrangements and then applying a recursive technique of parameter estimation still based on a 2 resistance model, as in the classic TRT theory. In such a way the effective BHE resistance R_{bhe} and the (transient) ground one (which in turn depends on the ground thermal conductivity k_g) have been calculated by minimizing the error between the measured and predicted carrier fluid temperature.

EXPERIMENTAL SETUP AND THE PRESENT PILE HEAT EXCHANGERS

In order to design an energy piles field part of a geothermal heat pump system serving a new building in the North of Italy, TRT measurements were carried out on six geopiles to determine the effective ground thermal conductivity and geopiles thermal resistance.

Knowledge of the ground stratigraphy results from experimental ground field tests performed by structural designers, so a preliminary estimation of ground thermal properties is possible. The values of thermal conductivity and volumetric heat capacity, determined from the Italian Standard UNI 11466 (UNI, 2012) are shown in Table 1 for each ground layer. Calculated mean thermal conductivity is 2.1 W/(m K).

Three TRT were carried out on 3 helicoidal pipe geopiles and other three on three double – U geopiles, placed on site, in different positions, chosen at a considerable distance each other to avoid any possible thermal interference.

The project includes two different cast-in-place geopiles geometries (Table 1 and Figure 1), a continuous helix system and a double U system.

Table 1 Ground layers and thermal properties for each layers from UNI 11466

ground layer	depth	layer thickness	thermal conductivity	volumetric heat capacity
	m	m	W/(m K)	kJ/(m³ K)
Silty sand	2	2	1.605	2165
Sand - gravel	4	2	1.605	2150
Sandy gravel – water saturated	2.5	0.5	2.1	2450
Silty sand	8.7	6.2	2.1	2450
Sand	13.5	4.8	2.4	2500

Table 2 Features of the two different tested geopiles geometries

GEOPILES TESTED			Type 1	Type 2
pile	geometry		continuous helix	double - U connected in series
	diameter	m	1	0.6
	depth	m	13.5	13.5
	grouting material		concrete - RCK 350	concrete - RCK 350
pipe	diameter	mm	25	20
	material		PEX-a	HDPE
	total length	m	100	54

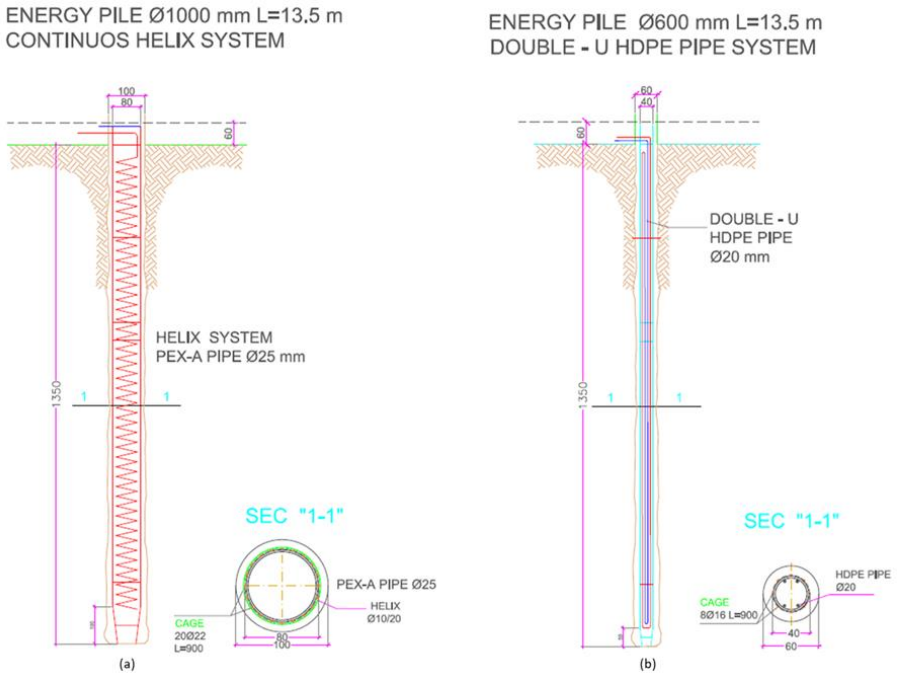

Figure 1 Tested energy piles configurations: continuous helix system with PEX-a pipes (a), double U system with HDPE pipes (b).

The TRT experimental setup consists in a standard TRT device, equipped with three modular electric resistances. The accuracy of the temperature sensors employed was ±0.1°C while the flow rate sensor accuracy was ±3% of the readings. All the tests were performed by imposing a controlled and constantly measured heat flux on the geopile-

ground system, by means of electric resistances, for 50 h (except 70 h for the second test), circulating water at constant flow rate. In this case the lowest heating power rate available (900 W, corresponding to 67 W/m considering the borehole depth) was chosen. Only for the first two tests, the heating power was set at 1900 W (corresponding to 141 W/m considering the borehole depth). Experimental data were logged every minute; the system measures and saves the following variables: external air dry bulb temperature, water flow rate, inlet (to the geopile) and outlet (from the geopile) water temperatures, power, current and voltage.

MODELLING THE GROUND RESPONSE FOR TRT PARAMETER ESTIMATION

The heat transfer process that regulates the thermal interaction between the ground and a vertical heat exchanger can be described by the three-dimensional time-dependent Fourier equation, when the ground water circulation can be neglected and the presence of pure conduction phenomena can be assumed.

The explicit analytical solution of the conduction equation can be obtained only for relatively simple geometries and a number of additional assumptions need to be introduced in order to develop suitable models able to tackle specific engineering problems. Under the assumptions of constant heat flux, constant and homogeneous ground thermo-physical properties, 1D and 2D solutions can be derived from the Fourier differential equation and specified for a particular heat source geometry. Considering Borehole Heat Exchangers (BHE), the generic expression for these solutions is shown in Eq. (1):

$$T_{\text{bhe}} - T_{g,\infty} = \dot{Q}' \cdot R_g = \frac{\dot{Q}'}{C \cdot k_g} \cdot \Gamma(\text{Fo}) \tag{1}$$

Where the BHE wall temperature T_{bhe} is the BHE wall temperature, T_g is the undisturbed ground temperature, $\dot{Q}'$ is the heat flux and R_g is the ground thermal resistance. A non dimensional Temperature Response Factor (TRF) Γ as a function of the Fourier number can be introduced to express the time variant nature of the ground thermal resistance. Finally, k_g is the ground thermal conductivity and C is a constant that depends on the geometrical approximation through which the BHE is modelled.

According to the Infinite Line Source solution (ILS, Ingersoll et al. 1954) the heat exchanger is modelled as an infinite line while according to the Infinite Cylindrical Source solution (ICS, Carslaw and Jaeger 1947) the heat exchanger is modelled as an infinite cylinder. Further solutions have been developed to model the thermal interaction between the ground and a Finite Line Source heat exchanger (FLS, Eskilson 1987, Zeng et al. 2002, Lamarche and Beauchamp 2007, Javed and Claesson 2011).

In general, spatial superposition can be applied to all the 1D and 2D solutions in order to obtain Temperature Response Factors (TRF) able to describe the 3D thermal field of multiple ground heat exchangers. The TRF based on the FLS model and resulting from a spatial superposition are traditionally named g-function.

Moreover, a temporal superposition scheme can be employed to overcome the strict assumption of considering a fixed heat flux. If a given time varying heat flux $\dot{Q}'(t)$ can be approximated as a step-wise function of N heat pulses, Eq. (1) can be extended as shown in Eq. (2):

$$T_{\text{bhe}} - T_{g,\infty} = \sum_{i=1}^{N} \frac{\dot{Q}'_i - \dot{Q}'_{i-1}}{C \cdot k_g} \cdot \Gamma\left[\text{Fo}(t_{\text{N}} - t_{i-1})\right] \tag{2}$$

To consider the carrier fluid temperature circulating in the BHE, the expression in Eq. (1) should be modified as

shown in Eq. (3) , where $\bar{T}_f$ is the average of the carrier fluid temperature inside the BHE and R_{bhe} is the borehole thermal resistance.

$$\bar{T}_f - T_{g,\infty} = \dot{Q}' \cdot R_g + \dot{Q}' \cdot R_{bhe} \tag{3}$$

Eq. (3) is based on the assumption of considering the evaluation of the temperature difference between the fluid circulating in a BHE and the ground undisturbed temperature according to the 2-resistance model where the BHE thermal resistance in series with the time variant ground thermal resistance. Therefore, with a suitable TRF, if the ground thermal conductivity, undisturbed ground temperature and borehole thermal resistance are known, Eq. (3) allows the calculation in time of the carrier fluid temperature circulating in a BHE.

The 2-resistance model was the scheme under which the modern TRT analysis has been conceived by Mogensen (1983). According to the TRT procedure proposed by Mogensen (1983) to estimate the ground thermal conductivity and the BHE thermal resistance, Eq. (3) is applied to solve an inverse problem where the average fluid temperature $\bar{T}_f$, the heat transfer rate $\dot{Q}'$ and the undisturbed ground temperature $T_{g,\infty}$ are known and an inverse procedure is employed to evaluate the BHE thermal resistance R_{bhe} and the ground thermal conductivity k_g. In particular, during a TRT, a constant heat transfer rate is injected (or extracted) into the ground and the resulting time variant fluid temperature profile is analysed. The temporal superposition principle can be applied if the heat transfer rate is varying with time (Eq. 2).

With reference to the temporal superposition scheme shown in Eq. (2) and the described 2-resistance model (Eq. 3), an optimum search procedure can be implemented in order to estimate the BHE thermal resistance and the ground thermal conductivity. In particular, from the profile of the heat transfer rate $\dot{Q}'$(t) measured during the TRT, the combination of Eq. (2) and Eq. (3) can be used to calculate the profile of fluid temperature circulating in the BHE ($T_{calculated}$) depending on tentative values of R_{bhe} and k_g. An objective function F can therefore be defined (Eq. 4) as the average of the percentage error between the fluid temperature measured during the TRT ($T_{measured}$) and the fluid temperature calculated ($T_{calculated}$) through Eq. (3).

$$F(k_g, R_{bhe}) = \frac{1}{N} \sum_{i=1}^{N} \frac{\left| T_{measured,i} - T_{calculated,i} \right|}{T_{measured,i}} \tag{4}$$

The minimization of the objective function F allows the estimation of the correct values of R_{bhe} and k_g.

The ILS model is the TRF typically employed to allow the analysis of TRT data. In case of ordinary BHE, the ILS solution has been widely adopted in TRT analysis as a suitable model to describe the thermal response vertical ground heat exchanger with typical depth between 50 and 300m. On the other hand, the geometry of a shallow geothermal pile is not as slender as in traditional BHE and the line source models can be proven to be not suitable to describe the heat transfer process related to a geo pile. For this reason, a new approach based on the employment of the FLS model for the data analysis is proposed in this paper. Two TRFs have been calculated to model the thermal interaction of the geo piles presented in the previous paragraph and shown in Figure 1.

The two g-functions have been obtained considering the schemes shown in Figure 2. The TRF for helicoidal heat exchanger (Figure 2a) has been modelled considering 8 heat sources in a circle configuration with a diameter (D) of 0.65m. A source radius r_b of 0.01m and source depth equal to 14m have been considered. Similarly, the TRF for the double U pipe heat exchanger (Figure 2b) has been modelled considering 4 heat sources in a square configuration. The excess temperature from the FLS action is evaluated at a radius of 0.01m and a source spacing (B) of 0.3m has been

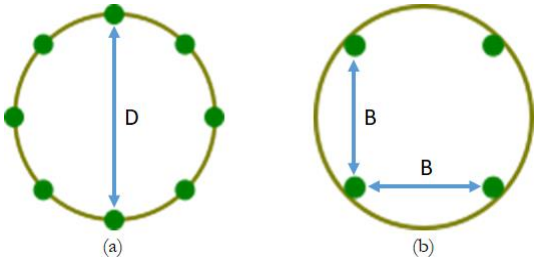

Figure 2 g-function calculation scheme developed for modelling the helicoidal (a) and double U (b) geo piles.

adopted. The depth of each source has been considered to be equal to 14m.

The respective g-functions have been adopted for the implementation of an optimum search procedure based on the minimization of the objective function shown in Eq. (4). This method is here proposed as a valuable alternative technique for the estimation of the ground thermal conductivity and the pile thermal resistance.

This approach has been developed and employed for the first time for the evaluation of the TRT measurement data of shallow geothermal piles. In the following paragraph, a comprehensive discussion of the obtained results is proposed.

RESULTS

As described in the previous paragraph, measured temperature values have been employed into a 2 resistance model where the ground is modelled according to a pure heat conduction approach. In particular the ground thermal response is expected to follow TRF solutions that have been built according to a spatial superposition of FLS solutions. Moreover a temporal superposition scheme has been applied for taking into account the variations in the heat rate transferred to the thermal fluid. The number of geopiles that have been investigated is equal to 6, as previously described. Some experimental measurements are presented in Figures 3a and 3b, for test case #1, #2 and #4. Figure 3a is of

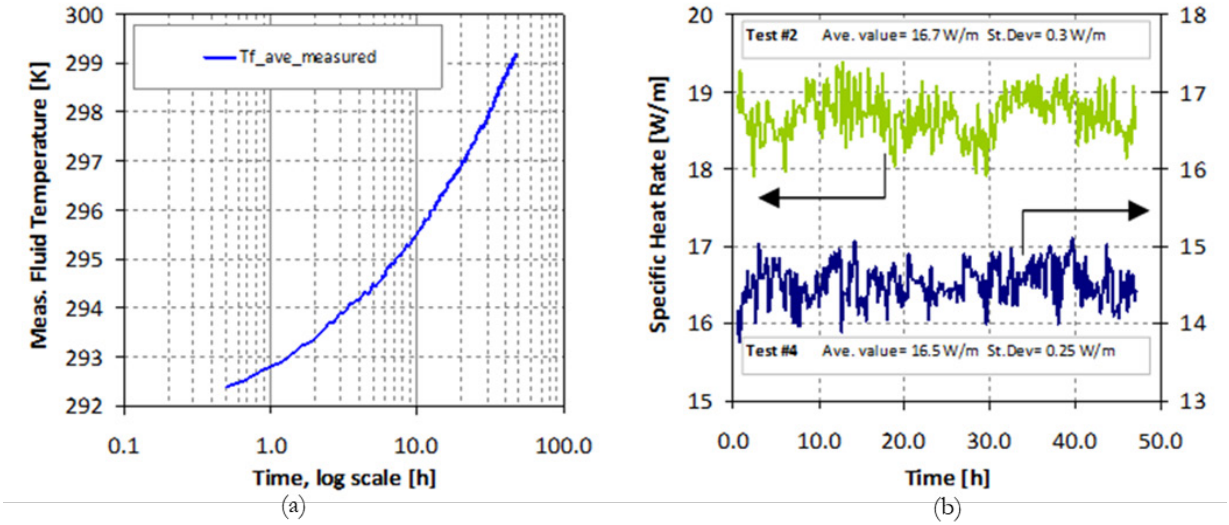

Figure 3 Measured values. (a) average fluid temperature (Test #1, helix pipe). (b) specific heat rate during tests #2 (helix pipe) and #4 (U pipes).

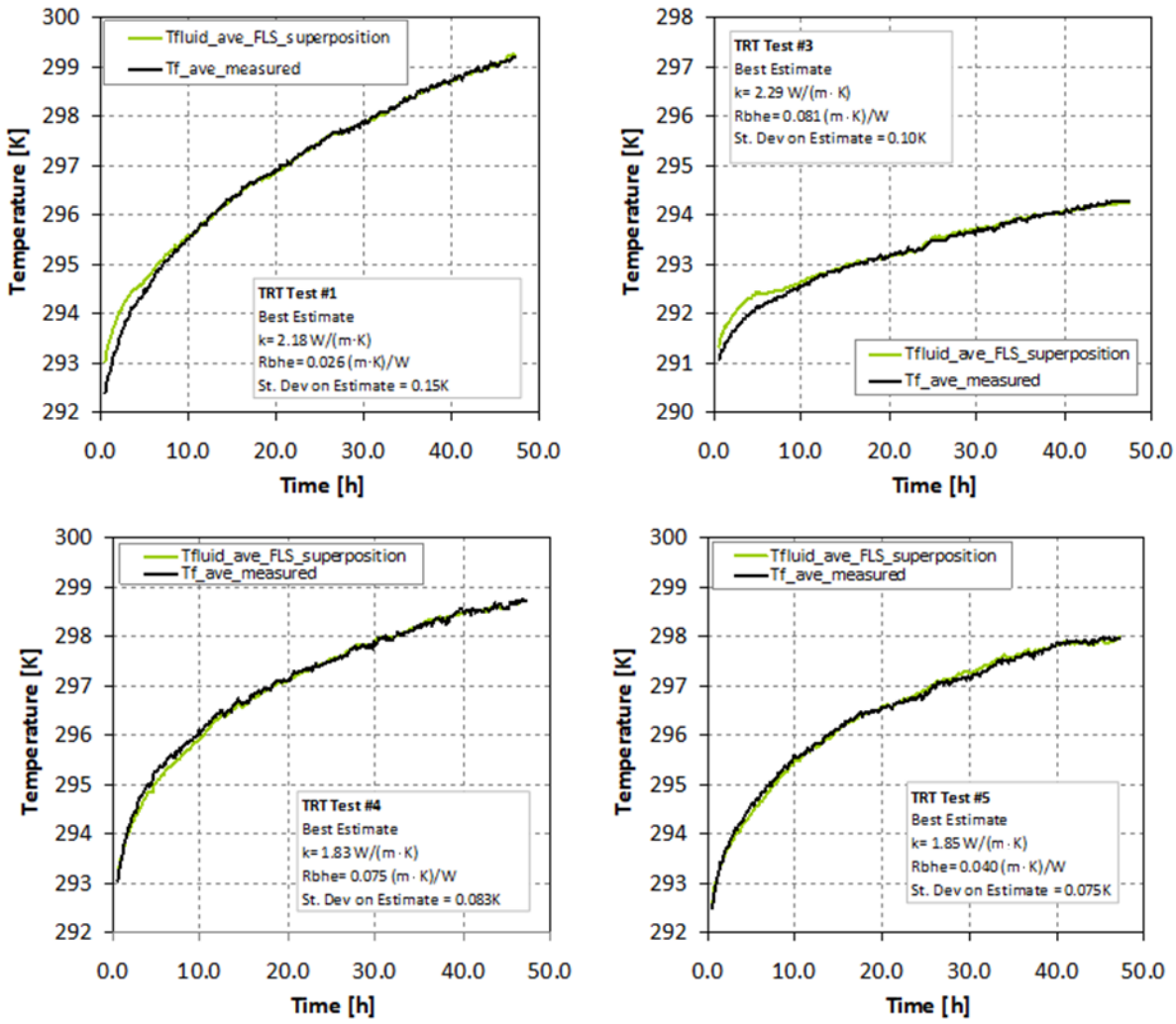

Figure 4 Experimental and Predicted temperature profiles after parameter optimization Inner captions show the final k_{gr} and R_{bhe} values at calculation convergence and related Test Number. Tests #1 and #3, helix pipe. Tests #4 and #5, U pipes.

particular interest according to Authors since it shows that the fluid temperature profile is not linear when represented as a function of the logarithm of time, hence demonstrating that the ILS solution is not adequate for the present analysis. Figure 3b shows the typical fluctuations of the heat rate to the fluid, that are of the order of about 8%, considering as a reference the observed standard deviation and the 95% confidence interval. The above profiles (and statistical meanings) can be considered representative for all the tests here carried out.

Figures 4 show the experimental temperature profiles together with the predicted ones at parameter estimation convergence. Each figure refers to a particular test number and hence to a particular pile geometry and related TRF model. For the sake of paper shortness only 4 test are represented, those not present here have very similar temperature trends. The differences among the measured temperatures and the theoretical ones resulted to be very small of the orders of tenths of degrees, with a typical standard deviation of 0.1 K. The impressive (even at Authors' eyes) result is the so close estimate agreement with the experimental profile since the very beginning of the experiment. The other interesting and peculiar result is the low R_{bhe} values that have been predicted, ranging from 0.03 to 0.08 mK/W.

A series of comments can be done either for explaining the present results or addressing further measurements

and theoretical analyses to the same problem. First of all the distance from pipe to pipe (about 0.3m for either the real situation or its modelling counterpart) and the TRF reference radius r_b makes the R_{bhe} term mainly constituted by the plastic pipe and fluid terms, since the surrounding medium is the grout/ground mass which is accounted for by the transient response described by the TRF solution employed in the iterative procedure. This can be the explanation of the low R_{bhe} values calculated after optimization and also an explanation for the good agreement of predictions from the very beginning of the experiments. Secondly the superposition scheme demonstrated to be able to cope also with high frequency heat rate variations, as a close inspection of the above time profile can demonstrate.

The third and more important result is in principle also the most controversial one, since it refers to the predicted thermal conductivity of the thermal mass embracing the pipe/sources. To which medium does this conductivity pertain? The only reasonable answer is probably to either the ground volume or the concrete one since probably the two thermal masses in this particular lithology case have similar thermal properties. In this sense a longer experiment, lasting for example 10 time more with respect to the present measuring sessions could provide further information on the concrete/ground behaviour and about the limits (if any) of the 2 resistance approach. For sure, this is an experimental evidence, the present modelling approach, based on the use of custom TRFs together with temporal superposition, is able to provide very good predictions of the ground heat exchanger behaviour in a short period ranging from hour fractions to few days.

CONCLUSIONS

A series of Thermal Response Test have been performed with real geopiles having diameter of 1000 and 600mm and a depth of about 15m. Measurements have been recast by calculating the temperature response factor of the different pipe arrangements and then applying a recursive technique of parameter estimation, namely the effective BHE resistance and the ground thermal conductivity. The results of the analysis show a very good agreement between the measured and predicted carrier fluid temperature profiles (standard deviation errors of about 0.1K). Apart the so encouraging results, the present findings are necessarily affected by the thermal properties of either the concrete structure or the surrounding ground, being the former unknown and not estimated by the present algorithm.

An additional issue is related to the duration of the experiments:(i.e. are they long enough for describing the ground response ?). All the above issues deserve further numerical and experimental investigations starting from the present findings which demonstrate that a proper temperature response factor different from the usual Infinite Line Source can be successfully applied for predicting the early period response of thermal piles.

NOMENCLATURE

T	=	temperature (K)
Γ	=	temperature response factor (-)
Fo	=	Fourier number (-)
$\dot{Q}'$	=	specific heat rate (W/m)
k	=	ground thermal conductivity (W/mK)
R	=	thermal resistance (mK/W)
t	=	time (s)

SUBSCRIPTS

g	=	ground
f	=	fluid
bhe	=	borehole

REFERENCES

Abramovitz M. and I. Stegun, 1964. Handbook of mathematical functions with formulas, graphs, and mathematical tables, National Bureau of Standards, 228–233.

Bernier M., P. Pinel, R. Labib and R. Paillot, 2004. *A multiple load aggregation algorithm for annual hourly simulations of GCHP systems*, International Journal of Heating, Ventilating, Air-Conditioning and Refrigeration Research 10: 471–488.

Carslaw H.S. and J.C. Jaeger, 1947. Conduction of Heat in Solids, Claremore Press, Oxford, UK.

Claesson J. and S. Javed, 2011. *An analytical method to calculate borehole fluid temperatures for time-scales from minutes to decades*, ASHRAE Transaction 117(2): 279–288.

Cui P., X. Li, Y. Man and Z. Fang, 2011. *Heat transfer analysis of pile geothermal heat exchangers with spiral coils*, Applied Energy 88: 4113-4119.

Dehghan B., A. Sisman and M. Aydin, 2016. *Parametric investigation of helix ground heat exchangers for heat pump applications*, Energy and Buildings 127: 999-1007.

Eskilson P., 1987. *Thermal Analysis of Heat Extraction Boreholes*. Ph.D. Thesis, Lund University of Technology, Sweden.

Fossa M., B. Stutz, A. Priarone, A. Coperey, 2017. *Thermal Response of helix ground heat exchangers*, in: IGSHPA Technical/Research Conference and Expo, Denver (CO) March 14-16.

Fossa M., 2017. *Correct design of vertical borehole heat exchanger systems through the improvement of the ASHRAE method*, Science and Technology for the Built Environment 23(7): 1080-1089.

Go G.H., S.R. Lee, H.B. Kang, S. Yoon and M.J. Kim, 2015. *A novel hybrid design algorithm for spiral coil energy piles that considers groundwater advection*, Applied Thermal Eng. 78: 196-208.

Ingersoll L.R. and H.J. Plass, 1948. *Theory of the ground pipe heat source for the heat pump* ASHVE transactions.

Ingersoll L.R., O.J. Zobel and A.C. Ingersoll, 1954. Heat Conduction with Engineering, Geological, and other Applications, McGraw-Hill, New York.

Lamarche L. and B. Beauchamp, 2007. *A new contribution to the finite line-source model for geothermal boreholes*, Energy and Buildings 39: 188–198.

Loveridge, F., T. Brettmann, C.G. Olgun and W. Powrie, 2014a. *Assessing the applicability of thermal response testing to energy piles*. In: Global Perspectives on the Sustainable Execution of Foundations, Sweden. 21 - 23 May 2014. 10 pp.

Loveridge, F., W. Powrie and D. Nicholson, 2014b. *Comparison of two different models for pile thermal response test interpretation*. Acta Geotechnica 9, 367–384.

Man Y., H. Yang, N. Diao, J. Liu and Z. Fang, 2010. *A new model and analytical solutions for borehole and pile ground heat exchangers*, International Journal of Heat and Mass Transfer 53: 2593-2601.

Man Y., H. Yang, N. Diao, P. Cui, L. Lu and Z. Fang, 2011. *Development of spiral heat source model for novel pile ground heat exchangers*, HVAC&R Research 17: 1075-1088.

Moch X., M. Palomares, F. Claudon and B. Souyri, 2014. *Geothermal helical heat exchangers: Comparison and use of two-dimensional axisymmetric models*, Applied Thermal Engineering. 73: 689-696.

Priarone A. and M. Fossa, 2016. *Temperature response factors at different boundary conditions for modelling the single borehole heat exchanger*, Applied Thermal Engineering 103: 934–944.

Rabin Y. and E. Korin, 1996. *Thermal analysis of helical heat exchanger for ground thermal energy storage in arid zones*, International Journal of Heat and Mass Transfer 39: 1051-1065.

UNI, 2012. UNI 11466:2012 Geothermal Heat Pump Systems: Sizing and design technical issues.

Yavuzturk C. and J.D. Spitler, 1999. *A short time step response factor model for vertical ground loop heat exchangers*, ASHRAE Transactions 105: 475–485.

Zeng H., N. Diao and Z. Fang, 2003. *Heat transfer analysis of boreholes in vertical ground heat exchangers*, International Journal of Heat and Mass Transfer 46: 4467–4481.

[This page has been intentionally left blank]

IGSHPA SWEDEN 2018 Research Conference

DOI: 10.22488/okstate.18.000005

Preliminary research for eight possible groundwater energy utilisation sites in Southern Finland

Teppo Arola, Isa Witick, Joonas Kouvo, Jussi Kuusela

ABSTRACT

Groundwater energy utilisation has not been widely regognised as a significant renewable energy source for industry in Finland. This investigation provides example of cost-effective study to map groundwater energy utilisation possibilities. The purpose of this investigation is to increase knowledge and promote groundwater energy utilisation in Finland. The investigation was carried out for eight industrial sites located on Nastola, Southern Finland. The research include geological site investigation with groundwater temperature measurements and existing geological, hydrological, geotechnical and environmental literature review. Based on investigations and sites energy consumption data site specific groundwater energy capacity was estimated. Possible environmental barriers for groundwater energy utilisation and preliminary economical calculation was also assessed. Groundwater pumping and infiltration demand for all sites is approximately 43.3 l/s. No significant environmental issues was observed in this investigation. By utilising groundwater energy it is possible to save approximately 600 000 to 800 000 € in yearly energy costs. Hence groundwater energy utilisation can provide cost-effective renewable energy option to all sites. It is possible to plan common groundwater energy system for 2 to 3 companies and hence reduce investment costs. Further actions to continue site investigations is recommended to all sites.

INTRODUCTION

The consequences of climate change has forced international policy to focus increasingly to the energy sector development (Stehfest, et al. 2009; Valkila, et al. 2010). For example, the European Union has committed to reduce greenhouse gases from 85% to 90% below 1990 levels by 2050 (European Commission 2011). Special attention has been paid to the utilisation of renewable energy resources, such as geothermal energy. Geothermal energy utilisation can be divided to two main categories; a) deep geothermal energy which source is the earth's internal energy and systems normally operates in temperature regime of over 100 °C and b) shallow geothermal energy which source is mainly solar energy, which is absorbed by and stored to the upper part of the ground and system's operational temperature is much lower than in deep geothermal energy systems. In Nordic countries term geothermal is widely used to describe the deep geothermal systems and term geoenergy to describe shallow geothermal systems respectively. The term geoenergy is used in this artickle.

Geothermal energy utilisation for heating has increased in Europe (EGEC 2017). Due to technical, economical, climatological and geological reasons geoenergy utilisation is currently the most widely used geothermal resource in the Nordic countries, excluding Iceland. One option to produce geoenergy is to utilise groundwater reservoirs for

Teppo Arola (teppo.arola@gtk.fi) is a chief expert and Isa Witick is a researcher in the Geological Survey of Finland. Joonas Kouvo is a student and Jussi Kuusela is a project manager in the Lahti University of Applied Science.

energy production. Groundwater has been widely used for decades as an energy resource, for instance in China (Banks 2009) and in North America (Ferguson and Woodbury 2005). In Europe, the Netherlands is currently leading groundwater energy producers, having over 2740 systems that utilise both heating and cooling energy from groundwater (Sommer 2014). Sweden has approximately 100 groundwater energy sites with a minimum capacity of 100 kW (Gehlin and Andersson 2016).

The groundwater energy utilisation (GEU) technique is called an open-loop energy system or open-loop system (Bonte, et al. 2011; Haehnlein, et al. 2010) where groundwater is pumped from extraction well, conveyed throught an energy-transfer system and returned the subsurface via an injection well. Short time energy storage can be added to the GEU system by designing the groundwater circulation to operate in two directions. This means that warm groundwater pumped from an extraction well in the winter is used for heating and hence returned to the injection well at a cooler temperature. In the summer the system is reversed with the purpose of the winter time injection well becomes an extraction well from where cooler groundwater is utilised for cooling purposes. This system is known as aquifer thermal energy storage (ATES) (Andersson 1998; Bonte, et al. 2011). Critical parameters to GEU are the amount of utilizable groundwater and its temperature. Suitable geological conditions, i.e. relatively high hydraulic conductivity are necessary to provide adequate groundwater flow. Urbanisation has significantly elevated groundwater temperatures under cities (Benz, et al. 2015; Memberg, et al. 2013), also in Finland (Arola and Korkka-Niemi 2014).

Even geological and climatological conditions in Finland are largely similar than in Sweden (Ehlers 1996) GEU systems are not widely used in Finland; only two industrial size ATES systems are in pilot phase. Hence, there is significant renewable energy reservoir (Arola, et al. 2014) which has not mobilized so far. This industrial related research report provides examples of cost-effective preliminary study to map GEU possibilities. The purpose of this investigation is to increase knowledge and promote GEU.

MATERIAL AND METHODS

The investigation was carried out for eight industrial sites located on Nastola, Southern Finland, approximately 100 km north-east from Helsinki (Fig.1). Geologically all sites are located on the Salpausselkä end-moraine complex (Fig. 2). Salpausselkä in Nastola is narrow east to west oriented ridge shape formation which topographically is approximately 20 to 30 m higher than surrounding landscape. The Centre for Economic Development, Transport and Environment (ELY) have categorized aquifers that are suitable for drinking water utilisation in Finland. These classified aquifers have legal status. All investigated sites are located inside classified aquifer in Nastola (Fig. 1 and 2).

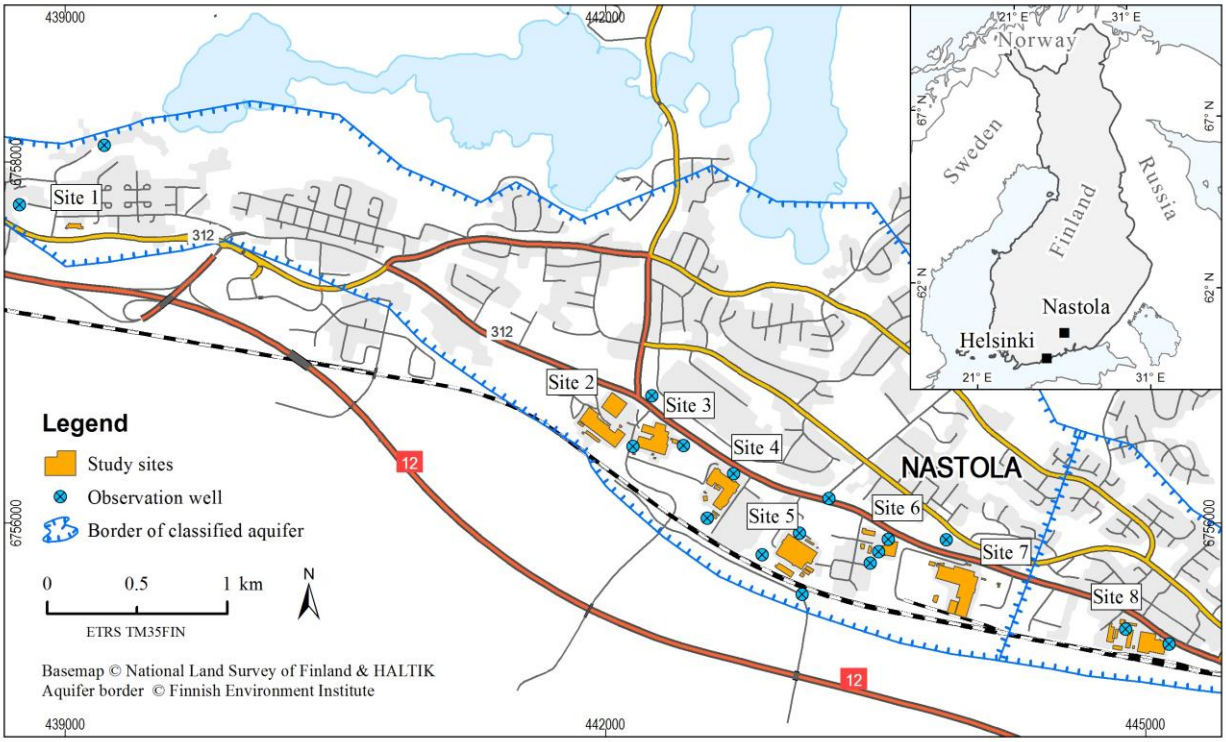

Figure 1 Location map including capital Helsinki (small map) and the study sites. The buildings in investigated property are highlighted with light brown colour. The border of classified aquifer and groundwater monitoring wells is also shown.

Site investigations. The work included literature review of existing geological, hydrological, geotechnical and environmental reports. Publically available information from the classified aquifer database and soil contamination database was investigated. A site visit to all locations were completed in June 2017. Site visit include interview of site manager, geological mapping and groundwater temperature measurements from existing groundwater wells.

Energy consumption data. Hourly based heating energy consumption data was available from seven sites and monthly based heating energy consumption data from one site. Hourly or monthly based cooling energy comsumption data was not available. The heating and cooling energy consumption varied significantly between sites; cooling energy is needed only in three sites. Cooling energy consumption was assessed based on the power demand of coolers and estimating the time needed for cooling. Several studies (i.e. Arola, et al. 2016; Holopainen, et al. 2010; Rosen, et al. 2001) has showed that economically the most suitable option is to dimension geoenergy heat pump system to cover 50% to 60% of the peak design heating power. Noticing above and the sites heating energy demand we calculate the scenarios where 30 % and 60 % of heating power and 100% of cooling power will be covered by GEU system. The results revealed which of the two scenarios would be more pragmatic both technically and environmentally and that scenario was selected for further estimations.

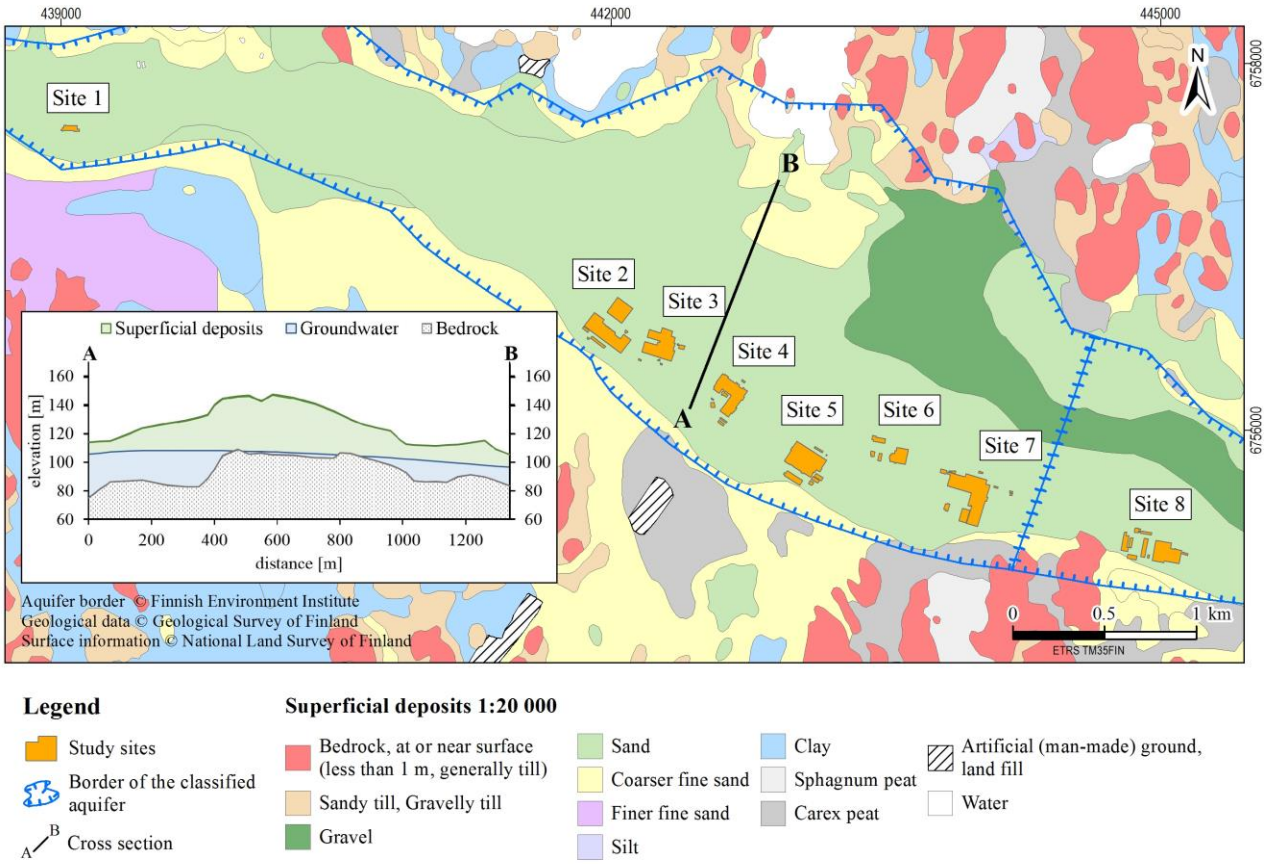

Figure 2 Superficial deposit map and cross section from the research area.

Groundwater pumping demand. The groundwater pumping requirements needed to achieve heating and cooling power were calculated on an hourly basis (8760 hours in a year) using the following equations (Allen, et al. 2003; Banks 2012):

Groundwater flux for heating: $$F_H = H(1-(\frac{1}{COP_H}))/(\Delta T_{in-out} C_w) \quad (1)$$

Groundwater flux for cooling: $$F_C = C(1+(\frac{1}{COP_C}))/(\Delta T_{in-out} C_w) \quad (2)$$

where F_H = flux of water (kgs^{-1}) for heating and F_C for cooling respectively, H is heating power (W) and C cooling power (W), ΔT_{in-out} = temperature difference between incoming and outgoing water in the heat pump / heat exchanger (K), C_w = specific heat capacity of water ($J\ kg^{-1}\ K^{-1}$), COP_H = coefficient of performance of the heat pump for heating (dimensionless), and COP_C = coefficient of performance of the heat exchanger system for cooling (dimensionless). The groundwater flux unit kgs^{-1} was changed to ls^{-1} as the change has no real effects on the results and ls^{-1} is universally used to describe groundwater flow. In heating mode, groundwater utilisation down to a temperature of +1 °C was assumed, and measured average groundwater temperature was used as T_{in} value. Based on sites cooling system technique 16 °C or 22 °C was used as a groundwater returning temperature in cooling calculations. The specific heat capacities of water were taken from Yaws (1998). A heat pump was assumed to be used for heating and a heat exchanger for cooling applications. Based on the information presented by Allen et al. (2003),

Bayer et al. (2011), Saner et al. (2010) and the European Heat Pump Association, EHPA (2009), a COP_H of 4 and COP_C of 30 was used in this analysis.

Environmental effects. The area of groundwater depression cone was calculated by following equation (Fetter 2001):

$$L_{max} = \pm \frac{Q}{2Kbi} \quad (3)$$

where L_{max} is the theoretical maximum width of depression cone (m), Q is the amount of pumped groundwater in day (m^3/d), K is the hydraulic conductivity of soil (m/d), b is the depth of aquifer (m) and i is hydraulic gradient (dimensionless).

Site specific information of soil and groundwater contamination was gathered during the site visit by interviewing site managers.

Preliminary economical calculation. The unit costs of current heating and cooling power were gathered during site visits and yearly energy costs was calculated from each site. Preliminary energy savings was calculated in situation where current heating and cooling energy is replaced by GEU. The costs related to heat and water pump electricity was noticed in calculations.

RESULTS

Total groundwater pumping demand is approximately 1 457 081 m^3 per year (table 1). Groundwater pumping demand varied significantly between sites due to differences in energy consumption. Average groundwater pumping demand, and injection demand in case of ATES, for all sites is approximately 4000 m^3/d which corresponds to 43.3 l/s and maximum daily pumping demand is approximately 7300 - 7400 m^3. In property scale maximum groundwater pumping demand was 20 l/s and minimum 3 l/s. The GEU experiment was estimated for office building only on site 8 due to technical and economic reasons. Hence, groundwater pumping demand is low on site 8.

No glacial sediments or groundwater is known to be contaminated on the area of investigated properties. The width of groundwater depression cone was calculated to be between 40 to 500 metres (table 2). The depression cone was not estimated to reach the nearest communal groundwater intake well.

Groundwater temperature in non-urbanised area was observed to be 6.0 °C, in traffic areas outside the industrial property between 6.6 to 7.1 °C and in industrial property near the buildings between 7.9 to 9.0 °C respectively.

Table 1. Groundwater pumping demands

Site no:	Yearly total demand (m^3)	Hourly avarage (m^3/h)	Daily average (m^3/d)	Max. (l/s)	Max. (m3/h)	Max. (m3/d)
1	55082	7.36	177	3.1	11.1	246
2	255932	29.2	701	11.3	40.6	973
3	317837	36.3	871	19.8	71.3	1712
4	353255	40.3	968	15	54	1302
5	300084	34	820	16	56	1355
6	35906	4	98	3	11	271
7	105737	12.1	290	13.7	49.4	1184
8	33248	4	91	4	15	308
Total	1457081		4016			7351

Table 2. Calculated widht of groundwater depression cone and site distance to the nearest communal water intake station

Site	Widht (m)	Distance to the nearest water intake well (m)
1	40	700
2	200	1300
3	300	1200
4	400	1300
5	500	1500
6	70	1600
7	150	1600
8	100	2000

Economical calculation revealed that it is possible to save approximately 600 000 to 800 000 € in yearly energy costs by utilising groundwater energy in every site.

DISCUSSION

The groundwater pumping demand for each site is realistic and achievable. The ELY-centre has estimated that total recharge of the aquifer in question is 7800 m^3/d. Permissions for current groundwater intake wells situated in aquifer allows groundwater pumping of 9800 m^3/d. In principle ATES system does not affect to the total groundwater balance as same amount of groundwater is injected back to the aquifer as has been pumped out. However, it can be estimated that in Salpauselkä environment 100 % groundwater injection may not be possible. Salpausselkä is heterogeneous and contains several different grain size units which is known to create semi-confined aquifer conditions.

Urbanisation and industrial activity has arisen groundwater temperature 1 to 3 °C from its natural temperature. Observed temperatures are within same limit as measured before from industrial areas in Finland (Arola and Korkka-Niemi 2014). Due to elevated groundwater temperature less groundwater is needed to pump to achieve targeted heating power. One degree increase in groundwater temperature results approximately 20% decrease in groundwater pumping demand if the pumping amount is 4016 m^3/d. Hence urbanisation has significant positive effect to groundwater heating utilisation, both economic and environmentally. Similarly it has negative impact to cooling energy utilisation. However, groundwater temperature is still low even in industrial areas and hence will provide cost-effective solution to cooling also.

Although no soil or groundwater chemical contamination is known it is possible that soil and groundwater is contaminated on the research area. This is due to several decades of industrial activity. Hence industrial activity was in place in Nastola before environmental legislation in Finland. Groundwater pumping and injecting can accelerate groundwater contaminants movement and hence it is essential to know possible contaminant sources in GEU. In general, groundwater quality is suitable for low-temperature groundwater energy utilisation and storage in Finland. However, high Fe and Mn concentrations exist in confined aquifers, where clay deposits overlay sand or gravel units creating unoxic environment (Korkka-Niemi, 2001). Similar unoxic environment is also possible to exist in Salpausselkä region. Hatva (1989) reported maximum Fe concentrations of 27 to 37.4 mg/l and Mn concentrations of 1.9 to 2.3 mg/l in aquifers where clays overlay coarse-grained soil material. These circumstances may cause technical obstacles to GEU system functioning.

Economically yearly savings in GEU system are significant compared to modern heating and cooling costs.

However, this preliminary research concentrates only for thermogeological aspects and engineering changes to energy utilisation, such as piping, drilling, heat pumps etc. is not covered meaning that investment costs are not known at the moment. Banks (2009) and Arola et al. (2016) showed that ATES system increased groundwater energy potential compared to heating or cooling energy utilisation only. The investment costs are more critical on the sites where no current cooling system exists. In these sites it might be more cost-effective to plan simply groundwater heat pump (GWHP) system instead of ATES even cooling energy production from groundwater is extremely cost effective.

Sites 2,3,4,5, and 6 and 7 are locating on neighbour properties. Hence it is possible to plan common ATES systems for example 2 to 3 sites where all sites would utilise same pumping and injection wells. This solution would decrease investment costs. However, common ATES system for 2 or 3 sites will need significant planning for operating phase due to heterogeneous energy consumption between the sites. The geological media, sand and gravel , and groundwater temperature regime is similar than reported from Swedish and Norwegian ATES sites (Andersson, 1998; Eggen and Vangnes, 2005).

CONCLUSION

Groundwater energy utilisation in all research sites is thermogeologically possible and can provide cost-effective solution for heating and cooling energy utilisation. It is also possible to plan common ATES systems where 2 or 3 sites will pump and inject groundwater from common wells. Utilising ground for heating in urbanised area is partly reuse of former waste energy.

Further HPAC, geotechnical and groundwater investigation has been recommended to all sites. Further investigations will provide more accurate information for feasibility study which is needed for decision makers.

This study provided necessary thermogeological information to companies to plan the next steps in GEU process. Investigation showed that thermogeological resource estimation in the first phase of GEU process is essential but can be done in very cost-effective way without massive in situ investigations and tests.

ACKNOWLEDGMENTS

We want to thank all the companies and the Nastolan Energiasäätiö for the opportunity to provide research on your sites.

NOMENCLATURE

ATES = aquifer thermal energy storage
GEU = groundwater energy utilisation
HPAC = heating, plumbing, air-conditioning
F_H = flux of water for heating (kgs^{-1})
F_C = flux of water for cooling (kgs^{-1})
H = heating power (W)
C = cooling power (W)
T = groundwater temperature (K)
C_w = specific heat capacity of water ($J\ kg^{-1}\ K^{-1}$)
COP_H = coefficient of performance of the heat pump for heating (dimensionless)
COP_C = coefficient of performance of the heat exchanger system for cooling (dimensionless)
L_{max} = theoretical maximum width of groundwater pumping depression cone (m)
Q = the amount of pumped groundwater in day (m^3/d)
K = the hydraulic conductivity of soil (m/d)
b = the depth of aquifer (m)
i = the hydraulic gradient (dimensioless).

REFERENCES

Allen, A. Milenic, D and Sikora, P. 2003. Shallow gravel aquifersand urban 'heat island'effect: a source of low entalphy geothermal energy. Geothermics 32:569-578. doi:10.1016/S0375-6505(03)00063-4.

Andersson, O. 1998. *Heat pump supported ATES applications in Sweden*. IEA Heat Pump Centre Newsletter 16:20-21.

Arola T. Okkonen J and Jokisalo J. 2016. *Groundwater utilisation for energy production in the Nordic environment: an energy simulation and hydrogeological modelling approach*. Journal of Water Resource and Protection 8, 642-656. doi: org/10.4236/jwarp.2016.86053.

Arola, T and Korkka-Niemi, K. 2014. *The effect of urban heat islands on geothermal potential: examples from Quaternary aquifers in Finland*. Hydrogeology Journal 22, 1953-1967. doi: 10.1007/s10040-014-1174-5.

Arola T. Eskola L. Hellen J and Korkka-Niemi K. 2014. *Mapping the low entalphy geothermal potential of shallow Quaternary aquifers in Finland*. Geothermal Energy 2:9. doi:10.1186/s40517-014-0009-x.

Banks, D. 2012. An introduction to thermogeology. Ground source heating and cooling. Wiley -Blackwell Publishing. Oxford England.

Banks, D. 2009. *Thermogeological assessment of open-loop well-doublet schemes: a review and synthesis of analytical approaches*. Hydrogeology Journal 17:1149-1155. doi: 10.1007/s10040-008-0427-6.

Bayer, P., Saner, D., Bolay, S., Rybach, L and Blum, P. 2011. *Greenhouse gas emission savings of ground source heat pump systems in Europe: A review*. Renew Sust Energ Rev, 16, 1256 - 1267. doi 10.1016/j.rser.2011.09.027.

Benz, SA., Bayer, P., Menberg, K., Jung, S and Blum, P. 2015. *Spatial resolution of anthropogenic heat fluxes into urban aquifers.* Science of the Total Environment 524-525: 427-439.

Bonte, M., Stuyfzand, P., Hulsmann, A and van Beelen, P. 2011. *Underground thermal energy storage: Environmental risks and policy developments in the Netherlands and European Union*. Ecology and Society 16(1):22.

EGEC. 2017. *2016 EGEC geothermal market report*. European geothermal energy counsil. Brussels.

Eggen, G and Vangsnes, G. 2005. *Heat Pump for district cooling and heating at Oslo airport, Gardemoen*. In proceedings of the 8th IEA Heat Pump Conference. Las Vegas, Nevada, USA May 30 – June 2 2005.

EHPA. 2009. *European heat pump statistic – Outlook 2009*. European Heat Pump Association. pp. 65. Brussels.

Ehlers, J. 1996. Quartenary and Glacial Geology. John Wiley & Sons

European Commission. 2011. *Energy roadmap 2050*. European Commission. Brussels.

Ferguson, G and Woodbury, AD. 2005. *Thermal sustainability of groundwater-source cooling in Winnipeg, Manitoba.* Canadian Geotechnical Journal 42: 1290-1301. doi: 10.1139/T05-057.

Fetter, CW. 2001. Applied Hydrogeology. 4rd edition. Prentice-Hall inc. USA.

Gehlin, S and Andersson, O. 2016. *Geothermal Energy Use, Country Update for Sweden.* European Geothermal Congress 2016.

Haehnlein, S., Bayer, P and Blum, P. 2010. *International legal status of the use of shallow geothermal energy.* Renewable and Sustainable Energy Review 14: 2611-2625. doi: 10.1016/j.rser.2010.07.069.

Hatva, T. 1989. *Iron and manganese in groundwater in Finland. Occurrence in glaciofluvial aquifers and removal by biofiltration*. National Board of Waters and the Environment. Helsinki. Finland.

Holopainen, R., Vares, S., Ritola, J and Pulakka, S. 2010. *Maalämmön ja viilennyksen hyödyntäminen asuinkerrostalon lämmityksessä ja jäähdytyksessä.* VTT – Research notes 2546. 56 pp. Espoo Finland.

Korkka-Niemi, K. 2001. *Cumulative geological, regional and site-specific factors affecting groundwater quality in domestic wells in Finland*. Monograph of the Boreal Environment Research vol. 20. 102 pp.

Menberg, K., Bayer, P., Zosseder, K., Rumohr, S and Blum, P. 2013. *Subsurface urban heat islands in German cities.* Science of the Total Environment 442: 123-133. doi: 10.1016/j.scitotenv.2012.10.043.

Rosen, B., Gabrielsson. A., Fallsvik. J., Hellström, G and Nilsson, G. 2001. *System för värme och kyla ur mark – En nulägesbeskrivning.* Varia 511. Statens Geotekniska Institut, Lindköping, Sweden.

Saner, D., Juraske, R., Kübert, M., Blum, P., Helweg, S and Bayer, P. 2010. I*s it only CO2 that matters? A life cycle per-spective on shallow geothermal system*. Renew Sust Energ Rev, 14, 1798-1813. doi: 10.1016/j.rser.2010.04.002.

Sommer, W. 2014. *Large scale application of Aquifer Thermal Energy Storage*, in 5th European Geothermal PhD Day. Abstracts, pp. 79-81. Technical University of Darmstadt, Germany.

Stephfest, E., Bouwman, L., van Vuuren, DP., den Elzen, MGJ and Eichout, B. 2009. *Climate benefits of changing diet*. Climatic Change 95: 83–102.

Valkila, N and Saari, A. 2010. *Urgent need for new approach to energy policy: the case of Finland.* Renewable&Sustainable Energy Reviews: 14: 2068–76.

Yaws, C. 1998. Chemical properties handbook: physical thermodynamic, environmental, transport, safety and health related properties for organic and inorganic chemicals. McGraw-Hill: New York.

IGSHPA SWEDEN
2018 Research Conference

DOI: 10.22488/okstate.18.000004

The impact of a demand-side management strategy in operating a hybrid geo-district energy system for a high-rise mixed-use residential building in Toronto, Canada

Adam Alaica, M.A.Sc., E.I.T.

ABSTRACT

In Ontario, Canada, the building thermal energy market is largely driven by the low cost of natural gas as a heating fuel source, with natural gas rates being approximately five times less per unit energy than electricity. The hybridization of geo-exchange with conventional building energy systems is a well-established means of optimizing the economics of geo-exchange and accelerating the adoption of this technology as a standard building thermal energy system. Demand-side management (DSM) is a mechanism which can be utilized in Ontario's electricity market (or others with similar demand charge structures) to manipulate a user's overall electricity cost. This case study presents the results of a project currently under development in Ontario for a hybrid geo-exchange system, comprised of an in-house Ground-Source Heat-Pump (GSHP) supplemented by a hot/chilled water district energy system. Utilizing the GSHP as a flexible load, the heat-pump is deactivated during the electrical grid's peak periods, shifting the building's demand to the district system. Transferring the load to the district results in a reduction in the high-rise building's contribution to the electrical grid's peak power demand, and consequently a reduction in the building's blended annual electricity rate. This case study illustrates the potential to reduce a high-rise building's blended annual electricity rate by up to 52%, impacting both the building's plug load and geo-exchange operating costs, proportionally. The simulated results indicate a potential geo-heating and geo-cooling operational cost savings of 14% and 67%, respectively.

INTRODUCTION

In the face of climate change, there is a prominent need for the adoption of low-carbon technology to displace our current dependence on fossil fuel-based building energy systems. According to the U.S Energy Information Administration, the building sector consumed 47.6% of total energy used in the United States (EIA 2012). In Canada the building sector contributed to 17% of the national carbon emissions by economic sector (NRCan 2017). With space heating/cooling requirements typically accounting for 50% of a building's annual energy usage, the integration of high efficiency low-carbon solutions present the potential for significant reductions in both energy consumption and green-house gas emissions.

Ontario's Energy Market

In recent years Ontario's Heating Ventilation and Air-Conditioning (HVAC) market has been predominantly driven by the "spark-spread" between natural gas and electricity, representing the costs differential present between these

Adam Alaica (adam.alaica@enwave.com) is Senior Associate of Community Energy Planning at Enwave North America.

commodities. As it stands, the spark-spread is significant with natural gas costing approximately five times less than electricity, on a per unit energy basis (OEB 2018). The result of this imbalance has guided the HVAC market in the direction of combustion-based heating systems, which has proven to be a difficult hurdle to overcome for GSHP technology.

The environmental benefits of utilizing a GSHP as a building energy provider is dependent on the carbon intensity of the local distribution network powering the mechanical systems. From an emissions perspective, Ontario's electrical grid provides a clean source of low-carbon power, generating less than 5% of energy from gas/oil (IESO 2018); standing among the top five provinces in country with the cleanest electrical grid (NRCan 2017). Through the electrification of building energy systems, significant emissions reductions can be realized. In Ontario, this benefit has been identified and supported with capital subsidies for single family dwelling retrofit programs for GSHPs; however, no funding programs have been established for commercial, institutional, or mixed-use high-rise developments.

For large developments like mixed-use high-rise, commercial, and institutional facilities, the provincial power grid imposes a demand charge mechanism used to cover the cost of providing generation capacity and conservation programs in Ontario. This demand charge mechanism is referred to as Global Adjustment (GA), which is the difference between the hourly provincial electricity price and the regulated price on generation. The GA component of an average customers blended electricity rate can be greater than 50% (IESO 2018). The province allows lager consumers, defined as a customer with monthly average peak power draw of > 1 MW_e, to opt-into a designation referred to as a "Class A Customer". Class A customers are provided the flexibility to manage their grid electrical demand, as GA fees are apportioned based on the customer's percentage contribution to the five provincial peak hours during the previous year. Which would otherwise be administered on a cost per unit energy consumption basis for Class B customers. Through proactively avoiding peak contribution to the provincial grid, Class A customers can strategically manipulate greater than 50% of their blended electricity rate to manage building operating costs.

The Building

This paper introduces the results of a case study for a new development located in Toronto's downtown core. The building is a 70 – storey mixed-use high-rise; its occupancy is predominately residential, with commercial and institutional usage located in the building's 10 – storeys of podium. This development will deliver 63,000 m^2 of gross floor area to the newly developed precinct.

The base case mechanical system for the building would consist of a central penthouse plant with natural gas boilers and electric chillers; in-building forced-air distribution is accomplished via a four-pipe fan coil system. Due to the city's energy efficiency standard imposed on new developments, the base case mechanical design was insufficient in meeting the minimum threshold. However, the city's energy efficiency criteria provides an optional compliance path by incorporating an onsite GSHP system sized to meet a minimum of 20% of total building energy.

The System

To assist the new mixed-use high-rise in meeting their energy efficiency targets while providing a financially viable solution, a hybrid GSHP system was developed. The system consists of an in-building GSHP, an electric boiler, and a hot/chilled/domestic hot water Energy Transfer Stations (ETS). Table 1 provides a summary of the system's equipment selections.

Table 1. Hybrid geo-district equipment specifications

Unit	Specification	Duty
Heat Recovery Chiller	Trane – RTWD	878 kW_{th}
Electric Boiler	Clever Brooks – CR	563 kW_{th}
Chilled Water ETS	Alfa Laval – Gasketed Plat and Frame Heat Exchanger	2,975 kW_{th}
Hot Water ETS	Alfa Laval – Gasketed Plat and Frame Heat Exchanger	4,799 kW_{th}
Domestic Hot Water ETS	Alfa Laval – Double Walled Braised Plat and Frame Heat Exchanger	682 kW_{th}

The in-building GSHP was sized to meet 20% of the building's total energy consumption, translating to a system operated to meet 24% of the peak cooling and 6% of peak heating. With the GSHP operating as a baseload provider, the capacity deficiency is supplemented by the precincts low-temperature district hot and chilled water systems.

Figure 1 provides a schematic representation of the hybrid geo-district system. The proposed system employs a Trane RTWD heat pump to reclaim heat from the building chilled water distribution system (dark/light blue CW S/R circuit) and reject it to the building hot water distribution system (orange/yellow HW S/R circuit). Under simultaneous heating and cooling conditions, the heat recovery chiller allows for waste heat to be reclaimed within the building, sustaining its own internal demand before relying on external sources such as the Ground Heat Exchanger (GHX) or the district ETS. The building chilled water system utilizes the heat recovery chiller and district chilled water ETS piped in a parallel configuration to meet the building's design cooling demand; the heat recovery chiller operates as a GSHP base load provider in cooling only demand scenarios, with the building hot water circuit operating in GHX switch over mode by drawing fluid from the bore-field (dark/light green GHX S/R circuit). The building hot water system utilizes the heat recovery chiller and hot water ETS in a series arrangement. With a cascading arrangement the output of the heat recovery chiller can be polished to the design supply temperature via the district hot water ETS; cascading operation will occur under high demand (>1,100 kW_{th}) and in scenarios where the heat recovery chiller's condenser outlet temperature is below the design hot water supply temperature. The heat recovery chiller will operate as a GSHP base load provider in heating only demand scenarios, with the building chilled water circuit operating in GHX switch over mode by drawing fluid from the bore-field (dark/light green GHX S/R circuit). The hybrid geo-district system utilizes an electric boiler connected in parallel to the building's Domestic Hot Water (DHW) ETS. The electric boiler's primary function is to act as a false electrical load, used to artificially inflate the building's average monthly peak electricity demand to meet the Class A 1 MW_e threshold; with a secondary function of providing DHW heating redundancy with high output temperature capabilities.

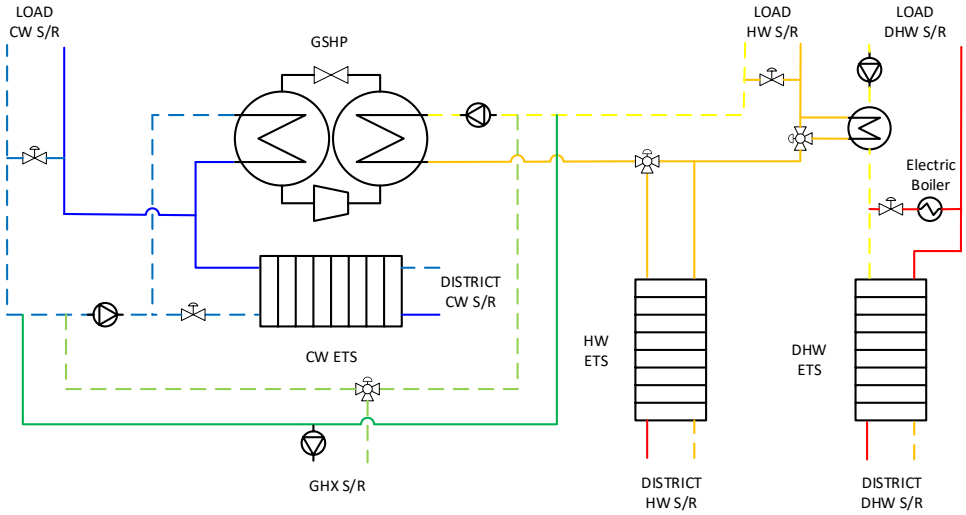

Figure 1 Process flow schematic of the hybrid geo-district energy system

The Control Strategy

The hybrid geo-district energy system for the proposed building case utilizes a DSM control strategy to manipulate the building's blended electricity rate; applicable in any electricity market that has a demand-based rate structure, like Ontario. DSM control strategies for hybrid GSHP plants have shown strong potential in all sectors, academia and industry alike (Carvalho *et. al* 2015; Jassen *et. al* 2015). In Ontario's market, GA drives a significant portion of an end-user's electricity rate. Operating costs of electrical loads can be intelligently managed to provide significant cost savings to an end-user, under the condition they are able to opt-into a Class A rate structure (average monthly peak power demand >1 MW_e).

The hybrid geo-district system was conceived to provide the building with the capability to meet the Class A GA designation, while reserving the flexibility to shift the building's central plant electricity demand to the district energy system. The hybrid geo-district system operates in a manner that is consistant with conventional hybrid GSHP control logic. The GSHP operates as a based load thermal energy provider for the building, with the district energy system being dispatched to provide supplementary heating and cooling under high demand conditions. The proposed DSM strategy introduces two unique operational sequences in addition to the conventional hybrid control logic: (1) artificial monthly peak inflation and (2) grid peak contribution avoidance. The monthly peak inflation sequence is introduced to elevate the building's base case monthly peak power draw to a degree which satisfies the GA Class A, 1 MW_e threshold. The monthly peak inflation is realized through the operation of the electric boiler; when the building experiences its monthly peak demand, the electric boiler (connected in paralled to the DHW ETS in Figure 1) is activated for a maximum of one utility meter sampling cycle, inflating the building's apparent peak power demand.
The grid peak avoidance sequence is a critical element to the success of the DSM strategy, as it has a direct impact on the resulting blended electricity rate. This sequence occurs only 5-hours a year, during the provincial grid's five peak demand hours; under these states, the on-site GSHP and electric boiler are deactivated, and all thermal demand is placed on the district energy system. The result of the grid peak avoidance sequence is a significant reduction in the build's grid power draw and associated Peak Demand Factor (PDF), the ratio the building's peak demand contribution to the provincial grid's demand during the province's five peak demand hours. The DSM strategy targets a maximum reduction in the PDF as this is the critical variable in the GA cost allocation for Class A customers; with the maximum reduction in the PDF, and end-user can minimize their blended electricity rate.

METHODOLOGY

This study consisted of a three-part process in evaluating the implications of the DSM control strategy on the proposed hybrid geo-district energy system. First, a building energy model was developed to establish the building's annual hourly thermal and electrical load profiles. The output of the building energy model was used as an input to numerical simulation of the hybrid geo-district system. Finally, a financial model was developed to assess the economic impact the proposed hybrid system and operational strategy have on the building's blended electricity rate and heating/cooling operational costs.

Building Energy Model

Using eQuest 3-65 (DOE 2009) building energy modelling software, a simulation was conducted for the proposed building to develop annually hourly thermal and electrical load profiles. The simulated profiles were used as inputs to the numerical model of the hybrid geo-district system. Table 2 provides a summary of the simulated thermal and electrical energy requirement for the proposed building. As indicated in Table 2, there is a significant thermal imbalance in the building's demand, with approximately four times more heating required than cooling. With this thermal imbalance, a hybrid GSHP solution provides the necessary flexibility in both design and system operation, allowing the GHX economics to be managed and risk of ground thermal saturation to be mitigated.

Table 2. Summary of thermal and electrical energy requirements

Unit	Demand	Consumption
Space Heating	4,799 kW_{th}	7,790,927 kWh_{th}
Space Cooling	2,975 kW_{th}	2,437,612 kWh_{th}
DHW	682 kW_{th}	1,882,429 kWh_{th}
Electrical Plug Load	383 kW_e	2,627,562 kWh_e

Hybrid Geo-District Numerical Simulation

A numerical simulation of the proposed hybrid system was conducted utilizing the modelling platform Ground-Loop Design (GLD) 2016 Premier (Gaia Geothermal 2016); with a numerical time-step of one hour, simulated for a 20-year period. Table 3 presents a summary of the numerical model assumptions used in the GLD simulations.

Table 3. Summary of numerical model assumptions

Input	Assumption	Unit
GHX Design Flow Rate – Heating Mode	0.06	LPS/kW
GHX Working Fluid	Water – Propylene Glycol (12.9% by Weight)	-
Undisturbed Ground Temperature	10	°C
Soil Thermal Conductivity	2.34	W/m*K
Soil Thermal Diffusivity	0.074	m^2/day
Borehole Thermal Resistance	0.118	m*K/W
Nominal Pipe Size	40	mm
Pipe Type	SDR11	-
GHX Flow Type	Turbulent	-
Borehole Diameter	108	mm
Grout Thermal Conductivity	2.09	W/m*K
Borehole Grid Pattern	12 X 5	-
Borehole Spacing Centre-to-Centre	5	m
Borehole Depth	229	m
Annual Average Load EWT, Cooling	13.3	°C
Annual Average Load EWT, Heating	40.6	°C

Table 4 presents a summary of the GSHP's performance over the 20-year simulation period. The simulated minimum/maximum Entering and Leaving Water Temperatures (EWT and LWT) are reflective of the design day operational peak hour over the 20-year period. The maximum operating capacity in heating and cooling mode represent the GSHP's controlled thermal output to ensure ground thermal loading is seasonally balanced, mitigating the risk of ground thermal saturation. As a result, the GSHP is operated to 24% of peak cooling and 6% of peak heating, meeting 66% and 24% of cooling and heating energy, respectively.

Table 4. Summary of the simulation results

Output	Result	Unit
	GSHP Cooling Performance	
Maximum Sink EWT	28.7	°C
Maximum Sink LWT	33.8	°C
Maximum Operating Capacity	714.1	kW
Design Day COP	5.5	-
Seasonal COP	7.4	-
	GSHP Heating Performance	
Minimum Source EWT	4.2	°C
Minimum Source LWT	2.9	°C
Maximum Operating Capacity	319.5	kW
Design Day COP	3.1	-
Seasonal COP	3.5	-

RESULTS AND DISCUSSION

In this study, the proposed DSM control strategy's impact on the building's hybrid geo-district system operational cost is evaluated. Figure 2 presents the building's hourly grid power demand including the hybrid geo-district plant operation. In Figure 2, the building's power demand (green profile) represents the actual power required to operate the building's various electrical loads. The artificial building power demand (red profile) represents the demand induced on the grid during the building's monthly peak demand hour, through strategically operating the 563 kW_{th} electric boiler to inflate the hourly grid power draw. This strategy allows the 1 MW_e threshold of the Class A designation to be satisfied, providing the building the flexibility of managing the GA operating costs by avoiding the peak contribution during the provincial grid's five peak demand hours.

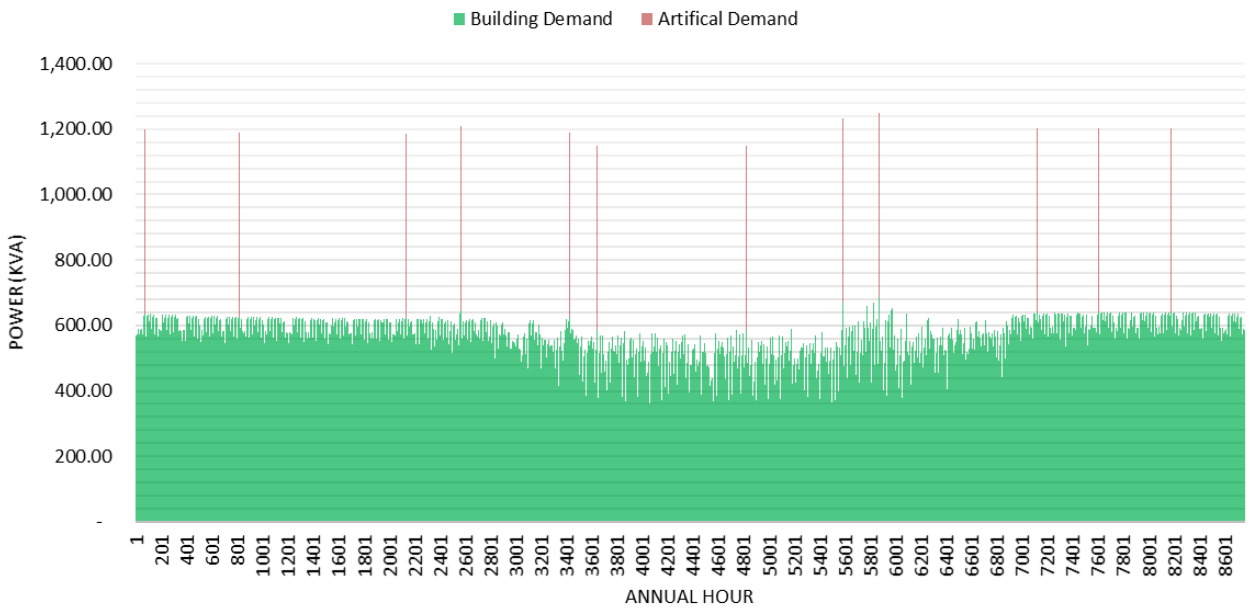

Figure 2 The building annual hourly grid power demand

Three scenarios have been evaluated, the base case Class B (GA cost administered by consumption on a $/kWh basis), Class A with conventional hybrid GSHP system operation, and Class A with GA avoidance (all plant electrical loads deactivated during the five hours of the provincial grid's peak demand). Table 5 presents a summary of the Class A operating scenarios' (regular and avoided GA) PDF. In Table 5, the building peak contribution in kW represents the sum of the building's peak electrical demand during the grid's five peak demand hours, and the provincial grid peak represents the sum of the grid peak power demand during the province's five peak demand hours. The resulting PDF characterises the ratio of the building's peak contribution to the grid's provincial peaks, representing the portion of GA cost paid by a connected customer. As illustrated in Table 5, the avoided GA control strategy reduces the PDF by 47% when compared to a Class A customer operating irrespective of the grid's peak demand hours.

Table 5. Summary of Class A peak demand factor results

Operation Case	Building Peak Contribution (kW)	Provincial Grid Peak (MW)	PDF
Regular	1,796	111,575	0.00001610
Avoided GA	852	111,575	0.00000764

Figure 3 illustrates the building's average monthly blended electricity rate for all three hybrid geo-district system operating scenarios. In Figure 3, the stacked column plots represent the operationally independent cost components of the building's blended electricity rate; the line plots represent the cost of GA for the three proposed operational cases; the scatter plot represents the total blended electricity rate, being the sum of the stacked column and line plot for each operational scenario. As indicated in Figure 3, the results indicate significant financial savings attributed to proposed operational strategy. The base case scenario of the building operating under a Class B rate structure indicates an average annual blended rate of $ 0.156/kWh. When the building's demand is artificially inflated (through dispatching the electric boiler) and operated under a Class A rate structure, the building experiences an average annual blended rate of $ 0.103/kWh, a 34% reduction compared to the base case scenario. Through implementing the proposed DSM control strategy (avoiding the central plant peak power contribution to the grid's five peak demand hours) the building experiences and average annual blended rate of $ 0.074/kWh, a 52% reduction compared to the base case scenario.

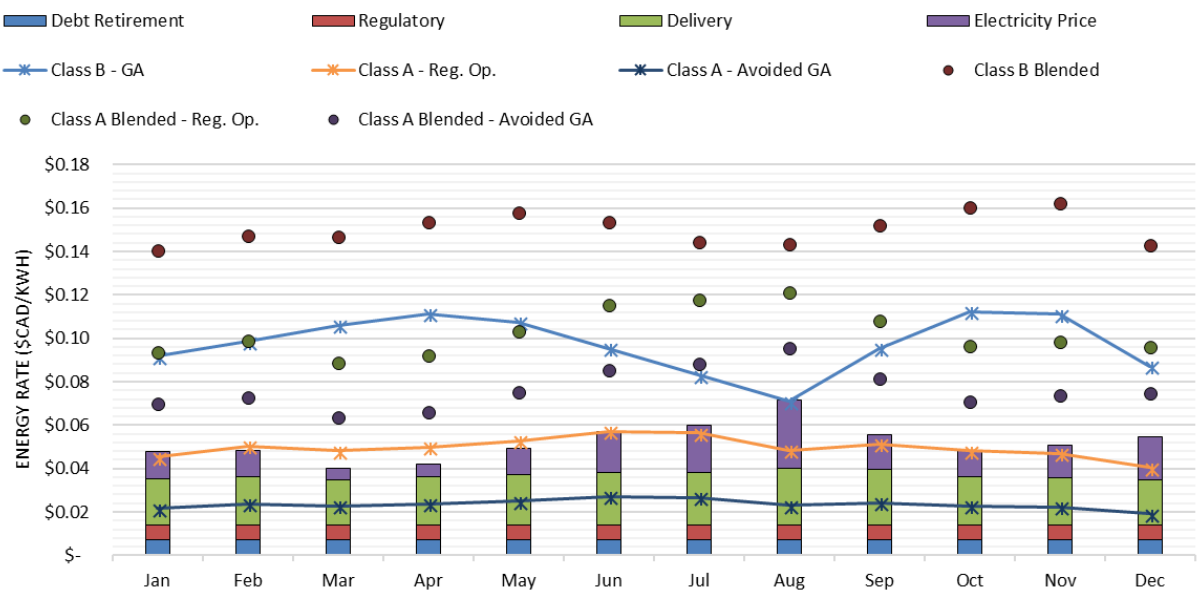

Figure 3 The building's monthly electrical energy rate components and average blended rates

With the proposed DSM operating strategy, the spark-spread between natural gas and electricity has been reduced, allowing geo-heating to become more economical than a natural gas-based solution. The Class A GA avoidance scenario produced a heating and cooling operational cost of $ 0.038/kWh$_{th}$ and $ 0.018/kWh$_{th}$, respectively. When compared to the base case central plant alternative, the GA avoidance scenario reduces the heating and cooling rates by 14% and 67%, respectively.

The integration of the GSHP into the proposed building's district energy based mechanical system provides the means to satisfy the development's energy efficiency and sustainablility targets imposed by the city. Without the hybridization of the building's district energy-based system with a GSHP, the afromentioned operation cost savings would not have been realized. The on-site GSHP and electric boiler combination provide the critical electical load to elevate the building from a Class B to Class A customer designation. The GSHP is an instrumental asset to the proposed building, which makes the use of the DSM control strategy capable of manipulating the building's blended electricity rate, significantly improving the operational economics of the GSHP system in Ontario's challenging energy market.

CONCLUSION

In this study, a DSM control strategy is proposed for a hybrid geo-district energy system, serving a mixed-use high-rise development in Toronto, Canada. The effect of the DSM control strategy on the building's blended annual electricity rate and heating/cooling operating costs were investigated. The proposed DSM strategy has shown strong potential for improving the business case of a hybrid GSHP system in Ontario's energy market and others with similar demand charge structures, even when facing a prominent spark-spread.

The proposed hybrid geo-district system was studied under two electrical rate structures with three operational strategies. Scenario one examined the system under a Class B rate structure (average monthly demand of < 1 MW$_e$) and a conventional hybrid GSHP control strategy; results indicated an average annual blended rate of $ 0.156/kWh. Scenario two evaluated the system under a Class A rate structure (average monthly demand > 1 MW$_e$) and a conventional hybrid GSHP control strategy; results indicated an average annual blended rate of $ 0.103/kWh, a 34% reduction compared to scenario one. Scenario three investigated the system under a Class A rate structure and a DSM control strategy; results revealed an average annual blended rate of $ 0.074/kWh, a 52% reduction compared to scenario one, while reducing the building heating and cooling rates by 14% and 67%, respectively.

ACKNOWLEDGMENTS

The author would like to acknowledge the Ontario Centre of Excellence (OCE) for their financial support.

REFERENCES

Carvalho, A. D., P. Moura, G. C. Vaz and A. T. de Almedia. 2015. *Ground source heat pumps as high effficient solutions for building space conditioning and for integration in smart grids*, Energy Conservation and Managment, vol. 103, pp. 991-1007.

Independent Electrical Systems Operator. 2018. *Transmission-connected generation, supply overview*. Available: www.ieso.ca/power-data/supply-overview/transmission-connected-generation

Independent Electrical Systems Operator. 2018. *Global adjustment components and costs*. Available: http://www.ieso.ca/en/sector-participants/settlements/global-adjustment-components-and-costs

Jassen, E., D. Zhang and T. VanSeters. 2015. *Performance assessment of ubran geo-exchange projects in the greater Toronto area*, Toronto and Region Conservation Authority Technical Report, Toronto. Available: http://www.sustainabletechnologies.ca/wp/wpcontent/uploads/2015/03/GeoExchangeMonitoring_Final_Feb2015.pdf

Natural Resources Canada. 2017. *Energy Fact Book 2016 – 2017*. Available: https://www.nrcan.gc.ca/sites/www.nrcan.gc.ca/files/energy/pdf/EnergyFactBook_2016_17_En.pdf

Ontario Energy Board. 2018. *Rates and your bill, historical energy rates*. Available: https://www.oeb.ca/rates-and-your-bill

United States Energy Information Administration. 2012. *Monthly energy review: energy consumption by sector*. Available: http://www.eia.gov/totalenergy/data/monthly/#consumption.

Gaia Geothermal. 2016. *Ground Loop Design (GLD) 2016 Premier*. Available: http://www.gaiageo.com/desktopindex.html

U.S. Department of Energy (DOE). 2009. *eQuest, the quick and simulation tool*. Available: http://www.doe2.com/eQuest/

IGSHPA SWEDEN
2018 Research Conference

DOI: 10.22488/okstate.18.000036

High temperature borehole thermal energy storage – A case study

Malin Malmberg **Willem Mazzotti** **José Acuña**

Henrik Lindståhl **Alberto Lazzarotto**

ABSTRACT

Combining High-Temperature Borehole Thermal Energy Storages (HT-BTES) with existing Combined Heat and Power (CHP) systems running on waste fuels seems to be a promising approach to increase the energy efficiency of district heating systems through recovery of excess heat summertime from the waste-to-energy operation. This paper presents a case study from Sweden where the potential for charging and discharging waste heat at 95°C from a CHP-plant in summer into and from a HT-BTES is investigated. The interaction between the HT-BTES and the CHP-plant has been simulated with the software tool TRNSYS using the DST (Duct Ground Heat Storage Model) and a number of other TRNSYS tools. The aim of the study has been to design the size and operation of the HT-BTES with regard to energy and power coverage. Several different potential system configurations are presented in this paper, with 1 300 to 1 500 boreholes of 300 m depth. The result shows that it is possible to retrieve around 93 GWh/year of stored heat winter time, with the use of heat pumps using ammoniac as refrigerant. The discharge temperatures from the BTES range between 40-60°C, and up to 70°C in the initial discharge period.

INTRODUCTION

In the 1980s, Sweden was first in constructing a High Temperature Borehole Thermal Energy Storage (HT-BTES) in bedrock: the Luleå Heat Store (Nordell, 1994; Hellström, 1991). New interest for HT-BTES has arose during recent years in Sweden, especially within the district heating sector. A large part of the Swedish district heating production takes place in Combined Heat and Power (CHP) plants. These plants are often waste-to-energy plants that run at high loads and work almost continuously when they constitute a part of a waste management system, resulting in large quantities of waste heat in summer when the district heating demand is low. Furthermore, due to uneven heating demand over the year, the capacity of the CHP plants is often insufficient during peak heat demand in winter and is hence complemented by auxiliary boilers using fossil fuels or expensive biofuels as primary energy source. Operation during peak demand is costly and contributes to a larger carbon footprint. Due to the few annual operational hours the capital invested in such peak load plants is also poorly utilized.

Based on this background, the possibility of shifting some of the surplus heat from summer to winter has been investigated through a case study, in order to increase the flexibility between energy supply and demand in the district heating network and to phase out fossil fuels. The investigated case involves the connection of a HT-BTES to a CHP-plant with large quantities of surplus heats in the summer (approximately 260 MWh).

Malin Malmberg (malin.malmberg@bengtdahlgren.se) is a civil engineer at Bengt Dahlgren Geoenergi, Willlem Mazzoti is a PhD candidate at KTH Royal Institute of Technology and GSHP consultant at Bengt Dahlgren Geoenergi, José Acuña is PhD and a researcher at KTH Royal Institute of Technology and GSHP consultant at Bengt Dahlgren Geoenergi, Henrik Lindståhl is a civil engineer at Tekniska Verken i Linköping AB, and Alberto Lazzarotto is a postdoctoral fellow at KTH Royal Institute of Technology.

A BTES system consists of closely placed vertical boreholes working as ground heat exchangers. It can be drilled in rocks, clays or soils and is applicable in most locations. It is therefore one of the most popular forms of Underground Thermal Energy Storage (UTES) systems. In Sweden, the procedure for authority approvals is usually somewhat simple, the ground loop is easy to construct, and the system requires limited maintenance when using closed borehole heat exchanger loops.

When the Luleå Heat Store was constructed in the 80s, it was built for experimental and demonstrational purpose for Luleå University of Technology. The storage was charged with excess heat from gas combustion in the steelwork of the Swedish Steel Company (SSAB) and supplied space heating for one of the university buildings. This HT-BTES was taken out of operation in 1990 due to lower performance than expected regarding energy storage and extraction (Nordell, 1994). Nonetheless, this project managed to show the potential of HT-BTES and provided experiences about the design, construction and operation of such systems. Twenty years after, a large storage was constructed in Emmaboda, Sweden, and started to operate in 2010 (Nordell, 2016). The HT-BTES in Emmaboda works both as an energy research project and as a part of the Xylem Water Solutions AB plant with the aim to increase the energy efficiency of the plant. Another HT-BTES installation in Sweden is the Anneberg residential area where solar thermal heat is seasonally stored in boreholes and distributed to houses through a low temperature space heating system (Lund and Dalenbäck, 2007). The system has been operated since 2003 with overall good performance.

Several other HT-BTES have also been built outside of Sweden, such as the HT-BTES in Brædstrup, Denmark (Tordrup, et al. 2017; PlanEnergi, 2013), and in Necklarsum and Crailsheim in Germany (Nußbicker, et al., 2003; Schneider, 2013), Okotoks, Canada (Sibbitt, et al., 2015) and in Paskov, Czech Republic (Grycz, et al., 2014; Rapantova, et al., 2016). In Table 1 a summary including years of operation, storage volume and maximal storage temperature reached for the above-mentioned HT-BTES, including the ones in Sweden, is given. The installations in Sweden are constructed in hard crystalline bedrock which is especially suitable for BTES due to the relatively easy drilling procedure. The borehole depth for the HT-BTES presented in Table 1 reaches between 30 m (Necklarsum) to 150 m (Emmaboda) and is, except the Swedish ones, mostly built in soils and clay.

The HT-BTES in Anneberg, Necklarsum, Crailsheim and in Okotoks are all seasonal storages of solar thermal energy and are connected to local low-temperature district heating networks supplying heat to residential areas, whereof the system in Okotoks (Drake Landing Solar Community) has reached a solar fraction as high as 97% after the fifth year of operation. Furthermore, the BTES in Brædstrup is solar-assisted while being connected to the local CHP-plant supplying district heating to the community.

The BTES in Paskov is an experimental HT-BTES charged by excess heat from a CHP-unit taken into operation in 2011 (Grycz, et al., 2014; Rapantova, et al., 2016). The storage was built for experimental purpose with the aim to study the storage system and the rock environmental behavior during different operating states of charging and discharging. The use of a CHP unit gives a continuous supply of heat compared to storing of solar collector heat. The project was initiated to gain more knowledge of BTES with high heat carrier temperatures of 70-90°C.

Table 1. Design Parameters of Existing HT-BTES

Location	Years of operation	Storage volume [m³]	Maximum storage temperature [°C]	Source of charge
Luleå, Sweden	1983-1990	115 000	65	Industrial waste heat
Emmaboda, Sweden	2010-	323 000	45	Industrial waste heat
Anneberg, Sweden	2003-	50 600	45	Solar thermal
Brædstrup, Denmark	2012-	19 000	60	Solar thermal
Necklarsum, Germany	1999-	63 360	65	Solar thermal
Crailsheim, Germany	2008-	37 500	65	Solar thermal
Okotoks, Canada	2007-	34 000	74	Solar thermal
Paskov, Czech Republic	2011-	Unknown	78	CHP

In the majority of these HT-BTES the boreholes have been grouted. The regulations for grouting the boreholes with a sealing material differ between countries. In Sweden groundwater filled boreholes are most common, except in water protected areas or in risk of salt water contamination as it can decrease the risk for contamination of groundwater significantly (Gehlin, 2016). In the case of BTES the magnitude of induced natural convection from groundwater flow in fractures and cracks can furthermore be reduced (Gehlin, 2002).

METHODOLOGY

The aim of this work has been to evaluate potential system configurations for effective extraction and storage of excess heat from a CHP-plant in connection to a HT-BTES. The software TRNSYS (Klein, et al. 2004) has been used to simulate the system performance. TRNSYS is a transient system simulation software tool used worldwide by researchers and consultant engineers which enables modeling of a wide range of thermal energy systems, with the possibility to combine a large variety of system component models (Simulation Studio components). The system has been simulated with two different configurations, with and without heat pumps during discharge of the HT-BTES. Figure 1 and 2 below shows a flow chart of the CHP-plant connected to the HT-BTES respectively the layout of the TRNSYS model used for the simulations, both with the configurations including heat pumps. The TRNSYS model has been iteratively developed at the *Royal Institute of Technology (KTH)* and *Bengt Dahlgren AB*.

The vertical BHEs and their interaction with the surrounding rock has been model with Type 557b available in TESS library in TRNSYS. Type 557b assumes uniformly placed ground heat exchangers in a hexagonal pattern, based on the well-known DST approach, developed by Claesson et al. (1981), Hellström (1989;1991) and Pahud & Hellström (1996). The Type 557b has been widely used for dimensioning of BTES. The temperature in the ground, at a specific point, is derived by superposition of three parts: the global temperature, a local solution and a steady-flux part. The local and the global part are solved using the explicit finite difference method (FDM) while the steady-flux part is solved by an analytical solution. The temperature response is derived through thermal interaction between the BHE regarding the injected/extracted load of the modelled BTES (Hellström 1989).

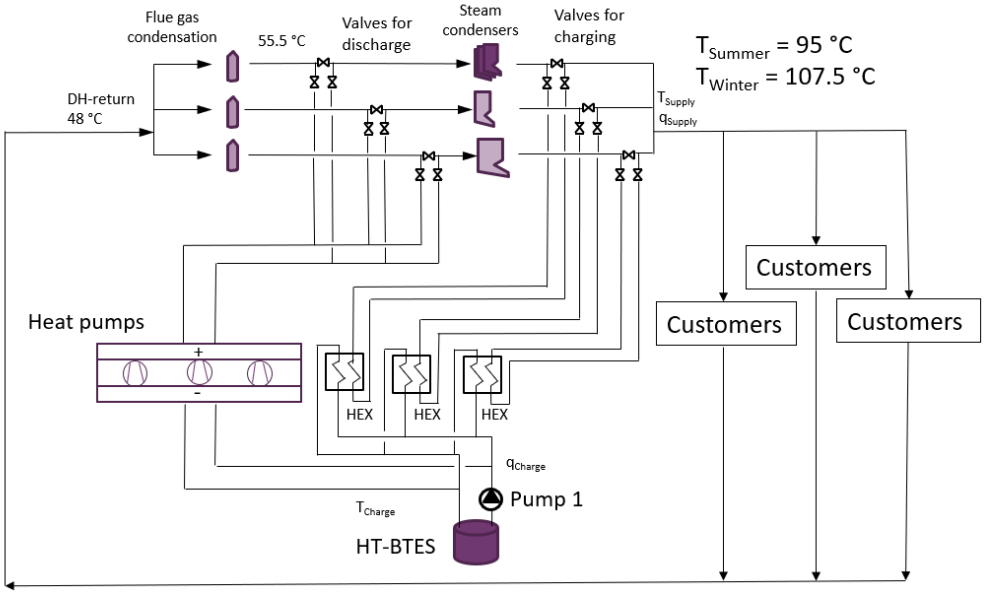

Figure 1 Flow chart for the CHP-plant including a HT-BTES and heat pumps.

In addition to simulation studio components, custom equations were utilized in the TRNSYS model. Furthermore, different data reader components are included. These contains pre-determined input data for operation of the CHP-plant such as district heating temperature, flow rates and power levels. The input data is given as daily mean values. However, the simulations are carried out with a timestep of one-hour. The simulation start corresponds to the first of May and a simulation period of 10 years has been used. The discharge period of the HT-BTES is considered to be between the end of October to the beginning of April. In the simulations the HT-BTES is not discharged during the first year of operation in order to heat up the surrounding ground. This means that it is charged for two periods before discharged.

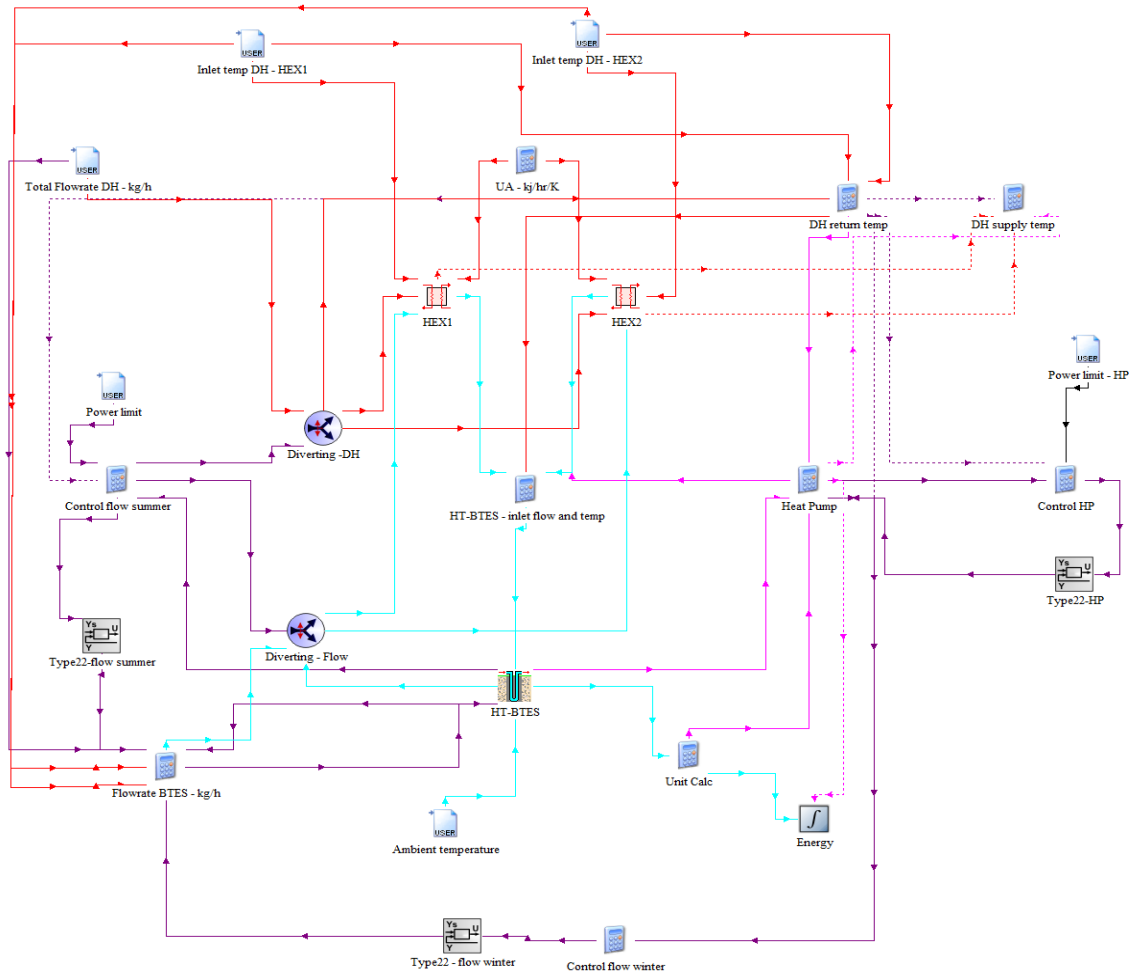

Figure 2 TRNSYS model of the interaction between the CHP-plant, the BTES and the heat pumps.

In the considered system layout (Figure 1) the HT-BTES is charged using the steam condensers of the electricity production unit in the CHP plant. The temperature at the condenser outlet is assumed to be maintained constant at 95°C during summer operation, corresponding to the required district heating supply temperature. During discharge, the HT-BTES is considered to be connected to the CHP-plant with discharge valves placed placed before the steam condensers, but after the flue gas condensers. Depending on the configuration the HT-BTES is discharged through heat pumps (Figure 1) alternatively directly through heat exchangers. In this way, the BTES preheats the district heating return flow without affecting the efficiency of the flue gas condensers. A more thoroughly investigation of how this

configuration would affect the operation of the CHP-plant is needed but has not been included in this study.
The district heating return temperature after passing the exhaust gas condensation is considered to be around 55°C winter time. During discharge phases of the HT-BTES, this temperature is used as inlet temperature to the water side of the heat pumps' condensers (or heat exchangers). The district heating flow varies over the year to obtain the desired supply temperature to the district heating network, with higher flowrates during the colder months when the demand is high. In Figure 3 a) the temperature levels and flowrates used for the simulations in the district heating system can be seen, as well as the ambient temperature.
In Figure 3 b) the power limits for charge and discharge of the BTES is shown in the form of a load duration curve. This limits the maximum possible power levels available or deliverable in the CHP-plant as excess heat (charge) and peak heat demand (discharge including heat pumps). The maximum delivered discharge power, with the use of heat pumps, has been limited to a maximum of 50 MW in the simulations, estimated as the maximum additional power supply that can be handled through the CHP-plant.

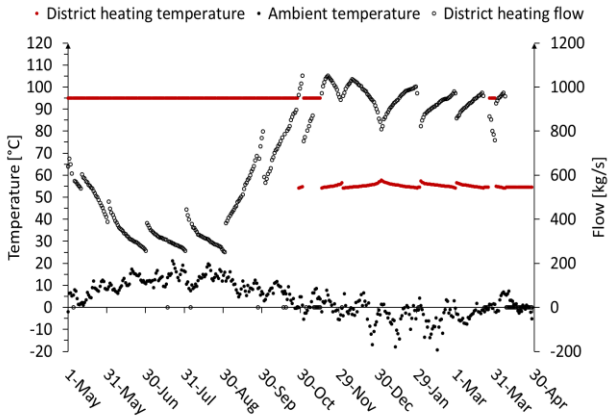

a) Temperatures and flowrates in the district heating network during charge and discharge of the BTES, as well as the ambient temperature

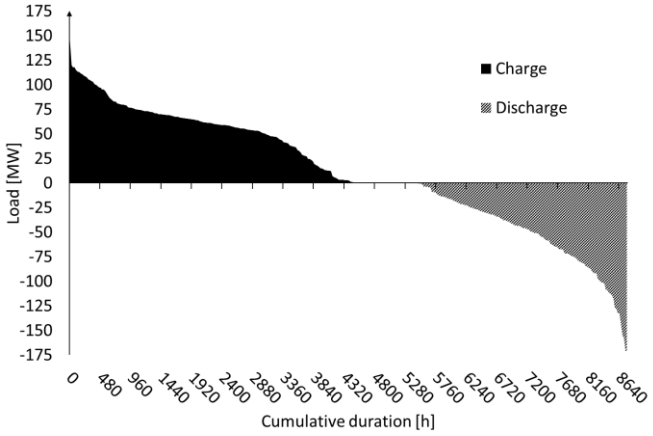

b) Duration diagram for available power levels in the system for charge and discharge of the BTES.

Figure 3 Input data used in the simulations regarding temperatures, flowrates and power levels in the district heating system.

When simulated without heat pumps the charge and discharge of the BTES was made through heat exchangers with the volumetric flow rate in the BTES loop controlled to match respectively not exceed the power limit in Figure 3 b). When simulated with heat pumps different control strategies have been applied in TRNSYS for summer and winter operation of the BTES, during charging and discharging, respectively. In summer mode, the system is controlled in a way similar to the case without heat pumps, with heat exchangers and control of the flow in the BTES. In the winter mode heat pumps are running for discharge of the BTES, connected in parallel to the heat exchangers. The number of heat pumps running during discharge, as well as the compressor speed (indirectly handled in the model) are controlled so that the delivered heating power from the heat pumps match the power limit shown in Figure 3 b), but at maximum 50 MW.
The heat pump model used for the simulations has been developed through a regression analysis from manufacturer's data for a two-stage high-temperature industrial heat pump unit, consisting of five individual 10 MW heat pumps which evaporators and condensers are respectively connected in series. The heat pump model has been applied to the TRNSYS model using custom equations. In winter mode the flow in the HT-BTES loop is furthermore controlled to give a

temperature difference of around 2 K over each evaporator. The number of heat pumps running in the model is not necessarily an integer, but it is representing an equivalent number of heat pumps running on full capacity (3600 RPM). The actual number of heat pumps is always rounded up and works with variable compressor speed at the high stage compressor. See Equation 1. The first compressor in each heat pump is always running on nominal speed (2950 RPM). The heat pump model is a simplification of the reality but is capturing the general behavior of the system.

$$RPM_{2^{nd}\ compressor} = 3600 \cdot \left(\frac{Number\ of\ HP}{Equvivalent\ number\ of\ HP_{Full\ speed}} \right) \quad (1)$$

The HT-BTES has been simulated with the number of boreholes varied between 1000-2000, borehole depth varied between 250-300 m and borehole spacing varied between 4-6 m, with a serial connection of up to three boreholes to induce thermal stratification of the storage. The system was furthermore simulated with two different borehole heat exchangers (BHEs): double U-pipes and coaxial. Some general input values used in the simulations are shown in Table 2 below. With regard to the higher density gradient of water at the operating temperatures, the borehole resistance is assumed to be 0.05 $K \cdot m \cdot W^{-1}$ for double U-pipes and 0.025 $K \cdot m \cdot W^{-1}$ for coaxial collectors, based on experience from field tests. The thermal conductivity of the ground is assumed as 2.9 $W \cdot m^{-1} \cdot K^{-1}$. All simulations have been made without regard of heat losses occurred due to ground water flow.

Table 2. Assumed Input Data for the Simulations

Parameter	Value
Borehole radius [m]	0.055
Heat transfer conductivity ground [W/(m·K)]	2.9
Heat capacity of the rock [kJ/(m³·K)]	2241
Heat capacity of the heat carrier fluid [kJ/(m³·K)]	4.2
Density of the heat carrier fluid [kg/m³]	976
Insulation thickness (on top of storage) [m]	0.4
Heat transfer conductivity insulation [W/(m·K)]	0.13
Undisturbed ground temperature [°C]	8.0
Borehole resistance (double U-pipes) [(K·m)/W]	0.05
Borehole resistance (coaxial) [(K·m)/W]	0.025

RESULTS

Results from the initial simulations, all made with 1 500 boreholes, 300 m depth and 5 m borehole spacing, showed that the use of a heat pumps are required if the system is to deliver the desired power and temperature level to the CHP-plant during discharge. With the use of heat pumps the discharged energy showed to increase with up to 84%. The heat pumps require operational energy as opposed to direct heat exchange. The TRNSYS simulations furthermore showed that when boreholes were coupled in series of three, compared to all being coupled in parallel, the available energy discharge increased with up to 17%. When increasing the flow in the BTES, from 0.5 m³/s to 1.0 m³/s the discharge energy also showed to increase with up to 17%, though the discharge temperature decreased with 5-7%. The result furthermore shows about 30% lower operational energy for the circulation pumps in the BTES when simulated with coaxial BHE compared to double U-pipes.

Based on several simulations three designs were found with similar performance: 1 400 boreholes with double U-pipes and a borehole depth of 300 m (Case 1), 1 300 boreholes with coaxial BHEs and a borehole depth of 300 m (Case 2), and a design with 1 500 boreholes and 275 m borehole depth with double U-pipes (Case 3) – all three designs with a borehole spacing of 5 m and with loops of 3 boreholes connected in series. The three BTES designs showed similar

results with a potential to store around 107 GWh/year and to extract around 93 GWh/year with the use of a GSHP after the fourth simulation year.

In Figure 4 a)-c) some results from the simulations with 1 300 boreholes, coaxial collectors and a borehole depth of 300 m is shown. Figure 4 a) shows how the control of the heat pumps is handled in the simulations, as was previously explained. In Figure 4 b) the system temperatures can be seen for the fifth simulation year for the heat pumps, BTES and district heating system. The resulting discharge temperature from the BTES ranges between 40-60°C and up to 70°C in the initial discharge period with the mean temperature during discharge reaching almost 60 °C in the tenth simulation year. In Figure 4 c) the corresponding system power levels are presented for the fifth simulation year. As can be seen the charged and discharged power of the BTES is respecting the power limit of the district heating network, and the maximum power delivered from the heat pumps is limited to 50 MW.

In general, the capacity of the system increases with time. Experience from existing HT-BTES, and the simulations, the system requires 3-4 years of operation before reaching its expected performance. The energy output-to-input ratio, calculated as the ratio between charged and discharged energy of the HT-BTES increases with time to reach about 90% in the tenth simulation year (Figure 4 d). As can be seen in Figure 4 d the performance of the HT-BTES is similar for the three configurations presented in this paper.

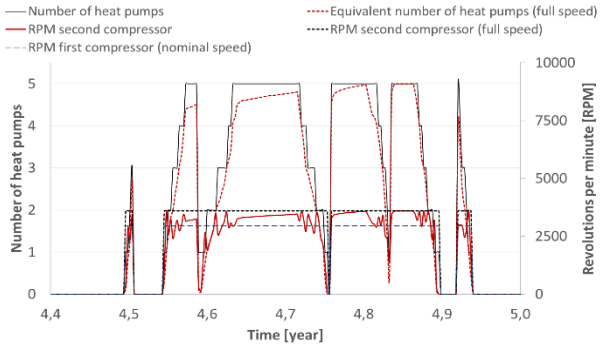

a) Visualization of how the heat pump model works regarding the number of heat pumps running and the compressor speed of the two stage compressors in each heat pump.

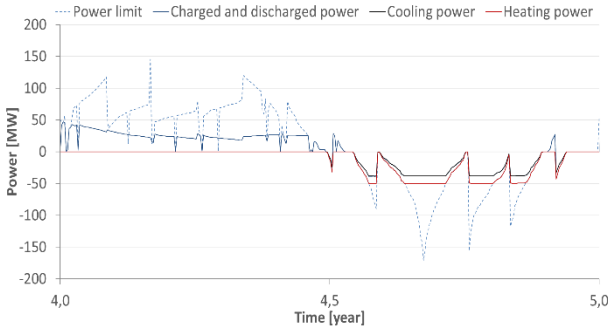

b) Charged and discharged power of the BTES and the heating and cooling power of the heat pumps, with respect to the power limit.

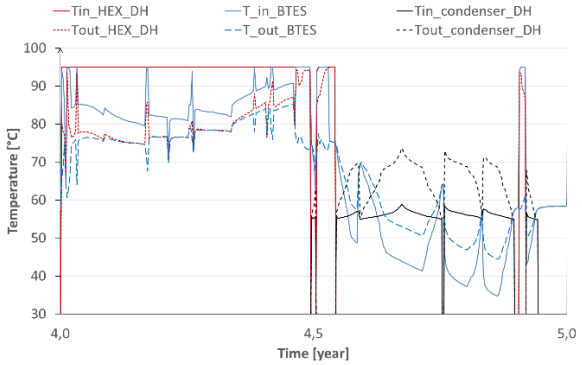

c) System temperatures for the heat pumps, BTES and district heating system

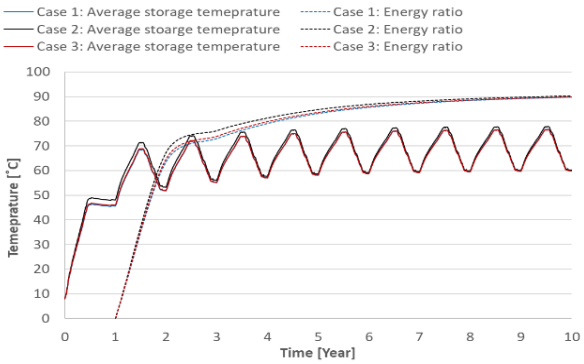

d) Average storage temperature and energy output-to-input ratio for the three HT-BTES configurations.

Figure 4 a)-c) Results from the TRNSYS simulations for the case with 1 300 boreholes and coaxial collectors; d) performance of the three HT-BTES configurations.

DISCUSSIONS AND CONCLUSION

In this project, a HT-BTES for seasonally storing excess heat from summer operation of a CHP-plant has been simulated in the software tool TRNSYS using the DST (Duct Ground Heat Storage Model). With the use of a HT-BTES as a part of the district heating system the flexibility between energy supply and demand in the district heating network can be increased. The BTES was simulated with two different BHEs: double U-pipes and coaxial. The tested geometries that showed the most favorable results consists of 1 400 boreholes and 1 300 boreholes with double U-pipes and coaxial collectors respectively, both with a borehole depth 300 m and a spacing of 5 m. When simulating with a lower borehole resistance, corresponding to coaxial collectors, the storage capacity of the system increased due to the improved heat exchange in the BHE and the size of the BTES could be decreased. Furthermore, a geometry with 1 500 boreholes and 275 m borehole depth with double U-pipes showed similar results regarding energy, power and system temperatures. The three systems showed a potential to store around 107 GWh/year and to extract around 93 GWh/year with the use of a GSHP. The resulting discharge temperature from the BTES ranges between 40-70°C.

The pressure drop in the BHE is overall rather high for the simulated systems, with up to 6 bars with double U-pipes, a borehole depth of 300 m and 3 boreholes in series. If the number of boreholes in series would be reduced the pressure drop would decrease significantly, both as the total collector length is decreased in each loop and that the number of borehole loops would increase resulting in a lower volumetric flowrate in each loop. How this would affect the thermal performance should be investigated further. Coaxial collectors would decrease the pressure drop, and thus the required operational energy for the circulation pumps in the BTES by about 30%. Using coaxial collectors should then be considered as they both improve the heat exchange and leads to lower pressure drop in the BHEs and thereby decreasing the required pumping energy. Further investigation is needed to ensure the market availability of a coaxial BHE that can withstand the high temperatures of this application.

Another subject where further investigation is needed is the influence on microbiology and geochemistry in HT-BTES applications. BTES systems operating at temperatures above 40°C can increase the risk of causing geochemical disturbance and affecting the microbiological balance in the ground (Gehlin, 2016). Several studies have shown no evidence for increasing number of bacteria or growth of pathogens related to increased temperature in the ground, but have showed a change in the composition of bacterial species (Bonte, et al., 2011). However, this is one subject regarding HT-UTES where the information is very limited.

Abbreviations

BHE = Borehole heat exchangers
BTES = Borehole thermal energy storage
CHP = Combined heat and power
GSHP = Ground source heat pump
HT = High temperature
RPM = Revolutions per minute
TRNSYS = TRansient system simulation program
UTES = Underground thermal energy storage

REFERENCES

Bonte, M., Stuyfzand, P. J., Hulsmann, A. & Beelen, P. V., 2011. *Underground Thermal Energy Storage: Environmental Risks and Policy Developments in the Netherlands and European Union.* Ecology and Society, 1 March.16(1)(22).

Claesson, Eftring, Hellström, Johansson. 1981. *Duct storage model*, Dept. of mathematical physics, Lund institute of technology, Sweden.

Erlström, M. et al., 2016. *Geologisk information för geoenergianläggningar: en översikt*, s.l.: Sveriges Geologiska Undersökning (SGU).

Gehlin, S., 2002. *Thermal Response Test - Method Development and Evaluation,* Luleå: Luleå University of Technology.

Gehlin, S., 2016. *Borehole Thermal Energy Storage*. in: S. J. Rees, red. Advances in Ground-Source Heat Pump Systems. u.o.:Woodhead Publishing, pp. 295-327. ISBN: 978-0-08-100322-0.

Grycz, D., Hemza, P. & Rozehnal, Z., 2014. *Charging of the Experimental High Temperature BTES Via CHP Unit - Early Results*. Energy Procedia, Volume 48, pp. 355-360.

Hellström, G., 1989. *Duct Ground Heat Storage Model - Manual for Computer Code,* Lund: University of Lund, Department of Mathematical Physics.

Hellström, G., 1991. *Ground heat storage : thermal analyses of duct storage systems*, Lund: University of Lund, Department of Mathematical Physics.

Klein, S. A., et al. 2004. *TRNSYS 16 – A TRaNsient SYstem Simulation program*, Solar Energy Laboratory. Univ. of Wisconsin. USA.

Lundh, M., Dahlenbäck, J.-O. 2007. *Swedish solar heated residential area with seasonal storage in rock: Initial evaluation. Renewable Energy*, Volume 33, pp. 703–711.

Mangold, D. & Deschaintre, L., 2015. *Seasonal Thermal Energy Storage - Report on State of the Art and Necessary Further R&D,* Stuttgart: International Energy Agency - Solar Heating & Cooling Programme (SHC), Task 45 Large Systems.

Nordell, B., 1994. *Borehole heat store design optimization,* Luleå: Luleå University of Technology.

Nordell, B. o.a., 2016. *Long Term Evaluation of Operation and Design of the Emmaboda BTES: Operation and Experiences 2010-2015,* Luleå: Luleå University of Technology.

Pahud, D. & Hellström, G., 1996. *The New Duct Ground Heat Model for TRNSYS*. Eindhoven, Netherlands. 25-27 March, s.n.

PlanEnergi, 2013. *Boreholes in Brædstrup,* u.o.: Brædstrup Totalenergianlæg, Via University College, GEO, P. Aersleff, SOLITES.

Rapantova, N. et al., 2016. *Optimisation of experimental operation of borehole thermal energy storage*. Applied Energy, Volume 181, pp. 464-476.

Rees, S. J. 2016. *Advances in Ground-Source Heat Pump Systems*. Duxford, UK: Woodhead Publishing.

Reuss, M., 2015. The Use of Borehole Thermal Energy Storage (BTES) Systems. In: L. F. Cabeza, ed. *Advances in Thermal Energy Storage Systems: Methods and Applications*. s.l.:Woodhead Publishing , pp. 117-147. ISBN 978-1-78242-096-5.

Schneider, B., 2013. *Storing Solar Energy in the Ground,* Eggenstein-Leopoldshafen: FIZ Karlsruhe - Leibniz Institute for Information Infrastructure.

Sibbitt, B., McClenahan, D., Djebbar, R. & Paget, K., 2015. *Groundbreaking solar - Case study Drake Landing Solar Community.* High Performing Buildings (HPB), July, pp. 36-46.Sibbitt, B. et al., 2012. *The Performance of a High Solar Fraction Seasonal Storage District Heating System – Five Years of Operation*. Energy Procedia, Volume 30, pp. 856-865.

Tordrup, K.W., Poulsen, S.E., & Bjørn, H. 2017. *An improved method for upscaling borehole thermal energy storage using inverse finite element modelling.* Renewable Energy, Volume 105, pp. 13-21.

[This page has been intentionally left blank]

IGSHPA SWEDEN
2018 Research Conference

DOI: 10.22488/okstate.18.000049

A double source heat pump: a case study

Angelo Zarrella
Diego Guzzon
Giuseppe Emmi
Roberto Zecchin
Michael Ciantia
Philippe Pasquier
Michele De Carli

ABSTRACT

The design of a Ground Source Heat Pump (GSHP) system is critical because design choices affect the system's energy performance and operating conditions. If the thermal load profile on the ground side is unbalanced the ground temperature will change throughout the time and, consequently, also the energy efficiency of the heat pump. This phenomenon is known as "ground thermal drift". A possible solution to avoid this inconvenience is the adoption of a hybrid system.

In this work a double source heat pump is investigated, i.e. the heat pump can use air or ground as heat source or heat sink. The case study is an office building located in the city of Padova (Italy). The building load profile is cooling dominant and a thermal drift can be observed in the monitoring records. A new water-to-water heat pump coupled to the boreholes and also to an air-cooled condenser was recently installed in order to tackle the thermal drift of the ground.

Detailed computer simulations of the system were carried out via EnergyPlus software to investigate the energy performance of the system and the control strategy for switching between the heat sources (air or ground). The study shows the advantages of the double source heat pump.

INTRODUCTION

Ground source heat pump (GSHP) systems are an attractive as well as a promising and worldwide used technology for space heating and cooling of buildings (Bayer et al., 2012). The primary advantage of these systems is the use of the ground or groundwater as the heat source-sink for the heat pump instead of the outside air (Michopoulos et al., 2007). The main disadvantage of GSHP systems, compared to conventional ones, is surely the higher initial costs due to drilling for ground heat exchangers or groundwater wells.

An important aspect to consider is that the energy efficiency of heat pumps fully depends on the temperatures of the secondary heat-carrier fluids on the condenser and evaporator sides. The temperatures on the building side in the heating and cooling modes are usually fixed or controlled, whereas the temperature of the external heat-carrier fluid, in the case of borehole heat exchangers depends on the ground thermal-physical properties and temperature as well as on the annual ground load profile and the borehole field layout. In fact, if the annual amount of heat extracted from the ground in the heating mode is higher (lower) than that injected into it in the cooling mode, the long-term

Angelo Zarrella (angelo.zarrella@unipd.it) is Assistant Professor of Energy Science at University of Padua. Roberto Zecchin (roberto.zecchin@unipd.it) is former Professor of Thermal Systems at University of Padua and partner at Manens-Tifs S.p.A. Philippe Pasquier (philippe.pasquier@polymtl.ca) is Professor of Hydrogeology at Polytechnique Montréal. Diego Guzzon (dguzzon@manens-tifs.it) and Michael Ciantia (mciantia@manens-tifs.it) are mechanical engineers at Manens-Tifs S.p.A. Michele De Carli (michele.decarli@unipd.it) is Associate Professor of Energy Buildings at University of Padua. Giuseppe Emmi (giuseppe.emmi@unipd.it) is Research Assistant at University of Padua.

ground temperature decreases (increases). This behaviour is well-known as thermal drift of the ground and affects the system's energy efficiency. Hybrid GSHP systems can help to reduce this disadvantage since the annual load profile on the ground can be balanced through an auxiliary system, e.g. a cooling tower or an air-to-water chiller in cooling and a gas boiler or solar thermal collectors in heating mode. Moreover, the hybrid systems can also reduce the initial investment. Recently, a double source heat pump for heating, cooling and domestic hot water production was investigated in the framework of a H2020 European project named Geot€ch (2018); in this case, the control system of the heat pump selects the most favourable source or sink between air or ground. Ruiz-Calvo et al. (2017) and Corberán et al. (2018) analysed the thermal performance of that dual source heat pump in an office building in the Netherlands.

In this work a retrofit of an existing ground source heat pump is analysed. The retrofitted system consists of a new heat pump coupled with both the ground, by means of the existing borehole heat exchangers, and an air-condenser used during the cooling season. A simulation model, tuned on eleven years of monitoring of the previous system, was used to carry out multi-year integrated simulations in order to evaluate the long-term thermal behaviour of the entire system and investigate the control strategy of the air-condenser.

METHOD

The computer simulations were carried out by means of the well-known energy simulation program EnergyPlus (U.S. Department Of Energy, 2016). Through this tool a detailed modelling of the building and the plant-system is possible. The borehole heat exchangers (BHEs) are simulated via the well-known g-functions approach (Eskilson, 1987). Given the dimensionless nature of the g-function, it is possible to precompute the transfer function and apply it to various BHE configurations and ground thermal properties. Once constructed, the g-function of the BHE is convoluted with the incremental heat flux signal to obtain the mean fluid temperature in accordance with the equation below:

$$T_f(\tau) = T_g + q(\tau)\cdot R_b + \sum_{i=1}^{n}\left(\frac{q_i - q_{i-1}}{2\pi\cdot\lambda}\cdot g\left(\frac{\tau-\tau_{i-1}}{\tau_s},\frac{r_b}{L_b}\right)\right) \quad (1)$$

where $\tau_s = L_b^2/(9a_g)$ is the characteristic time.

Eskilson's original work considered the situation of a uniform temperature along the borehole wall that was the same for all the boreholes present in the field. To explain the influence of the boundary conditions on early time steps, Eskilson proposed using a constant heat extraction–injection rate on the time-scale below:

$$\tau = \frac{5r_b^2}{a_g} \quad (2)$$

This time step for a typical borehole turns out to be between 2 to 6 hours.

At each time step, the energy efficiency of the heat pump can be calculated using the following equations; in the cooling mode:

$$\frac{Q_c}{Q_{c,nom}} = A_1 + A_2\cdot\left(\frac{T_{L,in}}{T_{ref}}\right) + A_3\cdot\left(\frac{T_{S,in}}{T_{ref}}\right) + A_4\cdot\left(\frac{\dot{V}_L}{\dot{V}_{nom}}\right) + A_5\cdot\left(\frac{\dot{V}_S}{\dot{V}_{nom}}\right) \quad (3)$$

$$\frac{P_{elc}}{P_{elc,nom}} = B_1 + B_2\cdot\left(\frac{T_{L,in}}{T_{ref}}\right) + B_3\cdot\left(\frac{T_{S,in}}{T_{ref}}\right) + B_4\cdot\left(\frac{\dot{V}_L}{\dot{V}_{nom}}\right) + B_5\cdot\left(\frac{\dot{V}_S}{\dot{V}_{nom}}\right) \quad (4)$$

in the heating mode:

$$\frac{Q_h}{Q_{h,nom}} = C_1 + C_2 \cdot \left(\frac{T_{L,in}}{T_{ref}}\right) + C_3 \cdot \left(\frac{T_{S,in}}{T_{ref}}\right) + C_4 \cdot \left(\frac{\dot{V}_L}{\dot{V}_{nom}}\right) + C_5 \cdot \left(\frac{\dot{V}_S}{\dot{V}_{nom}}\right) \quad (5)$$

$$\frac{P_{el\,h}}{P_{el\,h,nom}} = D_1 + D_2 \cdot \left(\frac{T_{L,in}}{T_{ref}}\right) + D_3 \cdot \left(\frac{T_{S,in}}{T_{ref}}\right) + D_4 \cdot \left(\frac{\dot{V}_L}{\dot{V}_{nom}}\right) + D_5 \cdot \left(\frac{\dot{V}_S}{\dot{V}_{nom}}\right) \quad (6)$$

where T_{ref} is a fixed value equal to 283.15 K.

The model of the heat pump when it operates with the air-condenser is implemented in the energy model by the following three equations: chiller capacity as function of leaving chilled fluid temperature and entering condenser air temperature ($Q_{c,FTemp}$), the ratio of electric power and cooling capacity (EIR_{FTemp}) as function of leaving chilled fluid temperature and entering condenser air temperature, EIR_{FPLR} function of partial load ratio (PLR).

$$\frac{Q_c}{Q_{c,nom}} = a + b \cdot T_{cf,l} + c \cdot T^2_{cf,l} + d \cdot T_{cond,e} + e \cdot T^2_{cond,e} + f \cdot T_{cf,l} \cdot T_{cond,e} \quad (7)$$

$$EIR_{FTemp} = a + b \cdot T_{cf,l} + c \cdot T^2_{cf,l} + d \cdot T_{cond,e} + e \cdot T^2_{cond,e} + f \cdot T_{cf,l} \cdot T_{cond,e} \quad (8)$$

$$EIR_{FPLR} = a + b \cdot PLR + c \cdot PLR^2 \quad (9)$$

These equations are implemented in EnergyPlus tool for the energy performance evaluation of the heat pump. In this study, the coefficients of the equations (A_i, B_i, C_i, D_i, a, b, c, d, e, f) have been calculated according to Tang (2005) using data provided from the manufacturer and they fit the behaviour of the heat pump. Finally, at each time step the energy delivered and the electrical power of the heat pump can be calculated.

CASE STUDY

The building used as a case study is located in the city of Padova, in the northern part of Italy. It is a four-storey office building with a total floor area of 2,200 m^2. Three floors are above ground and one level is underground (Figure 1.a). Approximately 90 people work inside this building. The North and South facades are completely glazed (the south is a double-skin type). The west-side wall is opaque with a large central window on the first two floors, while the top west-side floor is fully glazed. The main characteristics of the building are shown in Table 1. The construction was completed in 2003 and the whole building has been operational since 2004. A radiant and primary air HVAC system is installed: during the daytime the air handling unit is on, whereas the thermally activated radiant building system is switched on during the night (Currò Dossi et al., 2003).

The heating and cooling demand of the building was originally provided with a double circuit, four compressors R407C water to water heat pump (see Table 2) coupled to 16 borehole heat exchangers, 95 m long and 7 m apart and arranged in an L-shape (Figure 1.b). The heat pump is used for both space heating and cooling as well as for the air handling unit; it operates with one temperature setpoint in heating mode, i.e. 35°C, and with two different setpoints in cooling mode, i.e. 7°C and 15°C in daytime and night time, respectively, to improve the energy efficiency when no air handling is required. In this case, the supply temperature produced by the heat pump does not depend on the external air temperature in order to simplify the control system.

The borehole heads are buried at about 1 m beneath the ground surface. Double U-tube heat exchangers are

installed inside the boreholes and the outside (inside) diameter of the pipe is 32 mm (26 mm); the borehole diameter is 140 mm. The two U-tubes inside each borehole heat exchanger are coupled in parallel. The heat-carrier fluid inside the ground heat exchangers is pure water with a total constant mass flow rate equal to 5.56 kg/s.

Table 1 – Thermal transmittance of the building's envelope.

	[W/(m² K)]
External Wall – West Side	0.45
Ground Contact Wall	0.49
External Wall – East Side	0.18
Roof	0.57
Ground Contact Floor	0.33
Glazed Facade – Nord Side	1.86
Double Skin Facade – South Side	1.30
Skylight – East Side	1.45

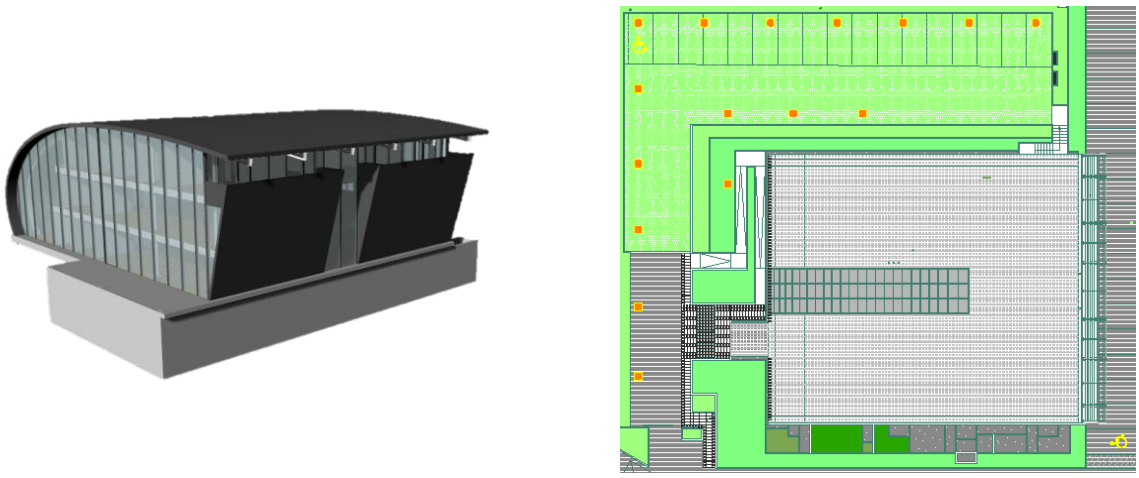

(a) (b)

Figure 1 – North and West view of the building of the EnergyPlus model (a) and plant of the real boreholes field (b).

On the building side, the total mass flow rate of water (i.e. the heat-carrier fluid) is equal to 6.10 kg/s. The fluid mass flow rates in the loops were considered constant over the simulation time. An equivalent ground layer was used to carry out the simulations: the mean weighted thermal conductivity was 1.9 W/(m K) and the volumetric heat capacity was 2.24 MJ/(m³ K). The undisturbed ground temperature was assumed to be 14°C. The area's groundwater flow effect was considered negligible. The heating and cooling demand of the building was calculated by means of the EnergyPlus tool over eleven years. To this purpose, real weather data provided by the regional environmental agency ARPAV (ARPAV, 2017) for the weather station of Legnaro (at about ten kilometers from the building) were used.

The energy model of EnergyPlus was built dividing the whole building in 59 thermal zones, and for each of them, the geometric and thermal properties of the opaque walls, glazed surfaces, and solar shading surfaces were assigned. Then, for each zone the internal heat gains were set. Figure 2 shows the thermal loads of the heat pump. The ratio between the annual heating and cooling energy demand ranges from 0.56 initially, to 0.4 at the end of the considered period. This confirms that the building's annual load profile is cooling dominant.

As above mentioned an integrated simulation simultaneously considering the building, heat pump and BHEs were implemented in EnergyPlus. For this purpose two blocks were used: one for the water condensing operation and one for the air-condensing operation, together with the pertaining control logic (see Figure 3). In Figure 3.a, in the supply section of the cooling circuit two blocks relative to the different operating conditions (water and air) can be

seen, while in the lower part (demand section) the two ideal heat exchangers relative to daytime operation (supply to air-handling unit, 7°C set-point) and night operation (supply to thermal active building storage, 15°C set-point) are shown. In Figure 3.b, the model shows only the geothermal operation, as during the winter the air heat exchanger is not used. Finally, the block concerning the borehole field was implemented using the g-functions calculated via GHLEPRO (Spitler, 2000).

The building is equipped with a BMS (Building Management System) that measures and stores not only the data concerning the control of the HVAC system but also those concerning the overall behaviour of the building-plant system; this was done specifically for research purposes.

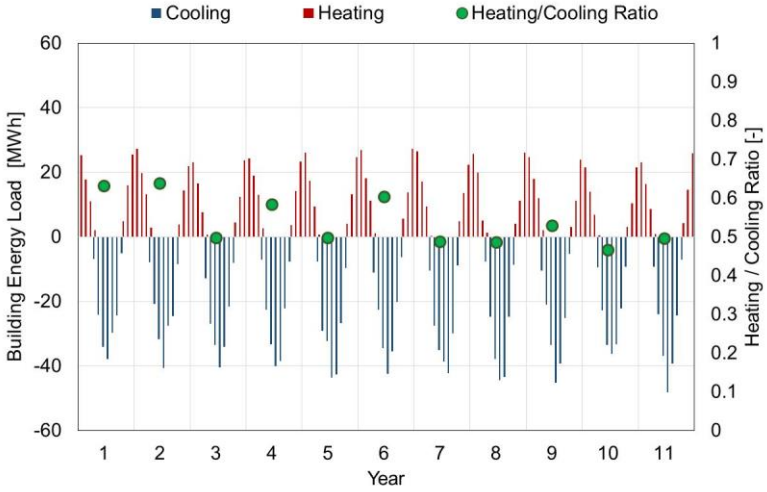

Figure 2 – Synthesis of the building's monthly load profile derived from hourly calculations.

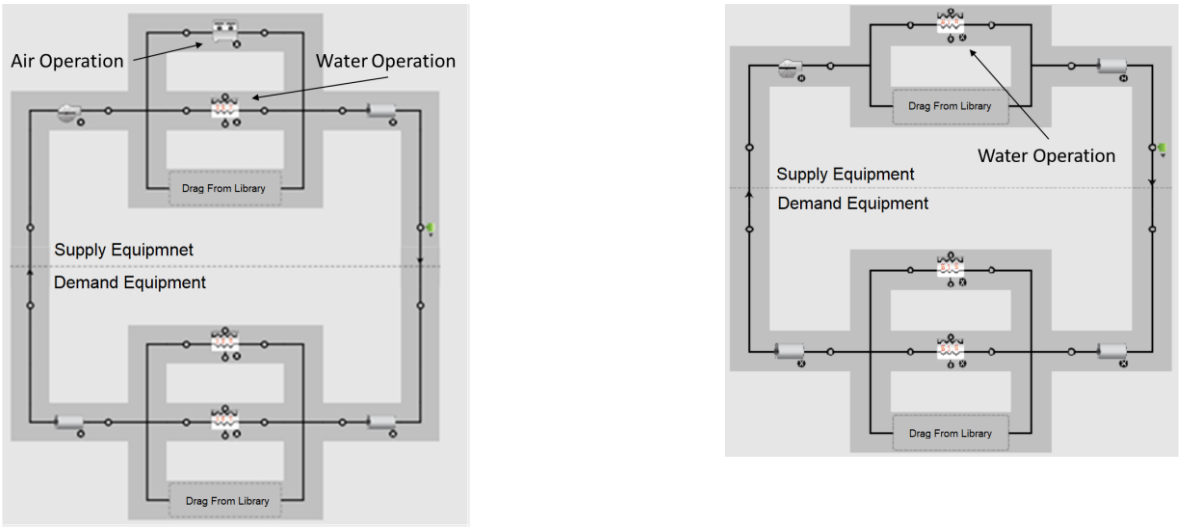

(a) (b)

Figure 3 – Model of the cooling (a) and heating (b) mode of operation of the double source heat pump.

Table 2 – Characteristics of the old and new heat pump.

	OLD	NEW	
		AIR	WATER
Refrigerant:	R407C	R410A	
Cooling Capacity (T_{fevap}: 10/7 °C, T_{fcond}: 25/29°C), EER	84.0 kW, 4.71	-	105.4 kW, 4.47
(T_{fevap}: 10/7 °C, T_{air}: 35°C), EER	-	92.6 kW, 2.97	
Cooling Capacity (T_{fevap}: 20/15°C, T_{fcond}: 24/30), EER	111.9 kW, 5.98	-	132,8 kW, 5.59
(T_{fevap}: 20/15 °C, T_{air}: 35°C), EER	-	115.4 kW, 3.52	
Heating Capacity (T_{fevap}: 8/15°C, T_{fcond}: 31/35°C), COP	92.0 kW, 4.6	-	119.6 kW, 4.49

COMPUTER SIMULATIONS

The above described model has been applied to simulate the system from year 2005 (date of completion of the building) to year 2026. As for the interval 2006-2017 the real climatic data for the considered location were used, while for the coming years, following the change of the heat pump, the Test Reference Year for the same location was used (see the temperature profile in Figure 4). The results of the simulations have been also compared with the data collected by the monitoring system during the period 2006-2017. In April 2017, the heat pump was changed with a new device and the air-condenser was also installed, consequently the parameters of the new heat pump were implemented. The simulations were carried out without interruptions between the two periods in order to consider the thermal history of the ground due to previous operation through 2006-2017 years.

To analyse the predictable behaviour of the new double source heat pump, different control strategies have been applied to the model, namely different outdoor temperature switch (22°C, 25°C, 28°C) from air cooled condenser to ground heat exchangers and vice-versa; e.g. when the external air temperature was lower than 22°C the air-condenser was switched on, whereas when it was higher than that the condenser of the heat pump was switched on the borehole heat exchangers.

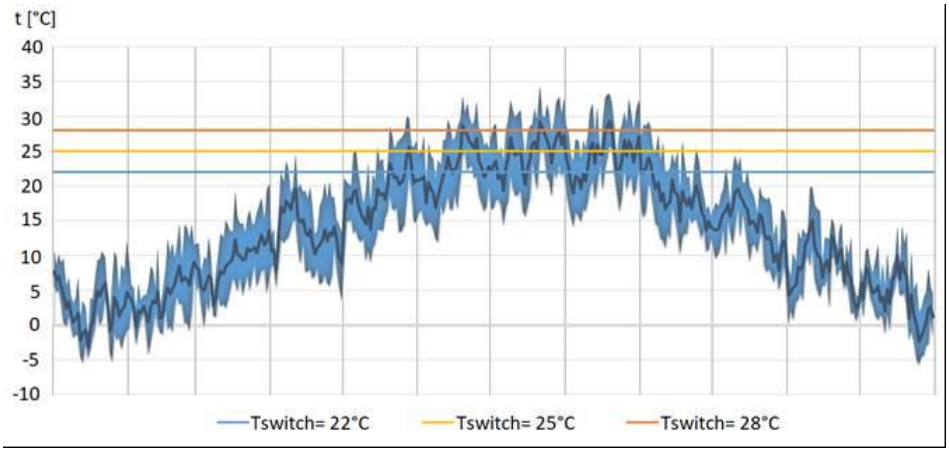

Figure 4 - Temperature profile of the Test Reference Year for Padova (Italy) with highlight of the air temperature switches considered in this work.

RESULTS

A representational output of the simulations is given in Figure 5 that shows the average monthly fluid temperature leaving the borehole heat exchangers (i.e. entering the heat pump on the ground side). In this figure also the measured values are reported during the years 2006-2017. As can be seen, the simulation results fit satisfactorily

the measured trend of ground temperature drift throughout the years. As for the prediction of the future trend, the influence of the switch air temperature can be appreciated. If the air-condenser was not installed and the heat pump was not changed, a thermal drift of the ground can be observed considering the weather data of the test reference year. With the new heat pump, when the switch temperature from air to ground decreases the fluid outlet temperature from borehole heat exchangers decreases since the heat load on the ground side decreases. As Figure 5 outlines, the thermal drift of the ground is controlled via air-condenser.

Figure 6 outlines the seasonal energy efficiency of the system taking into account the electrical consumption of the heat pump, ground loop pump and air fans. As the figure shows, the seasonal energy efficiency in heating mode increases whereas that in cooling decreases during 2006-2017 years due to the cooling dominant load profile of the building. With the air-condenser the effect of the thermal drift on the energy efficiency is limited.

Figure 7 shows the electrical consumption of the system. As it can be seen, with the switch temperature equal to 28°C from air to ground, the energy consumption is quite the same for air and ground loop; moreover, the total consumption is lower than other cases with switch temperature of 25 and 22°C. In addition, without the air-condenser, the total energy consumption would be higher than all cases.

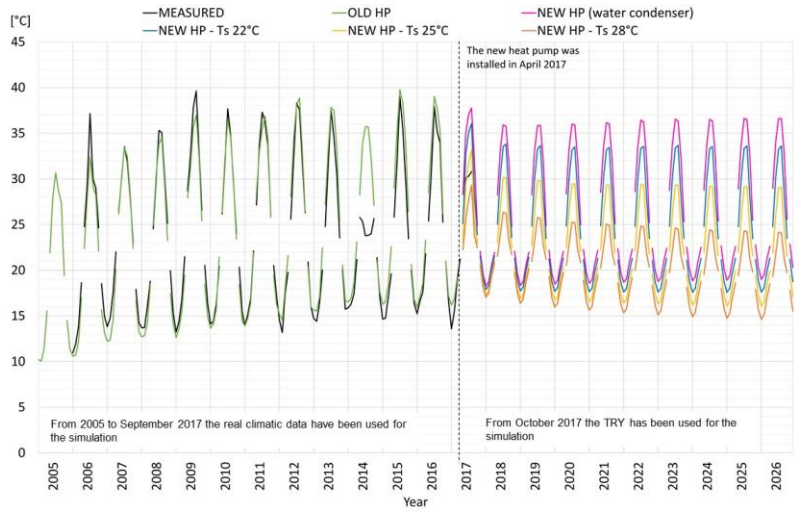

Figure 5 - Profiles of average monthly fluid temperatures leaving the boreholes throughout the simulation period.

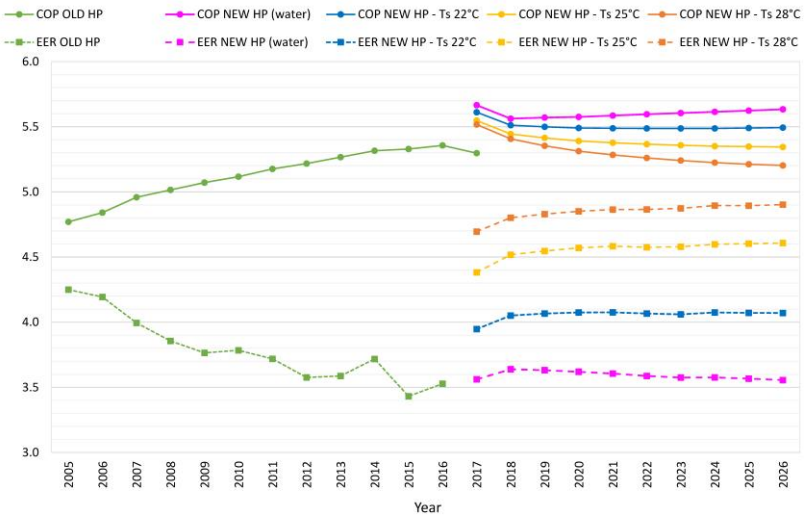

Figure 6 - Profiles of seasonal COP and EER of the heat pump, under different hypotheses of air temperature switch.

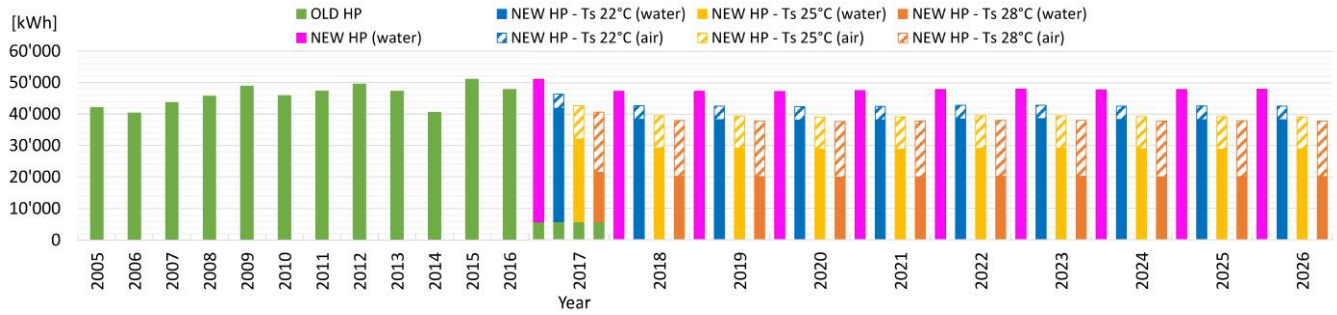

Figure 7 – Electrical energy consumption under different hypotheses of air temperature switch.

CONCLUSIONS

This study shows that the adoption of air as a secondary source/sink in ground source heat pump systems is suitable to hinder the ground temperature drift which is practically unavoidable when a building exhibits an appreciable unbalance between heating and cooling requirements

The simulations performed demonstrate that a simple control logic as a fixed value of temperature switch between the two condensing media, is good to contrast the temperature drift and improve the energy performance. Moreover, it arises that a relatively high value of switch temperature is sufficient to achieve the above mentioned goals.

ACKNOWLEDGMENTS

Special thanks are due to HiRef S.p.A. for providing the full set of performance data concerning the heat pump examined in this work.

NOMENCLATURE

a = Thermal diffusivity (m^2/s)

EIR_{FTemp} = Ratio of electric power and cooling capacity (EIR) as function of leaving chilled fluid temperature and entering condenser air temperature.

EIR_{FPLR} = Ratio of electric power and cooling capacity (EIR) as function of partial load ratio (PLR).

λ = Thermal conductivity (W/(m K))

L = Borehole length (m)

PLR = Partial Load Ratio.

$Power_c$ = Power in cooling of the heat pump (W)

$Power_h$ = Power in heating of the heat pump (W)

Q_c = Heat rate in cooling of the heat pump (W)

Q_h = Heat rate in heating of the heat pump (W)

q = Specific heat load (W/m)

r = Radial distance from the line source (m)

R_b = Borehole thermal resistance (m K/W)

τ = Time (s)

T = Temperature (°C)

T_g = Undisturbed ground temperature (°C)

$T_{L,in}$ = Entering heat pump fluid temperature on the load side (K)

$T_{S,in}$ = Entering heat pump fluid temperature on the source side (K)

$T_{cf,l}$ = Leaving chiller fluid temperature (°C)

$T_{cond,e}$ = Entering condenser fluid temperature (°C)

V_L = Volumetric flow rate on the load side of the heat pump (m^3/s)

V_s = Volumetric flow rate on the source side of the heat pump (m^3/s)

$V_{S,ref}$ = Reference volumetric flow rate on the source side of the heat pump (m^3/s)

$V_{L,ref}$ = Reference volumetric flow rate on the load side of the heat pump (m^3/s)

Subscripts

b = borehole

cond = condenser

f = fluid

evap = evaporator

g = ground

nom = nominal conditions

ref = reference

s = steady state

REFERENCES

ARPAV Agenzia Regionale per la Prevenzione e per la Protezione Ambientale del Veneto. 2017. http://www.arpa.veneto.it

Bayer, P., Saner, D., Bolay, S., Rybach and P. Blum. 2012. *Greenhouse gas emission savings of ground source heat pump systems in Europe: a review*. Renewable and Sustainable Energy Reviews 16: 1256–1267.

Corberán, J. M., Cazorla-Marin A., Marchante-Avellaneda, J. and C. Montagud. 2018. *Dual Source Heat Pump, a High Efficiency and Cost-Effective Alternative for Heating, Cooling and DHW Production*. International Journal of Low-Carbon Technologies 13: 161–176.

Currò Dossi, F., De Carli, M., Del Bianco, R., Fellin, F., Tonon, M. and R. Zecchin. 2003. *A pilot project for a low energy building equipped with thermal slabs, heat pump and ground heat storage*. 8th International IBPSA Conference Eindhoven, Netherlands, August 11-14.

Eskilson, P. 1987. *Thermal analysis of heat extraction boreholes*. Ph.D. Thesis, Lund University, Department of Mathematical Physics. Lund, Sweden.

GEOT€CH, Geothermal Technology for €conomic Cooling and Heating. (sub-programme H2020-LCE-2014-2, 656889). http://www.geotechproject.eu/ (10 May 2018, date last accessed).

Michopoulos, A., Bozis, D., Kikidis, P., Papakostas, K. and N.A. Kyriakis. 2007. *Three-years operation experience of a ground source heat pump system in Northern Greece*. Energy and Buildings 39: 328–334.

Ruiz-Calvo, F., Montagud, C., Cazorla-Marín, A. and J.M. Corberán. 2017. *Development and Experimental Validation of a TRNSYS Dynamic Tool for Design and Energy Optimization of Ground Source Heat Pump Systems*. Energies 10: 1510.

Spitler, J.D. 2000. *GLHEPRO a design tool for commercial building ground loop heat exchangers*. In: Proceedings of fourth international heat pumps in cold climates conference. Aylmer, Quebec; 17th – 18th August.

Tang, C.C. 2005. *Modeling Packaged Heat Pumps in a Quasi-steady State Energy Simulation Program*. Oklahoma State University,. Stillwater, Oklahoma (US).

U.S. Department Of Energy. 2016. *Engineering Reference Manual*. In EnergyPlus V8.5.

[This page has been intentionally left blank]

IGSHPA SWEDEN 2018 Research Conference

DOI: 10.22488/okstate.18.000038

Design of a Laboratory Borehole Storage model

Willem Mazzotti **Yifeng Jiang** **Patricia Monzó** **Alberto Lazzarotto** **José Acuña** **Björn Palm**

ABSTRACT

This paper presents the design process of a 4x4 Laboratory Borehole Storage (LABS) model through analytical and numerical analyses. This LABS is intended to generate reference Thermal Response Functions (TRFs) as well as to be a validation tool for borehole heat transfer models. The objective of this design process is to determine suitable geometrical and physical parameters for the LABS. An analytical scaling analysis is first performed and important scaling constraints are derived. In particular, it is shown that the downscaling process leads to significantly higher values for Neumann and convective boundary conditions whereas the Fourier number is invariant. A numerical model is then used to verify the scaling laws, determine the size of the LABS, as well as to evaluate the influence of top surface convection and borehole radius on generated TRFs. An adequate shape for the LABS is found to be a quarter cylinder of radius and height 1.0 m, weighing around 1.2 tonnes. Natural convection on the top boundary proves to have a significant effect on the generated TRF with deviations of at least 15%. This convection effect is proposed as an explanation for the difference observed between experimental and analytical results in Cimmino and Bernier (2015). A numerical reproduction of their test leads to a relative difference of 1.1% at the last reported time. As small borehole radii are challenging to reproduce in a LABS, the effect of the borehole radius on TRFs is investigated. It is found that Eskilson's radius correction (1987) is not fully satisfactory and a new correction method must be undertaken.

INTRODUCTION AND LITERATURE REVIEW

Ground-source heat pump (GSHP) systems with vertical, closed-loop borehole heat exchangers (BHEs) are among the most energy-efficient systems for heating and cooling buildings, when properly designed. A key part in the design process of these systems is the borehole field sizing, performed in such a way that the secondary fluid circulating in the BHEs remains within pre-determined temperature limits over the lifetime of the installation. The long-term changes in secondary fluid temperature are predominantly influenced by heat transfer phenomena in the ground; accurately modelling these phenomena is thus important to reach a proper design. For a given borehole field geometry, a common method to calculate temperature changes over time is to use a Thermal Response Function (TRF) linking the increase in temperature at the borehole wall to a given, constant heat rate and given ground properties.

TRFs and ground heat transfer modelling. Broadly-cited TRFs are Eskilson's g-functions (1987) which are dependent on similarity parameters of the borehole field, namely, $r_b^* = r_b/H$, $B^* = B/H$, and $t^* = t/t_s = 9Fo$. Eskilson's g-functions may be defined by $T_b - T_0 = \frac{\bar{q}}{2\pi\lambda} g(r_b^*, B^*, t^*)$ which relates the temperature increase at the borehole wall, $T_b - T_0$, to the specific heat injection rate, $\bar{q}$, and the thermal conductivity, λ. Eskilson generated g-functions numerically, assuming that all borehole walls in the field have the same temperature, which is additionally uniform with depth.

Claesson and Eskilson (1987) furthermore introduced an analytical solution based on uniform heat injection along a Finite-Line-Source (FLS) in a semi-infinite medium, which was later discussed and developed by other authors (Cui et al., 2006; Javed & Claesson, 2011; Lamarche, 2011; Lamarche & Beauchamp, 2007; 2002). Although convenient for fast computation, the different FLS methods failed to reproduce Eskilson's g-functions for large borehole fields because of the difference in boundary conditions (BCs) applied along the borehole wall between the two models. Although none of these BCs duly represent a real case, g-functions will better represent temperature changes in the borehole field when

Willem Mazzotti (willem.mazzotti@energy.kth.se) is a PhD candidate at the Royal Institute of Technology (KTH). Yifeng Jiang is a master student at INSA Lyon. Patricia Monzó is a PhD from the Royal Institute of Technology (KTH). Alberto Lazzarotto is post-doctoral fellow at the Royal Institute of Technology (KTH). José Acuña is a PhD and researcher at the Royal Institute of Technology (KTH). Björn Palm is a professor at the Royal Institute of Technology (KTH).

all boreholes are fed in parallel, as highlighted by Cimmino et al. (2013). This FLS vs. g-function issue was tackled by several authors who proposed modelling straight (Cimmino & Bernier, 2014) and inclined (Lazzarotto, 2016; Lazzarotto & Björk, 2016) boreholes as stacks of FLS while imposing a uniform temperature BC. Cimmino (2015) coupled such as stack-FLS mode to a quasi-steady-state borehole heat transfer model, thereby moving the BC outside of the boreholes, allowing to impose the same inlet temperature for all boreholes in the field.

Besides Eskilson (1987), other authors have numerically generated TRFs. A novel approach to numerically model borehole fields using a highly conductive material (HCM) was presented by Monzó et al. (2015) and later improved (Monzó, 2018). Other numerical models have been developed but are not discussed here.

Experimental and monitoring work. As highlighted in the previous section, many authors have focused on developing analytical and numerical models or methods to predict temperature changes in borehole fields, with the aim to improve the accuracy of GSHP design. However, due to the slow transitory nature of heat transfer phenomena in long boreholes, long-term experimental and monitoring studies have been scarce. This has been emphasized in the literature (Cimmino & Bernier, 2015; Cullin et al., 2015; Montagud et al., 2011; Spitler & Bernier, 2011, 2016). Spitler & Bernier (2016) identified the relevance and usefulness of long-term monitoring of thermally unbalanced borehole fields.

Some installations have been monitored over longer periods of 1 to 5 years (Cullin et al., 2015; Montagud, Corberán, Montero, & Urchueguía, 2011; Yavuzturk & Spitler, 2001) although none of the studies has been used to validate ground heat transfer models. In fact, validation of ground heat transfer models in real systems is harden by the long time scale involved. Moreover, uncontrolled or unknown parameters such as groundwater flow, thermal properties or geological conditions may complicate the validation process in real installations. Practical difficulties such as data gaps, unknown control strategies or lack of documentation may also arise. Additionally, uncertainties are hard to assess in operating systems and rarely reported.

An alternative is to perform lab experiments in small-scale physical models. Such laboratory apparatuses are attractive because the time scale is reduced and the tests can be performed in a controlled environment. A lab-scale apparatus was successfully built by Cimmino and Bernier (2015) based on a previous work (Salim Shirazi & Bernier, 2014). The authors obtained an experimental TRF that could be compared to a semi-analytical method. In the reviewed literature, this is the only attempt to validate ground heat transfer models on the long-term. A discrepancy between the experimental TRF and the analytical one was observed, although the difference is comprised within the measurement uncertainty at a 95% confidence level (Cimmino & Bernier, 2015). The authors proposed an explanation for this observed difference based on the air temperature variation above the tank, though the proposed correction did not fully succeed in reproducing the observations. The present article proposes another explanation for the difference based on scaling laws and natural convection. Other lab-scale models were constructed although their use was limited to analysis of short-term models or other purposes (Beier et al., 2011; Eslami-nejad & Bernier, 2012; Hellström & Kjellsson, 2000; Kramer et al., 2015).

This article presents the design process and sizing of a LABS simulating multiple vertical BHEs. The design process is based on an analytical scaling analysis as well as a numerical model which is a modified version of the model presented by Monzó et al. (2015). Additionally, some technical, practical and uncertainty limitations are used as constraints to determine the different design parameters.

METHODOLOGY

The main goal of this work is to determine adequate dimensions, materials and conditions for the LABS, which was preliminary thought as a vertical cylindrical container filled with a material simulating the ground and in which boreholes are placed at the center as shown in Figure 1. This figure also includes important parameters to be determined under the design process. The first step in this scaling process is to ensure that the solutions obtained with the LABS will be the same as for the real-scale model. A general analytical analysis of the effect of downscaling on the heat transfer phenomena is thus performed at first. Then, the borehole field to model is chosen, as well as the LABS size and related time scale. A preliminary selection of materials must also be performed before numerical simulations can be performed. Although seemingly sequential, the design procedure has consisted of many iterations and cross-investigations.

Scaling analysis

Some scaling requirements may be obtained analytically by stating the governing equations for the real and lab-scale cases. Assuming constant and uniform thermal properties, the two heat equations may be written, respectively, as

$$\frac{1}{\alpha}\frac{\partial T}{\partial t} = \frac{1}{r}\frac{\partial}{\partial r}\left(r\frac{\partial T}{\partial r}\right) + \frac{1}{r^2}\frac{\partial^2 T}{\partial \varphi^2} + \frac{\partial^2 T}{\partial z^2} \text{ and } \frac{1}{\alpha'}\frac{\partial T'}{\partial t'} = \frac{1}{r'}\frac{\partial}{\partial r'}\left(r'\frac{\partial T'}{\partial r'}\right) + \frac{1}{r'^2}\frac{\partial^2 T'}{\partial \varphi'^2} + \frac{\partial^2 T'}{\partial z'^2} \quad (1)$$

Note that the apostrophe symbol is be used to refer to the lab-scale parameters and variables. For similar Initial Condition (IC) and Boundary Conditions (BCs), the behavior of the real and lab-scale cases will be the same if the governing equations are the same. By introducing a proportional and isotropous geometrical scaling factor, β, a thermal diffusivity scaling factor, γ, as well as a time scaling factor, τ, such that

$$\beta = \frac{r}{r'} = \frac{z}{z'} = \frac{H}{H'} \;\; ; \;\; \tau = \frac{t}{t'} \;\; ; \;\; \gamma = \frac{\alpha}{\alpha'} \quad (2)$$

and applying the corresponding change of variables to the first eq. in 1, the latter may be rewritten as

$$\frac{\beta^2}{\alpha\tau}\frac{\partial T}{\partial t'} = \frac{1}{r'}\frac{\partial}{\partial r'}\left(r'\frac{\partial T}{\partial r'}\right) + \frac{1}{r'^2}\frac{\partial^2 T}{\partial \varphi'^2} + \frac{\partial^2 T}{\partial z'^2} \quad (3)$$

Note that $\varphi = \varphi'$ and that an anisotropic scaling would set requirement for an anisotropic material in the LABS, which is difficult to achieve. For similar IC and a set of BCs, the 2nd eq. in 1 and eq.3 have the same solution if $\frac{\beta^2}{\alpha\tau} = \frac{1}{\alpha'}$ which is equivalent to the invariance of the Fourier number: $Fo_r = \frac{\alpha t}{r^2} = \frac{\alpha' t'}{r'^2} = Fo_{r'}$ or $Fo_H = Fo_{H'}$. Therefore, as expected, the Fourier number must be conserved, constituting a first scaling requirement. One of the advantages of downscaling becomes clear from the previous eq., as τ is proportional to β, which takes large values ($\beta \gg 1$).

As previously mentioned, the IC and BCs must also be analogous in order to obtain the same solution in the real and LABS cases. Dirichlet BCs will not be affected by the downscaling as opposed to Neumann and convective BCs. Such BCs may arise at the borehole wall, as well as the bottom and top boundaries. At the borehole wall, a Neumann BC is expressed as $-\lambda\frac{\partial T}{\partial r}(r_b, z, t) = \frac{q}{2\pi r_b}$, $\forall (z,t) \in ([D;H] \times \mathbb{R}^{+*})$, where D is the buried depth. Applying the same change of variable as for the heat equation, one obtains $q' = q \cdot \frac{\lambda'}{\lambda}$, constituting a second requirement. Hence, the linear heat flux is slightly modified when downscaling.

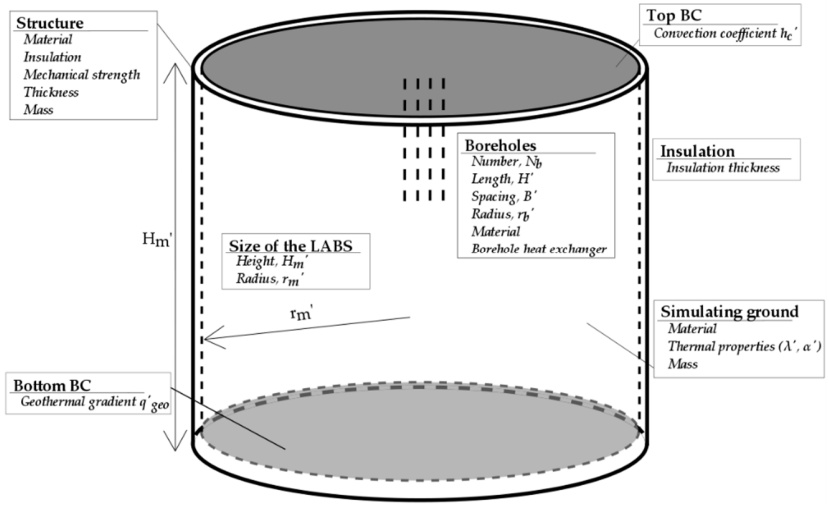

Figure 1. Preliminary outline of the lab-scale model (LABS) including important design parameters to be determined

Similarly, relations may be obtained for the geothermal heat flux BC and the top convective BC

$$\frac{\lambda'}{\lambda}\beta q_{geo} = q'_{geo} \quad \text{and} \quad \frac{\lambda'}{\lambda}\beta h_c = h'_c \tag{4}$$

Eq.4 also become requirements if the BC applied at the top and bottom of the model are a convective and a Neumann BC, respectively. The β appearing in eq.4 implies large increases in the equivalent geothermal heat flux and convection coefficient when downscaling the model ($\beta \gg 1$). For instance, a 300 m deep borehole field modelled by a 0.5 m LABS will lead to $\beta = 600$. Assuming a natural convection coefficient of 10 W·m^{-2}·K^{-1} on top of a real-scale system, the required convection on top of LABS would be of 6000 W·m^{-2}·K^{-1} for equal thermal conductivities. Thus, forced convection will likely be required at the top of the LABS to reproduce the behavior of real-scale installations having natural convection as top BC. Note that radiation is considered to be accounted for in the convection coefficient.

It is later shown that a Neumann BC with a typical natural convection coefficient of 10 W·m^{-2}·K^{-1} leads to similar results than a Dirichlet BC in the real-size case but not in the LABS case.

Choice of the borehole field to be modelled and sizing criteria for the LABS

Borehole field to be modelled. In order to perform a downscaling, the geometry of the real-scale borehole field must be set. A 4x4 borehole field has been arbitrarily chosen with the intention to observe thermal interactions between boreholes. Since TRFs only depend on non-dimensional geometrical parameters (r_b^*, B^* and $D^* = D/H$) for a given configuration, only those values need to be chosen in theory. However, for the purpose of the design, a borehole field with the following fixed geometrical parameters is chosen as a starting point for the downscaling process: H = 300 m, r_b = 5.75 cm and $D = B$ = 5 m corresponding to r_b^* = 1.92·10^{-4}, $B^* = D^*$ = 1.67·10^{-2}.

Sizing criteria for the LABS. The sizing of the LABS consists of two parts. The 1st one is the determination of β or, in other words, H'while the 2nd part is the determination of the dimensions of the LABS, H'_m and r'_m. H' is set as 50 cm, corresponding to β = 600, because this leads to a test duration of about a few days, which is what is wanted. The test duration is determined as the time at which the solution approach asymptotic condition (eq.6). A H' value of 50 cm is also considered a reasonable size for laboratory facilities although it implies reaching a challenging 0.11 mm for r'_b, given the parameters chosen in the previous paragraph. This radius issue is discussed later in the paper.

The dimensions of the LABS must be designed so that it fits in laboratory facilities; the maximum allowable size is thus arbitrarily set as 1.8 m in height and width. The size also affects the LABS mass that may be significant. To exactly determine the required dimensions of the LABS for β = 600, sizing criteria must be defined. The LABS boundaries should influence as least as possible conduction in the simulating ground over the test duration. Since the main goal of the LABS is to generate and validate TRFs, the sizing criteria may arbitrarily be defined as

$$\left|\overline{\Delta T}(r_b, t_{ss}) - \overline{\Delta T_{ref}}(r_b, t_{ss})\right| < 0.5 \cdot U(T, 95\%) \tag{5}$$

where $\overline{\Delta T_{ref}}(r_b, t_{ss})$ is the depth-integral mean of the temperature increase at the borehole wall at the end of the test, t_{ss}, emanating from a reference model with a large domain; thus one in which the boundaries negligibly influence the TRF. $U(T, 95\%)$ is the expanded uncertainty of temperature measurement at the borehole wall at a 95% confidence level. The targeted value for $U(T, 95\%)$ is 0.5 K. The criterion expressed in eq.5 is arbitrary but the aim is to limit the uncertainty in the determination of the TRF. Note that the test duration is chosen for the evaluation of criterion 5 because this is when the boundary effects will be the largest. The following criterion is thus used to determine t_{ss}

$$\forall t > t_{ss}\,, \frac{\left|\overline{\Delta T}_{ref}(r_b, t) - \overline{\Delta T_{ref}}(r_b, t_{ss})\right|}{\overline{\Delta T_{ref}}(r_b, t)} < 0.5\% \tag{6}$$

Lab-Scale Numerical Model (LSNM) and choice of materials

LSNM. To find the LABS dimensions that suit criterion 5, a Lab-Scale Numerical Model (LSNM) is used. A

real-scale numerical model is also built to verify the scaling laws found in previous sections. Both numerical models are an adaptation of Monzó et al. (2015). It is chosen to use a numerical tool instead of an analytical one for flexibility reasons, for instance in the type of BCs applied. Notably, the top and bottom BCs can be shifted between Dirichlet or convective BC, and geothermal heat flux or adiabatic condition, respectively. All vertical boundaries are adiabatic. The LSNM simulates the 4x4 borehole field presented earlier but symmetry is used to reduce the model to a 1/8 of the original domain. Analytical analyses were also undertaken but are not presented here.

Simulating ground. The simulating ground refers to the material in the LABS, as opposed to the simulated ground that refers to the real-scale material. The thermal properties of the simulating ground are of primary importance since they directly influence the heat diffusion process in the LABS. Indeed, a larger thermal diffusivity in the model will lead to shorter test durations but the heat plume will reach further away from the boreholes, thereby increasing the required LABS size. A lower thermal conductivity will on the other hand lead to a larger temperature increase that may create some practical problems. Another important feature of the simulating ground is its interchangeability, which is why saturated sand is chosen as simulating ground. The thermal properties assumed for the simulated and simulating ground are as follow: λ = 3.5 W·m^{-1}·K^{-1}, α = 1.58·10^{-6} m^2·s^{-1} and λ' = 3.0 W·m^{-1}·K^{-1}, α' = 7.00·10^{-7} m^2·s^{-1}, respectively (Arkhangelskaya & Lukyashchenko, 2017; Sundberg, 1991; Tarnawski et al., 2011). The thermal properties of the simulating ground should be well characterized before experiments are to be performed.

Structure and insulation. For practical reasons, steel was chosen as a structural material. Since steel has a relatively high thermal conductivity, the container should be thermally isolated from the ground to avoid thermal disturbances. An insulation layer is thus needed between the steel and the simulating ground. This insulation layer moreover reduces the potential thermal influence from the environing air as well as heat losses. Although not presented here, a 2D steady-state numerical model is used to assess the impact of the insulation thickness on the heat losses. The used thermal conductivity and heat transfer coefficient are of 0.035 W·m^{-1}·K^{-1} and 10 W·m^{-2}·K^{-1}, respectively.

Establishment of initial temperature gradient

The establishment of the initial temperature gradient in the LABS from a uniform ambient temperature may be significantly long as compared to the actual test duration. A LSNM is used to assess the establishment time. The time needed for the establishment of the initial gradient may also be estimated analytically by superposing the solutions for 1D conduction in two semi-infinite solids which intersection corresponds to any vertical cross-section of the LABS. Each semi-infinite solid is applied a constant heat flux on the boundary surface, the heat fluxes being equal in magnitude but of opposite sign for each solid. Taking a reference depth at the mid-depth of the LABS and defining $z^+ = H'_m/2 + z$ and $z^- = H'_m/2 - z$, the temperature increase may be expressed as such, for $Fo < 0.2$

$$\Delta T = q_{geo} \cdot \frac{H'_m}{\lambda}\left(\frac{2}{\sqrt{\pi}}\sqrt{Fo}\left(e^{-\frac{z^{+2}}{4\alpha t}} - e^{-\frac{z^{-2}}{4\alpha t}}\right) + z^- \cdot erfc\left(\frac{z^-}{2\sqrt{\alpha t}}\right) - z^+ \cdot erfc\left(\frac{z^+}{2\sqrt{\alpha t}}\right)\right) \quad (7)$$

RESULTS AND DISCUSSIONS

Verifications on the real-scale numerical model

The real-scale numerical model is not validated per say but several verifications have been performed in order to ensure the reliability of the results. In this part, the model has Dirichlet and adiabatic BCs at the top and bottom boundaries, respectively. The first verification regards the steady-state distribution of heat flow between boreholes which is in accordance with that of Cimmino (2015). The second verification performed is a comparison between the LSNM, the Infinite Line Source (ILS) and Lazzarotto and Björk (2016). Results from the LSNM are in accordance with those two analytical models (only at early times for the ILS). The largest relative difference between Lazzarotto and Björk and the numerical g-function is of 4.0% at $ln(t/t_s)$ = -5.5. This difference tends to be reduced when a finer discretization is used for the stacked-FLS model of Lazzarotto and Björk (40 elements are used).

Real-scale numerical model vs LSNM

In order to verify the scaling relations expressed previously, the real-scale numerical model presented in the previous section is compared to a LSNM, with similar geometry but different thermal properties. Note that thermal properties do not affect TRFs but are important in downscaling the BC. $\beta = 600$ is used leading to $r'_m = H'_m = 1.4$ m and $H' = 50$ cm. Geothermal heat flux is applied to both the real-scale numerical model and the LSNM. Geothermal heat flux means an initial vertical temperature gradient making the determination of the g-function not formally possible. However, a TRF may be defined in a similar way as $T_b - \overline{T_0} = \frac{\bar{q}}{2\pi\lambda} TRF(r_b^*, B^*, D^*, t^*)$. The TRFs obtained for each model are presented in Figure 2. The maximum absolute relative difference between the TRF obtained with the real-scale model and with the LSNM is of 15% at early times. The difference is lower than 2.6% after $ln(t/t_s) = -12$, corresponding to 16 hours in the real-scale application. This relative difference shows a decreasing trend as time increases, reaching values as low as 0.05 % towards the simulation end. The LSNM thus give very similar result to the real-scale numerical model on the long-term.

Ground dimension of the LABS

The ground dimension of the LABS is determined according to the criteria given in eq.5-6. A LSNM with the same scaling factor as previously used ($\beta = 600$) but of radius and height 5 m is used to generate the reference solution mentioned in eq.5-6. This reference solution is then utilized to determine t_{ss}. It is found that t_{ss} is about 131.8 hours (5.5 days). This corresponds to a non-dimensional logarithmic time, $ln(t_{ss}/t_s)$, of 2.48. LSNMs of different dimensions are then run to find a size matching the criterion expressed in eq.5.

Each model has equal radius and height. The resulting differences in borehole average temperature between the reference solution and the solutions for the different LSNM sizes are shown in Figure 3. These differences are shown for two different dimensionless times corresponding to the two different colored sets of points in the figure. The limit in criterion 5 is also represented by the black dashed line. The smallest model that satisfies eq.5 has a height and radius of 1 m. This model has an average borehole temperature 0.19 K higher than the reference model at $ln(t_{ss}/t_s) = 2.48$. The difference increases to 0.72 K at $ln(t_{ss}/t_s) = 4$. The sand mass for such a model would be around 4.9 tons. Nevertheless, in the same way as the LSNM domain can be reduced to a 1/8 cylinder by applying symmetry, the LABS size may be reduced as to limit its weight. It is chosen to reduce the LABS to a 1/4 cylinder in order to avoid the physical modelling of half boreholes. The sand mass is then reduced to 1.2 tons.

Challenges with the borehole radius

A problem arising from the chosen scale factor ($\beta = 600$) is that the borehole radius becomes very small in the LABS: r'_b indeed turns out as 0.2 mm, which is challenging to reproduce in a physical model.

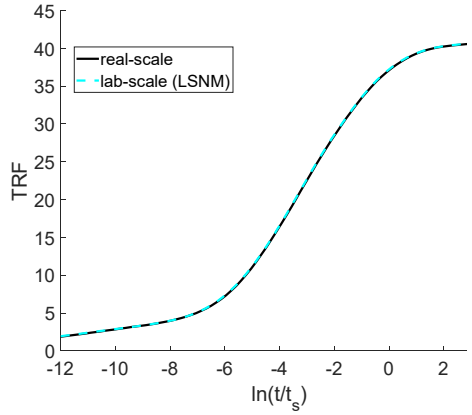

Figure 2. TRFs for real-scale and LSNM for a 4x4 borehole field with $r_b^* = 1.92 \cdot 10^{-4}$ and $B^* = D^* = 0.0167$

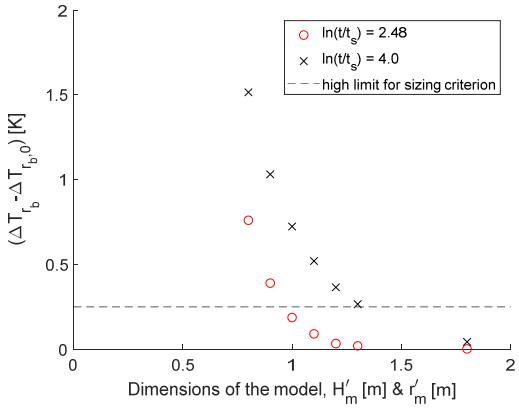

Figure 3. Difference in borehole average temperature between the reference solution and the solutions for different model sizes. The height, H'_m, and radius, r'_m, are equal.

As the results are scale-independent, one could decrease β in order to increase the borehole radius. This would however lead to unrealistic dimensions for the LABS: a borehole radius of 2 mm would for instance mean a LABS of 10 m in radius and height. This issue could be bypassed by considering that the LABS simulates shorter boreholes, thereby reducing β. The limits of this method may, however, be noted as the increase in borehole radius is directly proportional to the reduction in borehole depth; a 2 mm borehole radius in the LABS would then limit the simulated real-scale borehole depth to about 30 m. Another method is to use a correction factor such as the one suggested by Eskilson (1987),

$$g(r_1^*, B^*, t^*) = g(r_2^*, B^*, t^*) + \ln(r_2^*/r_1^*) \quad (8)$$

which is derived by assuming steady-state radial conduction between the two radii. This approximation may be valid for small differences in radius but axial effects may become important for larger ones, leading to underestimated values of the TRF for large times. On the contrary, the correction will lead to overestimated values of the TRF for short times, when the quasi-steady-state regime has not yet been established between the two considered radii. These two features can be observed in Figure 4 that shows the numerically-generated TRF for three different r_b^* in graph (a), while graph (b) shows the same TRF corrected with eq.8. Note that a more accurate correction factor could be derived from analytical or numerical analysis but this is left to a later stage of the project. Anyhow, experimentally-obtained TRF for a given r_b^* would allow the determination of other TRF corresponding to different r_b^* values.

Influence of the top convective BC

As noted in previous sections, the convection heat transfer coefficient, h_c, at the top boundary layer must be scaled up when downscaling the borehole field. Values of h_c around 10 W·m^{-2}·K^{-1} can be expected at the top of real size borehole fields, corresponding to a h_c' of 5142 W·m^{-2}·K^{-1} given the chosen scale factor and thermal conductivities. The latter value is challenging to achieve; hence, the influence of h_c' and, thus, h_c, is evaluated using the LSNM in order to assess the possible deviations in TRF for lower h_c', namely 514.2, 51.42 and 5.142 W·m^{-2}·K^{-1} corresponding to h_c of 1, 0.1 and 0.01 W·m^{-2}·K^{-1}. Note that the ambient temperature is set as 0°C.

The resulting TRFs are shown in Figure 5 together with the TRF obtained for constant temperature BC at the top. As could be expected, decreasing h_c' leads to increasing TRF values. At $\ln(t/t_s) = 4$, relative differences with the TRF generated with constant temperature BC are of 0.4%, 3.1%, 15.4% and 54.2% for h_c' of 5142, 514.2, 51.42 and 5.142 W·m^{-2}·K^{-1}, respectively. It may be observed that a h_c of 10 W·m^{-2}·K^{-1} in a real size borehole field (h_c' = 5142 W·m^{-2}·K^{-1} in the LABS) leads to an almost identical TRF than with the constant temperature BC.

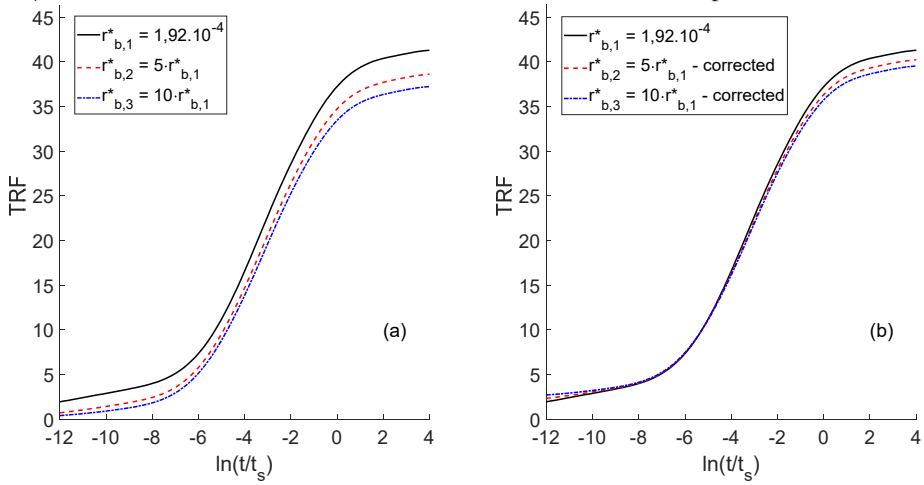

Figure 4. Influence of the borehole radius-to-depth aspect ratio on the numerically generated TRF for a 4x4 borehole field: (a) without correction, (b) with Eskilson's correction

A h'_c, of 514.2 W·m^{-2}·K^{-1} leads to a reasonable error while being easier to achieve than 5142 W·m^{-2}·K^{-1}. A value of 514.2 W·m^{-2}·K^{-1}, or higher, can be reached by circulating constant temperature water in micro-channels or by using a phase-change material (Kim et al., 2017). Note that the diverging TRF for h_c = 5.142 W·m^{-2}·K^{-1} is due to the finite size of the LSNM, the adiabatic BC on the sides and the close-to-adiabatic BC at the top.

As previously noted, the top BC appears to have been left uncontrolled in Cimmino and Bernier (2015), entailing natural convection on the surface. In those conditions, one may expect h'_c values between 1 to 6 W·m^{-2}·K^{-1}. Considering radiation, heat transfer coefficients could go up to 15 W·m^{-2}·K^{-1} (Bergman et al., 2011). A LSNM reproducing as faithfully as possible the conditions reported by Cimmino and Bernier (2015) is made using values of h'_c of 1 and 10 W·m^{-2}·K^{-1}, as well as a Dirichlet BC on top. The results are shown in Figure 6 which also displays results for h'_c = 10 W·m^{-2}·K^{-1} and borehole radii changing by ± 0.5 mm due to the uncertainty on the actual borehole radius used during the tests. A convection coefficient of 10 W·m^{-2}·K^{-1} seems to reproduce fairly well the behavior observed during their test with differences of 3.5% and 1.1% at the first and last reported time points, respectively. This could thus be one of the reasons for the observed discrepancy between the experimental and analytical results in Cimmino and Bernier (2015).

Heat losses and establishment of initial temperature gradient

Heat losses through vertical plates. Heat losses through the side of the LABS have so far been disregarded but it is important to limit those losses as much as possible to improve accuracy. A 2D steady-state model of the LABS corner is used with the radial temperature from the LSNM at 0.5 m depth and $ln(t/t_s)$ = 4.4 as the inner BC and a heat transfer coefficient of 10 W.m^{-2}.K^{-1} as outer BC. The maximum relative heat loss is found to be 8.2% and 3.8% for 5 cm and 10 cm insulation thickness, respectively, as compared to the heat injected in the LABS. Although this calculation represents a worst-case scenario, the losses are relatively high. This could be improved by adding insulation on the outer part of the metallic structure as well as reducing the radiation losses using a low-emissivity layer. The corner of the LABS should be particularly well-insulated as the temperature there will be higher and the heat losses will moreover directly affect the thermal response because of the direct proximity with the boreholes.

Establishment of initial temperature gradient. Using the analytical model described previously, it is found that the steady-state condition is reached after about 70 hours. This, however, corresponds to an ideal situation in which an extraction heat flux of same magnitude as the geothermal heat flux can be maintained at the surface. A numerical simulation shows that the time for establishment of the initial temperature gradient keeping a constant temperature at the top BC could be as long as 30 days. Hence, the establishment of the initial temperature gradient may be a time-consuming process that ought to be optimized to reduce test duration. Similarly, the recovery period – not studied here – could be optimized to avoid long waiting time between tests.

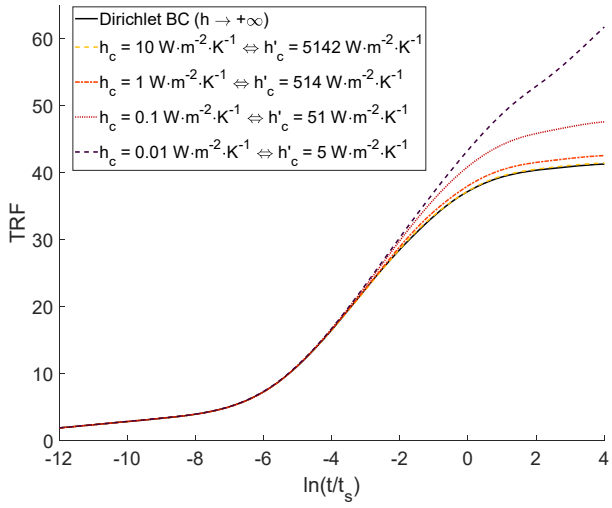

Figure 5. Influence of the top BC convection heat transfer coefficient on the TRF for 4x4 borehole field

CONCLUSION

The dimensioning of LAboratory-scale Borehole Storage (LABS)with 4x4 boreholes was investigated in this study; first by deriving scaling laws from an analytical analysis and then through the use of a numerical model. The analytical analysis shows that the invariance of the Fourier number is a requirement and that Neumann or convective boundary conditions (BC) are scaled up proportionally to the geometrical scaling factor, when downscaling. This BC scale-up is notably proposed as a possible explanation for the observed discrepancy between experimental and analytical results in Cimmino and Bernier (2015). A numerical reproduction of their experiment indeed shows a good agreement with their test results when natural convection is accounted for: the relative difference in Thermal Response Functions (TRFs) is of 1.1% at the last reported time.

It is found that, for the considered LABS, natural convection as top BC leads to TRF values at least 15% higher than those obtained with a Dirichlet BC. Therefore, forced convection or PCM must be used on the top BC to accurately reproduce real-scale TRFs.

The geometrical downscaling factor is fixed as 600, leading to scaled borehole depth of 50 cm and a test duration of about 5.5 days. For this configuration, a radius and height of both 1.0 m are found to be appropriate dimensions for the LABS, which is assumed of cylindrical shape. For these dimensions, the borehole temperature increase induced by boundary effects is indeed less than 0.25 K, which is half the expected uncertainty of temperature measurements. Symmetry is used to reduce the LABS to a ¼ cylinder, thereby reducing its weight to 1.2 instead of 4.9 tonnes.

The scaling laws found through the analytical analysis are confirmed through numerically modelling real-scale and laboratory scale borehole fields. The relative differences in TRFs between the two models is lower than 2.6%.

As small borehole aspect ratios are challenging to reproduce in a LABS, the effect of the borehole radius on TRFs is numerically investigated and it is found that Eskilson's radius correction (1987) is not fully satisfactory. A new correction method based on analytical or numerical analysis must be undertaken.

Heat losses as high as 8.2% of the total injected power are found to possibly occur towards the end of the tests, even with 5 cm insulation. This stresses the need for a larger insulation layer and/or the use of a low-emissivity layer on the outer shell of the LABS. The time needed for the establishment of the temperature gradient in the LABS is found to be at least 70 hours and may be as long as a month. The LABS should be optimized so that this duration and the time needed for recovery are as short as possible.

Future work includes the prediction and minimization of uncertainties, design of the measurement system and the system to implement on top of the LABS, testing of the simulating sand, as well as the construction of the LABS.

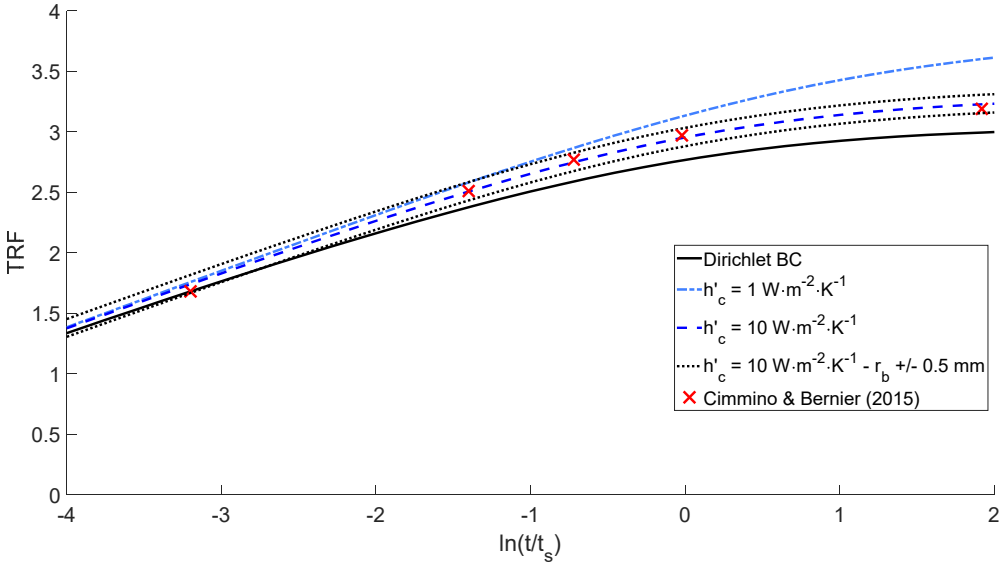

Figure 6. Numerical reproduction of the test performed by Cimmino and Bernier (2015)

ACKNOWLEDGMENTS

This work is financed by the Swedish Energy Agency through the EFFSYS Expand program. The authors thank all the sponsors involved in the project: Anergy, Asplan Viak, Avanti System, Bengt Dahlgren, Brf Ingemar 5, Brugg Cables, Båsum Boring, Cooly, E-ON, Finspångs Brunnsborrning, Geobatteri, HP borrningar, IVT Värmepumpar, LaPlast, Nibe, Nowab, NTNU, PMAB, Sindeq borrteknik, Stures brunnsbornningar, Sweco, Swedish Diamondtool Consulting, Team Wåhlin, Thermia Värmepumpar, Triopipe geotherm, University of Genoa, Uponor, Värmex Konsult, Wermer Energi, Wessman Drilling Solution, Wilo.

NOMENCLATURE

B = Borehole spacing (m)
D = Buried depth (m)
Fo = Fourier number (-)
g = G-function (-)
H = Active borehole depth (m)
h = Convection / global heat transfer coefficient ($W \cdot m^{-2} \cdot K^{-1}$)
q = Specific heat rate ($W \cdot m^{-1}$) or heat flux ($W.m^{-2}$)
r = Radius (m)
T = Temperature (°C or K)
t = Time (s)
z = Depth (m)
α = Thermal diffusivity ($m^2 \cdot s^{-1}$)
β = Spatial scale factor (-)
γ = Thermal diffusivity scale factor (-)
λ = Thermal conductivity ($W \cdot m^{-1} \cdot K^{-1}$)
φ = Azimuth angle (°)

Subscripts

b = borehole
c = convection
m = model or LABS
geo = geothermal
s = characteristic time
ss = test duration (asymptotic time)
0 = initial

Superscripts

$'$ = relative to the LABS
* = dimensionless parameter
$\bar{x}$ = integral mean of x

REFERENCES

Arkhangelskaya, T., & Lukyashchenko, K. (2017). Estimating soil thermal diffusivity at different water contents from easily available data on soil texture, bulk density, and organic carbon content. Biosystems Engineering. https://doi.org/10.1016/j.biosystemseng.2017.06.011

Beier, R. A., Smith, M. D., & Spitler, J. D. (2011). Reference data sets for vertical borehole ground heat exchanger models and thermal response test analysis. Geothermics, 40(1), 79–85. https://doi.org/10.1016/j.geothermics.2010.12.007

Bergman, T. L., Lavine, A. S., Incropera, F. P., & Dewitt, D. P. (2011). Fundamentals of heat and mass transfer (7th ed). Hoboken, NJ: Wiley.

Cimmino, M. (2015). The effects of borehole thermal resistances and fluid flow rate on the g-functions of geothermal bore fields. International Journal of Heat and Mass Transfer, 91, 1119–1127. https://doi.org/10.1016/j.ijheatmasstransfer.2015.08.041

Cimmino, M., & Bernier, M. (2014). A semi-analytical method to generate g-functions for geothermal bore fields. International Journal of Heat and Mass Transfer, 70, 641–650. https://doi.org/10.1016/j.ijheatmasstransfer.2013.11.037

Cimmino, M., & Bernier, M. (2015). Experimental determination of the g-functions of a small-scale geothermal borehole. Geothermics, 56, 60–71. https://doi.org/10.1016/j.geothermics.2015.03.006

Cimmino, M., Bernier, M., & Adams, F. (2013). A contribution towards the determination of g-functions using the finite line source. Applied Thermal Engineering, 51(1–2), 401–412. https://doi.org/10.1016/j.applthermaleng.2012.07.044

Claesson, J., & Eskilson, P. (1987). Conductive Heat Extraction by a Deep Borehole. Analytical Studies. (Technical Report). Lund: University of Lund.

Cui, P., Yang, H., & Fang, Z. (2006). Heat transfer analysis of ground heat exchangers with inclined boreholes. Applied Thermal Engineering, 26(11), 1169–1175. https://doi.org/10.1016/j.applthermaleng.2005.10.034

Cullin, J. R., Spitler, J. D., Montagud, C., Ruiz-Calvo, F., Rees, S. J., Naicker, S. S., … Southard, L. E. (2015). Validation of vertical ground heat exchanger design methodologies. Science and Technology for the Built Environment, 21(2), 137–149. https://doi.org/10.1080/10789669.2014.974478

Eskilson, P. (1987, June). Thermal analysis of heat extraction boreholes. Lund University, Sweden.

Eslami-nejad, P., & Bernier, M. (2012). Freezing of geothermal borehole surroundings: A numerical and experimental assessment with applications. Applied Energy, 98, 333–345. https://doi.org/10.1016/j.apenergy.2012.03.047

Hellström, G., & Kjellsson, E. (2000). Laboratory Measurements of Heat Transfer Properties for Different Types of Borehole Heat Exchangers. In Proc. of Terrastock. Stuttgart, Germany.

Javed, S., & Claesson, J. (2011). New analytical and numerical solutions for the short-term analysis of vertical ground heat exchangers. ASHRAE Transactions, 117(1), 3.

Kim, Y., Kim, M., Ahn, C., Kim, H. U., Kang, S.-W., & Kim, T. (2017). Numerical study on heat transfer and pressure drop in laminar-flow multistage mini-channel heat sink. International Journal of Heat and Mass Transfer, 108, 1197–1206. https://doi.org/10.1016/j.ijheatmasstransfer.2016.12.025

Kramer, C. A., Ghasemi-Fare, O., & Basu, P. (2015). Laboratory Thermal Performance Tests on a Model Heat Exchanger Pile in Sand. Geotechnical and Geological Engineering, 33(2), 253–271. https://doi.org/10.1007/s10706-014-9786-z

Lamarche, L. (2011). Analytical g-function for inclined boreholes in ground-source heat pump systems. Geothermics, 40(4), 241–249. https://doi.org/10.1016/j.geothermics.2011.07.006

Lamarche, L., & Beauchamp, B. (2007). A new contribution to the finite line-source model for geothermal boreholes. Energy and Buildings, 39(2), 188–198. https://doi.org/10.1016/j.enbuild.2006.06.003

Lazzarotto, A. (2016). A methodology for the calculation of response functions for geothermal fields with arbitrarily oriented boreholes – Part 1. Renewable Energy, 86, 1380–1393. https://doi.org/10.1016/j.renene.2015.09.056

Lazzarotto, A., & Björk, F. (2016). A methodology for the calculation of response functions for geothermal fields with arbitrarily oriented boreholes – Part 2. Renewable Energy, 86, 1353–1361. https://doi.org/10.1016/j.renene.2015.09.057

Montagud, C., Corberán, J. M., Montero, Á., & Urchueguía, J. F. (2011). Analysis of the energy performance of a ground source heat pump system after five years of operation. Energy and Buildings, 43(12), 3618–3626. https://doi.org/10.1016/j.enbuild.2011.09.036

Monzó, P. (2018). Modelling and monitoring thermal response of the ground in borehole fields (PhD Thesis). KTH Royal Institute of Technology, Stockholm, Sweden. Retrieved from http://urn.kb.se/resolve?urn=urn:nbn:se:kth:diva-222007

Monzó, P., Mogensen, P., Acuña, J., Ruiz-Calvo, F., & Montagud, C. (2015). A novel numerical approach for imposing a temperature boundary condition at the borehole wall in borehole fields. Geothermics, 56, 35–44. https://doi.org/10.1016/j.geothermics.2015.03.003

Salim Shirazi, A., & Bernier, M. (2014). A small-scale experimental apparatus to study heat transfer in the vicinity of geothermal boreholes. HVAC&R Research, 20(7), 819–827. https://doi.org/10.1080/10789669.2014.939553

Spitler, J., & Bernier, M. (2011). Ground-source heat pump systems: The first century and beyond. HVAC&R Research, 17(6), 891–894. https://doi.org/10.1080/10789669.2011.628221

Spitler, J., & Bernier, M. (2016). 2 - Vertical borehole ground heat exchanger design methods. In S. J. Rees (Ed.), Advances in Ground-Source Heat Pump Systems (pp. 29–61). Woodhead Publishing. https://doi.org/10.1016/B978-0-08-100311-4.00002-9

Sundberg, J. (1991). Termiska egenskaper i jord och berg (No. 12). Swedish Geotechnical Institute.

Tarnawski, V. R., Momose, T., & Leong, W. H. (2011). Thermal Conductivity of Standard Sands II. Saturated Conditions. International Journal of Thermophysics, 32(5), 984–1005. https://doi.org/10.1007/s10765-011-0975-1

Yavuzturk, C., & Spitler, J. D. (2001). Field validation of a short time step model for vertical ground-loop heat exchangers / Discussion. ASHRAE Transactions; Atlanta, 107, 617.

Zeng, H. Y., Diao, N. R., & Fang, Z. H. (2002). A finite line-source model for boreholes in geothermal heat exchangers. Heat Transfer?Asian Research, 31(7), 558–567. https://doi.org/10.1002/htj.10057

[This page has been intentionally left blank]

IGSHPA SWEDEN 2018 Research Conference

DOI: 10.22488/okstate.18.000044

An experimental setup to measure the heat-exchange processes by controlling thermal and hydraulic conditions

Paolo Scotton **Giordano Teza** **Daniele Rossi**
Giorgia Dalla Santa **Antonio Galgaro**

ABSTRACT

The design of a Borehole Heat Exchanger (BHE) is based on the evaluation of the thermal exchange capacity of the whole system constituted by the probes and the surrounding ground. The energy performance of a BHE mainly depends on the thermal properties of the sediments, the possible groundwater flow and the changes in the thermal gradient in the probe's surroundings due to the continuous heat exchange with the subsoil. The interpretation of the in-field applications is often difficult because in many instances the information needed is unavailable due to difficulties of in-field measurements. An experimental device was built in order to assess, under controlled conditions, the evolution in time and space of the energetic processes that occur between a thermal probe and the surrounding ground. A copper probe was placed into a soil control volume of 1m³ and 24 high precision temperature sensors were distributed inside this volume at different distances from the probe. The configuration of the experimental settings was built to allow alterations in terms of sediments, groundwater flow conditions, thermal probe properties and operations, in order to simulate different physical conditions and to better understand the complex physical processes involved. Another goal of the experimental research was to produce reliable experimental data that can be used for the calibration and set up of numerical models. This paper describes the experimental apparatus and two experiments performed in order to assess its capability to satisfy the design requirements.

INTRODUCTION

The physical phenomena that occur in a borehole heat exchanger (BHE) are generally well known and well-defined technical solutions are currently available thanks to the achievements obtained worldwide in the last 20-30 years in terms of design, installation and use of ground coupled heat pumps (GCHPs). However, there are still some open issues. The design of a BHE to be used in a shallow geothermal system is based on the evaluation of the thermal exchange capacity of the whole system constituted by the BHE itself and the surrounding ground. The energy performance of the system mainly depends on the thermal properties of the sediments and on possible groundwater flow (Sutton 2003). Moreover, the continuous heat exchange with the subsoil modifies the thermal status of the subsoil itself which, in turn, affects the thermal gradient in the BHE surroundings. The approach to BHE modeling can be analytical (see e.g. Philippe et al. 2009) or numerical (see e.g. Al-Khoury et al. 2005; Al-Khoury and Bonnier 2006). Examples of modeling focusing on district heating, i.e. teleheating, also exist (Carlini et al. 2012). Regardless to the used approach, the thermal alteration induced in the ground and the BHE performance are usually evaluated by means of models of heat transfer and groundwater flow that need to be validated through the comparison with experimental data, which are often missing due to the difficulties of in-field measurements. Therefore, in some cases

Paolo Scotton (paolo.scotton@unipd.it), Giordano Teza (giordano.teza@unipd.it), Giorgia Dalla Santa (giorgia.dallsanta@unipd.it) and Antonio Galgaro (anotonio.galgaro@unipd.it) perform their reserach activities at the Department of Geosciences, University of Padua, Italy. Daniele Rossi (danielerossi74@gmail.com) is a consultant engineer.

the design of a BHE may not be enough accurate and an assessment of its environmental and economic benefits could be inadequate.

Physical models are valid tools for the solution of many natural phenomena that are difficult to solve analytically or numerically as initial value problems or boundary value problems, or whose solution obtained with these methods has some uncertainties (Green 2014; Volkov et al. 2017). This tools are often used to verify the results of an analytical or numerical application obtained through appropriate simplifications. Physical modeling can also be used to describe the complex hydro-thermodynamic interaction that occurs when a thermal probe exchanges energy with the surrounding environment. For example, Wang et al. (2013) built a 900 × 800 mm experimental setup in order to investigate the interactions between soil and pipes in case of ground freezing phenomena: they analyzed the effects of soils with different grain sizes on the movement of the freezing front and on the deformations induced on the pipes. Cimmino et Bernier (2015) built an experimental setup constituted of a small-scale 400mm-long borehole inserted into a 2 m^3 sand tank with known thermal properties in order to obtain the experimental g-function, starting from measurements of the borehole wall temperature and of the net heat injection. Subsequently, the experimental g-function was compared to the g-function obtained analytically. Recently, Li et al (2018) built a 6.25 m × 1.5 m × 1 m experimental box to investigate the transient heat transfer performance of a double-U probe in a layered ground, then comparing the results with the outputs of a 3D numerical model.

A physical model of a probe-ground system was built (Scotton 2017) in order to measure, under controlled conditions, the evolution in time and space of the thermal alteration induced in the ground by a thermal probe. It was a single probe, inserted into a volume of 1 m^3, where 24 high precision temperature sensors were distributed at different distances from the probe. The experimental settings could be varied in a wide range of configurations in terms of sediments (with their different porosity, thermal properties, and hydraulic permeability), groundwater flow conditions and thermal probe operations. In order to better understand the complex physical processes involved, in the present early stages of the experimentations the thermal exchange was magnified by using a copper probe instead of a PE probe, obtaining a thermal power per unit length higher than the typical one. This paper shows details about the experimental setup and preliminary experimental results.

THE EXPERIMENTAL APPARATUS

Supporting structure

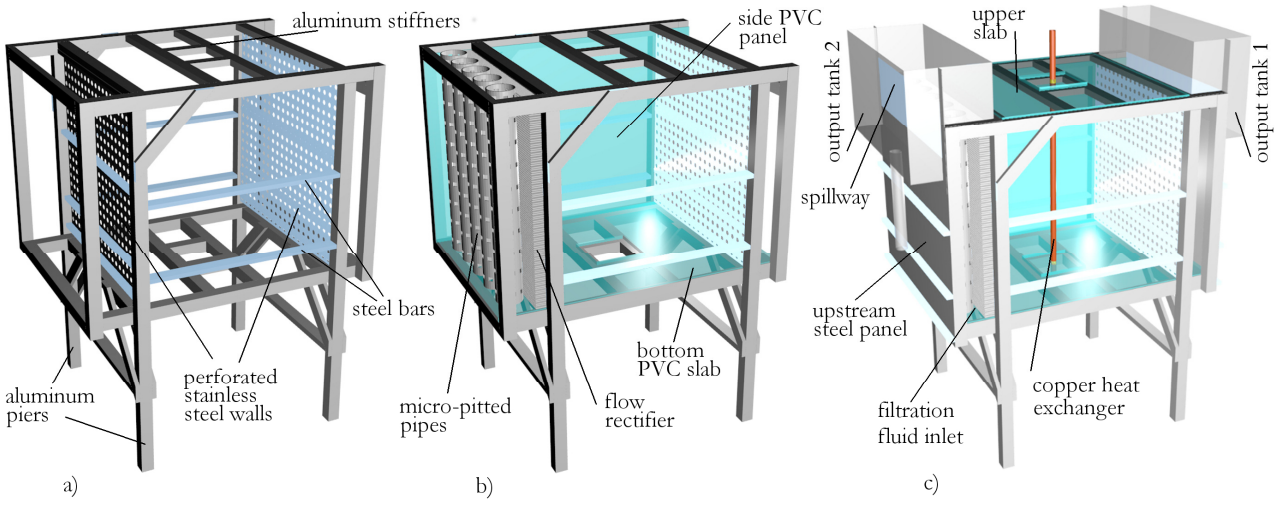

Figure 1 The bearing structure of the experimental apparatus. The materials used are aluminum, steel and PVC.

The supporting structure of the experimental apparatus is shown in Figure 1. It has a height of approximately 2 m, a length of 1.5 m, a width of 1.1m and a mass of 200 kg. The maximum weight of the experimental device, in test

configuration, is 3000 kg. The load-bearing structure is made of aluminum. The aluminum piers have a square section of 6cm side. The supporting elements of the side walls, the steel bars, have a rectangular section of 6cm x 2cm.

The internal support of the granular material is obtained using 2-mm thick perforated stainless steel walls (Figure 1.a). The area of the holes, which accounts for approximately 50% of the total surface, allows the free passage of the filtration fluid, inlet and outlet from the porous medium. The bottom of the apparatus is made of a 20mm thick opaque PVC slab. The side walls are made of 10mm thick transparent PVC panels. Figure 1.b shows the distributors of the filtration fluid, made with micro-pitted PVC pipes, and the flow rectifiers, made of polycarbonate honeycomb sheets. Figure 1.c displays the upstream and downstream closure steel walls of the model and the output tanks of the filtration fluid. The two tanks are equipped with spillways to stabilize the piezometric elevation of the filtration fluid in and out of the model. The maximum piezometric gradient obtainable is about 0.25 m/m. Figure 1.c also shows the copper pipe, used as a heat exchanger in the experimental tests reported in this article. The copper pipe was chosen to enhance the effects of the energy exchange between the probe and the surrounding environment. The internal diameter of the pipe is 28mm, the thickness is 2mm, the length is 0.95m. The upper closing plate is a 1cm thick transparent PVC slab.

Figure 2 shows the physical model carried out according to the design. The aluminum piers rest on height-adjustable supports which allow to level the structure.

Figure 2 a) The experimental apparatus in test configuration. The insulated circuit of the copper heat exchanger is visible; b) A view from the top of the filtration fluid inlet tank with the micro-pitted pipes; c) The perforated stainless steel wall; d) A detail of the flow rectifier located between the micro-pitted pipes and the perforated wall.

Hydraulic circuits

The physical apparatus described above has two hydraulic circuits: the hydraulic circuit of the cold fluid (HCC) and the hydraulic circuit of the hot fluid (HCH). Both circuits can be plugged into the probe circuit or into the filtration fluid circuit. The structural part of the experimental device and the connection points of the circuit of the thermal probe and of the filtration fluid are schematized in Figure 3, on the left. The probe circuit inserts the fluid into the upper part of the copper probe (inputCS) and reacquires it at the lower end of the probe (outputCS). The filtration fluid circuit inserts the fluid into the lower part of the loading tank (inputCF). The stability of the filtration motion through the porous medium of the experimental device is ensured by means of two spillways, placed in the loading tank and in the discharge tank respectively. Therefore, there are two discharges of the filtration circuit: one from the discharge tank (outputCF1) and one from the loading tank (outputCF2). The two circuits are designed to ensure a steady flow rate with constant temperature at the model inputs.

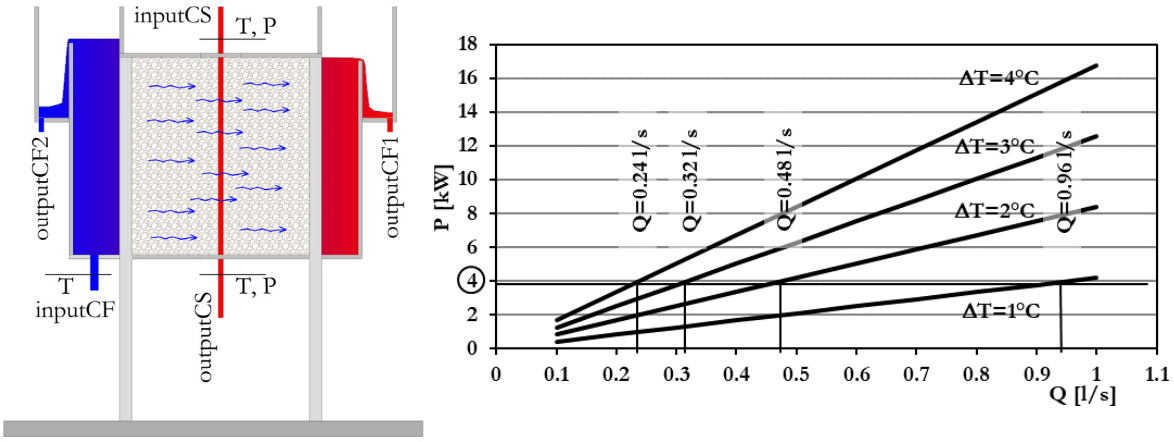

Figure 3 On the left, a scheme of the experimental apparatus with indication of input and output points of the cold and hot hydraulic circuit; on the right, power of the thermal machine vs flow rate when the temperature in the probe circuit fluid (water) varies between 1°C and 4°C.

Thermal power, flow rate and flow regime in the hydraulic circuits. The flow rate in the hydraulic circuits is a function of the temperature variation that the fluids undergo by covering the entire circuit. This temperature difference, in heating or cooling, must be restored by a machine of adequate power. Figure 3, on the right, shows the dependence between the power of the thermal machine and the flow rate that can be managed when the assumed temperature variation in the circuit varies between 1°C and 4°C. If a 4kW power machine is used, the flow rate varies between 0.24 l/s (4°C temperature variation in the circuit) and 0.96 l/s (1°C temperature variation in the circuit).

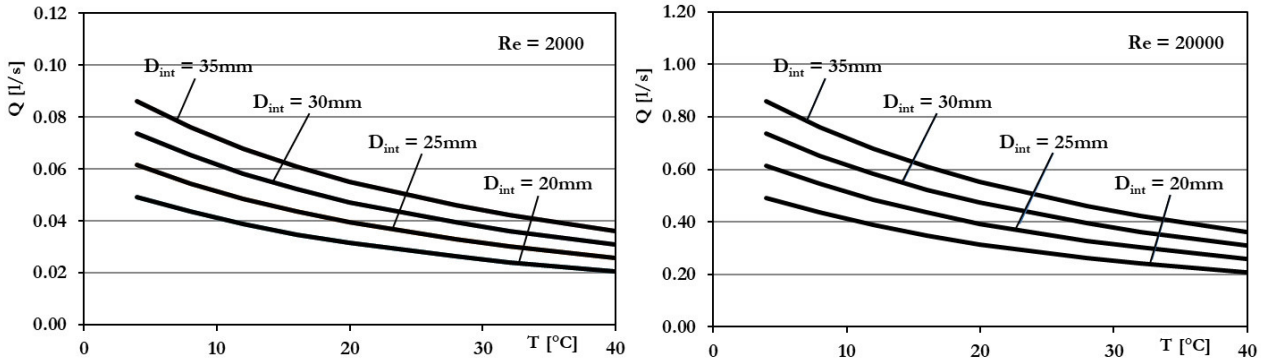

Figure 4 Flow rate vs. temperature of the thermal probe circuit, for two Reynolds numbers and some probe diameters.

Figure 4 shows the flow rate in the probe circuit when the temperature of the fluid (water) and the diameter of the probe tube vary. On the left, a description of the situation at the limit of laminar flow (the Reynolds number, Re, is 2000). The maximum flow rate, ~0.10 l/s, is obtained at low temperatures with the maximum diameter considered of 35 mm. This flow rate is easily achieved with the designed power of the circuit. On the right, a description of the case in which the Re in the probe circuit reaches 20000. Considering the maximum diameter, at temperatures slightly above 0°C the flow rate is 0.9 l/s, close to the maximum value obtainable from the system under the conditions described previously. These Re values are close to the maximums technologically used. The limits of the filtration fluid velocity in the porous medium are obtained as a function of the maximum generable rate of flow (between 0.25 l/s and 1 l/s), the maximum piezometric gradient (~0.2 m/m) and the filtration area (~1 m^2). The velocity ranges between $2.7x10^{-4}$ m/s and $1.21x10^{-3}$ m/s. In the case of a Darcy flow, the hydraulic conductivity varies between $1.4×10^{-3}$ m/s and $5.5×10^{-3}$ m/s, which is the case of clean sand, sand and gravel.

Temperature sensors

The temperature measurement was carried out by means of Resistance Temperature Detectors (RTDs). The thermocouples were excluded due to their insufficient accuracy and the thermistors were excluded because of their highly non-linear calibration curves. In particular, PT100 RTDs with three-wire connections were used. They have an adequate sensitivity (less than 0.1 °C) and a calibration curve very close to linearity, although their response time is not particularly short, especially if the sensor is protected by a copper capsule saturated with thermally conductive resin. The experimental tests performed on the bare probes showed a behavior consistent with the manufacturer data (variation of 90% of the temperature jump in a time of 0.3 s), while the probes protected with copper capsules of different shapes and lengths presented a response time of approximately 10 s. To reduce the response time up to 2-3 seconds, the protection was achieved by means of a water-permeable metal sock. This response time is considered compatible with the temperature variation times that occur in the physical model.

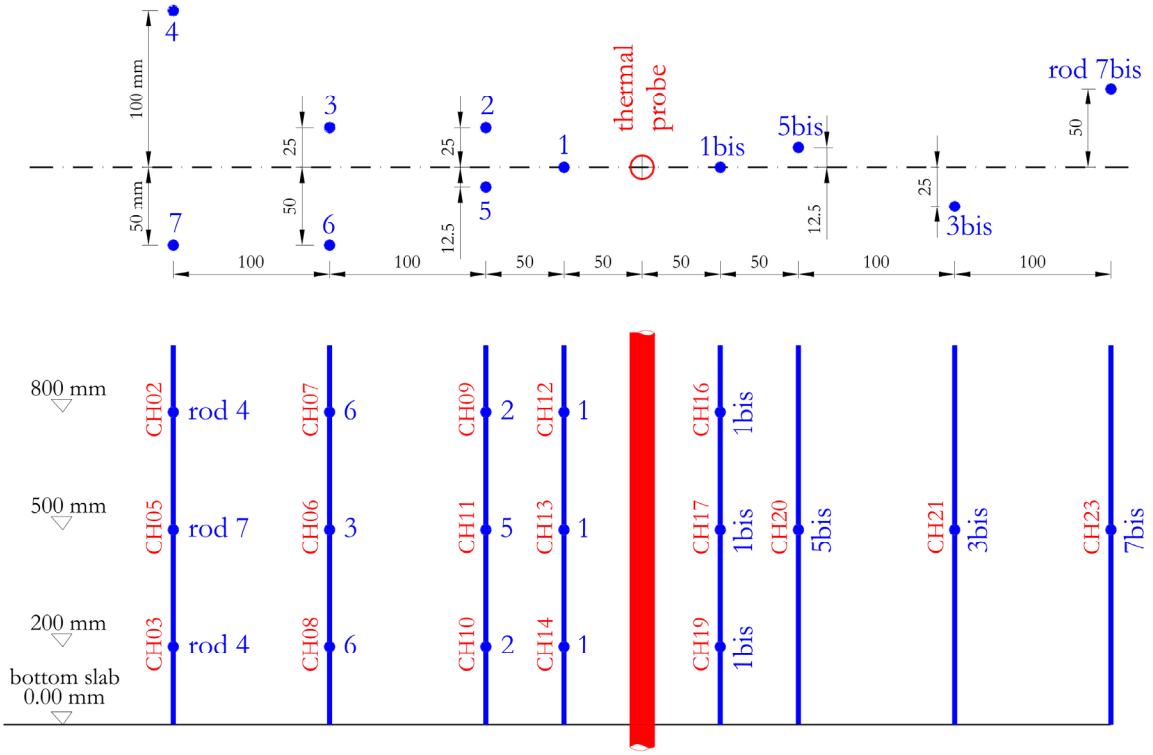

Figure 5 Above: planimetric position of the rods supporting the RTDs inside the control volume; below: rod and elevation with respect to the bottom of the control volume of each RTD.

In the tests described here, the RTDs are used to measure the temperature of: the fluid in the copper probe (input and output fluid temperature); the filtration fluid entering the control volume; the environment; 18 positions within the control volume. The RTDs are arranged within the control volume on the basis of a preliminary finite element analysis carried out by means of Comsol Multiphysics, taking into account the test configurations in the absence and in the presence of filtration water. The planimetric and altimetric layout is shown in Figure 5. Wooden vertical rods with 6mm diameter are placed in the positions indicated in the plan. The RTDs are placed on these rods, in the points shown in the Figure 5, and facing the copper probe. The rods are placed at different distances from the copper probe and are arranged mainly in the direction of the flow in the tests with filtration motion, in greater number downstream of the probe (rods 1, 2, 3, 4, 5, 6, 7) but also upstream (rods 1bis, 5bis, 3bis, 7bis). The

arrangement of the downstream rods is aimed at characterizing the temperature plume which is formed in a limited-width area downstream of the probe in the case of simulation of the groundwater flow. In the absence of groundwater flow, the temperature distribution should assume an axis-symmetrical behavior with respect to the thermal probe. The limits of this hypothesis are evaluated by means of the RTDs placed on the rods located upstream, in a symmetrical position with respect to the rods arranged downstream. The acquisition system has been designed to serve a maximum of 42 analogic channels.

THE FIRST TESTS

The assessment of the behavior of the experimental device was carried out by filling the control volume with different materials, leading to 5 experimental configurations: (i) water; (ii) moving water; (iii) dry granular material; (iv) saturated granular material; and (v) saturated granular material with moving water. The experimental results obtained in configurations (iv) and (v) are shown here. Figure 6 shows two images (on the left and in the middle) of the device in the configuration of the tests with saturated granular material. The image on the right shows the rods used as a support for the RTDs distributed inside the control volume. The volume was filled with "Risetta del Brenta" (literally, small rice from the Brenta river), a sandy material obtained from the riverbed of the Brenta river near Padua. The deposition of the granular material inside the model was obtained by letting the granular material fall into still water. The measurement of the extracted water volume (0.505 m^3) and of the mass of the material put into the model (1365.17 kg) allowed the estimate of the average density of the solid component, 2700 kg/m^3, and of its porosity, 0.43 (Figure 6).

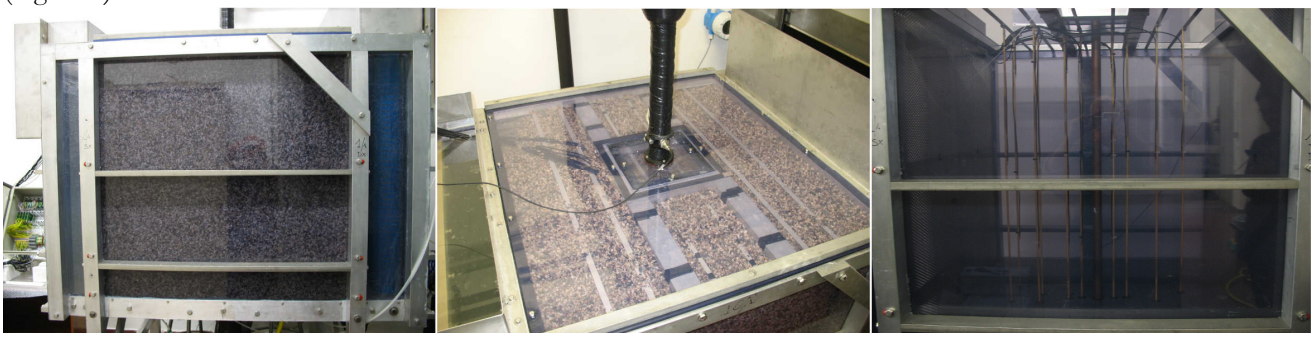

Figure 6 On the left and in the middle, two images of the experimental device filled with granular material saturated with water. On the right, a view of the inside of the control volume with the RTDs supporting rods. .

Figure 7 shows the experimental data acquired during the test carried out without filtration motion. The average input and output fluid temperatures at the copper probe are 43.0°C (standard deviation, SD, of 0.4°C) and 42.4°C (0.4°C SD) respectively. The average temperature difference between the two sensors is 0.57°C (0.06°C SD). The average room temperature is 18.7°C (0.3°C SD). The flow rate of the fluid in the copper probe is 10.12 l/min (0.03 l/min SD). Figure 7, on the left, shows that permanent boundary conditions of the input temperature, as well as permanent flow rate in the thermal probe and permanent room temperature can be achieved with the proposed device. The difference between input and output temperatures of the thermal probe is significant compared to the accuracy of the RTDs used (~0.025°C) and leads, through the application of the energy balance equation, to an estimate of the probe power per unit length of 400 W/m, slightly decreasing over time (an order of magnitude higher than the peak technological values). Figure 7, on the right, shows the temperature trends in symmetrical positions within the control volume (CH12-CH16; CH13-CH17; CH14-CH19; CH11-CH20; CH06-CH21; CH05-CH23). The temperature pattern is almost symmetric, as expected. The arrival times of the thermal wave are substantially concordant. The differences in temperature detected could be mainly related to a possible lack of homogeneity of the granular material and to the non-precise symmetry in the positioning of the probes within the control volume,

especially near the thermal probe where the temperature gradients are greater.

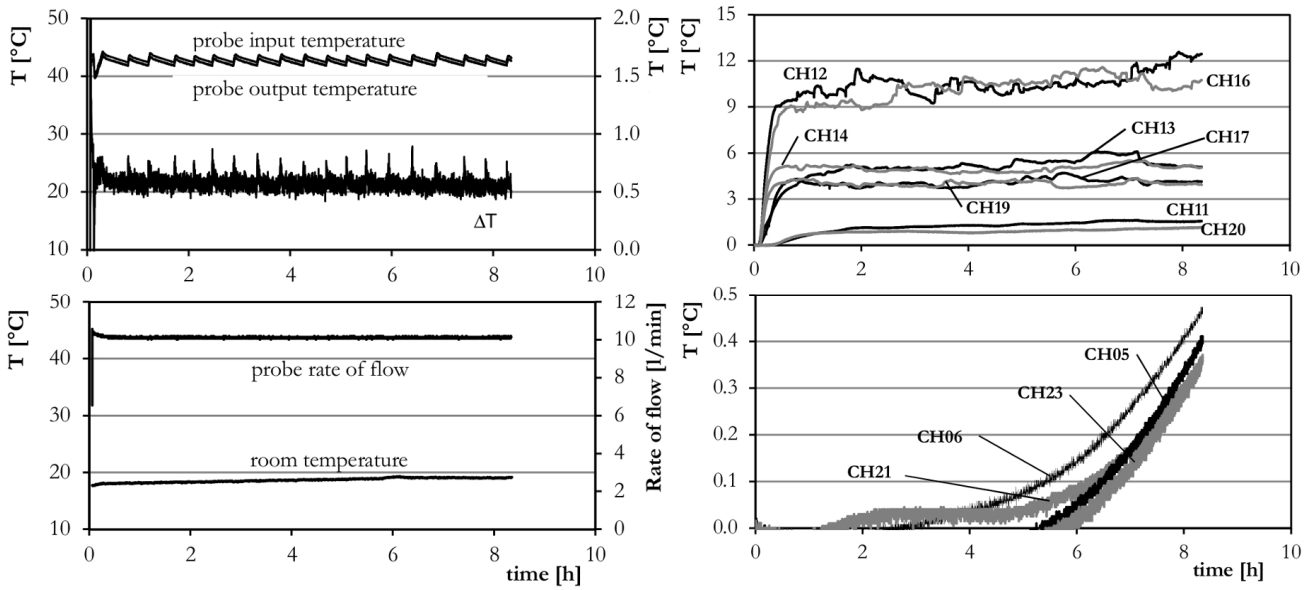

Figure 7 Experimental data acquired during the test with granular material saturated with still water. On the left, the input and the output temperature of the thermal probe fluid, its discharge and the room temperature. On the right, the temperature measured by some RTDs inside the control volume in a symmetrical position to the thermal probe.

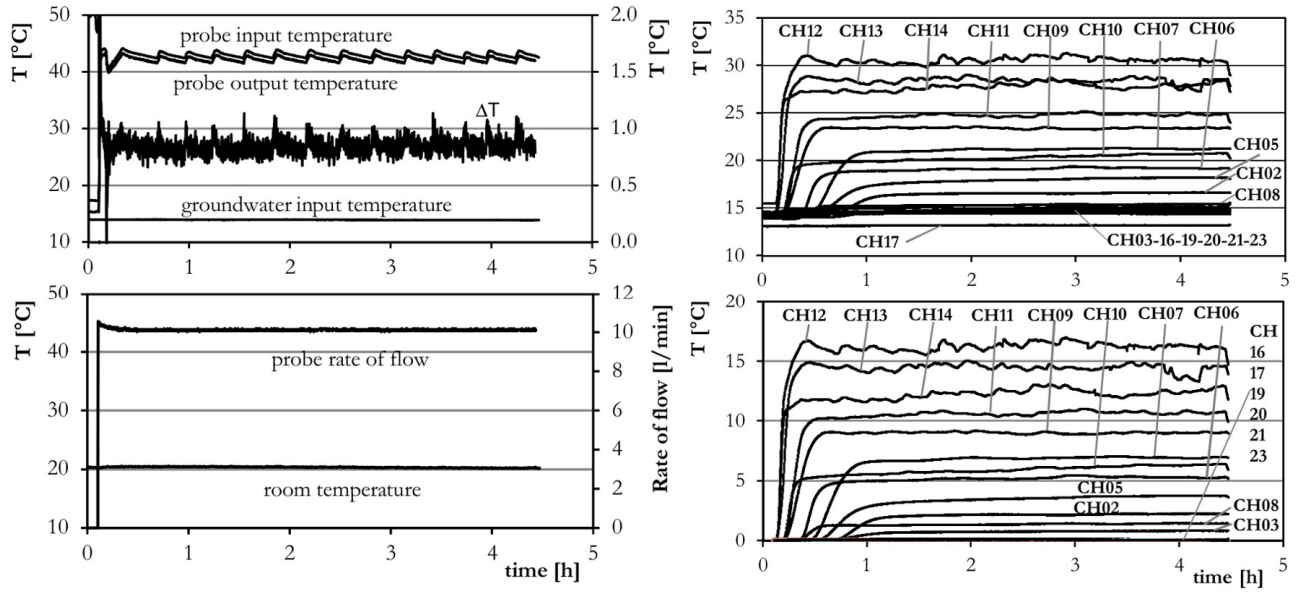

Figure 8 Experimental data acquired during the test with granular material saturated with filtration flow. On the left, the input and the output temperature of the thermal probe fluid, the temperature of the filtration fluid, the discharge of the probe fluid and the room temperature. On the right, above, the temperature measured by the RTDs inside the control volume; below, the temperature values with respect to the initial values.

Figure 8 shows the experimental data acquired during the test carried out with filtration motion. The average input and output fluid temperatures at the copper probe are respectively 43.0°C (0.4°C SD) and 42.2°C (0.4°C SD).

The average temperature difference between the two sensors is 0.84°C (0.07°C SD), much higher than in the previous test. The average room temperature is 18.7°C (0.3°C SD). The flow rate of the fluid in the copper pipe is 10.12 l/min (0.03 l/min SD). The velocity of the fluid in the copper probe is 0.274 m/s and the corresponding Reynolds number, at the temperature of 40°C, is 11654. This implies that the flow regime in the probe is a transition between laminar and turbulent motion. The filtration flow rate, obtained by mean of the volumetric method, is 4.721 l/min (0.017 l/min SD). The average filtration velocity is $8.4 \cdot 10^{-5}$ m/s. Based on the measurements made with piezometers, the piezometric drop is 0.0166 m/m. In the reasonable hypothesis of validity of Darcy's law, a hydraulic conductivity of $5.06 \cdot 10^{-3}$ m/s is obtained, which agrees with data from literature. The average temperature of the input filtration fluid is 13.92°C (0.03°C SD). In this case the estimate of the probe power per unit length is 595 W/m. Figure 8, on the left, shows the same data of the previous test plus the temperature of the filtration fluid: the boundary conditions are stable. On the right, the figure above shows the temperature trends measured by the RTDs inside the control volume; below, the same trends referring to the initial local temperature values. It should be noted that the temperatures at the beginning of the test are not equal in the various positions within the control volume. This should be due mainly to the difficulty of obtaining homogeneous initial conditions within the volume of control because of the significant size of the physical model and the size of the environment in which it is located, and, in a minor part, to a possible alteration of the temperature sensor calibration curves. In this test temperature variations are significant only downstream from the thermal probe: all RTDs located upstream (Figure 5) do not experience any temperature modification.

CONCLUSIONS

A new experimental apparatus was designed and constructed in order to study the physical processes that take place when a thermal probe exchanges energy with the surrounding environment. This paper presents the apparatus and two tests performed in order to evaluate its capability to fulfil design requirements.

In the tests carried out with saturated granular material, at rest or moving, the amplitudes of the temperature variations induced in the fluid inside the thermal probe were significantly higher than the sensitivity of the RTDs and an accurate analysis of the energy exchange between the thermal probe and the surrounding environment was possible, together with the description of the temperature field in the control volume over time. In the tests carried out with still water, the expected axial symmetry of the temperature pattern emerged clearly.

The thermal probe circuit is suitable for the purposes of the tests. A highly stable fluid discharge was obtained. The stability of the temperature sensors appeared to be adequate. The results also suggested some improvements of the system for further experimental stages (e.g., methods of RTDs positioning in the control volume more accurate could be used).

It is reasonable to assume that the experimental apparatus here proposed is a powerful tool for the analysis of the complex phenomena under study. Its use can be aimed at understanding the role of the different physical parameters involved in the phenomena and at characterizing different materials and different technical solutions for heat exchangers. Moreover, the experimental data can be used in the construction and calibration process of numerical models.

ACKNOWLEDGMENTS

The research has been funded in the framework of the research project "GEOTERM (Thermal Geo-Exchange in the Province of Trento)", REET-FBK, Trento, Italy. Moreover, the authors wish to thank Tecnopenta s.r.l., Teolo (Padua) for their aid in the development of the experimental device and Simonetta Cola, head of the Geotechnical Engineering Laboratory, DICEA, University of Padua, where the experimental set up was installed.

REFERENCES

Al-Khoury, R., Bonnier, P.G. and R.B. Brinkgreve. 2005. *Efficient finite element formulation for geothermal heating system. Part I: Steady state*. International Journal for Numerical Methods in Engineering 63: 988–1013.

Al-Khoury, R., and P.G. Bonnier. 2005. *Efficient finite element formulation for geothermal heating system. Part II: Transient*. International Journal for Numerical Methods in Engineering 67: 725–745.

Carlini,M., Castellucci, S., Allegrini, E. and A. Tucci. 2012. *Down-Hole Heat Exchangers: Modelling of a Low-Enthalpy Geothermal System for District Heating*. Mathematical Problems in Engineering 2012(845192): 1-11.

Cimmino, M., and M. Bernier. 2015. *Experimental determination of the g-functions of a small-scale geothermal borehole*. Geothermics 56: 60-71.

Green, D.L. 2014. *Modelling Geomorphic Systems: Scaled Physical Models*. Section 5.3 in Cook, S.J., Clarke, L.E. and J.M. Nield (Eds.) Geomorphological Techniques. London: British Society for Geomorphology

IEA. 2011. Technology Roadmap - Geothermal Heat and Power. Technical report. Paris: International Energy Agency.

Li, W., Li, X., Peng, Y., Wang, Y., and J. Tu. 2018. *Experimental and numerical investigations on heat transfer in stratified subsurface materials*. Applied Thermal Engineering 135: 228-237.

Philippe, M., Bernier, M. and D. Marchio. 2009. *Validity ranges of three analytical solutions to heat transfer in the vicinity of single boreholes*. Geothermics 38: 407–413.

Scotton, P. 2017. Un apparato sperimentale per lo studio dello scambio energetico tra sottosuolo e sonda geotermica, Project GEOTERM (Geoscambio nella Provincia Autonoma di Trento). Trento: Reet-FBK.

Sutton, M, Nutter, D., and R. Couvillion. 2003. *A ground resistance for vertical bore heat exchangers with groundwater flow*. Journal of Energy Resources Technology **125:** 183–189.

Volkov, A.V., Ryzhenkov, A.V., Kurshakov, A.V., Grigoriev, S.V. and V.V. Bekker. 2017. *Physical Modelling of Temperature's Potential Decrease for Near-Wellbore Rocks during Extraction of Thermal Energy*. International Journal of Applied Engineering Research Volume 12(17): 6570-6575.

Wang, Y., Gao, Q., Zhu, X., Yu, M., and X., Zhao. 2013. *Experimental study on interaction between soil and ground heat exchange pipe at low temperature*. Applied Thermal Engineering 60(1-2): 137-144.

[This page has been intentionally left blank]

IGSHPA SWEDEN 2018 Research Conference

DOI: 10.22488/okstate.18.000032

Vertical Hydraulic Conductivity of Borehole Heat Exchanger Systems Before and After Freeze-Thaw Cycle Stress

Alexander Kirschbaum **Jens M. Kuckelkorn** **Kilian Hagel**

ABSTRACT

Quality assurance is a very important aspect in the planning, implementation and operation of borehole heat exchangers (BHE). Within the research project Quality Assurance for Borehole Heat Exchangers (QEWS) the hydraulic sealing behaviour of industrial grouting materials was investigated. Important aspects therein were the capability for sealing between different aquifers and aging resistance against freeze-thaw cycle stress. For this purpose, a large-scale test rig for determining the hydraulic conductivity of borehole heat exchanger systems (BHES) was developed and put into operation. Compared to samples of the pure grouting material, the system samples exhibited significantly increased permeability, which was further increased by freeze-thaw cycle stress. It could be shown that the first freeze-thaw cycle caused the most significant aging effect. Aging caused by further freeze-thaw cycles could be partly compensated by regeneration effects. But the large-scale test rig has a substantial disadvantage: due to the length of the system sample, depending on the hydraulic permeability of the grouting material, the experimental program is very complex and time-consuming. Therefore, a downscaled test rig will be developed within the current project Quality Assurance for Borehole Heat Exchangers II (QEWS II).

INTRODUCTION

In the field of shallow geothermal energy, borehole heat exchangers (BHE) are widely used as low temperature sources for heating and cooling purposes. In Germany, double-U-pipes are frequently used in these systems.

Quality assurance is very important in planning, construction and operation of these systems. Reliable sealing of the borehole over a long period of time has a high priority. The best possible groundwater protection must be ensured and should not be impaired by influences such as improper pressure testing or freeze-thaw cycle stresses. (VDI 4640, 2015)

A long-term stable vertical sealing of the borehole heat exchanger system (BHES) is of fundamental importance for approval by the water authorities, particularly when intersecting different groundwater layers, which are separated by sealing layers. This is not only a matter of the impermeability of the grouting material but also of the overall BHES under in-situ conditions. Therefore, a collective consideration of grouting material, heat exchanger pipes (HEP) and possible installations such as spacers or centering devices as well as the connection to the surrounding soil must be carried out at realistic operating conditions.

Dr. Jens M. Kuckelkorn is head of the Systems Engineering group at the Bavarian Center for Applied Energy Research. Alexander Kirschbaum (alexander.kirschbaum@zae-bayern.de) and Kilian Hagel are research engineers in this group.

A large-scale test rig was built at the Bavarian Center for Applied Energy Research in Garching near Munich, Germany, to investigate an BHES under realistic pressure and temperature conditions with regard to its hydraulic conductivity. A system sample, 150 mm in diameter and 3.5 m long, consisting of grouting material, 4 HEPs with an outer diameter of 32 mm, U-bend, grouting hose and spacers can be installed into this test rig. (Kuckelkorn, et al. 2010; Kuckelkorn and Reuß 2010; Kuckelkorn and Reuß 2012; Reuß, et al. 2012; Kuckelkorn 2013; Anbergen, et al. 2014b; Anbergen, et al. 2015)

Yet, the vertical hydraulic conductivity of a BHES under in-situ conditions and the resistance of the grouting material against freeze-thaw cycle stresses and high temperature gradients has not been satisfactorily investigated.

In the meantime, another test method has been developed, suited to investigate a 7 cm tall sample with a diameter of around 10 cm and a central HEP with a diameter of 40 mm (Anbergen et al., 2012; Anbergen and Sass, 2013; Anbergen et al., 2014a, Anbergen et al., 2014b; Anbergen et al., 2015). This test method also allows for stressing of the sample with freeze-thaw cycles. These samples are comparably short and have only one HEP installed.

In comparison, the large-scale test rig has a substantial disadvantage: due to the length of the system sample and depending on the hydraulic permeability of the grouting material, it can take several weeks to reach a fully saturated condition. From sample preparation to sample disassembly, 4 to 6 months can pass. This is clearly too long to serve as a material testing method for manufacturers.

Therefore, the Bavarian Center for Applied Energy Research is developing a downscaled test rig in a running project. The installation of system samples of lengths up to 100 cm with a double-U-pipe and diameter of 15 cm as well as samples with only one HEP and 10 cm in diameter should be possible (Kirschbaum, et al. 2017).

LARGE-SCALE TEST RIG

Experimental setup and operation

The system tests include the evaluation of full BHES-samples in a large-scale laboratory test rig. The system sample has a diameter of 150 mm and a hydraulic measurement length of 2.75 m. It consists of grouting material, 4 HEPs with a diameter of 32 mm, a U-bend, grouting hose and spacers. The borehole wall is simulated by a plastic tube, which has been sanded on the inside. For this purpose, a suitable sanding process was developed which is intended to prevent water from flowing between the plastic tube and grouting material.

The system sample is prepared by tremie method by filling it with grouting material from bottom to top with the help of a grouting hose, a colloidal mixer and a screw pump. After curing under water for at least 28 days, the system sample is installed into the test rig. The test rig is shown in Figure 1.

According to DIN 18130-1 (DIN 18130-1, 1998) the system sample is saturated with tap water at a pressure of 9 bar after installing it into the test rig. When the saturating process is confirmed the system sample is subjected to a hydraulic gradient at isothermal conditions with the higher pressure at the bottom of the test rig. The volume of the water flowing through the 2.75 m long measurement section from the bottom to the top of the test rig is recorded.

The permeability coefficient (k_f-value) for water, used to characterize porous rocks according to Darcy (Hölting and Coldewey 2008) can be used as a measure for the hydraulic permeability of the entire BHES. Using the recorded volume flow, the mean temperature, the hydraulic gradient and the dimensions of the system sample, the k_{f10}-value (water permeability coefficient at 10 °C) can be determined.

To determine the influence of freeze-thaw cycle stress or high temperature gradients, the system samples are subjected to predefined thermal stress and, subsequently, measured again. Analogous to the in-situ operation of a BHE the system sample can be frozen from the inside out via the HEPs. The plastic tube simulating a borehole wall and the cell pressure mechanically stabilizes the grouting material of the system sample during the freeze-thaw cycle. A temperature control device allows for defined stressing of the system sample with inlet flow temperatures ranging from -10 °C to +80 °C. It also allows for keeping a constant internal temperature in the thermally insulated pressure vessel during the saturation process and measurements. These isothermal conditions are monitored by several Pt100

sensors installed in the vessel and system sample. To ensure precise volume measurement, the volumetric meter is installed in a temperature controlled and insulated chamber.

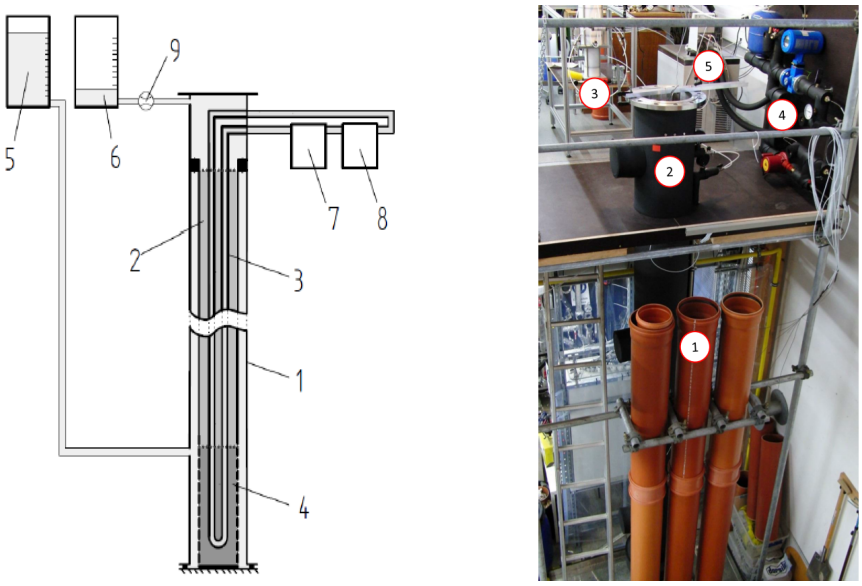

Figure 1 Large-scale test rig for the measurement of the hydraulic conductivity of BHES samples. Left: Schematic construction. The system sample, consisting of grouting material (2), double-U-pipe (3) and a sample bottom with U-bend (4), is installed into the pressure vessel (1). With the help of a cooling and heating device (7 & 8), isothermal conditions for the measurement and simulation of freeze-thaw cycle stress is possible. Using the pressurized water intake (5), the water outlet (6) and a volume flow sensor (9), the water volume flowing through the system sample from bottom to top is recorded and the hydraulic conductivity of the sample can thus be determined. Right: Picture of the test rig with sample storage for preparing and curing system samples (1), pressure vessel without installed lid (2), volume flow sensor (3), hydraulic circuit (4) and temperature control device (5).

For the design of the large-scale test rig and the experimental procedure, the following parameters were relevant, especially due to their influence on the sealing effect of the grouting materials:

- Mineral composition of the grouting material
- Methodology of mixing and/or properties of the suspension during filling
- Method of injection into the borehole
- Time and duration of the hydraulic pressure test of the in-situ BHE
- Sample age and curing time at beginning of measurement
- Thermal stress, especially minimum temperature and number of freeze-thaw cycles
- Height of the temperature gradient between the HEPs and surrounding rock

Special focus was put on the aging behavior of the grouting materials during freeze-thaw cycle stress and on transferability of the results. Thus, based on the methodology of hydraulic tests of triaxial cells (DIN 18130-1, 1998), the permeability coefficient of several system samples was determined. These system samples had to be comparable to an in-situ borehole heat exchanger regarding their dimensions, properties and the operating conditions. The results were compared to the parameters of standard triaxial cells determined in preliminary material tests.

So far, four different grouting materials were measured in combination with PE100 HEPs (polyethylene pipes, 32 mm in diameter), stressed with freeze-thaw cycles, remeasured and visually inspected after removal from the test rig. After preparation, the system samples were stored under water for a curing period of at least four weeks. After installation in the experimental apparatus, the samples were saturated for about four weeks due to their size and the low permeability of the material. The freeze-thaw cycle was defined according to a standard load profile which was derived from data of building facilities measured in operation. Load states of under dimensioned BHES in winter were considered in particular. On this basis, a standard load profile for freeze-thaw cycles was developed in which the inlet fluid temperature of the sample circuit is reduced to -6 °C (see Figure 2). For the first 11 freeze-thaw cycles this specified temperature profile was performed on all four system samples.

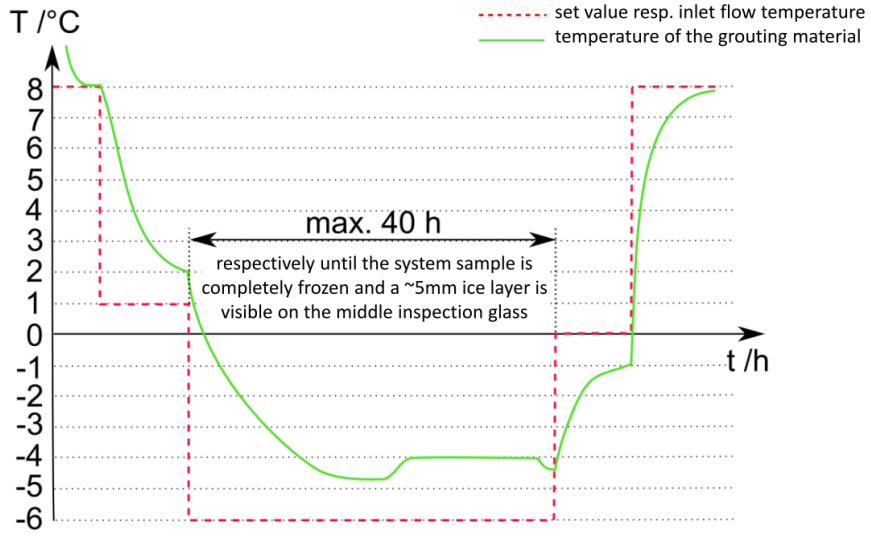

Figure 2 Scheme of the standardized freeze-thaw cycle. After lowering the sample inlet flow temperature to -6 °C, the reduction in temperature progresses radially from the heat exchanger pipes. The phase change to solid in the grouting material tracks the temperature profile.

Test results for vertical hydraulic conductivity

The main focus of the system sample tests was on vertical hydraulic conductivity, also in comparison with samples consisting of only the grouting materials; the effect of freeze-thaw cycle stress; visible changes in the structural conditions (e.g. crack formation, ring gap formation); water drifts — for example along the surface of the HEPs.

Furthermore, it had to be ensured that the measuring method was not affected by boundary conditions such as temperature fluctuations or additional water drifts along the "borehole wall". Therefore, the boundary conditions of the individual measurements were varied as follows to check if the k_{f10}-values were stable:

- Variation of the hydraulic gradient to check for water flow between sanded plastic tube and grouting material.
- Variation by increasing and reducing the hydraulic gradient to determine storage effects.
- Variation of the experimental temperature to determine the temperature dependence of the method.

The evaluation of the variation showed that the results of the measurements were not affected by the experimental setup.

The determined values of the system permeabilities of unstressed system samples showed considerable differences between the four system samples, which correlates with the material samples examined in the preliminary tests. It was possible to quantify how the inclusion in a BHE system as well as freeze-thaw cycle stress affects the k_{f10}-value and contribute to an increase in the systems' vertical hydraulic conductivity. In the case of the freeze-thaw cycles, the first thermal stress causes the greatest influence. Figure 3 shows this increase in permeability by comparing the unstressed sample permeability with the results after freeze-thaw cycle for one of the four system samples.

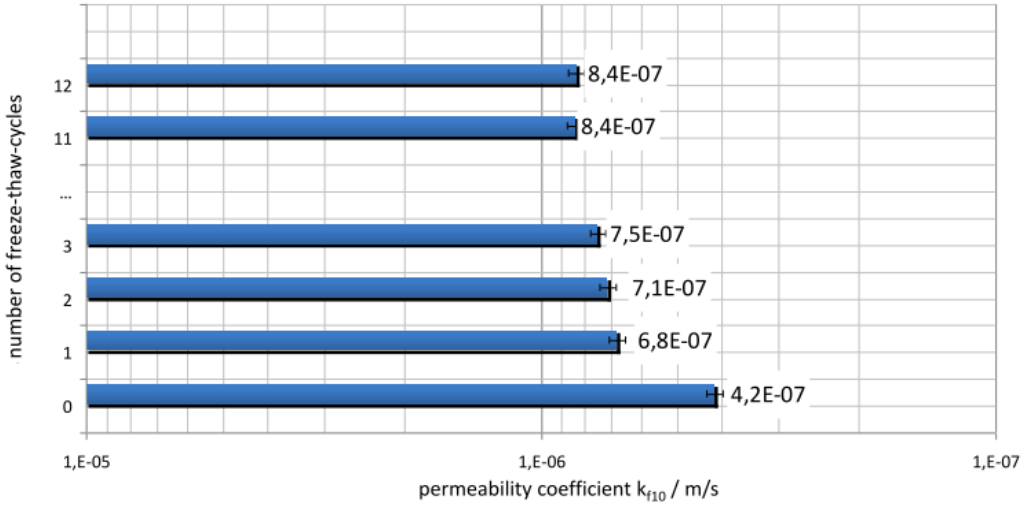

Figure 3 Vertical hydraulic conductivity of system sample B before and after freeze-thaw cycle stress. The first cycle caused the most significant increase in permeability.

The comparison with the reference measurements of the preliminary tests with grouting material samples showed that the k_{f10}-values of the system samples were about 2 orders of magnitude above the values of the pure material samples (see Figure 4). The first freezing cycle had the second largest influence, the remaining freezing cycles were the third largest influence. For all materials, the first 11 freeze cycles led to a degradation of approximately 0.5 to 1 order of magnitude. In contrast, the system samples showed individual regeneration behavior, so that the sum of the effects at the end of the experiment came to 2.5 to 3 orders of magnitude. Figure 4 shows this relation for four grouting materials. The temporal relations must be considered as follows: the age of the material samples corresponds to about 2 months. The measured values of the system samples, expressed as mean values, correspond to an age of 3 to 5 months for the undisturbed system samples and about 4 to 9 months after 11 freeze-thaw cycles. Higher sample age generally leads to lower permeability.

After the measurements, the system samples were removed from the pressure vessel and sliced. Significant visible changes in the structure or detachment of the HEPs from the grouting material could not be verified. Air holes in the backfill material and accumulations below spacers were observed but did not result in a continuous porous matrix.

The sanded layer on the inside of the plastic tube, which was supposed to prevent water flow between the grouting material and plastic tube, was fully intact. In system sample C and D a dye tracer was used and was mainly detectable in the very direct vicinity of the layer around the U-bend it was deposited in. For the area in which dye tracks could be found, coloration occurred mainly at the transition between the grouting material and the HEPs.

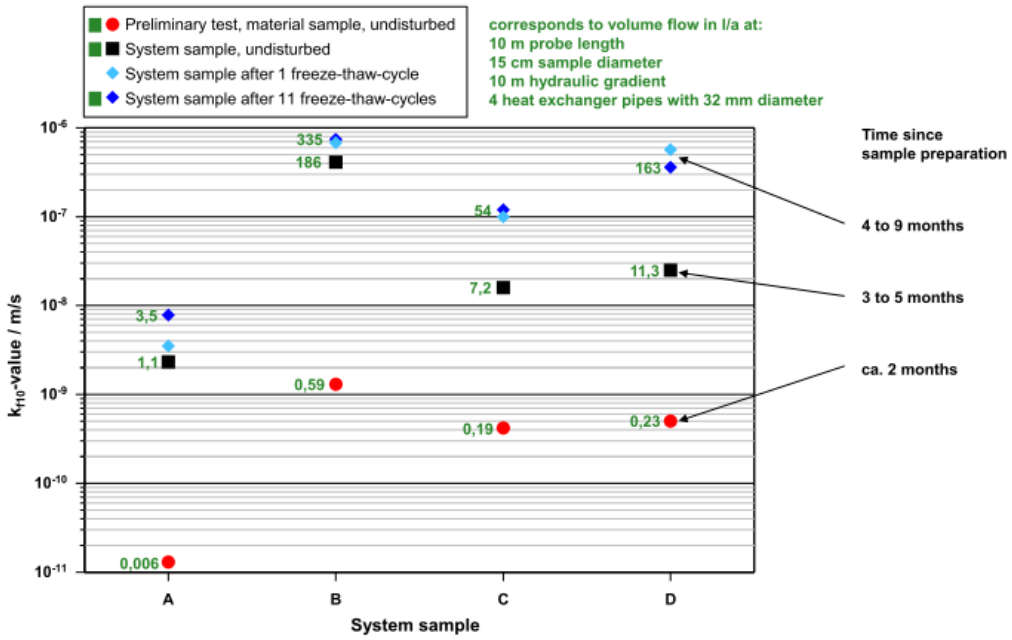

Figure 4 Comparison between the results from four system samples in the large-scale test rig and the material samples of the preliminary tests. The mean values of the system samples show markedly increased permeability, which is further increased by freeze-thaw cycle stress. The first freeze-thaw cycle generally caused an increase, the value stabilizes during the following cycles and was partially compensated, in particular for sample D, by regeneration effects. The green figures represent the water flow in a hypothetical 10 m sample with 15 cm diameter and hydraulic gradient of 10 m. This is a realistic example for a geological barrier layer at an in-situ BHE.

DOWNSCALED TEST RIG

The aim of this rig is to develop a test method which combines the advantages of the known approaches. For example, the geometry and installation conditions of a BHE are to be reproduced in a realistic manner. The borehole diameter and HEPs, including internal installations such as a grouting hose and spacers, need to correspond to the condition in an in-situ BHE. The operational conditions, especially the depth of the borehole, have to be represented by a corresponding pressurization of the entire test rig. Also, the backfilling procedure for producing a sample is the same as for a real BHE. The sample length, however, is chosen to allow for an acceptable duration of the measurements and easier handling of the samples.

Requirements definition

The following is a list of the essential requirements which resulted from considering the known methods.

- A membrane (e.g. made of latex) should be used analogously to the triaxial cells according to DIN 18130-1 (DIN 18130-1, 1998) to avoid water flow around the test specimens.
- The size of the test rig should allow for the installation of system samples with a length of up to 1000 mm.
- The installation of system samples with a diameter of 150 mm and four HEPs with a diameter of 32 mm each or samples with a diameter of 100 mm and one HEP with a diameter of 40 mm should both be possible.
- The test rig should withstand saturation pressures of up to 9 bar.

- For visual evaluation of the freeze-thaw cycle and the condition of the latex membrane, the pressure vessel should be transparent or partly transparent
- Freeze-thaw cycle stress should be achievable without the test specimen being depressurized or removed from the test rig.
- The freeze-thaw cycle stress of the system sample should take place from the center to the outside.
- The system samples should be produced in a realistic manner using the tremie method
- Optionally, the system sample can be radially clamped to prevent expansion during the freeze-thaw cycle.

Based on these requirements, the following concept was developed for measuring the vertical hydraulic conductivity of BHES samples.

Concept for the downscaled test rig

The new test rig is based on the model of a triaxial cell according to DIN 18130-1 (DIN 18130-1, 1998). All the above listed requirements are met. Especially the rig's ability to hold various types of samples should be emphasized. The length of the system samples can be up to one meter. With a simple modification of the test rig, samples of 150 mm or 100 mm diameter can be used. Optionally, other sample sockets can be designed to fit various sample diameters and HEP configurations.

The partly transparent pressure vessel shown in Figure 5 allows for observation of the freeze-thaw cycle stress as well as the entire testing procedure. This is useful, for example, to monitor the state of the latex membrane.

Compared to the large-scale test rig, the downscaled one has the important advantage of shorter sample sizes, which facilitates test execution. For example, the test specimens are easier to handle and the test duration is significantly shortened.

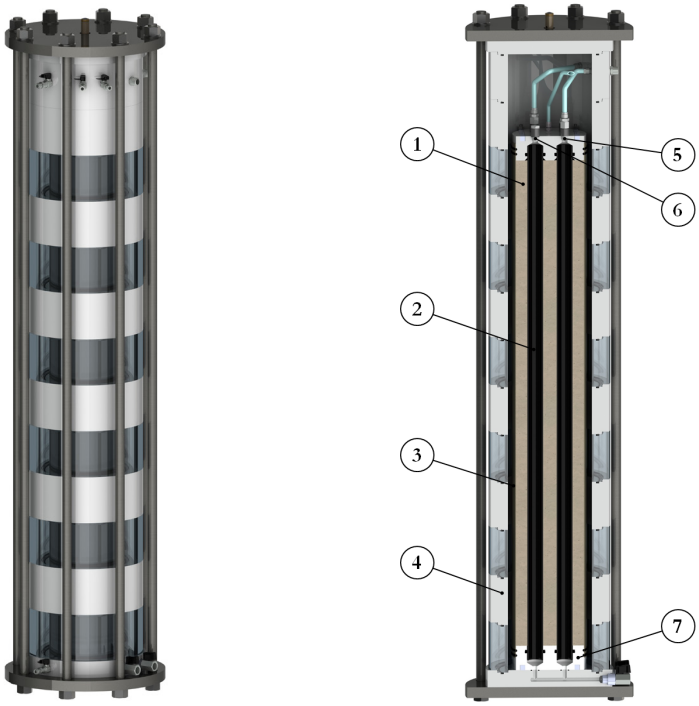

Figure 5 Concept for the downscaled test rig in isometric view (left) and sectional view (right). 1) grouting material, 2) heat exchanger pipes, 3) latex membrane, 4) pressure vessel wall, 5) fluid circulation inlet, 6) fluid circuit outlet and 7) sample socket. The vessel wall is made of alternatingly transparent and opaque rings due to cost and production process.

The possibility to vary sample length, sample cross section, number and diameter of the HEPs allows for free dimensioning of the sample. The experimental concept allows for experiments to be carried out to find the optimal experimental setup for a suitable material testing method for BHES. For example, experimental investigation on whether a simplified sample geometry is comparable to that of an in-situ installed double-U-pipe. Also, an experimental determination which minimal sample length is possible without reducing the significance of the k_f-value measurements.

By choosing different saturation pressures, optimized saturation can be achieved and different depth positions of the BHE can be simulated. In addition, the separation of the inlet and the outlet of the sample fluid circuit can be used to realize a depth dependent, horizontal temperature gradient by means of a corresponding external interconnection. For example, it would be feasible for the inlet of the system sample to exhibit a temperature difference of 5 K to the outlet.

CONCLUSION

The previous examination of industrially produced grouting materials has proven that the vertical hydraulic system conductivity increases after freeze-thaw cycle stress at -6 °C. However, even after several cycles the increase of the k_f-values is in the range of one order of magnitude, which is acceptable. It must yet be considered that the permeability of the grouting material always needs to be adjusted to the individual permeability of the geological surroundings of the borehole. The difference of the k_f-values of three orders of magnitude between the system samples and material samples shows an obvious restriction and applies only to the type of system tested here using PE100-pipes. Therefore, each material must be evaluated individually since general derivations cannot be applied to individual materials.

Another challenge is to cover a wide measuring range from 10^{-5} m/s to 10^{-11} m/s for the k_{f10}-values. For this purpose, high measurement accuracy and reproducibility of the results were achieved by optimizing the temperature stability of the test rig. The experimental setup is very complex and time-consuming. For example, the evaluation (incl. freeze-thaw cycles) of a single system sample takes at least 2 months.

Moreover, it has been found that an extremely careful execution of the experimental procedure and precisely controlled boundary conditions are crucial to achieve the necessary high measuring accuracy.

Consequently, the Bavarian Center for Applied Energy Research is building a smaller scaled test rig in a running project, which brings together the advantages of the previously known methods in one test rig. Due to the possibility of variable sample dimensions, the method is not restricted by predetermined scaling conditions of the test rig.

At the time of submission of these proceedings, the experimental setup is in the detail-planning phase and some parts have already been constructed. By the time of the presentation at the IGSHPA Research Track, the construction of the test rig will have been finalised and the first downscaled system sample will have been installed.

ACKNOWLEDGMENTS

We would like to thank the German Federal Ministry for Economic Affairs and Energy for granting the two projects (Grant Numbers: 0327453A and 03ET1386A).

REFERENCES

Anbergen, H., Frank, J., Müller, L. and Sass, I. 2014a. *Freeze-Thaw-Cycles on Borehole Heat Exchanger Grouts: Impact on the Hydraulic Properties*, Geotechnical Testing Journal, Vol 37, Num. 4, 2014.

Anbergen, H., Frank, J., Reuß, M., Kuckelkorn, J. M., Müller, L. and Sass, I. 2015. *Hydraulische Integrität des Systems Erdwärmesonde.* bbr – Fachmagazin für Brunnen- und Leitungsbau, 02-2015: 34-41.

Anbergen, H., Frank, J. and Sass, I. 2012. *Quality assurance of grouting for Borehole Heat Exchangers*. The 12th International Conference on Energy Storage, Innostock 2012. Lleida, Spain.

Anbergen, H., and Sass, I. 2013. *Freeze-thaw-behaviour: Observations in Grouted BHES*. Thirty-Eighth Workshop on Geothermal Reservoir Engineering, Stanford University. Stanford, California.

Anbergen, H., Reuß, M., Kuckelkorn, J. M., Frank, J., Müller, L. and Sass, I. 2014b. *Hydraulische Integrität des Systems Erdwärmesonde*. Der Geothermiekongress 2014. Essen, Germany.

DIN 18130-1. 1998. *Baugrund – Untersuchung von Bodenproben; Bestimmung des Wasserdurchlässigkeitsbeiwertes – Teil 1: Laborversuche*. Berlin: Deutsches Institut für Normung e. V. [PP], Beuth Verlag.

Hölting, B. and Coldewey, G. 2008. *Hydrogeologie: Einführung in die Allgemeine und Angewandte Hydrogeologie*. Heidelberg, Germany: Spektrum Akademischer Verlag.

Kirschbaum, A., Kuckelkorn, J. M. and Hagel, K. 2017. *Konzept für einen Versuchsaufbau zur Messung der hydraulischen Systemdichtheit von Erdwärmesonden*. Der Geothermiekongress 2017. Munich, Germany.

Kuckelkorn, J. M. 2013. *Systemdichtheit von Verfüllbaustoffen*. 12. Internationales Anwenderforum Oberflächennahe Geothermie, OTTI. Regensburg, Germany.

Kuckelkorn, J. M., Biank M. and Reuß, M. 2010. *Großversuchsstand zur Bestimmung der hydraulischen Durchlässigkeit von Erdwärmesonden-Systemen*. 10. Internationales Anwenderforum Oberflächennahe Geothermie, OTTI. Regensburg, Germany.

Kuckelkorn, J. M. and Reuß, M. 2010. *Untersuchung der hydraulischen Durchlässigkeit von Erdwärmesonden-Systemen*. Der Geothermiekongress 2010. Karlsruhe, Germany.

Kuckelkorn, J. M. and Reuß, M. 2012. *Methodik und Ergebnisse zur hydraulischen Durchlässigkeit von Verfüllbaustoffen bei Erdwärmesonden - Bestimmung des kf-Wertes und Alterung von Erdwärmesonden-Systemen in einem Großversuchsstand*. 3. VDI-Fachkonferenz Wärmepumpen, VDI Wissensforum GmbH. Düsseldorf, Germany.

Reuß, M., Koenigsdorff, R., Zorn, R., Kuckelkorn, J., Steger, H., Pröll, M. and Feuerstein, P. 2012. *Final Report, Qualitätssicherung bei Erdwärmesonden und Erdreichkollektoren. Bundesministerium für Wirtschaft und Technologie* (Grant Number 0327453A).

VDI 4640 – Blatt 2 2015. *Thermische Nutzung des Untergrundes – Erdgekoppelte Wärmepumpenanlagen* (Entwurf). Berlin: Verein Deutscher Ingenieure (PP), Beuth Verlag.

[This page has been intentionally left blank]

IGSHPA SWEDEN
2018 Research Conference

DOI: 10.22488/okstate.18.000042

Impacts of injection temperature on the relevant heat transport processes in groundwater heat pump (GWHP) systems

Byeong-Hak Park **Kang-Kun Lee***

ABSTRACT

In many hydrogeological applications, the influence of temperature on fluid density and viscosity have often been neglected. However, high contrasts in temperature which occurs in the field applications such as groundwater heat pump (GWHP) systems, can make the effects of variable density and viscosity on flow and transport significant. A theoretical study suggests that free convection occurs in an infinitely extensive horizontal layer when the Rayleigh number exceeds about 40. Experimental investigations are still lacking on the conditions where the influence of temperature can be important.

In this study, a laboratory experimental system was developed to investigate the impacts of injection temperature on the relevant heat transport processes. First of all, the experiments such as sieve analysis and constant-head permeability test were performed to estimate the physical properties of the saturated porous medium. Laboratory tracer tests using a resistor as a heat source were conducted with/without background flow conditions to derive the thermal properties of the medium. Lastly, tracer tests using injected water with different temperatures were performed to identify the certain conditions where the variations in fluid density and viscosity play an important role in the subsurface flow and transport.

INTRODUCTION

In many hydrogeological applications, the temperature dependency of fluid properties is often assumed to be negligible. However, high temperature difference which occurs in the field applications such as groundwater heat pump (GWHP) systems, can make the effects of variable density and viscosity on flow and transport significant. A theoretical study suggests that free convection occurs in an infinitely extensive horizontal layer when the Rayleigh number exceeds about 40 (Domenico and Schwartz, 1998). Experimental investigations are still lacking on the threshold conditions where the influence of temperature should be considered.

In this study, a laboratory experimental system which can simulate the subsurface flow and heat transport was designed to examine the impacts of injection temperature on thermal plume propagation. First of all, preexperiments were performed to estimate the physical properties of the saturated porous medium. Heat tracer tests using a resistor were conducted at various background flow velocities to derive the thermal properties of the medium. Lastly, heat tracer tests using injected water with different temperatures were performed to identify the certain conditions where the variations in fluid density and viscosity play an important role in the subsurface flow and transport.

Methodology

Experimental design. The experimental system mainly consists of the acrylic glass tank filled with fully-saturated sand. The size of the sand tank is 1.3 m × 0.6 m × 0.8 m (L × W × H) and the tank is devided into three

School of Earth and Environmental Sciences, Seoul National University, Seoul 08826, Rep. of Korea
*Corresponding author. Tel.: +82-2-880-8161
E-mail addresses: pbh3000@snu.ac.kr (B. Park), kklee@snu.ac.kr (K. Lee)

chambers: two constant-head chambers on both sides and one chamber in the middle filled with sand (see Fig. 1). By changing the water level at constant-head chambers, background flow rate was adjusted in the experiments. Figure 1b shows the location of heat sources and temperature sensors installed in the middle chamber. Two different heat sources of a resistor and injected water were used as a heat tracer. In a case of heat tracer tests using injected water, hot water in a thermostatic barrel was injected by a peristaltic pump into an injection well inside the middle chamber. Temperature change was detected by RTD sensors and logged in a data aquisition system developed in the LabVIEW 2009 programming environment.

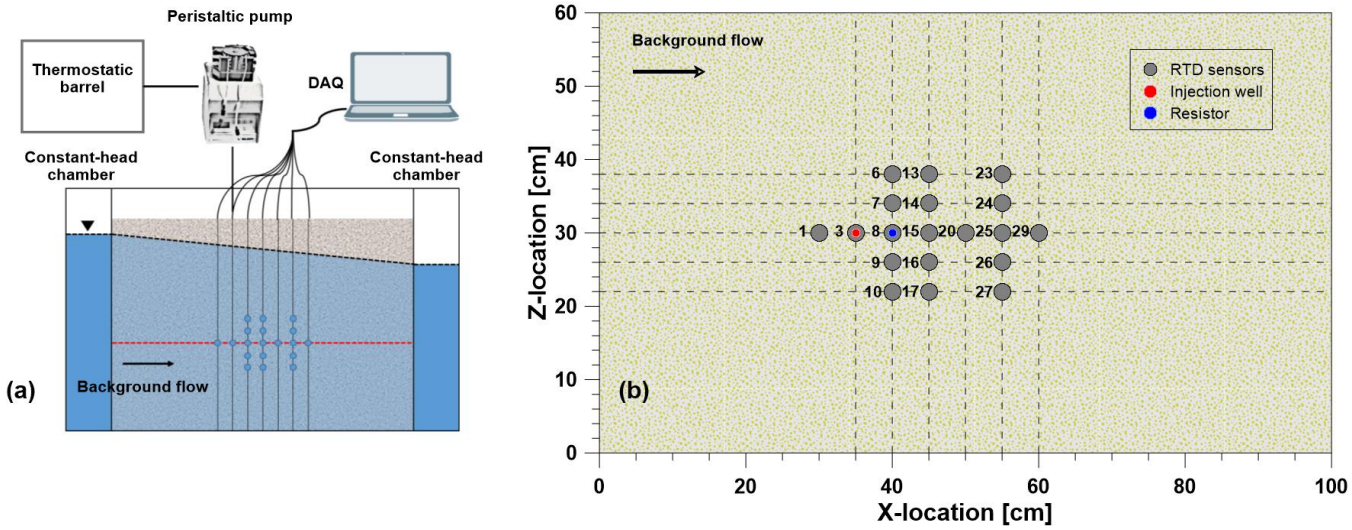

Figure 1 (a) Schematic diagram of a laboratory experimental system and (b) location of heat sources and RTD sensors.

Properties of porous medium. Before heat tracer tests were conducted, preexperiments were performed to estimate the physical properties of sand. Sieve analysis were performed to evaluate the mean grain size and uniformity of the porous medium. The analysis results showed that the mean diameter of the sand is 0.52 mm and its uniformity is 1.41, indicating relatively homogeneous material. The porosity of the sand was determined to be about 0.3306 by measuring the moisture contents in the experimental setup. Static permeability tests were repeatedly conducted with different hydraulic gradients. The linear regression method was applied to the measured hydraulic gradients and specific discharges, and hydraulic conductivity of the sand was estimated to be 2.041×10^{3} m/s with high R^2 value over 0.9981. The estimated properties of the sand are listed in Table 1.

Table 1. Hydrogeologic and thermal properties of sand

Properties	Unit	Value (m ± σ)	Source/comment
Mean grain size (d_{50})	mm	0.52 ± 0.01	Sieve analysis
Uniformity (U)	–	1.41 ± 0.01	Sieve analysis
Porosity (n)	–	0.3306	Moisture content
Hydraulic conductivity (K)	10^{-3} m/s	2.041	Permeability test
Thermal conductivity of sand	W/m-K	3.383 ± 0.204	Resistor test
Vol. heat capacity of sand	10^{6} J/m^{3}-K	2.078 ± 0.081	Resistor test

Laboratory heat tracer test. In this study, two different heat sources of a resistor and injected water were used as a thermal tracer to investigate the effect of injection temperature on thermal plume propagration in the subsurface. First, heat tracer tests using a resistor were performed with a constant heat source of 4.517 W without background flow to estimate the thermal conductivity and volumetric heat capacity of the porous medium. Then, heat tracer tests using a resistor were conducted at various background flow rates ranging from 5.301×10^{-5} to 1.448×10^{-4} m/s. Lastly, hot water 5–15K higher than background water was injected into the porous medium with an injection rate of about 100 ml/min.

The observed temperature breakthrough curves were analyzed by a curve-fitting procedure with analytical models. The resistor tests under no-flow condition were analyzed by a continuous point source (CPS) model expressed in Equation 1 (Carslaw and Jaeger, 1959; Stauffer et al., 2013) and thermal properties of the sand were evaluated. Equation 2, called a moving continous point source (MCPS) model, was used to interpret the resistor tests with various background flow rates (Carslaw and Jaeger, 1959; Rau et al., 2012), and thermal dispersion coefficients and thermal front velocities were derived from the analysis results. Equation 2 was also applied to the thermal breakthrough curves obtaind from injection tests. In the analysis, the quality of fit was assessed by the root mean square error (RMSE) value (Equation 3), and thermal properties were determined from the best-fitted model minimizing the RMSE value. More details on the parameter estimation procedure can be found in the recent literature (Park et al., 2018). To quantify a transport regime, the thermal peclet number, characterizing the relative contribution of convective and conductive heat transport, was defined as in Equation 4 (de Marsily, 1986; Anderson, 2005; Rau et al., 2014).

$$T(x,y,z,t) = T_0 + \frac{Q}{4\pi\lambda R'} erfc\left(\frac{R'}{\sqrt{4D^t t}}\right) \qquad (1)$$

$$T(x,y,z,t) = T_0 + \frac{Q}{8\pi D_T^t \rho c R} \exp\left(\frac{xv^t}{2D_L^t}\right) \cdot \left[\exp\left(-\frac{Rv^t}{2D_L^t}\right) erfc\left(\frac{R - v^t t}{2\sqrt{D_L^t t}}\right) + \exp\left(\frac{Rv^t}{2D_L^t}\right) erfc\left(\frac{R + v^t t}{2\sqrt{D_L^t t}}\right) \right] \qquad (2)$$

$$RMSE = \sqrt{\sum_{i=1}^{n} \frac{(T_{o,i} - T_{m,i})^2}{n}} \qquad (3)$$

$$Pe^t = \frac{\rho_w c_w q d_{50}}{\lambda} \qquad (4)$$

RESULTS

Figure 2 shows the thermal breakthrough curves observed at center and off-center locations (cross symbol) and the CPS model results (solid lines). As can be seen in Figure 2, the best-fitted model agrees very well with the oberved temperature data (RMSE < 0.007 K). From the best fit between the observations and modeling results, the thermal conductivity and volumetric heat capacity of sand were estimated to be 3.185–3.878 W/m-K and 1.770–2.190 MJ/m^3-K, respectively. Based on the estimated thermal properties, resistor tests performed at various background flow rates were analyzed with the MCPS model.

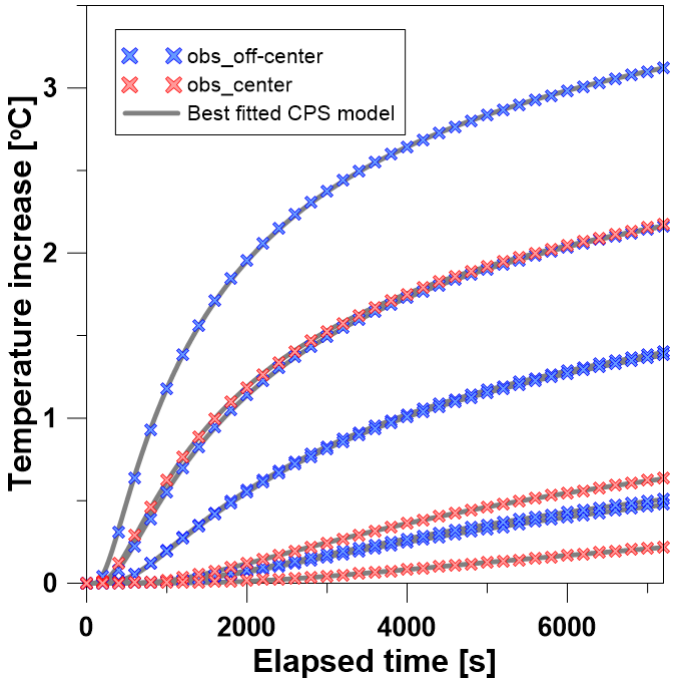

Figure 2 Thermal breakthrough curves observed at center and off-center locations (cross symbol) and best-fitted CPS models.

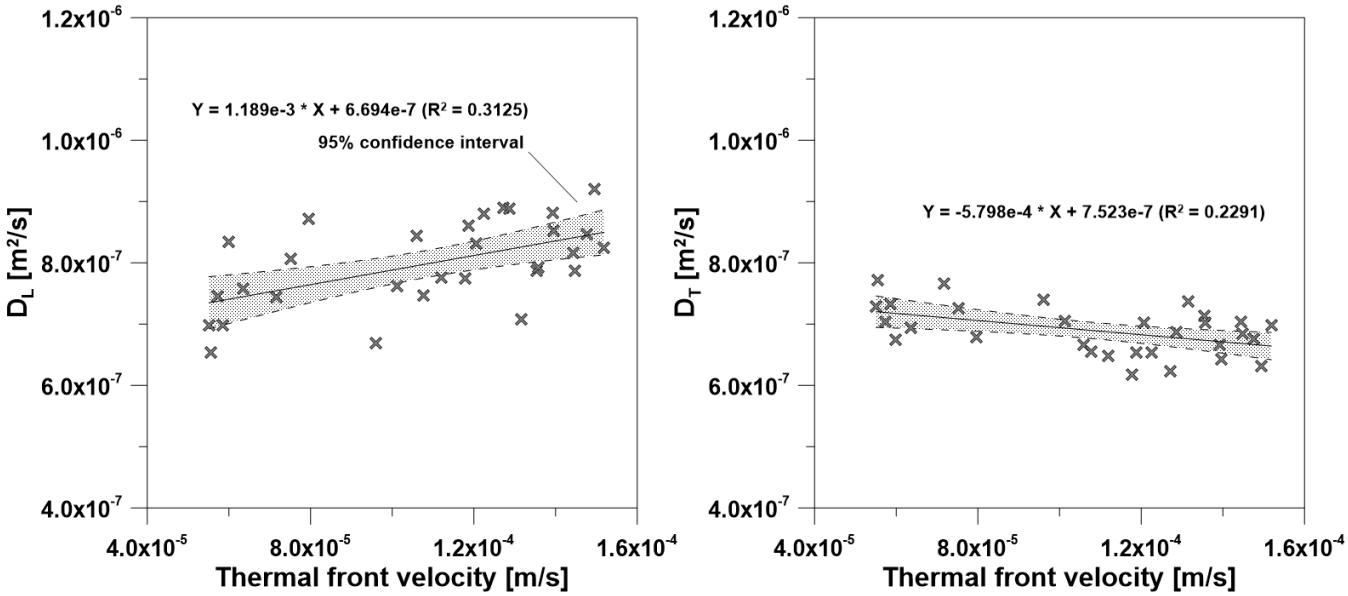

Figure 3 Relationships between the thermal dispersion coefficients and thermal front velocities: (a) longitudinal and (b) transverse directions.

Figure 3 describes the relationships between the thermal dispersion coefficients and thermal front velocities derived from the best-fitted MCPS model. The results showed that the longitudinal thermal dispersion coefficients increase with flow velocity, while the transverse thermal dispersion coefficients decrease with flow velocity. However, there were a lot of scatter in the relations with low R^2 values of 0.3125 (longitudinal) and 0.2291 (transverse). Such scatter can be partly caused by low flow velocities as explained in previous studies (Yuan et al., 1991; Rau et al., 2012). Although we tried to increase hydraulic gradient, it was found that thermal peclet numbers (Pe^t) for all the tests are less than 0.2. In the conduction dominant regime ($Pe^t < 1$), the effective thermal diffusivity is the dominant part of the thermal dispersion coefficient, and the contribution of flow velocity to that is very small (Yuan et al., 1991).

Injection tests were also analyzed by the MCPS model in Equation 2. Figure 4 describes the thermal front velocities estimated from the resistor (black cross) and injection (colored symbol) experiments at various background flow velocities. As shown in Figure 4, the estimated thermal front velocities from hot injection tests were higher than those from resistor tests. There can be two reasons for that. Even when the temperature difference is small ($\Delta T = 5$ K), the flow velocity was estimated to be faster. This indicates that injection increases the background flow velocity. When focusing on the injection tests results (colored symbols in Figure 4), themal front velocities have a higher value with increaing temperature. This is because hydraulic conductivity, which is a function of fluid density and viscosity, increases with temperature.

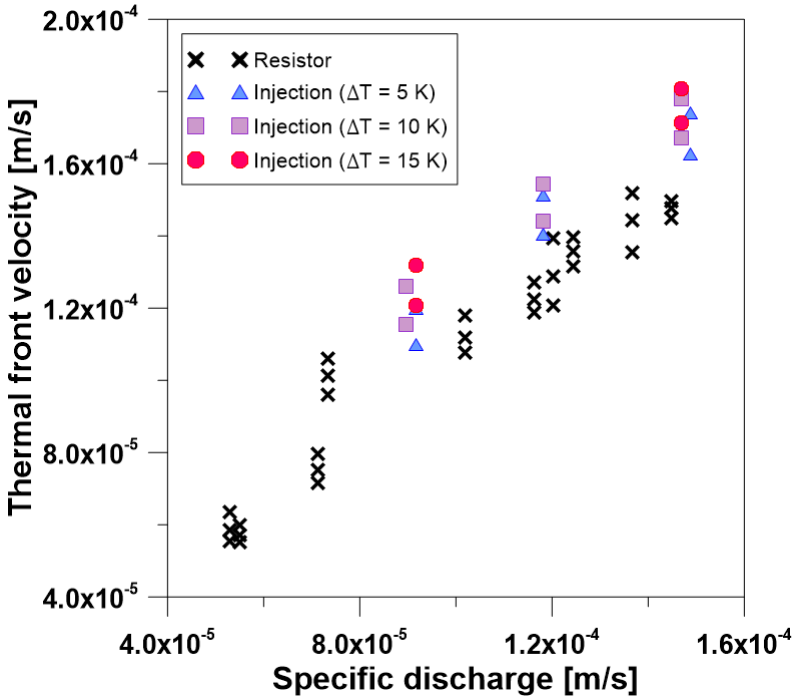

Figure 4 Thermal front velocities estimated from the resistor (black cross) and injection (colored symbol) experiments at various background flow velocities.

CONCLUSION

In this study, the laboratory experimental system was developed to investigate the effect of the temperature dependency of fluid properties on the relevant heat transport processes in GWHP systems. First, preexperiments were conducted to estimate the physical properties of the porous medium. Then, heat tracer tests using two different heat sources of a resistor and hot water were performed to estimate the thermal properties of the sand and to examine the influence of injected hot water on thermal plume propagation. The observed thermal breakthrough curves were repeatedly analyzed by the analytical (CPS and MCPS) models in Equation 1 and 2. The analysis results of resistor tests showed that the thermal dispersion coefficient has an unclear tendency with low R^2 values (< 0.32) and a lot of scatter. This is because heat tracer tests in this study was conducted in conduction dominated regime (Pe^t < 0.2) despite the effort to increase the hydraulic gradient. The thermal front velocities analyzed from injection tests suggest the effect of the injection and temperature difference on the thermal plume propagation. Further experimental and numerical study will be performed to investigate the vertical impacts as well as horizontal effects of variable fluid properties.

ACKNOWLEDGMENTS

This work was supported by the National Research Foundation of Korea (NRF) grant funded by the Korea government (MSIP) (No. 2017R1A2B3002119).

NOMENCLATURE

σ = standard deviation
λ = thermal conductivity (m^2/s)
ρc = volumetric heat capacity (J/m^3-K)
D = dispersion coefficient (m^2/s)
d_{50} = mean grain size (m)
K = hydraulic conductivity (m/s)
m = mean value
n = porosity (-)
Pe^t = thermal Peclet number (-)
Q = heat source strength (W)
q = specific discharge (m/s)
R = $\sqrt{x^2 + \frac{D_L^t}{D_T^t}(y^2 + z^2)}$ (m)
R' = $\sqrt{x^2 + y^2 + z^2}$ (m)
v^t = thermal front velocity (m/s)
T = temperature of the porous medium (°C)
T_o = initial temperature of the porous medium (°C)
t = time (s)
U = Uniformity indicating a measure of homogeneity (-)

Supscripts

t = thermal

Subscripts

L = longitudinal
T = transverse
m = modeling result
o = observation
s = solid property
w = water property

REFERENCES

Carslaw, H.S., and Jaeger, J.C. 1959. Conduction of heat in solids. NY: Oxford University Press.

Domenico, P. A., and Schwartz, F. W. 1998. Physical and chemical hydrogeology. New York: Wiley.

Park, B. H., Lee, B. H., and Lee, K. K. 2018. *Experimental investigation of the thermal dispersion coefficient under forced groundwater flow for designing an optimal groundwater heat pump (GWHP) system*. Journal of Hydrology. 562: 385-396.

Rau, G.C., Andersen, M.S., and Acworth, R.I. 2012. *Experimental investigation of the thermal dispersivity term and its significance in the heat transport equation for flow in sediments*. Water Resources Research. 48: W03511.

Stauffer, F., Bayer, P., Blum, P., Molina-Giraldo, N., and Kinzelbach, W. 2013. Thermal use of shallow groundwater. CRC Press.

Yuan, Z.G., Somerton, W.H., and Udell, K.S. 1991. *Thermal dispersion in thick-walled tubes as a model of porous media*. International journal of heat and mass transfer. 34(11): 2715-2726.

[This page has been intentionally left blank]

IGSHPA SWEDEN 2018 Research Conference

DOI: 10.22488/okstate.18.000019

Thermal influence of neighbouring GSHP installations: relevance of heat load temporal resolution

Maria Letizia Fascì **Alberto Lazzarotto** **José Acuña** **Joachim Claesson**

ABSTRACT

In densely populated areas where many ground source heat pump (GSHP) systems are present, it becomes important to consider the thermal influence of neighbouring GSHP installations while designing these systems. This question has started to become frequent in cities like Stockholm in Sweden. For the design and performance analyses of the GSHP systems, simulations at different detail levels regarding time step are used. Borehole heat loads of real installations can be estimated with different time resolution from case to case. This article presents a first step towards the development of a model to calculate the mutual influence of neighbouring GSHP installations: a first elementary model is developed to quantify such influence, then the error introduced when performing simulations with different heat load steps, i.e. annual and hourly, is analyzed from a perspective of multiple neighbouring GSHP installations. It is found that a negligible error is derived when considering low temporal resolution data.

INTRODUCTION

Ground source heat pumps (GSHPs) are systems that can extract/reject heat from/to the underground to provide domestic heating/cooling and hot water. The extraction can occur in several ways, the most common way is using borehole heat exchangers (BHEs): vertical pipe loops buried in the ground through which a fluid is circulated (Lund and Boyd, 2016). GSHPs became popular in western countries after the oil crisis of the '70s thanks to their higher energy efficiency compared to boilers, most commonly used solution to provide heat at that time. The number of installed GSHP systems has increased since then (Sanner, 2016).

In Sweden around one fifth of the single-family buildings use a GSHP; most of them are single-family houses using the systems for heating and hot water (Gehlin and Andersson, 2016). Using the GSHP for heat extraction only leads to a successive depletion of the heat surrounding the borehole that can decrease the system performance and eventually influence the surrounding installations. The decrease of a system performance due to its own operation is already taken into account during the design phase of the system, but the effects on surrounding systems are not considered nowadays. This induced the Swedish authorities to set up rules to avoid thermal interaction among neighbouring systems. The general rule for single-family buildings recommends 20 m as minimum distance between 2 boreholes on neighbouring properties (SGU, 2016). Such distance may be enough to guarantee that two neighbouring BHEs do not influence each other significantly during the first 15 years of operation. For example, for a typical heat extraction BHE (see table 1) it was calculated that the temperature variation at 20 m from the borehole, after 15 years of operation, is around 0.3 °C, while the temperature variation at 0.1 m from the borehole is 3.2 °C. This means that the influence of a borehole on an identical neighbouring borehole distant 20 m is around 10% of the influence of the boreholes on itself.

Though the influence of a single borehole can be negligible at greater distances than 20 m, in dense ground source heat pump areas (DGSHPAs), here referred to as areas where several independent GSHPs are installed, their influences add up and may result in a non-negligible effect. Another factor that should be taken into account is that, although the lifetime of a heat pump is around 20 years, the lifetime of the borehole can be longer; there are areas in Stockholm were boreholes and heat pumps have been operating for more than 30 years already (SKVP 2017). Extending the operation

Maria Letizia Fascì (mlfasci@kth.se) is a PhD student, Alberto Lazzarotto and José Acuña are researchers, and Joachim Claesson is docent at Royal Institute of Technology (KTH).

time of a borehole where only heat extraction occurs means extending its radius of influence and the intensity of its influence: the temperature variation at 20 m due to the borehole of the previous example increases to around 0.4 °C after 30 years and around 0.5 °C after 100 years.

Table 1. Example of borehole and ground characteristics for a Swedish villa

Borehole properties		Ground properties			
Total annual borehole heat load ($HL_{b,a}$) [kWh/year]	Length [m]	Conductivity [W/m/K]	Density [kg/m^3]	Specific heat [J/kg/K]	Undisturbed temperature [°C]
10000	100	3,1	2300	870	8

Currently, several models, both commercial and developed by researchers, are available for estimating the temperature evolution at the borehole wall in a BHE field; a summary of the models is given by Yang, et al. (2010). However, the authors of this paper are aware of only one recent model specifically designed to take into account the presence of neighbouring GSHP installations and so to model DGSHPAs; the model is based on the infinite line source (Witte, 2018). It is therefore the goal of the authors to develop a complete model for DGSHPAs. The main difference between the dedicated models for BHE fields and the model that the authors want to develop is that, in the latter, the borehole operating conditions (i.e. secondary fluid temperature and flow rate) are independent. Therefore the designer of an individual borehole in a DGSHPA has little information about the operating conditions of the surrounding boreholes. Thus, the new model, in addition to solving the heat transfer problem, has to estimate the uncertainty on the solution due to the uncertainties on the input data: boreholes positions, loads, and ground thermal properties, among others.

Among the input data, the BHEs' loads is the most difficult information to accurately assess without a direct interaction with all the house owners. For the sake of use, the model should be able to provide this values given easily accessible information. Building loads, and consequently also BHE loads vary from year to year and are not constant throughout the year, but vary over the seasons and the hours of the day. The difficulty in estimating the heat load increases as the heat load resolution increases. It is easier to estimate the loads with yearly resolution. Besides, using coarser time resolutions decreases the computational time of the model. Several studies are available about the importance of the heat load resolution and the possibility to use aggregated loads to estimate the borehole wall temperature in borehole fields (Yavuzturk and Spitler, 1999, Bernier et al, 2004, Marcotte and Pasquier, 2008, Claesson and Javed, 2012). They show that it is important to know the recent BHE history with hourly resolution, but it is possible to aggregate the least recent history. Although it is known that the further from the borehole the coarser the load time resolution can be without significantly compromising the accuracy of the results, no study focused on quantifying the accuracy of annual load aggregation for distances higher than 20 m has been found.

This paper represents a first step towards the development of the aforementioned model. The work consisted in two parts: in the first part an elementary model to calculate thermal influence in densely populated areas was developed. The model was used to estimate the possible influence between boreholes in Stockholm. The second part consisted in the evaluation of the error in case of load aggregation for long distances (>20 m). The error was calculated for individual boreholes and DGSHPAs.

METHODOLOGY

Thermal influence in densely populated areas

The first part of the study consisted in calculating the thermal influence of neighbouring GSHP systems on a central borehole (CB) in a DGSHPA. Two borehole grids characterized by a minimum distance among the BHEs where considered: a square grid and a triangular grid. The triangular configuration is the one that maximizes the number of neighbouring boreholes within a certain radius and minimizes the borehole-to-borehole distances. Figure 1 shows an

example of the two possible configurations described.

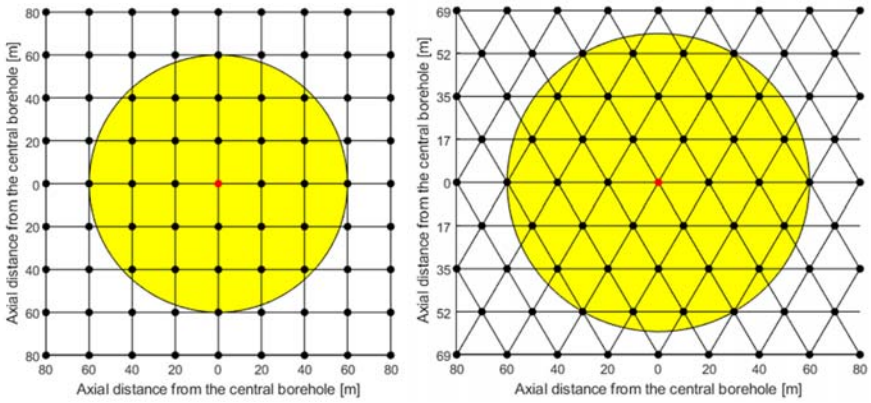

Figure 1 Borehole configurations: in each configuration the red dot is the influenced borehole, the black dots are the neighbouring boreholes. The boreholes in the yellow area are the ones influencing the central borehole after a certain period of operation.

All the boreholes in the grids were assumed to be equally deep and have the same annual heat load and profile. The region of influence, i.e. the region containing the BHEs influencing the central BHE was found iteratively: an initial radius of influence (RI) was set equal to 20 m, minimum distance among the boreholes. The number of BHE within the RI and their distances from the central borehole were calculated. The thermal response due to each single BHE after 100 years of operation at constant load was calculated. The results for all the boreholes were then superimposed; thus the thermal response due to all the surrounding BHEs was calculated. This was repeated for increasing radii of influence until the difference in the thermal response for two consecutive RIs was lower than 0.001 °C.

To calculate the thermal response due to each single borehole, the boreholes were considered as continuous line heat sources with uniform and constant heat flux in a semi-infinite, uniform, isotropic media with constant properties. The validity of the uniform heat flux assumption for the distances considered must be further investigated, as it might lead to an over- or underestimation of the boreholes influence. The validity of the constant heat flux assumption is showed later in this article. The boreholes and ground characteristics are described in table 1. The temperature evolution was then calculated using the finite line source model (Spitler and Bernier, 2016); the formulation given by Lamarche and Beauchamp (2007) was used for the calculation of the ground thermal response g.

For both configurations the thermal responses due to the boreholes within certain radii were calculated. The radius of influence after given operation times, the number of influencing boreholes and their effect on the central borehole are shown in the results section.

Errors due to load averaging

The second part of the study consisted in estimating the error on the thermal response calculation when the heat load time resolution used for the calculation was coarser than a reference calculation with a finer time heat load resolution. This was done for single boreholes first and then for DGSHPAs. To do so the temperature response due to a known hourly heat load (finest resolution) was calculated and compared with the results obtained using annual averaged heat loads.

To create an hourly load profile over a year, the total annual building heat load was divided into space heating and hot water loads. The values given by the Swedish Energy Agency for an average Swedish villa were used as reference, both for the total annual building heat load and the ratio between heating and hot water demand (Energimyndigheten 2017); the values used are shown in table 2.

The heating load was considered dependent on the ambient temperature. The ambient temperature considered was the one given for Stockholm by the Swedish meteorological and hydrogeological institute (SMHI 2017). Several

hourly profiles were created: for year 2010 to 2016. A base temperature of 15.5 °C was taken; the houses need mechanical heating when the ambient temperature falls below the base temperature (EEA, 2017). The heating load was considered 0 during the hours when the ambient temperature was higher than the base temperature, calculated as follows otherwise:

$$HL_{h,j} = HL_{h,a} \cdot \frac{T_{base} - T_{amb,j}}{\sum_{j=1}^{8760} T_{base} - T_{amb,j}} \tag{2}$$

where the sum at the denominator of the formula only considers the positive differences between the base and ambient temperatures. The hot water profile was considered the same for every day of the year, the hourly profile over the day was chosen among the ones in the literature (Ulseth, et al. 2017). The hourly loads were then calculated for every hour of the year as the sum of heating and hot water hourly loads. The total annual heat load was assumed constant from year to year and the load profile being the same every year. The temperature trend along the influenced borehole wall was calculated for 100 years of operation.

Table 2. Heat loads for a typical Swedish villa

Total annual building heat load ($HL_{h,a}$) [kWh]	Heating load [% of the total load]	Hot water load [% of the total load]
15000	86	14

The borehole load was calculated from the house load assuming that the COP of the HP was constant and equal to 3 (Energimyndigheten 2017); it was calculated as follows:

$$HL_b = HL_h \frac{COP - 1}{COP} \tag{3}$$

The thermal response from constant heat load was calculated as described in the previous section. The superposition method (Spitler and Bernier, 2016), without load aggregation, was used to calculate the response from non-constant heat loads:

$$T_b(t_n) - T_0 = \sum_{i=1}^{n} \frac{q_i - q_{i-1}}{2\pi k} g(t_n - t_i, H, d, \alpha) \tag{4}$$

Several borehole distances and lengths were considered. The results obtained using the hourly profile were compared with the ones obtained with yearly profiles.

The borehole grids described in the previous paragraph were then considered. The results obtained for single boreholes suggested that the error is not strongly dependent on the boreholes length (figure 5), therefore only grids of 100 m long boreholes were considered for DGSHPAs. The thermal response on the central borehole was calculated considering both yearly and hourly resolution heat loads in the surrounding boreholes. The errors associated to coarse load resolutions were calculated as previously done for individual boreholes.

RESULTS AND DISCUSSION

Thermal influence in densely populated areas

The radii of influence after 15, 30, 50 and 100 years of operation were calculated as discussed in the methodology section. The boreholes and ground properties are shown in table 1. The results are shown in table 3. It should be considered that table 3 shows the results of the algorithm discussed in the methodology and not empirical results.

Table 3. Influencing radii for several operational times.

Years of operation	15	30	50	100
Radius of influence [m]	140	180	220	300

Figure 2 shows that considering an RI of 80, 100 or 300 m after 15 years of operation does not lead to any significant difference in the results; while table 3 shows that the RI suggested by the algorithm used is 140 m. The algorithm used is then very conservative and can be improved so to decrease the computational time of the simulation without losing significantly in accuracy.

The number of boreholes within certain radii is shown below for the square and triangular grids.

Table 4. Number of boreholes in square and triangular grid

Radius [m]	20	40	60	80	100	150	200	250	300	
Boreholes within the radius	4	12	28	48	80	176	316	488	708	Square grid
	6	18	36	60	90	198	366	570	720	Triangular grid

The thermal responses of the central borehole of square and triangular grids were calculated over 100 years of operation. The responses accounting for all influencing boreholes within certain radii are shown below.

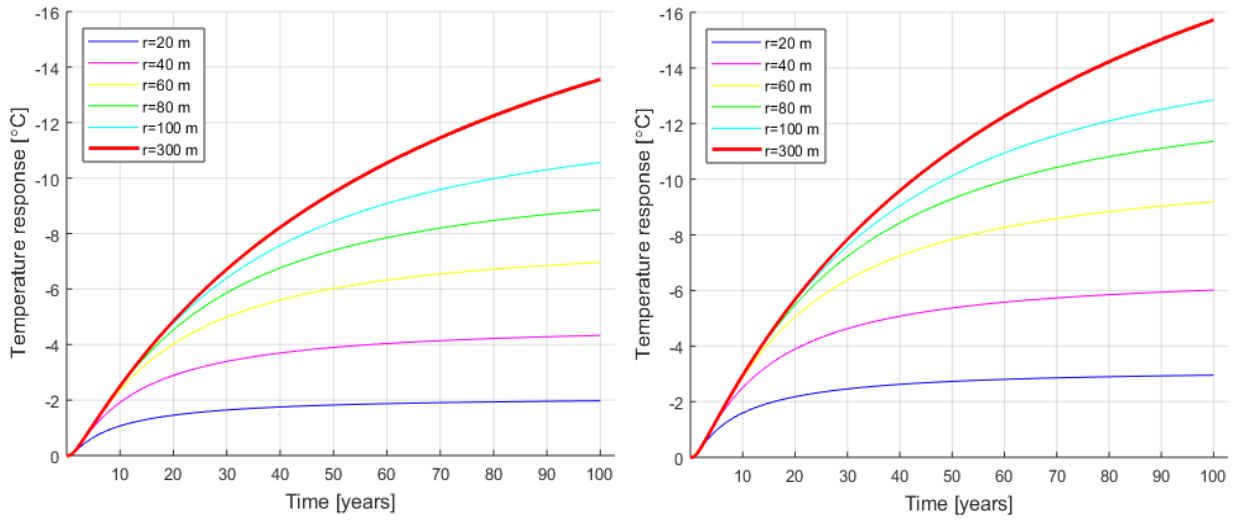

Figure 2 Thermal response of the central borehole of a square grid (left) and triangular grid (right).

As expected, in case of triangular grid the temperature response is more significant; in particular, after 100 years of operation the temperature decrease in a square grid is 14 °C, in a triangular one it is 16 °C. Figure 2 also shows that already after 15 years of operation the thermal response of the central borehole is around 4 °C, therefore not negligible.

It is clear that under the conditions considered in this study, the exploitation of the underground heat cannot be considered sustainable. These results are however insufficient for strong conclusions as many phenomena occurring in the ground were not considered: heat conduction was the only heat transfer type considered, the ground properties

were not considered temperature dependent, and the surface boundary condition set was uniform with constant temperature equal to the initial underground temperature. Besides phase change was not taken into account; considering it could change the results as the undisturbed ground temperature in Stockholm is around 8 °C, lower than the calculated temperature decrease. However ground freezing is not recommended, therefore rather than creating a model able to account it, the neighbouring systems should be designed to avoid it.

Errors due to load averaging

In the calculation of the error due to load approximation, the results obtained do not differ significantly depending on the hourly profile considered. The results obtained with the hourly profile for year 2011 are shown, as the errors obtained using this profile are slightly higher than in all the other cases and therefore lead to the most conservative conclusions.

Figure 3 shows on the left the thermal influence of a 100 m-deep borehole at 20 m distance. The annual heat load on the borehole is 10 MWh. The results obtained using both hourly and yearly resolution are shown. The two curves match very well. The absolute difference between them is shown in the graph on the right.

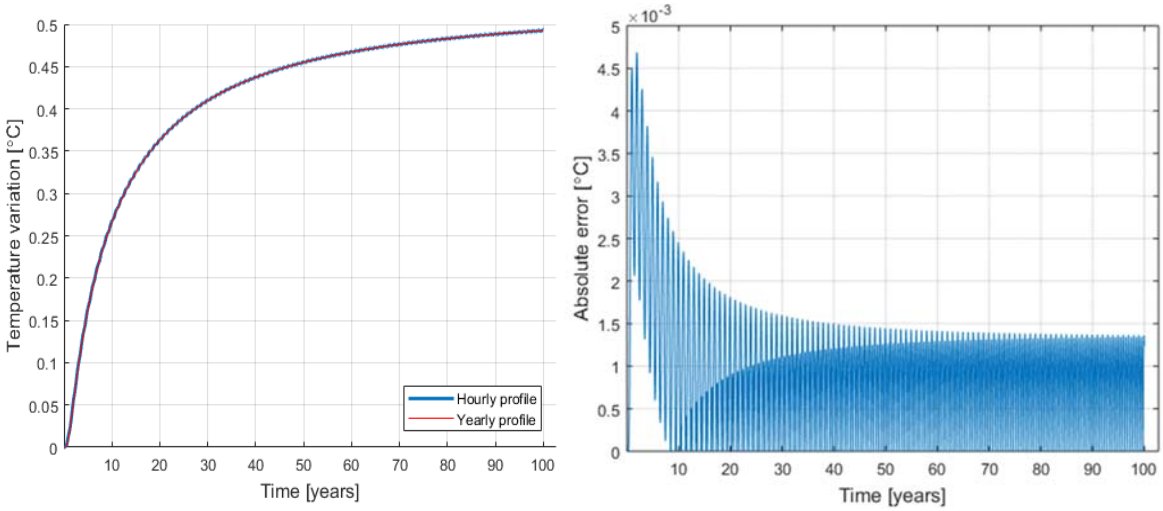

Figure 3 Temperature influence of neighbouring borehole obtained with hourly and yearly load resolution (left). Absolute difference between the results obtained with hourly and yearly resolution (right).

The maximum error, in case of yearly load resolution, is reached during the first years of operation and decreases logarithmically until reaching a steady state. For the case considered the steady state error is lower than 0.0015 °C.

In figure 4, the maximum error obtained due to the load resolution is shown for several borehole depths and distances. The total heat load on the borehole is the same for all the cases, so the heat load per borehole length differs from case to case. The graph shows that the error made decreases for longer distances and increasing borehole depth. Using yearly load resolution leads to unacceptable errors for short borehole-to-borehole distances (<5 m), but the authors feels confident in stating that the errors made for distances over 20 m are acceptable (<0.01 °C). Similarly to figure 4, figure 5 shows the maximum error obtained due to the load resolution for several borehole depths and distances, the difference with figure 4 is that it is the heat load per unit length of borehole to be the same for all the boreholes and not the total borehole heat load. The figure shows that for a fixed specific linear heat load the influence of the borehole length on the error is lower, though it can be observed that slightly higher errors are made for longer boreholes. In particular the curve for a 50 m long borehole differs significantly for longer distances. The explanation suggested by the authors is that the mitigative effect of the heat exchange in the axial direction is lower for longer boreholes, so is the attenuation of the fluctuating response due to fluctuating loads.

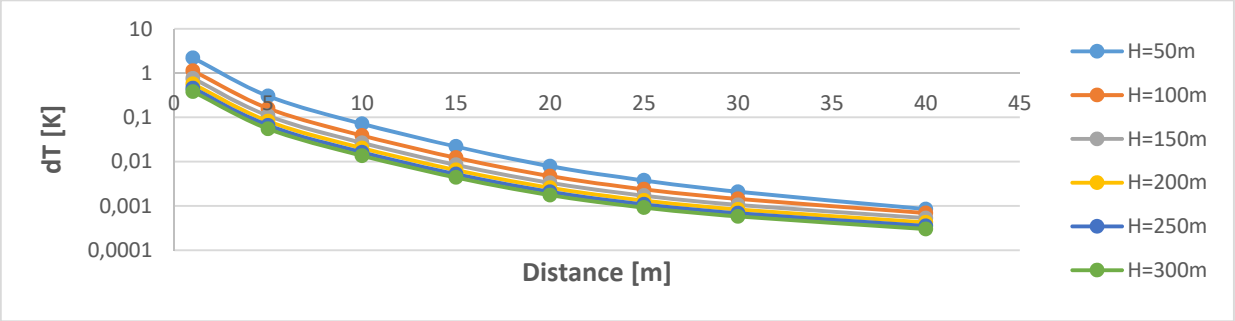

Figure 4 Maximum absolute errors made using yearly load resolution. Annual borehole heat load = 10000 kWh.

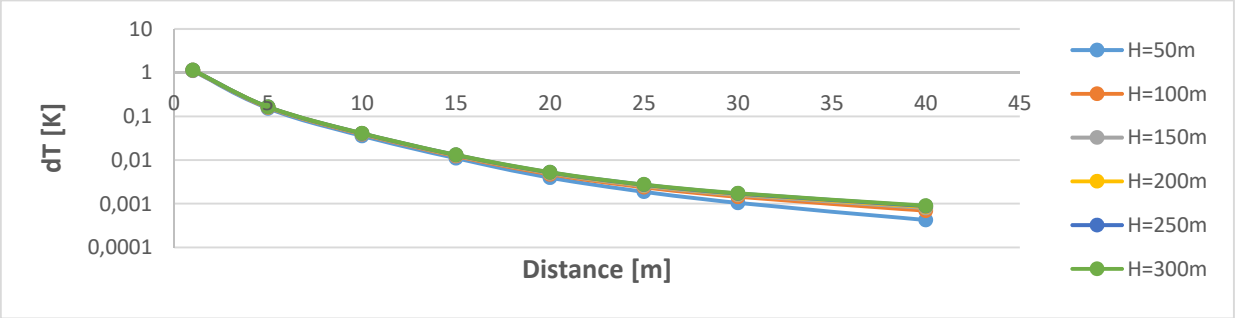

Figure 5 Maximum absolute errors committed using yearly load resolution. Annual borehole heat load per unit length = 100 kWh/m.

The errors obtained for the whole DGSHPAs are finally shown in figure 6.

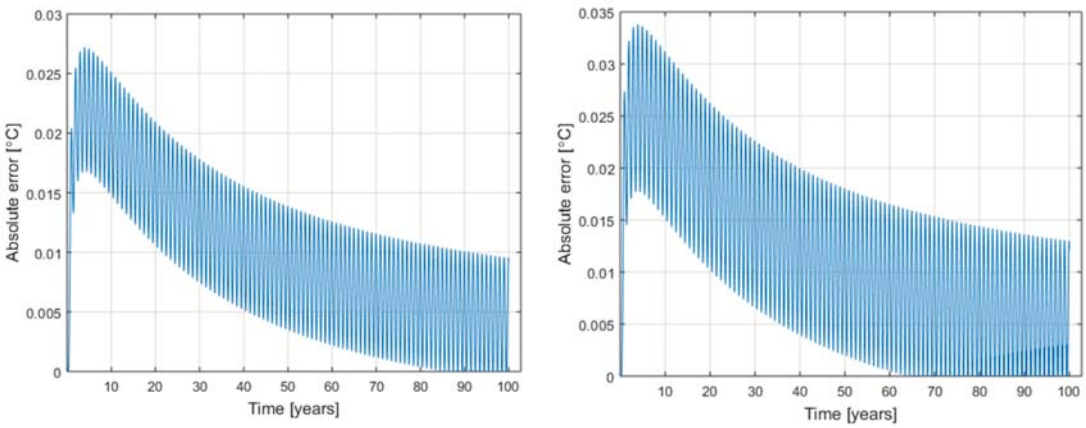

Figure 6 Absolute difference between the results obtained with hourly and yearly resolution for the square grid (left) and the triangular grid (right).

For both configurations the error is always lower than 0.035 °C. It is noteworthy that the load approximation error for a borehole field is not the mere sum of the errors of the individual boreholes, but is lower due to the different time-shift of the thermal responses at different distances from the heat source. Therefore using yearly load resolution is considered an acceptable approximation by the authors.

CONCLUSIONS

The results showed that measures need to be taken to prevent strong thermal interference between boreholes in densely populated areas. A tool that allows an accurate estimation of the boreholes thermal interaction is necessary to be able to forecast the evolution of ground temperature. The tool should be able to forecast the thermal behaviour of the ground where several boreholes, in arbitrary configurations and subject to different loads, are operating. The tool could be also useful to determine guidelines for how systems in densely populated areas should be designed.

One step has been taken towards the development of such a model by evaluating the importance of borehole load resolution for distant neighbouring boreholes (>20 m). It has been concluded that having yearly averaged loads leads to an acceptable accuracy of the results.

The next step towards the development of the model is to add the possibility to set not uniform temperature at the top surface. In particular the surface temperature is influenced by the presence of buildings and asphalt, therefore is on average higher than the undisturbed ground temperature. With such condition the resulting ground temperature response would be mitigated.

ACKNOWLEDGMENTS

This work was supported by the Swedish Energy Agency.

NOMENCLATURE

α = Thermal diffusivity (m^2/s)
d = Radial distance from the line source (m)
g = Thermal response function
H = Borehole length (m)
HL = Heat load (kWh)
k = Thermal conductivity (W/m/K)
q = Specific heat load (W/m)
t = Time (s)
T = Temperature (°C)
T_o = Initial temperature of the ground (°C)

Subscripts

a = annual
b = borehole
h = house

REFERENCES

Bernier, M.A., P. Pinel, R. Labib, R. Paillot, 2004. *A Multiple Load Aggregation Algorithm for Annual Hourly Simulations of GCHP Systems.* HVAC&R Research 10, 471–487.

Claesson, J., S. Javed, 2012. *A load-aggregation method to calculate extraction temperatures of borehole heat exchangers.* ASHRAE Transactions 118, 530–539.

Energimyndigheten, 2017. *Bergvärmepumpar- mätningar i hus.* Available online at: http://www.energimyndigheten.se/tester/tester-a-o/bergvarmepumpar/bergvarmepumpar---matningar-i-hus/

European Environment Agency, 2017. *Heating and cooling degree days*. Available online at: https://www.eea.europa.eu/data-and-maps/indicators/heating-degree-days/assessment

Gehlin, S., O. Andersson, 2016. *Geothermal Energy Use, Country Update for Sweden*. Proceeding of European Geothermal Congress 2016, Strasbourg, France, September 19-24th 2016.

Lamarche, L. and B. Beauchamp. 2007. *A new contribution to the finite line-source model for geothermal boreholes*. Energy and Buildings 39: 188–198.

Lund, J.W., T.L. Boyd, 2016. *Direct utilization of geothermal energy 2015 worldwide review*. Geothermics 60: 66-93.

Marcotte, D., P. Pasquier, 2008. *Fast fluid and ground temperature computation for geothermal ground-loop heat exchanger systems*. Geothermics 37: 651–665.

Sanner, B., 2016. *Shallow geothermal energy–history, development, current status, and future prospects*. European Geothermal Congress. Strasbourg, France: 19–24.

Spitler, J.D. and M. Bernier. 2016. *Vertical borehole ground heat exchanger design methods*. In: S.J. Rees Advances in Ground-Source Heat Pump Systems. London: Woodhead Publishing.

Svenska kyl och värmepump föreningen, 2017. *Värmepumpförsäljning*. Available online at: https://skvp.se/aktuellt-o-opinion/statistik/varmepumpsforsaljning

Sveriges geologiska undersökning, 2016. *Vägledning för att borra brunn*. Available online at: https://resource.sgu.se/produkter/broschyrer/vagledning-normbrunn-16.pdf

Swedish Meteorological and Hydrogeological Institute, 2017. *Meteoralogiska observationer*. Available online at: https://opendata-download-metobs.smhi.se/explore/?parameter=0#

Ulseth, R., K.B. Lindberg, L. Georges, M.J. Alonso, Å. Utne, 2016. *Measured load profiles and heat use for "low energy buildings" with heat supply from district heating*. 15th International Symposium on District Heating and Cooling. Seoul, South Korea: 180–190.

Witte, H.J.L., 2018: *A Novel Tool for Assessing Negative Temperature Interactions between Neighbouring Borehole Heat Exchanger Systems*. 14th international conference on energy storafge, April 2018, Adana Turkey.

Yang, H., P. Cui, Z. Fang, 2010. *Vertical-borehole ground-coupled heat pumps: A review of models and systems*. Applied Energy 87: 16–27.

Yazuzturk, C., J.D. Spitler, 1999. *A short time step response factor model for vertical ground loop heat exchangers*. Ashrae Transactions 105, 475.

[This page has been intentionally left blank]

IGSHPA SWEDEN 2018 Research Conference

DOI: 10.22488/okstate.18.000017

Near-instant g-function Construction with Artificial Neural Networks

Bernard Dusseault **Philippe Pasquier**

ABSTRACT

A g-function is a useful tool that simplifies the calculations of heat exchanges in a ground-coupled heat pump system. In this work, we show how an artificial neural network can be trained to construct a g-function with high efficiency and reliability. First, we show how a block matrix formulation can be used to construct rapidly a g-function. This method is then used to assemble a database of 27,000 g-functions with a variety of input parameters. This database of g-functions is used to train a feed-forward neural network having three hidden layers using the back-propagation algorithm to update the weights and biases of the neurons. The network we developed in this work can estimate the long-term g-function of a ground heat exchanger made of 1 to 10 boreholes over a duration of 100 years with various ground thermal properties, borehole field configurations, length and buried depth in a few milliseconds. The contribution of this work is to lay out the methodology to allow anyone to construct a g-function with an artificial neural network.

INTRODUCTION

Geothermal heat exchangers (GHE) are useful constructs that allow for heating and cooling of buildings at a fraction of the operating costs of conventional systems. The most common type is made of vertical boreholes through which a heat-carrying fluid flows. Calculating the thermal response of a GHE to a heating or cooling load can be accomplished using the elegant concept of g-function (Eskilson 1987). A g-function is a smooth and monotone function that links a heat extraction rate to the average borehole wall temperature in a GHE. Such function varies according to many thermal properties and geometrical relations and is different for each GHE. In the last years, many authors have come up with new strategies to construct g-function under different assumptions (Cimmino and Bernier 2014; Lazzarotto and Björk 2016; Marcotte and Pasquier 2014; Cimmino, et al. 2013; Dusseault, et al. 2017).

The modelling of GHE is also useful for distributed thermal response tests, model-based optimisation and sizing, and can even be used in model-based control of ground-source heat pump systems (Atam and Helsen 2016a; Atam and Helson 2016b; Atam, et al. 2016).

The ever-increasing computational capability of computers have led to the democratization of artificial neural networks (ANNs). Such networks, whose primary objective is to emulate the learning capabilities of a biological brain, can be trained to perform different tasks. In the field of geothermal energy, ANNs have been used to predict heat pump's COP (Esen, et al. 2008; Sun, et al. 2015), efficiency of a district geothermal system (Arat and Arslan 2017), model a direct expansion system (Fannou, et al. 2014), control district (Yabanova and Keeba 2013) and hybrid (Gang, et al. 2014) systems or construct the short-term g-function of a borehole (Pasquier, et al. 2018).

ANNs can also be trained to approximate smooth and monotone multivariable functions. Indeed, the universal approximation theorem (Cybenko 1989; Hornik, et al. 1989) states that a network with a single hidden layer with a finite number of neurons can approximate any continuous function on compact subsets, under mild assumptions on its activation function. In this paper, the learning abilities of ANNs are used to train a network that

Bernard Dusseault (bernard.dusseault@polymtl.ca) is Ph.D. candidate and Philippe Pasquier is Professor, both at Polytechnique Montréal.

can be used to construct a g-function. To assemble a training set, a block matrix formulation is used to build a database made of 27,000 g-functions. We illustrate in the paper how to train an ANN to reproduce accurately in a split second the g-function of a GHE placed on a regular grid made of up to 10 boreholes.

CONSTRUCTION OF A G-FUNCTION WITH A BLOCK MATRIX FORMULATION

To create a database of g-functions used to train the ANN, the block matrix formulation presented by Dusseault, et al. (2017) was selected mainly for its speed and efficiency. Indeed, this approach can construct a g-function for a GHE made of 50 boreholes over 40 years in only 0.46 second. This efficiency was a necessity to obtain under a reasonable time a large database of tens of thousands of g-functions. The core concept behind the block matrix formulation is to construct a linear system of equations accounting simultaneously for the thermal interactions between all *m* boreholes in a GHE at all *n* time steps.

All thermal interactions (ΔT) are calculated using the finite line-source model of Claesson and Javed (2011) described by Eq 1 to 3 and computed with a unit heat load of $\tilde{q}$ = 1 W/m.

$$\Delta T(r_{j\to i}, t_k) = \frac{\tilde{q}}{4\pi k_s} \int_{\frac{1}{\sqrt{(4k_s t_k)/C_s}}}^{\infty} e^{-r_{j\to i}^2, s^2} \frac{Y(Hs, Ds)}{Hs^2} ds \tag{1}$$

$$Y(h,d) = 2\,\mathtt{ierf}(h) + 2\,\mathtt{ierf}(h+2d) - \mathtt{ierf}(2h+2d) - \mathtt{ierf}(2d) \tag{2}$$

$$\mathtt{ierf}(X) = X\,\mathtt{erf}(X) - \frac{1}{\sqrt{\pi}}\left(1 - e^{-X^2}\right) \tag{3}$$

First, consider a GHE composed of a single borehole. To calculate its g-function, one would first have to calculate the mean borehole wall temperature T_b at each time step of the simulation. This can be done using Eq (4) with m = 1 (one borehole):

$$T_{b_i} = T_g + \sum_{j=1}^{m} \Delta T_{j\to i} \tag{4}$$

where *j* and *i* stand for emitting and receiving borehole, which in this case is the same borehole, and where T_g is the initial ground temperature. All values of ΔT can be found simultaneously using a convolution product in the spectral domain (Marcotte and Pasquier 2008). Convolution in the time domain can however be accomplished by the right-end part of Eq (5):

$$\Delta T(r_{1\to 1}, q, t) = (\mathbf{f} * \mathbf{g})(t) = \sum_{k=1}^{n} f(t_k)\, g(t - t_{k-1}) \tag{5}$$

where *f* represents the incremental heat load emitted by a borehole throughout the simulation. In Eq (5), the function $g\,(t - t_{k-1})$ is used to indicate the solution of the FLS model (Eq 1-3) under a heat load $\tilde{q}$ over the duration specified in the parentheses.

For convenience, Eq (5) can also be presented in a matrix form as shown by Eq (6).

$$\begin{bmatrix} \Delta T(t_1, r_{1\to 1}) \\ \Delta T(t_2, r_{1\to 1}) \\ \Delta T(t_3, r_{1\to 1}) \\ \vdots \\ \Delta T(t_n, r_{1\to 1}) \end{bmatrix} = \begin{bmatrix} g(t_1 - t_0) & 0 & 0 & \dots & 0 \\ g(t_2 - t_0) & g(t_2 - t_1) & 0 & \dots & 0 \\ g(t_3 - t_0) & g(t_3 - t_1) & g(t_3 - t_2) & \dots & 0 \\ \vdots & \vdots & \vdots & \ddots & \vdots \\ g(t_n - t_0) & g(t_n - t_1) & \dots & g(t_n - t_{n-2}) & g(t_n - t_{n-1}) \end{bmatrix} \begin{bmatrix} f(t_1) \\ f(t_2) \\ f(t_3) \\ \vdots \\ f(t_n) \end{bmatrix} \tag{6}$$

Using a more compact format and generalizing for any emitting (*j*) and receiving (*i*) boreholes, the matrix formulation of Eq (6) becomes:

$$\Delta \mathbf{T}_{i \to j} = \mathbf{G}_{j \to i}\, \mathbf{f}_j \tag{7}$$

To account for the thermal interactions between the m boreholes of a field, Eq (7) can be replicated $m \times m$ times and presented in a compact matrix form to integrate all spatial superpositions (Eq (8)). The g-function is obtained by solving a linear system of equations under the constraint of a unit heat load expressed in matrix form by:

$$\mathbf{I}\,\mathbf{f} = \mathbf{\Lambda} = [1 \quad 0 \quad 0 \quad \ldots \quad 0]' \tag{8}$$

Adding the previous constraints to guarantee the uniqueness of the solution, the resulting linear system is given by:

$$\begin{bmatrix} \mathbf{G}_{1\to1} & \mathbf{G}_{2\to1} & \mathbf{G}_{3\to1} & \cdots & \mathbf{G}_{m\to1} & \mathbf{I} \\ \mathbf{G}_{1\to2} & \mathbf{G}_{2\to2} & \mathbf{G}_{3\to2} & \cdots & \mathbf{G}_{m\to2} & \mathbf{I} \\ \mathbf{G}_{1\to3} & \mathbf{G}_{2\to3} & \mathbf{G}_{3\to3} & \cdots & \mathbf{G}_{m\to3} & \mathbf{I} \\ \vdots & \vdots & \vdots & \ddots & \vdots & \vdots \\ \mathbf{G}_{1\to m} & \mathbf{G}_{2\to m} & \mathbf{G}_{3\to m} & \cdots & \mathbf{G}_{m\to m} & \mathbf{I} \\ \mathbf{I} & \mathbf{I} & \mathbf{I} & \cdots & \mathbf{I} & \mathbf{0} \end{bmatrix} \begin{bmatrix} \mathbf{f}_1 \\ \mathbf{f}_2 \\ \mathbf{f}_3 \\ \vdots \\ \mathbf{f}_m \\ -(\mathbf{T}_b - T_g) \end{bmatrix} = \begin{bmatrix} 0 \\ 0 \\ 0 \\ \vdots \\ 0 \\ \mathbf{\Lambda} \end{bmatrix} \tag{9}$$

where $\mathbf{I}$ is the identity matrix and $\mathbf{0}$ is either a null matrix or vector. Once Eq (9) is solved for $\mathbf{T}_b$ and T_g, the adimensional g-function is simply obtained with:

$$\tilde{g}(t) = 2\pi k_s (\mathbf{T}_b - T_g)/\tilde{q} \tag{10}$$

ARTIFICIAL NEURAL NETWORKS

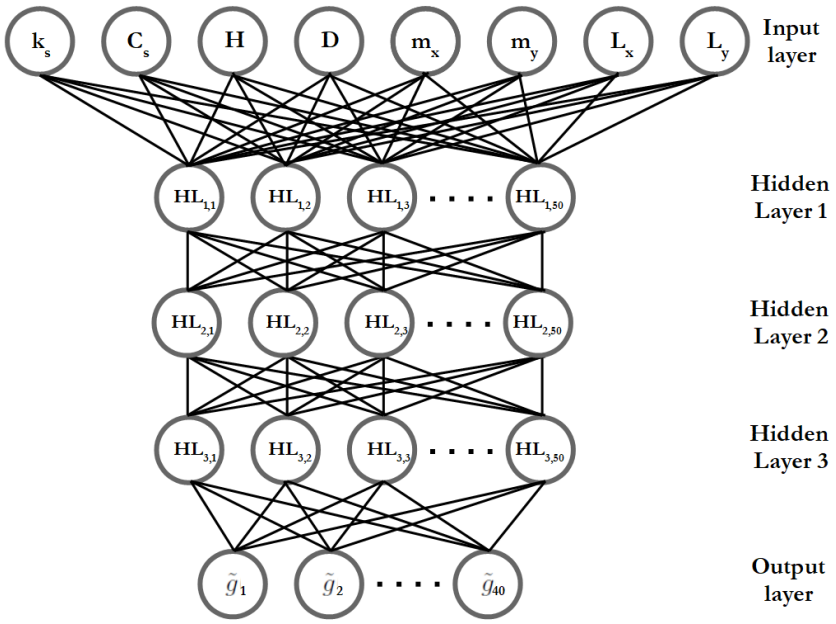

Figure 1 Artificial neural network with 3 hidden layers used to approximate a g-function.

Artificial neural networks come in many flavors, but all rely on the same building block. Indeed, artificial neurons (Rosenblatt 1958) are at the core of their learning ability and are connected with each other according to different architectures. In an ANN, each neuron gets its inputs from all the neurons of the previous layer and passes its output to all the neurons of the next layer. Every time an artificial neuron receives some signals as input, it must decide, just like its biological counterpart, which output signal to transmit to the next layer as a result. This behavior

can be summarized by Eq (11):

$$y_k = \varphi\left(\sum_{j=1}^{m} w_{kj}x_j + b_k\right) \tag{11}$$

where k is the neuron index, x_j is the input provided by neuron j, w_k and b_k are the neuron' weight and bias respectively. The resulting summation is submitted to an activation function φ to introduce an element of non-linearity between the input and output of the neuron. They are many types of activation function in the literature that are meant to be used for specific tasks. As of today, the choice of an activation function is empirical at best and is usually driven by the experience of the user, by trial and error and by the type of phenomenon being modelled. In this work, the linear function as well as the hyperbolic tangent sigmoid function were chosen after a few tests. The linear function, linking the last layer to the output of an ANN, is a prerequisite to the universal approximation theorem. The other function, linking the input and all the hidden layers, was selected for its transitional nature after some testing.

As mentioned earlier, the universal approximation theorem only requires a single hidden layer of a finite number of neurons. However, the arbitrary number of neurons, which needs to be fine tuned by the user, can grow quite large for the modelling of complex processes such as heat transfer in a GHE. To circumvent part of the problem, we resorted to use three hidden layers as illustrated in Fig 1. By adopting such an architecture, an ANN can be trained to performed more complex tasks while having a smaller total number of neurons. This results in faster training times.

METHODOLOGY

The objective of this paper is to train an ANN to approximate a g-function over a period of 100 years for GHE made of 1 to 10 boreholes placed on regular grids. They are 27 unique ways in which boreholes can be distributed between rows and columns on regular grids of a GHE made up of 1 to 10 boreholes. For example, 3 boreholes can be placed on grids in two different ways, 1×3 and 3×1, while 8 boreholes can be placed in four different ways, 1×8, 2×4, 4×2 and 8×1. In addition, the ANN must be able to approximate accurately the g-function while subjected to varying values of ground thermal conductivity (k_s), volumetric heat capacity (C_s), borehole length (H), buried depth (D), boreholes per row (m_x), boreholes per column (m_y), row spacing (L_x) and column spacing (L_y) (Fig 2) taken between the intervals presented in Table 1. Note that m_x and m_y are integers that can both vary from 1 to 10 under the constraint that ($m_x \times m_y$) ≤ 10. The input parameters should then be selected so that the total number of boreholes in the resulting GHE does not exceed 10. Finally, all boreholes share the same radius of 0.075 m.

Table 1. Ranges of inputs parameters of the ANN

Parameters (units)	Units	Lower bound	Upper bound
k_s	W/ (m °C)	1.0	3.5
C_s	MJ/ (m³ °C)	1.0	3.5
H	m	50	250
D	m	0	2.5
m_x	-	1	10
m_y	-	1	10
L_x	m	1	5
L_y	m	1	5

Inputs of the ANN

The ANN developed uses a total of 8 inputs as illustrated in Fig 1. To properly train the ANN, all input parameters were centered and scaled between the interval [0 1]. This ensures, for example, that some combinations of high inputs parameters won't saturate a neuron that has otherwise been trained to respond to small values.

Outputs of the ANN

The number of output neurons has a direct impact on the training time as well as the format in which the g-functions are produced by the ANN. To limit their number without losing information on the g-functions, the geometrical sampling scheme proposed by Marcotte and Pasquier (2008) was implemented. The progression that was selected starts at one hour and doubles every two time steps, allowing 100 years to be covered in 40 steps. The output layer then contains 40 neurons, each one corresponding to the g-function of a given time step. The whole g-function can later be reconstituted at every time step using cubic spline interpolation. Again, the training data set was normalized for the training.

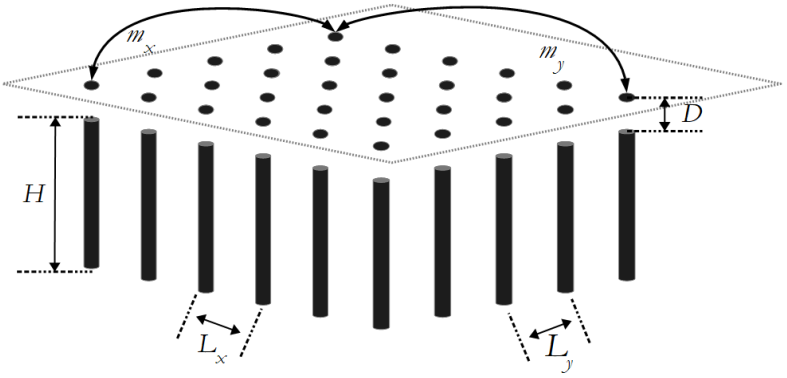

Figure 2 Geometrical parameters used as inputs.

Architecture and Training Algorithm

After some testing, we decided to use an ANN containing three hidden layers of 50 neurons each. This was found to be a good trade-off between training time and accuracy. We also decided to train our ANN with the scaled conjugate gradient with backpropagation (Hagan, et al. 1996) using the mean squared residuals (mse) as objective function. Random initial weights and biases were also used. As a rule of thumb, about 1000 training examples are needed per parameter to train an ANN. In our case, we observed that the number of different regular grids is the force that drives mostly the training. This is because the ANN can learn easily the impact of the first four parameters (k_s, C_s, H and D) no matter the GHE configuration. On the other hand, the 1 to 10 boreholes can be arranged in 27 different regular grids and their impact is hard to predict. Therefore, their contribution to the output is harder to learn to approximate for the ANN. Hence, we used the block matrix formulation presented earlier to generate a data set of 27,000 g-functions used for training.

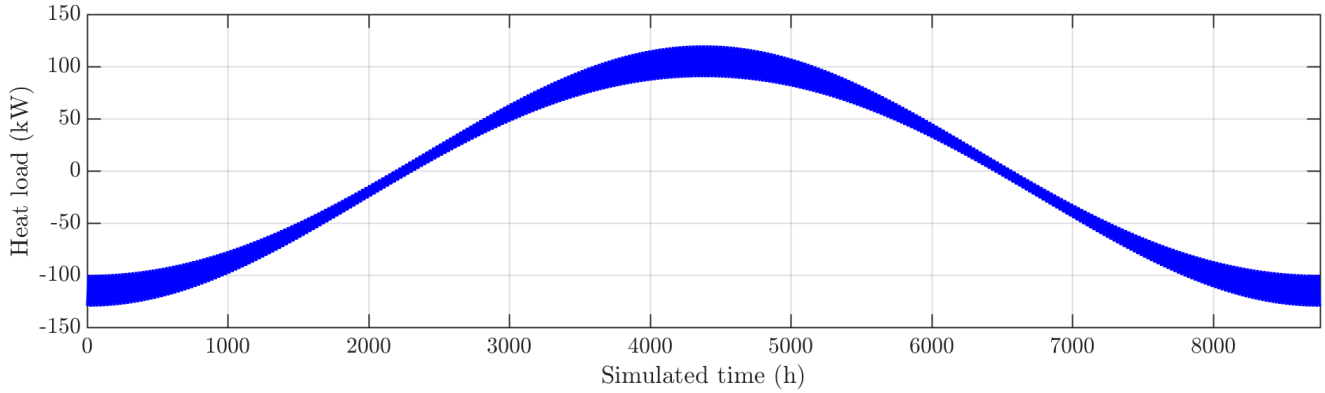

Figure 3 Hourly heat load signal used to verify the accuracy of the ANN.

It is important to note that the accuracy of an ANN is not verified using the same training data, as overfitting can sometimes exaggerate the accuracy of the network and lead to poor generalizations capabilities. Therefore, the trained ANN is tested using 27 independent g-functions generated after the training phase, one for each different grid arrangement. After comparison, both the approximated and reference g-functions are convolved with the same heat load signal (Fig 3) in the spectral domain to calculate fluid temperatures throughout the simulation duration (100 years).

RESULTS AND DISCUSSION

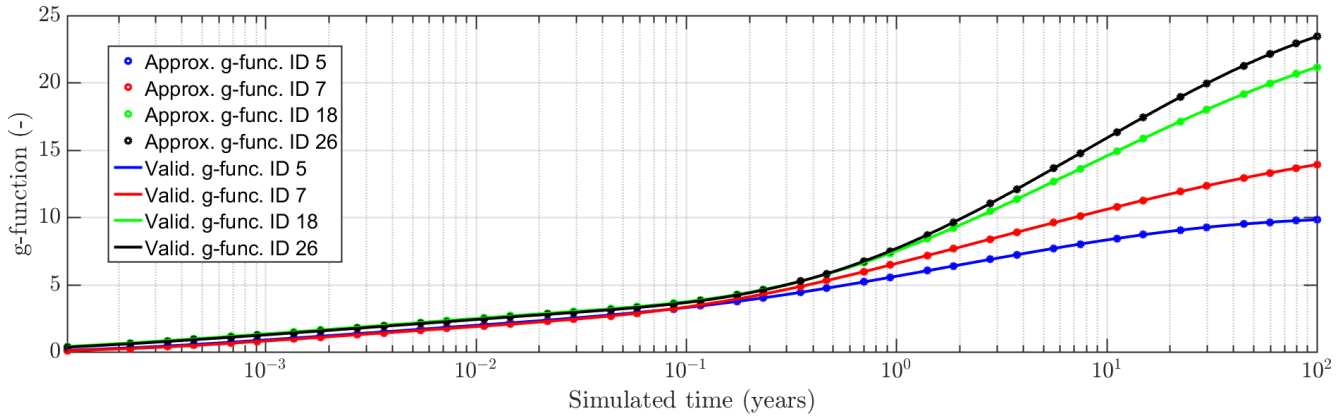

Figure 4 Comparison between the reference and ANN g-functions of ID 5, 7, 18 and 26.

Figure 4 compares a few g-functions obtained with the block matrix formulation and those produced by the ANN after its training for four sets of input parameters chosen randomly. The four g-functions shown are coming from a set of 27 g-functions (1 per geometrical layout) and are the cases having the worst fits. Nevertheless, one can see that the g-functions constructed by the ANN are visually practically superimposed.

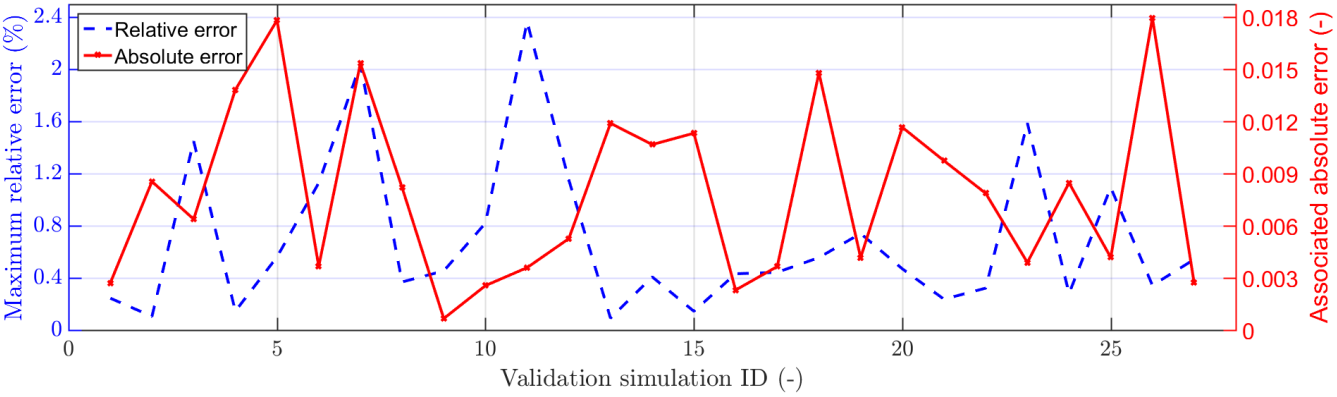

Figure 5 Maximum relative error and corresponding absolute errors committed by the ANN.

Figure 5 illustrates the error made by the ANN when approximating the g-functions for each of the 27 possible layouts with input parameters chosen randomly. From Fig 5 it is clear that no correlation is observed between

the error produced by the ANN and the layout of the ground heat exchanger. Also, we can see that even in the worst cases (ID 5, 7, 18 and 26), the absolute error is small with maximum relative errors that barely exceed two percent. Although it is not intrinsically bad, the universal approximation theorem suggested that a better accuracy could be achieved with the ANN we implemented. To find out why, we observed that the maximum error occurred mostly (10 times out of 27) at the first time step. Moreover, in most cases the errors are decreasing from the second neuron onwards as illustrated in Figure 6. This was a proof that 27,000 simulations are probably not enough to perfectly train our ANN and that a larger training set could have better its response on the first neuron.

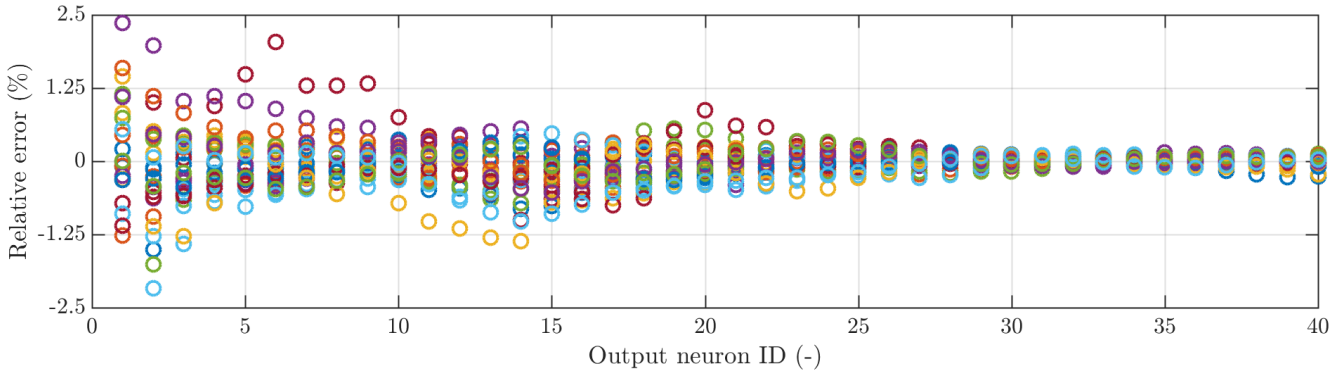

Figure 6 Relative error per output neuron for all 27 approximated g-functions.

Figure 7 compares the resulting fluid temperatures that were obtained after convolving in the spectral domain the approximated g-functions and the reference g-functions to the same heat load signal. Fig 7 clearly shows that the relative errors on fluid temperatures are up to an order of magnitude less important than the ones on g-functions. Indeed, most of the simulations are within an error of 0.1 °C and never exceed 0.3 °C, which is more than enough for sizing and simulation purposes. The sinusoidal heat load signal and the convolution process probably damp the error made at the first time step of the g-function, which results in a lower error.

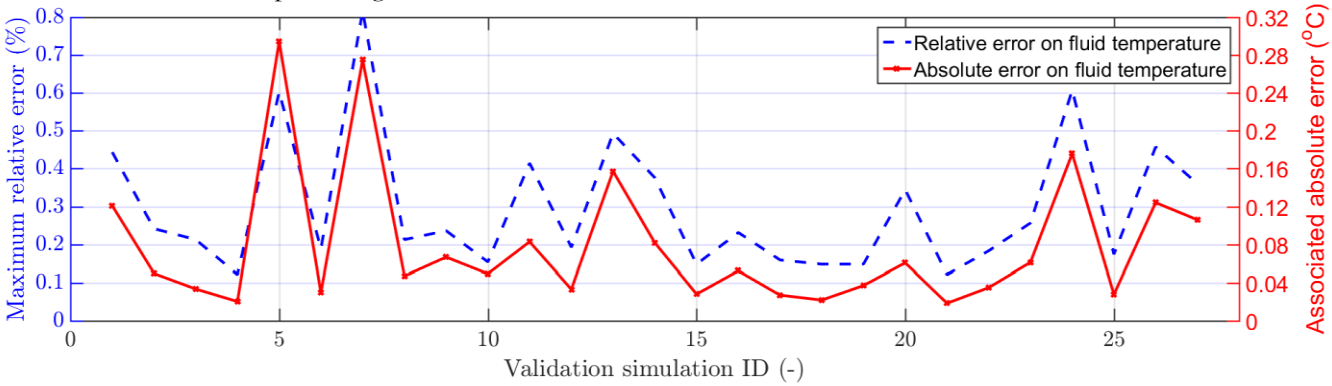

Figure 7 Maximum relative and absolute errors committed on the fluid temperatures after convolution with the heat load signal of Figure 3.

Finally, we emphasized the computational gain associated with the use of the ANN. Indeed, only 14 milliseconds are required to construct 27 g-functions over a period of 100 years (1 per configuration). By comparison,

construction of the same 27 g-functions by the block matrix formulation is achieved in 11.74 seconds, a ratio of 1 to 838. Such efficiency could be useful when optimizing ground-coupled heat pump systems or assessing the uncertainty of a design, which could require several thousands of g-function evaluations.

CONCLUSION

In this article, we demonstrated the feasibility of using artificial neural networks to approximate g-functions of ground heat exchangers varying from 1 to 10 boreholes placed on regular grids. We covered the architecture of the network we developed, how we trained it and its efficiency and accuracy when compared to a benchmark of g-functions calculated with an independent method. Our results show that a g-function of a 100 years duration can be calculated almost instantaneously with good accuracy. Moreover, we showed that the maximum imprecision of the ANN g-functions is very localised at the first time step, which could eventually be improved by additional works. The methodology developed in this article can easily be adapted to construct and train artificial neural networks for any number of boreholes.

BLOCK MATRIX NOMENCLATURE

$\mathbf{\Lambda}$	=	Constraint vector (-)
C	=	Volumetric heat capacity (MJ/m^3°C)
D	=	Boreholes' buried-depth (m)
f, $\mathbf{f}$	=	Incremental heat-flux function (W/m)
g	=	Finite-line source solved under $\tilde{q}$ (m°C/W)
$\mathbf{G}$	=	Lower-triangular matrix of g (°C)
$\tilde{g}$	=	g-function (-)
H	=	Borehole length (m)
$\mathbf{I}$	=	Identity matrix (-)
k	=	Thermal conductivity (W/m°C)
m	=	Number of boreholes (-)
n	=	Number of time steps (-)
$\tilde{q}$	=	Unit heat load (1 W/m)
t	=	Simulation time (s)
$\mathbf{T}$	=	Temperature (°C)
ΔT, $\mathbf{\Delta T}$	=	Thermal perturbation (°C)
r	=	Distance (m)

ANN NOMENCLATURE

$\mathbf{\Sigma}$	=	Combination function (-)
φ	=	Activation function (-)
b	=	Neuron's bias (-)
w	=	Neuron's weight (-)
x	=	Neuron's input (-)
y	=	Neuron's output (-)
X, Y	=	Boreholes' cartesian coordinates (m, m)
θ, r	=	Boreholes' polar coordinates (rad, m)

Subscripts

b	=	Borehole
g, s	=	Surrounding ground, soil
i	=	Receiving borehole
j	=	Emitting borehole
$j \rightarrow i$	=	Influence of borehole j on borehole i
m	=	Number of input in a neuron

REFERENCES

Arat, H. and O. Arslan. 2017. *Optimization of district heating system aided by geothermal heat pump: A novel multistage with multilevel ANN modelling*. Applied Thermal Engineering 111: 608-623.

Atam, E. and L. Helsen. 2016. *Ground-coupled heat pumps: Part 1- Literature review and research challenges in modeling and optimal control*. Renewable and Sustainable Energy Reviews 54: 1653-1667.

Atam, E. and L. Helsen. 2016. *Ground-coupled heat pumps: Part 2- Literature review and research challenges in optimal design*. Renewable and Sustainable Energy Reviews 54: 1668-1684.

Atam, E., D. Patteeuw, S. Antonov and L. Helsen. 2016. *Optimal control approaches for analysis of energy use minimization of hybrid ground-coupled heat pump systems*. IEEE Transactions on Control Systems Technology 24(2): 525-540.

Claesson, J. and S. Javed. 2011. *An Analytical Method to Calculate Borehole Fluid Temperatures for Time-scales from Minutes to Decades*. ASHRAE Transactions 117(2):279-288.

Cimmino, M. and M. Bernier. 2014. *A semi-analytical method to generate g-functions for geothermal borefields*. International Journal of Heat and Mass Transfer. 70: 641-650.

Cimmino, M., M. Bernier and F. Adams. 2013. *A contribution towards the determination of g-functions using the finite line source*. Applied Thermal Engineering. 51(1-2): 401-412.

Cybenko, G. 1989. *Approximation by superpositions of sigmoidal functions*. Budapest, Hungary: Eötvös Loránd University.

Dusseault, B., P. Pasquier and D. Marcotte. 2017. *A block matrix formulation for efficient g-function construction*. Renewable Energy In Press, Accepted Manuscript.

Esen, H., M. Inalli, A. Sengur and M. Esen. 2008. *Performance prediction of a ground-coupled heat pump system using artificial neural networks*. Expert Systems with Applications 35 (4): 1940-1948.

Eskilson, P. 1987. *Thermal Analysis of heat extraction borehole*. Lund, Sweden: University of Lund.

Fannou, J.-L. C., C. Rousseau, L. Lamarche and S. Kajl. 2014. *Modeling of a direct expansion geothermal heat pump using artificial neural networks*. Energy and Buildings 81: 381-390.

Gang, W., J. Wang and S. Wang. 2014. *Performance analysis of hybrid ground source heat pump systems based on ANN predictive control*. Applied Energy 136: 1138-1144.

Hagan, M. T., H. B. Demuth., M. H. Beale and O. De Jesus. 2014. Neural network design 2nd edition. Stillwater, Oklahoma. Oklahoma State University.

Hornik, K., M. Stinchcombe and H. White. 1989. *Multilayer feedforward networks are universal approximators*. Neural Networks 2 (5): 359-366.

Lazzarotto, A. and F. Björk. 2016. *A methodology for the calculation of response functions for geothermal fields with arbitrarily oriented boreholes: Part 2*. Renewable Energy. 86: 1353-1361.

Marcotte, D. and P. Pasquier. 2008. *Fast fluid and ground temperature computation for geothermal ground-loop heat exchanger systems*. Geothermics. 37 (6): 651-665.

Marcotte, D. and P. Pasquier. 2014. *Unit-response function for ground heat exchanger with parallel, series or mixed borehole arrangement*. Renewable Energy. 68: 14-18.

Pasquier, P., A. Zarrella and R. Labib. 2018. Near-instant construction of short-term g-functions by artificial neural network. TO BE SUBMITTED.

Rosenblatt, F. 1958. The Perceptron: A Probabilistic Model for Information Storage and Organization in The Brain. Psychological Review 65 (6): 386-407.

Sun, W., P. Hu, F. Lei, N. Zhu and Z. Jiang. 2015. *Case study of performance evaluation of ground source heat pump system based on ANN and ANFIS models*. Applied Thermal Engineering 87: 586-594.

Yabanova, I. and A. Keeba. 2013. *Development of ANN model for geothermal district heating system and a novel PID-based control strategy*. Applied Thermal Engineering 51 (1-2): 908-916.

[This page has been intentionally left blank]

IGSHPA SWEDEN 2018 Research Conference

DOI: 10.22488/okstate.18.000026

Application of matched asymptotic expansion techniques to the analysis of geothermal heat exchangers

Miguel Hermanns **Santiago Ibáñez**

ABSTRACT

Most theoretical models for the thermal response of geothermal heat exchangers assume the mean azimuthal borehole wall temperature to be uniform along the boreholes. This simplifying assumption, closely related to the g-functions introduced by Eskilson in 1987, has dominated the research field for the past 30 years, allowing the analysis of large geothermal heat exchangers in reasonable amounts of time. The assumption, however, is not physically correct, which hinders the attainable accuracy. By using matched asymptotic expansion techniques, analytical models for the thermal response of geothermal heat exchangers are derived, which do not require the aforementioned simplification. The resulting expressions, applicable to geothermal heat exchangers with irregularly placed heterogeneous boreholes, show accuracy and flexibility levels comparable to SBM, but with a computational cost in line with the use of g-functions.

INTRODUCTION

Geothermal heat exchangers have an increasingly fundamental role in the design and construction of sustainable buildings. An HVAC system based on geothermal energy can only be considered truly renewable, however, if the geothermal heat exchanger and the heat injection/extraction strategy are properly designed. Otherwise, thermal exhaustion of the ground occurs, and the geothermal heat pump's efficiency decreases over time.

To ensure the long-term efficiency of geothermal HVAC systems, its thermal behavior after 25, 50, or even 100 years of operation must be known, reason why their theoretical and numerical modeling is extremely relevant to the industry. Extensive literature exists on this topic, being the contributions by the research group at Lund University the most influential ones (Bennet et al. 1987; Claesson and Hellström 2011; Eskilson 1986, Eskilson 1987; Eskilson and Claesson 1988; Hellström 1991). They proposed two models. The *Superposition Borehole Model* (SBM) solved numerically the governing equation in the ground and the one-dimensional energy conservation equations for the transfer of heat along the pipes. In order to connect both, a network of thermal resistances was used to describe the quasi-steady two-dimensional thermal response of the grout and of the ground close to the borehole (Eskilson 1986). The extension to borehole fields was done by superposing the exerted temperature perturbation of neighboring boreholes. This approach rendered the model very accurate but also very slow, especially for large borehole fields. The second one, the *g-function model*, assumed a uniform mean azimuthal borehole wall temperature along the boreholes (Eskilson 1987). This simplification allowed the uncoupling of the heat conduction problem in the ground from the heat transfer problem inside the boreholes. For the former problem, a large database of precomputed borehole field configurations, the so called *g-functions*, was obtained using a tailored version of SBM, while the latter problem was solved analytically thanks to the introduced simplifying assumption. The result was a less accurate and less flexible model than SBM, but an extremely fast one.

Miguel Hermanns (miguel.hermanns@upm.es) is assistant professor at *Universidad Politécnica de Madrid***, Spain, and Santiago Ibáñez is visiting professor at** *Universidad Carlos III de Madrid***, Spain.**

A lot of effort has been made to develop efficient but accurate methods to calculate the *g-functions* (Li and Lai 2015). In recent years, *g-functions* have been obtained using a commercial finite-element simulation tool (Monzó et al. 2016), but this approach is very time consuming. On the other hand, a family of models assimilates the borehole to a line of heat sources of uniform intensity (Eskilson 1987). The infinite line source (ILS) (Ingersoll et al. 1954), the infinite cylindrical-surface source (ICS) (Ingersoll et al. 1954) and the finite line source (FLS) (Zeng et al. 2002; Lamarche and Beauchamp 2007) models have been used respectively to model the borehole for increasing values of the characteristic injection time. All these models assume that the heat injection rate per unit borehole length q is uniform along the borehole, contrary to the original *g-function* definition proposed by Eskilson that assumes a uniform mean azimuthal borehole wall temperature T_b along the borehole. As the resulting value of T_b is not uniform along the borehole, its mean value is used instead to define the *g-functions* (Zeng et al. 2002; Lamarche and Beauchamp 2007; Claesson and Javed 2011; Cimmino and Bernier 2014; Cimmino et al. 2013) and its calculation can be reduced to a single integral (Lamarche and Beauchamp 2007; Claesson and Javed 2011) that is discretized using the midpoint rule with one (Cimmino et al. 2013) or more segments (Cimmino and Bernier 2014; Lazzarotto and Björk 2016) or the trapezoidal rule with multiple segments along the boreholes (Lamarche 2017). Furthermore, a primitive function for the integral can be obtained for the steady-state and time-harmonic cases (Hermanns and Ibáñez 2018) leading to simple analytical expressions. This alternative *g-function* definition results in very efficient methods. However, discrepancies up to 30% have been reported between Eskilson's original definition with uniform T_b and the alternative definition with uniform q (Cimmino and Bernier 2014; Malayappan and Spitler 2013) that grow as the number of thermally interacting boreholes increases (Cimmino and Bernier 2014; Cimmino et al. 2013).

Those two simplifications that assume uniform values along the borehole are inherently limited in accuracy as shown in Malayappan and Spitler (2013), Hermanns and Ibáñez (2017), and Ibáñez and Hermanns (2018) among others. Besides these accuracy problems, the mathematical problem that the original Eskilson's definition of the *g-function* gives rise to, becomes ill-posed under certain circumstances (Hermanns and Ibáñez 2018). Therefore, a well-posed theoretical model that can retain axial variations of the mean azimuthal borehole wall temperature and the heat injection rate per unit borehole length is needed.

Using matched asymptotic expansion techniques (Lagerstrom 1988), the leading author and his research group have derived analytical expressions for the thermal response of geothermal heat exchangers without requiring the aforementioned simplifications. The resulting model is comparable to SBM in terms of flexibility and accuracy, but with a computational cost in line with the *g-function model*. Despite being also an analytical method, the proposed method clearly differs from the *g-function model* in that the thermal responses of the pipes and the liquid inside it, the grout, and the ground, all are tackled at once without assuming neither T_b nor q to be uniform along the borehole, that is, the developed solutions directly give the thermal response of the geothermal heat exchanger.

The present conference paper is a summary of the work done so far by the leading author and his research group. First, a description of the characteristic times that appear in the problem is given. The resulting inner and outer regions and the asymptotic matching process that weaves them are then described. An overview of the process carried out to obtain an asymptotic solution is given afterwards. The extension of the proposed model from one to multiple boreholes is discussed here for the first time. The proposed model is compared against existing models for a test case of a time-harmonic sub-annual excitation applied to a borehole field comprised by two coaxial probes of different lengths. These preliminary results state clearly the differences between the *g-function model* and the asymptotic model developed by the authors. Finally, conclusions and indications on the expected achievements to accomplish in the coming years are given.

SLENDER GEOTHERMAL BOREHOLES

A vertical geothermal borehole consists of a set of pipes placed in a vertical drilling, filled with grout, and through which a liquid flows and exchanges heat with the surrounding ground. Typical boreholes present depths H of the order of hundreds of meters and radii r_b of the order of tens of centimeters, leading to aspect ratios $\Lambda \sim H / r_b$ of the order of thousands. This extreme slenderness is responsible for the appearance of two distinct regions, an inner one located at

radial distances to the borehole of order r_b, and an outer one located further away. To obtain the thermal response of the borehole, the solutions to these two regions need to be combined, something that is accomplished through asymptotic matching at an intermediate scale (Lagerstrom 1988).

Closely related to the previous two length scales are the characteristic transversal diffusion time, $t_b \sim r_b^2/\alpha$, and the characteristic longitudinal diffusion time, $t_H \sim H^2/\alpha$, where α is the thermal diffusivity of the ground. Considering the typical values attained by the different parameters, these two characteristic times are respectively of the order of hours and centuries (Hermanns and Pérez 2014). Two additional characteristic times can be identified in the problem. The first one is the residence time of the liquid in the pipes, $t_r \sim V/H$, with V being the mean flow velocity of the liquid. Due to the requirement of turbulent flow regime to enhance the heat exchange between the liquid and the pipe wall, this characteristic time is of the order of tens of minutes, so that $t_r \ll t_b \ll t_H$ (Hermanns and Pérez 2014). The second one is the characteristic heat injection time t_q. Since the heat injection/extraction from the ground depends on the cooling/heating needs of the building, this characteristic time varies from minutes to months. Also, characteristic values of years or even decades are common, as certain heat injections/extractions are sustained over time.

The thermal problems to solve in the inner and outer regions depend on the relationship between t_q and the other three characteristic times. The following discussion will focus on the realistic case in which $t_r \ll t_b \ll t_q \ll t_H$. For the sake of simplicity, the presentation will be limited to simple U-pipe or coaxial pipe configurations with two pipes connected at the bottom, one with the flow downwards (pipe 1) and one with the flow upwards (pipe 2). A straightforward extension to other borehole configurations, like double U-pipes and energy piles, is possible if certain thermal symmetries are preserved (Hermanns and Ibáñez 2017; Ibáñez and Hermanns 2018).

Inner region

The inner region encompasses the pipes and grout inside the borehole, and the ground located at radial distances to the borehole of order r_b. In the pipes, the convective transport of heat by the liquid prevails, while heat conduction takes place in the pipe walls, grout, and ground.

In the heat conduction equation to solve, the vertical heat conduction terms are of order Λ^{-2} times smaller than the radial ones, rendering them negligible. Additionally, when the characteristic heat injection time t_q is large compared to the characteristic transversal diffusion time t_b, the thermal inertia in the heat conduction equation is of order t_b/t_q times smaller than the radial heat conduction terms, rendering it also negligible. All this allows the heat conduction problem in the inner region to be interpreted as taking place in two-dimensional planes perpendicular to the borehole, only coupled to each other through the pipes and the outer region, and in which a quasi-steady two-dimensional heat conduction problem must be solved.

Far from the borehole, at large radial distances compared to r_b, the behavior of the inner and outer regions must coincide. The boundary condition to impose there, when solving the aforementioned quasi-steady two-dimensional heat conduction problem, is given by the first two terms of the asymptotic expansion of the inner solution for $r \gg r_b$ (Hermanns and Pérez 2014):

$$r \gg r_b: \quad T(r,z,t) = -\frac{q(z,t)}{2\pi k}\ln\left(\frac{r}{r_b}\right) + T_a(z,t) + o(1), \tag{1}$$

where q is the heat injection rate per unit borehole length and T_a is the apparent temperature at which the inner region perceives the ground. This temperature, whose value results from the asymptotic matching with the outer region, differs from the unperturbed ground temperature due to the presence of the borehole and its operation.

It was shown by Hermanns and Pérez (2014), that the heat injection rates per unit pipe length q_i, obtained as part of the solution to the quasi-steady heat conduction problem in the inner region, must obey the very specific mathematical structure

$$q_1 = \frac{1+S}{2}\frac{T_m - T_a}{R_b} + \frac{T_1 - T_2}{R_a}, \qquad q_2 = \frac{1-S}{2}\frac{T_m - T_a}{R_b} + \frac{T_2 - T_1}{R_a}, \tag{2}$$

where R_a and R_b are respectively the thermal resistance between the pipes and the thermal resistance between the borehole and the ground. The thermal skewness parameter S, introduced for the first time by Ibáñez and Hermanns (2018), represents how the borehole's thermal resistance R_b is distributed among the pipes. Its value lies in the range [-1,1], corresponding the extreme values to coaxial probes.

The weighted mean fluid temperature T_m, given in terms of the temperatures T_i of the liquid in the pipes by

$$T_m = \frac{T_1 + T_2}{2} - S\frac{T_1 - T_2}{2}, \tag{3}$$

was introduced for the first time by Hermanns and Pérez (2014) and represents the temperature at which the borehole exchanges heat with the ground. This interpretation can easily be inferred from adding q_1 to q_2:

$$q = q_1 + q_2 = \frac{T_m - T_a}{R_b}. \tag{4}$$

The use of T_m and S is very convenient, because several different borehole configurations can be described using the same system of equations. For instance, single U-pipes and coaxial pipes, which in the literature are treated using different sets of equations, are treated in a unified manner here.

By substituting the expressions for q_i into the energy conservation equations for the pipes, which are quasi-steady because of the characteristic residence time t_r being small compared to the characteristic heat injection time t_q, a set of ordinary differential equations for $T_1 - T_2$ and T_m can be obtained, which combined with (4) constitutes the mathematical problem to solve in the inner region. Using the nondimensional variables

$$\Delta = \frac{T_1 - T_2}{Q_c/(\dot{m}c)}, \qquad \Theta = \frac{T_m - T_{mean}}{Q_c/(kH)}, \qquad \overline{q} = \frac{q}{Q_c/H}, \qquad \Theta_a = \frac{T_a - T_{mean}}{Q_c/(kH)}, \tag{5}$$

in which Q_c is the characteristic heat injection rate, $\dot{m}$ the mass flow rate in the pipes, c the specific heat capacity of the liquid, k the thermal conductivity of the ground, and T_{mean} the mean annual temperature at the considered geographical location, the following system of differential and algebraic equations results (Hermanns and Ibáñez 2017; Ibáñez and Hermanns 2018):

$$\frac{d\Delta}{d\xi} = -\overline{q}, \qquad \frac{d\Theta}{d\xi} = \Omega S\overline{q} - \frac{\Omega^2}{A}\Delta, \qquad \Theta - \Theta_a = \overline{q}B, \tag{6}$$

where $A = kR_a$ and $B = kR_b$ are the nondimensional thermal resistances of the borehole, $\Omega = kH/(\dot{m}c)$ is a nondimensional parameter that compares the characteristic temperature difference $Q_c/(\dot{m}c)$ between the pipes with the characteristic temperature difference $Q_c/(kH)$ between the borehole and the ground located at radial distances of order $\sqrt{\alpha t_q}$, and $\xi = z/H$ is the nondimensional vertical coordinate.

The boundary conditions to impose at the top, $\xi = 0$, and bottom, $\xi = 1$, of the borehole are

$$\xi = 0: \ \Delta = f(\tau), \qquad \xi = 1: \ \Delta = 0, \tag{7}$$

being $f = Q(t)/Q_c$ the nondimensional heat injection rate and $\tau = t/t_q$ the nondimensional time.

The formulated mathematical problem requires an additional relationship between the four unknowns, Δ, Θ, $\overline{q}$, and Θ_a, to be solvable. This relationship is supplied by the outer region and its asymptotic matching with the inner region.

Outer region

Far from the borehole, at radial distances of order $\sqrt{\alpha t_q}$, the thermal inertia of the ground becomes important, and a slender borehole is perceived in first approximation as a finite line source of heat, as inferred from the behavior of the inner region far from the borehole, given in (1) (Hermanns and Pérez 2014; Ibáñez and Hermanns 2018). Thus, the unsteady outer region is in first approximation axisymmetric, and an analytical solution for the nondimensional ground temperature, $\Theta_g = \left(T_g - T_{mean}\right)/(Q_c/(kH))$, can be obtained by superposition of point sources of heat (Carslaw and Jaeger 1959):

$$\Theta_g(\xi,\eta,\tau) = \Theta_\infty(\xi,\tau) + \frac{1}{8\epsilon\pi^{3/2}}\int_0^\tau\int_0^1 \frac{\overline{q}(\xi_0,\tau_0)}{(\tau-\tau_0)^{3/2}}\left[\mathrm{e}^{-\frac{\eta^2+\frac{(\xi-\xi_0)^2}{\epsilon^2}}{4(\tau-\tau_0)}} - \mathrm{e}^{-\frac{\eta^2+\frac{(\xi+\xi_0)^2}{\epsilon^2}}{4(\tau-\tau_0)}}\right] d\xi_0 d\tau_0, \tag{8}$$

where $\eta = r/\sqrt{\alpha t_q}$, $\epsilon = \sqrt{\alpha t_q}/H$, and Θ_∞ is the nondimensional unperturbed ground temperature:

$$\Theta_\infty(\xi,\tau) = G\xi + \sum_{n=-\infty}^{\infty} \hat{T}_{sn}\mathrm{e}^{i\omega_n t_q \tau}\mathrm{e}^{-\sqrt{i\omega_n t_q}\frac{\xi}{\epsilon}}, \tag{9}$$

being $G = q_{geo}H^2/Q_c$ the nondimensional geothermal heat flux at the considered geographical location and $\hat{T}_{sn}$ the nondimensional harmonic modes, with nondimensional angular frequency $\omega_n t_q$, of the ground surface temperature oscillations with respect to the mean annual temperature T_{mean}.

Asymptotic matching

The asymptotic matching procedure states that both the inner and outer solutions are valid in an intermediate region defined by $r_b \ll r \ll \sqrt{\alpha t_q}$, or expressed in non-dimensional variables $(\epsilon\Lambda)^{-1} \ll \eta \ll 1$, in which their asymptotic expansions must coincide. The asymptotic behavior of the outer solution close to the borehole can be obtained by taking the limit $\eta \ll 1$ in (8). The resulting expression depends on the position along the borehole. Near the top and the bottom of the borehole, asymptotic boundary layers appear that must be analyzed separately. Also, the logarithmic singular behavior near the borehole must be extracted carefully before comparing with expression (1). Thus, the remaining non-logarithmic terms that appear in the outer solution near the borehole correspond to the nondimensional apparent temperature Θ_a that expressed in compact form in terms of the nondimensional heat injection rate per unit borehole length $\overline{q}$ is

$$\Theta_a = F(\xi,\tau,\overline{q}). \tag{10}$$

All the details for the cases of steady-state excitation and time-harmonic sub-annual excitation have already been completed and submitted for publication (Hermanns and Ibáñez 2017; Ibánez and Hermanns 2018) while the case of arbitrarily time-varying heat injection rate is still under development.

Solution procedure

The solution to the integro-differential problem formed by (6), (10), and the boundary conditions given in (7) is obtained through asymptotic expansions of the unknown variables in terms of the small parameter δ present in the problem (Hermanns and Ibáñez 2017; Ibáñez and Hermanns 2018):

$$\Delta = \Delta_0 + \delta\Delta_1 + o(\delta), \qquad \delta\Theta = \Theta_0 + \delta\Theta_1 + o(\delta), \qquad \bar{q} = \bar{q}_0 + \delta\bar{q}_1 + o(\delta). \tag{11}$$

The small parameter δ is proportional to $log(\epsilon\Lambda)^{-1} \ll 1$ and its exact value depends on the case studied. In this expansion, the nondimensional weighted mean fluid temperature Θ is preceded by a factor δ that is foreseen by analyzing the order of magnitude of that variable in (6) (Hermanns and Ibáñez 2017; Ibáñez and Hermanns 2018). The expansions in (11) are introduced in (6) and similar order terms are grouped to obtain simpler systems of equations to be solved for each order of the expansions. The resulting analytical expressions for Δ, Θ, and $\overline{q}$ describe the thermal response of vertical geothermal boreholes and are computationally inexpensive to evaluate.

Worth to mention that the obtained apparent temperature is not uniform along the borehole, presenting deviations of around ±20% with respect to a mean value. This result is important, as the mean azimuthal borehole wall temperature coincides in value with the apparent temperature (Hermanns and Pérez 2014), showing that the simplifying assumption introduced by the *g-function model*, that the mean azimuthal borehole wall temperature is uniform along the borehole, is not accurate.

EXTENSION TO BOREHOLE FIELDS

Although most of the work done so far has been on single boreholes, the extension to geothermal heat exchangers comprised of tens or hundreds of boreholes has already been initiated, and preliminary results for the case of a time-harmonic sub-annual excitation will be presented for the first time in this conference.

When a time-harmonic excitation is imposed at the top of the borehole, the characteristic time of variation of the heat injection rate becomes $t_q = 1/\omega$, where ω is the angular frequency of the oscillation. The total heat injection rate can then be expressed as $Q(\tau) = \mathrm{Re}\left[\hat{Q}e^{i\tau}\right]$. Consequently, all variables can be expressed as harmonic functions,

$$\Delta(\xi,\tau) = \mathrm{Re}\left[\widehat{\Delta}(\xi)\, e^{i\tau}\right], \qquad \Theta(\xi,\tau) = \mathrm{Re}\left[\widehat{\Theta}(\xi)\, e^{i\tau}\right], \qquad \bar{q}(\xi,\tau) = \mathrm{Re}\left[\hat{q}(\xi)\, e^{i\tau}\right], \tag{12}$$

and only the complex-valued harmonic modes $\widehat{\Delta}$, $\widehat{\Theta}$, and $\hat{q}$ need to be obtained. These complex values, that are functions of the nondimensional vertical coordinate ξ, include information of the amplitude of the oscillation as well as of the phase difference with respect to the total heat injection rate at any section of the borehole. A system of equations equivalent to (6) must be solved now for each borehole, and additional conditions fix the total heat injection rate Q transferred to the ground by the N_b boreholes and the common inlet temperature of the boreholes. The apparent temperature of each borehole contains now $N_b - 1$ new terms which correspond to the temperature perturbations exerted by the remaining boreholes. These contributions are obtained by setting $\eta = B_{ij}/\sqrt{\alpha t_q}$ in (8), where B_{ij} is the distance between the borehole and the remaining boreholes. Finally, the solution of the problem is obtained by expanding $\widehat{\Delta}$, $\widehat{\Theta}$, and $\hat{q}$ in terms of a set of N_b small parameters as in (11). Details of the solution procedure and the resulting expansions can be found in Hermanns and Ibáñez (2018b).

A first implementation of the developed model in a computer program shows that the solution to a geothermal heat exchanger comprised of 100 boreholes can be obtained in 30 milliseconds using a single CPU core on an Intel Core i7-7700K PC. Thus, the advantage of having analytical expressions for the thermal response of geothermal heat exchangers is that they can be used for the analysis of heterogeneous borehole fields with irregular placement of the boreholes without requiring the excessive computational cost of SBM or the loss in accuracy of the *g-function model*.

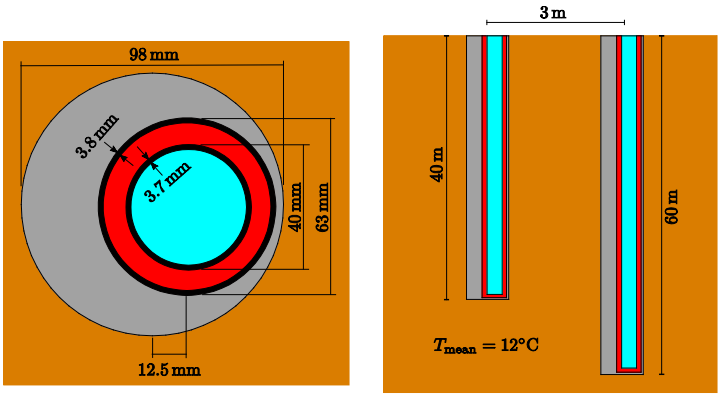

Ground (Granite)	Conductivity	3.7 W/(m K)
	Diffusivity	$1.5 \cdot 10^{-6}$ m^2/s
Grout	Conductivity	2.2 W/(m K)
	Diffusivity	$6.79 \cdot 10^{-7}$ m^2/s
Liquid	Density	997.2 kg/m^3
	Specific heat capacity	4180 J/(kg K)
	Conductivity	0.608 W/(m K)
	Dynamic viscosity	$8.9 \cdot 10^{-4}$ kg/(m s)
	Mass flow rate (per borehole)	0.168 kg/s
Pipes	Conductivity	0.42 W/(m K)

Figure 1 Diagram of the configuration used for the comparison of the derived asymptotic model with three existing models. (Left) Cross section of the coaxial borehole. The liquid flows downwards through the pipe shown in red and upwards through the pipe shown in cyan. The grout is shown in grey and the ground in brown. (Middle) Longitudinal section of the borehole field. Borehole 1 is at left and Borehole 2 is at right. (Right) Table of properties of the different materials used in the simulation.

COMPARISON WITH EXISTING MODELS

To assess the accuracy of the derived asymptotic expressions, comparisons with three existing models with different levels of accuracy are carried out. The first and most accurate model is a detailed numerical simulation (DNS) of the governing equations using a commercial finite-element simulation tool. The second model is the *Superposition Borehole Model* (SBM) developed by Eskilson and Claesson (Eskilson 1986; Eskilson and Claesson 1988). Since the original implementation is not meant for steady-state or time-harmonic excitations, a reimplementation of the method has been performed (Hermanns and Ibáñez 2017; Ibáñez and Hermanns 2018). The third model is the *g-function model* proposed by Eskilson (Eskilson 1987). For the steady-state case, the *g-functions* have been taken from the literature (Eskilson 1987; Zeng, et al. 2003; Conti 2016), while for the other regimes they have been computed using the reimplemented SBM and following the specifications given in the literature (Eskilson 1987; Eskilson and Claesson 1988; Hellström 1991; Blomberg, et al. 2017). The *g-function* solution has been implemented using an equally-spaced discretization with 20 segments along the boreholes, as in Cimmino and Bernier (2014).

The results from all the comparisons performed so far can be found in the work submitted for publication (Hermanns and Ibáñez 2017; Ibáñez and Hermanns 2018). Here, some preliminary results are shown for the time-harmonic sub-annual excitation of a geothermal heat exchanger comprised by two parallel coaxial boreholes of different lengths. Figure 1 contains a diagram of the borehole field studied as well as a table including the properties of all materials involved in the simulation. A total heat injection rate of modulus $\left|\widehat{Q}\right| = 2100$ W and period of one year (365.25 days) is distributed among the boreholes through which a mass flow rate of $\dot{m} = 0.168$ kg/s per borehole is supplied.

Figure 2 shows the modulus and argument of the complex-valued harmonic modes $\widehat{\Delta}$, $\widehat{\Theta}$, and $\widehat{q}$ for each of the two boreholes as functions of $\xi = z/\overline{H}$, where $\overline{H} = 50$ m is the mean depth of the boreholes. The modulus of each harmonic mode is a measure of the maximum value attained as it oscillates. On the other hand, the argument of each harmonic mode is a measure of the difference in phase that appears between that variable and the total heat injection rate.

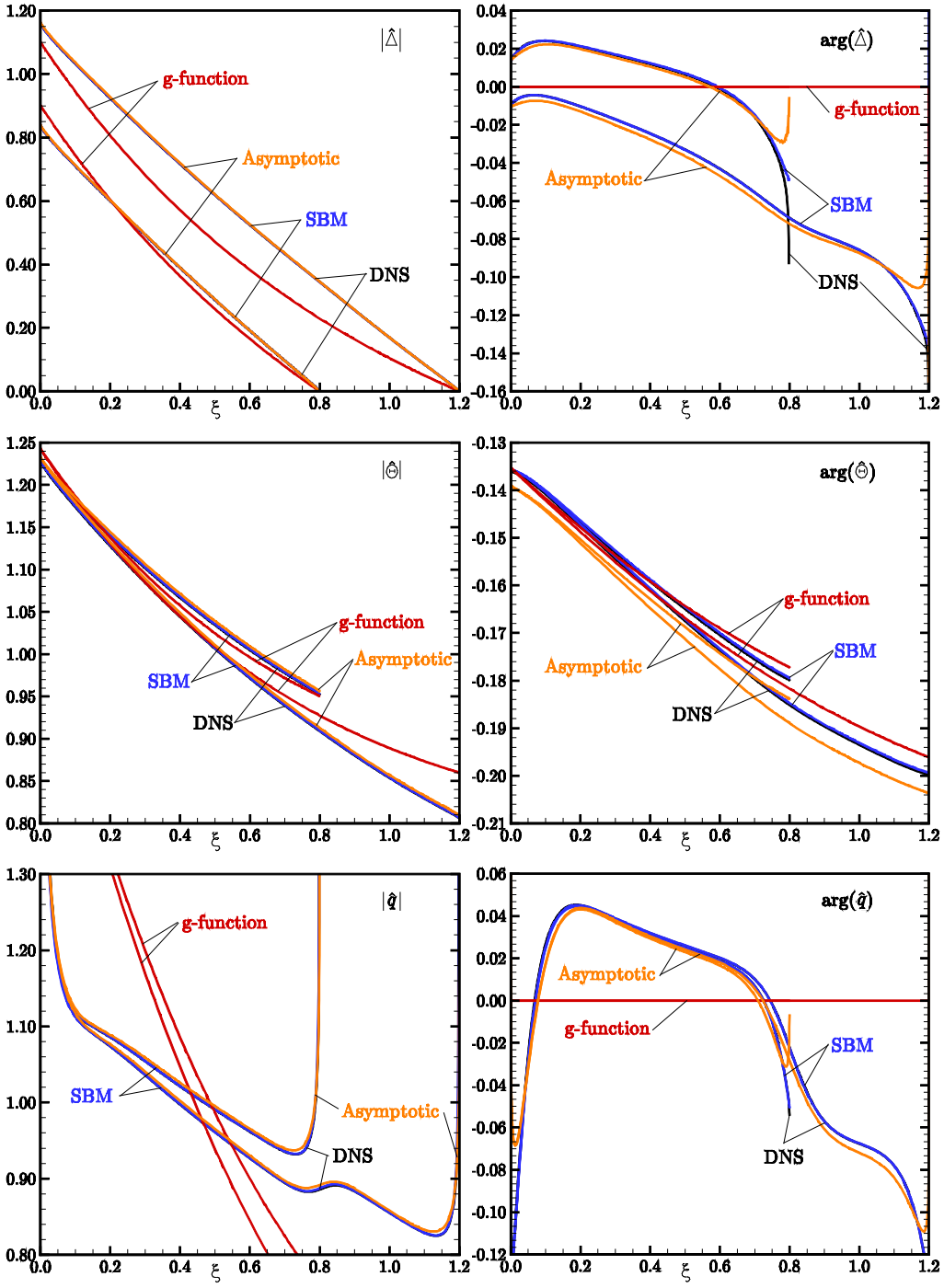

Figure 2 Time-harmonic thermal response of a geothermal heat exchanger, comprised of two heterogeneous coaxial boreholes with nondimensional depths h equal to 0.8 and 1.2, to a time-harmonic heat injection rate with a one-year period. (Left) modulus and (right) argument of the (top) nondimensional temperature difference $\widehat{\Delta}$, (middle) nondimensional weighted mean temperature $\widehat{\Theta}$, and (bottom) nondimensional heat injection rate per unit borehole length $\hat{q}$ of the two boreholes as functions of the nondimensional axial coordinate ξ and for the considered models.

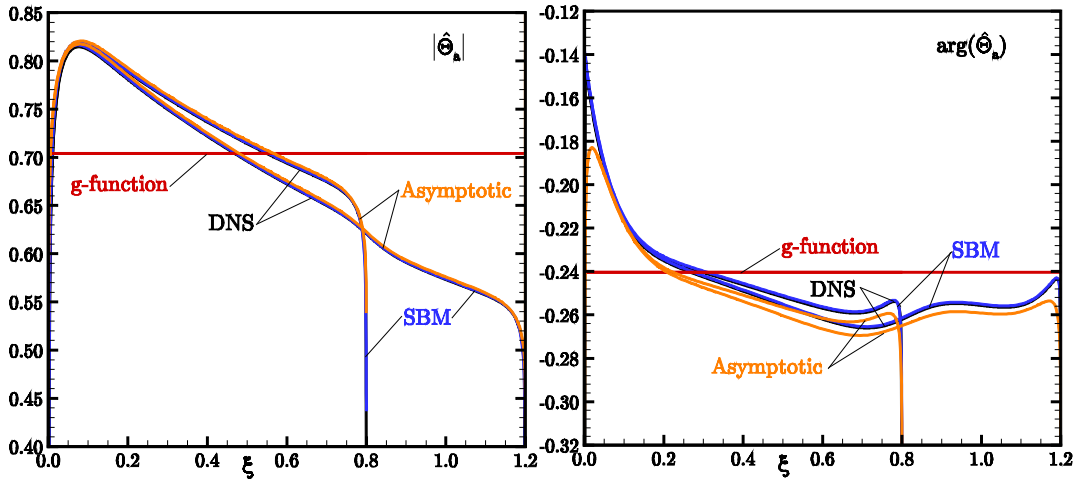

Figure 3 Time-harmonic thermal response of a geothermal heat exchanger, comprised of two heterogeneous coaxial boreholes with nondimensional depths h equal to 0.8 and 1.2, to a time-harmonic heat injection rate with a one-year period. (Left) modulus and (right) argument of the nondimensional apparent temperature $\widehat{\Theta}_a$ of the two boreholes as functions of the nondimensional axial coordinate ξ and for the considered models.

While the developed asymptotic model, SBM, and DNS present small differences, the *g-function model* is unable to correctly represent the temperature and heat injection rate distributions along the boreholes. The *g-function model* predicts a uniform zero value of the argument of both $\widehat{\Delta}$ and $\widehat{\Theta}$ while the remaining models display notable axial variations and non-zero mean values of those variables. The most noticeable discrepancies between the *g-function model* and the remaining models arise in the modulus of the nondimensional heat injection rate per unit borehole $\hat{q}$. In a small region near the top and the bottom of each borehole, the nondimensional heat injection rate per unit borehole $\hat{q}$ increases abruptly (Hermanns and Ibáñez 2017). These regions, which coincide with the asymptotic boundary layers mentioned before, are correctly represented by all models except the *g-function* one.

Figure 3 shows the nondimensional apparent temperature $\widehat{\Theta}_a$ for the same configuration. The developed asymptotic model, SBM, and DNS deliver very similar results, with deviations of up to ±23% with respect to a mean value. These results confirm that neither the nondimensional apparent temperature $\widehat{\Theta}_a$ on Figure 3, nor the nondimensional heat injection rate per unit borehole length $\hat{q}$ on Figure 2, are uniform along the borehole. Hence, the simplifying assumptions made by Eskilson's definition of the *g-function* (uniform mean azimuthal borehole wall temperature) and the alternative definition found in the literature (uniform heat injection rate per unit borehole length) are not justified by the physics of the problem.

CONCLUSIONS AND FUTURE WORK

By means of scale analysis and matched asymptotic expansion techniques, a new approach for the modeling of the thermal response of geothermal heat exchangers was initiated in 2011. A first publication, whose main focus was the asymptotic matching process and the structure of the solution to the quasi-steady heat conduction problem in the inner region, was published in 2014 (Hermanns and Pérez 2014), followed by a recent extension of that analysis to the steady-state thermal response of complete boreholes (Ibáñez and Hermanns 2018). Further work related to the time-harmonic thermal response of single boreholes (Hermanns and Ibáñez 2017) and its extension to whole borehole fields (Hermanns and Ibáñez 2018b) is in reviewing process at the moment. Also, a critical analysis of the *g-function model* and its different versions was recently sent for publication (Hermanns and Ibáñez 2018). In it, a mathematical explanation is given to the ill-posedness that appears in the original definition of the *g-function model* when no initial insulated length is used.

Still in the present year, the analysis of the thermal response of single boreholes to arbitrarily time-varying heat injection rates will be finished and sent for publication. Then, in the next year, the case in which the characteristic heat injection time t_q is comparable to the characteristic transversal diffusion time t_b will be addressed. This regime of operation is relevant for peak loads, in which the inner region is unsteady. The same applies to the flow in the pipes in case the characteristic heat injection time t_q is comparable to the characteristic residence time t_r. Also, the extension to borehole fields of the thermal response to arbitrarily time-varying heat injection rates will be performed.

The outcome of all this work will ultimately be a coherent theoretical framework for the thermal response of geothermal heat exchangers with irregularly placed heterogeneous boreholes, in which extensions such as stratified grounds, time-varying mass flow rates, and groundwater flow will be possible, and whose reduced computational cost will allow the implementation of automatic optimization strategies at borehole field level.

ACKNOWLEDGMENTS

Work was funded by the Spanish *Ministerio de Economía y Competitividad* through project ENE2015-68703-C2-2-R.

REFERENCES

Bennet, J., J. Claesson and G. Hellström. 1987. *Multipole method to compute the conductive heat flows to and between pipes in a composite cylinder*. Technical report of the Lund Institute of Technology. Lund, Sweden.

Blomberg, T., J. Claesson, P. Eskilson, G. Hellström and B. Sanner. 2017. EED – Earth Energy Designer 4.17. BLOCON. Lund, Sweden.

Carslaw, H. and J. Jaeger. 1959. Conduction of Heat in Solids. Oxford, UK: Oxford University Press.

Cimmino M. and Bernier M., 2014. *A semi-analytical method to generate g-functions for geothermal bore fields*, International Journal of Heat and Mass Transfer, 70: 641-650.

Cimmino M., Bernier M. and Adams F. 2013. *A contribution towards the determination of g-functions using the finite line source*. Applied Thermal Engineering, 51: 401-412.

Claesson, J. and G. Hellström. 2011. *Multipole method to calculate borehole thermal resistances in a borehole heat exchanger*. HVAC&R Research 17: 895-911.

Claesson J. and Javed S. 2011. *An analytical method to calculate borehole fluid temperatures for time-scales from minutes to decades*. ASHRAE Transactions. 117: 279-288.

Conti P. 2016. *Dimensionless maps for the validity of analytical ground heat transfer models for GSHP applications*. Energies. 9: 890.

Eskilson, P. 1986. *Superposition Borehole Model, Manual for Computer Code*. Technical report of the University of Lund. Lund, Sweden.

Eskilson, P. 1987. *Analysis of Heat Extraction Boreholes*. PhD Thesis at Lund Institute of Technology. Lund, Sweden.

Eskilson, P. and J. Claesson. 1988. *Simulation model for thermally interacting heat extraction boreholes*. Numerical Heat Transfer 13: 149-165.

Hellström, G. 1991. *Ground Heat Storage: Thermal Analyses of Duct Storage Systems, I. Theory*. PhD Thesis at Lund Institute of Technology. Lund, Sweden.

Hermanns, M. and J.M. Pérez. 2014. *Asymptotic analysis of vertical geothermal boreholes in the limit of slowly varying heat injection rates*. SIAM Journal on Applied Mathematics 74: 60-82.

Hermanns, M. and S. Ibáñez. 2017. *Thermal response of slender geothermal boreholes to sub-annual harmonic excitations*. Submitted to SIAM Journal on Applied Mathematics.

Hermanns, M. and S. Ibáñez. 2018. *On the ill-posedness of the g-function model for the thermal response of geothermal heat exchangers*. Submitted to International Journal of Thermal Sciences.

Hermanns, M. and S. Ibáñez 2018b. *Thermal response of geothermal heat exchangers to sub-annual harmonic excitations*. Submitted to SIAM Journal on Applied Mathematics.

Ibáñez, S. and M. Hermanns. 2018. *On the steady-state thermal response of slender geothermal boreholes*, SIAM Journal on Applied Mathematics 78: 1658-1681.

Ingersoll L. R., O. J. Zobel, A. C. Ingersoll. 1954. Heat conduction with engineering, geological, and other applications. New York, USA: McGraw-Hill.

Lagerstrom, P.A. 1988. Matched asymptotic expansions: ideas and techniques. New York, USA: Springer-Verlag.

Lamarche L. 2017. *g-function generation using a piecewise-linear profile applied to ground heat exchangers*. International Journal of Heat and Mass Transfer 115: 354-360.

Lamarche L. and B. Beauchamp. 2007. *A new contribution to the finite line-source model for geothermal boreholes*. Energy and Buildings. 39: 188-198.

Lazzarotto A. and F. Björk. 2016. *A methodology for the calculation of response functions for geothermal fields with arbitrarily oriented boreholes -part 2*. Renewable Energy 86: 1353-1361.

Li M. and C. K. Lai. 2015. *Review of analytical models for heat transfer by vertical ground heat exchangers (GHEs): A perspective of time and space scales*. Applied Energy. 151: 178-191.

Malayappan V. and J. D. Spitler. 2013. *Limitations of using uniform heat flux assumptions in sizing vertical borehole heat exchanger fields*. Proceedings of the Clima 2013 World Conference.

Monzó P., P. Mogensen, J. Acuña, F. Ruiz-Calvo and C. Montagud. 2016. *A novel numerical approach for imposing a temperature boundary condition at the borehole wall in borehole fields*. Geothermics. 56: 35-44.

Philippe M., M. Bernier and D. Marchio. 2009. *Validity ranges of three analytical solutions to heat transfer in the vicinity of single boreholes*. Geothermics 38: 407-413.

Zeng H., N. Diao and Z. Fang. 2002. *A finite line-source model for boreholes in geothermal heat exchangers*. Heat Transf Asian Res 31: 558–67.

Zeng, H., N. Diao and Z. Fang. 2003. *Heat transfer analysis of boreholes in vertical ground heat exchangers*. International Journal of Heat and Mass Transfer 46: 4467-4481.

[This page has been intentionally left blank]

IGSHPA SWEDEN
2018 Research Conference

DOI: 10.22488/okstate.18.000028

Field Performance of a District Central Ground Source Heat Pump System in the US

Piljae Im, PhD **Xiaobing Liu, PhD** **Hugh Henderson**

ABSTRACT

This case study discusses the field performance of a district central ground source heat pump (GSHP) system installed at Ball State University (BSU) in Muncie, IN., USA. This district GSHP system replaces the existing central steam plant and water-cooled chiller plants and designed to serve 47 major buildings in BSU. The field performance of the GSHP system was analyzed based on measured data from August 2015 through July 2016, construction drawings, maintenance records, personal communications, and construction costs. It was compared with the performance of a baseline scenario— a conventional water-cooled chiller and natural-gas-fired boiler system, both of which meet the minimum energy efficiencies allowed by the American Society of Heating, Refrigerating and Air-Conditioning Engineers (ASHRAE 90.1-2013). The comparison was made to determine source energy savings, energy cost savings, and CO_2 emission reductions achieved by the GSHP system. This paper presents the results of the analysis, the lessons learned, and recommendations for improvement in the operation of this district central GSHP system.

INTRODUCTION

High initial costs and a lack of public awareness about ground source heat pump (GSHP) technology are the two major barriers preventing rapid deployment of this energy-saving technology in the United States (Hughes 2008). To tackle these barriers, 26 GSHP projects were competitively selected by the US Department of Energy in 2009 and awarded grants funded by the American Recovery and Reinvestment Act to demonstrate the benefits of GSHP systems and innovative technologies for cost reduction and/or performance improvement. A district central GSHP system that ultimately would replace the existing coal-fired steam boilers and conventional water-cooled chillers on the campus of Ball State University (BSU) in Muncie, IN was one of the 26 selected demonstration projects. This case study evaluates the performance of the demonstrated district central GSHP system based on measured performance data, utility bills, and other relevant information. The evaluated performance metrics include the energy efficiency of the overall GSHP system, electricity usage of all major equipment of the GSHP system, and the achieved benefits (e.g., energy and cost savings) compared with a new conventional HVAC system. This case study also identifies opportunities for improving the operational efficiency of the system.

SITE DESCRIPTION

Prior to implementing the district GSHP system, 47 major buildings in BSU were served by a central steam plant with 4 coal-fired and 3 natural gas-fired steam boilers. Cooling was provided by 5 water-cooled centrifugal chillers at the District Energy Station South (DESS). Faced with the need to eliminate the coal-fired boilers and aging chillers, BSU considered several options, including circulating fluidized bed coal boilers and improved stack controls.

Piljae Im (imp1@ornl.gov) and Xiaobing Liu (liux2@ornl.gov) are R&D Staff at the Oak Ridge National Laboratory in the US. Hugh Henderson is Vice President of Frontier Energy, Inc. (formerly CDH Energy).

Finally, a geothermal system with heat recovery (HR) chillers was selected to meet the simultaneous heating and cooling needs in the campus. Although the district GSHP system has a cost premium compared to other options, it has higher energy savings potential. It was one of major reasons for the final selection.

The implementation of the GSHP system was taken in two phases. Phase 1 included constructing a geothermal field with 1,803 vertical boreholes, as well as a new District Energy Station at the North side of the campus (referred as DESN). This energy station includes two new 2,500 ton two-stage HR chillers connected to the phase 1 geothermal fields (Figure 1). These chillers can simultaneously produce chilled water (at 42°F or 5.6°C) and hot water up to 150°F (65.6°C). In Phase 2, the existing conventional chillers in DESS were replaced with other two 2,500 ton (8,750 kW_clg) two-stage HR chillers. These chillers are connected to the phase 2 geothermal fields at the south end of the campus. This case study focuses on evaluating the field performance of the GSHP system implemented in phase 1. Buildings in the BSU campus were retrofitted and connected to the district GSHP system gradually over several years. As more buildings were connected to the GSHP system, the heating and cooling loads imposed on DESN increased from year to year. Control and operation of the GSHP systems has been adjusted by the facility operators to improve the performance of the GSHP system.

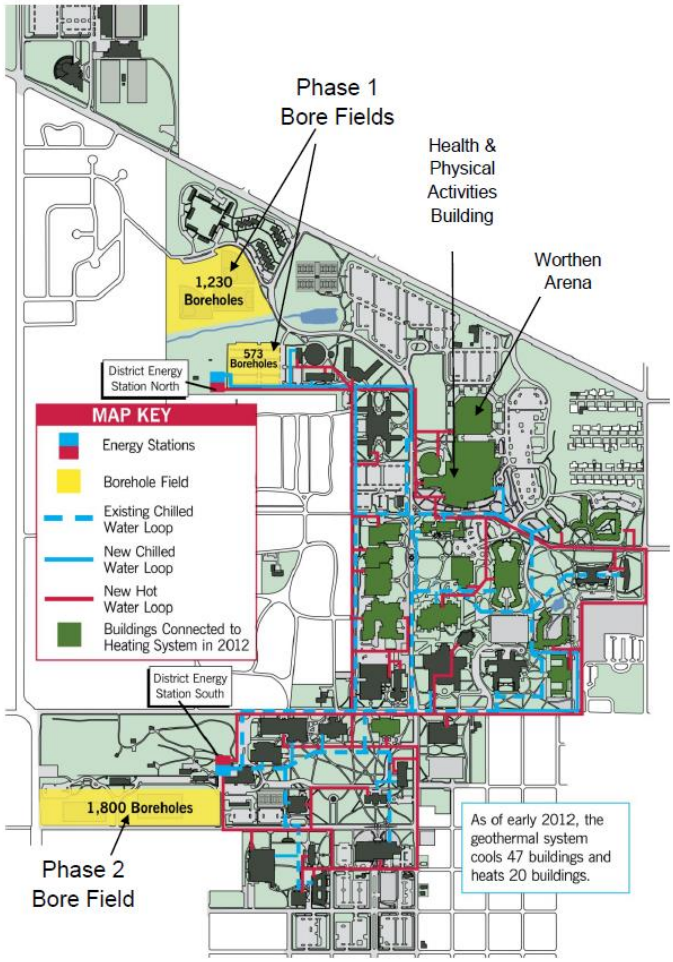

Figure 1. Ball State University campus map showing the energy stations, chilled water and hot water loops, and geothermal borehole fields in Phase 1 and Phase 2 of the district central GSHP system. As shown in this map is the buildings connected to the GSHP system in 2012.

GSHP System Description

The district GHP system implemented in phase 1 includes two geothermal borehole fields, two HR chillers, three water loops, and a new campus-wide control and monitoring system. All the chillers and pumps are installed in a new building (DESN). Chilled water and hot water are produced by the HP chillers and distributed to buildings in the campus through a chilled water (CHW) loop and a hot water (HW) loop. As of May 2106, 47 buildings are connected to the CHW loop and 30 buildings are connected to the HW loop. Note that there were only 20 buildings connected to the HW loop in 2012. Expansion of the HW loop to serve more buildings is still ongoing.

Geothermal Borehole Fields. Two geothermal borehole fields were constructed during Phase 1 as shown in Figure 1. One borehole field includes 1,230 bores and the other has 573 bores. Each bore is 400 ft (122 m) deep and the bores are spaced by 15 ft (4.6 m) between centers. Two 1-inch diameter high density polyethylene (HDPE) U-shape loops filled with water are inserted into each bore, which is then grouted with a mixture of sand, bentonite, and water. All the HDPE pipes are routed into DESN through 5 major circuits that are buried 5 ft (1.5 m). under the ground. An in-situ ground thermal conductivity test was performed in a borehole at the site. The test result indicated that the effective ground thermal conductivity at the test site is about 1.68 Btu-hr^{-1}-ft^{-1}-F^{-1} (2.9 W-m^{-1}-K^{-1}), and the undisturbed ground temperature is about 56°F (13.3°C).

Heat Recovery Chillers. Two 2,500-ton (8,750 kW_clg) HR chillers (CH #1 and CH #2) are installed in DESN. Figure 2 shows the schematic of the two HR chillers with the associated control valves and pumps. During typical operation, CH #1 is run to produce both HW and CHW. If the HW load is smaller than the available heating capacity, then the HW return temperature starts to rise above the desired set point. The HW return is then directed to the geothermal field (referred as ground loop hereinafter), and water retuning from ground loop is directed back to the condenser of the chiller. This is achieved by opening valves CV-LFW-01 and CV-LFW-03, which connect the ground loop to the condenser side of the chiller. Then control valves CV-CW-01 and CV-CW-03 (for chiller #1 or CV-CW-05 and CV-CW-07 for chiller #2) modulate in opposite directions to control the HW return temperature (back to the condenser side of the chiller) at the desired temperature (the set point was 106°F or 41.1°C). As the second stage of control, the circulation pumps for the ground loop are staged to maintain HW return temperature at the desired set point. On the other hand, when cooling load is too small, resulting the CHW return temperature drops below a set point, valves CV-LFW-02 and CV-LFW-04 are opened to allow some returned CHW going through the ground loop and then mixing with other returned CHW. These valves are cycled ON and OFF to increase the CHW return temperature.

Besides, there are other four chillers in the South Plant (DESS)—two HR chillers (CH #3, and CH #4) are connected to the phase 2 geothermal borehole fields; and two conventional centrifugal chillers (CH #5, and CH#6) are connected to a cooling tower. The six chillers in DESN and DESS are staged to meet the cooling demands in the campus. The two chillers in DESN are used at first stage1. When the cooling demand is larger than the capacity of CH #1 and CH #2, other chillers will be added on following the sequence of CH#3, CH#4, CH#5 and CH#6.

Pumps. There are three sets of pumps in DESN and each is used for the ground loop, CHW loop, and HW loop, respectively. In addition, the condenser and evaporator sides of each chiller, as well as the cooling tower, have their own dedicated (primary) pumps. Three 350 HP pumps are connected parallelly to distribute CHW throughout the campus, and similarly, three 300 HP pumps are used to distribute HW. When the HW or CHW produced by the chiller excesses the demand, it is circulated through the geothermal borehole field with three in parallelly connected pumps (250 HP each). The dedicated pumps used in condenser and evaporator sides of each chiller, as well as the cooling tower, all have 125 HP power. Each building has its own internal water loops and (tertiary) pumps to extract CHW and CW from the main campus-wide CHW and CW loop and return it back to the main loop. The tertiary pumps are controlled to maintain a pre-defined temperature difference across the building's internal water loop.

[1] Measured data showed that there was not any occasion that both CH#1 and CH#2 were operated at the same time. While CH #1 ran most time, CH #2 only ran sporadically.

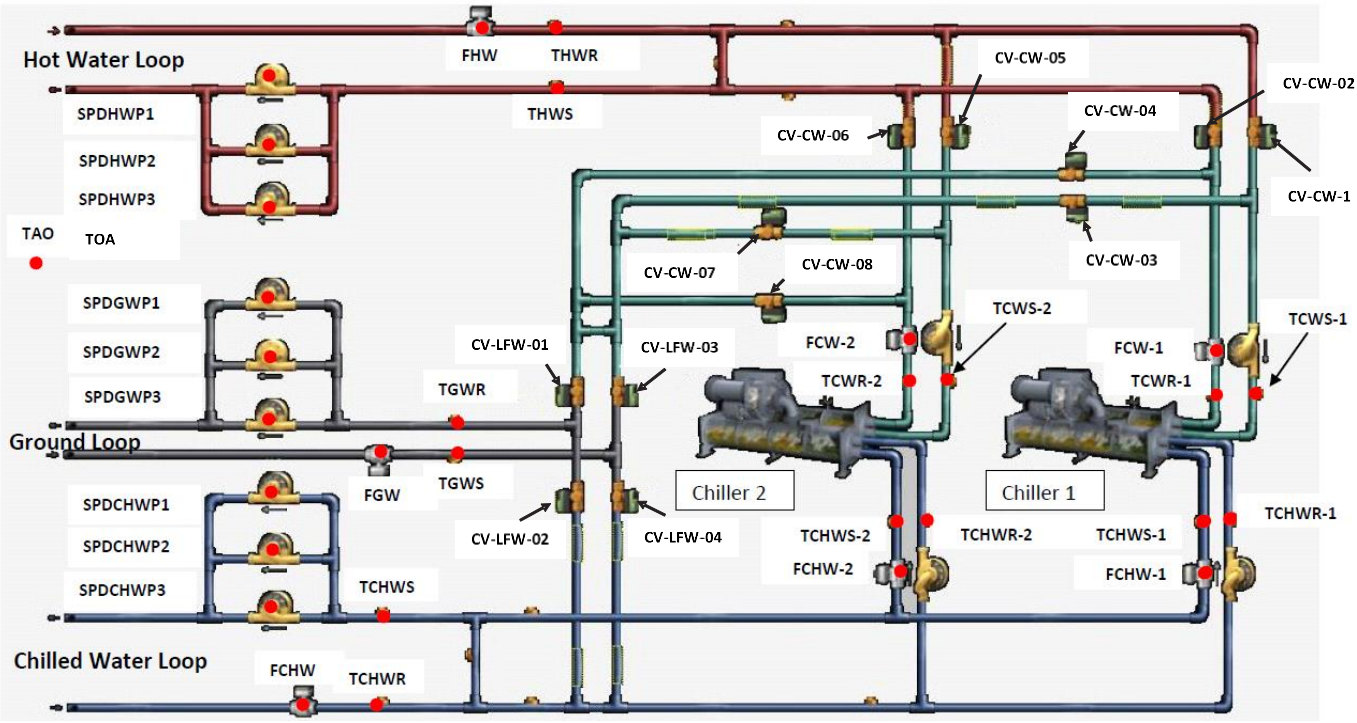

Figure 2. The schematic of the central GSHP system in DESN shown in BSU's Building Energy Management system (red dots indicating measured data)

Brief explanation of the acronyms used in the above schematic is given in following table:

CV	Control valve	CW	Condenser water
FCHW	Chilled water flow rate	FHW	Hot water flow rate
FGW	Ground loop flow rate	TCHWR	Chilled water return temperature
TCHWS	Chilled water supply temperature	THWR	Hot water return temperature
THWS	Hot water supply temperature	TGWR	Ground loop return temperature
TGWS	Ground loop supply temperature	SPDCHWP	single speed chilled water pump
SPDHWP	single speed hot water pump	SPDGWP	single speed ground loop pump

Supplemental Heat Rejection. A fluid cooler (a wet cooling tower – not shown in Figure 2) was added to the ground loop in the spring of 2015 to reduce the excessively high ground loop temperatures experienced in the first a few years of operation.

DATA ANAYLSIS RESULTS

Ground Loop Temperatures

Error! Reference source not found. shows the monthly average supply and return temperatures of the geothermal borehole field (ground loop temperatures) and monthly average outdoor air temperature from August 2015 through July 2016. As shown in this figure, the difference between the monthly average supply and return temperatures during summer and winter ranged within 5-7ºF (3-4ºC) and 2-4ºF (1-2ºC), respectively. The ground loop temperatures in this period is lower than that one year ago (see **Error! Reference source not found.**). For example,

the monthly average ground loop supply temperature during 2014-2015 was 89 to 101°F (32 to 38°C), while it ranged from 82 to 95°F (28 to 35°F) in 2015-2016. The decrease of the ground loop supply temperature is thought to be due to following reasons: (1) supplemental heat rejection through the fluid cooler, which was added to the ground loop in April 2015[2]; and (2) more heating load in 2015-2016 as more buildings were connected to the campus-wide HW loop (see discussion in Heating and Cooling Outputs). The high ground loop temperature led to high heating efficiency of the HR chiller in winter but resulted in poor cooling efficiency in summer. Low heating loads and the sub-optimal operation of the HR chillers are thought to be the main reason of the high ground loop temperature. While the central GSHP system provided chilled water to most buildings in the campus, it took several phases to retrofit the existing heating systems in these buildings. As a result, the current heating load is lower than that when all the heating systems are retrofitted.

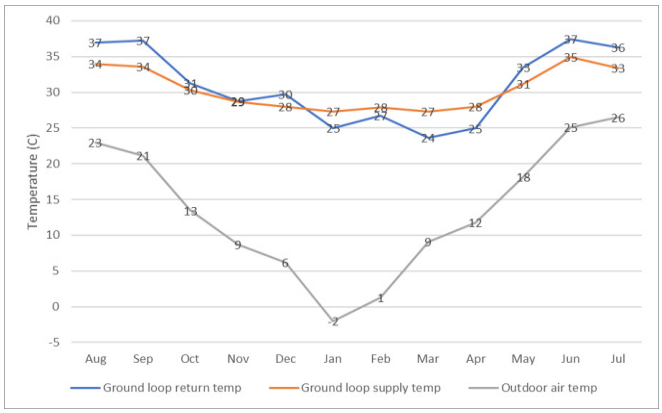

Figure 3. Monthly ground loop supply and return water temperatures at DESN and the outdoor air temperature (August 2015 through July 2016)

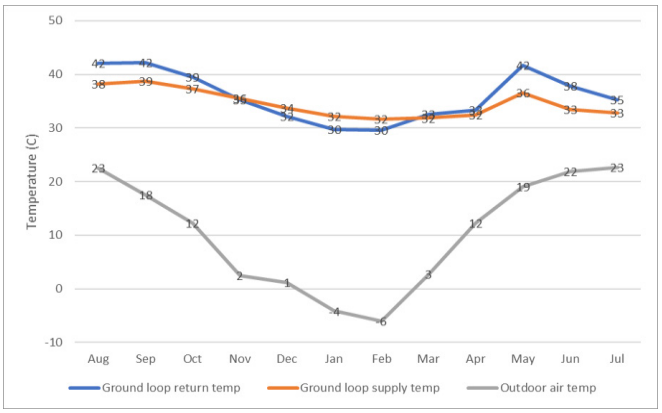

Figure 4. Monthly ground loop supply and return water temperatures at DESN and the outdoor air temperature (Previous year: August 2014 through July 2015)

Heating and Cooling Outputs

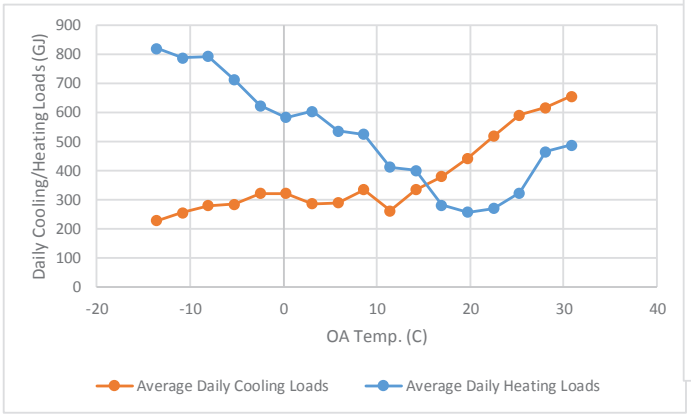

(a)

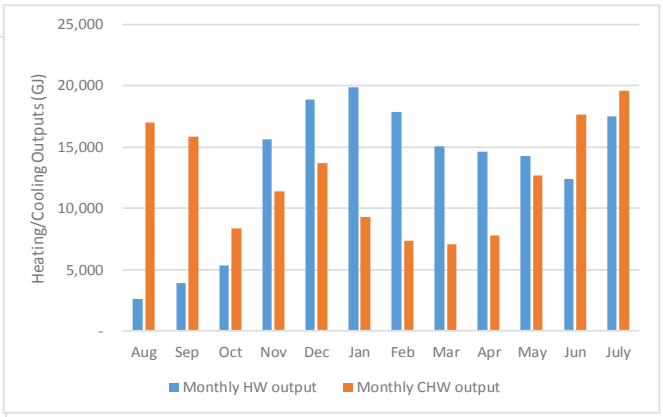

(b)

Figure 5 (a) shows the average daily heating and cooling energy provided by the GSHP system in DESN to the campus-wide CHW and HW loops. Each data point in this figure is the average of daily heating or cooling outputs

[2] Performance data of the fluid cooler were not measured, and the impact of the fluid cooer cannot be quantified.

when the associated daily average outdoor air temperature is within a specific 5°F (2.8°C) bin (e.g., from 40-45°F or 4-7°C). The year-round cooling demands are due to high internal heat gains, which are typical in university buildings. The year-round heating demands are due to domestic hot water (DHW) preheating and reheating needs in variable air volume (VAV) HVAC systems, which are used in many buildings in the campus. Further investigation (Fig. 5b) reveals that the new GSHP system in DESN provided most HW to the campus in the summer of 2016 while it was the existing boilers in DESS that provided most HW in the summer of 2015. It resulted in an increase in the average daily heating loads when OA temperature was higher than 20°C as shown in Fig. 5(a). The total heating and cooling energy provided by the HR chillers in DESN was 149,738 MMBtu (157,988 GJ) and 140,032 MMBtu (147,747 GJ), respectively. During the same period in previous years (August 2014 through July 2015), the total heating and cooling energy was 79,124 MMBtu (83,483 GJ) and 108,065 MMBtu (114,019 GJ), respectively. It shows that there was a significant increase (i.e., about 89%) in heating demand in 2015-2016.

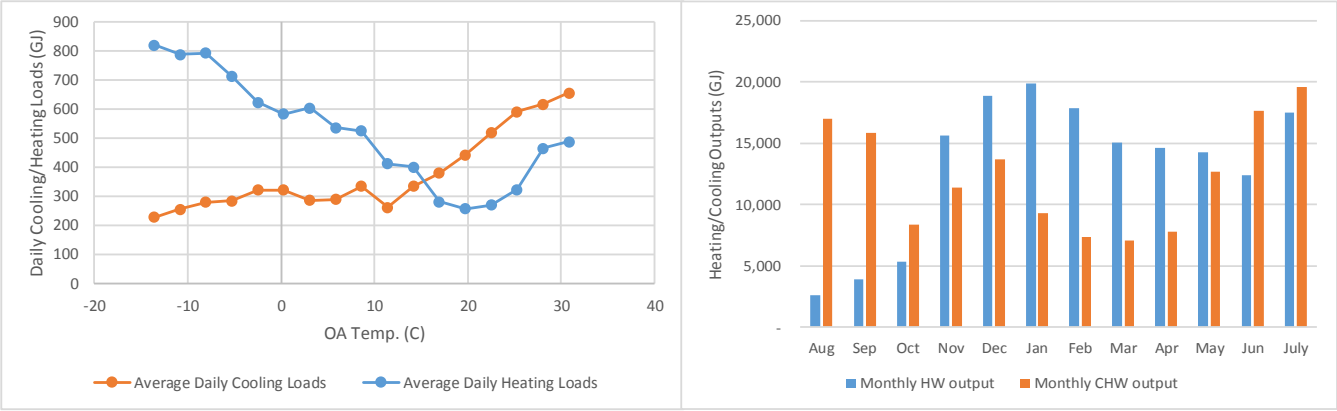

(a) (b)

Figure 5. Heating and cooling outputs: (a)average daily at various outdoor air temperatures; and (b) monthly total

While the heating and cooling demands were balanced in 2015-2016, it was not the case for the heat extracted from and rejected to the ground. The annual heat rejection to and extraction from the ground were 71,684 MMBtu (75,633 GJ) and 16,120 MMBtu (17,008 GJ), respectively. The heat rejection to the ground is only about 52% of the total cooling outputs, and the heat extracted from the ground is only about 11% of the total heating output. Based on the heat balance of the chiller, the heat recovered from the condenser of the chiller (Q_HR) can be calculated with following Equation (1).

$$Q\_HR = Q\_clg + Q\_clg/COP - Q\_rej\_GL \quad (1)$$

where, Q_HR is the heat recovered from the condenser of the chiller when it produces chilled water; Q_clg is the cooling output of the chiller; COP is the chiller cooling efficiency expressed as Coefficient of Performance[3]; and Q_rej_GL is the heat rejected to the ground loop

The calculated annual Q_HR is 116,635 MMBtu (123,061 GJ), which is about 78% of the annual heating output to the HW loop. While it is an expected benefit of the HR chiller, it may not be the optimal operation for the

[3] According to the HR chillers' catalog data, when it produces both 42°F (5.6°C) chilled water (from evaporator) and 125°F (51.7°C) hot water (from condenser), the cooling COP is 2.9.

GSHP system. Since a large portion of the heating output is from the recovered heat at the condenser, the GSHP system did not extract much heat from the ground. As a result, the heat rejected to and extracted from the ground is significantly unbalanced even with the relatively balanced heating and cooling demands from the buildings. The significantly unbalanced thermal load of the ground is one of the reasons for the high ground loop temperature.

Power Consumption

Chillers' power consumption was measured continuously starting in August 2015. To verify the quality of the measured power consumption and other performance data of the chillers, the measured monthly chiller power consumption was compared with that calculated with other measured performance data using a heat balance equation (equations 2 and 3), and the analysis shows a close match between the calculated and the measured monthly chiller power consumption. It indicates good quality of the measured performance data.

$$WCH1 = (Q\_CW\_1 - Q\_CHW\_1) \quad (2)$$

$$WCH2 = (Q\_CW\_2 - Q\_CHW\_2) \quad (3)$$

where, WCH1 and WCH2 are the monthly power consumptions (in kWh) of chiller #1 and #2, respectively; Q_CW_1 and Q_CW_2 are the monthly condensing heat (in kWh) of chiller #1 and #2, respectively; and Q_CHW_1 and Q_CHW_2 are the monthly cooling outputs (in kWh) at the evaporator of chiller #1 and #2, respectively.

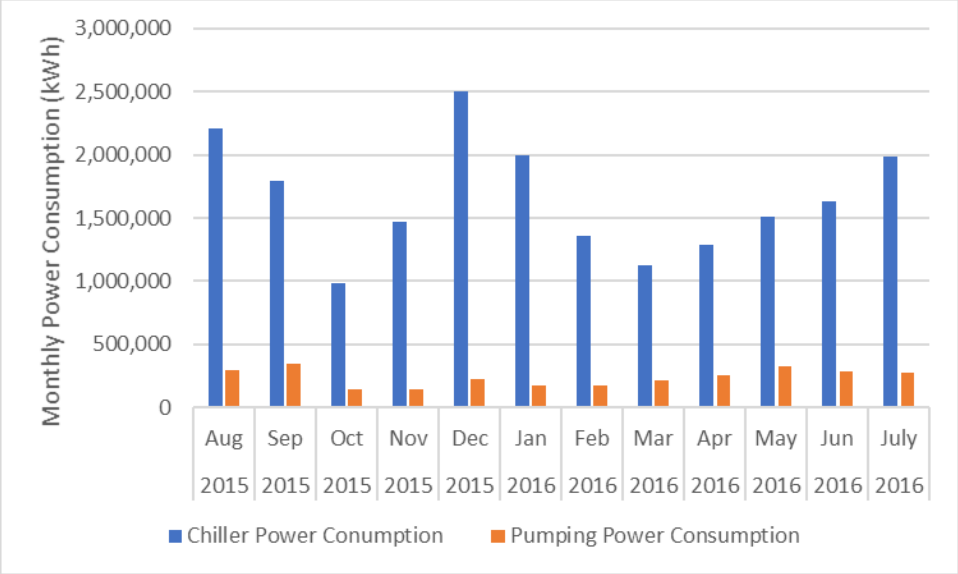

Figure 6. Monthly chiller power and pump consumption

Figure 6 shows the monthly chiller and pumping power consumption. The contribution of pumping power (excluding the tertiary pumps in each building) to the total GSHP system power consumption ranges from 8% to 18% at different months. On an annual basis, the pumping energy was 12.6% of the total power consumption of the district GSHP system at DESN.

Energy Efficiency

According to the HR chillers' catalog data, when it produces both 42°F (5.6°C) chilled water (from evaporator) and 125°F hot water (from condenser), they use 1.2 kW of power per each ton (3.5 kW) of cooling supplied, which is

equivalent to a cooling COP of 2.9. With this efficiency, for each ton of cooling produced, there are 1.34 tons (4.7 kW) of heating available. The HR chiller could operate very efficiently (i.e., with an effective COP as high as 6.83) if both the produced chilled and hot water were fully used to satisfy the cooling and heating demands of the campus. However, if the produced CHW and HW are not fully used, and the surplus heating or cooling energy is thus dumped to the ground (as discussed before), the ECOP of the HR chiller is lower than the COP of conventional chiller or heat pump. Figure 7 shows ECOP of the HR chiller vs. the ratio of the daily HW demand (the heating output to the HW loop) to the daily CHW demand (the cooling output to the CHW loop). Each data point in this figure is the average of ECOPs within a 0.2 bin of the HW/CHW ratio. As shown, the minimum average daily ECOP of the HR chiller was about 2.5 when the HW/CHW ratio is less than 0.2 (i.e., most of the heating energy is dumped into the ground), and the ECOP was around 5 when the HW/CHW ratio is near 1.3 (the ratio between the heating and cooling output of the HR chiller). The ECOP varied between 4 and 5 when the HW/CHW ratio is higher than 1.3, which means heating demand is much higher than the cooling demand. Based on measured annual cooling and heating outputs and the measured annual power consumption of the chiller, it is calculated that the annual average ECOP of the chiller was 4.28±0.2. Accounting for annual pumping power consumption, the annual average ECOP of the district GSHP system at DESN was 3.74±0.2. The ±0.2 uncertainty of ECOPs is calculated based on the accuracies of the sensors following the procedure described in ASHRAE Guideline 14-2014 – Measurement of Energy, Demand, and Water Savings (ASHRAE 2014).

The operational efficiency of the GSHP system could have been higher if the two chillers were operated separately—with one chiller always producing CHW, and the other operating as a heat pump to produce HW. Given the relatively balanced HW and CHW loads, these separate operations would reduce the ground loop temperature because (1) the (heat pump) chiller would produce only the needed HW necessary to satisfy the heating demand, eliminating dumping of 125°F (51.7°C) HW into the ground loop; and (2) heat extraction from and heat rejection to the ground would be more balanced since the (heat pump) chiller would extract more heat from the ground. To satisfy the same heating and cooling demands, the two separately operated chillers using the ground loop as both heat source and heat sink would consume 17,806 MWh electricity. Compared with the electricity consumption of the as-built/operated GSHP system (19,853 MWh), the separate operations will save 2,047 MWh electricity. However, the separate operations will result in an increase in ground loop pumping energy use since more heat is extracted from and rejected to the ground loop. The calculation result indicates that the ground loop pumping energy use will increase by 715 MWh, so the net savings in electricity is 1,331 MWh, which is of $106,557 value given the $0.08 per kWh electricity rate.

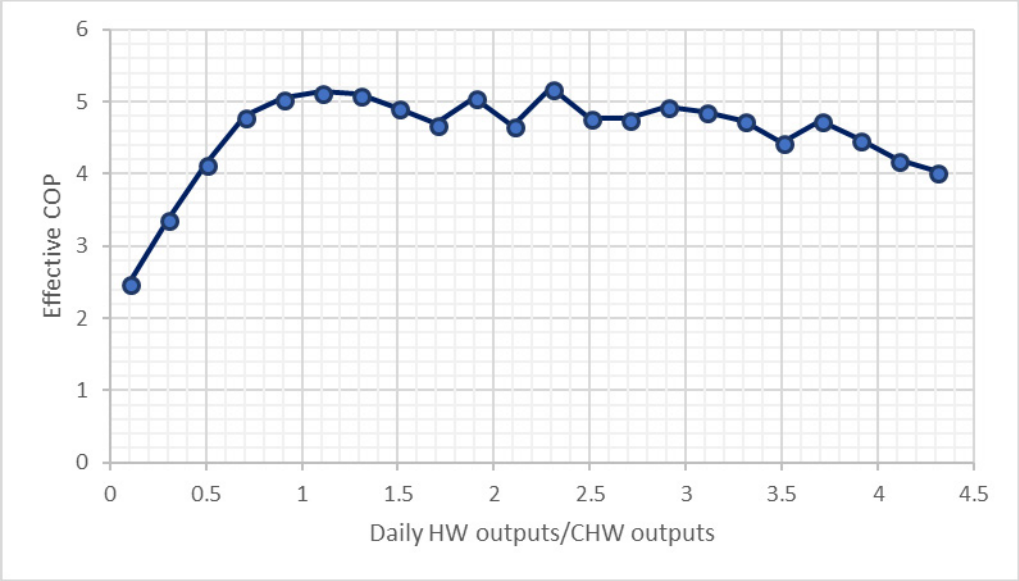

Figure 7: Average ECOP of the heat recovery chiller

Energy Savings

The energy savings achieved by the district GSHP system was determined by calculating the difference in measured energy consumptions between the GSHP system and the calculated energy consumption of a baseline HVAC system. The energy consumption of previous HVAC system in the campus was not sub-metered and thus can't be compared against. The baseline HVAC system includes a conventional water-cooled chiller and a natural gas boiler, which have the minimum energy efficiency as specified in ASHRAE Standard 90.1-2013 (ASHRAE 2013). The baseline chiller efficiency is 0.57 kW/ton (COP = 6.1), and the boiler efficiency is 80%. It was assumed that there are two 2,500-ton (8,750 kW) water-cooled centrifugal chillers, four 1,000-ton (3,500 kW) cooling towers, and three 20,000 kBtu/hr (5,860 kW) natural gas boilers. The baseline energy use was estimated using the measured cooling and heating outputs of the GSHP system, and a computer simulation of the centrifugal chillers and gas-fired boilers with DOE-2/eQUEST (Hirsch 2016). Our calculation shows that the baseline HVAC system would consume 10,970 MWh electricity (including power consumptions of circulation pumps and a cooling tower) and 212,806 MMBtu (224,531 GJ) natural gas, respectively, in a year to provide the same heating and cooling outputs as the GSHP system. The source energy factor for delivered electricity is 3.443, which is an average value for U.S. Eastern Interconnection according to Deru and Tocellini (2007). The same literature also provides the CO_2 emission factors for delivered electricity (i.e., 0.74 kg of pollutant per kWh of electricity) and natural gas (including 49.1 kg per GJ from on-site combustion and 4.6 kg per GJ from pre-combustion). These emission factors are used to calculate the CO_2 emissions. The annual source energy savings achieved by the GSHP system is about 96,281 MMBtu (101,586 GJ), or a 27% reduction from the baseline source energy consumption. The annual energy cost savings is calculated based on the difference in annual energy consumption for electricity and natural gas between the simulated baseline HVAC system and the measured data of the district GSHP system. Assuming $0.08/kWh for electricity and $7.6/GJ for natural gas, the calculated annual energy cost savings is $764,200 (a 30% savings compared with the baseline). In addition, the GSHP system has reduced CO_2 emission by about 8,494,540 lbs (3,853 ton) each year, which is a 19% reduction compared with the baseline system. More detailed information is presented in a technical report of this case study (Im et al. 2016).

CONCLUSIONS AND LESSONS LEARNED

- This case study indicates that the average system ECOP during the monitoring period was about 3.74, while the chiller ECOP is about 4.28. The monthly pumping power contribution to the total system power consumption ranges from 8% to 18%.
- Compared with a baseline HVAC system with code-compliant efficiencies, the GSHP system in each year could avoid 101,586 GJ (a 27% saving) source energy consumption, reduce 3,853 tons (a 19% reduction) carbon emissions, and save $764,200 (a 30% saving) energy cost.
- The operational efficiency of the GSHP system could have been higher if the two chillers were operated separately—one chiller dedicates on producing chilled water, and the other chiller operates as a heat pump to produce only hot water. In this case, there is no need to dump the energy of the chilled or hot water to the ground. In addition, it will help balance the ground loop loads since more heat will be extracted from the ground to satisfy the heating demand.

ACKNOWLEDGMENTS/DISCLAIMERS

This manuscript has been coauthored by UT-Battelle, LLC under Contract No. DE-AC05-00OR22725 with the U.S. Department of Energy. The United States Government retains and the publisher, by accepting the article for publication, acknowledges that the United States Government retains a non-exclusive, paid-up, irrevocable, world-wide license to publish or reproduce the published form of this manuscript, or allow others to do so, for United States Government purposes.

REFERENCES

ASHRAE Standard 90.1-2013, Energy Standard for Buildings Except Low-Rise Residential Buildings, ASHRAE standard.
ASHRAE Guideline 14-2014, Measurement of Energy, Demand, and Water Savings, ASHRAE standard.
Deru, M., and P. Tocellini. 2007. *Source Energy and Emission Factors for Energy Use in Buildings*, Technical Report, NREL/TP-550-38617, National Renewable Energy Laboratory, Golden, Colorado.
Hirsch J. (2016). *eQUEST program*. www.doe2.com
Hughes, P. 2008. "Geothermal (Ground-Source) Heat Pumps: Market Status, Barriers to Adoption, and Actions to Overcome Barriers." Rep. No. ORNL/TM-2008/232. Oak Ridge National Laboratory, Oak Ridge, TN.

IGSHPA SWEDEN 2018 Research Conference

DOI: 10.22488/okstate.18.000033

Simulated temperature evolution of large BTES – case study from Finland

Kimmo Korhonen **Nina Leppäharju** **Petri Hakala**
Teppo Arola

ABSTRACT

The largest borehole thermal energy storage system in Finland (also one of the largest systems in Europe) is located in Sipoo, Southern Finland. The system produces heating and cooling energy for a large logistics centre and consists of 157 vertical borehole heat exchangers that are grouped into 10 blocks. The temperature of the heat carrier fluid circulated in each block has been monitored since the operation was started. A numerical model of the system was created using the finite element software COMSOL Multiphysics® in order to simulate the temperature evolution of the system and the surrounding rock mass using the monitoring data as input. Simulation results indicate that the temperature within the rock mass embodying the system has decreased as the system is imbalanced but the decrease is moderate. The temperature disturbance created by the system was found to extend 50 metres from the borehole field. Based on the simulation the shallow geothermal reservoir will suffice for the designed lifetime of the system.

INTRODUCTION

In recent years Finland has been undergoing a similar increase in the number of large-scale ground-source heat pump (GSHP) systems and borehole thermal energy storage (BTES) systems as the neighbouring Sweden and Europe in general (e.g. Gehlin, et al. 2015; The European Heat Pump Association 2015). There is no national database storing information about the number of installed borehole heat exchangers (BHEs) in Finland but the statistics of The Finnish Heat Pump Association (2018) indicate growing sales numbers of large-scale GSHPs.

Designing a large-scale BTES or GSHP system requires detailed background information about the site and the desired energy loads. In these kinds of systems, the investments are likely to be massive so a good reliability of the system and significant annual savings on energy costs are naturally expected. In the design phase, the dimensioning of the BHE field is made based on the information available at that time. However, in many cases changes occur, for example, in energy loads during the utilization of a system. One may prepare for these changes by making the system versatile and adjustable and also by adding monitoring tools to the system. Monitoring of GSHP system operation can also play an important role in identifying and resolving problems at an early stage as stated by Sanner, et al. (2016). Taking these considerations into account, the reliability of large-scale BTES systems can be increased and thus these systems can be made more appealing to investors.

Monitoring data from GSHP systems in operation have been used for system performance analysis (e.g. Luo, et al. 2015) and for the assessment of design models (e.g. Naicker and Rees 2011; Cullin, et al. 2015). Data from a well-designed monitoring system also enables simulating the temperature response of the BHE field as well as forecasting the adequacy of the system in the upcoming years of operation. For example, Derouet, et al. (2015) used a method based on the finite line source theory to forecast the temperature decrease in a BHE field and to calculate the decrease in seasonal performance factor (SPF) in the upcoming 20 years. Lanini, et al. (2014) and Rapantova, et al. (2016) both used experimental data to calibrate a numerical BTES model. They used the models to optimize BTES operation and to formulate guidelines for BTES design. Tordrup, et al. (2016) used a numerical model validated with monitoring data to upscale a pilot-size BTES to full scale.

Kimmo Korhonen and Nina Leppäharju are Geophysicists, Petri Hakala is a Research Scientist and Teppo Arola is a Chief Expert at the Engineering Geology and Geoenergy Unit of the Geological Survey of Finland. E-mail addresses are in form firstname.lastname@gtk.fi.

Recently, new tools have been introduced for GSHP performance monitoring. Monzo, et al. (2016; 2017) presented a large-scale BTES installation with a carefully designed monitoring system and the first measurements from data collection sensors and distributed temperature sensing (DTS) optical fibre cables. DTS offers detailed information of the vertical variations of the thermal response of the ground. In large BHE fields, differences may also exist between the thermal performances of different parts of the field, for example, between the inner and outer BHEs, or due to varying geological properties of the site.

In this paper we present long-term monitoring data and simulated temperature response of one of the largest BTES systems in Europe. The BTES has been in operation since 2012 and the performance of the system has been monitored since the beginning. A numerical model was developed to simulate the temperature response of the BHE field and to evaluate the thermal performance of the system. This BTES system and the monitoring data starting from 2012 will be studied in more detail in further work. This kind of long-term monitoring of BTES operation is called for in order to further improve designing of large-scale systems and enable commercial development.

THE BOREHOLE THERMAL ENERGY STORAGE

Description of the BTES

The BTES system provides heating and cooling energy for a large logistics centre located in Sipoo, Southern Finland. The system has been in operation since 2012. The BTES is operated jointly with a pellet fuel bioenergy system forming a hybrid energy system. The heat pumps provide approximately 5,100 MWh of space heating energy and 1,200 MWh of cooling energy annually (according to the average values from 2012–2017). The SPF of the system in heating mode has been around 3.5 on average over the years based on the amount of heating energy produced and electrical energy input.

The BTES system consists of an array of vertical groundwater filled BHEs, which are installed nearly symmetrically on a rectangular grid (Figure 1). Most of the BHEs are located under the logistics centre building. The extent of the BHE field is 310 m by 270 m and the average distance between the boreholes is 25 m. The total number of BHEs is 157 and the average active depth is 280 m (ranging from 68 m to 303 m with a mode of 300 m). In 7 cases the nominal depth of 300 metres could not be reached while drilling and a secondary borehole was drilled close to the first one and the two boreholes were connected in series. The BHEs are grouped into 10 blocks (i.e. into 10 manifolds). The borehole diameter is 140 mm. The collectors are single U pipes (40 mm diameter) in 9 blocks and TurboCollector® pipes (40 mm diameter) in one block. All the BHEs were installed with collector spacers having a shank spacing of 75 mm.

In winter time in heating mode all the blocks are normally in use. In summer time each block can be recharged using energy from space cooling. In addition, solar energy is collected using horizontal heat exchanger pipes installed under part of the tarmac covering the loading bay for trucks. The collected solar energy can be fed to selected BHE blocks for recharging.

The geology of the site was mapped in detail in 2008 before the BTES was designed. Field observations and analyses of drill cuttings (from test boreholes) suggested 2 different sorts of igneous rock types, diorite and granitic gneiss, with a relatively ragged boundary (Figure 1).

Monitoring of the BTES

The performance of the BTES system has been monitored since the beginning of the operation in 2012. The temperature of the heat carrier fluid entering and exiting each block is measured with Ni1000 temperature sensors. The volumetric flow rates were measured for each BHE using an ultrasonic flow meter. The flow rates are not monitored continually. Instead, the flow rates are considered constant over time since the circulation pumps have been operating on non-stop since 2012.

The monitoring system also includes DTS measurements using optic fibre cables in selected BHEs and

additional monitoring boreholes interior to the BHE field. In total, 15 kilometres of optic cable has been installed into the BTES system. However, the DTS data will not be addressed in this paper but will be a subject for future studies.

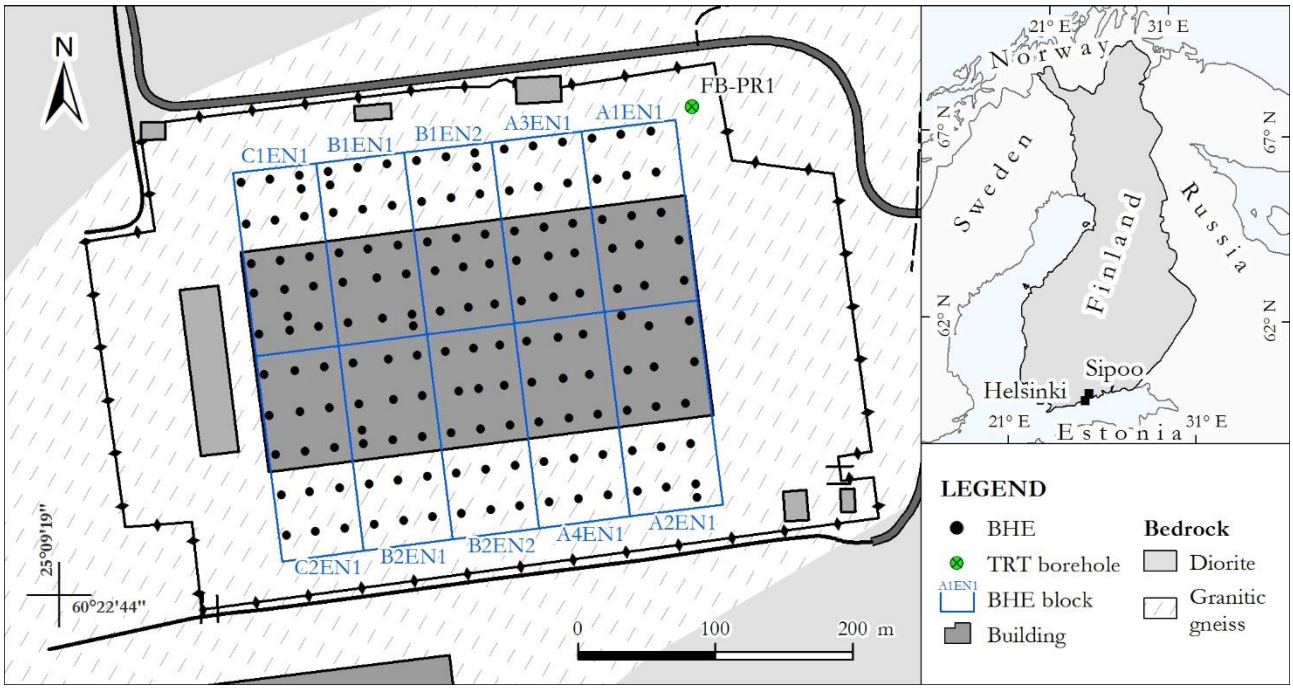

Figure 1. Plan view of the borehole thermal energy storage system located in Sipoo, Southern Finland. The extent of the borehole heat exchanger (BHE) field is 310 m x 270 m. It consists of 157 vertical BHEs, most of which are located under a logistics centre building. The BHEs are grouped into 10 blocks. For reference, the area of each block is approximately that of a standard football field. The BHE field is situated in granitic gneiss bedrock.

NUMERICAL BTES MODEL

A numerical model of the BTES was constructed using the finite element modelling software COMSOL Multiphysics® (version 5.3). The purpose of the model was to simulate the operation of the BTES in order to determine its temperature evolution and the extent of the temperature disturbance created by it.

Geometry and mesh

Modelling such a large BTES requires a large number of elements. In order to keep the number of elements at a manageable level for a desktop computer, three simplifications were made. The first simplification was to assume that all the boreholes were completely vertical and to round the lengths of the boreholes to the nearest 25 metres. This reduced the number of different borehole lengths from 42 to 8 (Figure 2a).

The second simplification was to solve the equations describing heat transfer inside the BHEs in two dimensions on the boundaries representing the walls of the boreholes. This allowed to exclude the detailed three dimensional internal structure of the BHEs from the model geometry and meshing which reduced the complexity of the model significantly. The boreholes were represented by cylinders which were carved out of the volume representing the bedrock using constructive solid geometry operations (Figure 2b).

The third simplification was to use sweep meshing (Figure 2b). The edges comprising the collars of the boreholes were first meshed with edge elements having the maximum length of 25 mm. Then the ground surface boundary was meshed using triangular elements. Finally, the mesh at the ground surface was swept down to the bottom of the model at intervals having the maximum length of 25 metres. The final mesh consisted of 1,397,126

elements, of which, 1,354,494 were prismatic (97 %).

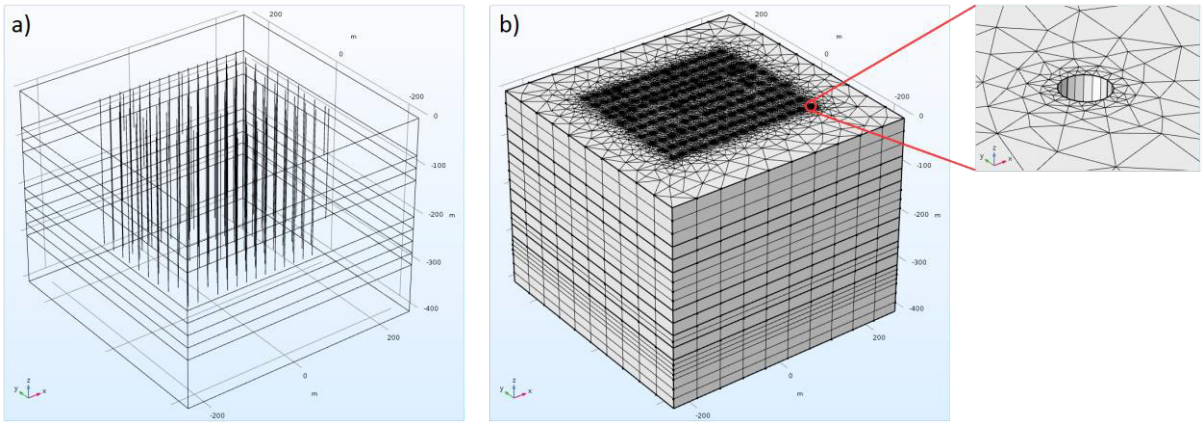

Figure 2. Geometry and meshing of the borehole thermal energy storage model. a) The model consists of 157 boreholes of 8 different lengths that are carved out of the three-dimensional volume representing the bedrock. b) The final three-dimensional mesh was generated by sweeping the two-dimensional ground surface mesh down to the bottom of the model.

Governing equations

The heat transfer inside a BHE can be described accurately enough using three coupled partial differential equations without resorting to the use of three dimensional elements. The equations describe the heat transfer in the downflow shank, in the upflow shank, in the grouting, and between the pipes and grouting. This solution was presented, for example, in Saeid, et al. (2013), Diersch, et al. (2011) and Al-Khoury, et al. (2010). However, they solved the equations in one dimensional line elements while we solved them in two dimensional quadrilateral boundary elements representing the borehole walls.

Heat transfer in the downflow shank (denoted by the subscript d) was described using the equation

$$\rho_f C_f \frac{\partial T_d}{\partial t} dV_p - k_f \nabla^2 T_d dV_p - \rho_f C_f u \frac{\partial T_d}{\partial z} dV_p = b_{fg}(T_g - T_d) dS_p, \quad (1)$$

in the upflow shank (denoted by the subscript u) using the equation

$$\rho_f C_f \frac{\partial T_u}{\partial t} dV_p - k_f \nabla^2 T_u dV_p + \rho_f C_f u \frac{\partial T_u}{\partial z} dV_p = b_{fg}(T_g - T_u) dS_p \quad (2)$$

and in the grouting (denoted by the subscript g) using the equation

$$\rho_g C_g \frac{\partial T_g}{\partial t} dV_g - k_g \nabla^2 T_g dV_g = b_{fg}(T_d - T_g) dS_p + b_{fg}(T_u - T_g) dS_p + b_{gr}(T_r - T_g) dS_g. \quad (3)$$

In these equations the subscript f refers to heat carrier fluid, g refers to grouting, and r refers to bedrock. Density is ρ, C is specific heat capacity (in constant pressure), k is thermal conductivity, T is temperature and t is time. Heat transfer between the heat carrier fluid and the grouting is characterized by the heat transfer coefficient b_{fg} and between the grouting and the surrounding bedrock by the heat transfer coefficient b_{gr}. Furthermore, the volume element dV_p represents the volume of a pipe element of height dz, dS_i represents the surface area of the same pipe element, dV_g represents the volume of a grouting element of height dz, and dS_g represents the surface area of the grouting element at the borehole wall. The equation governing heat transfer in the bedrock domain was

$$\rho_r C_r \frac{\partial T_r}{\partial t} + \nabla \cdot (-k_r \nabla T_r) = b_{gr}(T_g - T_r) \quad (4)$$

which was solved in three dimensions.

Equations (1)–(3) solve the flow of heat between the heat carrier fluid and the grout on two-dimensional boundary elements. The magnitude of heat flow between the pipes and the grout is determined based on the heat transfer coefficient b_{fg}. The grout acts as mediator of heat between the heat carrier fluid and the bedrock. Equations (3) and (4) (two-dimensional and three-dimensional elements) are coupled to each other through the heat transfer coefficient b_{gr} which determines the magnitude of heat flow between the grout and the bedrock.

Model parameters

The thermal properties of the heat carrier fluid were estimated using the polynomial interpolation equation of Melinder (2007). The thermal conductivity, specific heat capacity and density of a water-alcohol mixture with 28 weight-% ethanol at 15 °C with were estimated to be 0.418 W/m·K, 4239 J/kg·K and 960.1 kg/m^3 respectively. As the boreholes are groundwater-filled, the density and specific heat capacity of the grouting were estimated to be 999 kg/m^3 and 4185 J/kg·K respectively, based on Incropera, et al. (1990). To account for natural convection occurring in the borehole water, the thermal conductivity of the groundwater filling was set to the value of 1.8 W/m·K (3 times that of stagnant water). The density and specific heat capacity of the bedrock were set to the values of 2700 kg/m^3 and 890 J/kg·K respectively.

The heat transfer coefficients together with the bedrock thermal conductivity were estimated by fitting the model to TRT data (refer to Figure 1 for the location of the borehole in which the test was carried out). The heat transfer coefficients b_{fg} and b_{gr} were estimated to be 149.658 W/m^2·K and 39.800 W/m^2·K respectively, and the bedrock thermal conductivity was estimated to be 3.6 W/m·K.

Initial values and boundary conditions

The ground temperature distribution was measured in 2010 in one of the boreholes comprising the BTES using DTS. The measurements were carried out before the construction work of the logistics centre was begun, thus, giving the undisturbed ground temperature profile. The measured profile was smoothed and used as the initial temperature in the model.

The constant temperature boundary condition was applied to the ground surface boundary. The temperature at the ground surface was chosen to be 6.698 °C which was the measured initial temperature at the ground surface. The flux boundary condition was applied to the bottom boundary of the model. The flux was set equal to the geothermal heat flux of 43.912 mW/m^2 which was solved from the measured ground temperature profile assuming the thermal conductivity of the bedrock to be 3.6 W/m·K. The no-flux boundary condition was applied to all the vertical boundaries of the model which were taken far enough from the BTES so as not to be affected by the temperature disturbance created by it.

RESULTS

Simulation of the BTES operation was carried out by feeding the observed inlet temperature of a block to the inlets of each of the BHEs comprising that block. The BHEs in a block were connected in parallel except in seven cases in which two BHEs were connected in series. In these cases, the calculated outlet temperature of the first BHE was fed as the inlet temperature to the second BHE. The simulated outlet temperatures for each block were calculated as the average temperature of all the BHE outlet temperatures in that block.

The simulation time step was chosen to be 1 day to make the computational time reasonable (8 hours). The length of the simulation time period was 1937 days (5.3 years). The temperature records for each block were logged typically at the time intervals of 10, 20 and 60 minutes. However, the logging interval changes irregularly in each temperature record and may be even as small as few seconds or as large as one day. Thus, the irregular temperature

records needed to be made uniform using averaging. Moreover, smoothing using a 10-day moving window was used to average out the highly variable records in order to avoid numerical instabilities which would have otherwise arisen due to large time step and element size. The time step and mesh size were chosen based on a convergence analysis. Finer space and time discretization would have only a minimal effect on the result.

Figure 3 shows the observed inlet and outlet fluid temperatures together with the simulated outlet temperatures and the differences between the observed and simulated outlet temperatures (residuals) for each borehole block. The difference between the observed and simulated temperatures is virtually zero in blocks B1EN2 and B2EN2. In other blocks the simulated outlet temperatures trace the observed temperatures with a margin of few tenths of kelvins. However, in blocks A2EN1 and B2EN2 the misfit during the first year of the simulation is significantly larger (the residuals reach even 1.5 K). Similarly, in block B1EN1 the misfit is significantly larger but during the second year of simulation.

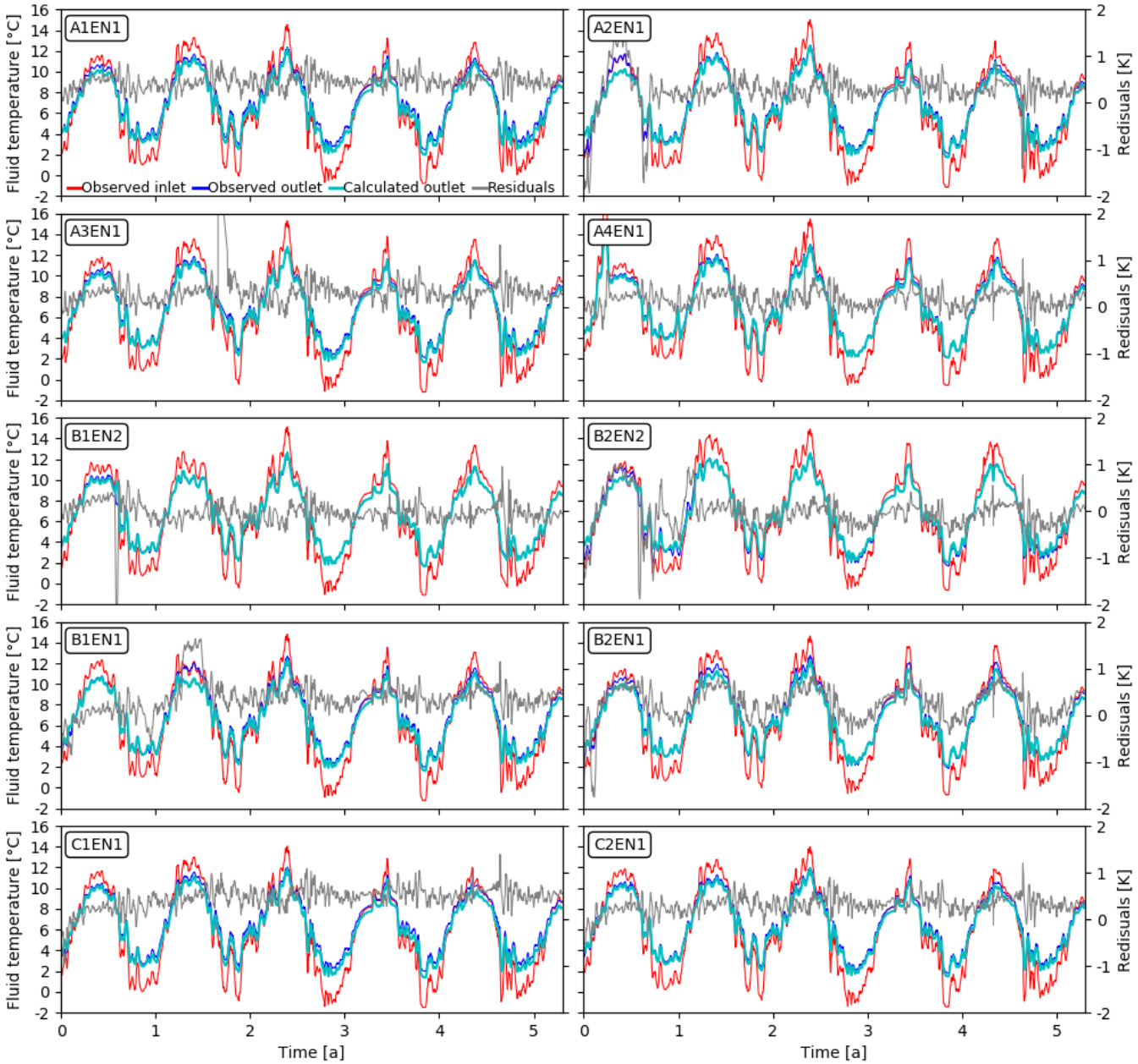

Figure 3. Observed and simulated temperatures, and residuals (the difference between observed and simulated outlet temperature) for each borehole heat exchanger block.

Table 1 lists the observed and simulated total energy amounts utilized each year and the relative error. The total energy amounts were calculated as the sums of injected and extracted energy for each year. The years 2012 and 2017 are not fully covered by data (they lack 3 and 6 months of data respectively). There is a large relative error in the simulated energy amount for the year 2012 but otherwise the relative errors are not larger than 5 %.

Table 1. Total energy loads extracted from the BTES.

Year	Observed load [MWh]	Simulated load [MWh]	Relative error [%]
2012	2649	3191	20.5
2013	4686	4755	1.5
2014	4519	4391	2.8
2015	4212	4119	2.2
2016	4730	4798	1.4
2017	2360	2243	5.0

Figure 4 shows the horizontal and vertical temperature disturbances created by the BTES on horizontal and vertical planes cutting through it. The disturbance was calculated by first averaging the temperature over the last year of the simulation and then subtracting the undisturbed temperature from the calculated average. The extent of the horizontal and vertical temperature disturbances appear to be 50 metres judging by the −1 mK isotherms (which was considered as negligible disturbance) shown in Figure 4.

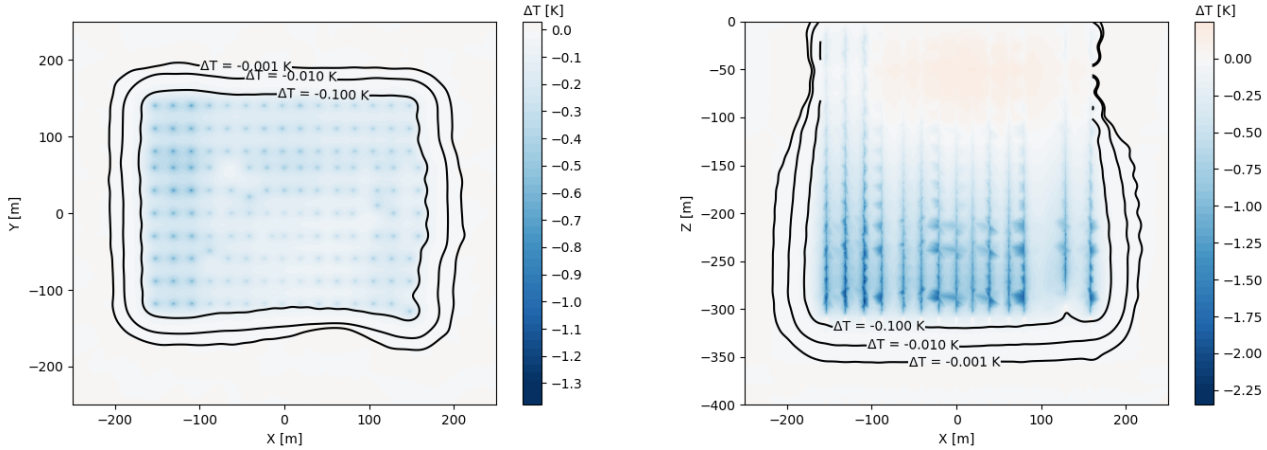

Figure 4. Spatial extent of the simulated temperature disturbance created by the BTES. The left panel shows the horizontal extent on the XY plane at the depth of 150 metres. The right panel shows the vertical extent on the XZ plane throught the center of the BTES.

DISCUSSION AND CONCLUSIONS

The simulated outlet temperatures agree quite well with the observed outlet temperatures as is shown by Figure 3. In some cases the fit is not excellent (the residuals reach 0.5 K) but for the objective of this study the accuracy is considered sufficient. In the case of blocks A2EN1, B1EN1 and B2EN2 the simulated outlet temperatures do not appear to fit the observed temperatures well during specific periods of time (the first or second year of the simulation). This is most likely due to errors in the outlet temperature sensors as the temperature difference between the inlet and outlet is virtually or close to zero during those periods even though the blocks have been in full use. Inaccuracies in the monitoring data were detected already before this study and improvements are planned in order to increase the usability of the monitoring data. The simulation results further highlight the need for improvements.

However, for this study the quality of the data was considered to be sufficient.

The observed and simulated total energy amounts extracted from the BTES also appear to agree well as is shown by Table 1. The large relative error of 2012 is likely due to the identified sensor problems as well as adjustments made in the operation of the system (for example in fluid flow rates).

The temperature disturbance created by the BTES has not advanced far even though the BHE field is large and the amount of thermal energy extracted from the system has been larger than the amount of injected thermal energy. The advancing negative temperature disturbance illustrated by the isotherms in Figure 4 is due to this unbalance in the energy loads. There is also a slight downwards trend in the observed inlet and outlet temperatures seen in Figure 3 which could be removed if the BTES was recharged more. The unbalance in the loads was, however, acknowledged and taken into account in the design phase of the system. Within the first 5 years of operation the temperature decrease appears to be about 2 K. The BTES was designed for a 25-year lifetime and as the steepest decrease in temperatures is expected during the first years of operation the results indicate that with these load levels the heat reservoir will not be depleted. However, balancing the energy loads would improve the performance of the system.

As a next step, we aim to improve the fit between the observed and simulated temperatures. To achieve this, we will fit each block individual model parameters and carry out simulations using a finer mesh and a smaller time step. As the BTES is equipped with a DTS monitoring system, the DTS data will also be used in order to further validate the model and investigate the temperature evolution of the BTES in more detail. In future we also intend to investigate the thermal performance of each BHE block individually.

ACKNOWLEDGMENTS

We thank S Group and Adven for their support regarding our reseach and for the permission to use the monitoring data. We also thank our colleagues Ilkka Martinkauppi and Isa Witick whose help was vital for the completion of this paper.

NOMENCLATURE

ρ	=	density (kg/m^3)
C	=	specific heat capacity (J/kg·K)
k	=	thermal conductivity (W/m·K)
T	=	temperature (K)
t	=	time (s)
b	=	heat transfer coefficient (W/m^2·K)
$\mathrm{d}V$	=	infinitesimal volume (m^3)
$\mathrm{d}S$	=	infinitesimal surface area (m^2)
$\mathrm{d}z$	=	infinitesimal height (m)

Subscripts

d	=	downflow shank of a U pipe
u	=	upflow shank of a U pipe
g	=	grouting of a borehole heat exchanger
f	=	heat carrier fluid
r	=	bedrock

REFERENCES

Al-Khoury, R., Kolbel, T. and Schramedei, R. 2010. *Efficient numerical modeling of borehole heat exchangers*. Computers & Geosciences, 36, pp. 1301–1315.

Cullin, J.R., Spitler, J.D., Montagud, C., Ruiz-Calvo, F., Rees, S.J., Naicker, S.S., Konečný, P. and Southard, L.E. 2015. *Validation of vertical ground heat exchanger design methodologies*. Science and Technology for the Built Environment, 21, 137–149.

Derouet, M., Monzó, P. and Acuña, J. 2015. *Monitoring and Forecasting the Thermal Response of an Existing Borehole Field*. World Geothermal Congress 2015. Melbourne, Australia. April 19-25. Available online at: https://www.kth.se/polopoly_fs/1.571163!/published%20paper.pdf

Diersch, H.-J.G., Bauer, D., Heidemann, W., Ruhaak, W. and Schatzl, P. 2011. *Finite element modeling of borehole heat exchanger systems. Part 1. Fundamentals.* Computers & Geosciences, 37, pp. 1122–1135.

European Heat Pump Association. 2015. *European Heat Pump Market and Statistics Report 2015. Executive Summary.* Available online at: http://www.ehpa.org/fileadmin/red/07._Market_Data/2014/EHPA_European_Heat_Pump_Market_and_ Statistics_Report_2015_-_executive_Summary.pdf

Gehlin, S., Andersson, O., Alm, P-G. and Rosberg, J-E. 2015. *Country Update for Sweden*. World Geothermal Congress 2015. Melbourne, Australia. April 19-25. Available online at: https://pangea.stanford.edu/ERE/db/WGC/papers/WGC/2015/01021.pdf

Incropera, F. P. and de Witt, D. P. 1990. Fundamentals of Heat and Mass Transfer. 3rd edition, Wiley, New York, 919 p.

Lanini, S., Delaleux, F., Py, X., Olivès, R. and Nguyen, D. 2014. *Improvement of borehole thermal energy storage design based on experimental and modelling results*. Energy and Buildings, 77, pp. 393−400.

Luo, J., Rohn, J., Bayer, M., Priess, A., Wilkmann, L. and Xiang, W. 2015. *Heating and cooling performance analysis of a ground source heat pump system in Southern Germany.* Geothermics 53, 57–66.

Melinder, Å. 2007. *Thermophysical Properties of Aqueous Solutions Used as Secondary Working Fluids.* Doctoral thesis, Royal Institute of Technology, Stockholm, Sweden, 130 p.

Monzó, P., Lazzarotto, A., Acuña, J., Tjernström, J. and Nygren, M. 2016. *Monitoring of a borehole thermal energy storage in Sweden*. 12th REHVA World Congress – Clima 2016. Aalborg, Denmark. May 22-25. Available online at: http://kth.diva-portal.org/smash/get/diva2:932875/FULLTEXT01.pdf

Monzó, P., Lazzarotto, A. and Acuña, J. 2017. *First Measurements of a monitoring BTES system*. IGSHPA Technical/Research Conference and Expo 2017. Denver, USA. March 14-16.

Naicker, S.S. and Rees, S.J. 2011. *Monitoring and Performance Analysis of a Large Non-domestic Ground Source Heat Pump Installation*. CIBSE Technical Symposium 2011. Leicester, UK. Sept 6-7.

Rapantova, N., Pospisil, P., Koziorek, J., Vojcinak, P., Grycz, D. and Rozehnal, Z. 2016. Optimisation of experimental operation of borehole thermal energy storage. Applied Energy, 181, pp. 464−476.

Saeid, S., Al-Khoury, R. and Barends, F. 2013. *An efficient computational model for deep low-enthalpy geothermal systems.* Computers & Geosciences, 51, pp. 400–409.

Sanner, B., Bockelmann, F., Kühl, L. and Mands, E. 2016. *System optimisation of ground-coupled heat and-cold supply of office buildings*. European Geothermal Congress 2016. Strasbourg, France. Sept 19-24.

The Finnish Heat Pump Association. 2018. *Heat Pump Investments up to Half a Billion a Year in Finland.* Press release 1/2018. Available online at: https://www.sulpu.fi/documents/184029/0/Press%20Realaese%20-%20Heat%20Pump%20Investments%20up%20to%20a%20Half%20Billion%20a%20Year%20in%20Finland%2C%202.pdf

Tordrup, K.W., Poulsen, S.E. and Bjørn, H. 2016. An improved method for upscaling borehole thermal energy storage using inverse finite element modelling. Renewable Energy, 105, pp. 13−21.

[This page has been intentionally left blank]

Index

A

B

C

D

E

F

G

H

I

J

K

L

M

N

O

P

Q

R

S

T

U

V

W

X

Y

Z

IGSHPA SWEDEN
2018 Research Conference